

This material is a declared work of the U.S. Government and is not subject to copyright protection in the United States. Approved for public release; distribution unlimited. Any opinions expressed in this material are those of the author and do not represent the opinions of the U.S. Government

Report Documentation Page				Form Approved OMB No. 0704-0188	
Public reporting burden for the collection of information is estimated to average 1 hour per response, including the time for reviewing instructions, searching existing data sources, gathering and maintaining the data needed, and completing and reviewing the collection of information. Send comments regarding this burden estimate or any other aspect of this collection of information, including suggestions for reducing this burden, to Washington Headquarters Services, Directorate for Information Operations and Reports, 1215 Jefferson Davis Highway, Suite 1204, Arlington VA 22202-4302. Respondents should be aware that notwithstanding any other provision of law, no person shall be subject to a penalty for failing to comply with a collection of information if it does not display a currently valid OMB control number.					
1. REPORT DATE 01 OCT 2007		2. REPORT TYPE N/A		3. DATES COVERED -	
4. TITLE AND SUBTITLE An Experimental Investigation Into The Effect Of Plasma On The Flow Features Of An Axisymmetric Jet				5a. CONTRACT NUMBER	
				5b. GRANT NUMBER	
				5c. PROGRAM ELEMENT NUMBER	
6. AUTHOR(S)				5d. PROJECT NUMBER	
				5e. TASK NUMBER	
				5f. WORK UNIT NUMBER	
7. PERFORMING ORGANIZATION NAME(S) AND ADDRESS(ES) University of Illinois at Urbana-Champaign				8. PERFORMING ORGANIZATION REPORT NUMBER	
9. SPONSORING/MONITORING AGENCY NAME(S) AND ADDRESS(ES) AFIT/ENEL WPAFB, OH 45433				10. SPONSOR/MONITOR'S ACRONYM(S)	
				11. SPONSOR/MONITOR'S REPORT NUMBER(S)	
12. DISTRIBUTION/AVAILABILITY STATEMENT Approved for public release, distribution unlimited					
13. SUPPLEMENTARY NOTES The original document contains color images.					
14. ABSTRACT					
15. SUBJECT TERMS					
16. SECURITY CLASSIFICATION OF:			17. LIMITATION OF ABSTRACT UU	18. NUMBER OF PAGES 386	19a. NAME OF RESPONSIBLE PERSON
a. REPORT unclassified	b. ABSTRACT unclassified	c. THIS PAGE unclassified			

AN EXPERIMENTAL INVESTIGATION INTO THE EFFECT OF PLASMA ON THE
FLOW FEATURES OF AN AXISYMMETRIC JET

BY

RICHARD E. HUFFMAN

B.S., Purdue University, 1994

M.S., Air Force Institute of Technology, 1995

DISSERTATION

Submitted in partial fulfillment of the requirements
for the degree of Doctor of Philosophy in Aerospace Engineering
in the Graduate College of the
University of Illinois at Urbana-Champaign, 2007

Urbana, Illinois

Abstract

The main goal of the research presented was to determine the differences between a plasma field and neutral field flow structure (both mean and turbulent effects) for varying Mach number. The overall objective was to describe the effect of radio frequency capacitively coupled plasma on the flow features of compressible axisymmetric jets in Nitrogen. Three flows were investigated: perfectly expanded jets, highly underexpanded jets, and jets created by a constant-diameter nozzle which produced developing pipe flow. High subsonic to supersonic pressure ratios were investigated to determine the influence of compressibility.

Particle image velocimetry was used to quantify the mean and turbulent fluctuations of velocity in the jet flow field. The tracking of seed particles in rarefied and compressible jets was characterized by comparison with particle models and from mean velocities obtained by molecular tagging velocimetry. Periodic, large scale structures were forced into the jet field and convective velocities were measured by tracking the structures. The plasma fields were measured to characterize the visible light emitted and rotational and vibrational temperatures were obtained by model matching to spectra recorded of the second positive system of diatomic Nitrogen.

The plasma did influence the mean and turbulent velocity profiles of the jets tested - allowing the jet core to penetrate further downstream. Large scale structure tracking indicated an increase in convective velocity of up to 5%. Heating of the shear layer by the plasma field was believed to bias the convective velocity towards the jet core by increasing the speed of sound in the shear layer. Rotational temperatures taken by model matching of spectroscopy data indicated shear layer heating which supports an equivalent increase in convective velocity as was measured in large scale structure tracking. In perfectly expanded jets, turbulent kinetic energy decreased along the jet centerline by 7% to 14% and were not influenced by compressibility which is consistent with increased jet penetration. However, in pipe-flow jets the centerline turbulent kinetic energy decreased at low equivalent Mach numbers, reversing to slight increases for equivalent Mach numbers over 1.4.

To my Lord, Jesus Christ - may this be to your glory. I am incredibly blessed by God to have the opportunity to research in such an exciting field. I wish to thank my wonderful wife Amy for being so supportive and forgiving to the many demands on my time - I love you honey! I also want to thank my children: Melissa, Joshua and Matthew for their cheerful hearts and understanding - it is truly a blessing to be in this adventure as a family.

Acknowledgments

There are so many people who provided time and effort to make this research a success, I apologize in advance if I leave someone out here. First, I want to thank my parents, you raised me with what I can only imagine was patience from above. Thank you for being there for me, I love you. My advisor, Prof Greg Elliott was really instrumental in guiding me and encouraging me through this endeavor. My wife and I chose this school after chatting with you and learning of a thing called ‘Papa Dels.’ Not that it was all about pizza mind you, it is difficult to find an advisor willing to work with a military student and the constraints put on us and we are truly grateful that God directed us to you. Next I want to thank Dr Martin Boguszko, my ‘Obe-wan’ in Raleigh scattering and molecular filtering, and my office mate Taylor Swanson, it was refreshing and encouraging to share an office with you.

I also want to thank the Department of Aerospace Engineering, your facilities and attitude were awesome - thank you! When it came to building parts for this research, I want to specifically thank Bob Coverdill in Mechanical Science and Engineering, you are truly a go-to man when it is fourth and long with time running out. I also want to thank Prof Yuanhui Zhang and Jong Min Lee who let me borrow their aerodynamic particle sizer and helped me collect the data from it. Finally, I would like to acknowledge the support of AFOSR (FA9550-04-1-0425) with contract monitor Dr. John Schmisser for support of this research. Any opinions, findings and conclusions or recommendations expressed in the material are those of the authors and do not necessarily reflect the views of AFOSR.

Table of Contents

List of Tables	ix
List of Figures	xi
List of Abbreviations	xviii
List of Symbols	xx
Chapter 1 Background	1
1.1 Axisymmetric Jet	2
1.1.1 Nominal Jets	2
1.1.2 Off-Nominal Jets	6
1.1.3 Free Shear Layers	10
1.2 Plasma	16
1.2.1 Thermal Equilibrium	17
1.2.2 Quasi-Neutrality	19
1.2.3 Electrostatically Ideal Plasma	19
1.2.4 Treanor Effect	20
1.2.5 Breakdown Mechanisms	21
1.2.6 Plasma Instabilities	23
1.2.7 Nonequilibrium Plasma Chemistry	23
1.3 Plasma Discharges	24
1.3.1 Glow	24
1.3.2 Arc	26
1.3.3 Corona	27
1.3.4 Dielectric Barrier	28
1.3.5 Radio Frequency	28
1.4 Plasma Flow Control	29
1.5 Plasma Effects on Turbulence	30
Chapter 2 Test Apparati	33
2.1 High Pressure Air	33
2.2 Vacuum System	34
2.3 Test Section	35
2.4 Nozzle Design	36
2.5 Flow Seeding	40
2.6 Plasma Generation	42
2.7 Electrode Design	45

Chapter 3	Test Techniques	48
3.1	Measurement Uncertainty and Error Propagation	48
3.2	Particle Image Velocimetry (PIV)	50
3.2.1	Experiment Setup	52
3.2.2	Test Procedures	54
3.2.3	Uncertainty Estimates	58
3.3	Molecular Tagging Velocimetry (MTV)	63
3.3.1	Experiment Setup	64
3.3.2	Test Procedures	66
3.3.3	Uncertainty Estimates	71
3.4	Laser Energy Deposition	72
3.4.1	Experiment Setup	72
3.4.2	Test Procedures	73
3.4.3	Uncertainty Estimates	75
3.5	Plasma Imagery of Visible Light Emission	76
3.5.1	Experiment Setup	76
3.5.2	Test Procedures	77
3.5.3	Uncertainty Estimates	79
3.6	Temperature Measurement with Spectroscopy of the Second Positive System of Diatomic Nitrogen	80
3.6.1	Experiment Setup	81
3.6.2	Test Procedures	81
3.6.3	Uncertainty Estimates	86
Chapter 4	Results and Discussion	87
4.1	Characterization of Particle Tracking	90
4.1.1	Particle Image Velocimetry Verification by Means of Molecular Tagging Velocimetry	91
4.1.2	Modeling Approach to Accuracy Estimation for Turbulence Measurements	101
4.2	Velocity and Turbulent Kinetic Energy Profiles from Particle Image Velocimetry	109
4.2.1	Mean and Turbulent Characteristics of Axisymmetric Jets	111
4.2.2	Mach 1.4, 5 Torr Converging-Diverging Axisymmetric Jet	119
4.2.3	The Effect of Plasma for Increasing Pressure Ratios in Perfectly Expanded Axisymmetric Jets	126
4.2.4	Mean and Turbulent Characteristics of Constant-Diameter Axisymmetric Jets	134
4.2.5	The Effect of Plasma for Increasing Pressure Ratios in Jets Formed out of Developing Pipe Flows	143
4.2.6	Mach 1.9 (Overexpanded), 8 Torr Converging-Diverging Axisymmetric Jet	149
4.2.7	Influence of Anode Design on Mean Flow and Turbulence	152
4.2.8	Summary of Important Findings from Particle Image Velocimetry Measurements	155
4.3	Large Scale Structure Tracking by Means of Laser Energy Deposition	161
4.4	Plasma Imagery of Visible Light Emission	168
4.4.1	Effect of Compressibility on Plasma Fields for Perfectly Expanded Jets	168
4.4.2	Effect of Anode Design on Visible Light Emissions from the Plasma Field	174
4.4.3	Effect of Compressibility on Plasma Fields for Developing Pipe Flow Jets	177
4.4.4	Comparison of Visible Light Emitted Between Plasmas at 8 Torr and 5 Torr	181
4.4.5	Visible Light Emissions from a Highly Underexpanded Jet at 8 Torr	182
4.4.6	Summary of Important Findings from Visible Light Emission Imagery	186
4.5	Temperature Measurement with Spectroscopy of the Second Positive System of Diatomic Nitrogen	187
4.5.1	Spectroscopy of the Highly Underexpanded Jet at 8 Torr	189
4.5.2	Effect of Compressibility on Plasma Field Temperatures for Perfectly Expanded Jets	192
4.5.3	Effect of Anode Design on Plasma Field Temperatures	193
4.5.4	Effect of Compressibility on Plasma Field Temperatures for Developing Pipe Flow Jets	194
4.5.5	Summary of Important Findings from Temperature Measurement by Spectroscopy	195

Chapter 5	Conclusions	197
5.1	Test Objectives	197
5.2	Findings	199
5.3	Recommendations	202
Appendix A	Archival of Particle Image Velocimetry Statistical Data	204
A.1	Mach 0.6 Converging-Diverging Nozzle at 9 Torr	206
A.2	Mach 1.1 Converging-Diverging Nozzle at 9 Torr	218
A.3	Mach 2.0 Converging-Diverging Nozzle at 8 Torr	230
A.4	Overexpanded Converging-Diverging Nozzle at 8 Torr	242
A.5	Mach 1.4 Converging-Diverging Nozzle at 5 Torr Using Anode with Serrated Conical Feature	254
A.6	Flow from a Tube Driven at a Mach 0.9 Pressure Ratio at 5 Torr Using Anode with Serrated Conical Feature	272
A.7	Flow from a Tube Driven at a Mach 1.4 Pressure Ratio at 5 Torr Using Anode with Serrated Conical Feature	290
A.8	Flow from a Tube Driven at a Mach 1.9 Pressure Ratio at 5 Torr Using Anode with Serrated Conical Feature	308
A.9	Mach 1.1 Converging-Diverging Nozzle at 9 Torr Using Anode with Serrated Conical Feature	326
Appendix B	Archival of Spectroscopy Based Temperature Measurements	338
Bibliography		343
Curriculum Vitae		364

List of Tables

1.1	Unique Plasma Properties	17
1.2	Room Temperature Air Plasma Properties, Adapted from Fridman[145]	20
2.1	Nozzle Contour Parameters	39
2.2	Condensation Monodisperse Aerosol Generator Settings [25]	41
2.3	Relative Inductance of the Manual Coil	43
3.1	Description of Optical Components in Figure 3.2, the Schematic of Particle Image Velocimetry	52
3.2	Scaling of Measurement Uncertainties in Particle Image Velocimetry	59
3.3	Conditions Chosen to Represent Test Conditions for the Analysis of Uncertainty Propagation in Particle Image Velocimetry	60
3.4	Propagation of Measurement Uncertainties in Calculations Performed on Particle Image Velocimetry Data	62
3.5	Description of Optical Components in Figure 3.5, the Schematic of Molecular Tagging Velocimetry	64
3.6	Conditions Chosen to Represent Test Conditions for the Analysis of Uncertainty Propagation in Molecular Tagging Velocimetry	71
3.7	Description of Optical Components in Figure 3.11, the Schematic of Laser Energy Deposition	73
3.8	Propagation of Measurement Uncertainties for the Plasma Imagery of Visible Light Emission	79
3.9	Description of Optical Components in Figure 3.15, the Schematic of Imaging Spectroscopy . .	81
3.10	Emission Lines of Iron Used to Perform Spectral Calibration, Taken from NIST [313]	82
4.1	Estimation of Jet Exit Conditions	89
4.2	Estimated Properties of Saturated Acetone Vapor in Nitrogen Gas	91
4.3	Exit Velocities for Two Supersonic Converging-Diverging Jets to Confirm the Assumed Ratio of Specific Heats	92
4.4	Test Conditions Examined with Molecular Tagging Velocimetry and Particle Image Velocimetry Using Nitrogen Saturated with Acetone	93
4.5	Comparison of Maximum Axial Velocity Measurements for Varying Particle Size and Varying Pressure Ratios	97
4.6	Configuration for the Highly Underexpanded Jet Created by a Sonic Orifice	98
4.7	Estimation of Particle Tracking of Turbulent Velocities	104
4.8	Estimation of the Uncertainty in Particle Tracking of Shear Layer Thickness	107
4.9	Estimation of Jet Exit Conditions for the Mach 1.4, 5 Torr Converging-Diverging Axisymmetric Jet	111
4.10	Estimation of Jet Exit Conditions for the 8-9 Torr Converging-Diverging Axisymmetric Jets .	127
4.11	Estimation of Jet Exit Conditions for the Mach 1.4, 5 Torr Converging-Diverging and Constant-Diameter Axisymmetric Jet	141
4.12	Estimation of Jet Exit Conditions for the 8-9 Torr Converging-Diverging Axisymmetric Jets .	143
4.13	Estimation of Jet Exit Conditions for the Mach 1.9, 8 Torr Converging-Diverging Axisymmetric Jet	151

4.14	Estimation of Jet Exit Conditions for the Mach 1.1, 9 Torr Converging-Diverging Axisymmetric Jet	154
4.15	Effect of Increasing Mach Number on Converging-Diverging Nozzles	156
4.16	Comparison Between Perfectly-Expanded and Overexpanded Jets	159
4.17	Comparison Between Flat Anode and Anode with Serrated Conical Tip Feature	160
4.18	Summary of Large Scale Structure Tracking Analysis	166
4.19	Plasma and Jet Configuration for the Series of Converging-Diverging Nozzles with Flat Anodes at a Chamber Pressure of 8-9 Torr	168
4.20	Plasma and Jet Configuration Comparing Anode Design for the Mach 1.1 Converging-Diverging Nozzle at a Chamber Pressure of 9 Torr	174
4.21	Plasma and Jet Configuration for the Series of Constant-Diameter Nozzles for an Anode with Serrated Conical Feature at a Chamber Pressure of 5 Torr	177
4.22	Comparison of Plasma and Jet Configuration for Increasing Chamber Pressure	182
4.23	Plasma and Jet Configuration for the Highly Underexpanded Jet Created by a Sonic Orifice with a Flat Anode	184
4.24	Rotational and Vibrational Temperatures Taken by Line Spectroscopy of the Highly Underexpanded Jet at 8 Torr	190
A.1	Test Conditions Reference	205
B.1	Rotational and Vibrational Temperatures Taken by Line Spectroscopy of the Mach 0.7 Jet at 9 Torr (Case A)	338
B.2	Rotational and Vibrational Temperatures Taken by Line Spectroscopy of the Mach 1.1 Jet at 9 Torr (Case B)	339
B.3	Rotational and Vibrational Temperatures Taken by Line Spectroscopy of the Mach 1.1 Jet at 9 Torr with Modified Anode (Case B')	339
B.4	Rotational and Vibrational Temperatures Taken by Line Spectroscopy of the Mach 2.0 Jet at 8 Torr (Case C)	339
B.5	Rotational and Vibrational Temperatures Taken by Line Spectroscopy of the Overexpanded Jet at 8 Torr (Case D)	339
B.6	Rotational and Vibrational Temperatures Taken by Line Spectroscopy of the Mach 1.4 Jet at 5 Torr (Case E)	340
B.7	Rotational and Vibrational Temperatures Taken by Line Spectroscopy of the Effective Mach 0.9 Jet at 5 Torr (Case F)	340
B.8	Rotational and Vibrational Temperatures Taken by Line Spectroscopy of the Effective Mach 1.4 Jet at 5 Torr (Case G)	340
B.9	Rotational and Vibrational Temperatures Taken by Line Spectroscopy of the Effective Mach 1.9 Jet at 5 Torr (Case H)	340
B.10	Rotational and Vibrational Temperatures Taken by Line Spectroscopy of the Highly Underexpanded Jet at 8 Torr (Case U)	341
B.11	Rotational and Vibrational Temperatures Taken by Line Spectroscopy of the Effective Mach 0.9 Jet at 5 Torr, with Decreased Gap Distance of 76.5 mm	341
B.12	Rotational and Vibrational Temperatures Taken by Line Spectroscopy of the Effective Mach 1.4 Jet at 5 Torr, with Decreased Gap Distance of 76.5 mm	341
B.13	Rotational and Vibrational Temperatures Taken by Line Spectroscopy of the Effective Mach 1.9 Jet at 5 Torr, with Decreased Gap Distance of 76.5 mm	342
B.14	Rotational and Vibrational Temperatures Taken by Line Spectroscopy of the Mach 2.0 Jet at 10 Torr	342
B.15	Rotational and Vibrational Temperatures Taken by Line Spectroscopy of the α -Discharge No-Flow Plasma Field	342

List of Figures

1.1	Flow Exiting From a Plenum into the Test Chamber Through a Nozzle	3
1.2	Cut-away View of an Axisymmetric Converging-Diverging Nozzle	4
1.3	Schematics of Nominal and Off-Nominal Jets in Air	7
1.4	Schematic of the Shock Structure of a Highly Underexpanded Jet Exiting from a Sonic Orifice	9
1.5	Mean Velocity Profile of an Axisymmetric Jet	10
1.6	Streamlines Between a Vortex Pair in the Convective Reference, Adapted from Coles[93]	11
1.7	Turbulent Regions of the Axisymmetric Jet	12
1.8	Schematic of Dominant Jet Instability Modes	14
1.9	Energy Distribution of Excitation for Air, Adapted from Fridman.[145]	24
1.10	Glow Discharge Regions, Adapted from Fridman.[145]	25
1.11	Glow Discharge Created During Testing	26
1.12	Arc Discharge Created During Testing	27
2.1	High Pressure Plumbing Diagram	33
2.2	High Pressure Air Delivery System	34
2.3	Vacuum Pump System	35
2.4	Test Section	36
2.5	Cross-Sectional View of the Nozzle Assembly	37
2.6	Nozzle Contours	40
2.7	Particle Size Distributions Measured with the Aerodynamic Particle Sizer, APS-3321 from TSi	41
2.8	Plasma Generation Components	42
2.9	Cross-Sectional View of Anode and Cathode Installed in Test Section	45
2.10	Cross-Sectional view of Semi-Torus Cathode	46
2.11	A View of Each Anode, Showing the Flat Anode and the Anode Modified with Serrated Conical Feature	47
3.1	Particle Image Velocimetry Description, From LaVision[388]	50
3.2	Schematic of Particle Image Velocimetry	52
3.3	Location of PIV Measurement Stations for Statistical Analysis	56
3.4	A Schematic of MTV Response at Increasing Time Steps	63
3.5	Schematic of Molecular Tagging Velocimetry	65
3.6	Relative Intensity of the Fluorescence/Phosphorescence of Acetone Vapor in Nitrogen at 5 Torr After Being Tagged by a UV Laser Beam at 266nm	67
3.7	Schematic of the Shock Structure of a Highly Underexpanded Jet Showing the Response Just Downstream of the Mach Disk of a Line of Molecular Tagging Velocimetry at Successive Time Steps	68
3.8	Time Lapse Imagery Indicating the Motion of an Acetone Seeded Flow Field (A Highly Underexpanded Jet Just Downstream of the Mach Disk) Imaged After Being Tagged by a UV Laser Beam at 266nm	69
3.9	Line of Acetone Phosphorescence Indicating Location of the Peak Determined from Curve Fitting Algorithm	70

3.10	Flow Visualization of Mie Scattering from Condensation of a Mach 2.0 Jet Showing Development of the Large Scale Structure from Laser Energy Deposition, from Adelgren et. al. (US Government Work) [11]	72
3.11	Schematic of Laser Energy Deposition	73
3.12	Contours of Tangential Velocity in the Convective Frame Showing Large Scale Structure Motion in the Shear Layer of a Mach 1.38 Perfectly Expanded Jet, From Adelgren et. al. (US Government Work) [11]	75
3.13	Schematic of Photon Emission from an Excited Molecule	76
3.14	Schematic of Imaging Visible Light Emission	77
3.15	Schematic of Imaging Spectroscopy	80
3.16	Spectrum of Plasma Emission from Near Ultraviolet to Near Infrared	82
3.17	Relative Intensity of Hollow Cathode Iron Emission Used to Calibrate the Imaging Spectrometer	83
3.18	Relative Intensity of Black Body Emission at 2659 K Used to Calibrate the Imaging Spectrometer	84
3.19	Sample of Spectrum Fitting Results	85
4.1	Photos of the Jet and Plasma with Flow from Left to Right, Note the Barrel Shock of Highly Underexpanded Jet is Visible with the Plasma On	88
4.2	A Summary of the Experiment Space by Chamber Pressure and Equivalent Mach Number	89
4.3	Contours of Axial Velocity Measured by Particle Image Velocimetry, Showing the Location of the Molecular Tagging Velocimetry Line	93
4.4	Comparison of Axial Velocity 1.1 Diameters from the Anode Face Measured by Molecular Tagging Velocimetry and Particle Image Velocimetry of a Flowfield Formed From Developing Flow Exiting a Constant Diameter Tube, Driven at a Pressure Ratio Equivalent to an Isentropic Mach Number of 1.9	94
4.5	Comparison of Axial Velocity 1.1 Diameters from the Anode Face Measured by Molecular Tagging Velocimetry and Particle Image Velocimetry of a Flowfield Formed From Developing Flow Exiting a Constant Diameter Tube, Driven at a Pressure Ratio Equivalent to an Isentropic Mach Number of 1.4	95
4.6	Comparison of Axial Velocity 1.1 Diameters from the Anode Face Measured by Molecular Tagging Velocimetry and Particle Image Velocimetry of a Flowfield Formed From Developing Flow Exiting a Constant Diameter Tube, Driven at a Pressure Ratio Equivalent to an Isentropic Mach Number of 0.6	96
4.7	Comparison of Axial Velocity 1.1 Diameters from the Anode Face Measured by Molecular Tagging Velocimetry and Particle Image Velocimetry of a Axisymmetric Jet From a Converging-Diverging Nozzle at Mach 1.4	96
4.8	Schematic of a Highly Underexpanded Flow Created by a Sonic Orifice	98
4.9	Contours of Axial Velocity Measured by Molecular Tagging Velocimetry of a Flow Field Created by a Sonic Orifice	99
4.10	Comparison of Axial Velocity Along the Jet Centerline Measured by Molecular Tagging Velocimetry and Particle Image Velocimetry of a Flow Field Created by a Sonic Orifice, Showing the Degrading Effect of Increasing Particle Size	100
4.11	Measurement Locations Investigated for the 8-9 Torr Series of Nozzles	110
4.12	Measurement Locations Investigated for the 5 Torr Series of Nozzles	110
4.13	Mean Axial Velocity Contours of the Mach 1.4 Axisymmetric Jet	111
4.14	Downstream Progression of Mean Axial Velocity and Axial Velocity Fluctuations for a Mach 1.36 Axisymmetric Jet Exhausting into Atmospheric Air, Based on Data From Mosedale et. al. [275] (<i>Note: Measurements Were made 45.8° Off the Jet Axis, Meaning the Axial Components are Larger by a Factor of 1.41</i>)	112
4.15	Downstream Progression of Mean and Turbulent Velocities for a Mach 1.4 Axisymmetric Jet	114
4.16	Downstream Progression of Second Moment Turbulent Fluctuations for a Mach 1.4 Axisymmetric Jet	115
4.17	Downstream Progression of Third Moment Turbulent Fluctuations for a Mach 1.4 Axisymmetric Jet	116

4.18	Downstream Progression of Skewness and Kurtosis of Axial Velocity Fluctuations for a Mach 1.4 Axisymmetric Jet	117
4.19	Plasma Effects on Downstream Progression of Centerline Jet Velocity and Shear Layer Thickness for a Mach 1.4 Axisymmetric Jet at 5 Torr	120
4.20	Plasma Effects on Mean and Turbulent Axial Velocities for a Mach 1.4 Axisymmetric Jet at 5 Torr	122
4.21	Plasma Effects on Second Moment Turbulent Fluctuations for a Mach 1.4 Axisymmetric Jet at 5 Torr	123
4.22	Plasma Effects on Third Moment Turbulent Fluctuations for a Mach 1.4 Axisymmetric Jet at 5 Torr	124
4.23	Plasma Effects on Skewness and Kurtosis of Axial Velocity Fluctuations for a Mach 1.4 Axisymmetric Jet at 5 Torr	125
4.24	A Path Showing The Progression Through the Experiment Space to Investigate Compressibility on Perfectly Expanded Axisymmetric Jets	126
4.25	Plasma Effects on Downstream Progression of Centerline Jet Velocity and Shear Layer Thickness for a Mach 0.7 Axisymmetric Jet at 9 Torr	128
4.26	Plasma Effects on Mean Axial Velocity and Turbulent Kinetic Energy for a Mach 0.7 Axisymmetric Jet at 9 Torr, 3.2 Diameters from the Anode Face	128
4.27	Plasma Effects on Downstream Progression of Centerline Jet Velocity and Shear Layer Thickness for a Mach 1.1 Axisymmetric Jet at 9 Torr	130
4.28	Plasma Effects on Mean Axial Velocity and Turbulent Kinetic Energy for a Mach 1.1 Axisymmetric Jet at 9 Torr, 4.5 Diameters from the Anode Face	130
4.29	Plasma Effects on Downstream Progression of Centerline Jet Velocity and Shear Layer Thickness for a Mach 2.0 Axisymmetric Jet at 8 Torr	132
4.30	Plasma Effects on Mean Axial Velocity and Turbulent Kinetic Energy for a Mach 2.0 Axisymmetric Jet at 8 Torr, 6.2 Diameters from the Anode Face	132
4.31	Downstream Progression of Mean Axial Velocity and Velocity Fluctuations for an Incompressible Axisymmetric Straight Pipe at Atmospheric Pressure Where U_b is the Exit Bulk Velocity Based on Mass Flux, From Ferdman, Otugen and Kim (with Permission) [133]	136
4.32	Mean Axial Velocity Contours of the Equivalent Mach 1.4 Axisymmetric Constant-Diameter Jet	137
4.33	Plasma Effects on Mean and Turbulent Axial Velocities for a Mach 1.4 Axisymmetric Jet at 5 Torr	139
4.34	Comparison of Centerline jet Velocity Between a Mach 1.4 Axisymmetric Jet and a Jet Created by Developing Flow Exiting from a Constant-Diameter Tube Driven at a Mach 1.4 Isentropic Pressure Ratio	140
4.35	Comparison of Mean Axial Velocity and Turbulent Kinetic Energy between a Mach 1.4 Axisymmetric Jet and Flow Created from a Tube Driven at a Mach 1.4 Pressure Ratio at 5 Torr, Near the Jet Exit ($x/D = 2.3$)	141
4.36	Comparison of Mean Axial Velocity and Turbulent Kinetic Energy between a Mach 1.4 Axisymmetric Jet and Flow Created from a Tube Driven at a Mach 1.4 Pressure Ratio at 5 Torr, Much Further Downstream ($x/D = 11.3$)	142
4.37	A Path Showing The Progression Through the Experiment Space to Investigate Compressibility on Developing Pipe Flow From Constant-Diameter Nozzles	143
4.38	Plasma Effects on Downstream Progression of Centerline Jet Velocity and Shear Layer Thickness for a Flow Created from a Tube Driven at a Mach 0.9 Pressure Ratio at 5 Torr	144
4.39	Plasma Effects on Mean Axial Velocity and Turbulent Kinetic Energy for a Flow Created from a Tube Driven at a Mach 0.9 Pressure Ratio at 5 Torr	144
4.40	Plasma Effects on Downstream Progression of Centerline Jet Velocity and Shear Layer Thickness for a Flow Created from a Tube Driven at a Mach 1.4 Pressure Ratio at 5 Torr	145
4.41	Plasma Effects on Mean Axial Velocity and Turbulent Kinetic Energy for a Flow Created from a Tube Driven at a Mach 1.4 Pressure Ratio at 5 Torr	146

4.42	Plasma Effects on Downstream Progression of Centerline Jet Velocity and Shear Layer Thickness for a Flow Created from a Tube Driven at a Mach 1.9 Pressure Ratio at 5 Torr	147
4.43	Plasma Effects on Mean Axial Velocity and Turbulent Kinetic Energy for a Flow Created from a Tube Driven at a Mach 1.9 Pressure Ratio at 5 Torr	147
4.44	Contours of Mean Axial Velocity, U [m/s] Comparing the Nominal Mach 2.0 Jet to the Overexpanded Jet, Driven at Mach 1.9 Isentropic Pressure Ratio	149
4.45	Plasma Effects on Downstream Progression of Centerline Jet Velocity and Shear Layer Thickness in an Overexpanded Jet Driven at a Mach 1.9 Pressure Ratio at 8 Torr	150
4.46	Plasma Effects on Mean Axial Velocity and Turbulent Kinetic Energy in an Overexpanded Jet Driven at a Mach 1.9 Pressure Ratio at 8 Torr	150
4.47	Comparison of Turbulent Kinetic Energy between a Flat Anode and an Anode with Serrated Conical Feature for a Mach 1.1 Axisymmetric Jet at 9 Torr - Plasma-Off	152
4.48	Plasma Effects on Downstream Progression of Centerline Jet Velocity and Shear Layer Thickness for a Mach 1.1 Axisymmetric Jet at 9 Torr for an Anode with Serrated Conical Feature .	153
4.49	Plasma Effects on Mean Axial Velocity and Turbulent Kinetic Energy for a Mach 1.1 Axisymmetric Jet at 9 Torr for an Anode with Serrated Conical Feature	153
4.50	Comparison of Turbulent Kinetic Energy between a Flat Anode and an Anode with Serrated Conical Feature for a Mach 1.1 Axisymmetric Jet at 9 Torr - plasma-on	154
4.51	Effect of Increasing Equivalent Mach Number on Constant-Diameter Tube Nozzles	158
4.52	Baseline Flow Undisturbed by Laser Energy Deposition	161
4.53	Schematic of Large Scale Structure Pointing Out the Tracking Feature	162
4.54	Influence of Plasma on Large Scale Structure Motion Using Time Phased Framing of Axial Velocity Relative to the Convective Frame of Motion	163
4.55	Influence of Plasma on Large Scale Structure Motion Using Time Phased Framing of Tangential Velocity Relative to the Convective Frame of Motion	164
4.56	Comparison of Large Scale Structure Motion by Centroid Tracking	165
4.57	Schematic of Photon Emission from a Collisionally Excited Molecule	168
4.58	Relative Intensity of Visible Emission from the Plasma Field for a Flat Anode Around a Mach 0.6 Axisymmetric Jet at 9 Torr	170
4.59	Relative Intensity of Visible Emission from the Plasma Field for a Flat Anode Around a Mach 1.1 Axisymmetric Jet at 9 Torr	171
4.60	Relative Intensity of Visible Emission from the Plasma Field for a Flat Anode around a Mach 2.0 Axisymmetric Jet at 8 Torr	172
4.61	Comparison Between Increasing Pressure Ratios of Relative Intensity of Visible Emission Along the Centerline of the Plasma Field for a Flat Anode around Axisymmetric Jets at Mach 0.6, 1.1 and 2.0 at 8-9 Torr	173
4.62	Relative Intensity of Visible Emission from the Plasma Field for an Anode with Serrated Conical Feature Around a Mach 1.1 Axisymmetric Jet at 9 Torr	175
4.63	Comparison Between Anode Designs of Relative Intensity of Visible Emission Along the Centerline of the Plasma Field for an Anode with Serrated Conical Feature and a Flat Anode Around a Mach 1.1 Axisymmetric Jet at 9 Torr	176
4.64	Relative Intensity of Visible Emission from the Plasma Field for an Anode with Serrated Conical Feature Around an Axisymmetric Jet of Developing Pipe Flow Driven at a Pressure Ratio Corresponding Isentropically to Mach 0.9	178
4.65	Relative Intensity of Visible Emission from the Plasma Field for an Anode with Serrated Conical Feature Around an Axisymmetric Jet of Developing Pipe Flow Driven at a Pressure Ratio Corresponding Isentropically to Mach 1.4	179
4.66	Relative Intensity of Visible Emission from the Plasma Field for an Anode with Serrated Conical Feature Around an Axisymmetric Jet of Developing Pipe Flow Driven at a Pressure Ratio Corresponding Isentropically to Mach 1.9	180

4.67	Comparison Between Increasing Pressure Ratios of Relative Intensity of Visible Emission Along the Centerline of the Plasma Field for an Anode with Serrated Conical Feature Around an Axisymmetric Jet of Developing Pipe Flow Driven at Pressure Ratios Corresponding Isentropically to Mach 0.9, 1.4 and 1.9	181
4.68	Comparison Between Chamber Pressures of 5 Torr and 8 Torr of Relative Intensity of Visible Emission Along the Centerline of the Plasma Field	182
4.69	Schematic of a Flow Created by a Sonic Orifice	183
4.70	Image of Visible Emission from the Plasma Field at 8 Torr for a Flat Anode Around a Flow Created by a Sonic Orifice Which Generated a Visible Barrel Shock Wave	184
4.71	Relative Intensity of Visible Emission from the Plasma Field at 8 Torr for a Flat Anode Around a Flow Created by a Sonic Orifice Which Generated a Visible Barrel Shock Wave . .	185
4.72	Schematic Showing the Imaging Focal Planes for Spectroscopy Orthogonal to the PIV, MTV and Visible Imagery Plane	188
4.73	Rotational and Vibrational Temperature of Flow Exiting from a Sonic Orifice from Spectra of Diatomic Nitrogen, Along the Centerline of the Jet	189
4.74	Summary of Temperature Comparisons for Increasing Mach Numbers from Spectra of Diatomic Nitrogen for Axisymmetric Jets at 8-9 Torr, Taken 10 mm Away from the Cathode . .	192
4.75	Temperature Comparisons Between Anode Designs from Spectra of Diatomic Nitrogen for a Mach 1.1 Axisymmetric Jet at 9 Torr, Along the Centerline of the Jet	193
4.76	Summary of Temperature Comparisons for Increasing Mach Numbers from Spectra of Diatomic Nitrogen for Developing Flow Exiting from a Constant-Diameter Pipe at 5 Torr, Taken 10 mm Away from the Cathode	194
A.1	Comparison of Plasma Effects on Mean Velocity and Fluctuations: Case 613LINE1024 . . .	206
A.2	Comparison of Plasma Effects on Second Moment Fluctuations: Case 613LINE1024	207
A.3	Comparison of Plasma Effects on Skewness and Kurtosis: Case 613LINE1024	208
A.4	Comparison of Plasma Effects on Mean Velocity and Fluctuations: Case 613LINE3024 . . .	209
A.5	Comparison of Plasma Effects on Second Moment Fluctuations: Case 613LINE3024	210
A.6	Comparison of Plasma Effects on Skewness and Kurtosis: Case 613LINE3024	211
A.7	Comparison of Plasma Effects on Mean Velocity and Fluctuations: Case 604LINE4673 . . .	212
A.8	Comparison of Plasma Effects on Second Moment Fluctuations: Case 604LINE4673	213
A.9	Comparison of Plasma Effects on Skewness and Kurtosis: Case 604LINE4673	214
A.10	Comparison of Plasma Effects on Mean Velocity and Fluctuations: Case 604LINE6655 . . .	215
A.11	Comparison of Plasma Effects on Second Moment Fluctuations: Case 604LINE6655	216
A.12	Comparison of Plasma Effects on Skewness and Kurtosis: Case 604LINE6655	217
A.13	Comparison of Plasma Effects on Mean Velocity and Fluctuations: Case 611LINE1051 . . .	218
A.14	Comparison of Plasma Effects on Second Moment Fluctuations: Case 611LINE1051	219
A.15	Comparison of Plasma Effects on Skewness and Kurtosis: Case 611LINE1051	220
A.16	Comparison of Plasma Effects on Mean Velocity and Fluctuations: Case 611LINE3051 . . .	221
A.17	Comparison of Plasma Effects on Second Moment Fluctuations: Case 611LINE3051	222
A.18	Comparison of Plasma Effects on Skewness and Kurtosis: Case 611LINE3051	223
A.19	Comparison of Plasma Effects on Mean Velocity and Fluctuations: Case 603LINE5011 . . .	224
A.20	Comparison of Plasma Effects on Second Moment Fluctuations: Case 603LINE5011	225
A.21	Comparison of Plasma Effects on Skewness and Kurtosis: Case 603LINE5011	226
A.22	Comparison of Plasma Effects on Mean Velocity and Fluctuations: Case 603LINE6993 . . .	227
A.23	Comparison of Plasma Effects on Second Moment Fluctuations: Case 603LINE6993	228
A.24	Comparison of Plasma Effects on Skewness and Kurtosis: Case 603LINE6993	229
A.25	Comparison of Plasma Effects on Mean Velocity and Fluctuations: Case 609LINE1012 . . .	230
A.26	Comparison of Plasma Effects on Second Moment Fluctuations: Case 609LINE1012	231
A.27	Comparison of Plasma Effects on Skewness and Kurtosis: Case 609LINE1012	232
A.28	Comparison of Plasma Effects on Mean Velocity and Fluctuations: Case 609LINE3011 . . .	233
A.29	Comparison of Plasma Effects on Second Moment Fluctuations: Case 609LINE3011	234
A.30	Comparison of Plasma Effects on Skewness and Kurtosis: Case 609LINE3011	235

A.31	Comparison of Plasma Effects on Mean Velocity and Fluctuations: Case 607LINE5024 . . .	236
A.32	Comparison of Plasma Effects on Second Moment Fluctuations: Case 607LINE5024	237
A.33	Comparison of Plasma Effects on Skewness and Kurtosis: Case 607LINE5024	238
A.34	Comparison of Plasma Effects on Mean Velocity and Fluctuations: Case 607LINE7001 . . .	239
A.35	Comparison of Plasma Effects on Second Moment Fluctuations: Case 607LINE7001	240
A.36	Comparison of Plasma Effects on Skewness and Kurtosis: Case 607LINE7001	241
A.37	Comparison of Plasma Effects on Mean Velocity and Fluctuations: Case 610LINE1033 . . .	242
A.38	Comparison of Plasma Effects on Second Moment Fluctuations: Case 610LINE1033	243
A.39	Comparison of Plasma Effects on Skewness and Kurtosis: Case 610LINE1033	244
A.40	Comparison of Plasma Effects on Mean Velocity and Fluctuations: Case 610LINE3032 . . .	245
A.41	Comparison of Plasma Effects on Second Moment Fluctuations: Case 610LINE3032	246
A.42	Comparison of Plasma Effects on Skewness and Kurtosis: Case 610LINE3032	247
A.43	Comparison of Plasma Effects on Mean Velocity and Fluctuations: Case 608LINE5018 . . .	248
A.44	Comparison of Plasma Effects on Second Moment Fluctuations: Case 608LINE5018	249
A.45	Comparison of Plasma Effects on Skewness and Kurtosis: Case 608LINE5018	250
A.46	Comparison of Plasma Effects on Mean Velocity and Fluctuations: Case 608LINE6996 . . .	251
A.47	Comparison of Plasma Effects on Second Moment Fluctuations: Case 608LINE6996	252
A.48	Comparison of Plasma Effects on Skewness and Kurtosis: Case 608LINE6996	253
A.49	Comparison of Plasma Effects on Mean Velocity and Fluctuations: Case 633LINE2229 . . .	254
A.50	Comparison of Plasma Effects on Second Moment Fluctuations: Case 633LINE2229	255
A.51	Comparison of Plasma Effects on Skewness and Kurtosis: Case 633LINE2229	256
A.52	Comparison of Plasma Effects on Mean Velocity and Fluctuations: Case 633LINE3227 . . .	257
A.53	Comparison of Plasma Effects on Second Moment Fluctuations: Case 633LINE3227	258
A.54	Comparison of Plasma Effects on Skewness and Kurtosis: Case 633LINE3227	259
A.55	Comparison of Plasma Effects on Mean Velocity and Fluctuations: Case 634LINE4789 . . .	260
A.56	Comparison of Plasma Effects on Second Moment Fluctuations: Case 634LINE4789	261
A.57	Comparison of Plasma Effects on Skewness and Kurtosis: Case 634LINE4789	262
A.58	Comparison of Plasma Effects on Mean Velocity and Fluctuations: Case 634LINE6785 . . .	263
A.59	Comparison of Plasma Effects on Second Moment Fluctuations: Case 634LINE6785	264
A.60	Comparison of Plasma Effects on Skewness and Kurtosis: Case 634LINE6785	265
A.61	Comparison of Plasma Effects on Mean Velocity and Fluctuations: Case 635LINE8792 . . .	266
A.62	Comparison of Plasma Effects on Second Moment Fluctuations: Case 635LINE8792	267
A.63	Comparison of Plasma Effects on Skewness and Kurtosis: Case 635LINE8792	268
A.64	Comparison of Plasma Effects on Mean Velocity and Fluctuations: Case 635LINE10787 . . .	269
A.65	Comparison of Plasma Effects on Second Moment Fluctuations: Case 635LINE10787	270
A.66	Comparison of Plasma Effects on Skewness and Kurtosis: Case 635LINE10787	271
A.67	Comparison of Plasma Effects on Mean Velocity and Fluctuations: Case 624LINE2260 . . .	272
A.68	Comparison of Plasma Effects on Second Moment Fluctuations: Case 624LINE2260	273
A.69	Comparison of Plasma Effects on Skewness and Kurtosis: Case 624LINE2260	274
A.70	Comparison of Plasma Effects on Mean Velocity and Fluctuations: Case 624LINE3253 . . .	275
A.71	Comparison of Plasma Effects on Second Moment Fluctuations: Case 624LINE3253	276
A.72	Comparison of Plasma Effects on Skewness and Kurtosis: Case 624LINE3253	277
A.73	Comparison of Plasma Effects on Mean Velocity and Fluctuations: Case 623LINE4808 . . .	278
A.74	Comparison of Plasma Effects on Second Moment Fluctuations: Case 623LINE4808	279
A.75	Comparison of Plasma Effects on Skewness and Kurtosis: Case 623LINE4808	280
A.76	Comparison of Plasma Effects on Mean Velocity and Fluctuations: Case 623LINE6799 . . .	281
A.77	Comparison of Plasma Effects on Second Moment Fluctuations: Case 623LINE6799	282
A.78	Comparison of Plasma Effects on Skewness and Kurtosis: Case 623LINE6799	283
A.79	Comparison of Plasma Effects on Mean Velocity and Fluctuations: Case 618LINE8800 . . .	284
A.80	Comparison of Plasma Effects on Second Moment Fluctuations: Case 618LINE8800	285
A.81	Comparison of Plasma Effects on Skewness and Kurtosis: Case 618LINE8800	286
A.82	Comparison of Plasma Effects on Mean Velocity and Fluctuations: Case 618LINE10812 . . .	287
A.83	Comparison of Plasma Effects on Second Moment Fluctuations: Case 618LINE10812	288

A.84	Comparison of Plasma Effects on Skewness and Kurtosis: Case 618LINE10812	289
A.85	Comparison of Plasma Effects on Mean Velocity and Fluctuations: Case 626LINE2260 . . .	290
A.86	Comparison of Plasma Effects on Second Moment Fluctuations: Case 626LINE2260	291
A.87	Comparison of Plasma Effects on Skewness and Kurtosis: Case 626LINE2260	292
A.88	Comparison of Plasma Effects on Mean Velocity and Fluctuations: Case 626LINE3253 . . .	293
A.89	Comparison of Plasma Effects on Second Moment Fluctuations: Case 626LINE3253	294
A.90	Comparison of Plasma Effects on Skewness and Kurtosis: Case 626LINE3253	295
A.91	Comparison of Plasma Effects on Mean Velocity and Fluctuations: Case 621LINE4808 . . .	296
A.92	Comparison of Plasma Effects on Second Moment Fluctuations: Case 621LINE4808	297
A.93	Comparison of Plasma Effects on Skewness and Kurtosis: Case 621LINE4808	298
A.94	Comparison of Plasma Effects on Mean Velocity and Fluctuations: Case 621LINE6799 . . .	299
A.95	Comparison of Plasma Effects on Second Moment Fluctuations: Case 621LINE6799	300
A.96	Comparison of Plasma Effects on Skewness and Kurtosis: Case 621LINE6799	301
A.97	Comparison of Plasma Effects on Mean Velocity and Fluctuations: Case 617LINE8814 . . .	302
A.98	Comparison of Plasma Effects on Second Moment Fluctuations: Case 617LINE8814	303
A.99	Comparison of Plasma Effects on Skewness and Kurtosis: Case 617LINE8814	304
A.100	Comparison of Plasma Effects on Mean Velocity and Fluctuations: Case 617LINE10809 . . .	305
A.101	Comparison of Plasma Effects on Second Moment Fluctuations: Case 617LINE10809	306
A.102	Comparison of Plasma Effects on Skewness and Kurtosis: Case 617LINE10809	307
A.103	Comparison of Plasma Effects on Mean Velocity and Fluctuations: Case 627LINE2260 . . .	308
A.104	Comparison of Plasma Effects on Second Moment Fluctuations: Case 627LINE2260	309
A.105	Comparison of Plasma Effects on Skewness and Kurtosis: Case 627LINE2260	310
A.106	Comparison of Plasma Effects on Mean Velocity and Fluctuations: Case 627LINE3253 . . .	311
A.107	Comparison of Plasma Effects on Second Moment Fluctuations: Case 627LINE3253	312
A.108	Comparison of Plasma Effects on Skewness and Kurtosis: Case 627LINE3253	313
A.109	Comparison of Plasma Effects on Mean Velocity and Fluctuations: Case 620LINE4808 . . .	314
A.110	Comparison of Plasma Effects on Second Moment Fluctuations: Case 620LINE4808	315
A.111	Comparison of Plasma Effects on Skewness and Kurtosis: Case 620LINE4808	316
A.112	Comparison of Plasma Effects on Mean Velocity and Fluctuations: Case 620LINE6799 . . .	317
A.113	Comparison of Plasma Effects on Second Moment Fluctuations: Case 620LINE6799	318
A.114	Comparison of Plasma Effects on Skewness and Kurtosis: Case 620LINE6799	319
A.115	Comparison of Plasma Effects on Mean Velocity and Fluctuations: Case 616LINE8814 . . .	320
A.116	Comparison of Plasma Effects on Second Moment Fluctuations: Case 616LINE8814	321
A.117	Comparison of Plasma Effects on Skewness and Kurtosis: Case 616LINE8814	322
A.118	Comparison of Plasma Effects on Mean Velocity and Fluctuations: Case 616LINE10809 . . .	323
A.119	Comparison of Plasma Effects on Second Moment Fluctuations: Case 616LINE10809	324
A.120	Comparison of Plasma Effects on Skewness and Kurtosis: Case 616LINE10809	325
A.121	Comparison of Plasma Effects on Mean Velocity and Fluctuations: Case 614LINE1331 . . .	326
A.122	Comparison of Plasma Effects on Second Moment Fluctuations: Case 614LINE1331	327
A.123	Comparison of Plasma Effects on Skewness and Kurtosis: Case 614LINE1331	328
A.124	Comparison of Plasma Effects on Mean Velocity and Fluctuations: Case 614LINE2831 . . .	329
A.125	Comparison of Plasma Effects on Second Moment Fluctuations: Case 614LINE2831	330
A.126	Comparison of Plasma Effects on Skewness and Kurtosis: Case 614LINE2831	331
A.127	Comparison of Plasma Effects on Mean Velocity and Fluctuations: Case 606LINE4706 . . .	332
A.128	Comparison of Plasma Effects on Second Moment Fluctuations: Case 606LINE4706	333
A.129	Comparison of Plasma Effects on Skewness and Kurtosis: Case 606LINE4706	334
A.130	Comparison of Plasma Effects on Mean Velocity and Fluctuations: Case 606LINE6701 . . .	335
A.131	Comparison of Plasma Effects on Second Moment Fluctuations: Case 606LINE6701	336
A.132	Comparison of Plasma Effects on Skewness and Kurtosis: Case 606LINE6701	337

List of Abbreviations

Acronyms and Abbreviations

AC	Alternating Current
CCD	Charge Coupled Device
CCP	Capacitively Coupled Plasma
CF	Completely Fouled
CMAG	Condensation Monodisperse Aerosol Generator
DC	Direct Current
DBD	Dielectric Barrier Discharge
FWHM	Full Width at Half Maximum
ICCD	Intensified Charge Coupled Device
ICP	Inductively Couple Plasma
LED	Laser Energy Deposition
LSS	Large Scale Structure
MTV	Molecular Tagging Velocimetry
NACA	National Advisory Committee for Aeronautics
Nd:YAG	Neodymium:Yttrium Argon Garnet
ND	Non Dimensional
PIV	Particle Image Velocimetry
PMT	Photo Multiplier Tube
PVC	Poly Vinyl Chloride
RF	Radio Frequency
VV	Vibrational to Vibrational Coupling
VR	Vibrational to Rotational Coupling
SH	Super High
SNAFU	Situation Normal: All Fouled Up

TU	Totally Unusable
TKE	Turbulent Kinetic Energy
2-D	Two Dimensional
UV	Ultra Violet

Units

cm	Centimeters
g	Grams
Hz	Hertz
K	Kelvin
Kg	Kilograms
KW	Kilowatts
MHz	Megahertz
μm	Micrometers
μs	Microseconds
mm	Millimeters
nm	Nanometers
ns	Nanoseconds
pm	Picometers

List of Symbols

a_1	Jet Core Speed of Sound
a_2	Jet Shear Speed of Sound
C_p	Coefficient of Specific Heats at Constant Pressure
D_e	Nozzle Exit Diameter
D^*	Nozzle Throat Diameter
δ_{10}	Shear Layer Thickness
δ_{ω_0}	Initial Vorticity Thickness
η	Free Jet Similarity Parameter
ϵ	Measurement Uncertainty
γ	Ratio of Specific Heats
k	Turbulent Kinetic Energy
Kn	Knudsen Number
λ	Wavelength
\dot{m}	Mass Flow Rate
M_c	Convective Mach Number
M_e	Exit Mach Number
M_g	Geometric Mach Number
M_i	Isentropic Mach Number, also Equivalent Mach Number
μ	Viscosity
N	Number of Samples
P_o	Plenum Pressure
P_e	Chamber Pressure
P_f	Fluid Pressure
R	Gas Constant
r	Tangential (Radial) Location Coordinate

$r_{1/2}$	Radial Location of Half Maximum Axial Velocity
Re	Reynolds Number
ρ	Density
ρ_e	Jet Exit Density
ρ_p	Particle Density
σ_u	Root Mean Square of Axial Velocity Fluctuations
σ_v	Root Mean Square of Tangential Velocity Fluctuations
T_o	Plenum Temperature
T_1	Jet Core Temperature
T_2	Jet Shear Temperature
T_e	Exit Temperature
T_f	Fluid Temperature
T_i	Isentropic Temperature
T_p	Particle Temperature
T_r	Rotational Temperature
T_v	Vibrational Temperature
τ	Time Scale Factor Ratio
τ_f	Fluid Time Scale Factor
τ_p	Particle Time Scale Factor
u	Axial Velocity
U	Axial Mean Velocity
U_e	Jet Exit Velocity
U_i	Isentropic Predicted Jet Exit Velocity
U_o	Jet Centerline Velocity
U_1	Jet Core Velocity
U_2	Jet Shear Velocity (0)
v	Tangential Velocity
V	Tangential Mean Velocity
x	Axial Location Coordinate
y	Tangential (Horizontal) Location Coordinate
z	Tangential (Vertical) Location Coordinate

Chapter 1

Background

This research sets out generally to find the influence of plasma on compressible turbulence. Compressible turbulence in plasma touches many fields of interest. Vehicles such as the space shuttle experience the combined effects of plasma and compressible turbulence on re-entry into the earth's atmosphere. As we learned in the space race of the 1960s, the stresses placed on a re-entry vehicle during the return to earth are severe and miscalculations carry devastating consequences. Plasmas are being used also in flow control to control separation over wings and to generate oblique shocks in jet inlets. In order to achieve an understanding of the underlying features of plasmas and to predict the impact of those features on future designs, modeling is required. And therein lies the strongest influence for this research - that this work provides data which will validate modeling of this rather complicated juncture of interwoven phenomena.

The main goal of the research presented here is to determine the differences between a plasma field and neutral field flow structure (both mean and turbulent effects) for varying Mach number. The overall objective is to describe the effect of Radio Frequency Capacitively Coupled Plasma (RF-CCP) on the flow features of compressible axisymmetric jets. This objective will be examined through three specific sub-objectives.

- Confirm the Measurement Technique Accurately Describes the Flow Field
- Define a Measure for Plasma Quality
- Measure the Effect of Plasma on the Flow Field

The first sub-objective is to confirm the measurement technique accurately describes the flow field. Research indicates that atomized liquid seed particles will be small enough to accurately track the flow dynamics of these nozzles. However, the accuracy of the particle tracking must be quantified. Measurements taken with seed particle based tracking techniques will be compared to molecular tracer techniques to confirm the particles accurately track the flow. Good theoretical models exist which will also be used for comparison. One aspect of this sub-objective is the concern that the plasma may induce motion in the seed particles. However, through observation prior to testing, the seed particles in these experiments were noted not to be disturbed electrically or thermophoretically by the plasma field. This sub objective will be considered

successful if two conditions are met. First, particles based velocity measurements must track the mean flow features to within 5% of the molecular tracer based velocimetry technique. Second, the model based approach to estimating uncertainty in turbulent fluctuations must determine that uncertainty is below 10%.

The next sub-objective is to define a measure for plasma quality. The goal of this sub objective is to quantify a factor which can be measured independent of the flow structure to determine the influence of the plasma on the flow structure. Success in this category will be through documenting plasma quality for all plasma fields tested.

Measuring the effect of plasma on the flow field is the next sub-objective. This sub-objective is the primary path to answering the test objective. Both mean and turbulent fluctuating velocity fields will be acquired for plasma and neutral fields at the same test conditions and flow locations. Success here will be acquiring these sets at at least two different Mach numbers for: a free shear flow, the same free shear flow with an induced large scale structure, and an oblique shock structure.

This section begins with a review of axisymmetric jet flow structures. Then to gain a better understanding of plasmas, this chapter will report on the mechanics of the fourth state of matter and the techniques used in generating sustained plasma in the laboratory. The plasma fields described here are important because many of them were encountered in testing and phenomena encountered in one type of plasma field are often used to describe features of other plasmas.

1.1 Axisymmetric Jet

The flow field for this research focuses on axisymmetric jets, that is a jet formed by a nozzle of circular cross section. This section will describe the characteristics of a jet and salient features exploited in the current effort.

1.1.1 Nominal Jets

Jets are created when a pressure differential causes fluid to flow through a nozzle. After the jet exits into a large open volume, the test chamber in this case, it is free to change its shape. This region is called a free shear layer. It is a shear layer because the jet exiting from the orifice may have a mismatch in velocity. The velocity mismatch causes frictional shear between the jet and the surrounding fluid in the chamber which forms a layer of flow dominated by viscous effects.[\[15, 284\]](#)

Figure 1.1 shows a jet formed by a pressure mismatch between the plenum and the test chamber $P_o > P_e$. The jet exhausts into the the chamber initially as the jet core, then interacting with the quiescent gas in

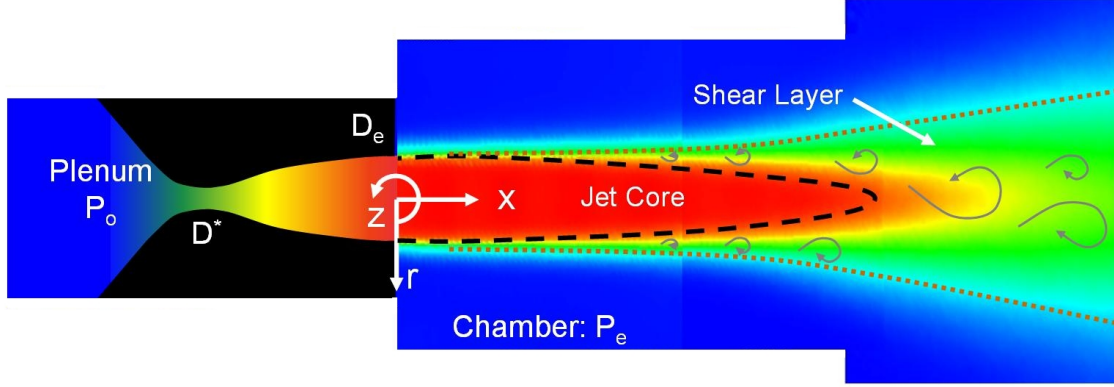


Figure 1.1: Flow Exiting From a Plenum into the Test Chamber Through a Nozzle

the chamber through the shear layer. The coordinate system is set up assuming an axisymmetric jet, where x is the axial coordinate aligned with the jet exit velocity and r is the radial, or tangential flow coordinate direction. The vertical component z is included as an indicator for some of the measurements taken in this research. While the flow velocity measurements are taken in the $x - r$ plane, temperature measurements are made in the $x - z$ plane.

For a compressible fluid, a nozzle can be contoured in such a way as to accelerate flow beyond the speed of sound. This is accomplished by a converging-diverging nozzle, also known as a de Laval nozzle after the Swedish inventor Gustaf de Laval. Acceleration up to the speed of sound occurs in the convergent portion of the nozzle and while the contour should be smooth to avoid viscous separations, the velocity acceleration to sonic conditions is relatively insensitive to the actual shape. This research effort uses a converging contour of 45° as described in Pope.[297] Pope also recommends very gradual contours with no seams near the throat. Even minor contour mismatches there can cause the flow to accelerate to sonic conditions prematurely resulting in undesired effects from shocks or separations to cascade into the divergent section of the nozzle. The designs used in this effort avoid these issues by manufacturing the converging-diverging nozzle as one piece to avoid seams and also provide a gentle parabolic transition from the convergent slope to the throat. The convergent slope used here transitions to the throat through a quarter ellipse with a major axis of D^* and minor axis of $D^*/2$. The throat is typically a short constant-diameter region which minimizes minor variations in the choke point from affecting flow in the divergent region. The design used in this effort are of a constant-diameter cylinder, one throat diameter D^* long. Once the flow is choked, the trend of fluid velocity with diameter reverses. Now for increasing nozzle diameter, the fluid velocity accelerates. This divergent portion of the nozzle is where the jet reaches supersonic conditions. Figure 1.2 shows a cut-away of an axisymmetric jet.[14, 226, 284]

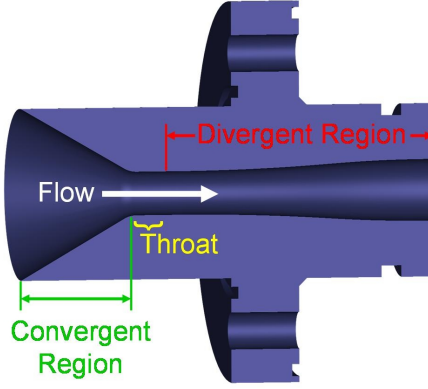


Figure 1.2: Cut-away View of an Axisymmetric Converging-Diverging Nozzle

The speed of sound a , for an ideal gas is determined by $a = \sqrt{\gamma RT}$, where γ and R are the ratio of specific heats and gas constant for the gas, respectively. The static temperature T varies as a function of the fluid velocity and the total temperature of the fluid at that point. To determine the static temperature, some assumptions are required. Therefore, assuming the flow process occurring in the nozzle is both adiabatic (by neglecting heat transferred into or out of the flow from the nozzle) and reversible (by neglecting the effects of frictional losses), then the isentropic relations for an ideal gas can be rearranged to describe the equivalent exit conditions of the jet.

$$M_i = \sqrt{\frac{2}{\gamma - 1} \left[\left(\frac{P_o}{P_e} \right)^{(\gamma-1)/\gamma} - 1 \right]} \quad (1.1)$$

$$T_i = \frac{T_o}{1 + \frac{\gamma-1}{2} M_i^2} \quad (1.2)$$

In these equations, P_o and P_e are the plenum and chamber pressures, respectively, and T_o is the plenum temperature. The plenum is designed to provide a settling chamber which reduces the turbulence and velocity fluctuations associated with providing the high pressure gas required to generate nozzle flow. The gas velocity in the plenum is very low due to its large cross-sectional area and therefore plenum measurements approximate the total pressure P_o and total temperature T_o nicely. For the remainder of this report, plenum conditions are subscripted by 'o' and infer the approximate measurement of total conditions of the gas upstream of the nozzle. The subscript 'i' is used to indicate that the calculated flow conditions are assumed to be isentropic, resulting in the moniker *equivalent* Mach number for M_i . Nozzle inefficiencies result in

losses which drive the actual Mach number lower than equivalent predictions and subsequently the measured static temperature of the actual jet is usually higher than T_i . By manipulating the conservation of energy, a prediction of the exit velocity of a jet can be found based entirely on the measurements of P_o , P_e and T_o .

$$U_i = \sqrt{2C_p T_o \left[1 - \left(\frac{P_e}{P_o} \right)^{(\gamma-1)/\gamma} \right]} \quad (1.3)$$

Where C_p is the coefficient of specific heat at constant pressure for the gas, related to the gas constant, R , by $C_p = \gamma R / (\gamma - 1)$. [14, 297]

If the exit velocity U_e for the jet is measured, then the equivalent approximations can be improved by now using the actual exit velocity to estimate the exit Mach number and temperature. This procedure begins with manipulating the conservation of energy to find an estimate of the exit temperature based on the measured plenum temperature and the exit velocity.

$$T_e = T_o - \frac{U_e^2}{2C_p} \quad (1.4)$$

This estimation assumes that the total temperature remains constant traveling through the nozzle. Then the exit Mach number is estimated by rearranging the isentropic relationship for temperature.

$$M_e = \sqrt{\frac{2}{\gamma - 1} \left(\frac{T_o}{T_e} - 1 \right)} \quad (1.5)$$

Where the estimate for static temperature T_e is used from Equation 1.4. [15]

The concept of a geometric Mach number is now introduced as the Mach number which would be achieved based on the area ratio (or nozzle diameter ratio) between the throat and the exit of the nozzle and is M_g in Equation 1.6. The ratio of throat to nozzle diameter is set by the desired geometric Mach number.

$$\left(\frac{D_e}{D^*} \right)^4 = \frac{1}{M_g^2} \left[\frac{2}{\gamma + 1} \left(1 + \frac{\gamma - 1}{2} M_g^2 \right) \right]^{(\gamma+1)/(\gamma-1)} \quad (1.6)$$

The desired mass flow then determines the throat diameter, leaving only the exit diameter as a function of M_g .

However, the divergent portion of the nozzle design is more complicated than a simple geometric ratio. In addition to accelerating the flow through a monotonic increase in nozzle diameter, the contour of the nozzle determines the profile of the exit velocity. In order to achieve uniform exit velocity, where the velocity across the jet exit is constant and aligned with the nozzle centerline, the method of characteristics is employed. For

this research, a software utility developed by Prof Addy at the University of Illinois, Urbana-Champaign - and later modified by Prof Samimy at The Ohio State University applies the method of characteristics to achieve uniform exit velocities with the desired geometric Mach number.[15, 226, 284]

The effects of boundary layer growth through viscous gas interactions with the nozzle wall are not accounted for in the method of characteristics solution. The boundary layer is a thin layer of fluid which is slower than the core nozzle velocity and influences the desired exit velocity by effectively decreasing the usable cross-sectional area of the jet. The result is a lower measured Mach number than desired at the exit of the jet. A slight increase in geometric Mach number (about 10%) is applied as a correction for the boundary layer.

1.1.2 Off-Nominal Jets

Experimentally, the process of matching the actual pressure ratio to a nozzle is somewhat iterative in nature. The boundary layer growth modifies the jet's effective area ratio. A jet driven at a pressure ratio (Equation 1.1) corresponding to the geometric Mach number of the nozzle will result in jet exit velocities which are not perfectly aligned with the nozzle centerline. The misaligned flow reverberates through the jet in a series of reflected expansions and compressions which contract or expand the jet boundary.[14, 228, 284]

Figure 1.3 shows the four cases encountered in matching the pressure ratio to the actual nozzle. Each of the panels show a schematic of the jet with the jet boundary and any compression, expansion or shock waves. Note that the interaction of the wave structure is more complicated than sketched here, as the concept of waves reflecting off the jet boundary and off each other is the one of importance in the illustration. The sketches are based on drawings found in Pai [284], Love [228] and Anderson [14] where expansion and compression waves are also shown as straight lines for clarity.

Panel (a) is the subsonic case in air, where the pressure ratio $P_o/P_e < 1.893$. For pressure ratios below this threshold, the jet will not produce supersonic flow. For this research, some subsonic jets were produced by this technique. Increasing the pressure ratio over the threshold develops a supersonic jet as seen in panels (b), (c) or (d). The goal in most cases is the perfect expansion in panel (b). In this case, the pressure ratio applied matches the effective area ratio and accounts for the effect of the boundary layer. If done perfectly, the jet which exits at this condition is free of shocks and produces a jet of uniform exit velocity U_e , with a thin boundary layer. In practice, the match is less than perfect and minor variations are seen in exit velocity across the width of the nozzle and very weak expansion and compression waves produce a slight oscillation in the core exit velocity traveling out of the jet, usually around 1% of the mean exit velocity. The off-nominal cases in panels (c) and (d) are for gross pressure mismatches. In both cases the jets develop radial velocity

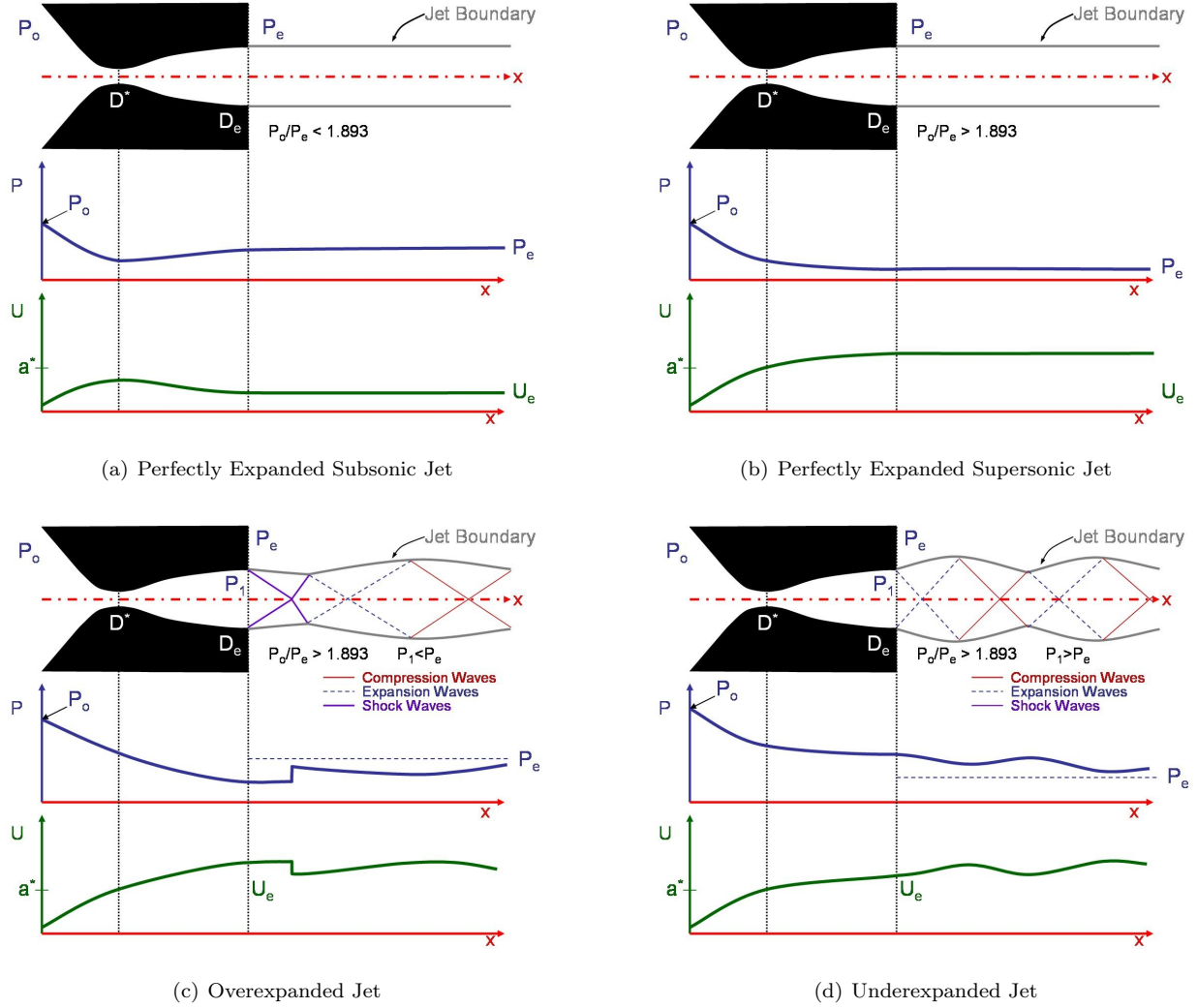


Figure 1.3: Schematics of Nominal and Off-Nominal Jets in Air

components of significance and stronger oscillations in the centerline velocity. To match the pressure ratio, measurements of the velocity field near the jet exit must be taken through an iterative procedure. The search begins near the geometric pressure ratio and examines initially large deviations to narrow the search range. The range is consecutively decreased through smaller variations in pressure ratio until the velocity field shows a matched condition.[14, 284, 297]

Rarefied Jets

In most fluid dynamics problems, it is assumed that there are so many molecules present in a volume of interest, that continuum dynamics can be applied to create transport coefficients which change smoothly in that volume. In rarefied gases that model breaks down. A rarefied gas has molecules, which on the mean,

are separated by a distance which is on the order of magnitude of the length scale of interest. The mean separation distance of the molecules is referred to as the mean free path λ ,

$$\lambda = \frac{kT_f}{\sqrt{2}\sigma^2 P_f} \quad (1.7)$$

where k is the Boltzmann constant ($1.38 \times 10^{-23} J/K$) and σ is the molecule diameter, which is 407 pm for air. The temperature and pressure of the fluid (T_f and P_f , respectively) are used as a substitution for the local fluid density by quantities which are more easily estimated for this scenario. The mean free path of air at standard atmospheric conditions is 69 nm. For the air to be considered rarefied, the characteristic length of interest needs to be on the order of that mean free path - making it a factor for nano-devices or the smallest of seed particles. However, when looking at jets exhausting into a vacuum, the situation changes. For a gas still at 295 K but now at 5 torr, the mean free path is $8.3\mu m$, 2 orders of magnitude larger. The flow is still not rarefied relative to a jet diameter of 1 cm, but standard seed particles used for flow tracers in many velocimetry techniques are now firmly in the rarefied regime. The Knudsen number is commonly used to determine the boundary of rarefaction and is $Kn = \lambda/L$, where L is the characteristic length. Rarefaction dominates the local dynamics as the Knudsen number increases to unity and beyond. The Knudsen number can be recast into Reynolds number Re and Mach number shown in Equations 1.8 through 1.10.

$$Re_L = \frac{\rho_f U L}{\mu_f} \quad (1.8)$$

$$M = \frac{U}{\sqrt{\gamma_f R_f T_f}} \quad (1.9)$$

$$Kn_L = \sqrt{\frac{\pi \gamma_f}{2}} \left(\frac{M}{Re_L} \right) \quad (1.10)$$

Where the local gas properties ρ_f , μ_f , γ_f and R_f are the density, viscosity, ratio of specific heats and the gas constant, respectively. The local velocity is represented by U and could be a relative velocity between a particle of interest and the fluid it travels in, or between the fluid and a stationary boundary in the flow.[\[77, 339\]](#)

Given the discussions trend toward the focus on small tracer particles, one rarefied flow feature of interest is thermophoresis. Thermophoresis is the force placed on an object in a quiescent gas with a thermal gradient. Under normal conditions, the object in the flow is so large, relative to the thermal gradient that motion does not occur. However, in the instance of small tracer particles which see thermophoretic forces, this issue must be dealt with carefully. For a small particle in a temperature gradient, the molecular collisions on

the warm face are more likely than on the cold face of the particle. Therefore, the thermophoretic force is one which drives a tracer particle away from warm gas toward cold gas. Thermophoresis effects are reduced significantly when the fluid is in motion, as the thermophoretic forces are small relative to forces on the tracer particles by the fluid in motion. However, the question of the effect of thermophoresis must be answered when using tracer particles in rarefied flow.[54, 339]

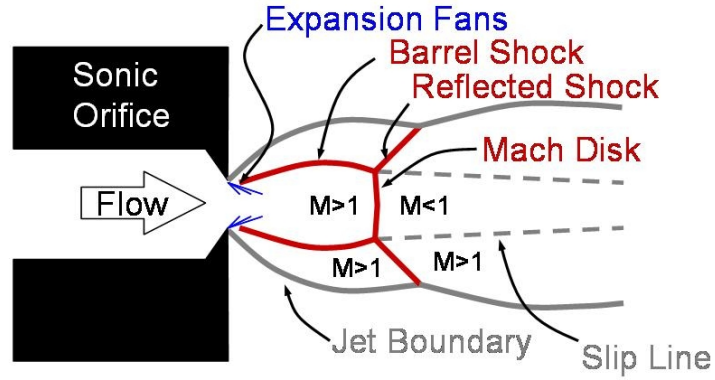


Figure 1.4: Schematic of the Shock Structure of a Highly Underexpanded Jet Exiting from a Sonic Orifice

On example of a rarefied flow is the highly underexpanded jet. Figure 1.4 shows the structure of a highly underexpanded jet. The jet is formed by flow exiting out of a sonic orifice, which is the location where the flow chokes. The jet exits into a relative vacuum and forms an expansion region and accelerates rapidly in the chamber with static pressures dropping well below that of the chamber. Next, the flow forms a barrel shock structure where the static pressure jumps to match the chamber pressure. This pattern will continue in a chain of shocks if the pressure ratio is high enough. An interesting place to examine the flow is directly downstream of the Mach disk. Many experiments [1, 8, 46, 78, 79, 106, 115, 143, 209, 220, 221, 283, 386] have been performed on this flow and empirical predictions of the shock location are known. Crist [100] provides a relation for the location of the Mach disk x_M , based on orifice diameter D_e and pressure ratio P_o/P_e .

$$x_M = D_e \sqrt{\frac{P_o}{2.4P_e}} \quad (1.11)$$

Just downstream of the Mach disk, the flow is subsonic, but the flow which surrounds the disk passed through a reflected oblique shock and is still supersonic producing a slipstream in the flow.[228]

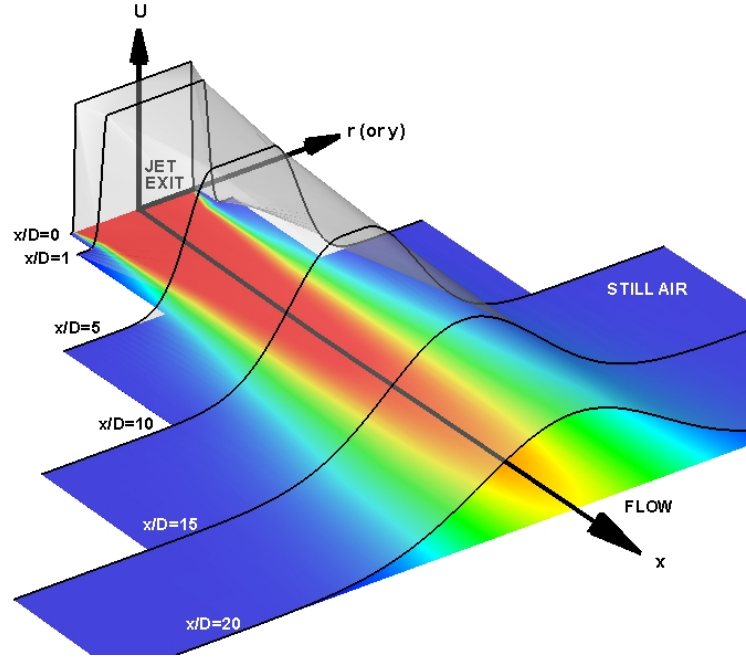


Figure 1.5: Mean Velocity Profile of an Axisymmetric Jet

1.1.3 Free Shear Layers

The baseline flow field of this investigation is the axisymmetric jet into a quiescent chamber. To understand the baseline flow better, examine Figure 1.5, which represents the flow of an ideally expanded supersonic jet with matched pressure between the test chamber and the nozzle exit flow. The jet exits from a plenum chamber, through a convergent divergent nozzle designed to provide reasonably uniform flow at the exit. The first mean velocity profile ($x/D=0$) is that of the ‘top-hat.’ The top hat represents the core of the jet, which is uniform. As the jet interacts with the still air in the test section, a shear layer develops between the core flow and the surrounding air due to viscosity. In this region, represented by the stations located at $x/D=1$ and 5, the core flow is still present, but is decreasing in width. Further downstream, in this example at $x/D=10$ and beyond, the shear layer has overtaken the entire jet. The core flow is no longer present here and the centerline mean flow speed represents the maximum. The flow continues to develop as it travels downstream. The flow is typically fully developed between 5 and 8 jet diameters (D) downstream. Fully developed flow is marked by self-similarity, where the flow features are no longer dependent on the downstream distance. Troutt and McLaughlin[376] found the mean velocity profiles collapse to a half-Gaussian represented in Equation 1.12 on the next page.[328, 367, 383]

$$\frac{U(\eta)}{U_o} = \begin{cases} e^{-2.773(\eta+0.5)^2} & \text{for } \eta > -0.5 \\ 1 & \text{for } \eta \leq -0.5 \end{cases} \quad (1.12)$$

The half-Gaussian profile accounts for the potential core region, as well as the self-similar region. The similarity parameter η , is related to the physical coordinate of radius off the jet centerline through the shear layer thickness δ and $r_{\frac{1}{2}}$. The parameter $r_{\frac{1}{2}}$ is the radial position where the flow speed is 50% of the maximum ($0.5U_o$) by $r = \eta\delta + r_{\frac{1}{2}}$.

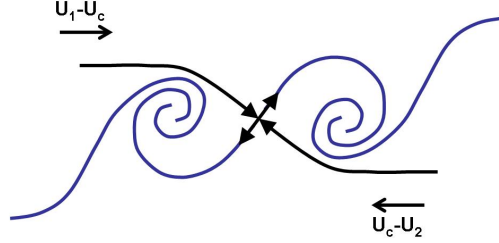


Figure 1.6: Streamlines Between a Vortex Pair in the Convective Reference, Adapted from Coles[93]

To consider the effect of large scale structures on free shear flows, a frame of reference must be developed. This reference frame is constant with respect to the flow of interest. The convective reference frame is the reference in which the largest turbulent structures move relative to the jet exit. To develop the theory behind the convective frame Bogdanoff[58] and Papamoschou and Roshko[287] considered a pair of counter-rotating vortices which represent this large scale turbulent structure. In a frame of reference traveling with the vortex pair, there is a stagnation point between them. Two streamlines, one traveling from each vortex collide at this stagnation point as depicted in Figure 1.6. Therefore, since the total pressure is fixed, the following relationship holds true - *assuming the flow along the streamlines are isentropic*. [11, 93, 344]

$$\left(1 + \frac{\gamma_1 - 1}{2} \frac{(U_1 - U_c)^2}{\gamma_1 R_1 T_1}\right)^{\gamma_1/(\gamma_1 - 1)} = \left(1 + \frac{\gamma_2 - 1}{2} \frac{(U_c - U_2)^2}{\gamma_2 R_2 T_2}\right)^{\gamma_2/(\gamma_2 - 1)} \quad (1.13)$$

In Equation 1.13 the convective speed is U_c and the flow speeds for the two flows are U_1 and U_2 , respectively. Some useful relations come from manipulating the above relation (assuming $\gamma_1 = \gamma_2$), and are presented in Equations 1.14 and 1.15

$$M_c = M_{c1} = (U_1 - U_c)/a_1 = M_{c2} = (U_c - U_2)/a_2 \quad (1.14)$$

$$U_c = \frac{a_1 U_2 + a_2 U_1}{a_1 + a_2} \quad (1.15)$$

For the case of a free jet into quiescent air, this relationship simplifies considerably. Since the medium of both flows is the same, $\gamma_1 = \gamma_2$ and also $U_2 = 0$. These simplifications yield the following relationships: $U_c = U_1/(\sqrt{T_1/T_2} + 1)$ and $M_c = U_c/a_2 = U_1/(a_1 + a_2)$. [352]

Differences from this ideal convective reference were observed. [71, 154, 163, 192, 287, 288] Researchers [86, 90, 142, 120, 271] surmised the vortex structure developed a three dimensional helicity which decreased the shear layer growth rate. Further discovery into the turbulent structure occurred when flows of involving supersonic jets into quiescent air were measured. In this compressible shear layer, the large scale structures were less evident. The difference was conjectured to be an effect of compressibility, namely turbulent eddies moving at supersonic speeds in the shear layer were forming shock waves which invalidated the isentropic assumption and worked to quickly breakdown the large scale structures. To account for this phenomenon, Murakami and Papamoschou [278] developed an empirical correction shown in Equations 1.16 through 1.18. [11, 67, 117]

$$U_{c \text{ corrected}} = U_1 - a_1 M_{c1 \text{ corrected}} \quad (1.16)$$

$$M_{c1 \text{ corrected}} = M_c + \frac{-dM_c}{\sqrt{1 + (a_1/a_2)^2}} \quad (1.17)$$

$$dM_c = 1.25 \ln(M_c) + 1.11 \quad (1.18)$$

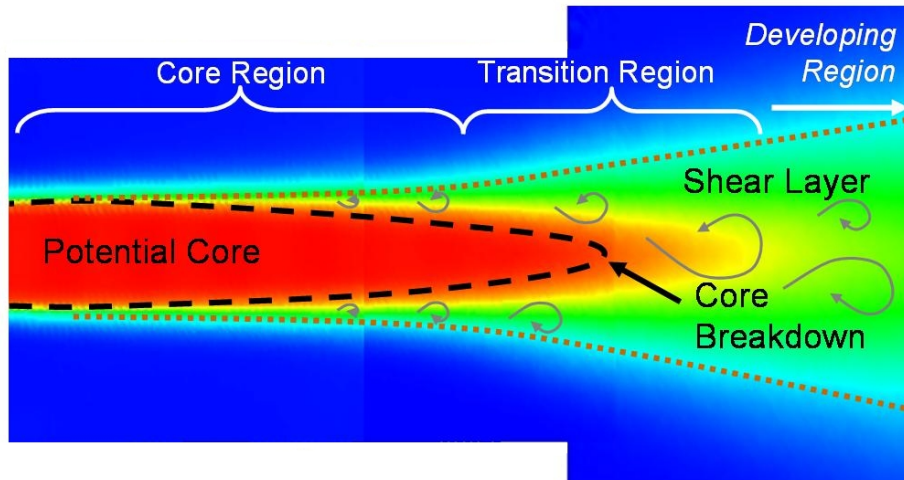


Figure 1.7: Turbulent Regions of the Axisymmetric Jet

The turbulent axisymmetric jet has received considerable investigation. Figure 1.7 shows the progression of turbulence in the axisymmetric jet. The jet begins with either a laminar or turbulent thin shear layer at the exit of the jet (depending on the boundary layer created in the nozzle). Hussain and Clark [187] state that the initial region is dominated by the irrotational jet core and is defined by two length scales, the jet diameter and the initial vorticity thickness. This core region persists for roughly one jet diameter. The shear layer grows in the transition region, feeding off of the momentum in the potential core. Yule [398] observed that the jet becomes dominated by turbulence near the point of core breakdown, roughly 4 jet diameters from the nozzle exit. Experiments [191, 389, 398, 403] have discovered that the mean velocity profile reaches self similarity first, roughly 8 to 15 diameters downstream. Self similarity implies the profile is independent of distance from the nozzle exit, e.g. the velocity profiles collapse onto one scaled curve. However, the turbulence velocity fluctuations take longer to reach full development, up to 40 jet diameters in the case of higher order fluctuation moments.

Researchers [45, 109, 134, 188] agree that above Reynolds numbers of ≈ 500 (based on nozzle exit diameter) that the axisymmetric jet is unstable and always transitions into a turbulent flow. And while the axisymmetric jet is always considered turbulent, the nature of turbulence is related to the Reynolds number. Dimotakis [109] found that two turbulence regimes exist for axisymmetric jets. For Re_D higher than 20,000 the turbulent fluctuations of the jet were very fine, resulting in a distribution of the velocity fluctuations tightly centered around the mean. When the Reynolds number falls below 20,000 however, the turbulence was dominated by large scale structures which spread the distribution of velocity fluctuations significantly farther from the mean value. The dominance of large scale structures at low Reynolds number decreased the effectiveness of the shear layer mixing.[376]

The variance in turbulence structure with Reynolds number has been reported by others [45, 66, 71, 73, 101, 400] and is tied closely with the instability modes of the axisymmetric jet. Figure 1.8 illustrates the dominant instability modes found in axisymmetric jets. Researchers [73, 101, 107, 276] have observed that an axisymmetric jet develops initially like a planar free shear flow with a roll-up into torroidal vortex rings initiated at the lip of the jet exit. These vortex rings are the axisymmetric mode. Corcos [96] postulates that the rings of this mode are unstable to three-dimensional perturbations. The vortex rings respond quickly to the disturbances and interact, forming vortex pairs and become three-dimensional. These vortex interactions transition into the 3-D helical mode. The transition point from axisymmetric to helical modes is sensitive to the jet's initial conditions; the initial vorticity thickness, whether the initial boundary layer was laminar or turbulent and Reynolds number. The thicker the initial vorticity thickness, it has been observed [66] that helical transition moves toward the nozzle exit. Some researchers [101, 191] compared initially laminar

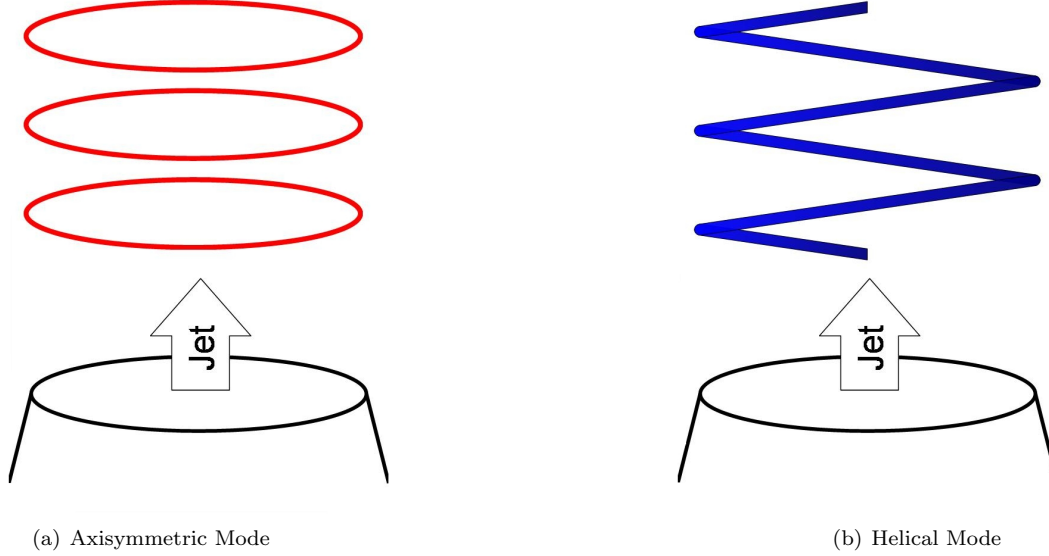


Figure 1.8: Schematic of Dominant Jet Instability Modes

shears to shear layers which were tripped into turbulence in the nozzle and found that the turbulent shear layers transitioned into the helical mode almost immediately. Finally, increasing Reynolds numbers have been observed [73, 101, 276, 398] to move the initiation of the helical mode towards the nozzle exit as well. It has been reported by Zaman and Hussain [403], that these instability modes are sensitive to particular frequencies. The axisymmetric mode favors frequencies with a Strouhal number $St_D = fD/U_e$ of 0.3, while the helical mode is driven for frequencies near $St_D = 0.85$ - where f is the forcing frequency, D is the nozzle exit diameter and U_e is the exit velocity. This frequency dependence has been investigated by other researchers as well.[73, 101, 188]

Compressibility affecting the turbulent structure of a free shear layer was first pointed to by Brown and Roshko [71]. Their experiment looked at large scale structures in a planar mixing layer with variations in flow speed and density. They noted a change in shear layer spreading rate for change in compressibility and ruled out the change in density between the two jets as the source, pointing to a effect only of Mach number. For planar flows the decrease in shear layer growth rate was confirmed by experiments.[86, 154, 322, 347] It was reasoned by Papamoschou and Roshko [287], that the decrease in growth rate was due to increased stability provided by a decreased region of influence at supersonic speeds. Given the parallels between planar mixing layers and the core region of the axisymmetric jet, the trend of decreasing growth rate for increasing convective Mach number was observed in axisymmetric jets.[89, 142, 162, 216]

The stability of supersonic axisymmetric jets was investigated by Tam and Hu [363]. They found three instability modes. The first was the Kelvin-Helmholtz instability which generates into the axisymmetric

mode. This mode was shown to be neutrally stable when the flow was assumed inviscid, but for finite shear layers this mode dominates the transition for Mach numbers below 4.4. The other two modes occurred in a bifurcation. The subsonic wave branch was found never to dominate the flow, while the supersonic wave branch dominated high supersonic flows. Fourgette, Mungal and Dibble [142] investigated this theory experimentally and could not observe the axisymmetric 2-D mode. Gutmark, Schadow and Yu [162] observed that shear layer thickness played a role in which mode was dominant and the helical mode dominates for lower thicknesses while both modes were on par for increasing shear thickness. Gutmark, Schadow and Bicker [161] also discovered that off-nominal supersonic jets exhibit increased growth rates over their perfectly expanded counterparts. They theorized that acoustic feedback from the shocks were interacting upstream at the nozzle lip to energize earlier transitions. Finally, the influence of heating on supersonic jet cores was observed by Lau.[214] Lau found that heating the jet core caused the potential core region to retract, while increasing Mach number caused the core region to extend further downstream.[164]

In addition to theoretical and experimental investigations of the turbulent axisymmetric jet, many numerical studies have also been accomplished. Corcos and Lin [96] used a linear perturbation model to augment their theoretical approach to instability modes. Acton [3] investigated the results of forced jets by Large Eddy Simulation (LES) of the axisymmetric mode and found good agreement to experiment suggesting the initial development of transition was largely influenced by the toroidal structure. Martin and Meiburg [242] used a vortex filament model and also found good agreement with subsonic growth rate. Compressibility on jet structure has also been investigated numerically. Investigators [144, 270] have used Direct Numerical Simulation (DNS) of the near-field of supersonic jets to examine the production of sound waves. And Aupoix [39] investigated turbulence models to improve the prediction of spreading rate reduction for supersonic jets. While this is by no means an exhaustive list of works in the numerical realm, it is meant to illustrate that this area is rich with possibility for further investigations.

In a departure from conventional jets formed by converging-diverging nozzles, Bradshaw [66] used a constant-area tube to look at axisymmetric transition. Additionally, Ferdman, Otugen and Kim [133] used a straight pipe nozzle and found increased turbulence in the jet. Therefore, to increase the turbulence in the core flow of a jet, the characteristics of pipe flow can be utilized. To accomplish this, a long, constant-diameter tube can be formed downstream of the nozzle. This tube produces pipe flow with turbulent intensities in the jet core on the order of those found in the shear layer. Tube lengths which are 50 times the tube diameter are considered fully developed, where the velocity profile is no longer a function of distance traveled down the tube. Shorter tubes produce a jet of developing pipe flow, which feature increased turbulent fluctuations in the jet core, but may still exhaust into the chamber with a top-hat profile.[328, 383]

A simpler approach to create developing pipe flow, is to use an aerodynamic nozzle at the beginning of a constant-diameter tube. The flow exhausting from a constant-diameter tube achieves supersonic conditions through what is suspected to be an aerodynamic nozzle formed by a separation bubble created at the tube entrance in the plenum chamber. Aerodynamic nozzles have been studied previously in annular ejector flows in constant-diameter mixing channels. Predictions of the occurrence of aerodynamic nozzles in ejector flows were initiated by Fabri and Siestrunk [130] and improved by Chow and Addy [82]. It was postulated that the separation regions commonly formed in aircraft inlets, can occur at the right angle formed at the inlet to the constant-diameter tube. Then, that separation region chokes the flow and accelerates it to supersonic speeds. A supersonic jet flow formed by a constant-diameter tube will be studied in this research.[35, 114, 165]

1.2 Plasma

Since most of this dissertation depends on measuring the influence of a jet passing through a plasma field, and since plasma fields are a relatively ethereal topic, this section describes the important properties of plasmas. Some additional plasma topics are covered here to help decipher the current types of plasma undergoing research in the field of turbulence.

A plasma is an ionized fluid. It is considered the fourth state of matter, plasmas typically occur in the gaseous phase where ions, neutral particles (atoms or molecules) and free electrons are unconstrained in their translational motion. The plasmas of interest in this study, ones which can be produced in the laboratory (ruling out thermo-nuclear fusion), are considered electrically quasi-neutral. These plasmas are called quasi-neutral because in the region of interest there is a relative balance in charge between free electrons and ions. However, since the plasma state contains free electrons and ions, the conductance is high (higher than gold in some cases) and a plasma is able to create an electrical circuit and is influenced by electric or magnetic fields. Table 1.1 on the following page summarizes the unique properties of plasmas.[5, 145]

The effect of plasmas on high speed flow is to create free electrons, and to pump energy into the vibrational modes of diatomic molecules. The rotational and translational energy of these molecules remains in equilibrium and thus the flows are considered ‘cold’ as the temperature which defines the random translational motion of the molecules is relatively constant.[5, 145]

$$E_{total} = E_{trans} + E_{rot} + E_{vib} + E_{elec} \quad (1.19)$$

This effect is similar to a highly expanded nozzle. The nozzle expansion produces a rapid drop in temperature as the mean motion of the flow accelerates toward the exit. The rotational and translational motion

Table 1.1: Unique Plasma Properties

Property	Description
Ionized Particles	Charged particles exist in high enough concentration that Coloumb forces effect the gas kinetics.
Thermal Nonequilibrium	The ability of a plasma to maintain non-Boltzman energy distributions by trapping energy in elevated vibrational quantum states. Thermal equilibrium exists in a plasma when translational energy is elevated to near that of the energized free electrons.
Quasi-Neutrality	The charged particles maintain a balance on a local scale.
Electrostatically Ideal	Coloumb forces are typically negligible in evaluating continuum properties.

of the molecules is in equilibrium through the expansion, as each molecule transfers energy between their neighbors through elastic collisions. The transfer of rotational and translational energy between particles is very efficient and energy is transferred effectively after only a handful of collisions. Thus, molecules which are moving quickly are more likely to strike adjacent molecules and transfer energy to them.[5, 145]

However, the vibrational states of these molecules remain in the state the plenum conditions, which was a much higher energy state. The collisional transfer of molecular energy between rotational/translational states and vibrational or electric energy states is inefficient and requires at least an order of magnitude more collisions to transfer energy out of the now elevated vibrational states. The vibrational energy remains trapped in the molecules and cannot be used in flow acceleration, the flow is considered 'frozen' in this state. The effect of a plasma is to elevate the vibrational modes of these diatomic molecules. If the plasma is created in a flow which is supersonic or hypersonic, the length scale required to achieve vibrational equilibrium with the translational and rotational modes is typically longer than the test section. Thus, the flow is similarly frozen.[5, 145]

1.2.1 Thermal Equilibrium

A plasma in thermal equilibrium is marked by 'high' (atmospheric) pressure and high temperature. This type of plasma is referred to as a thermal plasma. Examples of a thermal plasma include lightning and nuclear fusion. In a plasma where pressures are lower, which results in less frequent energy distributing collisions and thus resulting in a disparity between free electron temperature and neutral gas temperature. This temperature disparity in the plasma is called thermal non-equilibrium. An example of this type of plasma is the fluorescent light bulb. The non-equilibrium of molecules may be further segregated into the

translational, rotational, and electric energy modes. Particles can exchange energy with each other through collisions or interaction of Coulomb forces. The particle collisions can be described as elastic inelastic or super elastic. Elastic collisions only involve a transfer of kinetic energy between collision particles. Inelastic collisions involve transfer of kinetic energy into internal energy. Conversely, super-elastic collisions transfer internal energy back into kinetic energy.[145]

Elastic collisions involve a transfer of translational energy where particle momentum is conserved between the particles. An inelastic interaction involves additional transfers of energy into the electric, rotational or vibrational energy state and thus translational momentum is not conserved even though energy conservation applies. It is typically assumed translational and rotational energy are in equilibrium in a plasma and the gas temperature represents both of these particle motions. Non-equilibrium plasma will be the type of plasma used in this research due to the ability to contain the lower gas temperatures in the laboratory.[145]

A plasma is created in a non-charged gas by energizing atoms or molecules into quantum levels high enough for the liberation of an electron. Then through the collision of this highly energized free electron and another molecule (or atom) in a moderately elevated quantum energy state where more electrons are released. Under conducive conditions, this process blossoms in a condition called an electron cascade. Most plasma generation techniques are marked by initially high input energy levels to reach cascade conditions, followed by reduced input energy to maintain a plasma with a well populated free electron concentration.[145]

An equilibrium plasma is one where the gas temperature T_0 is near that of the electron temperature T_e (for most plasmas, $T_e \approx 1eV$ is used for estimation). For a nonequilibrium plasma, the ratio of T_e/T_0 can be as high as 100. In low pressure plasmas, the neutral gas loses heat to the chamber walls faster than the electron gas can transfer heat into it. Gas pressures below roughly 30 torr are needed to provide enough conductive heat losses for static gas plasmas. Above this pressure, a nonequilibrium plasma can be maintained through fluid velocity to increase the conductive heat transfer and to lower the residence time of the gas in the plasma field. The amount of energy transferred into a plasma has an upper bound which can be estimated from Equation 1.20

$$\frac{T_0 - 300[K]}{300[K]} = \frac{E_v(1 - \eta)}{C_p 300[K]} \quad (1.20)$$

where η is the energy efficiency of the plasma process, C_p is the specific heat coefficient at constant pressure, E_v is the specific energy input and T_0 is the gas temperature.[145]

1.2.2 Quasi-Neutrality

One of the qualitative definitions of a plasma is quasi-neutrality. In a localized sense, ions and free electron charges are in balance. When a plasma interacts with its boundaries, the charge balance is no longer quasi-neutral and the fluid is no longer defined as a plasma. For example, when a plasma comes in contact with a grounded (floating potential) wall, the free electrons go to ground and leave the remaining positively charged ions in the fluid. The ions are left behind since the electron thermal velocity is roughly 1000 times faster than the ion thermal velocity, $\sqrt{T_e/m} \gg \sqrt{T_i/M}$. This positively charged portion of the fluid is called the plasma sheath. The thickness of the sheath is typically on the order of three Debye radii, and can only exist if there are ions which have energy which is equivalent to the electron temperature. The Bohm sheath criterion codifies this as $u_i \geq u_B = \sqrt{T_e/M}$, where m is the electron mass and M is the ion mass.[145]

The Debye radius is characteristic length of plasma quasi-neutrality. Large values of the Debye radius (where $r_D \gg R$ R being the characteristic length of change of electron concentration) signify large separations of electrons from the ions and the breakdown of the quasi neutral assumption. Typically the plasmas dealt with in this research can be considered quasi-neutral with $r_D \ll R$. [145]

$$r_D = \sqrt{\frac{T_e \epsilon_0}{e^2 n_e}} = 742 \sqrt{\frac{T_e [eV]}{n_e [cm^{-3}]}} [cm] \quad (1.21)$$

Just as the Debye radius is the characteristic length, the characteristic time scale of the plasma is determined by the Langmuir frequency. The Langmuir frequency is the time required for an electron to travel one Debye radius at the thermal electron velocity to provide charge screening to a perturbation in the external electric field.[145]

$$\omega_P = \sqrt{\frac{e^2 n_e}{m \epsilon_0}} = 5.65 \times 10^4 \sqrt{n_e [cm^{-3}]} [cm] \quad (1.22)$$

1.2.3 Electrostatically Ideal Plasma

In an interaction between two electrostatically neutral particles, particle motion is governed by intermolecular collisions - forces which only become important when particles are in close proximity to each other. The interaction of two charged particles is governed by Coulomb law and affects particle motion over much longer distances than neutral particle collisions. An electrostatically ideal plasma is one in which free electrons and ions travel in straight lines. This description implies the kinetic energy of the particles is much higher than the interparticle potential energy and is neglected. Only the most extreme ionized particle densities can generate non-ideal conditions. These extreme plasmas are not found in nature and are very difficult to contain in the laboratory currently. The assumption of electrostatically ideal plasmas simplifies analysis.

Some of the results provided from this assumption are described next.[145]

Waves and oscillations in plasmas are enhanced compared to neutral gases due to the additional long distance effects of Coloumb forces created by local potential fields. The dispersion relation for electrostatic plasma waves is $\omega^2 = \omega_P^2 + \gamma T_e k^2/m$, where γ is the ratio of specific heats for an electron gas and k is the wave number. In the limit of wavelengths ($2\pi/k$) much higher than the Debye radius, the frequency approaches the Langmuir frequency. For very high frequencies, the phase velocity of the waves approaches the thermal speed of the electrons.[145]

Some common calculations useful in plasma design are provided in this section. Electron conductivity can be used to estimate the electron density.

$$\sigma = \frac{n_e e^2}{m \nu_e n}, \sigma = 2.82 \times 10^{-4} \frac{n_e [cm^{-3}]}{\nu_e n [sec^{-1}]}, Ohm^{-1} cm^{-1} \quad (1.23)$$

Where n_e is the electron density, e is the charge of an electron, m is the mass of an electron and ν_{en} is the frequency of electron neutral collisions. Note when gas pressure is used to calculate reduced electric field E/p it is commonly with the assumption of room temperature conditions. The gas concentration can be calculated from $n_0 [cm^{-3}] = 3.295 \times 10^{16} p [Torr]$. If the gas temperature T_0 is not room temperature, then use n_0 in scaling E or use the following correction $p_{eff} = p T_{act}/T_{room}$. Joule heating can be calculated from the following relation:

$$P = \sigma E^2 = \frac{n_e e^2 E^2}{m \nu_e n}, \quad (1.24)$$

For air at room temperature and a reduced electric field $E/p = 1 - 30 [V/cm Torr]$ the typical similarity parameters are listed in Table 1.2. At a pressure of 5 torr then, $\lambda = 0.06$ mm and $\nu_{en} = 2 \times 10^{10}$ 1/sec.[145]

Table 1.2: Room Temperature Air Plasma Properties, Adapted from Fridman[145]

Property	Value
Electron Mean Free Path	$\lambda p = 3 \times 10^{-2} [cm torr]$
Electron-Neutral Collision Frequency	$\nu_{en}/p = 4 \times 10^9 [sec^{-1} torr^{-1}]$
Electron Conductivity	$\sigma p/n_e = 7 \times 10^{-14} [torr cm^2 / Ohm]$

1.2.4 Treanor Effect

The Treanor effect is important in this study because it describes the temperature distribution which is present in non-equilibrium plasma to be studied. The effect is arrived at by way of a few simplifying assumptions which can be made in the case of plasma which originates from diatomic molecules. It has been

observed that the relaxation of vibrational energy through translation of nearby molecules (for constant pressure) is exponentially dependant on the neutral gas temperature. Additionally, diffusion of vibrational energy is exponentially dependant on vibrational temperature. Therefore, through an Arrhenius-like simplification, the relaxation of vibrational energy into translational energy (VT relaxation) can be neglected for cold nonequilibrium plasmas since vibrational temperatures are much higher than translational temperatures. Additionally, if the diffusion of vibrational energy through vibrational relaxation (VV relaxation) is considered harmonic (anharmonic VV' relaxation is neglected) then the vibrational and translational energy distributions are uncoupled.[145]

The biggest result of these approximations is that the gas is effectively frozen as in nozzle flow and two temperatures describe the condition of the plasma energy state. The neutral gas temperature T_0 describes the cold fluid translational mean property and describes temperature related fluid properties such as viscosity and specific heat. The energy stored in vibrationally excited molecules is then trapped in the vibrational temperature, T_V . Another implication of the Treanor effect is the resulting non-Boltzman temperature distribution, which is now described by the Treanor distribution in Equation 1.25.

$$T_V = \frac{\hbar\omega}{\ln\left(\frac{N_0}{N_I}\right)} \quad (1.25)$$

Where \hbar is Plank's constant, ω represents the dispersion frequency, N_0 and N_I are number of molecules and ions, respectively. The Treanor effect explains the high degree of efficiency in chemical reactions which are stimulated by vibrational excitation of plasma fields. The Treanor effect also explains how vibrationally rich molecules can take energy from molecules which are vibrationally excited (although at a lower state). Since the vibrationally richer molecule is higher in VV relaxation rate than the poorer molecule, the preferred direction of energy transfer is from the poor molecule to the rich molecule. The result of this effect is to enhance the creation of a population inversion, where the majority of molecules are in the vibrationally excited states. This effect additionally explains how molecules are efficiently excited to the point of radiating photons or liberating electrons.[145]

1.2.5 Breakdown Mechanisms

The transition from neutral gas to ionized plasma is referred to as breakdown, from the early observation of capacitive circuits with air gaps discharging in a failure due to overvoltage. Two models provide a description of breakdown: the Townsend mechanism and the spark mechanism. Both breakdown mechanisms are observed in this plasma research effort.

The Townsend Mechanism describes the point at which, through increasing voltage potential across a gap filled with a neutral gas, the non-conducting fluid breaks down - generating a plasma and carrying current. To describe the mechanism, consider a planar gap with cathode and anode in a uniform DC voltage potential of $E = V/d$, where V is the voltage and d is the gap distance. An initial electron near the cathode is liberated and travels across the gap towards the anode. Along its path it collides with a neutral atom or molecule and liberates another electron. Neglecting the electron affinity of electronegative gases and electrons recombining with ions, this geometric expansion implies that each of these initial electrons generates $e^{\alpha d} - 1$ positive ions and free electrons in an electron cascade, where α is the Townsend coefficient. Just as the electrons move to the anode, the positive ions now migrate toward the cathode. Depending on the cathode material properties, the ions which collide with the cathode liberate another electron, producing a secondary electron emission which sustains the plasma. At some point, as the electric field is increased, the electron avalanche is self-sustaining and the gas undergoes breakdown. Empirically, for air the Townsend coefficient predicting breakdown is $\alpha/p = 15[\text{Torr}/\text{cm}]e^{-365[V\text{Torr}/\text{cm}]/(E/p)}$.[\[145\]](#)

The spark breakdown mechanism is a very localized breakdown, as opposed to the Townsend breakdown which fills the entire field. Spark breakdowns occur at higher gap distances and gas pressures than the Townsend phenomenon. In this situation, an voltage across the gap increases faster than the ions can migrate to the cathode - which creates an overvoltage. As a result, secondary electron emission can be neglected and cathode material is irrelevant. The spark begins with a streamer which is a channel of positive ions created in the wake of an electron avalanche caused by the overvoltage. The avalanche is strong enough to stimulate photon radiation which causes additional avalanches nearby. The channel of positive ions grows, creating its own electric field and attracting nearby electron avalanches into it. This channel, called a streamer grows and quickly connects the electrodes to pass high currents and eliminate the overpotential.[\[145, 350\]](#)

Typically, when a neutral atom or molecule becomes excited enough, it will shed a highly energized electron. In a plasma, this explains the high concentration of free electrons and positively charged ions. However, the presence of certain gas elements, such as oxygen, radically alter the plasma initiation process. Molecules with an electron affinity actually attract free electrons and become negatively charged ions. This process enhances the ionization of the gas, as the negatively charged ion has significantly higher collision potential than the free plasma electrons and thus the reaction rate increases in the plasma formation and sustainment.[\[145\]](#)

1.2.6 Plasma Instabilities

A plasma can transition from thermal nonequilibrium into equilibrium through an instability. A transition to thermal equilibrium, with potentially catastrophic consequences can occur at surprisingly low input energies. For this research effort, plasma instabilities need to be recognized and avoided to prevent equipment failure. Plasma instabilities are characterized into two groups, striation and contraction. A striation instability is one which causes alternating light and dark regions in the plasma. A striation does not appreciably affect the plasma properties and will not be dealt with further in this article. A contraction instability causes the plasma to compress into a single filament and can be a problem for the plasmas intended in this research effort. An example of contraction instability is the thermal instability (ionization overheating). This instability phenomenon plays on the Arrhenius-like exponential feedback found in VT relaxation. The feedback loop initiates when a perturbation creates a locally elevated gas temperature. The elevated temperature lowers the local gas density and therefore raises the reduced electric field (E/n_0). The increase in local reduced electric field then raises the local electron temperature which feeds directly into increased vibrational molecular energy. The exponential dependance on gas temperature of VT relaxation rate then transfers vibrational energy into an increased local gas temperature, which closes the feedback loop and drives the system toward thermal equilibrium.[\[145\]](#)

1.2.7 Nonequilibrium Plasma Chemistry

Vibrational excitation of molecules is the most efficient way to stimulate an endothermic chemical process. Roughly 70% to 95% of the energy in the plasma electrons can be transferred into vibrational energy in the molecules found in air. Chemical processes have different activation energies based on which degree of freedom is excited. For example, the energy threshold for dissociation of diatomic Hydrogen by electronic excitation is twice that of vibrational excitation.[\[145\]](#)

Free electrons are typically responsible for the excitation of neutral particles in the plasma. When a free electron collides with a neutral diatomic molecule, it can impart only negligible translational momentum, due to the incredible difference in mass between the electron and molecule. And for many diatomic molecules, rotational motion is rarely affected, as these molecules have no dipole and are difficult to influence magnetically by the imbalance of free electrons in the local magnetic field. Therefore in non-thermal plasmas, it is common to treat translational and rotational degrees of freedom collectively in equilibrium with each other and represent the mean energy distribution by the gas temperature. Electronic excitation of a molecule by collision with a free electron requires a gigantic potential on the part of the free electron and is rare for non-thermal plasmas. Therefore, the influence of free electrons on diatomic molecules is most

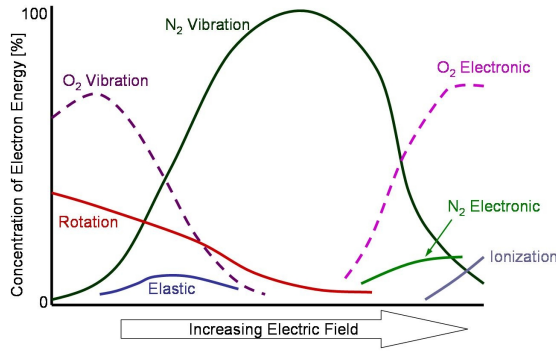


Figure 1.9: Energy Distribution of Excitation for Air, Adapted from Fridman.[145]

easily coupled into an increased vibrational state. Additionally, the relaxation time (time to go from a high energy state to a low energy state) of a vibrationally excited molecule is roughly 10^6 times longer than for an electrically excited molecule, which accounts for the predominance of vibrational non-equilibrium found in frozen nozzle flows and non-thermal plasmas. Figure 1.9 shows the excitation channels for free electrons as they are distributed in the formation of an air plasma. Diatomic molecules in particular, can be vibrationally excited to the point of dissociation to further fuel the ion concentration in plasma generation.[5, 145]

1.3 Plasma Discharges

This section provides a summary of the most common types of plasma discharge used in both industrial and research applications. Multiple plasma discharges are present in this research endeavor.

1.3.1 Glow

A glow discharge is a DC nonequilibrium plasma which is generated between electrodes. It is self sustaining, which means its electron source is provided solely by dissociation in the supplied electric field and is not augmented by electron beams or photon radiation. The glow discharge is self sustained by secondary electron emission from energetic ion collision with the cathode. This plasma experiences the thermal instability and to avoid transition to quasi-equilibrium this plasma is generated in low pressures, usually around 10 Torr. The thermal instability also limits the amount of power supplied. This plasma is common to fluorescent lighting. The glow discharge structure contains small light and dark regions which are not considered plasma due to charge separation where Townsend breakdown and Faraday effects are prevalent near the electrodes. Finally, a large volume of fluorescence is generated across the length of the tube in a plasma called the

positive column. If convective heat transfer is applied through high speed fluid motion, the pressure and applied power can be increased significantly to create a glow discharge for use in aerodynamic experiments. If the glow discharge is confined inside a cylinder of length d_0 , then to maintain a thermal balance yields a relation (Equation 1.26) for electron concentration.

$$n_e = \frac{2uc_p m k_{en}}{e^2 d_0 T_0 (E/p)^2} \quad (1.26)$$

Where in Equation 1.26, u is the flow speed through the cylinder and k_{en} is the rate coefficient for electron-neutral collisions. Turbulence in a glow discharge significantly increases the loss of charged particles by stimulating diffusion of charged particles to the walls of the discharge container. These losses reduce the chance of thermal instability and allow more power to be transferred through the system. Some systems enhance turbulence to increase the power input and stability characteristics of the glow discharge. The primary instability is a contraction of the plasma into a current filament which heats the gas into equilibrium and forms a short circuit. To stably increase the gas pressure to atmospheric conditions, electronegative gas and transonic or supersonic flow speeds must be used. Supersonic flow provides a stabilizing effect on the contraction instability through suppressing the influence of local contractions. Figure 1.10 illustrates the various regions of a glow discharge. [145, 186, 195, 201, 253, 336, 338, 358, 319]

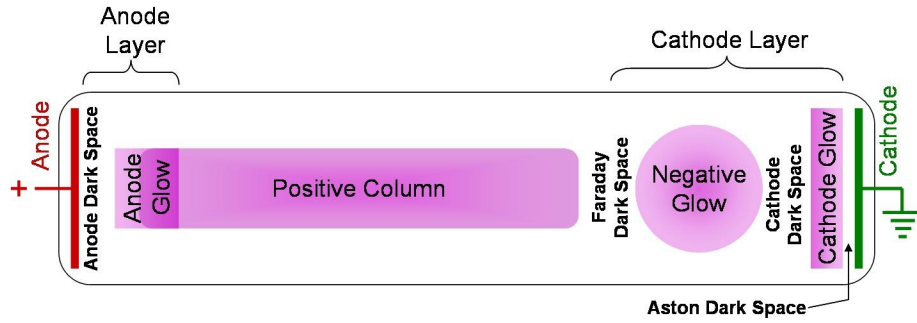


Figure 1.10: Glow Discharge Regions, Adapted from Fridman. [145]

Figure 1.11 shows a glow discharge which was observed during testing. The coordinates x/G and y/G are axial and tangential coordinates, scaled by the electrode gap distance G . All regions described in Figure 1.10 are visible in Figure 1.11 except the negative glow region.

An arrangement of electrodes in a strong magnetic field produces what is called the Penning glow discharge. The Hall effect occurs due to the crossed electric and magnetic fields and generates rotating clouds of electrons. It differs from the glow discharge above in that the Penning discharge has an order

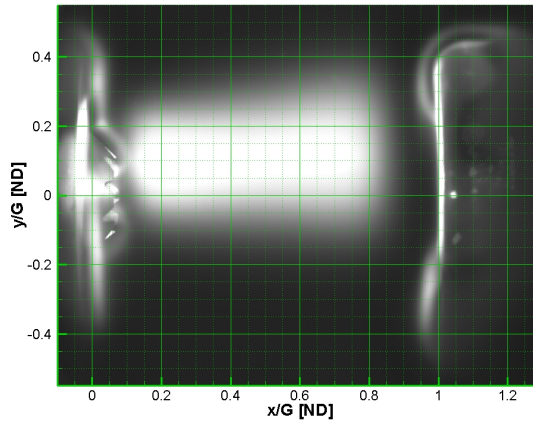


Figure 1.11: Glow Discharge Created During Testing

of magnitude higher electron gas densities. Plasma centrifuges can be created by the Hall effect and by arranging the magnets as a magnetron, cathode material can be sputtered onto other surfaces for thin film deposition.[145, 336, 320, 333]

1.3.2 Arc

Arc discharges are DC thermal plasmas which are self sustaining by thermionic emission (where hot metallic cathode emits electrons from the metal surface) and field electron emission (where a strong electric field emits electrons from a cold cathode through tunneling) from the cathode. Examples of arc discharge plasmas used in lighting include xenon and mercury vapor lamps, which produce positive columns as in glow discharges - except these are quasi-thermal plasmas. Plasma torches (also called arc jets) entrain surrounding flow to generate temperatures near that of the surface of the sun for industrial metal working applications. A special configuration of the arc plasma, called a gliding arc, allows buoyancy to create a traveling arc which begins as a thermal plasma and transitions to a nonequilibrium plasma as it climbs and stretches across gradually increasing gap distances.[145, 251]

Figure 1.12 is an example of an arc plasma encountered during testing. The coordinates x/G and y/G in the figure are the axial and tangential coordinates, respectively, scaled by the electrode gap distance G . When arc plasmas were encountered in actual testing, the plasma generator was turned off to avoid overheating.

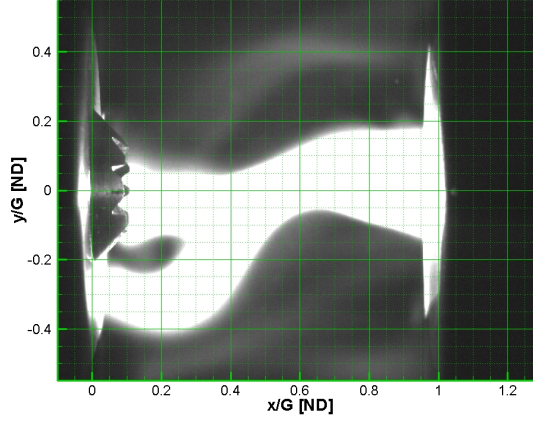


Figure 1.12: Arc Discharge Created During Testing

1.3.3 Corona

Up to this point in describing plasma discharges, the electric field has been constant in space and time. A corona discharge is a plasma with low luminous radiation only near one of the electrodes. To create this discharge, the electric field is nonuniform spatially and may be DC or alternating. Specifically, the electric field must be significantly higher near one electrode. A very high potential difference is required to generate the corona. However, if the voltage difference increases further, the discharge transitions into a spark. This type of discharge is found in the Aurora Borealis as well as on ship masts and near high voltage power lines (known as St Elmo's fire). To create the nonuniform electric field, a common method is through cylindrical electrodes with a large gap (such as power lines or ship masts). Corona discharges are initiated through Townsend breakdown and the subsequent self sustaining electron cascade is through secondary ion-electron emission with the cathode (negative corona) or from streamers (which is a precursor to spark breakdown) for the near-anode discharge (positive corona). A corona discharge can be predicted in air for parallel wires by Peek's Formula: $E_{cr}[kV/cm] = 30\delta(1 + 0.301/\sqrt{(\delta r[cm])})$ where δ is the ratio of air density to sea level standard conditions and r is the electrode radius. Peek's formula is valid for pressures from 0.1 atm to 10 atm and up to 1 KHz in alternating current frequency. To initiate a corona discharge between parallel wires, the following formula is applied $E_{cr} = \frac{V}{r} \ln(\frac{d}{r})$, where V is the voltage potential to be solved for and d is the distance between the wires. Continuous corona discharges are limited to very low currents, but provide a high concentrations of charged particles at atmospheric pressures. To increase the power input without spark breakdown, the corona discharge is pulsed.[145, 201]

1.3.4 Dielectric Barrier

Dielectric barrier discharges (DBDs) are a technique to modify the corona discharge to allow higher input voltages without transition to spark breakdown by application of a dielectric material in the discharge gap. The dielectric material prevents streamers generated at the anode from traveling to the cathode and short circuiting the discharge gap. The dielectric also inhibits DC discharges, making the DBD plasma a frequency driven system in the typical range of 0.5 to 500 KHz. DBD plasmas are used extensively in plasma displays, industrial stack scrubbers and CO_2 lasers. These plasmas can be generated with high input power and at atmospheric pressure. The breakdown phenomenon is through a series of distributed small streamers called microdischarges. Dielectric barriers can be used in a glow discharge configuration at atmospheric pressure when in the presence of only noble gases which lack the electron affinity of electronegative gases to limit thermal instabilities.[145, 126, 41, 337, 43]

1.3.5 Radio Frequency

In general, an oscillating electric field provides more effective ionization than a DC field due to the exponential dependance of ionization rate on electric field magnitude. Radio frequency (RF) discharges can be split into two groups based on pressure. Atmospheric (high) pressure RF plasmas are thermal equilibrium plasmas which are not part of the current research effort interest. For the moderate pressures (roughly 50 Torr) generated in the research facility for this effort, RF plasmas can be generated through inductive or capacitive coupling. A capacitive coupled RF plasma is generated between two electrodes which stimulate an electric field in the gap and produce a plasma. An inductively coupled plasma is created by a coil which creates an electromagnetic field and subsequently a plasma. In either coupling scenario, the power generation system must be in AC resonance with the discharge system - which requires tuning. Inductively coupled plasmas (ICPs) can exceed CCP electron concentrations by an order of magnitude, but are limited to lower pressures where the free electrons are effectively collisionless and involve a coil to generate the plasma vice electrodes. This research effort will focus on generation of capacitively coupled plasma (CCP) based on the available equipment.[145, 251, 393]

In a CCP, the ions may be considered at rest during an oscillation cycle forming an ion network, while the electrons oscillate based on the polarity of the electric field. Electrons for a plasma sheath reside near an electrode during part of the cycle, and vacate that region for the part of the cycle which is referred to as the space charge phase. The alternation of space charges is what completes the RF circuit and generates the plasma in a positive column similar to the DC glow discharge plasma. The CCP electrodes can be covered by a thin layer of dielectric material with low capacitive resistance and not significantly effect the RF plasma

generation. A CCP can be created in two regimes labeled the α and γ discharges respectively. The γ discharge is marked by a luminous region in the positive column, which is missing from the α discharge. The γ regime carries an order of magnitude higher current density and is marked by the influence of secondary electron-electron emissions from the electrodes which are then accelerated by the oscillating plasma sheath. The RF frequency for CCPs at moderate pressure has an upper limit related to the width of the plasma sheath which decreases with increasing frequency. When the mean free path of the electrons (a function of gas pressure) reaches the electron energy relaxation length, the plasma is then considered a low pressure CCP and are out of the range of frequencies generated by the equipment in this research effort. The lower bound of RF discharge is limited by time for an ion to travel across the discharge gap and is usually around a frequency of 1 MHz. A typical frequency used in industrial RF plasma generation is 13.6 MHz, as this frequency is reserved to avoid radio communication interference. Electron densities on the order of 10^{10} are typical for medium pressure CCPs.[145, 255]

1.4 Plasma Flow Control

Using plasmas in flow control can be done through a many techniques. In the first technique, the plasma field can be moved through magnetohydrodynamics. The charged particles in the plasma are accelerated when subjected to a magnetic field. The mean motion of the charged particles entrain the neighboring neutral gas and can be used to produce a significant flow field which is easily directed in different directions. In an interesting experiment by Meyer et. al. [257], a Mach 3 Nitrogen RF capacitively coupled plasma is generated in the divergent section of the 2-D nozzle. The plasma then travels into the constant cross-sectional area test section, sustained by a DC potential applied there. The test section is sandwiched between an electromagnet which can generate up to 1.5 Tesla. The generated magnetic field applies a Lorentz force axial to the flow either with the flow or against it. The decelerating Lorentz force was found to increase density fluctuations in the boundary layer by 10-20%, measured by laser differential interferometry.[320, 201, 202, 338]

Next, some pulsed or sinusoidally driven plasma generation schemes generate a plasma field and allow the thermal characteristics of the plasma expand a pocket of nearby flow to produce a frequency controlled forcing of the flow locally. A DBD plasma is used in a pulsed mode to decrease turbulence across an optical port for a high powered laser as reported in a paper by Zubair et. al. [408]. The turbulence decrease was measured by examining the laser aberrations of a beam which passed through the the port. The aberrations caused by turbulence to laser beams mounted on aircraft looking can compound pointing and tracking and the decrease in turbulence across the window is therefore important. The large scale turbulence

across the window was amplified by forcing at 60 KHz, but was dissipated with a forcing frequency of 30 KHz.[127, 56, 238, 380]

An alternate application of the pulsed plasma for control, is the use of high frequency sinusoidally driven plasmas described by Matlis, Corke and Gogineni [244]. In this application, an AC plasma is generated in a small gap and used as a high frequency anemometer. The plasma volume responds to fluid velocity across the gap in a fashion similar to a hot-wire, but with two times the frequency response of the smallest hot-wire anemometers.

The effect of shock waves by a plasma field has received quite a bit of attention in research. Bow shocks were reportedly weakened when ballistically fired through an RF capacitively coupled plasma in Argon in an experiment by Lowry et. al. [230] They found bow shock standoff distances increased more than 10% with the plasma on measured by holographic interferometry. The increased standoff distance infers a weaker shock and for Lowry et. al. matches with CFD calculations for Argon at the increased temperatures measured in the plasma field.[53, 4, 55, 57, 72, 76, 129, 193, 253, 255, 269]

Finally, a plasma field can be introduced on the surface of a plate, which heats the flow locally to form a low density pocket. This pocket closely resembles a separation bubble, and depending on its shape and forcing frequency, can generate vortices which alter the surrounding flow features to move turbulent transition and delay separation of the boundary layer. Corke and Post [99] used DBD plasma generators on the leading edge of various airfoils and found the leading edge generators delayed stall and increased post stall lift considerably.[203, 43, 186, 126, 195]

1.5 Plasma Effects on Turbulence

In one of the most promising studies on the effect of plasma on turbulence, Appartaim, Mezonlin and Johnson [36] suggest that plasma heating effects alone do not account for the increase in velocity of the shock wave of various halogens in a shock tube experiment they performed. After modeling the shock speed through the tube, heated to the same level as the measured plasma field in their experiment, they found that a reduced kinetic theory turbulence model was required. The use of this model suggests that the plasma process is interfering with the dissociation process in the shock wave as it travels by. The researchers further surmise that this effect may be capitalized on in reducing drag on hypersonic vehicles.

Another potential effect is the use of plasma interacting with a flow to produce turbulence. Roth, Sherman and Wilkinson [320] used an array of glow plasma actuators on the leading edge of a flat plate to prematurely trip a flow into turbulence. The forcing amplitude of the actuators was varied in this research,

causing the transition point to shift upstream for increasing forcing amplitudes at a frequency of 3 kHz. Conversely, Visbal, Gaitonde and Roy [380] used pulsed DBD actuators at the leading edge of a NACA 0015 airfoil to prevent or delay transition and consequently minimize the effects of turbulence.[110]

Research was accomplished recently on the effect of a plasma field on turbulence. In a paper by Grau and Messerschmid, a plasma field was introduced to provide translational heating of a hypersonic free jet to 12000K. The effect of the plasma field was to increase the temperature of the jet, and likewise the viscosity of the flow. The contribution of turbulent viscosity was dwarfed by the thermal effects. Unfortunately, no comparison of the flow with plasma on vice plasma off was accomplished to determine relative individual contribution of these effects.[145, 158]

It is believed that turbulence could influence the subsonic and supersonic free jet in four different ways. First, the increase in gas temperature caused by the plasma field could increase the viscosity of the shear layer. The shear layer should be more affected than the jet core by the plasma heating effects due to lower velocity and longer residence time in the plasma generating electric field. Additionally, research by Menart, et al. [251] indicates the jet core will be difficult for the RF plasma to penetrate and the plasma field will form in the shear region. The higher viscosity would serve to decrease turbulence. The temperature increase to the jet from the plasma heating is yet to be determined and therefore the relative viscosity increase will require experimental investigation.[149, 162]

Research on plasma fields in supersonic and hypersonic flow indicates thermal effects are present which influence shock structure through heating of the flow. The flow heating increases the local speed of sound and therefore reduces the strength of the shock wave. Additionally, the speed of sound is indirectly affected by the molecular weight of the gas mixture. When a molecular gas dissociates, the molecular weight of the gas mixture decreases, which results in an increased speed of sound. In non-equilibrium plasma, the ratio of ionization is usually many orders of magnitude lower than the background gas which results in a negligible change in molecular weight and therefore the primary influence on the speed of sound is derived directly from temperature affects.[145, 5, 384]

Finally, the plasma field in this research is a capacitively coupled radio frequency discharge. The oscillating nature of the plasma field may induce a forcing function into the flow field. Kimmel[199] indicates this forcing function can potentially couple into (or retard) the instabilities associated with the turbulent jet. An investigation into different plasma frequencies can potentially shed light on this phenomenon. In a Moscow State University program review paper by Aleksandrov et. al. [13] in 2005 the last recommendation reads: “New understanding is required of influence of plasma turbulence and moving gas turbulence (at presence of generated plasmas) and vortices on flow characteristics; influence of turbulence and vortices on generated

plasmas characteristics; interaction of generated plasmas with boundary layers; creation of vortices and other disturbances in boundary layers due to presence of charged particles.”[36, 200, 345]

In light of the previous research base on compressible axisymmetric jets, this effort seeks to use the jet flow field for its turbulent properties. Given the current desires to use plasmas in the control of turbulent flows it is important to understand the impact plasma has on turbulence. Then, the existence of plasmas in turbulent compressible flows (e.g. re-entry and hypersonic vehicles) further motivates this research. To better understand the impact of plasma on turbulence in the presence of compressibility, we offer this series of experiments.

Chapter 2

Test Apparati

This chapter describes the equipment used and developed for this research effort. First the facilities which deliver high pressure air and evacuate the test chamber are detailed. Next, the test section is described. Then, the nozzle design procedure is reported along with descriptions of all the nozzle contours as an aid to modeling with computational fluid dynamics. Next, the equipment used to generate seed particles is over-viewed. Finally, the plasma generation system is detailed, along with tuning philosophy and electrode design methodology.

2.1 High Pressure Air

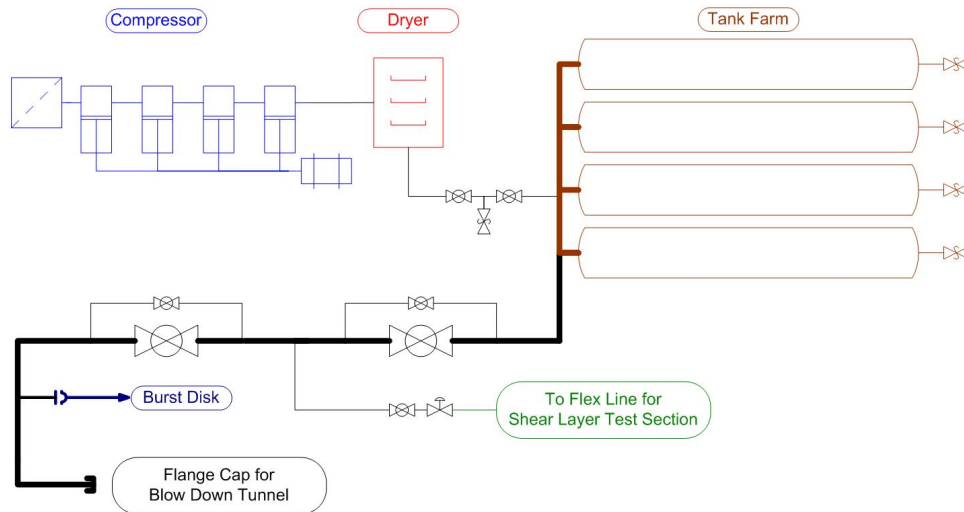


Figure 2.1: High Pressure Plumbing Diagram

To facilitate both the supersonic/hypersonic free shear testing and an upcoming supersonic blow-down wind tunnel, the first task in this research project was to design and build a high and low pressure air handling system. Figure 2.1 is a schematic of the high pressure plumbing and Figure 2.2 on the following page (a) through (c) are photos of the installed system. The system consists of a CompAir Mako compressor,

capable of producing 3.1 Kg/min at . The relative humidity of the compressed air is lowered by a Zander inline drier. Typically, the dew point is roughly $-40\text{ }^{\circ}\text{C}$. The air exits the drier and is stored in 4 cylinders with a total volume of 1.78 m^3 which can contain 255 Kg of air at 12.1 MPa and 293 K. The storage tanks are certified to 16.9 MPa and have pressure relief valves installed, which are set to 16.9 MPa. The compressor cut-off is set to charge the system to a maximum of 12.1 MPa and the system is designed with an additional pressure relief valve set to 13.8 MPa in the compressor shed. The compressed air enters the laboratory through a series of 7.62 cm Schedule 160 steel pipes, designed to handle the supersonic blow down facility mass flow rate. Two large gate valves are in series, one for flow control (e.g. on/off) and one for rough pressure regulation. Additionally, a burst disk is installed (which exhausts outside of the building safely upward) in the last section of pipe and is designed to be replaced based on the operating pressure of the installed test section. That section of pipe is currently open, awaiting installation of the blow-down facility later this year. To run the free shear jet experiments, a small Tescom regulator is threaded into a tap through the larger piping. Since the system is designed for a much larger wind tunnel, a fully charged system lasts through about a month of testing in the vacuum chamber configuration.



Figure 2.2: High Pressure Air Delivery System

2.2 Vacuum System

The test section is evacuated through 6 m of 20.32 cm schedule 80 PVC pipe by a Kinney KT-300 rotary piston vacuum pump. The PVC piping has pressure relief plate to prevent damage in the event of vacuum pump failure or other over pressure events. Figure 2.3 on the next page (a) and (b) show the pressure relief plate (and chamber vent valve) and the vacuum pump installed in the compressor shed, respectively.[\[24\]](#)

The vacuum pump is able to draw the system down to 100 mTorr with no flow through the chamber valve or the nozzle valve. Using the $M=3.8$ converging-diverging nozzle, the vacuum pump was run with varying mass flow rates and chamber pressure was found to be linearly dependent on mass flow until 4 g/s.

At mass flow rates higher than 4 g/s, the chamber pressure switches to a quadratic curve which was not investigated for this experiment as the chamber pressures are outside the region of interest. Figure 2.3 (c) shows the results of the mass flow experiment and the curve fit which was used in nozzle design in the next section. The chamber pressure curve is approximated by Equation 2.1.

$$P_{chamber}[torr] = 5165.1(\dot{m}[Kg/s]) + 1.1164 \quad (2.1)$$

The performance of the vacuum pump was improved significantly by open-loop cooling from the building tap water and monitored in the lab by means of a remote reading bulb thermometer with 4.6m long capillary. Previously, the vacuum pump oil temperature was controlled by a small closed-loop water chiller circulating through the cooling jacket of the vacuum pump. The closed loop system was unable to keep up with the thermal demand of the vacuum pump which allowed the oil temperature to rise and significantly degraded the performance of the vacuum pump. The result was rising chamber pressures for fixed mass flows during testing. The open-loop cooling and thermal monitoring allowed for continuous running and stable chamber pressures for these experiments.

2.3 Test Section

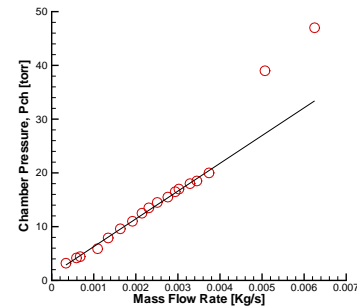
The test section is a cube (30.48 cm per side) made of 2.54 cm thick Plexiglas. Optical access is provided through 4 glass windows 15.24 cm in diameter and 1.91 cm thick. One face of the test section allows the nozzle and plenum to slide along the flow axis. The opposite face is mated to the vacuum system. The bottom window was replaced with a Plexiglas disk with threaded brass rods inserted to allow the electrical



(a) Pressure Relief Plate and Vent Valve



(b) Kinney KT-300 Vacuum Pump



(c) Chamber Pressure for Varying Mass Flow Rates

Figure 2.3: Vacuum Pump System

connections needed for various plasma generating electrodes. Figure 2.4 shows a CAD model of the test section.

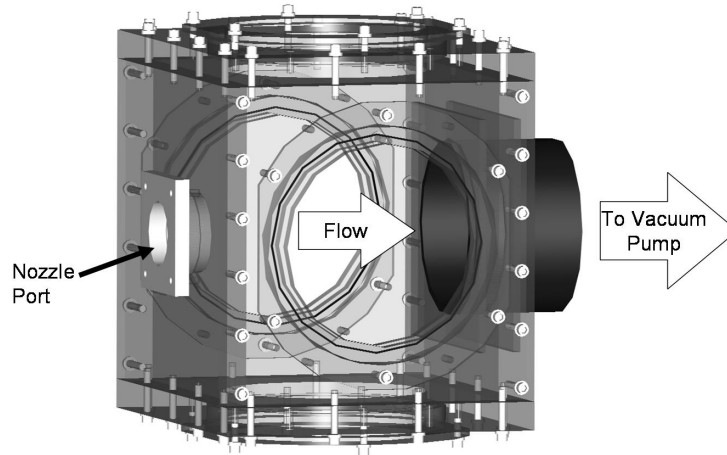


Figure 2.4: Test Section

The plenum section is bored out of the center of a 6.99 cm diameter Aluminum cylinder. The nozzle is bolted onto one face of the plenum. A valve arrangement is threaded into the opposite end of the cylinder to allow seeded or un-seeded flow into the plenum and to monitor plenum pressure. The high pressure air system is connected to the seeder to supply the test section with air which is low in water vapor and dust particles.

Additionally, testing in pure gases such as Nitrogen and Argon was accomplished by simply connecting a compressed gas cylinder to the plenum section with a regulator. Chamber pressure can be further adjusted by means of a vent valve located downstream of the test section, shown in Figure 2.3 (a).

2.4 Nozzle Design

The nozzle section comprised of six separate pieces which mated together and were joined by four 20.32 cm long hex head cap screws, as illustrated in Figure 2.5 on the following page. The nozzle section slid into the test section through a nylon block and was able to adjust the gap distance between the cathode and anode between testing. During testing, the nozzle section was bolted into place and the gap distance was measured (under vacuum to account for any flexing under load). The first piece of the assembly was the mating section. This 6061 aluminum alloy section allowed threaded 1.27 cm NPT brass pipe to be connected for air delivery as well as a block to join each of the pieces of the nozzle section together and to mount the

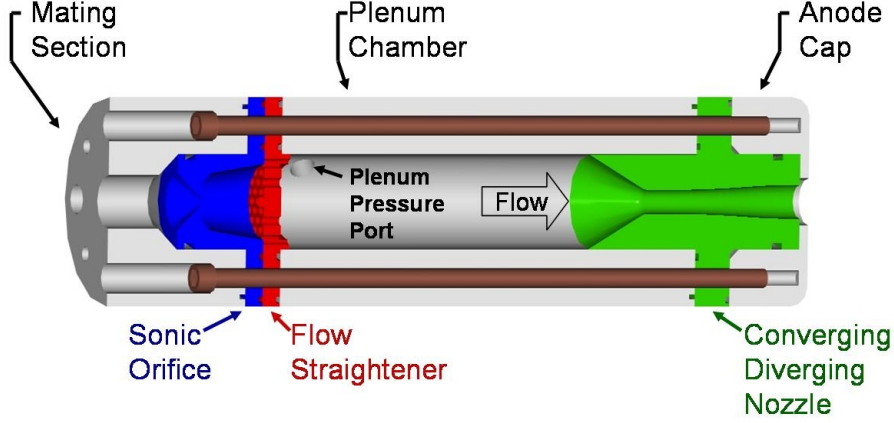


Figure 2.5: Cross-Sectional View of the Nozzle Assembly

nozzle section to the table. The 10.16 cm wide copper flashing was connected to the mating section as well, to provide the anode grounding.

The next section slid into the mating section and provided mass flow regulation through a small sonic orifice and was labeled the sonic orifice. Preliminary test results suggested particle seed concentration was severely restricted when using a ball valve to regulate the mass flow. As the ball valve closed, the gap between the ball valve and the valve wall decreased to the order of the seed particle diameter and a majority of the seed particles were removed from the flow by collision with this gap. To eliminate this problem, a series of axisymmetric sonic orifices were designed to provide mass flow regulation keeping the seed particles contained in the flow. The contour of the section leading up to the orifice began as a 45 degree incline, followed by an elliptical arc represented in Equation 2.2, where D^* is the throat diameter. The resulting elliptical arc segment was then rotated to the correct reference frame.[8, 46, 205, 220, 297]

$$r_{ell} = \frac{\sqrt{3}D^*}{4} \sqrt{1 - \frac{4x_{ell}^2}{D^{*2}}}, \quad 0 \leq x_{ell} \leq 1.30D^* \quad (2.2)$$

Using the predictions of extremely underexpanded jets, the normal shock location was predicted to be between 1.9 mm to 10.1 mm downstream of the sonic orifice for the anticipated test conditions. Two sonic orifice diameters were utilized in this experiment. For the 8-9 torr experiments, a 2.52 mm diameter orifice provided an estimated mass flow rate of 1.1 g/s. For the 5 torr experiments, a 1.50 mm diameter orifice was used with a mass flow rate estimated at 0.6 g/s.[79, 100, 221, 283]

The remainder of the ram plug was designed to mate the the next section and to provide enough clearance for the underexpanded jet to reach subsonic conditions prior to the flow straightener. Both the ram plug and

flow straightener sections were designed in AutoCAD 2005 and fabricated by stereo lithography in the 3D Systems Viper Stereo Lithography Apparatus from Accura SI 40 resin in the Ford Concurrent Design and Manufacture Lab lab in the University of Illinois, Urbana-Champaign’s Mechanical Engineering Laboratory.

The flow straightener was designed to provide relatively uniform flow into the plenum chamber and to eliminate any spurious large particles. Based on some research into particle sorting devices and preliminary test results, it was hypothesized that large particles passing through an underexpanded jet would travel down the center of the jet and would pass almost undisturbed through the shock produced in the resulting underexpanded flowfield. Therefore, in an attempt to eliminate these large particles, a cone shaped spike was placed in the center of the flow straightener to provide an impact point for those large particles. The base of the spike also served as a convenient location to place a thermocouple to measure plenum temperature. The thermocouple wire was fed through a small capillary to the exterior of this section and leaks were sealed with vacuum grease.[240, 279]

The flow straightener mated directly to the plenum chamber, which provided a 15.24 cm long, 3.18 cm diameter long interior cylinder made of 6061 aluminum alloy for the flow to be conditioned prior to acceleration through the converging-diverging nozzle. A hole was taped into the side of the plenum chamber to provide access to a Pirani style ConvecTech Model CVT-275-101 pressure transducer from Duniway Stockroom Corp.

The converging-diverging nozzle section then mated to the plenum chamber and was also constructed out of Accura SI 40 resin using stereolithography which is advertised to provide build tolerances of ± 0.1 mm. The nozzle contour began with a 45 degree slope from the wall of the plenum chamber, transitioning to an ellipse to meet with the throat (see Equation 2.2). The throat was a constant diameter section one throat diameter in length. Next the diverging section was designed using NOZCS software developed by Dr. A. Addy while at the University of Illinois, Urbana-Champaign and modified by Dr. M. Samimy at The Ohio State University. This method of characteristics routine produced an initial expanding region and then proceeded to align the flow and cancel any reflected expansion waves. The diverging section was based on an inviscid flow assumption and was corrected for by increasing the desired exit Mach number to counter the growth of the boundary layer and its resulting effective decrease to the contour radius. The results from the method of characteristics code were curve fit to a 10th order polynomial to allow for evenly distributed points along the contour, shown in Equation 2.3. Note that D^* was the throat diameter. Table 2.1 on the next page lists the input parameters used to create the nozzles built for this experimental investigation.[297]

$$\frac{r_{div}}{d^*} = \frac{1}{2} + \sum_{i=1}^{10} a_i \left(\frac{x_{div}}{D^*} \right)^i \quad (2.3)$$

Table 2.1: Nozzle Contour Parameters

d_{exit} [mm]	d^* [mm]	$2r_{cw}/d^*$ [ND]	M_{geom} [ND]	l_{DIV}/d^* [ND]	Divergent Section Polynomial Coefficients		
					a_1	a_2	a_3
					a_4	a_5	a_6
					a_7	a_8	a_9
					a_{10}		
9.52	8.78	50	1.40	1.73	1.926×10^{-3}	-9.240×10^{-3}	7.522×10^{-2}
					-1.456×10^{-1}	1.564×10^{-1}	-9.857×10^{-2}
					3.722×10^{-2}	-8.316×10^{-3}	1.016×10^{-3}
					-5.234×10^{-5}		
11.29	7.97	99	2.20	6.00	-4.382×10^{-3}	1.820×10^{-2}	-1.571×10^{-2}
					9.462×10^{-3}	-3.216×10^{-3}	6.513×10^{-4}
					-7.978×10^{-5}	5.781×10^{-6}	-2.280×10^{-7}
					3.772×10^{-9}		
15.66	15.17	50	1.30	1.37	1.505×10^{-3}	-1.036×10^{-2}	1.068×10^{-1}
					-2.774×10^{-1}	4.004×10^{-1}	-3.397×10^{-1}
					1.730×10^{-1}	-5.217×10^{-2}	8.607×10^{-3}
					-5.996×10^{-4}		
16.02	15.17	50	1.40	1.73	1.926×10^{-3}	-9.240×10^{-3}	7.522×10^{-2}
					-1.456×10^{-1}	1.564×10^{-1}	-9.857×10^{-2}
					3.722×10^{-2}	-8.316×10^{-3}	1.016×10^{-3}
					-5.234×10^{-5}		
20.76	20.29	5	1.25	0.72	-4.017×10^{-3}	2.073×10^{-1}	-8.899×10^{-1}
					2.482	-4.483	5.210
					-3.865	1.766	-4.518×10^{-1}
					4.946×10^{-2}		

During preliminary investigations, the initial radius of curvature (r_{cw} in Table 2.1) was found to be set too low and the resulting flowfield was measured to be still accelerating after exiting the diverging section of the nozzle. Several iterations on nozzle designs were constructed and investigated until uniform unaccelerating flow at several Mach numbers were achieved. Additionally, the uniform subsonic flow condition was achieved by using a rather large throat diameter converging-diverging nozzle. This technique was described by Pope [297] and the resulting flow was confirmed subsonic at the exit, through particle image velocimetry and molecular tagging velocimetry. The final design contours are presented in Figure 2.6 on the following page.

Chosen from preliminary experiments, another nozzle design was created for this study. The ‘nozzle’ was created from a constant diameter section to produce the increased turbulence found in straight pipe flow. The constant diameter was 9.52 mm and the section was 12.70 cm long. Varying subsonic and supersonic flow speeds were achieved by changing the plenum pressure through the use of a ram plug with 1.50 mm diameter orifice in combination with some ball valve regulation. The addition of the ram plug allowed the ball valve to effectively throttle the plenum pressure without significant particle elimination. To directly compare the effects of the straight pipe flow created from this constant area ‘nozzle,’ a converging-diverging

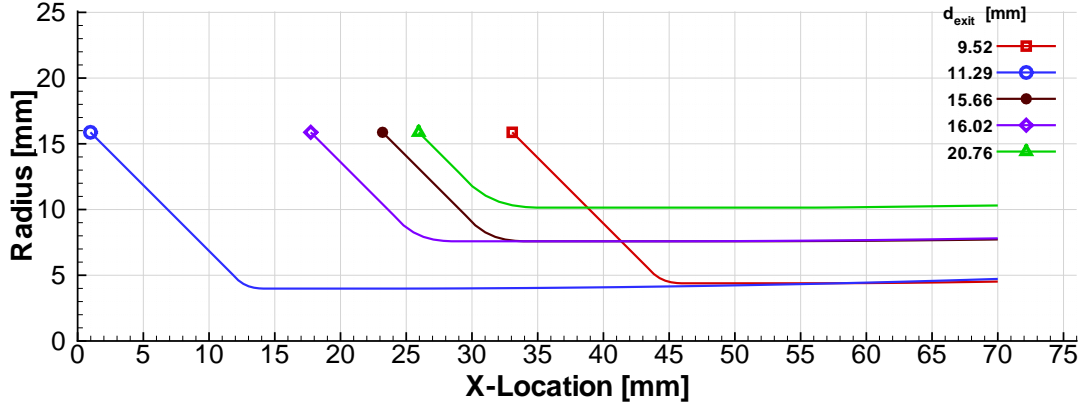


Figure 2.6: Nozzle Contours

nozzle with an exit diameter of 9.52 mm was tested at the baseline pressure ratio and is discussed further in Chapter 4.

The flow exhausting from a constant-diameter tube achieves supersonic conditions through what is suspected to be an aerodynamic nozzle formed by a separation bubble created at the tube entrance in the plenum chamber. Aerodynamic nozzles have been studied previously in annular ejector flows in constant-diameter mixing channels. Predictions of the occurrence of aerodynamic nozzles in ejector flows were initiated by Fabri and Siestrunck [130] and improved by Chow and Addy [82]. It was postulated that the separation regions commonly formed in aircraft inlets were occurring at the right angle formed at the inlet to the tube used in this experiment. Then, that separation region chokes the flow and accelerates it to supersonic speeds.[?, 114, 165]

The final assembly of the nozzle section was the anode cap. This was a cylindrical cap, constructed of 6061 aluminum alloy which slid over the diverging portion of the converging-diverging nozzle and had threaded holes for the cap screws to fasten the entire assembly together. The steel cap screws additionally provided the needed electrical connection to ground the anode for plasma generation.

2.5 Flow Seeding

Preliminary test results suggested that standard olive oil atomizers would not produce small enough particles. To counter this problem, the flowfield was seeded with a Condensation Monodisperse Aerosol Generator (CMAG) model 3475 produced by TSi Inc. The CMAG uses atomized NaCl crystals (nominally 10-100nm in diameter) as a condensation source for heated DEHS oil vapor. The particle size can be adjusted by

Table 2.2: Condensation Monodisperse Aerosol Generator Settings [25]

		Case A	Case B	Case C
NaCl Concentration	[mg/l]	200	20	20
Total Flow Rate	[l/h]	280	280	280
Saturator Flow Rate	[l/h]	280	280	280
Screen Bypass Flow Rate	[l/h]	0	0	0
Saturator Temperature	[°C]	300	300	300
Reheater Temperature	[°C]	140	140	170
Predicted Particle Diameter	[nm]	100	600	1000
Measured Geometric Mean Diameter	[nm]	< 500	651	929
Measured Geometric Standard Deviation	[ND]	–	1.19	1.28

concentration and flowrate of the airborne salt crystals, as well as through varying the temperature of the oil vapor and the condensation chimney.[25, 293]

Three settings were used to verify the particle size distribution against the results from the manufacturer. To validate the particle size distribution, a test was performed with the assistance of Jongmin Lee and Dr. Yuanhui Zhang of the Department of Agricultural and Biological Engineering at the University of Illinois, Urbana-Champaign. The settings listed in Table 2.2 were used to generate particles from the CMAG which were captured and analyzed with an Aerodynamic Particle Sizer (APS) model 3321 from TSi Inc. Figure 2.7 (a) through (c) show the particle size distributions of the three cases. Note the APS 3321 only measured particles with diameters larger than 500 nm and therefore Figure 2.7 (a) can only confirm the absence of larger particles. The mean geometric diameter and geometric standard deviation for cases B and C are summarized in Table 2.2 and compared to the results from the TSI manual.[25]

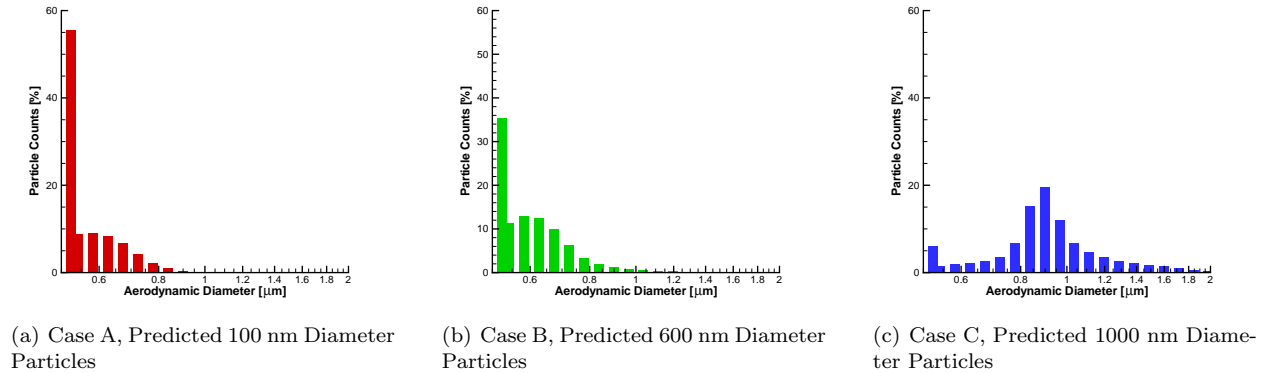


Figure 2.7: Particle Size Distributions Measured with the Aerodynamic Particle Sizer, APS-3321 from TSi

The CMAG 3475 was shipped with two output ports, one collected particles from the center of the condensation chimney and the remaining output particles were collected in the second output port. The manufacturer recommends discarding the seed particles from the secondary output to reduce the variation

in particle size. The CMAG 3475 was modified to combine the output from both ports to increase the number of seed particles and to prevent the loss of seed particles from a pressure differential across the output ports.[25]

Given the resulting increase in geometric standard deviation, which was expected from the modification to the CMAG 3475, excellent agreement was achieved in this validation experiment, therefore the mean particle diameter provided from the manufacturer is believed accurate. Under the settings used for this experiment, the CMAG is estimated to produce quasi-monodisperse seed particles with an estimated mean geometric diameter of 100 nm, which corresponds to Case A in Table 2.2. Additionally, to perform a study on the effect of particle size on the accuracy of flow measurement in rarefied flow, the settings from Case C were used, resulting in a measured mean geometric diameter of $0.93 \mu\text{m}$ with geometric standard deviation of 1.28.[25, 293]

2.6 Plasma Generation

The plasma generation system consisted of surprisingly few components. Most of the system monitoring was provided by the Dressler Cesar 1350 RF generator and accompanying Dressler VarioMatch VM-5000W automatic impedance matching network. The RF generator produced up to 2 KW of power at 13.56 MHz and is commonly used in electroplating and for the semiconductor industry. The generator actively monitored the system impedance and can automatically control the impedance matching network.[33, 34]

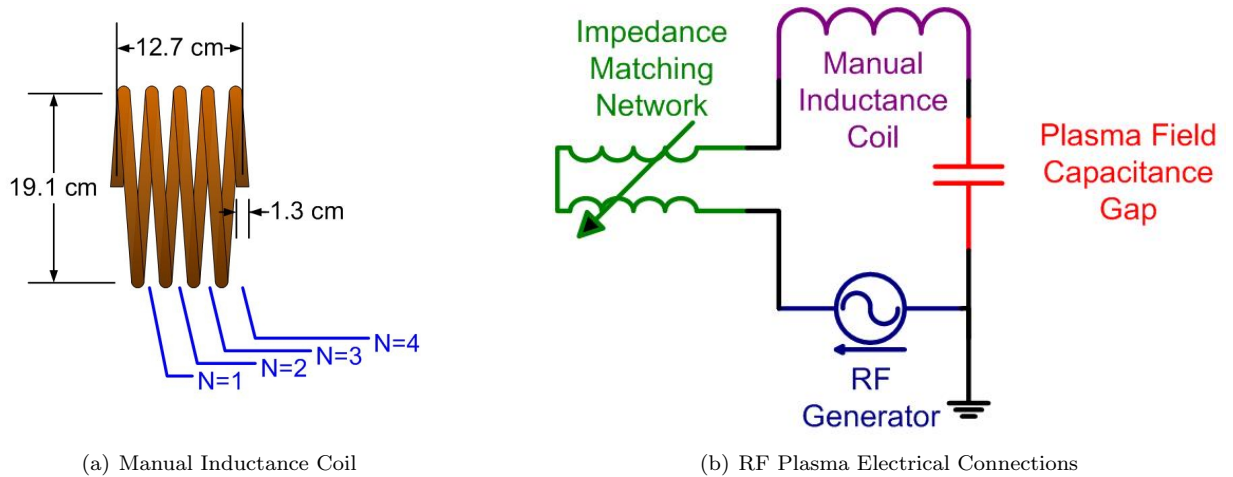


Figure 2.8: Plasma Generation Components

Impedance matching was critical in RF plasma generation, as reflected power in the transmission lines drastically reduced the power available to the electric field for plasma sustainment. Typically, to generate

a plasma the impedance matching network was augmented with an additional inductance coil. The coil was fashioned from 2.4 m of 1.3 cm ID copper tube. The coil was made of 4 turns with a diameter of 19.1 cm and a total length of 12.7 cm. The inductance of this coil was adjusted by using large battery clips to select the number of turns in which current can pass through. Figure 2.8 (a) is a schematic of the manual inductance coil. The greater the number of turns available increases the relative inductance. When the automatic inductance matching has reached its maximum or minimum capacity, the plasma generator was switched off and the number of turns selected on the manual coil was increased or decreased, respectively. Equation 2.4 was the calculation for inductance of a simple coil.

$$L[H] = \frac{\mu_o \mu_r N^2 \pi r^2}{l} \quad (2.4)$$

Inductance, L , increases with the number of turns N and with the radius of the turn r , while decreasing with the length of the coil l . The two factors μ_o and μ_r are functions of the winding material and the magnetic properties of the material which the coil is wrapped around. For a copper coil in air, the μ parameters are constant. Table 2.3 shows the relative inductance $L/\mu_o\mu_r$ available for each turn of the inductor.

To create plasma, the RF generator was connected to the impedance matching network with a RG-393 semi-rigid cable and a serial cable for automated impedance balancing. The variable impedance network was then connected to the manually tuned inductance augmentation coil with 10.2cm wide copper flashing. Electrical power at

Table 2.3: Relative Inductance of the Manual Coil

N [ND]	l [cm]	$L/\mu_o\mu_r$ [m]
1	3.2	28.8
2	6.4	57.5
3	9.5	86.2
4	12.7	114.9
For a coil of $d = 19.1$ cm with $l = 3.2$ cm/turn		

13.56MHz is transmitted by skin current, which required transmission lines to have at least 4cm of cross sectional width. The copper flashing provided the lowest impedance connection for RF power transmission and was recommended by the manufacturer for electrical connection to the plasma cathode and from the anode to the ground. The connection between the RF generator and the matching network used RG-393 cable and was already tuned for that connection. The output of the manual coil was then connected to the cathode in the test section. The anode was then grounded by a run of copper flashing to a true earth ground rod installed through the floor of the laboratory. Figure 2.8 (b) is a schematic of the electrical connections for RF plasma generation.[33, 34, 308]

To minimize the risk of electrical contact to the exposed metal required to generate the plasma field, the electrical connections were barricaded with a partition during operation. Additionally, only personnel re-

quired for the test are present in the lab while plasma generation equipment is in operation. Everyone present in the lab during plasma operation was instructed on the risks of contact with exposed electrical connections and the procedures for emergency shutdown and injury procedures prior to the start of testing.[33, 34]

Tuning of Optimal Plasma Fields

To achieve the best possible plasma field, the following procedure was used. First, a continuity check was accomplished to verify the copper flashing was not grounded out on nearby metal surfaces and that the electrical connectors were properly attached. The continuity check involved drawing the test chamber down to 500 mtorr with all valves closed (this also served as a leak check). Then an α -discharge plasma field was created. These plasmas were easy to create, using only 5 Watts of forward power. The quality of the plasma field was verified visually with indications of strong visible emission. Additionally, two criteria were verified. First, the bias voltage, measured by the plasma generator was confirmed to be over 5 Volts. Next, the reflected power was confirmed to be 1 Watt or less.[308]

After the continuity check, test conditions were set in the chamber - with plenum pressure set to the desired flow conditions and measured real time by the Pirani style ConvecTech Model CVT-275-101 pressure transducer from Duniway Stockroom Corp. The pressure measurement was displayed on a Terranova Model 906A Convection Gauge Controller also from Duniway Stockroom Corp. The chamber pressure was set at 5, 8 or 9 torr depending on the test and also measured by a separate CVT-275-101 pressure transducer and displayed on a Terranova Model 907 Hybrid Capacitance Diaphragm Gauge and Convection Gauge Controller. For these chamber pressures, a γ -discharge could be generated by setting the forward power control on the Dressler Cesar 1350 RF generator. Typical settings were between 50 and 150 Watts, increasing for chamber pressure and electrode gap spacing. After a plasma field was ignited, the field was examined for stability, uniformity and symmetry. The goal was to produce a uniform and symmetric (about the centerline of the jet) visible emission between the cathode and the anode. It was required that the plasma not transition into an unstable thermal mode such as an arc discharge. If the plasma emission did not reach the entire distance from the cathode to the anode, the power was incrementally adjusted to achieve the maximum plasma volume in the electrode gap. Note that the typical behavior of the plasma was to begin as a cathode layer and grow with a positive column towards the anode with increasing forward power. After plasma ignition, reflected power was monitored continually. The requirement achieved in all the testing was for 0 Watts reflected power. At some points during the increase in forward power, some minor adjustments were required in the tune or load capacitors to null out reflected power with matched impedance. Only one setting was used on the manual augmentation impedance coil, with all four turns being utilized (the

electrical connectors were attached to opposite ends of the, providing maximum impedance).[145, 308]

Forward power was increased until hints of instability appeared, the first signs of instability were typically asymmetries on the cathode which grew into visible waves which traveled toward the anode. At this point, the power was reduced slightly to eliminate the plasma waves. If the waves were left uncountered, they would transition to an arc later during testing. As chamber pressure increased the margin between power required to start the plasma field and the power of unstable transition shrank. At a gap space of 60 mm, the crossover for these two power levels occurred at 10 torr - requiring a smaller electrode gap to reach higher pressures.[145, 308]

2.7 Electrode Design

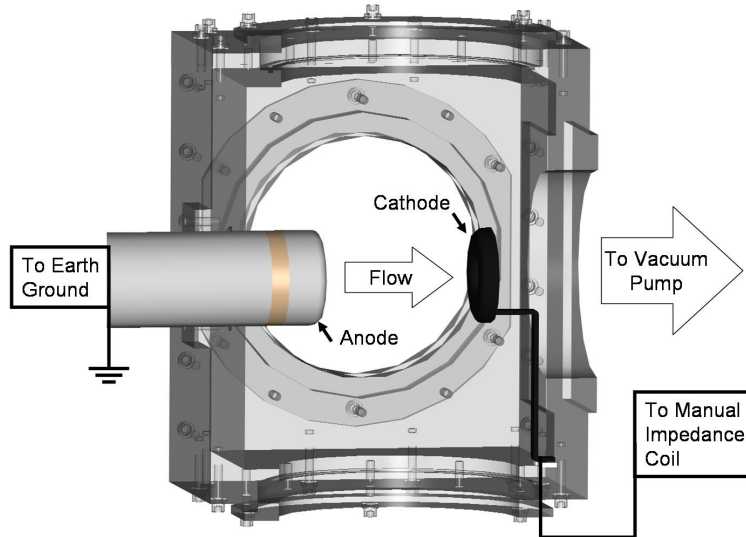


Figure 2.9: Cross-Sectional View of Anode and Cathode Installed in Test Section

The design of electrodes used in this experiment were based on a series of variations in preliminary testing. The arrangement settled upon was to utilize a cap covering the nozzle as the anode and allow the jet to exhaust through a semi-torus energized as the cathode. Desired features in this arrangement included:

- Flat surfaces on the cathode and anode face, to mimic efficient capacitors.
- Rounded edges to prevent arcing and corona discharges, making the plasma field more stable.
- Electrical connections easily passed into the test section, with minimal opportunity for vacuum leaks.

- Cathode position easily changed to vary the gap spacing between cathode and anode, a critical parameter in optimum plasma discharge.
- Plasma field concentrated in the shear layer of the jet to provide maximum effect to the turbulence in the shear layer.

Figure 2.9 on the preceding page details the cathode and anode in the test section.[145, 308]

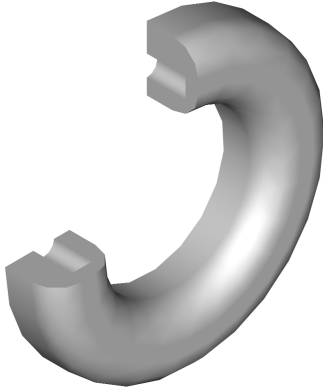


Figure 2.10: Cross-Sectional view of Semi-Torus Cathode

The cathode was a 6061 aluminum alloy semi-torus formed from a disk 7.0 cm in diameter and 1.9 cm thick. A 3.8 cm diameter hole was drilled through the center for the jet to flow through. The face pointing towards the cathode was rounded with a circular bevel of 0.6 cm. Figure 2.10 is a cutaway view of the cathode, showing the rounded face. The cathode was secured to the test section with a frame constructed of fiberboard and epoxy. The frame was designed to prevent anode vibration, as the vacuum pump provided minor excitation to the test section. Additionally, the frame was constructed out of non-conducting materials to eliminate arcing sources. The semi-torus was electrically connected to the test section wall through a 3.2 mm thick piece of 6061 aluminum alloy 1.9 cm wide, which was formed to avoid sharp angles to minimize corona discharges. This

aluminum stem was secured to the floor with threaded rod 6.4 mm thick. Sandwiched between the foot of the aluminum stem and the test section floor was a 3.2 mm thick piece of Macor ceramic to prevent melting of the plexiglas on the floor of the test section, should the cathode inadvertently become hot. The face of the semi-torus was coated with two layers of Boron Nitride, a dielectric paint, to prevent oxidation and arcing. The Boron Nitride was then coated with two coats of high temperature flat black spray paint to protect the Boron Nitride, which was easily scratched, and to reduce reflections as the Boron Nitride coating was white. After the electrical connection was secure in place, the stem and aft section of the semi-torus were coated in RTV to minimize corona discharges and to prevent arcing. The RTV was found to be very effective in reducing plasma fields from forming away from the gap between the anode and cathode. These plasma fields became strong enough to divert the entire plasma away from the desired location at pressures over 6 torr.[145, 308]

The anode was formed providing a grounding plate to the aft end of the nozzle assembly. The anode cap on the front of the nozzle was electrically connected by four 20.32 cm long steel cap screws, which joined the grounding plate and the anode cap. Great care was taken in shielding the copper flashing by enclosing the flashing in 10.16 cm diameter PVC pipe for most of the run from the grounding plate to

the grounding rod in the laboratory floor. Inadvertent contact between the grounding line and any metal surfaces, resulted in significant increases in reflected power from mismatched impedance in that portion of the circuit. In portions of the grounding line which were fatigued by repetitive bending, fractures developed which were readily apparent in increased reflected power, due to the interruption of eddy currents. Caution was exercised near the grounding plate to minimize bending and periodically, that portion of the grounding line was replaced with fresh copper flashing. The anode cap was left uncoated, as only the cathode was discovered to undergo oxidation.[145, 308]

A modified anode was designed to focus more plasma energy near the exit of the jet. The anode was formed from the conventional flat faced anode described above, by milling a cone segment which came to a lip at the opening drilled for the jet exit. The modification was then altered by filing 8 grooves into the lip to produce a weak corona discharge in the non-uniform electric field formed in the serrations. The modification to the anode was labeled the serrated conical feature. Figure 2.11 is an external view of each anode design clearly showing the serrations of in the conical lip.[145, 308]

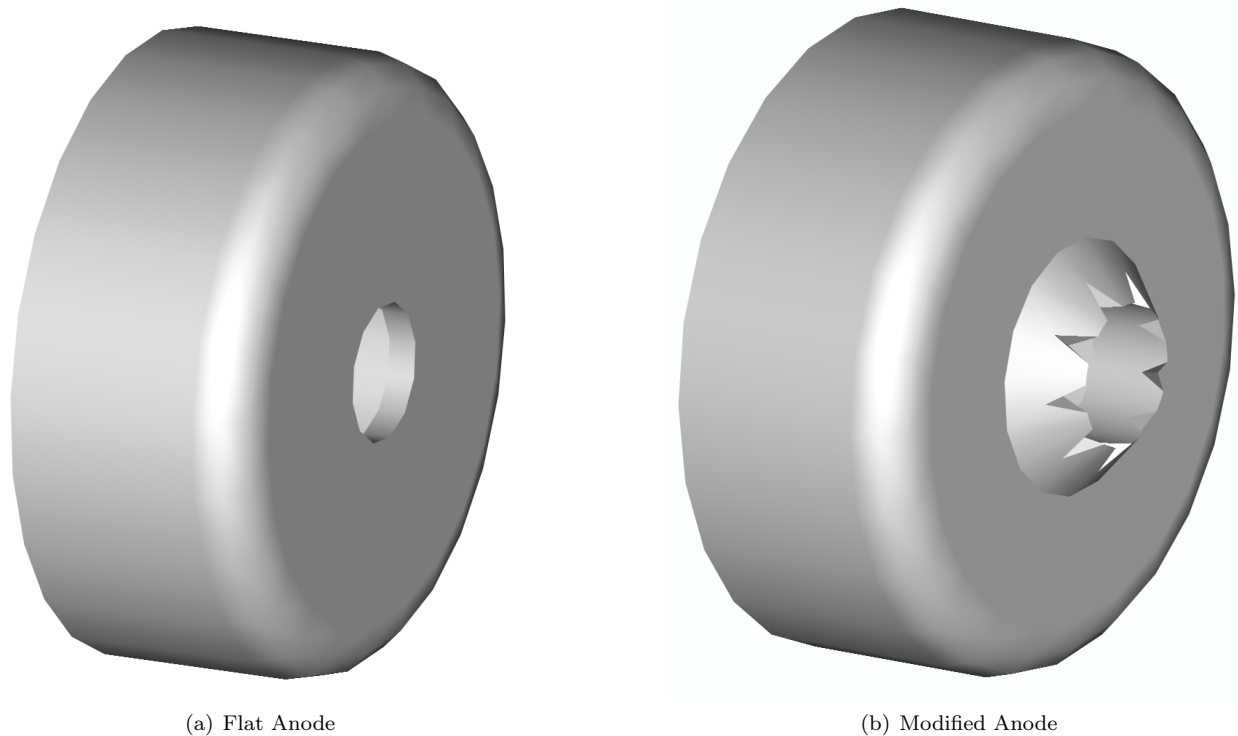


Figure 2.11: A View of Each Anode, Showing the Flat Anode and the Anode Modified with Serrated Conical Feature

Chapter 3

Test Techniques

This research effort concerns the changes in flow properties, particularly the mean and fluctuating properties of a subsonic and supersonic free shear flow fields due to changes based on the addition of a plasma field. Historically, the measurement of these flow properties would be accomplished through pitot probes, cone static probes and hot-wire anemometry. These invasive probes alter the flow, which implies they measure a different flow than exists in the absence of the probe. The use of these probes in combination can provide fluctuating quantities for the flow variables of pressure, density and velocity. However, the technique to reduce this data into the respective primitive variables requires the assumption that each probe individually sees the same flow field, even though the probes are traversed through the test section sequentially and the probes are of differing shapes and therefore, see different flows.[250, 371]

These detractors provide motivation for the use of non-intrusive diagnostics. Non-intrusive diagnostics are used in determining the flow properties of interest in this research effort. Each of the diagnostics are based on the measurement of light. The sections which follow describe each of the measurement techniques used, the test procedures and the measurement uncertainties.

3.1 Measurement Uncertainty and Error Propagation

Before proceeding through each measurement technique, it is important to mention a few concepts of the propagation of measurement errors. All measurements deviate from the truth by an unknown uncertainty. To that end, it is utterly impossible to ascertain the precise truth of what is trying to be measured. However through observation of numerous measurements it is believed that the truth lies somewhere within the center of our measurements. Each measurement has associated with it errors of two types, random and bias. Random errors correspond to the usually minor fluctuations in the data recorded, and are considered to be uncorrelated to neighboring measurements and unaffected by the conditions associated with the test. Random errors are assumed to be distributed around the truth by a Gaussian distribution and can be quantified and minimized by the taking of an ever increasing number of samples.[92, 183]

Errors of bias, on the other hand, are errors which are not distributed around the truth which we attempt to measure. Some bias errors are made by blunders in the setup or in data taking technique, while others are known prior to testing and unavoidable. Bias errors are unlike random errors in that larger data sets will not minimize their affect, as an error in bias is not represented by a Gaussian distribution and is usually highly correlated to the test conditions. The only hope in minimizing errors of bias, are through vigilance in data acquisition, care in planning and patience in troubleshooting.[92, 183]

In processing and combining raw data from many separate measurements, the combined effect of random and bias errors propagates through the system. It is customarily assumed that the errors are small with respect to the measurements being taken. Following that logic, it flows naturally that error propagation can be processed through linearizing the equations through which the uncertainties pass. To combine different errors, it is important to avoid overly cautious propagation. Specifically, the affect of errors which cancel each other must be considered. The standard treatment of canceling errors is to combine each error's contribution through the L_2 norm. This approach is the most common technique for error propagation and is the approach followed here, as represented by Equation 3.1. The variable ϵ_i represents the normalized uncertainty for measurement i , while ϵ_c is the combination of propagated errors through the L_2 norm technique.

$$\epsilon_c = \|\epsilon_i\|_2 = \sqrt{\sum_i \epsilon_i^2} \quad (3.1)$$

One of the key factors in producing a realistic measurement of uncertainty is in non-dimensionalizing each of the measurements by realistic values which represent the test conditions. The non-dimensionalizing process allows each of the factors of uncertainty to be combined under the L_2 norm. Errors of bias are estimated to provide 95% coverage of the uncertainty they introduce, while random errors are included as a ' 2σ ' source to provide the equivalent 20:1 odds. Finally, the effect of large sample sets is included where applicable, typically as a factor of $1/\sqrt{N}$, where N is the number of samples used to find the mean. In the sections which follow, each test technique will be scrutinized for applicable measurement uncertainties. The effect of measurement uncertainties will be propagated into the calculated results to quantify the impact of the combination of the uncertainties.[92, 183]

3.2 Particle Image Velocimetry (PIV)

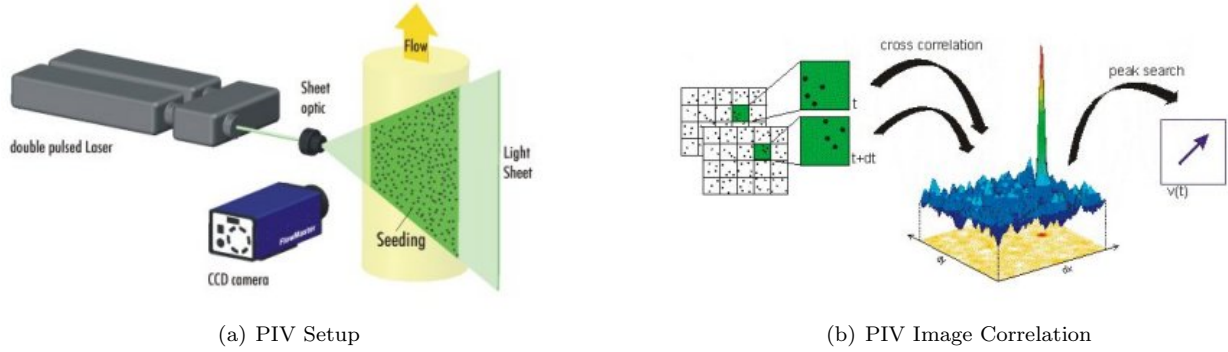


Figure 3.1: Particle Image Velocimetry Description, From LaVision[388]

Particle Image Velocimetry uses a pulsed, coherent illumination source focused into a plane to create a two dimensional interrogation region which is imaged by a charge coupled device (CCD). Naturally occurring or artificially injected seed particles scatter light in Mie, or Raleigh regimes and are recorded as bright pixels on the camera. Multiple frames are analyzed sequentially and computer software correlates the velocity field required to produce the recorded particle motion. The results from this technique are advantageous in that, a low power illumination source is acceptable, an entire two-dimensional region can be measured in one test and the setup is simple since frequency information is not required to determine path velocities. Figure 3.1 illustrates the setup for PIV and the image correlation technique. The correlation software works under the assumption that many of the particles in the first image remain in the subsequent images. The first image is compared to the second image by dissecting the image plane into smaller pieces.[12, 307, 388]

A section of the image (of size $M \times N$) at initial time t_a is introduced as a function of intensity $I_a(i, j)$, where i and j represent the pixel indices corresponding to the axial and tangential directions of the CCD image. The first thing to accomplish in processing is to calculate the cross-correlation function between the initial image a at t_a and the second image $I_b(i + k, j + l)$ at t_b , where the location of the second image is shifted by (k, l) with respect to the first image. The cross-correlation $R_{ab}(k, l)$ is a summation of the multiplied intensities at each pixel of the two images being compared.

$$R_{ab}(k, l) = \frac{1}{MN} \sum_{i=1}^M \sum_{j=1}^N I_a(i, j) I_b(i + k, j + l) \quad (3.2)$$

As it turns out, the Fourier transform of the image intensity can be used here to cut the number of mathematical operations from $O(N^4)$ to $O(N^2 \log_2 N)$. The cross-correlation function $R_{ab}(k, l)$ is found equivalently

by

$$R_{ab}(k, l) = \mathcal{F} \{I_a(i, j)\} \mathcal{F} \{I_b(i + k, j + l)\}^* \quad (3.3)$$

where $\mathcal{F} \{\}^*$ is the hermitian of $\mathcal{F} \{\}$. Since the image is a series of discrete pixels, the Fast Fourier Transform (FFT) is used to calculate the discrete Fourier transform of the image. Note that the FFT analysis assumes a periodicity to the data. Nyquist sampling theorem therefore imposes that data aliasing will occur if the particles in the image travel more than half the total sub-image in the time $\Delta t = t_b - t_a$. To get around this problem, the sub-image size can be increased, or the time Δt can be decreased. After computing the cross-correlation function, the maximum value determines the most likely shift of the second image with respect to the initial image. The accuracy of this displacement (k_{max}, l_{max}) is limited to $\pm 1/2$ a pixel. To improve this a Gaussian curve fit is applied to interpolate the true peak of the cross-correlation function $R_{ab}(k_{max}, l_{max})$. Most common is a three-point estimator, where $[k_{max} - 1, k_{max}, k_{max} + 1]$ and $[l_{max} - 1, l_{max}, l_{max} + 1]$ are investigated to determine the actual peak to sub-pixel accuracy (k_{sub}, l_{sub}) . [307, 373]

$$k_{sub} = k_{max} + \frac{\ln R_{ab}(k_{max} - 1, l_{max}) - \ln R_{ab}(k_{max} + 1, l_{max})}{2 \ln R_{ab}(k_{max} - 1, l_{max}) - 4 \ln R_{ab}(k_{max}, l_{max}) + 2 \ln R_{ab}(k_{max} + 1, l_{max})} \quad (3.4)$$

$$l_{sub} = l_{max} + \frac{\ln R_{ab}(k_{max}, l_{max} - 1) - \ln R_{ab}(k_{max}, l_{max} + 1)}{2 \ln R_{ab}(k_{max}, l_{max} - 1) - 4 \ln R_{ab}(k_{max}, l_{max}) + 2 \ln R_{ab}(k_{max}, l_{max} + 1)} \quad (3.5)$$

Two techniques are applied to this algorithm to improve the results. First, the Gaussian interpolation technique assumes that particle illumination is Gaussian. One case when this does not occur is when a particle is truncated on the border of a sub-image. If the peak displacement is near this region, the resulting interpolation is doomed. To improve this common situation a technique called correlation multiplication is used. This is a re-normalization technique where the cross-correlation function is weighted by overlapping windows which can provide the correct peak location even in the presence of image truncation. The next improvement comes through an iterative sub-imaging technique. This sub-imaging utilizes the displacement vector field calculated previously to cut the interrogation window in half and re-evaluate the cross-correlation to produce displacement vectors at twice the resolution. This technique can be applied multiple times, at the sacrifice of exponentially increasing processing time. [17, 168]

In some locations, the cross-correlation algorithm finds a spurious solution. These vectors are eliminated by two techniques. First, by estimating the maximum velocity expected in the flow field, the maximum pixel displacement can be determined prior to image processing. Using that prediction, vectors which are longer than a set threshold are eliminated from the analysis. Next, a nearest neighbor check is performed, where vectors which deviate more than two standard deviations in displacement from their nearest neighbors are

eliminated.[12, 17]

This technique relies on seed particles injected upstream to act as tracers of the gas motion, which requires some caution in use. If the flow field contains significant motion out of the plane of illumination, then the particle correlation accuracy quickly degrades as particles in the first image are no longer present in subsequent images. Seeding issues of large particle size and sufficient particle density are also an issue with this technique. The issue of particle tracking will be covered in detail in the results.[12, 195, 266, 307]

3.2.1 Experiment Setup

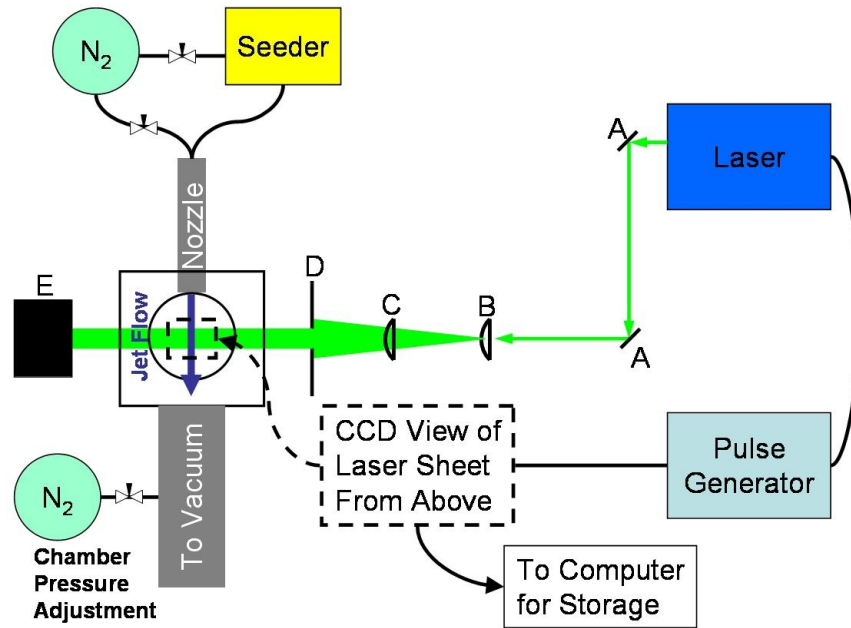


Figure 3.2: Schematic of Particle Image Velocimetry

Table 3.1: Description of Optical Components in Figure 3.2, the Schematic of Particle Image Velocimetry

Item	Description
A	Dichroic Mirror
B	Lens, Cylindrical-Convex $f = 500$ mm
C	Lens, Spherical-Convex $f = 750$ mm
D	Knife-Edge for Beam Forming and Reflection Minimization
E	Beam Dump

Figure 3.2 outlines the setup of the particle image velocimetry system schematically. Note that the optical components are labeled in the figure and those letters correspond to the component descriptions

found in Table 3.1. The initially round cross-section of the laser beam was formed into a sheet by means of a cylindrical plano-convex lens which spread the beam horizontally. Next, the beam was focused vertically by a spherical plano-convex lens with the focal point placed just to the left of the nozzle centerline to provide the thinnest sheet possible and avoid shadows in the camera field of view caused by particles located in the focus of the laser sheet.[125, 307]

To set the test conditions and provide seed particles in the test section, a compressed Nitrogen tank supplied gas primarily to the model 3475 Condensation Monodisperse Aerosol Generator (CMAG) by manufactured by TSI Inc. The exhaust of the seeder was at atmospheric pressure, and therefore the seeder was allowed to vent continually into the lab. The exhaust of the seeder was carried out of the room by an exhaust fan when particles were not being drawn into the test section. To ensure that the gas in the test section was Nitrogen, some of the gas from the cylinder was fed directly into the lab vent, providing slight positive pressure to the CMAG during the testing.[25, 125]

The seed particles were illuminated by the Gemini-15Hz PIV Nd:YAG laser made by New Wave Research. The laser produced two sequential pulses of light at a nominal frequency of 532 nm. The minimum spacing between laser pulses produced by the controller of the Gemini PIV laser system was over 1 μs . In order to sequence the laser pulses under the minimum threshold, the laser pulse timing was externally controlled by a Quantum Composers Model 565 8-channel pulse generator. This provided a significant reduction in the timing of the pulses. Pulse-to-pulse jitter was estimated at 0.5 ns, based on the Gemini Manual.[19, 30, 125, 307]

The images were captured by the PCO.1600 charge-coupled device (CCD) camera from Cooke Corp. The camera allowed for rapid interline acquisition of image pairs and was sequenced to capture one image from each of the two laser pulses from the Gemini PIV laser system. Images were then stored in a computer for post processing.[27, 125]

Downstream of the test section, 15.24 cm PVC tubing evacuated the test section to the desired pressure. Chamber pressure was adjusted by means of a vent located in the PVC evacuation plumbing and was fed by means of a regulated compressed Nitrogen cylinder. Vacuum was provided by the Kinney KT-300 rotary vacuum pump.[24]

3.2.2 Test Procedures

Initially important to each set of PIV runs, was the calibration and focusing of the optics. The laser sheet was aligned to be parallel to the laser table. Subsequently, the test section and jet orientation were confirmed to be parallel to the laser sheet. Next, the camera was aligned and focused onto the laser sheet by filling the test section with seed particles and illuminating them with the laser. The pixel locations were calibrated, first by taking an image of a ruler with 0.254 mm markings which was placed into the focal plane of the camera. Then, the location of the camera field of view was surveyed by viewing the anode face with the camera. The electrode gap distance, anode face location and camera position were measured relative to reference marks by means of a caliper with resolution down to 25.4 μm . From the surveyed position, the gap distance and camera position were able to be adjusted relative to the reference marks, which were recorded and used in post processing. Note that the survey position and any adjustments were made with the test section under vacuum to account for slight motion of the nozzle (typically 0.2 to 0.3 mm) due to bending of the rig attaching the nozzle to the table when the test chamber was evacuated.[125, 307]

Next, the maximum jet velocity to be tested was estimated from isentropic relations. That velocity and the camera scale factor were then used to set the delay between laser pulses. The pulse delay was set to allow a seed particle to travel approximately 13 pixels between pulses at maximum velocity. Then, the images were synchronized with the laser pulses. A sample set of images were taken: to confirm the particles were visible and focused throughout the entire image, to confirm seeding was optimized in concentration and uniformity, laser power was optimized to prevent blooming and provide adequate illumination. The images were post-processed to confirm the expected maximum velocity was achieved, that the jet was centered in the field of view and that the camera was acquiring the portion of the laser sheet which was Gaussian in illumination. Non-Gaussian illumination was easily identifiable in unexpected drop-offs in maximum velocity and in processing errors which produced tell-tale shifts in the velocity field.[12, 307]

The test conditions were set with regard to the plenum pressure, chamber pressure and CMAG and were allowed to stabilize prior to data acquisition. Then, plasma off and plasma on cases were taken in an interleaved fashion. The first plasma off run was taken, to fill the camera memory buffer. While the first run was downloading, the plasma field was turned on and allowed to stabilize. Then the first plasma on case was taken. This sequence continued until the desired number of images were stored on the computer (1056 or 1150 depending on whether the images stored were 1200x1600 pixels or 1200x1200 pixels, respectively). Images were acquired at a rate of 8 to 10 Hz, depending on settings and one sequence of interleaved runs took about thirty minutes to set up and thirty minutes of acquisition.[125]

After the data were stored, they were transferred to two processing computers. The computers were

based on the ASUS P5W64 motherboard, running Intel Pentium Core Duo processors over-clocked to 3.0 GHz. The combined two computers allowed for four simultaneous batch jobs to be processed. Each one of the interleaved sequences took 14 hours of processing time. The images were correlated through DPIVB version 2.1 from ISSI Inc. The correlation software produced a field of vectors which matched the shift produced by the illumination of the seed particles in two successive images. Three stages of correlation were accomplished on each image pair. The first stage correlated 128x128 pixel windows in the image with 50% overlap. The second stage examined 64x64 pixel sub-windows, aided by the pixel shift information from stage one. Finally, 32x32 pixel windows produced a field of vectors spaced every 16 pixels with displacement in axial and tangential directions relative to the centerline jet flow. Correlation was enhanced through correlation multiplication. The four correlation maps were placed around the window of interest with 50% overlap and were the same size as the interrogation window. Additionally, between each stage, vectors calculated were examined according to filters. The first filter eliminated vectors which were longer than 15 pixels. The second filter performed a consistency check of the nearest neighbors to the vector being examined. Vectors were eliminated if the length of the vector of interest was more than two standard deviations longer than its neighbors.[12, 17, 83, 116, 307]

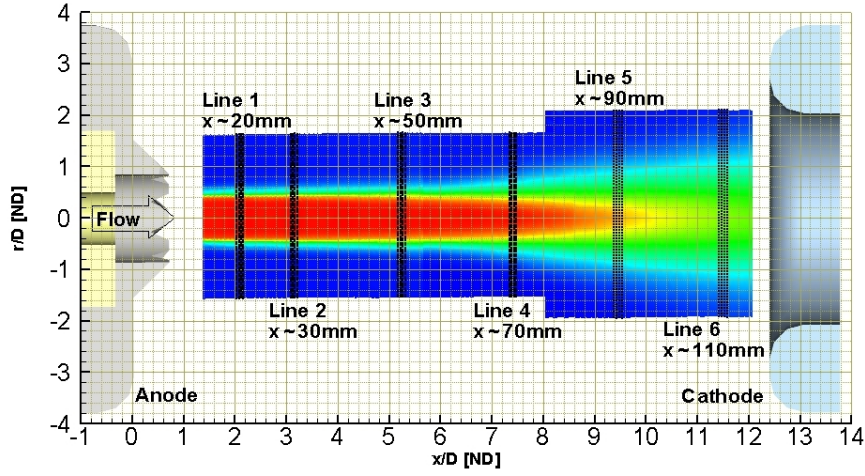
Next, the vector fields were further evaluated by a MATLAB program which was developed for this research effort. The program read in each of the vector files produced from DVIPB and applied the calibrations between pixel and physical distance as well as the time delay between laser pulses. Some points were eliminated from the velocity field at this time based on the result of the correlation algorithm. No more than 10% of the velocity vectors were eliminated through these processes. The mean velocity fields were then output into files for plotting. To perform statistical analysis on the velocity data, four rows of velocity information were combined at specific locations to provide more than 4,000 data points. The locations selected corresponded to cross-sections of the jet, displaced from each other by roughly 20 mm and are shown in Figure 3.3. The velocity fields were then subjected to statistical analysis.[12, 17, 116, 307]

The mean velocities in axial (U) and tangential (V) directions were calculated by

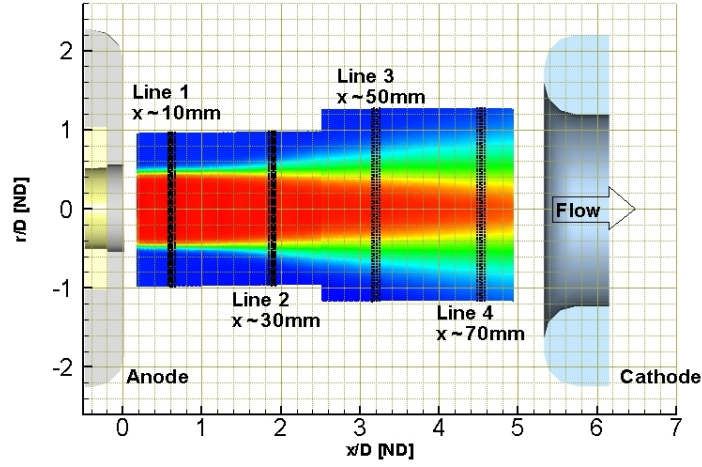
$$U = \frac{\sum \Delta x_i}{N \Delta t}, \quad V = \frac{\sum \Delta r_i}{N \Delta t} \quad (3.6)$$

where Δx_i and Δr_i are the pixel displacement in the axial and tangential locations, Δt is the temporal displacement between image pairs and N are the number of vectors summed. The standard deviations of velocity were then calculated by

$$\sigma_u = \sqrt{\frac{\sum u_i^2}{N}}, \quad \sigma_v = \sqrt{\frac{\sum v_i^2}{N}} \quad (3.7)$$



(a) Chamber Pressure of 5 Torr



(b) Chamber Pressure of 8-9 Torr

Figure 3.3: Location of PIV Measurement Stations for Statistical Analysis

where u_i and v_i are the fluctuations of velocity from the mean.[64, 307, 352]

Next second and third order moments were taken of the data and are represented in Equation 3.8 through 3.13

$$\overline{u^2} = \frac{\sum u_i^2}{N} = \sigma_u^2 \quad (3.8)$$

$$\overline{v^2} = \frac{\sum v_i^2}{N} = \sigma_v^2 \quad (3.9)$$

$$\overline{uv} = \frac{\sum u_i v_i}{N} \quad (3.10)$$

$$\overline{u^3} = \frac{\sum u_i^3}{N} \quad (3.11)$$

$$\overline{u^2 v} = \frac{\sum u_i^2 v_i}{N} \quad (3.12)$$

$$\overline{uv^2} = \frac{\sum u_i v_i^2}{N} \quad (3.13)$$

Most of the terms above were analyzed after scaling by the centerline velocity U_o at the location of interest. The Reynolds shear stress term was examined by two other scalings. When scaled by multiplication of the root mean square (standard deviation) of the velocity fluctuations, e.g. $\sigma_u \sigma_v$ this term was labeled the Reynolds shear stress correlation coefficient, C_{uv} and is an indication of correlation between fluctuations in the axial and tangential velocities. Values near unity indicate positive correlation, while values close to negative one indicate anti-correlation. Values near zero report that the fluctuations are uncorrelated. Another way to examine the Reynolds shear stress was through the structural parameter a_1 . Equations 3.14 and 3.15 show the scalings of Reynolds shear stress by velocity fluctuations to produce the correlation coefficient (C_{uv}) and structural parameter (a_1), respectively.

$$C_{uv} = \frac{-\overline{uv}}{\sigma_u \sigma_v} \quad (3.14)$$

$$a_1 = \frac{-\overline{uv}}{\sigma_u^2 + \sigma_v^2} \quad (3.15)$$

Turbulent kinetic energy (TKE), k , is a derived term, often used in turbulence modeling in computational fluid dynamics. TKE is aptly named, as it represents the amount of kinetic energy present the turbulent fluctuations of the flow field. Note the factor of two in the denominator in Equation 3.16 below.

$$k = \frac{\sigma_u^2 + \sigma_v^2}{2} \quad (3.16)$$

The parameter k is scaled by centerline kinetic energy $U_o^2/2$, which eliminates the factor of two from the relation.[\[64, 289, 307, 352\]](#)

Further examination of the velocity fluctuations can be found in analysis of the distribution of fluctuations. This was accomplished by examining skewness and kurtosis of the axial velocity fluctuations.

Equations 3.17 and 3.18 detail the computation for skewness and kurtosis, respectively.

$$\text{skewness} = \frac{\overline{u^3}}{\sigma_u^3} \quad (3.17)$$

$$\text{kurtosis} = \frac{\overline{u^4}}{\sigma_u^4} \quad (3.18)$$

Skewness is an indication of a shift in velocity fluctuations when compared to a purely Gaussian distribution. A Gaussian distribution has skewness of zero, which marks that the distribution of fluctuations is symmetric about the mean. Positive skewness represents a shift toward the right tail (positive fluctuations), while negative skewness is shifted toward negative fluctuations. A Gaussian distribution has kurtosis of three. Values lower than three represent a distribution of velocity with higher peakedness than a Gaussian distribution. While conversely, values above three represent flatter distributions. [75, 289, 307]

3.2.3 Uncertainty Estimates

This section accounts for the majority of uncertainty analysis performed for this research effort. Many calculations were accomplished on the velocity fields after processing. It is important to determine the effect of uncertainty as it propagates through the calculations. In order to determine the relative effect of a combination of uncertainties, the variables are all scaled by appropriate parameters. Thereby relative uncertainties may be compared to produce the overall effect on the calculated variables. Table 3.2 summarizes the scaling process used for all of the calculations accomplished on particle image velocimetry data. Note that the convention used throughout the uncertainty analysis is to designate ϵ as the scaled uncertainty in a particular parameter and is non-dimensional in nature. Δ is used to indicate a bias (or propagated error) in a measured (calculated) variable, while σ is the root mean square of the fluctuations in the measured sample. Finally, N is the number of samples taken in the data set.[92, 183]

The values chosen to provide scaling were taken from two conditions. The use of these conditions help illustrate that the effect of measurement uncertainty can vary for different points in the flow field. Note here, that when measurements are made of very small values (e.g. the velocity of fluid at rest), the uncertainties can become incredibly large. The baseline flow to be used in propagating PIV measurement uncertainty is based on the test conditions of the 9.5 mm exit diameter converging-diverging nozzle. The pressure ratio used drives the flow at Mach 1.4. The two conditions chosen are located 11.3 diameters downstream of the anode face and represent the furthest downstream measurement station. This station is where the primary statistical analysis was performed in the results section. The first condition is along the centerline of the

Table 3.2: Scaling of Measurement Uncertainties in Particle Image Velocimetry

Scaled Uncertainty	Scale Factor	Result
ϵ_U	U_o	$\Delta U/U_o$
ϵ_V	U_o	$\Delta V/U_o$
ϵ_{σ_u}	U	$\Delta\sigma_u/U$
ϵ_{σ_v}	V	$\Delta\sigma_v/V$
$\epsilon_{\overline{u^2}}$	U^2	$\Delta\overline{u^2}/U^2$
$\epsilon_{\overline{v^2}}$	V^2	$\Delta\overline{v^2}/V^2$
$\epsilon_{\overline{uv}}$	UV	$\Delta\overline{uv}/UV$
ϵ_k	k	$\Delta k/k$
ϵ_{a_1}	a_1	$\Delta a_1/a_1$
$\epsilon_{C_{uv}}$	C_{uv}	$\Delta C_{uv}/C_{uv}$
$\epsilon_{\overline{u^3}}$	U^3	$\Delta\overline{u^3}/U^3$
$\epsilon_{\overline{v^3}}$	V^3	$\Delta\overline{v^3}/V^3$
$\epsilon_{\overline{u^2v}}$	U^2V	$\Delta\overline{u^2v}/U^2V$
$\epsilon_{\overline{uv^2}}$	UV^2	$\Delta\overline{uv^2}/UV^2$
$\epsilon_{\text{skewness}}$	skewness	$\Delta\text{skewness}/\text{skewness}$
$\epsilon_{\overline{u^4}}$	U_o^4	$\Delta\overline{u^4}/U_o^4$
$\epsilon_{\text{kurtosis}}$	kurtosis	$\Delta\text{kurtosis}/\text{kurtosis}$

jet. The other condition takes into the account the increased turbulence and decreased velocity of the shear layer. Table 3.3 describes the actual scaling conditions used in propagation analysis.[92, 183, 307]

Note in Table 3.3 that the tangential velocity V was chosen to be 5 m/s as representative of the observed mean value and to prevent division by a very small number overwhelming the effects of its relatively small overall contribution to most propagated uncertainties. The values of x and r chosen correspond to the velocities U and V , respectively, and represent the number of pixels traveled in time t . The bias estimates were arrived at as follows. The error in timing between two pulses was arrived at by researching the manuals for both the pulse generator and the laser which generated the pulses. The timing error Δt was estimated to be 6 ns as the manual specification for pulse-to-pulse jitter of the laser, which was much higher than the timing uncertainty associated with the pulse generator. Therefore the percent uncertainty from timing was $\epsilon_{\Delta t} = 6\text{ns}/1096\text{ns} = 0.5\%$. The error in pixel displacement by correlation analysis provided by the DPIVB software program was commonly estimated at one-tenth of one pixel, assuming the laser sheet is providing Gaussian illumination. Sub-pixel accuracy was achieved by matching the intensity captured from illuminated particles through a Gaussian shaped peak locator. Therefore the position errors Δx and Δr were set at 0.1 pixel. The axial uncertainty therefore $\epsilon_{\Delta x}$ was that error, scaled by the mean value of 8.6 pixels, or 1.2 to 1.5%. In the radial direction, the error has a larger effect on $\epsilon_{\Delta r}$. In this case, even though the actual uncertainty is only 3.0 m/s, the radial velocity is approximately zero and therefore the relative uncertainty

Table 3.3: Conditions Chosen to Represent Test Conditions for the Analysis of Uncertainty Propagation in Particle Image Velocimetry

Parameter	Value	
	Centerline	Shear Layer
t	1096.0 ns	1096.0 ns
x	8.6 pix	6.7 pix
r	0.2 pix	0.4 pix
U_o	257.5 m/s	257.5 m/s
U	257.5m/s	200.9 m/s
V	5.0 m/s	12.9 m/s
σ_u/U_o	23.5%	26.0%
σ_v/U_o	14.0%	16.0%
N	4000. samples	4000. samples
Bias Estimates		
$\epsilon_{\Delta t}$	0.5%	0.5%
$\epsilon_{\Delta x}$	1.2%	1.5%
$\epsilon_{\Delta r}$	59.9%	23.2%

is 23.2% to 59.9%. This relative uncertainty is expected and acceptable.[17, 19, 30, 83, 92, 183, 307]

To begin looking at the propagation of uncertainties, the first example is to examine the mean velocity which is represented by Equation 3.19.

$$\epsilon_U = \frac{\|\epsilon_{\Delta x}, \epsilon_{\Delta t}, 2\sigma_u/U_o\|_2}{\sqrt{N}} \quad (3.19)$$

Two important points need to be made here. First, the bias uncertainties represented by Δx and Δt come from the simple time-of-flight calculation used to create velocity vectors from the correlation of PIV images. The bias uncertainties are estimated to contain errors with 20:1 odds. The uncertainty due to fluctuating measurements are then matched to roughly the 95% bounds of Gaussian distribution which is a multiplicative factor of 1.96. Since there are only a finite number of samples, convention suggests rounding the factor up to 2σ in order to account for the increased uncertainty introduced by finite data sets. The three contributions which propagate the uncertainty are combined under the L_2 norm.[92, 156, 307]

The second important point to mention is the influence of a large number of samples on uncertainty of the mean. The influence on mean velocity in Equation 3.19 is accounted for by the factor \sqrt{N} in the denominator as detailed in Coleman and Steele. [92] It is clear that the use of large data sets is advantageous in significantly reducing the error of mean measurements. However, a point is reached where decreasing gains make the cost of continued reductions exorbitant.[50, 307]

And by following the derivation of uncertainty in standard deviation of velocity outlined in Grant and

Owens[156], the uncertainty of σ_u is

$$\epsilon_{\sigma_u} = \sqrt{\frac{2}{N}} \sqrt{1 + 2 \left(\frac{\sigma_u}{U} \right)^2} \quad (3.20)$$

where ϵ_{σ_U} represents the uncertainty already scaled by the centerline velocity U_o . Note that the uncertainty of a standard deviation is dependent only on the number of samples taken. The last term in Equation 3.20 is introduced to account for the effect of uncertainty based on the measured fluctuations, which provides negligible effects when measured fluctuations are less than 30%. Similarly, the uncertainty in the tangential direction is given by Equation 3.21.[92, 289, 307]

$$\epsilon_{\sigma_v} = \sqrt{\frac{2}{N}} \sqrt{1 + 2 \left(\frac{\sigma_v}{V} \right)^2} \quad (3.21)$$

Because of judicious choices made in scaling, uncertainty in higher order moment fluctuations break into linear combinations of the uncertainty in standard deviation. For example, the Reynolds normal stress term $\overline{u^2}$ when scaled by the centerline velocity has twice the uncertainty of ϵ_{σ_U} . When calculated terms are scaled by the standard deviation in velocity, then the uncertainties are combined under the L_2 norm. Table 3.4 steps through each of the propagated uncertainties and provides an estimate for both the centerline of the jet and the shear layer for the baseline case. Again, the conditions chosen for this baseline case are detailed in Table 3.3.[50, 92, 183]

Table 3.4: Propagation of Measurement Uncertainties in Calculations Performed on Particle Image Velocimetry Data

Scaled Uncertainty	Derivation	Value	
		Centerline [%]	Shear Layer [%]
ϵ_U	$\ \epsilon_{\Delta x}, \epsilon_{\Delta t}, 2\sigma_u/U_o\ _2/\sqrt{N}$	0.7%	0.8%
ϵ_V	$\ \epsilon_{\Delta r}, \epsilon_{\Delta t}, 2\sigma_v/U_o\ _2/\sqrt{N}$	1.0%	0.6%
ϵ_{σ_u}	$\sqrt{\frac{2}{N}}\sqrt{1+2\left(\frac{\sigma_u}{U}\right)^2}$	2.4%	2.5%
ϵ_{σ_v}	$\sqrt{\frac{2}{N}}\sqrt{1+2\left(\frac{\sigma_v}{V}\right)^2}$	2.2%	2.2%
$\epsilon_{\sigma_u^2}$	$2\epsilon_{\sigma_u}$	4.7%	4.9%
$\epsilon_{\sigma_v^2}$	$2\epsilon_{\sigma_v}$	4.5%	4.5%
$\epsilon_{\overline{u^2}}$	$2\epsilon_{\sigma_u}$	4.7%	4.9%
$\epsilon_{\overline{v^2}}$	$2\epsilon_{\sigma_v}$	4.5%	4.5%
$\epsilon_{\overline{uv}}$	$\ \epsilon_{\sigma_u}, \epsilon_{\sigma_v}\ _2$	3.2%	3.3%
ϵ_k	$\ 2\epsilon_{\sigma_u}, 2\epsilon_{\sigma_v}, 2\epsilon_{U_o}\ _2$	6.7%	6.9%
ϵ_{a_1}	$\ 2\epsilon_{\sigma_u}, 2\epsilon_{\sigma_v}, \epsilon_{\overline{uv}}\ _2$	7.3%	7.5%
$\epsilon_{C_{uv}}$	$\ \epsilon_{\overline{uv}}, \epsilon_{\sigma_u}, \epsilon_{\sigma_v}\ _2$	4.6%	4.7%
$\epsilon_{\overline{u^3}}$	$3\epsilon_{\sigma_u}$	7.1%	7.4%
$\epsilon_{\overline{v^3}}$	$3\epsilon_{\sigma_v}$	6.7%	6.7%
$\epsilon_{\overline{u^2v}}$	$\ 2\epsilon_{\sigma_u}, \epsilon_{\sigma_v}\ _2$	5.2%	5.4%
$\epsilon_{\overline{uv^2}}$	$\ \epsilon_{\sigma_u}, 2\epsilon_{\sigma_v}\ _2$	5.1%	5.1%
$\epsilon_{\text{skewness}}$	$\ \epsilon_{\overline{u^3}}, 3\epsilon_{\sigma_u}\ _2$	10.0%	10.5%
$\epsilon_{\overline{u^4}}$	$4\epsilon_{\sigma_u}$	9.4%	9.9%
$\epsilon_{\text{kurtosis}}$	$\ \epsilon_{\overline{u^4}}, 4\epsilon_{\sigma_u}\ _2$	13.3%	14.0%

3.3 Molecular Tagging Velocimetry (MTV)

Molecular tagging velocimetry appears to be first introduced by Miles et. al. [261] in an experiment where lines of Oxygen were caused to fluoresce by laser tagging and a small jet flow was tracked. Since then, others have seeded water flow with soluble phosphorescent molecules [148, 182], and phosphorescent molecule vapor such as Biacetyl [176, 359]. The first use of molecular Acetone vapor for MTV traces back to Lempert et. al. [217] in an experiment where Acetone was used to make velocimetry measurements in supersonic microjets.[174]

This technique uses a gas (which will be termed the tracer molecule) seeded into the flow, that fluoresces when excited by the laser which is tuned to overlap the absorption line(s) of the molecule. The tracer molecules absorb a photon and rise to an excited electrical state. When the molecules transition back to their ground state, they release a photon at a longer wavelength. The tracer molecules have an absorption well, where they have an affinity for absorbing photons which result in a fluorescent release. Technically, fluorescence is the transition of the tracer molecule into an excited state, and then directly back to the ground state through a released photon relaxation. Typical fluorescence times are on the order of 10 ns. Some tracer molecules undergo phosphorescence, when after excitation, they transition to a triplet state where energy is held captive from milliseconds to hours and then released through photon relaxation back to the molecular ground state. Quenching can also occur, where the molecule initially excited by an incident photon then releases its energy through molecular collision. Diatomic Oxygen is very effective at quenching fluorescence and phosphorescence through an unusual triplet ground state.[175, 176, 217, 397]

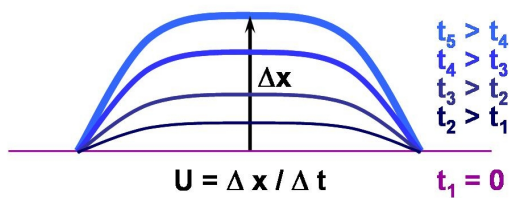


Figure 3.4: A Schematic of MTV Response at Increasing Time Steps

ing the delay time. Phosphorescent molecules are therefore desired due to the longer time they emit light, allowing longer delays between imaging. The longer delay produces better resolution of low speed flows, but produces a larger distortion in the shape of the line - which ultimately results in a limit to the maximum velocity resolution. Figure 3.4 shows a schematic of the typical MTV response with increasing time delay

The technique for MTV is relatively straightforward.

A flow, seeded with tracer molecules, is excited by a laser beam cutting through at a location of interest. Then, the tracer molecules are excited - typically to phosphorescence. The flow field is then imaged two times. The first image occurs quickly after excitation to capture the illuminated particles as a line. The next image is taken with a delay. The two images are compared and a mean velocity profile is deduced from the distance traveled during the delay time.

between the first and second image. Note the lines are increasing in thickness through dispersion and decreasing in intensity through phosphorescent decay in addition to traveling downstream with the flow which is up in this figure. Processing of the images is accomplished by slicing the image into columns, aligned with the direction of flow. Each of these slices is examined to determine the position of maximum image intensity. The first and second images are then compared to produce a displacement of the maximum intensity location for each slice. Velocity in the direction of the slice is then determined simply by $U = \Delta x / \Delta t$.[\[125, 218\]](#)

MTV is useful as a flow diagnostic at the low pressures expected for this investigation. However, the technique has some limitations. In regions of recirculation, the initial line of particles becomes smeared and results in an inability to resolve important portions of the flow of interest to this study. Additionally, the difference between excitation into fluorescence and phosphorescence becomes important, as fluorescent emission intensity is roughly an order of magnitude lower than phosphorescence. The transition into the quantum forbidden triplet state to produce phosphorescence is extremely dependent on the quantity of molecules excited to singlet and triplet states already, as well as the quantity of quenching molecules (such as Oxygen). For example, Acetone has a transition from singlet state fluorescence to triplet state phosphorescence which occurs at 10 torr - where higher pressures result in predominately phosphorescent emission, but lower pressures produce fluorescence.[\[218, 176, 370\]](#)

Acetone was the seed particle selected for use in this investigation. Acetone requires excitation by the 4th harmonic (266nm) of the Nd:YAG laser, which required the replacement of the glass windows with fused silica windows, which are transparent to the UV spectrum. One of the advantages of seeding with Acetone is the relative simplicity in the seeder arrangement, since it can be sprayed and evaporated into the flow upstream of the nozzle.[\[218, 232, 397\]](#)

3.3.1 Experiment Setup

Table 3.5: Description of Optical Components in Figure 3.5, the Schematic of Molecular Tagging Velocimetry

Item	Description
A	UV Dichroic Mirror
B	Fused Silica Lens, Spherical-Convex $f = 500$ mm
C	Beam Dump

Figure 3.5 is a schematic of components used in the molecular tagging velocimetry technique. In contrast to PIV, the CMAG seed particle generator is replaced by a model 9302 atomizer from TSI Inc. Nitrogen is fed into the atomizer and controlled through a regulator. Oxygen quenches Acetone phosphorescence and therefore the acetone placed in the atomizer was continually pressurized with Nitrogen gas. The output of

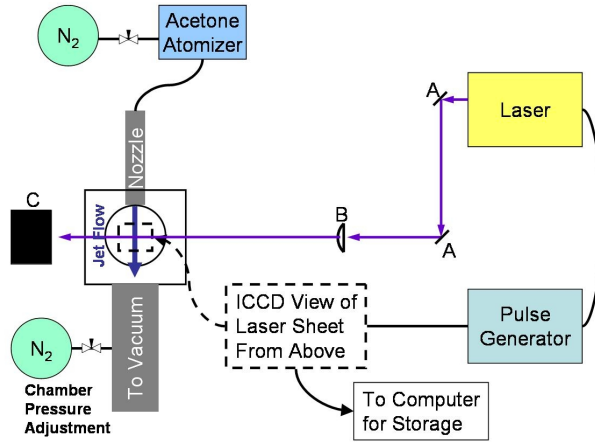


Figure 3.5: Schematic of Molecular Tagging Velocimetry

the atomizer was connected to 15 m of 3 mm diameter copper tube to ensure the acetone was completely vaporized. From this arrangement, the Nitrogen gas was assumed to be completely saturated with Acetone vapor - which at 20°C results in a molar concentration of 25.5%. Now while it is realized that this mixture of Acetone vapor and Nitrogen gas does not have the same molecular weight as pure Nitrogen, the mean flow results calculated by this technique are compared to PIV data with the same concentration of Acetone vapor and therefore provide the same flow field for particle tracking comparisons.[125, 232, 281, 370, 397]

The saturated mixture was then injected into the plenum chamber and regulated by means of a ball valve. The ConvecTech CVT-275-101 Pirani style pressure gauge connected to the plenum chamber was extremely affected by the addition of Acetone. The pressure gauge required calibration by means of diaphragm style absolute pressure transducer (Omega PX303-015A5V gauge read on an Omega PP302-E display). in order to be used for controlling the experiment. The same type gauge was used in monitoring chamber pressure, but was unaffected (maximum 3% offset noted) by Acetone addition due to the location of the chamber transducer and the dilution of the chamber with supplemental Nitrogen vented in downstream. The vacuum arrangement and venting to control chamber pressure is the same setup as detailed in the PIV technique and is not repeated here for brevity.[21, 23, 233]

The Spectra Physics GCR-230 Nd:YAG laser provided the beam source, nominally at 266 nm with pulse width measured at 8 ns. Since the beam was in the UV region, the optical components were made of fused silica. The beam was positioned by means of two dichroic mirrors optimized to reflect 266 nm light at 45° angles. The collimated laser beam was focused using a spherical plano-convex lens with focal length of 500 mm. The optical components shown in Figure 3.5 are described further in Table 3.5.[29]

Images of the Acetone phosphorescence were recorded on a Princeton Instruments ICCD-576-S cooled and intensified charge-coupled device (ICCD). The camera was cantilevered over the test section and was adjustable in axial and tangential directions relative to the flow through two large translation stages. Since the camera used an intensifier, gated images of 50 ns were able to be taken and were controlled by a Princeton Instruments PG-200 programmable pulse generator. The laser pulse and camera images were synchronized by use of the Quantum Composers Model 565 8-channel pulse generator. 1000 images were taken at each test condition and then downloaded to a computer connected through use of a proprietary card and custom cable.[22, 28, 30, 31]

3.3.2 Test Procedures

To begin the test, detailed position calibrations were made. The scale to convert between pixels and physical units was made by imaging a ruler placed at the center of the jet and parallel to the stimulating laser beam. The ruler had marks every 0.254 mm. After the calibration was known, the distance between the anode face and the center of the laser beam was measured from an image of the acetone filled test chamber. The chamber was evacuated to account for the shift of the nozzle under the load of vacuum. The florescence signal of the Acetone vapor was measured by centering the camera gate around the laser pulse. The location of the anode face was then known by a slight reflection off the metallic surface. Pixel damage from reflection of laser light into the ICCD was avoided by the use of standard glass in the camera lens as well as the optical access window over the test section. Standard glass has very low transmission of light at 266 nm, while the florescence and phosphorescence signals are in the visible region and pass through the glass components easily. Subsequent measurements of the phosphorescence signal were taken on a 50x576 pixel sub-region of the ICCD which was centered around the beam to reduce stored image file sizes and to speed the framing rate of the camera to match the laser pulse frequency of 10 Hz.[125, 174, 217]

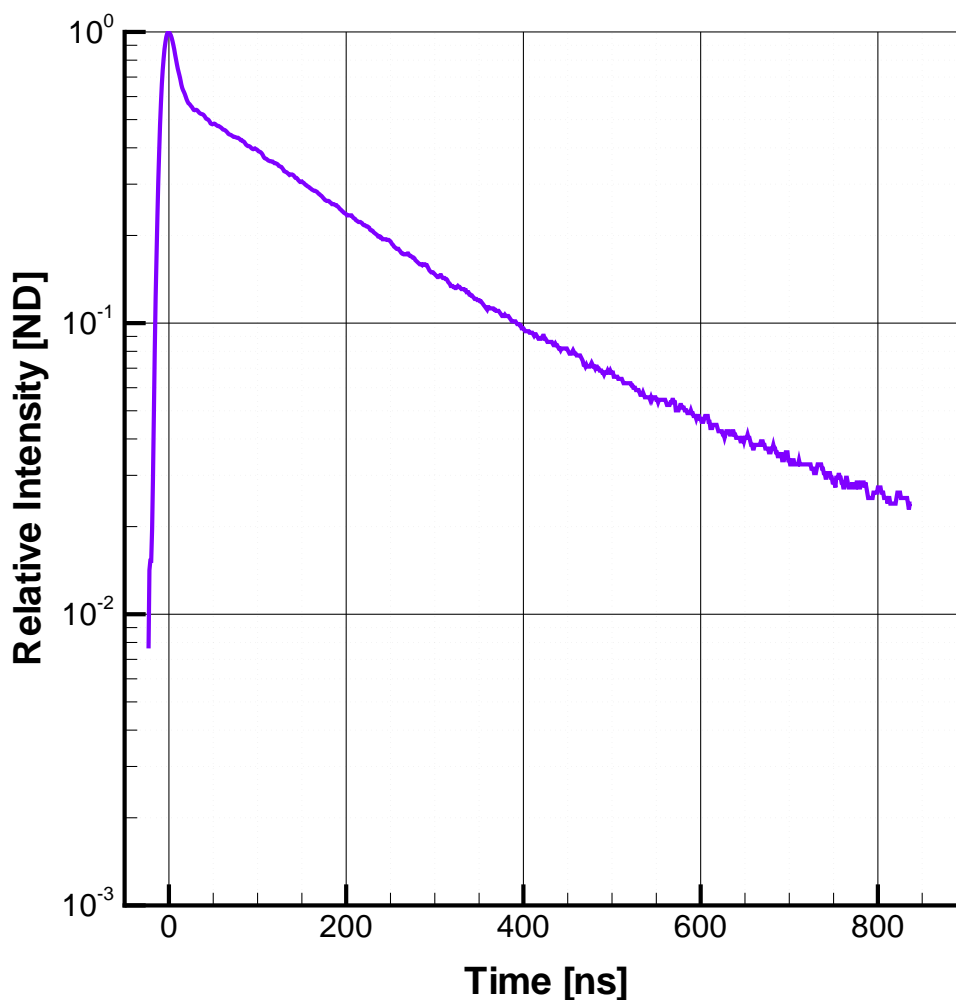


Figure 3.6: Relative Intensity of the Fluorescence/Phosphorescence of Acetone Vapor in Nitrogen at 5 Torr After Being Tagged by a UV Laser Beam at 266nm

To give an idea of the response of Acetone to stimulation by light at 266 nm, Figure 3.6 shows the relative intensity curve for saturated Acetone vapor in Nitrogen in the test chamber, taken at a chamber pressure of 5 torr by an Hamamatsu Model R-1306 photomultiplier tube and recorded by a Hewlett Packard 54542A oscilloscope. The initial slope of the response curve is the florescent decay and has a decay time constant measured at 38 ns. The exponential decay which follows is the phosphorescence of Acetone and has a measured decay time constant of 311 ns. [160, 206, 282]

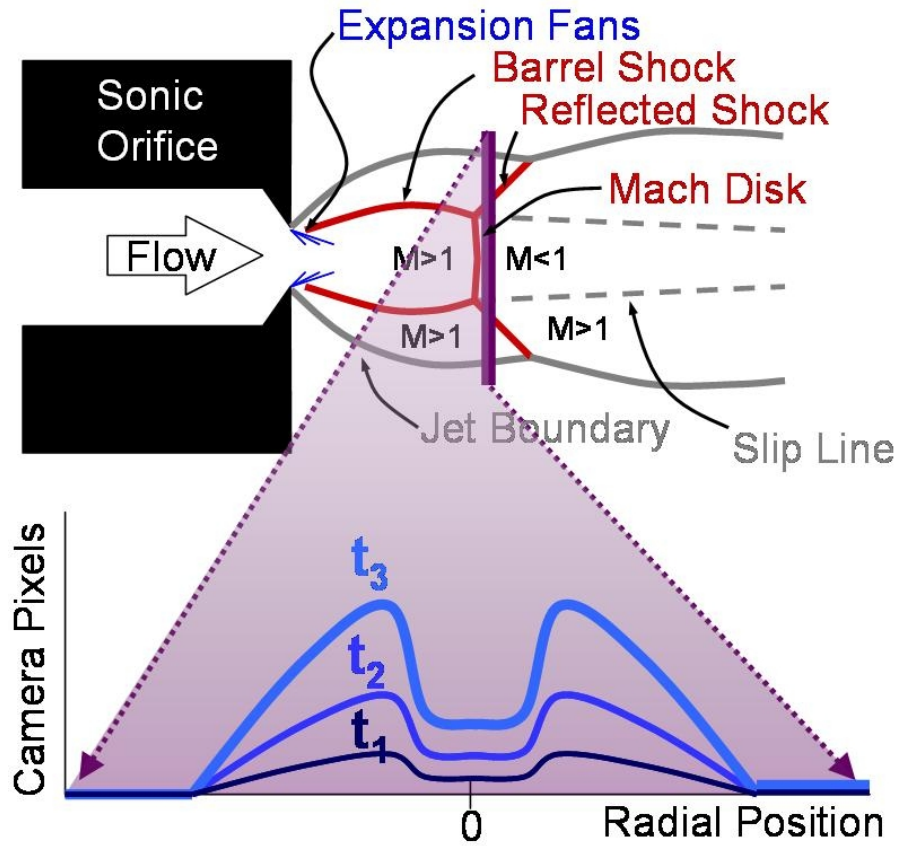


Figure 3.7: Schematic of the Shock Structure of a Highly Underexpanded Jet Showing the Response Just Downstream of the Mach Disk of a Line of Molecular Tagging Velocimetry at Successive Time Steps

Now, in order to investigate a sample of the response of a tagged line of the Acetone tracer in a jet flow, refer to Figure 3.7. This figure shows the structure of a highly underexpanded jet. The jet is formed by flow exiting out of a sonic orifice, which is the location where the flow chokes. The jet exits into a relative vacuum and forms an expansion region and accelerates rapidly in the chamber with static pressures dropping below that of the chamber. Next, the flow forms a barrel shock structure in order to match the chamber pressure. This pattern will continue in a chain of shocks if the pressure ratio is high enough. An interesting place to examine the flow is directly downstream of the Mach disk. Here, the flow is subsonic downstream of the normal shock, but the flow which surrounding the disk passed through the reflected oblique shock and is still supersonic. The morphing of the tagged line due to flow velocity at increasing time intervals is shown at the bottom of the figure. The Mach disk region is located in the center, surrounded by the higher speed flow which forms two lobes.[100, 228]

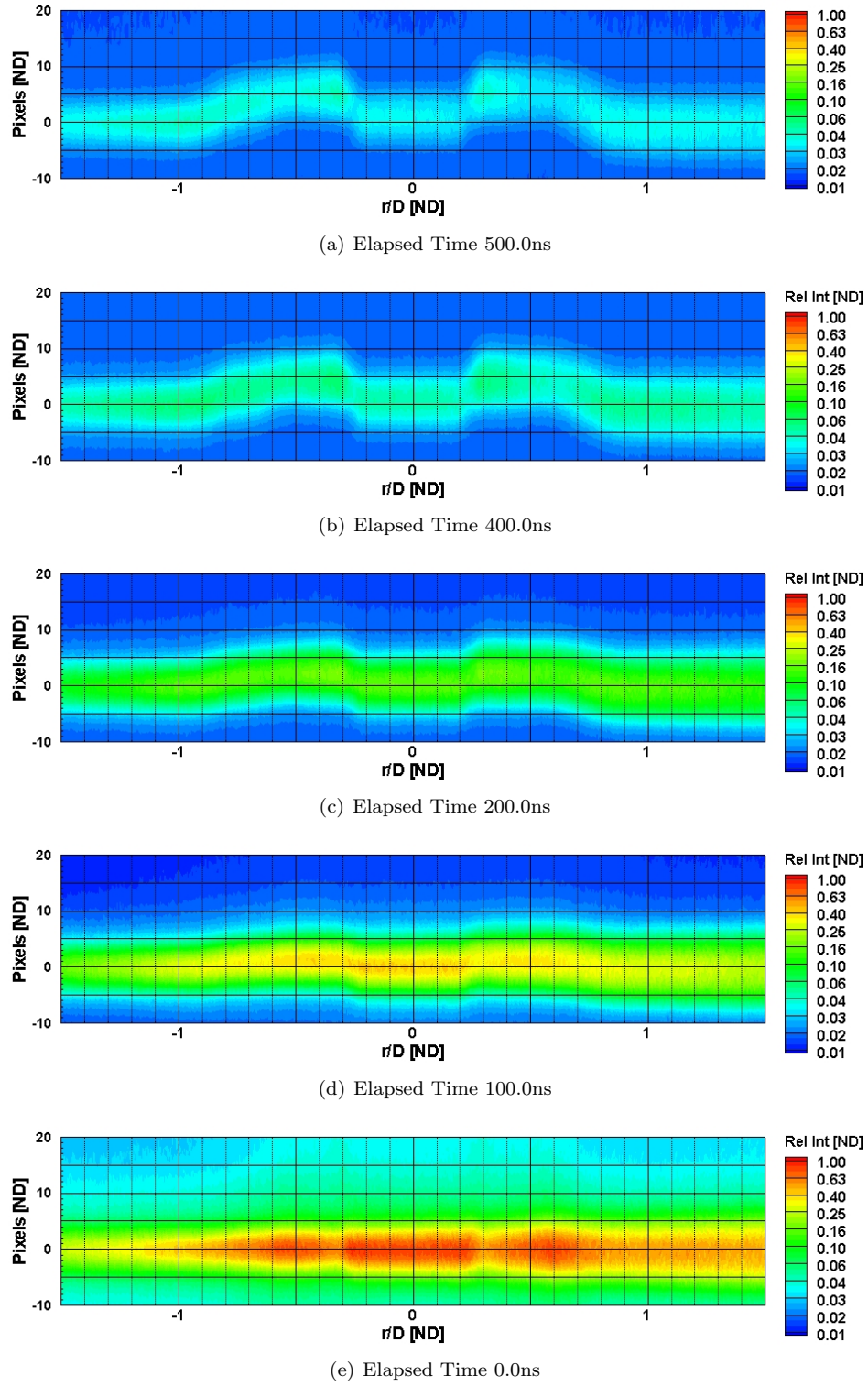


Figure 3.8: Time Lapse Imagery Indicating the Motion of an Acetone Seeded Flow Field (A Highly Underexpanded Jet Just Downstream of the Mach Disk) Imaged After Being Tagged by a UV Laser Beam at 266nm

This extended emission by means of phosphorescence presented in Figure 3.6 was key to utilizing Acetone in the molecular tagging technique. Figure 3.8 is made from a series of phase locked images with growing delay times from the exciting laser pulse. The images were taken for an underexpanded axisymmetric jet just downstream of the normal shock and the flow is from the bottom of the page towards the top. Given the upward direction of the flow, the time delay from laser pulse increases from the bottom of the page (panel (e)) towards the top (panel (a)). Note that for increasing delays, the intensity of the shifted beam decreases. The best combination of adequate intensity and maximum pixel travel was found to occur at 400 ns.[159, 171, 174, 207]

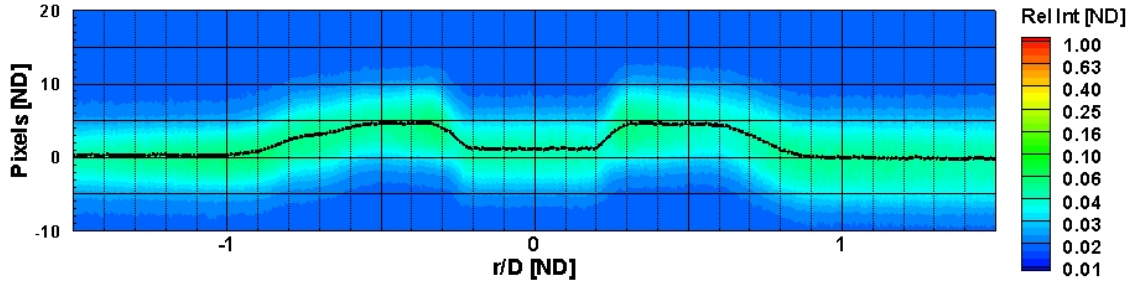


Figure 3.9: Line of Acetone Phosphorescence Indicating Location of the Peak Determined from Curve Fitting Algorithm

From images like these, the velocity in the axial direction was obtained by use of a Gaussian curve fitting routine. A MATLAB program based on the 'fminsearch' algorithm matched the following equation to the measurement of intensity at each pixel.

$$I_{fit} = a \exp \left(- \left(\frac{x_{pixel} - b}{c} \right)^2 \right) + d; \quad (3.22)$$

Where I_{fit} is the resulting intensity fit for a Gaussian peak centered at b . The constant a represents the maximum value of the peak, and the FWHM is c . A correction for constant floor d was included to improve the fit and never exceeded 1% of the peak value. The use of this curve fit provided sub-pixel accuracy, and assumed the illumination source is Gaussian. The result of the curve fit was a series of b values which indicated the location of the peak center, which was calculated individually for each column of pixels and at every frame acquired. Velocity information was easily obtained then by a simple time-of-flight calculation. The MATLAB code written for curve fitting also determined the pixel shift and corresponding mean velocity profiles. Figure 3.9 shows the performance of the peak locator. The contours represent relative intensity of the phosphorescence signal acquired for an axisymmetric jet flow. The abscissa of the contour plot is scaled by jet diameter, while the ordinate is in pixels. A black line is superimposed on the contour which represents

the calculated peak location and shows excellent tracking of the center of the contour. The computationally intensive nature of the Gaussian curve fitting routine required the use of the LINUX workstation cluster at the Air Force Institute of Technology.[125, 174, 182, 217, 375]

3.3.3 Uncertainty Estimates

The uncertainties in measured parameters are again followed through the same procedure used in the PIV calculations. However, the propagation through the calculations is significantly reduced as the only measurement made was mean velocity. Table 3.6 details the test conditions of the Mach 1.4 axisymmetric jet exhausting into a chamber pressure of 5 torr. The location of the measurements was made at 1.1 diameters downstream of the anode face and therefore differ from Table 3.3. Also, note that the flow speed is affected by the saturation of Nitrogen by Acetone vapor which doubles the molecular weight of the test gas without changing the ratio of specific heats.[370, 374, 397]

Table 3.6: Conditions Chosen to Represent Test Conditions for the Analysis of Uncertainty Propagation in Molecular Tagging Velocimetry

Parameter	Value
t	400.0 ns
x	3.1 pix
U_o	362.0 m/s
U	362.0 m/s
N	1000. samples
Bias Estimates	
$\epsilon_{\Delta t}$	2.0%
$\epsilon_{\Delta x}$	3.3%
σ_u/U_o	0.1%

The bias estimates were calculated in similar fashion to PIV analysis. The Gaussian curve fit routine provided 0.1 pixel accuracy, which was scaled by the 3.1 pixel motion in this example. To cover the spread of timing uncertainty to better than 20:1 odds, the value was estimated to be 8 ns which was the measured pulse-to-pulse jitter of the Spectra Physics laser used for phosphorescence excitation. This factor was scaled by the 400 ns delay between laser pulse and camera gate. Equation 3.23 provides the propagation of measurement uncertainties, with the consideration for improvement provided by large sample sets. By substituting in the values in Table 3.6, the uncertainty in estimating the mean velocity, ϵ_U was 0.1%. [29, 92, 183]

$$\epsilon_U = \frac{\|\epsilon_{\Delta x}, \epsilon_{\Delta t}, 2\sigma_u/U_o\|_2}{\sqrt{N}} \quad (3.23)$$

3.4 Laser Energy Deposition

The Laser Energy Deposition (LED) technique is used here to generate a predictable, periodic large scale structure in the shear layer of the jet. The large scale structure is visible and able to be tracked as it progresses downstream in the shear layer, moving at the convective velocity. Phased-locked particle image velocimetry is utilized to provide mean flow images of the large scale structure at increasing delay times in order to measure the convective velocity of the shear layer. From this technique, the influence of the plasma field on the convective velocity is observed.[11, 111, 149, 151, 364, 391]

The use of LED was introduced by Adelgren et.al [11] as a technique to measure convective velocity through tracking the development of a large scale structure. Figure 3.10 shows flow visualization from a perfectly expanded Mach 2.0 jet where the large scale structure created by LED at the nozzle exit develops and travels downstream. Two recognizable regions are marked in the images at ‘a’ and ‘b’. The primary structure ‘a’ is the vortex core which is trailed by an elongated secondary structure ‘b’. Note how the structure grows and spreads as it convects downstream. Adelgren et. al. found that the large scale structure position can be tracked by following contours of tangential velocity, where the vortical motion of the core vortex region shows up clearly. The large scale structure produces strong tangential velocities ($> 30\%$ of the convective velocity) in the swirl of the vortex. One the downstream side of the vortex, the tangential velocity is outward, away from the jet core, while on the upstream side, a lobe of velocity toward the core is created. Adelgren et. al. found these lobes provide excellent tracking contours.

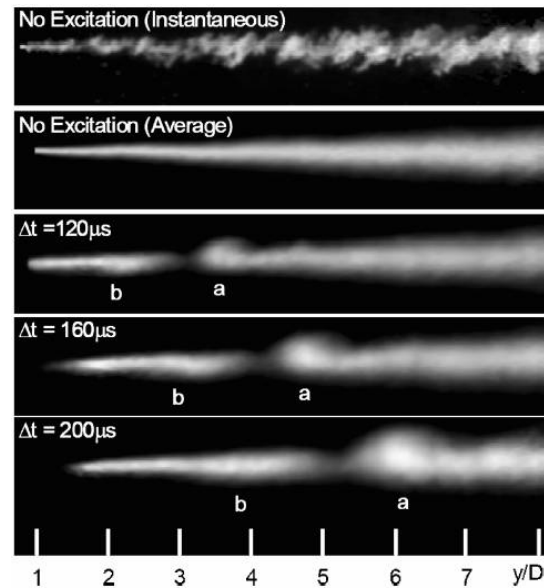


Figure 3.10: Flow Visualization of Mie Scattering from Condensation of a Mach 2.0 Jet Showing Development of the Large Scale Structure from Laser Energy Deposition, from Adelgren et. al. (US Government Work)[11]

3.4.1 Experiment Setup

Figure 3.11 is a schematic of the LED configuration for testing. The setup is similar to the particle image velocimetry schematic of Figure 3.2, with the addition of another laser and associated optics. All of the optical components are specified in Table 3.7. The LED laser source is the Spectra Physics GCR-230 Nd:YAG laser,

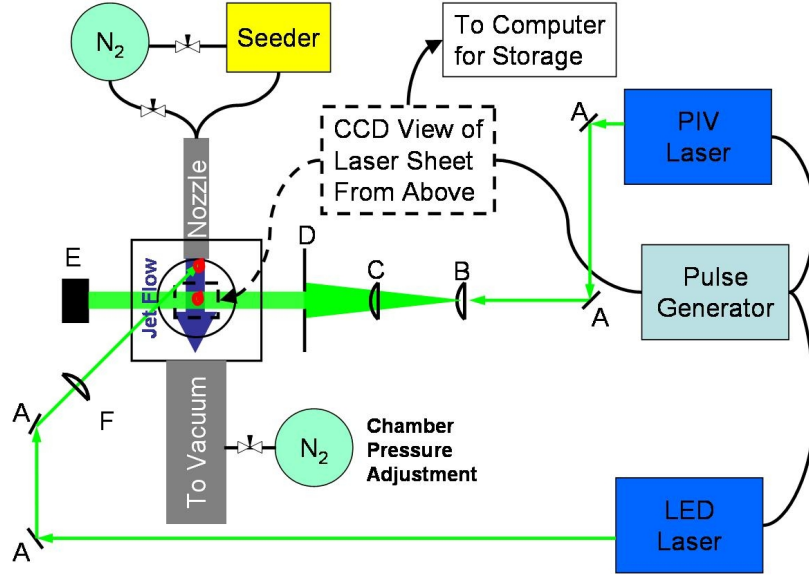


Figure 3.11: Schematic of Laser Energy Deposition

Table 3.7: Description of Optical Components in Figure 3.11, the Schematic of Laser Energy Deposition

Item	Description
A	Dichroic Mirror
B	Lens, Cylindrical-Convex $f = 500$ mm
C	Lens, Spherical-Convex $f = 750$ mm
D	Knife-Edge for Beam Forming and Reflection Minimization
E	Beam Dump
F	Lens, Spherical-Convex $f = 750$ mm

tuned to a nominal frequency of 532 nm. The PIV laser and LED laser are phase-locked to the PCO.1600 Cooke camera by means of an Quantum Composers Model 576 8-channel pulse generator.[\[29, 27, 30\]](#)

3.4.2 Test Procedures

The setup for LED was the same as described in the PIV section. After the camera was focused and calibrated for position and surveyed relative to the anode face, it was centered roughly between the cathode and anode and aligned to capture the full extent of the jet shear layer. Next, the LED laser entered through a glass window and was focused to a point in the test section. The focal point of the beam was placed on the anode lip, near the jet exit and in the plane of PIV imaging.

A small ablation region was created at the anode lip by creation of a small plasma at the beam's focal point. The LED laser was passed through a series of neutral density filters to cut the power per pulse down

to 20 mJ. The pulse power was monitored in between experiments through an Ophir Nova II power meter coupled to an Ophir Model 30(150)A-HE power head which measured average energy of a series of pulses. The power per pulse was determined by dividing the average energy by the pulse repetition rate of 10 Hz. Additionally, real-time pulses were monitored by observing a reflection of the laser beam off one of the dichroic mirrors by a DET-200 photodiode from Thor Labs. The resulting curve of intensity as a function of time was integrated by an Stanford Research Systems SR-250 boxcar integrator which was monitored during testing by a Fluke 89 IV multi-meter.[11, 111, 149, 151, 364, 391]

Synchronization of the LED pulses were first estimated by the time required for a structure to travel at one-half the jet exit velocity the distance from the anode face until centered in the CCD field of view. This approximation consistently placed the structure barely in the upstream portion of the CCD image. From there various time delays were examined to determine three or four delays in which the period structure created would be observable by PIV. The test then proceeded through the matrix of time delays where plasma off runs were interleaved with plasma on runs. The time delays were interleaved as well to account for any degradation of the large scale structure due to the drilling of small holes into the anode from the focused laser light. For each time delay more than 750 PIV image pairs were collected and processed. The resulting data set required 238 gigabytes of storage for the images and subsequent PIV vector fields.[11, 17, 307]

The large scale structure was tracked through post-processing analysis of the vector fields. The velocity fields were shifted into the convective reference frame allowing clear observation of the period structure for tracking. From there, contours of tangential velocity, scaled by convective velocity were gathered and stored in files. A contour representing the location of the structure at each time delay and plasma condition was then evaluated by a centroid tracker. The centroid tracker was written in MATLAB and preferred round contours, which required care when selecting contours. When possible, the same contour level was used for each different time step and plasma condition. In some cases, the contour level was adjusted to provide accurate centroidal position. The contour levels were adjusted by no more than 5% of the initial contour level. Convective velocity U_c was measured according to Equation 3.24

$$U_c = \frac{x_2 - x_1}{t_2 - t_1} \quad (3.24)$$

where the subscripts 1 and 2 correspond to two different time delays, x is the centroid position and t is the value of the time delay.[11]

A sample of the expected large scale structure tracking, is shown in Figure 3.12. The results presented are in an experiment from Adelgren et. al. [11] for a perfectly expanded Mach 1.38 jet into quiescent air

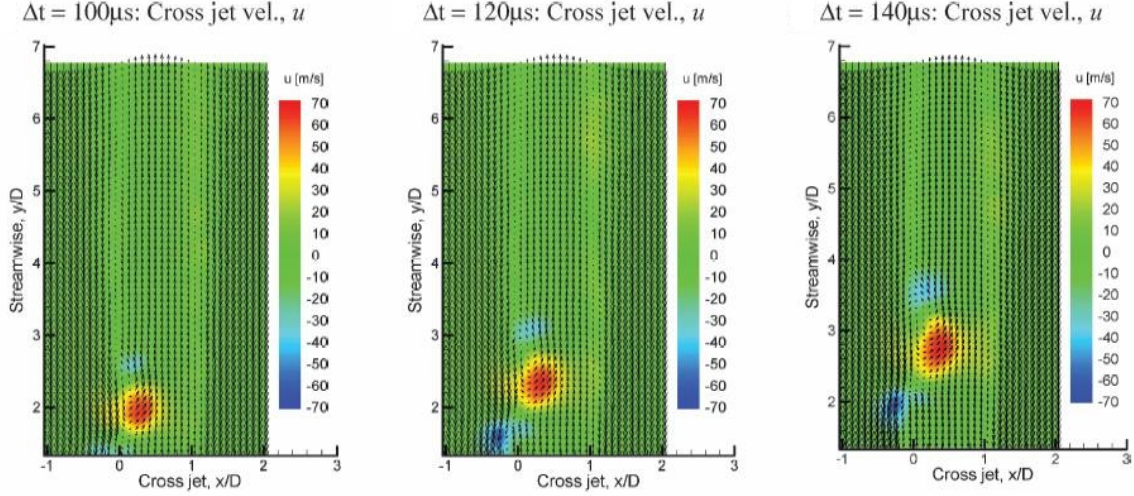


Figure 3.12: Contours of Tangential Velocity in the Convective Frame Showing Large Scale Structure Motion in the Shear Layer of a Mach 1.38 Perfectly Expanded Jet, From Adelgren et. al. (US Government Work) [11]

(with very low speed co-flow) at atmospheric pressures. Three successive time delays show the large scale structure in tangential velocity contours as well as the vector field in the convective velocity frame. Note how the motion of the large scale structure is readily apparent in the tangential velocity contours (u in their experiment).

3.4.3 Uncertainty Estimates

The uncertainty in this technique was overwhelmingly biased toward the error created by tracking the structure with the centroid tracker. The error in measuring position based upon a poor choice in contour was measured to be 0.2 mm. While, it is believed that the contour choices were much better than the worst case scenario the measurement error stands in order to conservatively contain 20:1 odds. The error in timing is so small (0.01%) that it is neglected as a contribution further downstream. Additionally, the errors associated with PIV image processing to determine the velocity field are not propagated forward as these errors are minimized by 750+ samples and are small when compared to the two measurements of centroid position. The centroid position error propagates forward into the uncertainty in convective velocity then by

$$\epsilon_{U_c} = \|\epsilon_{\Delta x_1}, \epsilon_{\Delta x_2}\|_2 \quad (3.25)$$

where $\epsilon_{\Delta x}$ is the uncertainty in centroid position, scaled by $(t_2 - t_1)U_c$. Given the large variation in time delays and convective velocities, the propagated uncertainty will not be tabulated here. Instead, the uncertainty in each measurement reported in the results has a column reporting the uncertainty associated with that

measurement and is found in Table 3.7 on page 73. [11, 92]

3.5 Plasma Imagery of Visible Light Emission

Light emitted by plasma excited molecules and atoms were collected by photography with a cooled charge-coupled device in this technique. Visible light emission from the plasma field is an easily observable phenomena which indicates the presence of a strong plasma field. The plasma works on the both the radicals and molecules, pumping the ions and neutrals into electronic states much higher than ground. Figure 3.13 is a drawing of an excited molecule releasing a photon and dropping from an excited electronic state E_2 , to a lower state E_1 . One of the readily apparent indicators of the presence of molecules in elevated electronic states is photon emission. And

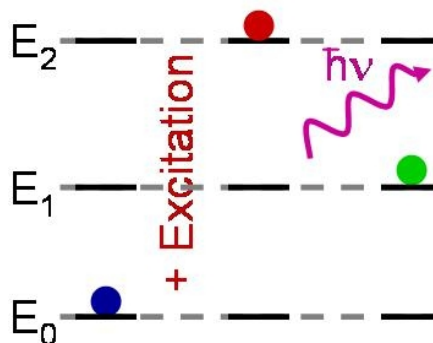


Figure 3.13: Schematic of Photon Emission from an Excited Molecule

therefore in locations where there are high concentrations of molecules and radicals emitting photons, it can be deduced that the field performing the work on those molecules is high. By capturing light on a charge-coupled device with constant exposure settings, the relative grayscale intensity of the light can be compared to provide a figure of merit on the plasma strength for each case. Calibrations were made so that different plasma fields could be compared to each other to provide a quantitative evaluation. This section provides the details regarding the setup and prosecution of the experiment. [125, 229, 308]

3.5.1 Experiment Setup

Figure 3.14 describes the layout used to collect visible light from plasma emission for use in quantitative analysis. Nitrogen was fed from compressed cylinders through a regulator into the plenum, where total pressure was measured by a ConvecTech CVT-275-101 Pirani style pressure transducer and total temperature was measured by a K type thermocouple read by an Omega HH81 digital thermometer. The flow was then accelerated onto conditions through the nozzle section which exhausted into the test section. The flow through the test chamber is from top to bottom, as indicated by the blue arrow with the light purple trapezoidal region signifying the plasma field. The test section was 30.48 cm in length, width and height with optical access provided on 4 sides (the sides without nozzle or vacuum ports) through 15.24 cm round

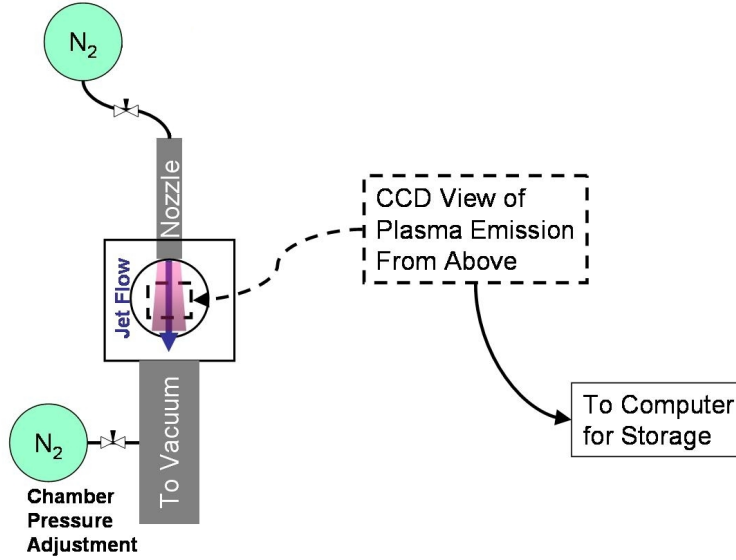


Figure 3.14: Schematic of Imaging Visible Light Emission

glass windows, 19.1 mm thick. Over the top access window, a PCO.1600 CCD camera from Cooke Corp. was cantilevered. The camera was allowed to traverse axially and tangentially with respect to the flow through two translation stages. If required for focusing, the camera could be adjusted perpendicularly to the focal plane by means of cap screws through slotted grooves attached to the cantilever assembly. A computer was connected to the camera control to acquire and store the images. Downstream of the test section, the flow exhausted into 15.24 cm PVC pipe which was evacuated by a Kinney KT-300 vacuum pump. To adjust and regulate chamber pressure, a bottle of compressed Nitrogen was vented into the PVC plumbing at a T-connector through a regulator.[24, 27, 23, 125]

3.5.2 Test Procedures

The goal of this test technique was to capture images which were calibrated in position and intensity, in order to compare the plasma field emissions of the various test conditions. To calibrate the images in position, the pixel size was calibrated by photographing a ruler with 0.254 mm increments. The camera was aligned to the anode face such that the pixel coordinates corresponded to axial and tangential coordinates relative to the flow. Given that the focal plane of the camera was parallel to the test section to within $\pm 2^\circ$, it was assumed that the pixel size was the same in both the axial and tangential directions.[125]

Next, the images were calibrated in intensity. To provide the highest resolution of intensity, the longest exposure time possible was desired. The exposure time was set using the no-flow α -discharge to allow

sufficient time for several cases to be evaluated. The exposure time was increased until the point of saturation occurred in the anode and cathode glow regions. The exposure time was set at 100 ms. The lack of overexposure was confirmed by checking some of the brighter plasmas tested and found that saturated pixels occurred only near the electrodes or in the case of an unstable plasma which transitioned to an arc discharge. With the exposure time fixed, the intensity between two plasma fields were able to be compared directly.[125, 145, 308]

Thirteen 100 ms images were acquired of the plasma field for each test case. These images were processed by subtracting the background counts and then averaged together. To further align the coordinate system of the camera to the plasma field, a post-processing technique was employed next to determine electrode gap space and to correct for misalignment. The image was investigated to determine the location of the electrode faces and the line connecting the centers of each electrode. Some minor difficulty was encountered when finding the location of the electrode faces due to saturation from cathode glow or lack of signal at the anode face. These were minimized by false color image displays and by picking multiple points and using averages to determine the actual location. After the points of interest were measured, the images were compared to the measurement. Gap distance errors between the electrodes were found to be no more than 2 mm. The alignment correction needed was found to average between 1° and 2° , never to exceed 2° . [125]

All of the plasma field intensities were imaged simultaneously with the spectroscopy measurements in order to help quantify the field imaged through spectroscopy. Note, that the spectroscopy measurements were made horizontally through a fused silica window in the side of the test section, while the visible images were obtained vertically through a glass window on the top of the test section. While the plasma was relatively axisymmetric, slight asymmetries were observed and therefore the plasma field was slightly dependant upon the viewing angle. The most noticeable asymmetry was in the misalignment of the electrodes. While great care was taken to align the electrodes, even misalignment of between one and two degrees (the typical measured error) caused the plasma field to become visibly stronger on the side with smallest gap distance between electrodes. Therefore the reader should be cautioned that comparing visible emission images to spectroscopy images will involve slight mismatches and that only trend information should be extracted in those comparisons.[145, 251, 308]

It was impossible to take visible imagery of the plasma field concurrently with particle image velocimetry data, as the same camera was used for both techniques. The process involved in reconfiguring the camera between PIV and visible intensity measurements involved changing lenses, recorder settings and refocusing. Therefore it was impossible to perform realtime on the exact same plasma fields, as the reconfiguration operation involved bringing the test section up to atmospheric pressure. And while the repeatability of

the plasma field generation was relatively consistent (by generator settings and by observation), the same electrode mismatch errors mentioned previously did occur. Again, caution must be wielded when comparing measurements of light intensity with PIV data in that only trends between the two are valid for the data were not collected simultaneously.

3.5.3 Uncertainty Estimates

Two uncertainties in the measurement of visible light intensity from the plasma field have been eluded to in the previous paragraphs. This section will quantify the effects on the measurements made. The first uncertainty was the measurement of gap distance. As previously mentioned, the error in measuring gap distance was found to be a maximum of 2 mm. For typical gap spaces of 80 mm, this represents an error of 2.5%. Since the alignment correction was found to be less than 2° and the correction was applied to effectively eliminate misalignment, the alignment error will be neglected in further contributions to downstream calculations. The position error of 2.5% with respect to gap distance is applied therefore to both axial and tangential directions as a conservative estimate of uncertainty in position reported. Table 3.8 provides a summary of the uncertainties found here, where I is the intensity relative to maximum counts ($I_{max} = 65535$), G is the gap distance between electrodes and x and r are axial and radial (tangential) positions, respectively.[92]

Table 3.8: Propagation of Measurement Uncertainties for the Plasma Imagery of Visible Light Emission

Normalized Error	Derivation	Value [%]
ϵ_x	$\Delta x/G$	2.5
ϵ_y	$\Delta x/G$	2.5
ϵ_I	$2.179\sigma_I/I_{max}\sqrt{13}$	0.2

Note that the estimate in uncertainty in relative intensity was calculated from the standard deviation, σ_I , from one of the representative image samples and was found to be 247 counts. Since the number of samples was 13, the student-T distribution was used to provide a factor of 2.179 as the confidence coefficient for 95% interval. The uncertainty in mean relative intensity is given by $\Delta I = 2.179\sigma_I/\sqrt{13}$ as outlined in Grant and Owens.[156] The resulting uncertainty ΔI was then scaled by the maximum counts to produce ϵ_I .[92]

3.6 Temperature Measurement with Spectroscopy of the Second Positive System of Diatomic Nitrogen

Spectroscopy is a calibrated technique of analyzing light emitted from various sources. It is a popular technique, used to measure gas concentrations and compositions on distant planets as well as for measuring combustion temperatures on this planet. In this case an imaging spectrometer is used to provide a vertical line of rotational and vibrational temperature measurements by focusing in on a small part of the spectrum to examine the light emitted from the second positive system of diatomic Nitrogen.[80, 113, 125, 131, 172]

The use of second positive system of diatomic Nitrogen to calculate rotational and vibrational temperatures by model matching in plasma fields has historical acceptance. Arc plasma temperature fields have been measured this in atmospheric air this way.[132, 234] Additionally, an RF capacitively-coupled plasma was generated in atmospheric air by use of microchannel electrodes, with spectroscopy providing the thermal measurements.[309] Dielectric Barrier Discharge plasmas in atmospheric air have also been measured.[198] At lower pressures, Palm et. al.[286, 384] used this technique to investigate temperatures in a CO laser, which was pumped with an RF capacitively-coupled plasma in a chamber pressure varying from 0.1 to 1.0 atmospheres. Finally, DC glow plasmas have been investigated in the pressure ranges of this research, both in quiescent Nitrogen [49] and supersonic to hypersonic flows.[341, 358]

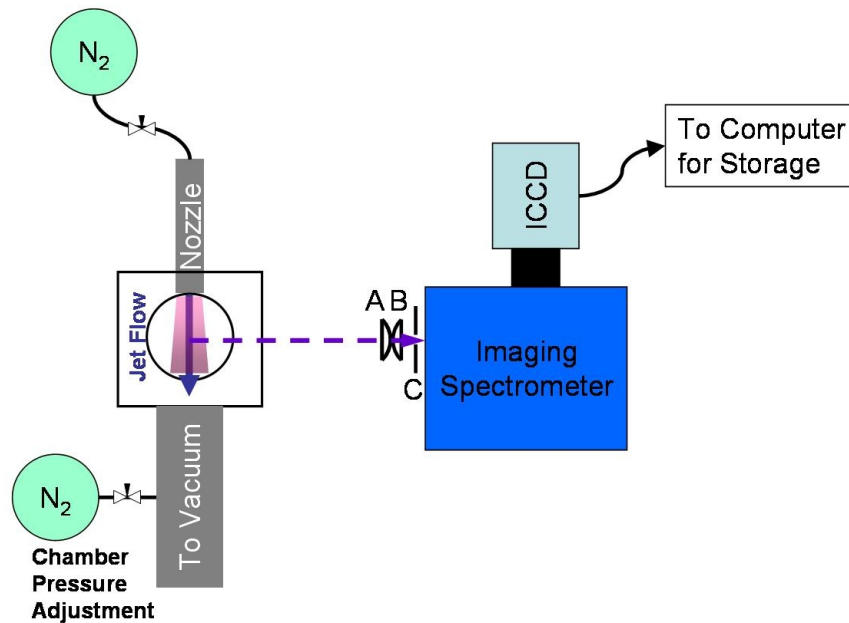


Figure 3.15: Schematic of Imaging Spectroscopy

Table 3.9: Description of Optical Components in Figure 3.15, the Schematic of Imaging Spectroscopy

Item	Description
A	Lens, Spherical-Convex $f = 600$ mm
B	Lens, Spherical-Convex $f = 75$ mm
C	Iris

Figure 3.15 is a schematic of the setup for imaging spectroscopy. The setup of the test chamber is similar to the PIV, LED and MTV experiments - noting the removal of any seed equipment here. The optical components of which are detailed further in Table 3.9. Two spherical plano-convex glass lenses were placed together with the convex sides towards each other in order to image a line about 8 cm high in the test section onto the 1 cm tall slit at the entrance of the spectrometer. The image was shaped slightly by placing an iris in the optical path to help eliminate light being emitted from the plasma field outside the region of interest from entering the spectrometer. The imaging spectrometer was an ISA Triax series 190 spectrometer and featured the ability to switch between three different diffraction grating mirrors. The grating used in this experiment contained 2400 gratings per mm. This spectrometer also featured an adjustable slit, which was set to 0.03 mm. The diffraction grating mirrors perform the same effect as a prism on the incoming light, spreading it out onto the intensified charge-coupled device which was a model ICCD-576-S from Princeton Instruments. The resulting wavelength resolution was 0.03 nm.[32, 22, 125, 131, 170]

3.6.1 Experiment Setup

To determine the broadband emission of the light being emitted by the plasma field, an experiment was performed with an Ocean Optics S2000 fiber optic spectrometer. This spectrometer has a $5\mu\text{m}$ slit producing 0.3 nm resolution over wavelengths from 250 nm to 850 nm. Figure 3.16 shows the results of this experiment. Note that the second positive system of diatomic Nitrogen is highlighted and that emission is relatively strong and free of overlapping emission from other species.[80, 113, 125, 131, 170]

3.6.2 Test Procedures

Again the test procedure section begins with the calibration procedure. In this case an index card was marked with black lines every 12.7 mm and placed at the focal point of the imaging spectrometer which coincided with the centerline of the jet. The black calibration lines were aligned to be parallel with the jet flow. These lines, when imaged, show up as dark regions on the ICCD and were used to provide a vertical position calibration of the recorded images. The index card was illuminated by a hollow cathode lamp with

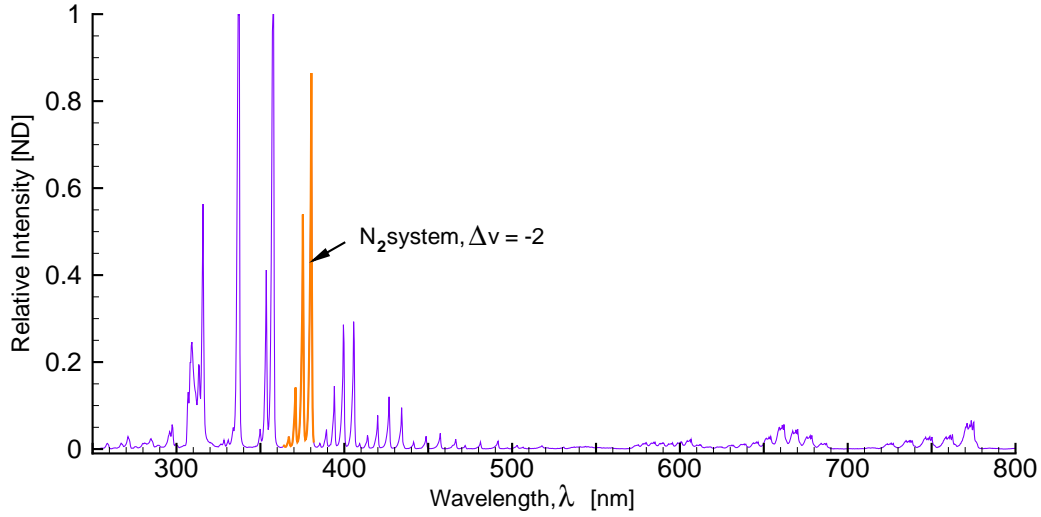


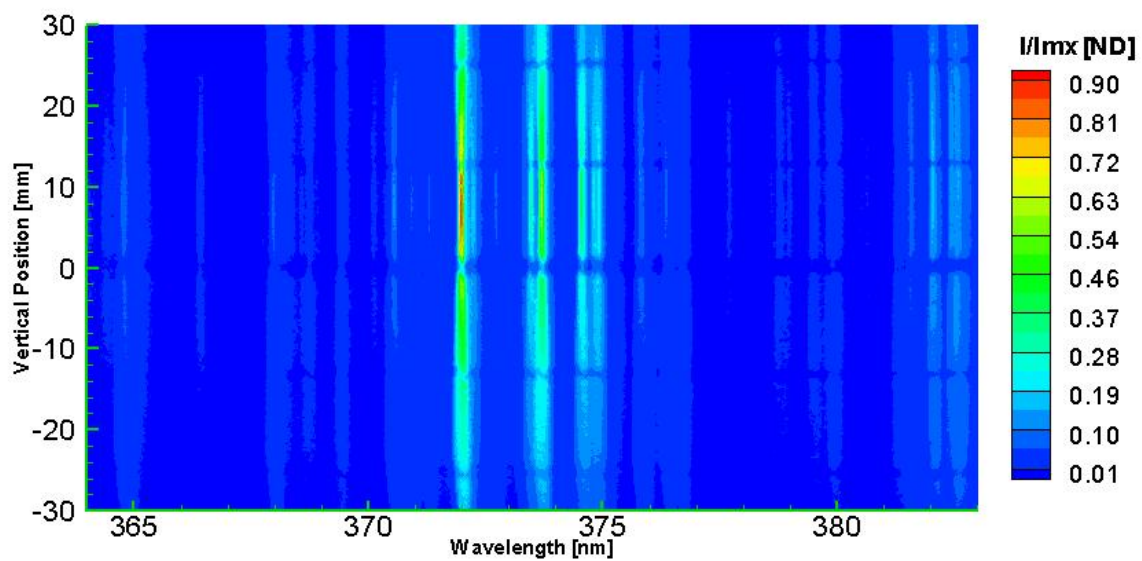
Figure 3.16: Spectrum of Plasma Emission from Near Ultraviolet to Near Infrared

a sample of iron inside. The lamp stimulated the emission of numerous Iron lines in the spectral region of interest.[125, 131]

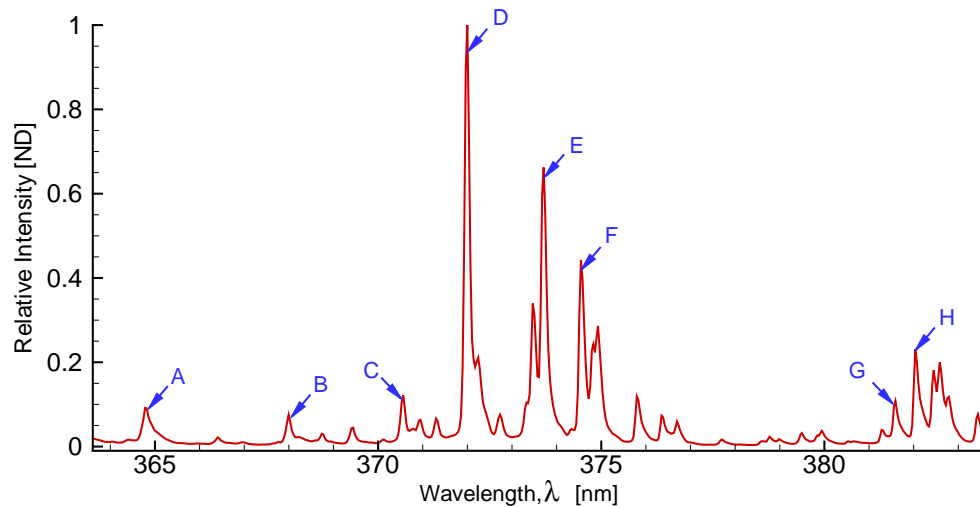
Figure 3.17 (a) is a contour image of relative intensity of the index card with calibration lines illuminated by the Iron sample hollow cathode tube lamp. Individual Iron emission lines show up vertically across the sample and are cut horizontally by the dark lines from the calibration marks on the index card. Figure 3.17 (b) is a line of intensity formed by binning 30 rows of the image in panel (a) together, centered about 14.7 mm. The features used to perform the wavelength calibration are indicated by the letters in the figure. The source for the calibration information was the NIST database, the results of which are tabulated in Table 3.10. The relative intensities are listed as an aid to distinguish between the different lines and to reject lines near the ones listed.[125, 131]

Table 3.10: Emission Lines of Iron Used to Perform Spectral Calibration, Taken from NIST [313]

Index	Wavelength [nm]	Relative Intensity [%]
A	364.7842	19
B	367.9913	19
C	370.5566	15
D	371.9935	100
E	373.7131	75
F	374.5561	75
G	381.5840	19
H	382.0425	31

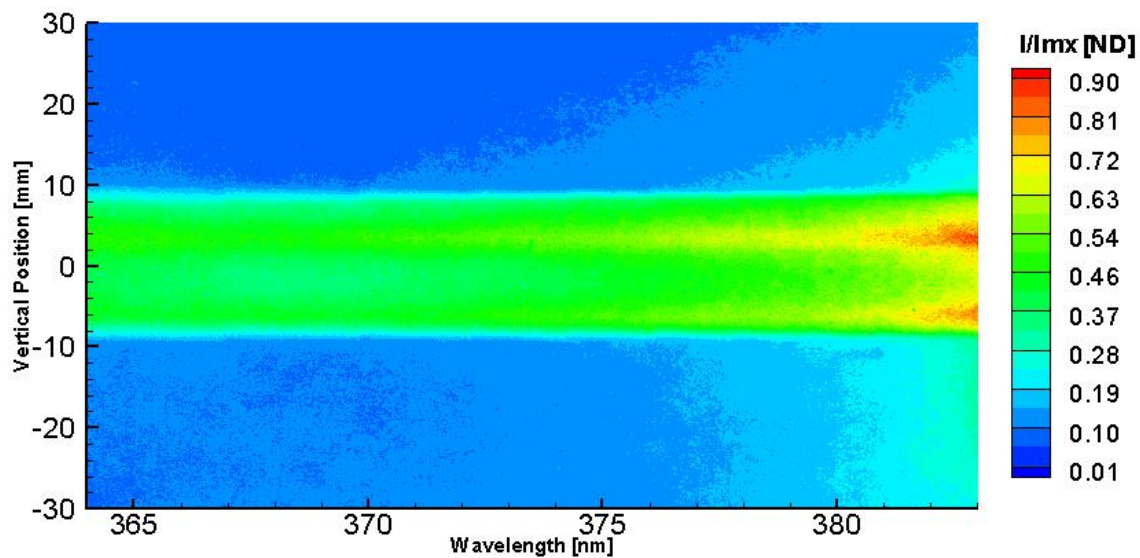


(a) Contours of Relative Intensity

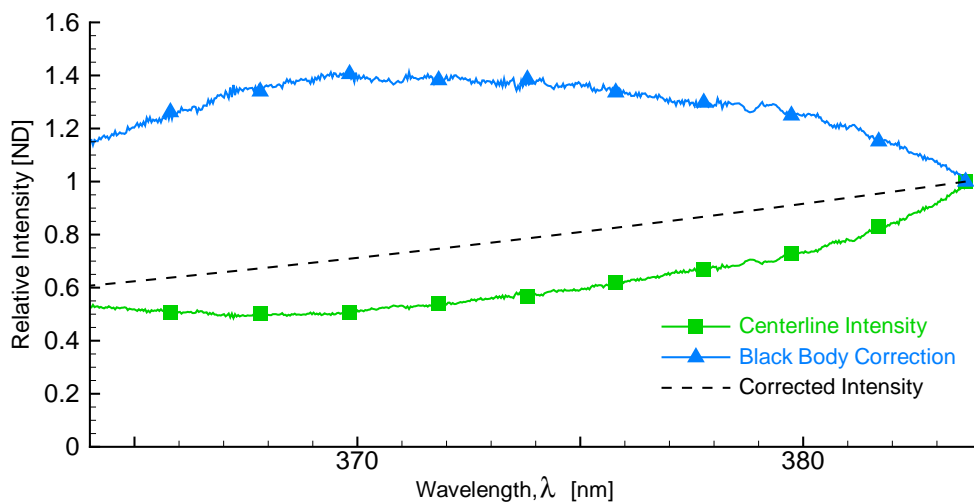


(b) Relative Intensity along a Line Centered at $z=14.7$ mm

Figure 3.17: Relative Intensity of Hollow Cathode Iron Emission Used to Calibrate the Imaging Spectrometer



(a) Contours of Relative Intensity



(b) Relative Intensity along the Centerline

Figure 3.18: Relative Intensity of Black Body Emission at 2659 K Used to Calibrate the Imaging Spectrometer

Next the intensity response of the optical train from the test section through to the ICCD is calibrated from a white light source created from a Tungsten lamp. The Tungsten lamp was calibrated by NIST standard to a black body at a temperature of 2659 K. The intensity response of the system was then corrected by a frequency dependant function which replicated the exponential decay of a black body source at the calibrated temperature. Figure 3.18 shows a contour image of relative intensity of the lamp in panel (a) with the binning to produce a line and subsequent correction process in panel (b). The lamp was 2.5 cm high and was placed on the jet centerline in the focal plane of the imaging spectrometer.[125, 131, 313]

With the extensive calibration complete, data collection began. The optics, spectrometer and ICCD were fixed to an optical breadboard and fastened to an optical table. The system was aligned to take readings in a line 10 mm upstream from the face of the cathode. This was chosen as the baseline plasma measurement location for two reasons. First, the location was far enough upstream to avoid the light emitted from the cathode glow. The cathode glow was the plasma field created in the immediate vicinity of the cathode and was not representative of the plasma field affecting the shear layer of the jet. Secondly, the location 10 mm from the cathode was in a region which was consistently illuminated for even the weakest plasma fields. Some plasma fields did not provide uniform emission across the electrode gap, but near the cathode, consistent emissions were recorded. Some plasma fields were mapped across the electrode gap by sliding the breadboard table in a track to keep the system focus aligned with the jet centerline. The displacement of the system from the baseline position was measured by a ruler, with marks every nearest mm.

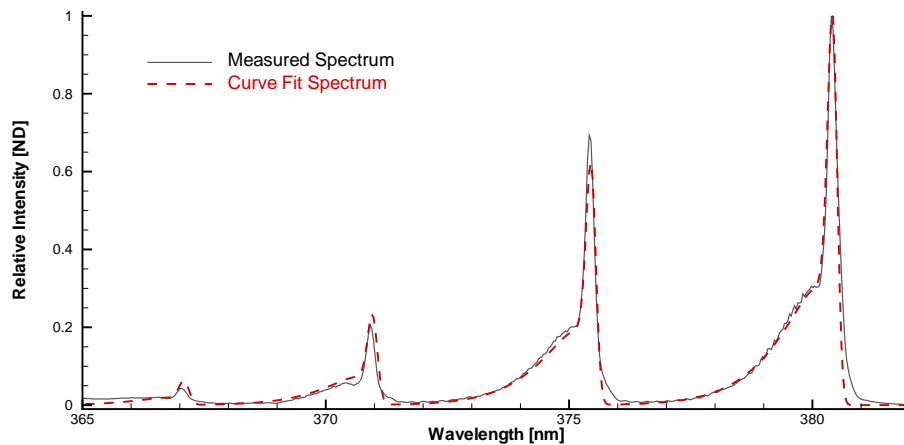


Figure 3.19: Sample of Spectrum Fitting Results

The emission of plasma spectra were recorded in batches of 50 images. The exposure time of the ICCD was adjusted as required to obtain enough signal for processing. Dark images were taken for each measurement

and also consisted of 50 frames recorded. All significant light sources were extinguished for both data and dark field images to eliminate contamination from other spectra. The images were processed by another custom MATLAB routine to first average the 50 frames of dark images. Then the data images were averaged, subtracting the average dark frame from each image before averaging. Finally, nine lines were created by binning 30 rows together. Separate calibrations of the Iron lines were made for each line to account for any differences based on vertical displacement and variations in dispersion. The calibrations were applied to the nine data lines, and included the transformation from location to wavelength, and the correction to intensity from the black body radiation source. Next each of the measured spectra were curve fit in a FORTRAN routine supplied by Dr. Nick Glumac at the University of Illinois at Urbana-Champaign, to a model of the second positive system of diatomic Nitrogen. The model iterated until convergence and calculated the vibrational and rotational temperature of Nitrogen by matching a modeled response to the measured and corrected data. Figure 3.19 is a sample of the curve fit response.[125, 131, 132, 198, 234]

3.6.3 Uncertainty Estimates

Estimates of the uncertainty and error propagation were difficult to determine with this technique. Re-searching similar experiments and investigating trends in the ability of the curve fitting routine to capture changes in temperature, it was estimated that rotational and vibrational temperature measurements are accurate to ± 25 K and ± 200 K, respectively. The location relative to the cathode face was uncertain to within ± 0.5 mm based on one-half the smallest increment on the ruler.[131, 152]

Chapter 4

Results and Discussion

This chapter documents the measurements conducted to characterize the plasma and its effect on the mean and turbulence quantities of the jet. It is divided into the specific test techniques used to investigate the jet flow fields. First, verification results are reported to investigate how well the seed particles track the flow. Then, with adequate tracking characterized, particle based velocimetry techniques were used for the quantitative measurement effort. The bulk of this chapter then focuses on the velocimetry results, examining the effect plasma had on mean and turbulent measurements of the velocity field for various jet conditions. Four different axisymmetric jets and their resulting shear layers were investigated to determine the influence of a plasma field on them: perfectly expanded subsonic and supersonic jets, jets created by developing pipe flow exhausting from a constant-diameter tube, and large scale structures created by forced laser energy deposition into jet flows. The plasma field is documented next by examining the intensity of light emitted in the visible spectrum. Finally, the plasma field is defined quantitatively by examining the rotational and vibrational temperatures of diatomic nitrogen through spectroscopy of the emission of near ultraviolet light from second positive system of diatomic nitrogen.

Figure 4.1 are a pair of photos of the plasma field. Note that flow is from left to right in this highly underexpanded jet flow. The anode is on the left, with the cathode coated in black paint on the right. With the plasma on, the barrel structure associated with the plasma field is visible at the jet exit through the anode. Note the darker region in the center of the jet which represents the jet core region.

Run Conditions

Figure 4.2 shows the chamber pressure and equivalent Mach number of the jets which were tested in this experiment. The experiment space in this figure is shown in terms of equivalent Mach number M_i on the abscissa which is derived by using the measured pressure ratio and in terms of measured chamber pressure on the ordinate. The letters designate a case identifier to aid in cross referencing. The primed letters (e.g. H') indicate that condition was tested using the anode modified with serrated conical feature. Cases without the primed mark were tested using the flat-faced anode.

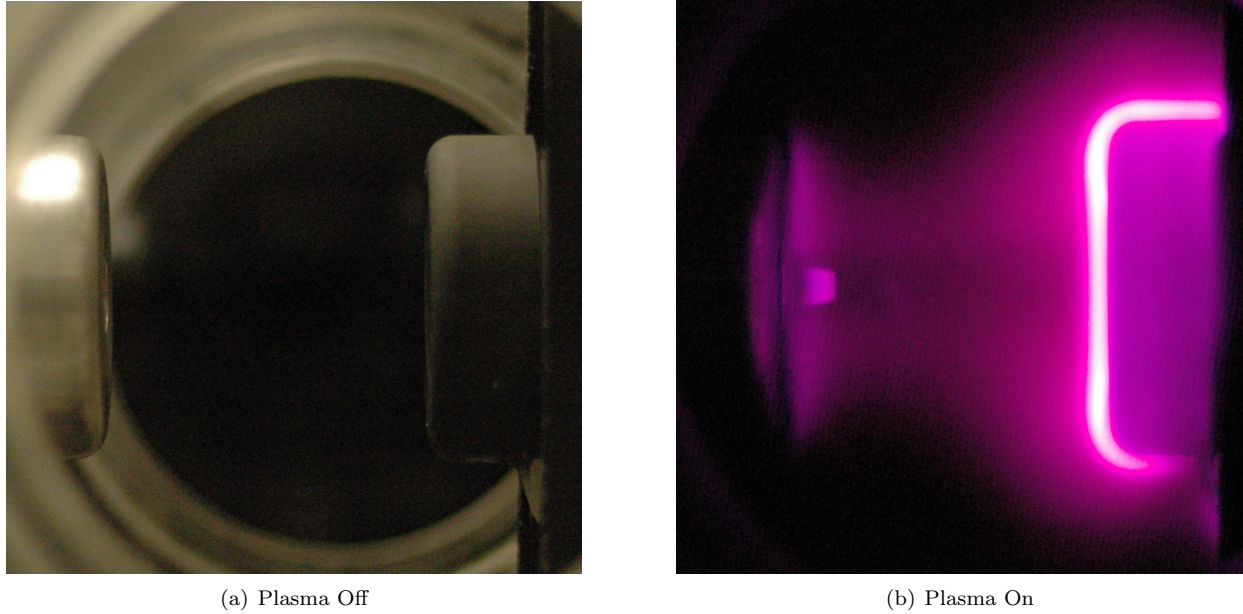


Figure 4.1: Photos of the Jet and Plasma with Flow from Left to Right, Note the Barrel Shock of Highly Underexpanded Jet is Visible with the Plasma On

Cases A, B, C, and E are experiments conducted on converging-diverging nozzles under pressure matched conditions. Case E was tested at 8 torr vice 9 torr to achieve the proper pressure matching. Cases F, G and H were conducted using a constant diameter nozzle. The constant-diameter nozzle was made of a tube, 13.3 diameters long. The resulting flow could be driven at subsonic or supersonic conditions with choking caused by an aerodynamic throat created by a separation at the tube entrance. This nozzle design was chosen as an alternative to the standard converging-diverging nozzles to produce increased turbulence in the core of the jet, an effect of developing pipe flow. In addition to these 7 cases, two off-nominal, non pressure matched conditions were examined. Case D represents an overexpanded jet, using the nozzle from Case C but with a decrease in plenum pressure. Case U is a highly underexpanded flow created by a sonic orifice. These two cases explore the possibility of plasma field influence on shocks and expansions.[36, 114, 130, 165, 194]

The goals of this experiment were to create stable, uniform, radio-frequency, capacitively-coupled plasma fields and investigate its affect on the mean and turbulent velocities of compressible axisymmetric jets. To that end, variations in jet exit speed were required in order to ascertain the plasma field influence on compressibility and explains the predominant trend to run along lines of roughly constant chamber pressure with increasing Mach numbers. Higher chamber pressures were desirable in this experiment in order to match test conditions achievable in larger scale supersonic tunnels. However, the uniformity and stability of the plasma field degraded significantly for chamber pressures over 10 torr which set a limit on the chamber pressure for testing.[69, 145, 308]

Another constraint on the experiment and run conditions was due to particle seeding issues. In order

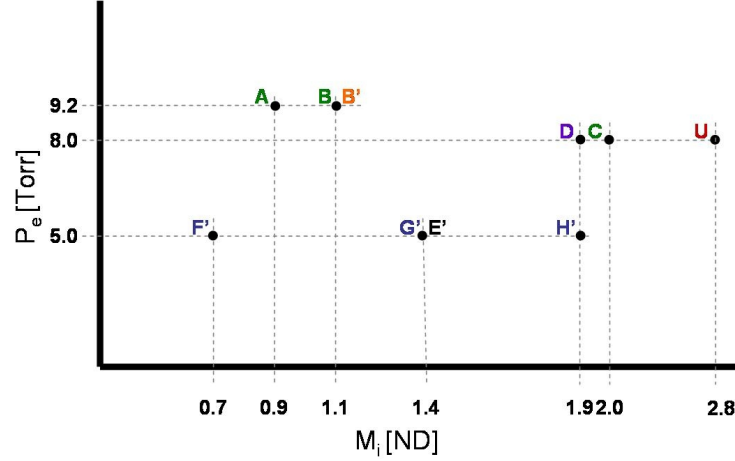


Figure 4.2: A Summary of the Experiment Space by Chamber Pressure and Equivalent Mach Number

to provide adequate seed particle concentration, the flow of Nitrogen and seed into the plenum chamber had to be controlled by a small diameter sonic orifice. Variable regulation by means of a ball valve had a devastating impact on seed particle concentration and uniformity in the flow. The diameter of the upstream sonic orifice effectively set the mass flow - and vacuum pump performance set the chamber pressure based on mass flow from the jet (combined with a regulated vent downstream of the test section). The nozzle design and pressure matching process became complicated as the upstream sonic orifice and the downstream test nozzle interacted with each other.[25, 219, 297]

Table 4.1: Estimation of Jet Exit Conditions

	P_o (1)	P_e (1)	T_o (1)	M_i (2)	U_i (2)	T_i (2)	M_e (3)	U_e (1)	T_e (3)	D_e (1)	Re_D (3)
	[torr]	[torr]	[K]	[ND]	[m/s]	[K]	[ND]	[m/s]	[K]	[mm]	[ND]
A	12.7	9.15	289	0.70	231	263	0.69	229	264	20.8	4470
B	20.5	9.15	293	1.14	353	232	1.13	350	233	15.7	8501
C	71.0	8.00	292	2.08	530	157	2.03	523	160	11.3	22430
D	62.0	8.00	293	1.99	518	163	1.94	510	167	11.3	20208
E'	16.5	5.00	296	1.43	421	210	1.35	404	217	9.5	6133
F'	8.2	5.00	293	0.87	283	254	0.75	247	263	9.5	2637
G'	16.5	5.00	295	1.43	420	209	1.27	387	222	9.5	5605
H'	34.0	5.00	294	1.91	507	170	1.63	460	192	9.5	8733
(1) Measured Quantity											
(2) Estimated From Pressure Ratio, Assuming Isentropic Flow Through Nozzle											
(3) Estimated From Plenum Temperature and Measured Exit Velocity											

In order to better quantify jet exit conditions in the absence of temperature measurements, the following approach is applied to both converging-diverging nozzles and constant-diameter tubes. First, the plenum temperature is taken as the stagnation temperature at the jet exit. Then, the measured exit velocity is

used to estimate the exit Mach number, temperature, density and viscosity - knowing that the developing pipe flow is not isentropic. This assumption appears reasonable, given that in all cases tested, the measured exit velocity is within 15% of the equivalent isentropic exit velocity for the same pressure ratio. Table 4.1 summarizes the exit conditions for the test cases. In the first section on the left in Table 4.1, each of the conditions is labeled by the case identifier introduced in Figure 4.2. Next, the measured pressures and temperatures are listed. The plenum pressure P_o and temperature T_o were measured by a CVT-275-101 Pirani style pressure transducer and an Omega K-type thermocouple through ports into the plenum chamber. The chamber pressure P_e was also measured by a CVT-275-101 transducer through a port drilled into the test section. Using the measured pressure ratio and stagnation temperature from the plenum, the following isentropic conditions were calculated: Mach number M_i (also referred to as equivalent Mach number for off-design cases), exit velocity U_i and exit temperature T_i . These are compared in the next block of Table 4.1 with the measured exit velocity U_e and corresponding Mach number M_e , and static temperature T_e which were calculated based on the measured exit velocity and assume adiabatic flow. Finally, based on T_e and the measured P_e (assuming matched flow) the exit density and viscosity were calculated to determine the Reynolds number. The characteristic length for an axisymmetric jet was the jet exit diameter D_e which is presented as well. While some approximations were applied in calculating these parameters, they are reasonable given the care taken to achieve near-matched conditions for these jets. In the case of the flow created by a constant-diameter nozzle, there is a pressure loss associated with the developing pipe flow. This does have an influence the total temperature, however the influence is believed minor.[14, 40, 297]

4.1 Characterization of Particle Tracking

Although particle image velocimetry (PIV) is a reliable and popular technique, its accuracy can be compromised with poor choices in flow seeding. In this case, the rarefied conditions of the test chamber and high flow speeds of the jet can couple to produce particle lag. Particle lag results when seed particles which serve as flow markers are too large or too heavy to accurately track the flow field of interest. In the rarefied gas of the test section, quantum molecular collision dynamics govern the particle motion. This effect serves to increase the distance a particle travels before it reaches local conditions, after a sudden change when compared to the continuum dynamics of higher density flows.[12, 227, 307, 323, 339]

Knowing that particle lag exists and is unavoidable (although able to be minimized), the next two sections take aim to quantify the effects of particle lag on the uncertainty of measuring mean and turbulent velocities. This section focuses on the uncertainty of mean velocity measurements, while Section 4.2 looks

at the turbulent velocities. The verification of good particle tracking can be accomplished in two ways. If a more accurate measurement of velocity can be made, then comparisons between the PIV measurement and the ‘truth’ can be quantified. This technique is employed for the mean flow verification. Secondly, much research has been accomplished in modeling particle motion through a gas flow. Of specific interest to this research is the modeling of particles under compressible and rarefied environments. Two models will be used in the next section to determine the ability of particles to track turbulent velocities and turbulent features of the jets tested.[227, 323]

4.1.1 Particle Image Velocimetry Verification by Means of Molecular Tagging Velocimetry

The current section describes the results of an effort to verify adequate particle tracking of rarefied flow of axisymmetric jets at the same subsonic and supersonic speeds tested. It is very important that the seed particles used as motion trackers accurately represent the flow features being measured. To confirm the accuracy of seed particle tracking, four axisymmetric jets were compared by measuring exit velocity using PIV and molecular tagging velocimetry (MTV). The MTV data was considered to be the most accurate measurement of velocity, given the measurement tracer was molecular acetone vapor which does not suffer with particle lag problems in tracking the flow.[217, 175, 176, 397]

Table 4.2: Estimated Properties of Saturated Acetone Vapor in Nitrogen Gas

Property	Value	
Vapor Pressure	194.0	[torr]
Molar Concentration	25.5	[%]
Molecular Weight	35.7	[g/mol]
Specific Heat at Constant Pressure	815.4	[J/Kg-K]
Ratio of Specific Heats (Assumed)	1.4	[ND]

Although the effect of Acetone seeding on the Nitrogen test gas was minimal, both PIV and MTV measurements reported in this section were made using the Nitrogen-Acetone gas mixture to eliminate any differences due to Acetone injection. The concentration of Acetone in Nitrogen was assumed to be saturated based on the atomizing technique. Lower concentrations were attempted, but the signal strength available for MTV imaging was too low. The partial pressure of acetone at 294.26K was calculated to be 194.0 torr.

The atomizing process occurred at room pressure before being introduced into the vacuum chamber, therefore from the partial pressure calculation, the molar concentration was determined to be 25.5%. Using the molar concentration, the gas constant was adjusted accordingly based on the molecular weights of Acetone

and Nitrogen. Not being able to measure the ratio of specific heats, it was assumed to be 1.4. Table 4.2 summarizes the properties of the nitrogen/acetone mixture. To confirm assumption of an unchanged ratio of specific heats, the exit velocities of two supersonic jets formed from converging-diverging nozzles and matched pressure conditions were measured and the results summarized in Table 4.3. The table represents the measured quantities of plenum pressure P_o , and temperature T_o , chamber pressure P_e and exit velocity $U_{measured}$. From the pressure ratio, the equivalent Mach number M_i and exit velocity U_i are calculated based on the assumptions of isentropic flow and $\gamma = 1.4$. Given the excellent agreement between the measured exit velocity, $U_{measured}$ and the exit velocity calculated assuming isentropic flow, U_i (with measurements of plenum pressure and temperature, and chamber pressure) - a ratio of specific heats of 1.4 appears valid.[14, 40, 213, 297]

Table 4.3: Exit Velocities for Two Supersonic Converging-Diverging Jets to Confirm the Assumed Ratio of Specific Heats

M_i [ND]	P_o [Torr]	P_e [Torr]	T_o [K]	U_i [m/s]	$U_{measured}$ [m/s]
2.1	71.0	8.00	289.2	468	466
1.1	20.5	9.15	289.3	312	315

Table 4.4 shows the jet conditions which were used to compare MTV and PIV measurements in this section. The case identifiers presented have the *MTV* subscript to indicate that although the nozzles used are the same for the corresponding cases, that the Nitrogen gas containing Acetone is exhausting at a slower speed than pure Nitrogen due to the increased molecular weight of the gas mixture. Therefore the reader is cautioned from making comparisons between the Acetone flows and the pure flows in other sections of this chapter. Case E_{MTV} is presented last in the sequence as it is the case where the nozzle was a conventional converging-diverging nozzle resulting in matched flow conditions. Cases F_{MTV} , G_{MTV} and H_{MTV} are created by the developing pipe flow of flow exhausting from a constant-diameter tube, 9.5 mm in diameter and 12.7 cm in length and will be used to investigate the effects of compressibility on the PIV seed particles. At the end of this section, the highly underexpanded jet (Case U) will be examined to show an example of the effect of a poor seeding strategy. The particle tracking models in the next section suggest the worst case particle latency region occurs at the most rarefied conditions near the jet exit and therefore, only 5 torr pressure chambers were scrutinized.

Figure 4.3 shows contours of axial velocity measurements from PIV, with a white line indicating the location of MTV data used to check the accuracy of the PIV measurements. The jet described in Figure 4.3 is formed by developing flow created by a constant-diameter tube 9.5 mm in diameter and 12.7 cm long.

Table 4.4: Test Conditions Examined with Molecular Tagging Velocimetry and Particle Image Velocimetry Using Nitrogen Saturated with Acetone

	P_o [torr]	P_e [torr]	T_o [K]	M_i [ND]	U_{e-MTV} [m/s]
H_{MTV}	34.0	5.00	294	1.9	433
G_{MTV}	16.0	5.00	294	1.4	327
F_{MTV}	6.5	5.00	294	0.6	174
E_{MTV}	16.0	5.00	294	1.4	362

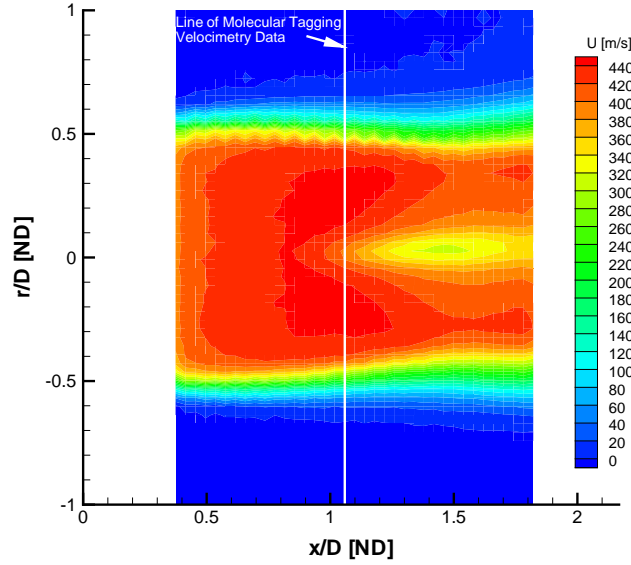


Figure 4.3: Contours of Axial Velocity Measured by Particle Image Velocimetry, Showing the Location of the Molecular Tagging Velocimetry Line

The pressure ratio used to drive the flow would result in an isentropic Mach number of 1.9. Shock and expansion structures are present and displays as the diamond shaped deceleration along the centerline of the jet in the contour image. Figure 4.4 is a cross-section of axial velocity at 1.1 diameters from the anode face which compares the MTV measurement to the PIV measurements for two particle sizes. The shock structure is evident in the MTV result as the velocity decrease along the centerline. The $0.1\mu m$ diameter particles appear to track the flow well until the shock structure was encountered, and at this location the PIV results show a 3% higher maximum velocity than the MTV baseline. Conversely, the larger, $1.0\mu m$, particles indicate a 6% lag in peak velocity, having not accelerated to core velocity before encountering the shock structure and therefore report a lower maximum velocity than the MTV baseline. Note that the PIV data shows excellent agreement to baseline data in tracking the mean structure of the shear layer, the region of most concern to this research effort.[\[219\]](#)

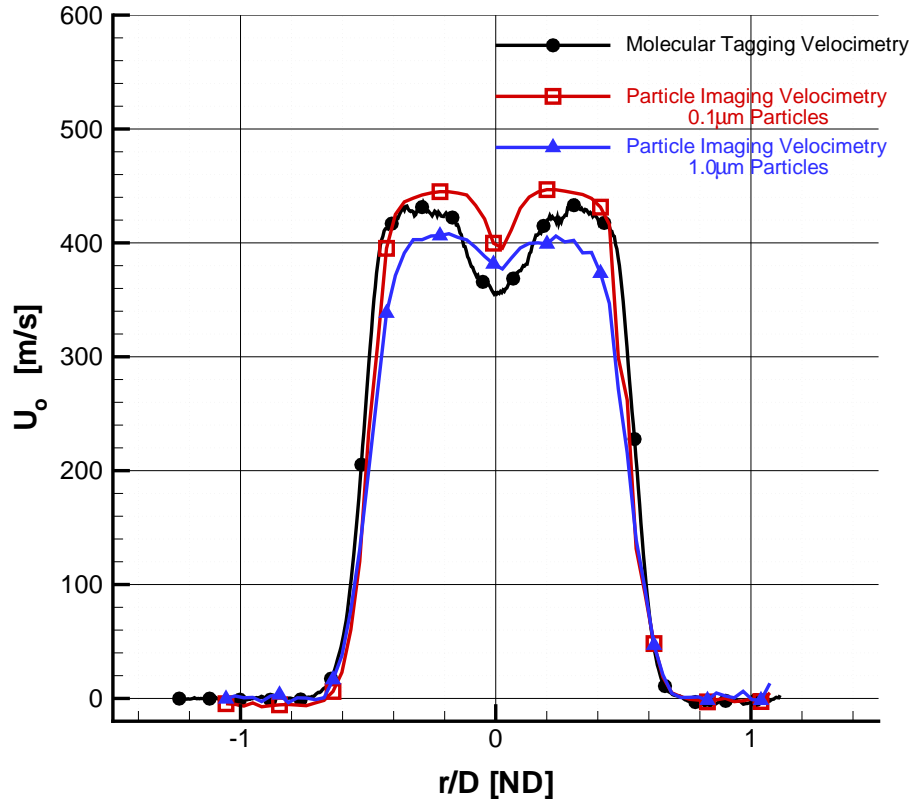


Figure 4.4: Comparison of Axial Velocity 1.1 Diameters from the Anode Face Measured by Molecular Tagging Velocimetry and Particle Image Velocimetry of a Flowfield Formed From Developing Flow Exiting a Constant Diameter Tube, Driven at a Pressure Ratio Equivalent to an Isentropic Mach Number of 1.9

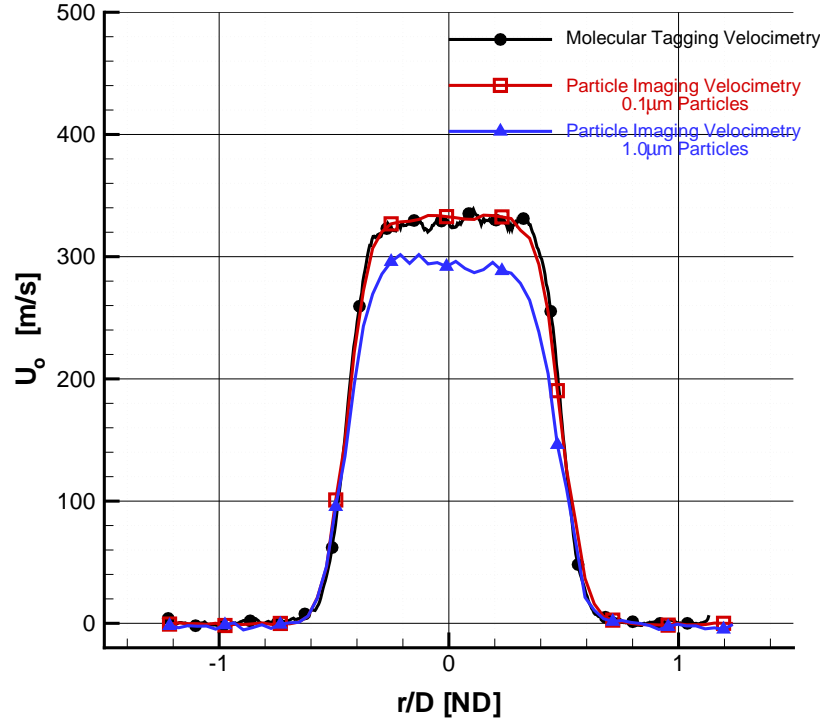


Figure 4.5: Comparison of Axial Velocity 1.1 Diameters from the Anode Face Measured by Molecular Tagging Velocimetry and Particle Image Velocimetry of a Flowfield Formed From Developing Flow Exiting a Constant Diameter Tube, Driven at a Pressure Ratio Equivalent to an Isentropic Mach Number of 1.4

Figure 4.5 compares MTV data to PIV measurements at the same location, with a pressure ratio equivalent to an isentropic Mach number of 1.4. In this case the $0.1\mu\text{m}$ diameter particles show excellent agreement to the MTV baseline, while the $1.0\mu\text{m}$ particles are still lagging the flow with now a 10% error. Note here that when measuring shear layer thickness, the PIV measurements tend to result in a larger calculated thickness than those calculated from MTV data. The shear layer thickness is calculated as δ_{10} , where the radial position of 90% of the centerline (maximum) velocity of the jet is subtracted from the radial location of 10% of the velocity. The PIV data tends to find the 10% location well, but the location of the 90% velocity tends to be slightly smaller, making the resulting difference between the two positions larger. For the $0.1\mu\text{m}$ particles, the error in this case is 1%, and of the four cases investigated in this section, the maximum error is 3%. The $1.0\mu\text{m}$ particles however, show much larger differences, indicating the need to take care in using shear layer calculations from PIV measurements.[328, 383]

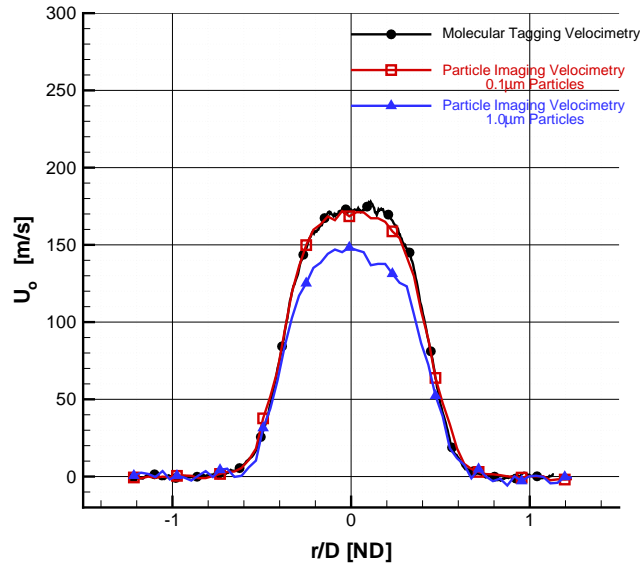


Figure 4.6: Comparison of Axial Velocity 1.1 Diameters from the Anode Face Measured by Molecular Tagging Velocimetry and Particle Image Velocimetry of a Flowfield Formed From Developing Flow Exiting a Constant Diameter Tube, Driven at a Pressure Ratio Equivalent to an Isentropic Mach Number of 0.6

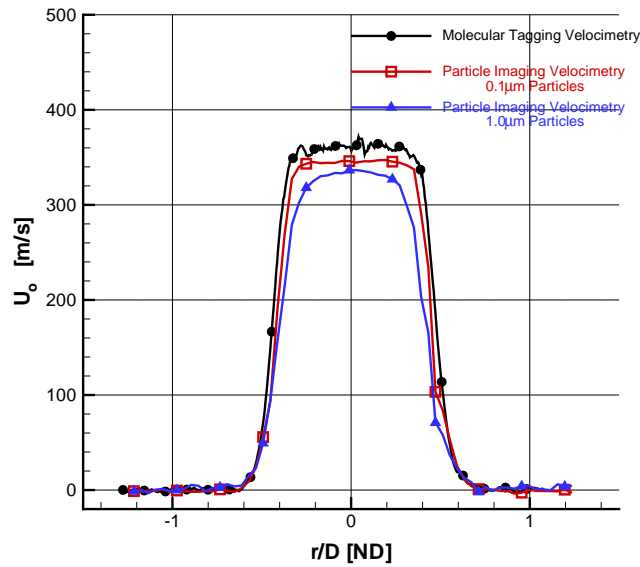


Figure 4.7: Comparison of Axial Velocity 1.1 Diameters from the Anode Face Measured by Molecular Tagging Velocimetry and Particle Image Velocimetry of a Axisymmetric Jet From a Converging-Diverging Nozzle at Mach 1.4

Continuing now with a pressure ratio which corresponds to an equivalent Mach number of 0.6, Figure 4.6 compares MTV data again to PIV measurements at 1.1 diameters from the anode face. The $0.1\mu m$ diameter particles again show excellent agreement (3% difference) to the MTV baseline, while the $1.0\mu m$ particles are lagging the baseline flow with an error of 15%.

The next comparison is between MTV and PIV measurements of axial velocity for a jet created by a converging-diverging nozzle at Mach 1.4. Figure 4.7 describes the velocity measurements at 1.1 diameters from the anode face. Here particle lag effects are evident with both particle diameters as a 4% difference for the $0.1\mu m$ diameter particles and 7% error for the larger $1.0\mu m$ diameter particles.

Table 4.5: Comparison of Maximum Axial Velocity Measurements for Varying Particle Size and Varying Pressure Ratios

	M_i [ND]	P_o [torr]	P_e [torr]	U_{MTV} [m/s]	$U_{PIV,0.1\mu m}$ [m/s]	$U_{PIV,1.0\mu m}$ [m/s]
H_{MTV}	1.9	34.0	5.00	433	446	407
G_{MTV}	1.4	16.0	5.00	327	332	296
F_{MTV}	0.6	6.5	5.00	174	168	148
E_{MTV}	1.4	16.0	5.00	362	346	335

Table 4.5 summarizes the findings of the particle tracking effort. The particles chosen to perform further experiments with were the smaller $0.1\mu m$ diameter particles. Note that while there are errors in tracking the centerline velocity near the exit of the jet, these represent the worst case tracking errors and that even at this location the tracking error for the smaller particles is under 5%. This difference is considered adequate for continued investigation into the mean flow features of rarefied axisymmetric jets in the absence of strong shock-expansion structures.[\[219, 249\]](#)

Further downstream, particle lag is minimized due to lower flow field acceleration away from the jet exit and increased time for quantum collisions to bring the particles up to the flow conditions. Particle lag effects were minimized in nozzle design, by two techniques. For the converging-diverging nozzles, the diverging region was lengthened an order of magnitude over original designs to provide increased distance for molecular collisions inside the nozzle. For the constant-diameter nozzle, the increased turbulence created by the developing pipe flow has a natural increase in collision rate to assist in particle tracking.[\[14, 40, 297\]](#)

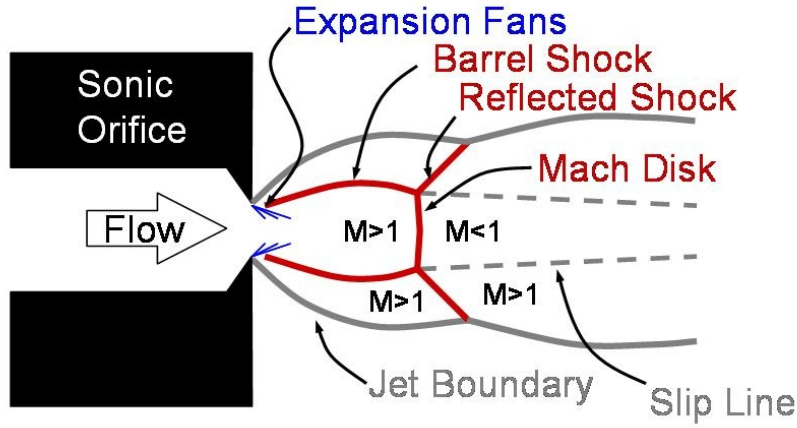


Figure 4.8: Schematic of a Highly Underexpanded Flow Created by a Sonic Orifice

The final case to be investigated was the highly underexpanded jet created by flow exiting a sonic orifice. The ability to track the flow features represented the worst case scenario for particle tracking and it was not expected that the particles would track this flow. The sonic orifice is aptly named because the flow chokes at the nozzle exit. The resulting near field flow is left to form its own nozzle with strong reflected shocks and expansions in order to equalize the pressure differential. The near field flow exiting from a sonic orifice is described in Figure 4.8. The barrel shock and Mach disk shown have been studied extensively and reasonably accurate empirical formulas exist to describe the location and diameter of the Mach disk based on the pressure ratio used to drive the jet and the diameter of the sonic orifice.[37, 100, 221, 228, 283]

Table 4.6: Configuration for the Highly Underexpanded Jet Created by a Sonic Orifice

	M_i [ND]	P_o [torr]	P_e [torr]	D_e [mm]
U_{MTV}	2.8	76.0	8.00	8.2

Next, the flow produced from a highly underexpanded jet formed from a sonic orifice was measured using both PIV and MTV. The flow was mapped with MTV, in a series of 16 lines spaced axially between 0.5 and 4 mm apart, with the tightest spacing occurring at the normal shock. Figure 4.9 shows the contours of axial velocity with the Mach disk clearly indicated by the sharp drop in velocity at 1.7 diameters from the jet exit, where the flow of the jet is from left to right. Table 4.6 describes the test conditions for the underexpanded jet. From the contour of axial velocity, many of the regions in Figure 4.8 are visible. The Mach disk, previously mentioned is sandwiched between the accelerating flow on the left and the subsonic

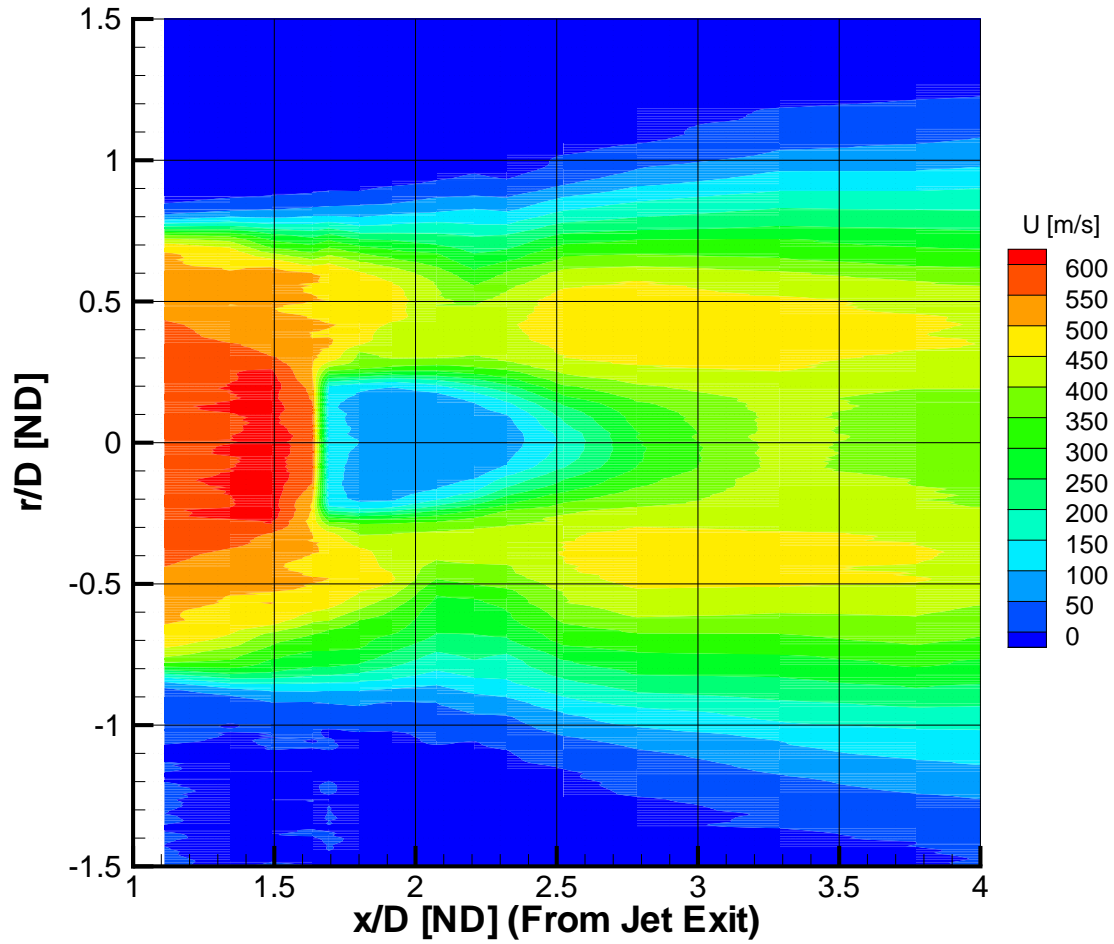


Figure 4.9: Contours of Axial Velocity Measured by Molecular Tagging Velocimetry of a Flow Field Created by a Sonic Orifice

region on the right, downstream of the normal shock. The weak shock and expansion waves above and below the Mach disk region produce flow which is still supersonic downstream of the point of the Mach disk. Some detail of the slip lines are also visible, where the outer supersonic flow is working to accelerate the subsonic flow which passed through the normal shock. It appears that a second compression region (through either a normal shock or oblique shock/compression waves) occurs at about 3.5 diameters from the jet exit. MTV measurements were made at 0.5 diameter intervals this far downstream which preclude more detailed analysis of the shock structure there.[37, 221]

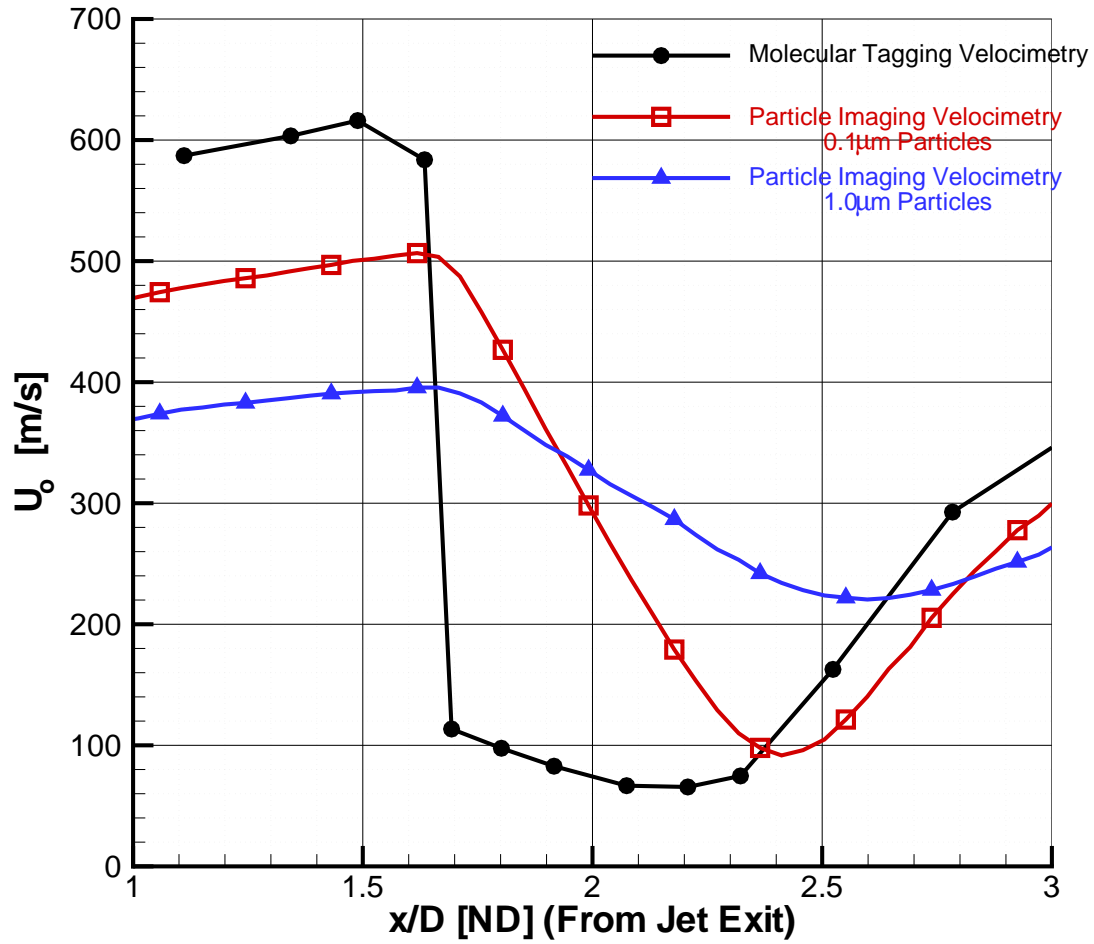


Figure 4.10: Comparison of Axial Velocity Along the Jet Centerline Measured by Molecular Tagging Velocimetry and Particle Image Velocimetry of a Flow Field Created by a Sonic Orifice, Showing the Degrading Effect of Increasing Particle Size

Figure 4.10 compares the centerline axial velocity for the underexpanded jet as measured by MTV and PIV. Two particle sizes were generated to emphasize the effect of poor particle tracking. While the normal shock location can be determined accurately by all three techniques (by looking for the slope change in PIV curves the shock location can be determined to within a grid point axially), the particle latency in these rarefied flow conditions is extreme. It is clear that accurate velocity information is not available from PIV for rarefied conditions in the presence of strong shocks or expansions and extreme care must be taken in interpreting PIV results if these features are present. The particles used exclusively for measuring the effect of plasma-on mean and turbulent fluctuations of velocity are nominally estimated to be 100nm in diameter and are represented by the red line in Figure 4.10.^[219]

Summary of Important Findings from Molecular Tagging Velocimetry

Here is a summary of the significant conclusions obtained in the comparison of particle image velocimetry and molecular tagging velocimetry to measure the effect of particle lag on mean flow measurements.

- Near the exit (1.1 diameters downstream of the anode), the effects of particle latency on mean flow determination resulted in up to a 5% error in PIV measurements of centerline axial velocity for the 100 nm seed particles. The larger $1.0\mu\text{m}$ particles resulted in errors of up to 15%. These larger seed particles were not used further in this testing.
- In general, the 100 nm seed particles showed excellent tracking ability of the mean flow of the jet, which is expected to improve as the flow gradients shallow and the jet core is dissolved.
- Mean flow tracking for both 100 nm and $1.0\mu\text{m}$ diameter particles were not acceptable in the presence of strong shocks. Flow test conditions under evaluation in the remainder of this effort minimize the effect of shocks through pressure matching jet conditions and focusing on flow features much further downstream than the expected location of shock structures.

4.1.2 Modeling Approach to Accuracy Estimation for Turbulence Measurements

Since PIV is a primary diagnostic tool used in this study and due to the problems associated with the particle motion representing the fluid motion, the ability of the particle to track with the flow needed to be assessed. Two techniques are used in the assessment. In the previous section, velocity fields made by PIV using particles were compared to a velocity field measurement made with molecular phosphorescent tags. Those molecular tags were on the order of the diameter of the gas they track and provide a more accurate measurement of the velocity from which comparisons were made regarding particle tracking. Next, in order to quantify the particle tracking of fluctuating velocity measurements, a model based validation approach is used. Two models are presented. The first model of Samimy and Lele [323] will be used later to estimate the uncertainty in a seed particle to track velocity fluctuations when measured by PIV. The model of Loth [227] will be described next to provide an estimate in the particle's ability to follow rapid deceleration in the shear layer. Both models will be employed in the results section to quantify uncertainties under measured test conditions.

There is a substantial art in placing particles into the flow which have a larger optical return than the surrounding flow which is to be measured. These larger particles may not follow the flow features of interest.

To that end, some preliminary calculations are needed to ensure proper particle characteristics are selected. Three general types of seed particles are available for flow measurement. Small solid particles like glass beads or aluminum salt crystals can be generated in sub-micron diameters and provide relatively uniform particle sizes. However, these particles are incompatible with the vacuum pump system and will not be considered for this effort. The second popular type seed particle is the fluid droplet.

These droplets are typically formed with air under pressure forced through low viscosity oil in an atomizer. For supersonic flows, water cannot be used, as it freezes into crystals of a significantly larger diameter than the original droplets. An ideal fluid would have the same density as the flow which it was trying to track. A fluid with low density and low freezing point is difficult to find at a reasonable price, therefore typical fluids of interest are significantly more dense than the surrounding air flow. This difference in density allows some simplification of the corresponding two-phase fluid dynamics, namely $\rho_{droplet}/\rho_{fluid} \gg 1$. Consider a droplet which is formed into a perfect sphere. If we examine this droplet surrounded by a viscous fluid, the Reynolds number (based on particle diameter) is $Re_p \ll 1$. Therefore the particle drag follows the Stokes drag law if the fluid is incompressible. If the particle is in a fluid which undergoes a step change in speed, the particle speed can be characterized by Equation 4.1.[219, 307]

$$\Delta U(t)_{particle} = \Delta U_{fluid} \left(1 - e^{(-t/\tau_s)}\right) \quad (4.1)$$

The relaxation time for a Stokes particle in Equation 4.1 is given by $\tau_s = \rho_p d_p^2 / 18\mu_f$. Given all of the assumptions used to derive the relaxation time, it does not produce a value which can be used to quantify or correct the actual particle tracking errors. However, this parameter is very useful in providing relational comparisons between various seed particles to select desired qualities. The relaxation time calculated in this manner for a 1 μm particle of olive oil ($\rho_p = 860 \text{ Kg}/m^3$) in air at room temperature (295 K) is $\tau_s = 2.6 \mu s$, using Sutherland's Law for the viscosity of air based on temperature T in Equation 4.2.[383]

$$\mu[Pa\cdot s] \approx 1.716 \times 10^{-5} [Pa\cdot s] \left(\frac{T}{273[K]}\right)^{(3/2)} \frac{384[K]}{T + 111[K]} = 1.823 \times 10^{-5} [Pa\cdot s] \quad (4.2)$$

Empirical corrections to a particle in compressible flows where the Reynolds Number is not necessarily small are available. Many model's exist based on the flow conditions. Walsh [381] provides an excellent archive for 7 different methods and compares each to experimental data. Based on an empirically corrected drag coefficient for a sphere, the resulting correction to the relaxation time is given by Equation 4.3 on the next page, where $\Delta U = |U_{particle} - U_{fluid}|$, $M_r = \Delta U / \sqrt{\gamma_f R_f T_f}$, $Re_r = \rho_f \Delta U d_p / \mu_f$ and $C_{D_{Stokes}} =$

24/Re_r. [379]

$$\tau_{corrected} = \tau_s \frac{C_{D_{Stokes}}}{C_D} = \frac{\rho_p d_p^2}{18\mu_f} \frac{C_{D_{Stokes}}}{C_D} \quad (4.3)$$

To investigate the quality of seed particles for this investigation, consider an ideally expanded M=1.2 jet from a stagnation temperature of 295 K exhausting into a 5 torr chamber which undergoes a step velocity change of 100 m/s. In the core of the jet the temperature is 229 K which yields a mean free path of $6.5\mu m$ ($8.3\mu m$ at the chamber temperature of 295 K). The Knudsen Number for a $1\mu m$ particle is 6.5, therefore a correction for quantum collision dynamics is required. The relative Mach Number and Reynolds Number at the core temperature are $M_r = 0.33$ and $Re_r = 0.07$, respectively. In this case, only a correction for quantum collision effect is required. The empirical correction to spherical drag coefficient for Knudsen Number effects is given in Equation 4.4, where $Kn_{d_p} = kT_f/\sqrt{2}\pi\sigma^2 p_f d_p$, k is the Boltzman constant ($1.38 \times 10^{-23} J/K$) and σ is the molecule diameter which is 407 pm for air. The correction to drag coefficient is substituted into the relaxation time equation and provided in Equation 4.5. The corrected relaxation coefficient for the example of a $1\mu m$ particle of olive oil at room temperature and 5 torr is $\tau_p = 61.3\mu s$, which is significantly higher than the Stokes approximation of $2.6\mu s$. [379, 381]

$$C_D = \frac{24}{Re_r(1 + 2.7Kn_{d_p})} \quad (4.4)$$

$$\tau_p = \frac{\rho_p d_p^2}{18\mu_f} (1 + 2.7Kn_{d_p}) \quad (4.5)$$

To provide a meaningful evaluation of the particles a fluid time scale is needed. Samimy and Lele [323] studied the problem of particle tracking in compressible free shear layers with convective Mach numbers of 0.2, 0.4 and 0.6 and found that a ratio $\tau = \tau_p/\tau_f < 0.2$ (where τ_f is the fluid time scale) produced an error of 2% in the measurement of velocity fluctuations by PIV. The fluid time scale for the compressible shear layer was determined to be $\tau_f = 10\delta_{w0}/(U_1 + U_2)$, where $U_2 = 0$ for this investigation and δ_{w0} is the initial vorticity thickness. This experiment could not collect velocity profiles at the jet exit, in order to determine the initial vorticity thickness. Therefore, recognizing that vorticity thickness was on the order of the shear layer thickness, the following procedure was used to estimate initial vorticity thickness. First, Samimy and Lele determined, for their free shear flow jets studied, the initial vorticity thickness resulted in a Reynolds number $Re_\delta = \rho_1(U_1 - U_2)\delta_{w0}/\mu_1$ to lie in the range from 100 to 400. Therefore, to estimate the fluid time scale for this investigation a Re_δ of 250 was used. The resulting value of δ_{w0} was then compared to the first available downstream shear layer thickness, calculated from the PIV measurements. In all cases, the estimate of δ_{w0} was on the same order as the closest shear layer thickness measurement.

Table 4.7: Estimation of Particle Tracking of Turbulent Velocities

	x/D_e [ND]	M_1 [ND]	U_1 [m/s]	T_1 [K]	τ_s [μ s]	Kn_p [ND]	τ_p [μ s]	$\delta_{\omega o}$ [mm]	τ_f [μ s]	τ [ND]	$\frac{\Delta\sigma_u}{U}$ [%]
A	3.2	0.65	215	267	0.028	41.1	3.169	1.17	54.316	0.06	0.9
B	4.5	1.05	330	237	0.031	36.4	3.100	0.60	18.107	0.17	2.3
C	6.2	1.93	507	166	0.042	29.1	3.380	0.23	4.473	0.76	8.6
D	6.2	1.74	475	181	0.039	31.8	3.408	0.25	5.242	0.65	7.5
E	11.3	0.79	258	258	0.029	72.5	5.735	0.80	31.243	0.18	2.4
F	11.4	0.50	171	276	0.028	77.6	5.813	1.93	113.111	0.05	0.8
G	11.3	0.70	230	264	0.029	74.3	5.763	0.89	38.728	0.15	2.0
H	11.3	0.99	315	242	0.031	68.1	5.667	0.57	18.122	0.31	3.9

Using these estimations for exit conditions found in Table 4.1, the particle time scales and fluid flow time scales are calculated following the procedure outlined previously in this section. Table 4.7 steps through each case, for the furthest downstream station where turbulent quantities are presented. Uncertainty values increase at locations closer to the jet exit, however the increase was less than one percent in most cases and therefore considered negligible for the focus of this research which was interested in the impact further downstream. The table begins on the left by defining the conditions of the jet in the region of interest. The case identifier is used again here for cross reference. The location is shown as distance from the anode face, scaled by the jet exit diameter and is the furthest downstream location where turbulence measurements are made. The Mach number, centerline velocity and temperature are subscripted with a ‘1’ in free shear nomenclature to designate the high speed flow and represent the centerline values of the jet at this location. Note that it is not possible to use U_e here as the centerline velocity decreases for a free jet as it travels downstream. The velocity is measured from PIV, while the temperature and Mach number are calculated based on the assumption that total temperature measured in the plenum is the same total temperature of the flow at this location. Next, the analysis of time scales is performed. The Stokes time scale τ_s is calculated based on the incompressible Stokes drag on a sphere by $\tau_s = \rho_p d_p^2 / 18\mu_1$ where the subscript p describes the seed particle properties ($\rho_p = 860 \text{ Kg/m}^3$, and $d_p = 100 \text{ nm}$) and μ_1 is found from Sutherland’s Law based on T_1 . The Knudsen number of the particle is based on the diameter of the particle and is determined by $\text{Kn}_p = kT_1 / \sqrt{2\pi}\sigma_1^2 p_1 d_p$, where k is the Boltzman constant, σ_1 is the molecule diameter (407 pm for air is used here) and p_1 is the measured chamber pressure. An empirical correction is applied for the effects of rarefied gas to create the particle time scale $\tau_p = \tau_s(1 + 2.7\text{Kn}_p)$. Next, the fluid time scale is determined. The characteristic length scale needed is the initial vorticity thickness which is estimated and compared to the measured shear layer thickness. The Reynolds number used to estimate the initial thickness is based on measured exit velocity using a viscosity and density based on measured chamber pressure and estimated static temperature.

Then, the fluid time scale $\tau_f = 10\delta_{\omega o}/U_1$, is calculated. The time scale ratio $\tau = \tau_p/\tau_f$ is then used to determine an uncertainty in velocity measurement $\Delta u/U$ from a curve fit of the results found in Samimy and Lele.[323] Finally, the contributions of particle tracking errors are combined using L_2 norm. To provide the most conservative approach, the uncertainty $\Delta\sigma_u/U$ from Table 4.7 is added directly to the uncertainties calculated from shear layer data used for PIV estimates. Given the large root mean square fluctuations of the shear layer and the advantage of 4000 samples, the resulting propagated uncertainty is effectively unchanged. The propagated uncertainty on the standard deviation of axial and tangential velocity ϵ_{σ_u} and ϵ_{σ_v} , respectively was between 2.3% and 2.6% for all cases tested, inclusive of the added particle tracking uncertainty. The calculations conclude that particle tracking appears to be adequate for turbulent measurements of the velocity field with particle image velocimetry.[92, 183, 383]

The next model was assembled by Loth [227] and is much more detailed, providing corrections for Knudsen number effects, Reynolds number effects and compressibility effects. The derivation of the model can be found in the article by Loth, while the steps used to employ the model for this situation will be described in detail here.

Four subscripts are used to describe the various conditions required to feed the semi-empirical model about to be presented. The properties of the particle such as density, diameter and temperature are designated by the subscript p . Conversely, the surrounding fluid properties are indicated by subscript f . And when considering the fluid of an axisymmetric jet, the convention of free shear layers are adopted where subscript 1 designates the high-speed flow (jet centerline conditions in this case) and subscript 2 indicates the low speed flow which is considered stagnant in this experiment. The 1 and 2 subscripts are required at times to indicate the shear characteristics at a particular location downstream of the jet exit where the jet exit velocity is not an appropriate value to use. With these considerations in mind, the model begins by looking at the particle Reynolds number Mach number and Knudsen number, shown in Equations 4.6 through 4.8, respectively.

$$\text{Re}_p = \frac{\rho_f(U_p - U_f)d_p}{\mu_f} \quad (4.6)$$

$$\text{M}_p = \frac{U_p - U_f}{\sqrt{\gamma_f R_f T_f}} \quad (4.7)$$

$$\text{Kn}_p = \sqrt{\frac{\pi\gamma_f}{2}} \left(\frac{\text{M}_p}{\text{Re}_p} \right) \quad (4.8)$$

Note here that the characteristic velocity used is the relative velocity of the particle with respect to the surrounding gas flow. In general the particle is treated as a solid sphere and therefore the fluid properties of temperature (T_f), density (ρ_f) and viscosity (μ_f) are used. To determine the best model to use, as some

variations of the model occur depending on the regime being modeled, a rough estimate of Re_p , M_p and Kn_p are needed now. Given the very small size of the particle diameters used (100 nm), the Reynolds number can be taken to below unity for all conditions encountered. Compressibility effects could play a significant role, as particle Mach numbers range from 0.5 to 1.1 and are detailed more in the results section. Finally, the rarefied condition of the gas in the vacuum chamber places the particle dynamics firmly in the free-molecular region with Knudsen numbers ranging from 100 to 200. Knowing these estimated values provides direction through the modeling to follow.[227]

Using the drag coefficient of a Stokes sphere as a baseline ($C_{D_s} = 24/\text{Re}_p$), corrections will now be applied to account for the effects of viscous, compressible, rarefied flow. A very slight correction (less than 1%) to the drag coefficient C_D is applied to account for Reynolds number effects when $\text{Re}_p < 800$ in Equation 4.9.

$$f_{\text{Re}_p} = 1 + 0.15\text{Re}_p^{0.687} \quad (4.9)$$

Where the corrected drag is given by $C_{D,\text{Re}} = C_{D_s}f_{\text{Re}_p}$.[227]

Next, the effect of free molecular flow about the sphere, and the resulting Maxwellian distribution of particle dynamics will be accounted for with a multiplicative correction f_{Kn_p} . The Knudsen number for the particles of interest lie in an intermediate region between continuum flow and free molecular flow and therefore the correction factor is

$$f_{\text{Kn}_p} = \frac{15c_w - 6c_w^2\text{Kn}_p + (1616c_w + 4\pi)(c_w^2 + 2)\text{Kn}_p^2}{15c_w + 24c_w^2\text{Kn}_p + 36c_w(c_w^2 + 1)\text{Kn}_p^2 + 72(c_w^2 + 2)(c_w + 1)\text{Kn}_p^3} \quad (4.10)$$

Where the factor c_w is approximately 1.22. The combination of corrections so far produces an intermediate drag coefficient $C_{D,\text{Re},\text{Kn}} = C_{D_s}f_{\text{Re}_p}f_{\text{Kn}_p}$. Given that the particle dynamics are rarefied and compressible, the molecular speed ratio S is introduced and is related to the particle Mach number as $s = \text{M}_p\sqrt{\gamma_f/2}$. A compressibility drag coefficient for free molecular flows is then given in Equation 4.11.

$$C_{D,\text{M}} = \frac{(1 + 2s^2)\exp(-s^2)}{s^3\sqrt{\pi}} + \frac{(4s^4 + 4s^2 - 1)\text{erf}(s)}{2s^4} + \frac{2}{3s}\sqrt{\pi\frac{T_p}{T_f}} \quad (4.11)$$

The next intermediate drag coefficient is created by correcting $C_{D,\text{M}}$ for finite Reynolds numbers in Equation 4.12.

$$C_{D,\text{M},\text{Re}} = \frac{C_{D,\text{M}}}{1 + (0.613C'_{D,\text{M}} - 1)\sqrt{\text{Re}_p/45}} \quad (4.12)$$

Note that $C'_{D,\text{M}}$ results from recalculating Equation 4.11 with T_f substituted in for T_p .[227]

Finally, compressibility effects are combined with the effects of Reynolds number and Knudsen number

through Equation 4.13

$$C_D = \frac{C_{D,\text{Re},\text{Kn}} + M_p^4 C_{D,\text{M},\text{Re}}}{1 + M_p^4} \quad (4.13)$$

Thermophoretic forces were not accounted for here, as the particle temperature and the gas temperature were relatively close to each other during normal testing. The effect of the plasma field on the particles by thermophoresis or by electrical forces was investigated by observing particles in the chamber while the plasma field was cycled on and off. The particles drifted toward the chamber walls at a slow rate, estimated to be under 1 m/s due to thermophoresis. The particles mass and electrically neutral properties combine to minimize reactions to the oscillating electric field generated in the plasma.[54, 145, 227, 308]

Table 4.8: Estimation of the Uncertainty in Particle Tracking of Shear Layer Thickness

	x/D_e [ND]	ΔU [m/s]	M_p [ND]	Re_p [ND]	Kn_p [ND]	C_{D_S} [ND]	$C_{D_{Loth}}$ [ND]	τ_p [ns]	Δx_{10} [μm]
A	0.5	229	0.48	0.0060	118.1	0.20	53.1	0.109	0.070
B	0.7	350	0.73	0.0092	118.1	0.20	30.3	0.214	0.208
C	0.9	522	1.09	0.0120	135.1	0.18	15.1	0.521	0.756
D	0.9	510	1.07	0.0117	135.1	0.18	15.7	0.484	0.686
E	2.3	404	0.96	0.0066	216.2	0.11	19.0	0.222	0.284
F	2.4	247	0.85	0.0058	216.2	0.11	23.9	0.160	0.179
G	2.3	387	0.52	0.0036	216.2	0.11	48.6	0.066	0.045
H	2.3	460	0.81	0.0056	216.2	0.11	25.8	0.144	0.155

The purpose of Table 4.8 is two-fold. First, the semi-empirical approach of Loth [227] for particle tracking is utilized. This model provides a much more rigorous development of particle drag coefficient and therefore serves as a check of the technique employed by Samimy and Lele [325]. The particle time factor, τ_p reported in Table 4.8 is the exponential decay rate for a particle to track a step decrease in velocity from the centerline axial velocity to zero. The approach of Loth includes compressibility effects of particle Mach number M_p , viscosity effects of particle Reynolds number Re_p , and rarefied gas effects of particle Knudsen number Kn_p . When comparing the time factors calculated in this table with those of Table 4.7, it is clear that the time factors of Samimy and Lele used to calculate particle tracking of velocity fluctuations are much higher than with the higher fidelity model of Loth. Therefore, it is believed that the uncertainty in standard deviation of velocity fluctuations, $\Delta\sigma$, presented in Table 4.7 is conservative.[54]

The second use of the data in Table 4.8 is in providing an uncertainty estimate for the effect of particle tracking on measuring the width of the shear layer. In order to make this approach as conservative as possible, the worst case particle tracking problems to be encountered were fed into the particle drag coefficient model. The velocity change ΔU used was a step change from the jet exit velocity to a fluid at rest. Additionally, a gas temperature in the shear layer, T_2 of 550 K was used to calculate the lowest possible density ρ_2 . Then,

the distance taken for a particle to travel from 90% of the centerline velocity to 10% of the centerline velocity (which are the measurement points of the shear layer thickness, δ_{10}) was calculated from an integration of the assumed exponential velocity profile. The result was $\Delta x_{10} = 2.778\Delta U\tau_p$ and is listed in the far right column of Table 4.8. The uncertainty in shear layer thickness produced by particle tracking errors is four orders of magnitude less than measured shear layer thicknesses and is therefore neglected in further uncertainty analysis.[92, 227, 323]

In further investigation of Figures 4.4, 4.5, 4.6 and 4.7, the 100 nm particles do show indications of predicting the shear layer thickness to be larger than the thickness measured by molecular tagging velocimetry. In all four cases the error in shear layer thickness is 3% or less. This is much larger than the error suggested by the particle tracking model previously, however note that the particles are not tracking a simple step as was implemented by the model. The environment which the particles are tracking is chaotic and severe, especially at the exit of the jet. This tracking only improves as the jet decelerates and spreads out further downstream.[216, 249, 323]

Summary of Important Findings from the Modeling Approach to Estimate Accuracy in Turbulence Measurements

Here is a summary of the significant conclusions obtained from the modeling of particle tracking to estimate uncertainties in turbulent measurements using particle image velocimetry.

- Using the model of Samimy and Lele [323], the effect of particle latency on turbulence measurements of axial and tangential velocity produced a propagated uncertainty of between 2.3% and 2.6% using sample sizes of 4000 velocity vectors.
- Using the model of Loth [227], particle tracking was found to have negligible effect on determining shear layer thickness. Measurement comparisons made in the previous section found errors of between 1% and 3% 1.1 diameters downstream of the anode face. Further downstream it was reasoned that this measurement error should decrease as particle tracking improves in the growing shear layer.

4.2 Velocity and Turbulent Kinetic Energy Profiles from Particle Image Velocimetry

This section contains a comprehensive description of the particle image velocimetry (PIV) data collected. First, PIV information is used to compare the rarefied perfectly expanded supersonic jet to a supersonic jet exhausting into quiescent atmospheric air. Next, to show the development of the features of a supersonic axisymmetric jet, mean and turbulent velocity jet data is presented as a sequence from near the jet exit downstream through the entire test region. Then, the influence of plasma on the calculated mean and turbulent quantities is presented at the furthest downstream location, where the plasma has the strongest influence. The PIV data collected for three perfectly expanded jets of increasing Mach number are examined next to better understand the influence of plasma with varying compressibility.

A new nozzle design is introduced next, with the goal of providing a flow field which interacts more with the plasma. The developing pipe flow of a constant-diameter tube type nozzle is used to increase the turbulence in the core of the jet and subsequently throughout the jet after the core breaks down. The results of this jet flow are compared to a jet created from fully-developed pipe flow exhausting into atmospheric conditions as a baselining technique, to understanding the flow structure before interaction with the plasma. Then the plasma influence is examined at three increasing pressure ratios to understand the effect plasma has through compressibility. Supersonic exit conditions are achieved with the constant-diameter pipe through an aerodynamic throat caused by a separation at the tube entrance.[\[130\]](#)

Next, an off-nominal case is examined to investigate the claim that plasma may influence weak shocks. A supersonic perfectly expanded jet is run at an overexpanded pressure ratio to provide a weak series of diamond shocks in the jet core. The influence of the plasma field is then examined through the velocity fields measured from particle image velocimetry.[\[76, 194, 193, 229\]](#)

Finally, the influence of anode design on mean and turbulent features of a jet exhausting through a plasma field is examined. The baseline flat anode is compared to an anode with a modified tip. The tip design was created to improve the strength of the plasma field near the jet exit. The truncated conical tip with serrated groves provides a non-uniform electrical field which generated small corona discharges to draw plasma strength towards the jet exit. PIV data are compared for both anodes, using the same jet and pressure ratio to quantify the effectiveness of the anode.[\[145, 308\]](#)

Figure 4.11 shows the measurement locations in increasing downstream distance from the jet exit, for the 8 and 9 torr plasma fields. The measurement are shown as a sequence of dots, with each dot representing an individual data point. The dots are organized into four columns and are superimposed on the axial velocity

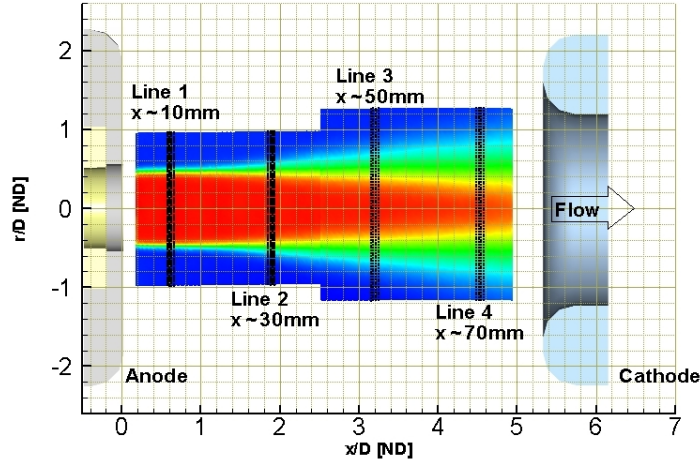


Figure 4.11: Measurement Locations Investigated for the 8-9 Torr Series of Nozzles

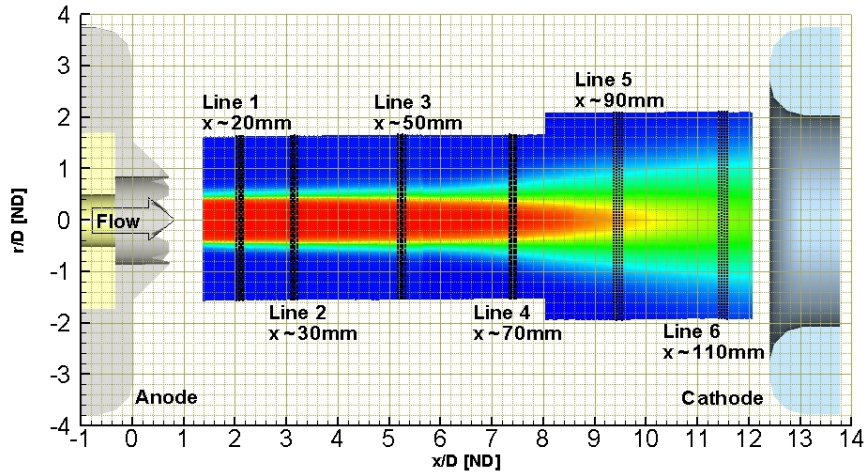


Figure 4.12: Measurement Locations Investigated for the 5 Torr Series of Nozzles

contours of a jet to highlight the jet structure at those locations. To report data of large enough sample size, the four adjacent columns of PIV data were combined. Each line consisted of velocity measurements made from 1,056 or 1,150 image pairs (depending on image size used). By combining four adjacent columns, over 4,000 velocity samples were available to perform statistical analysis on. Figure 4.12 shows the stations for the 5 torr plasma field cases. Note the additional two measurement stations for this sequence.[\[50, 156\]](#)

4.2.1 Mean and Turbulent Characteristics of Axisymmetric Jets

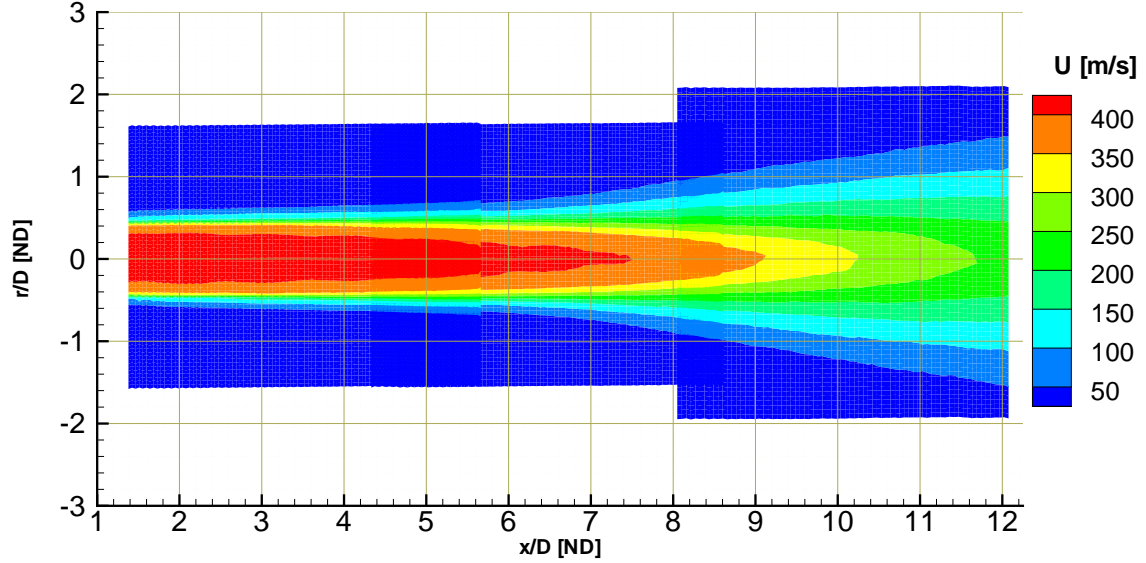


Figure 4.13: Mean Axial Velocity Contours of the Mach 1.4 Axisymmetric Jet

This section will focus on a detailed analysis of the evolution of mean velocity and turbulent velocity fluctuations of a perfectly expanded supersonic axisymmetric jet. Figure 4.13 is a carpet plot of contours of mean axial velocity for the Mach 1.4 jet. Three separate PIV collection stations comprise the overlapping data represented in the figure, covering 12 jet diameters in the axial direction and 2 diameters in the radial direction. Note that the initial profile of the jet includes a high speed core which is traveling at a constant speed of 421 m/s. This core decreases in width as the jet begins to spread, and at 7.5 jet diameters downstream the jet core is swallowed by the shear layers on both sides merging together. The jet slows and widens from that point, reaching near self-similar conditions by 12 diameters downstream.[133, 224, 376]

Table 4.9: Estimation of Jet Exit Conditions for the Mach 1.4, 5 Torr Converging-Diverging Axisymmetric Jet

Case	P_o (1) [torr]	P_e (1) [torr]	T_o (1) [K]	M_e (2) [ND]	U_e (1) [m/s]	T_e (2) [K]	D^* (1) [mm]	D_e (1) [mm]	Re_D (2) [ND]
E	16.5	5.00	296	1.35	404	217	8.9	9.5	6133
(1) Measured Quantity									
(2) Estimated From Plenum Temperature and Measured Exit Velocity									

The parameters detailed in the beginning of this chapter are reviewed here in Table 4.9. The table lists the measured pressures which drove the jet (P_o and P_e) and the plenum temperature, T_o . Calculations performed on the measured pressures and temperature assume isentropic conditions and yield equivalent

Mach number M_i , jet core velocity U_i and static temperature T_i . Next, using the measured core jet velocity U_e , the Mach number M_e and static temperature T_e were calculated assuming the total temperature was equal to the measured plenum temperature. Finally, using the jet exit diameter as the length scale, the Reynolds number for the jet was calculated with the measured chamber pressure. Viscosity and density were calculated from the static temperature T_e by Sutherland's law and the equation of state for an ideal gas. Following are a series of figures which show the mean and turbulent velocity features of the axisymmetric jet as a series of lines, progressing from near the jet exit in successive downstream increments.[14, 40, 383]

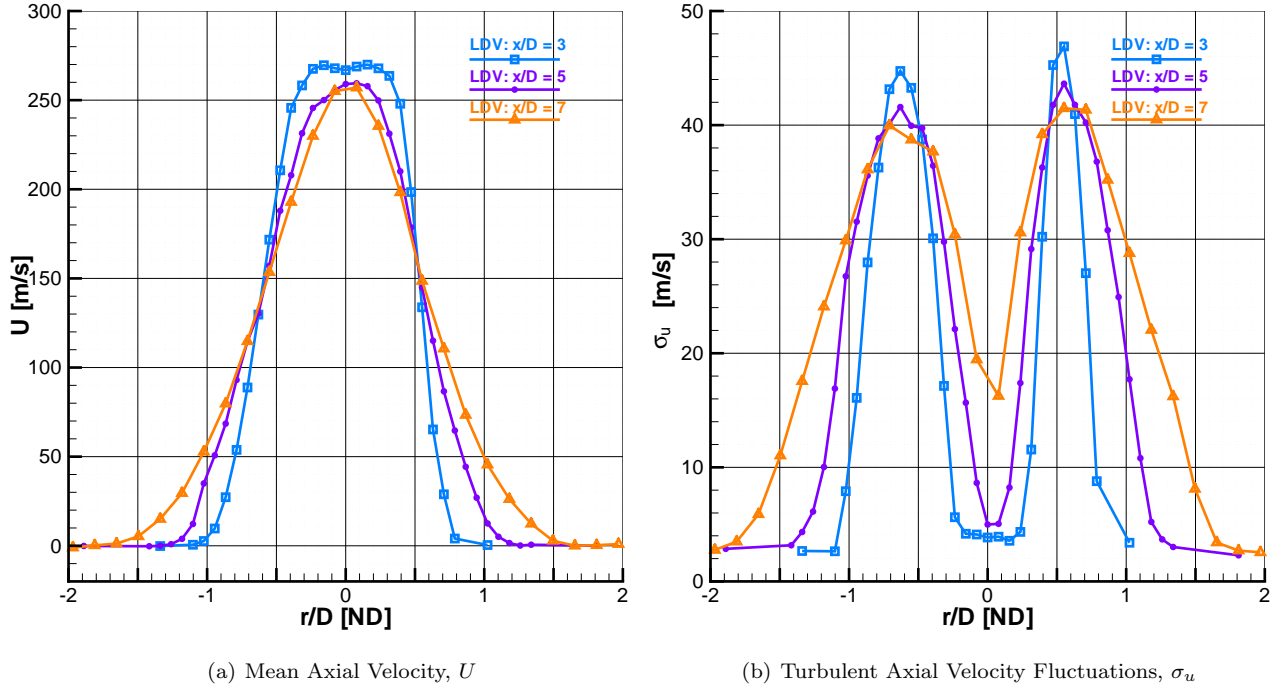
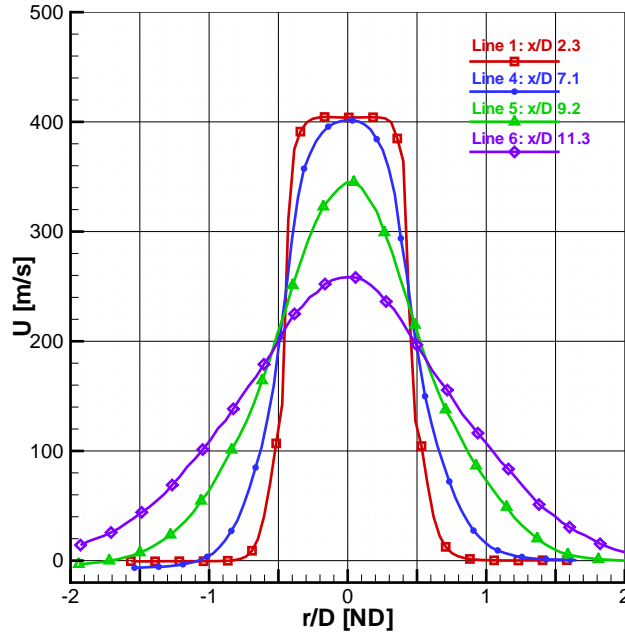


Figure 4.14: Downstream Progression of Mean Axial Velocity and Axial Velocity Fluctuations for a Mach 1.36 Axisymmetric Jet Exhausting into Atmospheric Air, Based on Data From Mosedale et. al. [275] (Note: Measurements Were made 45.8° Off the Jet Axis, Meaning the Axial Components are Larger by a Factor of 1.41)

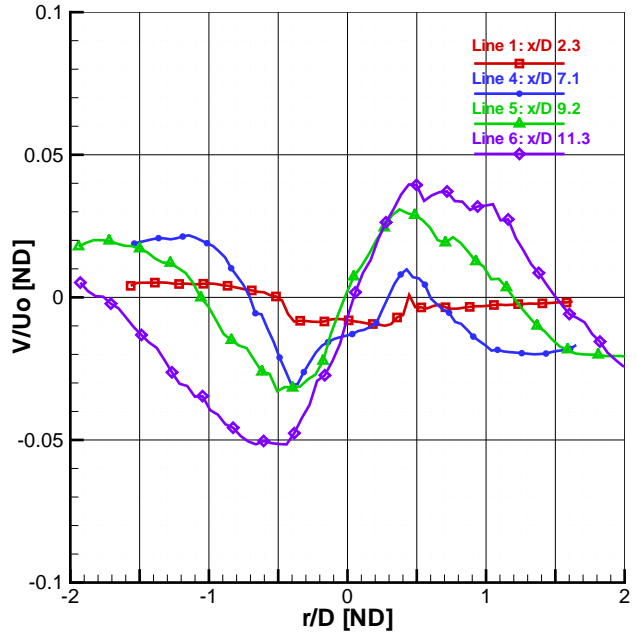
The two panels of Figure 4.14 provide a basis for comparison of measurements of a supersonic axisymmetric jet made at atmospheric pressure by Mosedale et. al. [274] with the measurements made here. The jet measured by Mosedale, et. al. was a perfectly expanded Mach 1.36 jet. The measurements were made by Laser Doppler Velocimetry (LDV). The panel on the left shows mean axial velocities at 3, 5 and 7 jet diameters downstream, respectively. On the right, the turbulent axial velocity fluctuations σ_u are presented at the same locations. Note that the measurements of Mosedale et. al. were made 45.8° off the jet axis, meaning the axial components are larger by a factor of 1.41. Figure 4.14 shows the core of the jet at three jet diameters with the signature top-hat profile, named because the cross-sectional shape resembles an outline the garment. As the jet progresses downstream, the mean velocity profiles show the shear layers merging

and engulfing the core of the jet. The turbulent fluctuations in this developing jet peak at roughly 17% of the jet centerline velocity. Note in the region where the jet core exists, the turbulent fluctuations are very low. However, in the shear layer, the axial velocity fluctuations peak. As the jet core is swallowed, the core turbulence correspondingly begins to rise.[224, 228, 376]

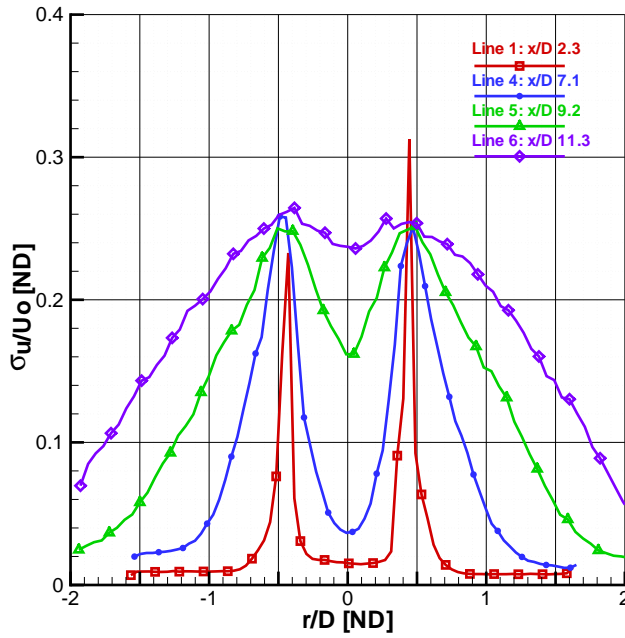
The next set of figures are a from the Mach 1.4 jet created for this research effort. Figure 4.15 on the following page contains four panels, each of which show one mean or turbulent quantity of interest in the jet analysis. Each panel shows the progression of that particular parameter from 2.3 to 11.3 jet diameters from the anode face. In panel (a) are lines of mean axial velocity. Note that the jet exit velocity is significantly higher than when compared to the measurements of Mosedale et. al.[275] The LDV and PDV results presented there were taken at an angle 45.8° off of the jet axis. The mean flow in the axial direction should be 1.41 times higher which agrees well with the isentropic predictions for a Mach 1.36 jet and also with the measurements taken here. The mean axial velocity profiles of Figure 4.15 follow the same trends as found in the work of Mosedale et. al., with the jet core disappearing in converging shear layers. Note that when comparing the axial fluctuating values in Figure 4.14 (b), (d), and (f) with those of Figure 4.15 (c), care should be taken with the off-axis results of Mosedale et. al. The measurements show a fluctuating peak of roughly 17% in an axis inclined halfway between axial and tangential flow. Blindly scaling that value by 1.41 yields 24%, which is near the measurements in Figure 4.15. However, all that can be truly said about the fluctuating velocities of Figure 4.14 are that they are anticipated to peak higher than 17% and that the trends shown there correspond well to the trends found in this current work. Hussein, Capp and George [192] used hot-wire anemometry and LDV to measure mean and turbulent fluctuations in the axial direction of a subsonic jet and found axial turbulence intensities peaked at 28%.[14]



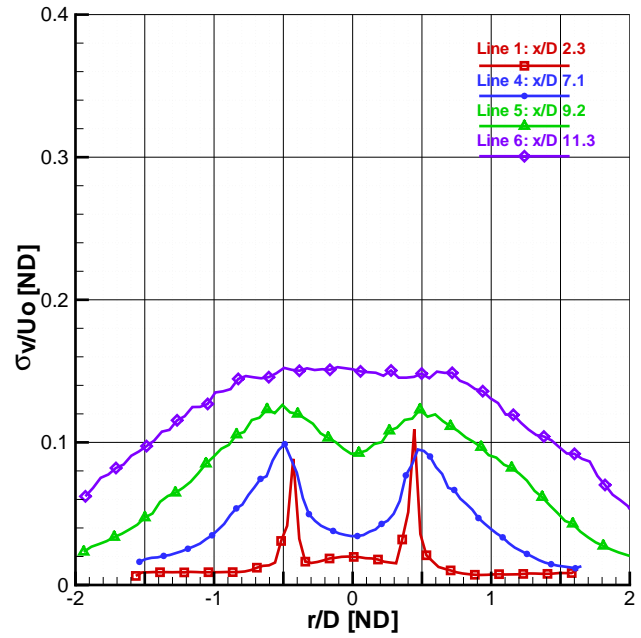
(a) Mean Axial Velocity, U



(b) Mean Tangential Velocity, V/U_o

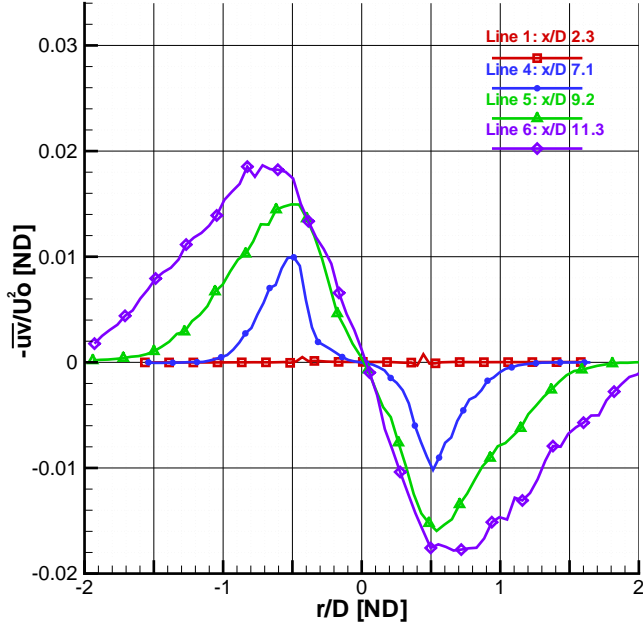


(c) Turbulent Axial Velocity Fluctuations, σ_u/U_o

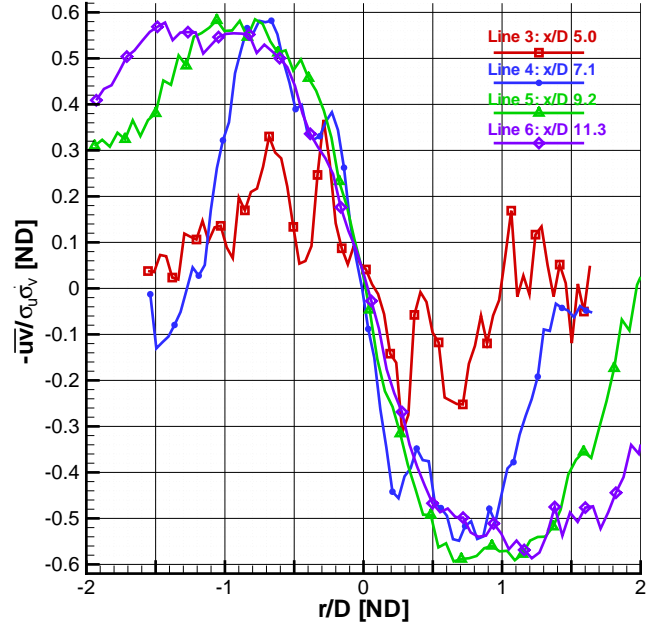


(d) Turbulent Tangential Velocity Fluctuations, σ_v/U_o

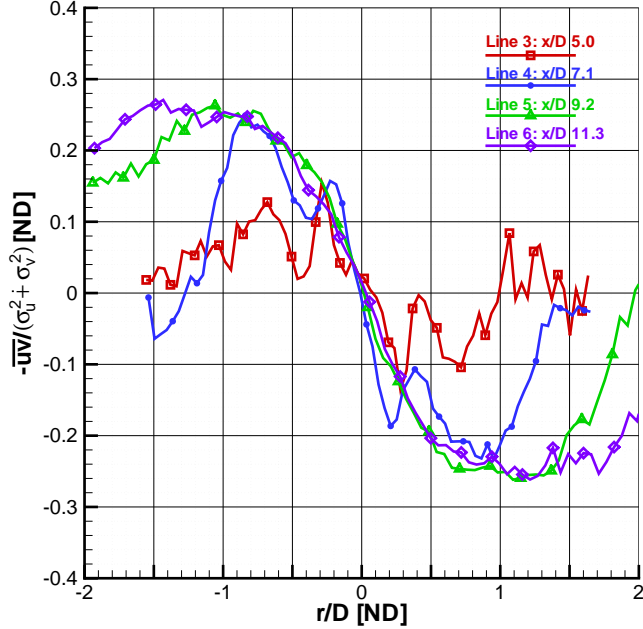
Figure 4.15: Downstream Progression of Mean and Turbulent Velocities for a Mach 1.4 Axisymmetric Jet



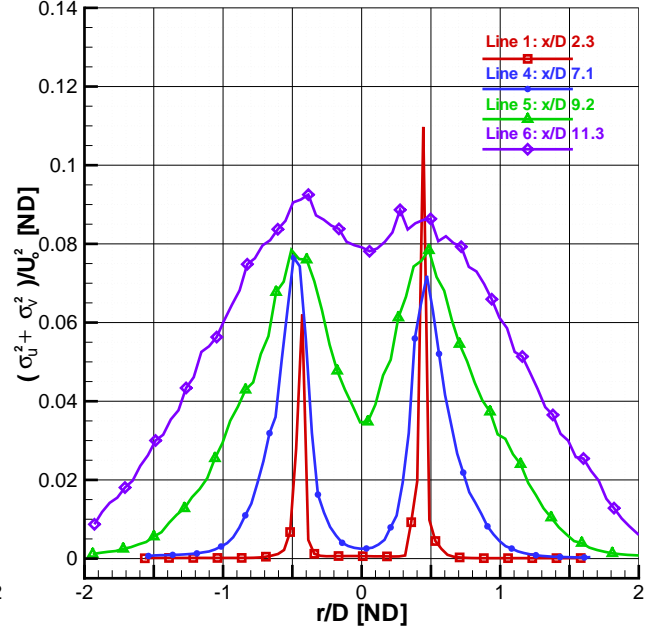
(a) Reynolds Shear Stress Term, $-\overline{uv}/U_o^2$



(b) Correlation Coefficient of Reynolds Shear Stress, $-\overline{uv}/\sigma_u\sigma_v$

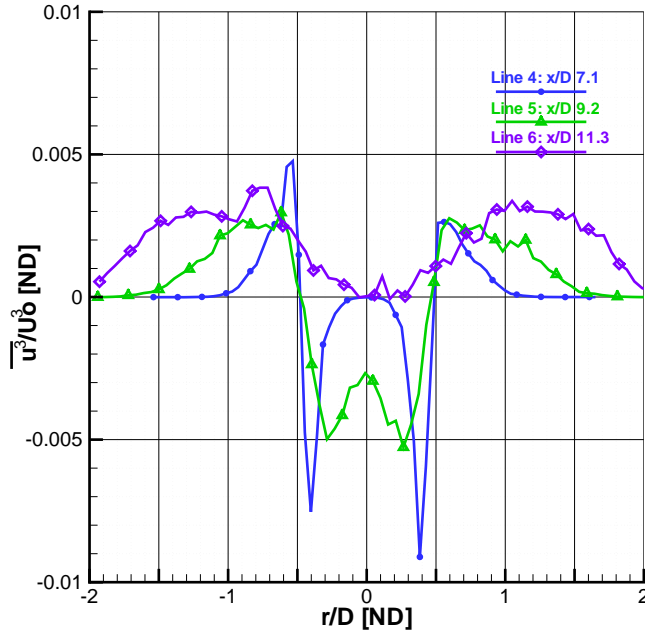


(c) Structural Parameter, $a_1 = -\overline{uv}/(\sigma_u^2 + \sigma_v^2)$

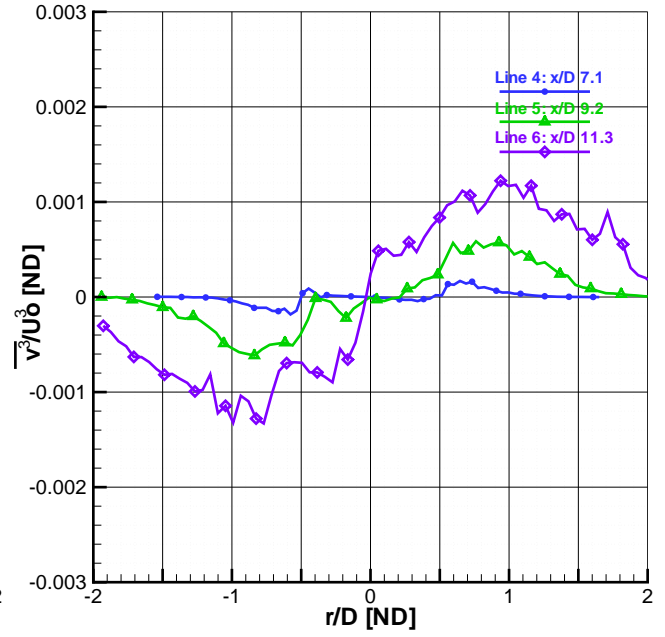


(d) Turbulent Kinetic Energy, $(\sigma_u^2 + \sigma_v^2)/U_o^2$

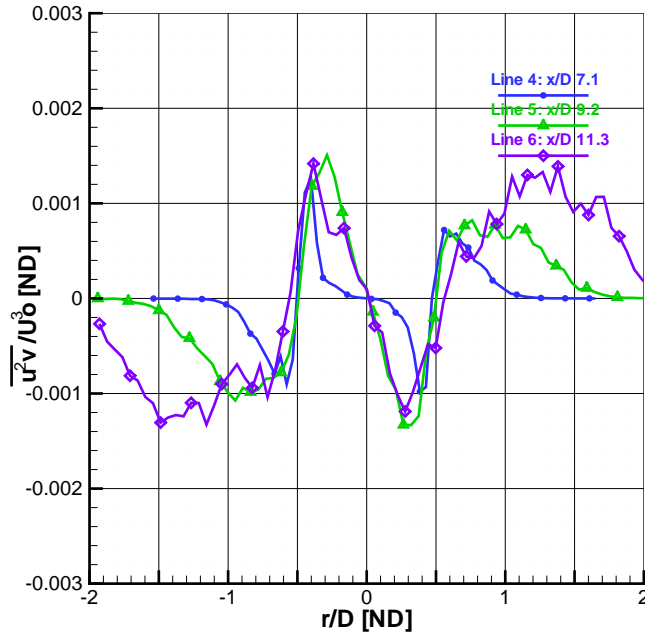
Figure 4.16: Downstream Progression of Second Moment Turbulent Fluctuations for a Mach 1.4 Axisymmetric Jet



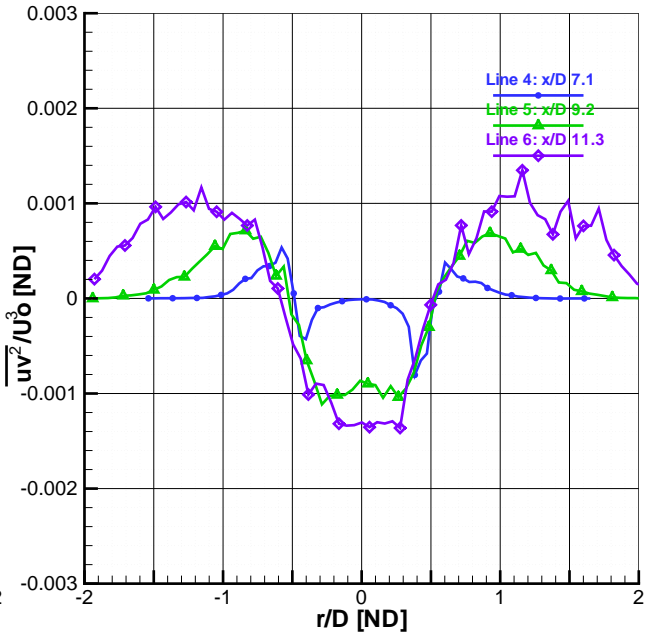
(a) Third Moment Axial Velocity Fluctuations, $\overline{u^3}/U_o^3$



(b) Third Moment Tangential Velocity Fluctuations, $\overline{v^3}/U_o^3$



(c) Third Moment Crossed Velocity Fluctuations, $\overline{u^2 v}/U_o^3$



(d) Third Moment Crossed Velocity Fluctuations, $\overline{uv^2}/U_o^3$

Figure 4.17: Downstream Progression of Third Moment Turbulent Fluctuations for a Mach 1.4 Axisymmetric Jet

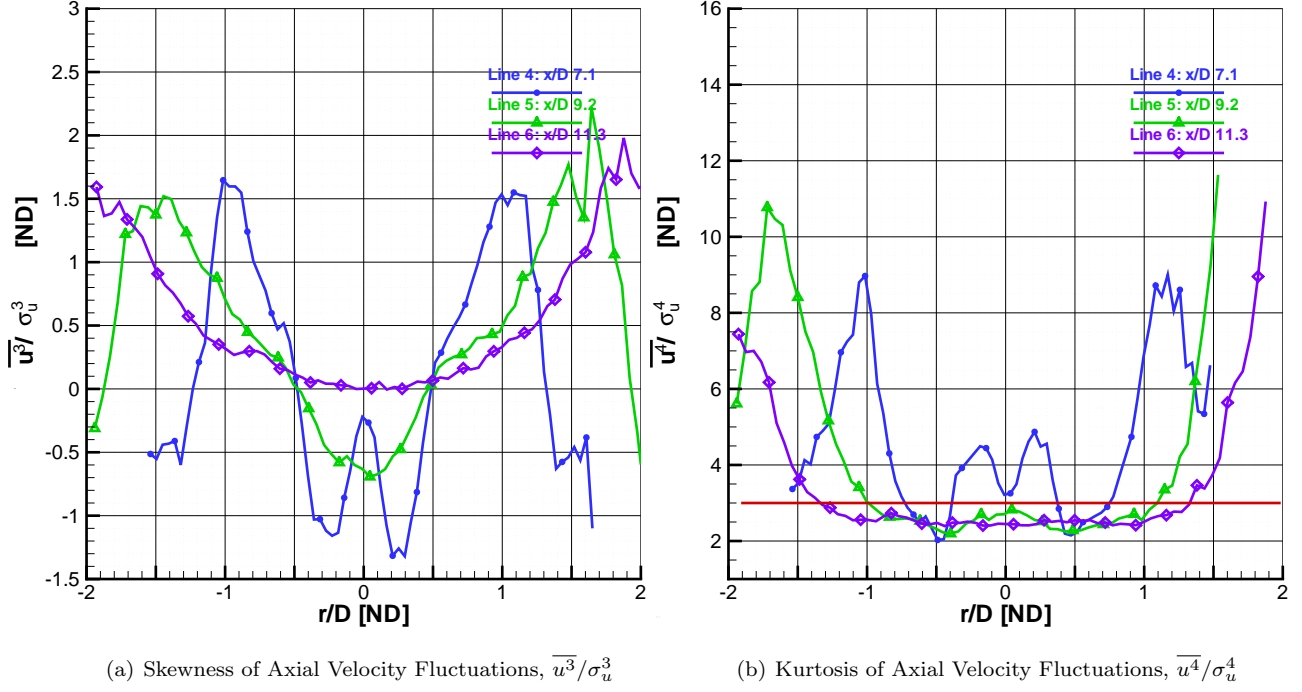


Figure 4.18: Downstream Progression of Skewness and Kurtosis of Axial Velocity Fluctuations for a Mach 1.4 Axisymmetric Jet

Panel (b) of Figure 4.15 are lines of tangential velocity at successive downstream locations for the same jet. Note that at the first downstream location, a 1% velocity to the left (toward negative radial positions) indicates a small angular misalignment between the camera and jet centerline. The spreading of the jet through the shear layer is visible in the tangential velocity increasing in magnitude away from the centerline initially and then decreasing as the extent of the shear layer is reached in each direction. Panels (c) and (d) show the standard deviation (or root mean square - RMS) of axial and tangential velocity, respectively, scaled by the jet centerline velocity U_o . The trends in both fluctuating measurements are the about same, except the axial fluctuations are twice the magnitude of the tangential component. Nearest the jet exit, the fluctuations appear as sharp peaks in the shear layer where the core of the jet abruptly interacts with the quiescent gas in the test section. As the jet core disappears further downstream, the turbulent fluctuations rise in the center of the jet and broaden with the growth of the shear layer. Finally, at 11.3 diameters downstream, the jet is nearing self-similar conditions where the mean and fluctuating profiles would take on a Gaussian shape. The values measured here match well with the RMS profiles found by Mosedale et al. [275], with the caution on the magnitudes of off-axis measurements of turbulence intensities in their work.[224, 274, 352, 376]

The influence of the jet on second moment statistics of the velocity fluctuations is examined in Figure 4.16 on page 115. Panel (a) is the progression of the Reynolds shear stress term $-\overline{uv}/U_o^2$. This cross coupled term

shows the characteristic antisymmetry about the centerline, created by the tangential spreading of the jet. At the jet exit the Reynolds shear stress term is nonexistent, but grows as downstream location increases. Panels (b) and (c) show two common variations of the Reynolds shear stress term. First, the cross-coupled velocity fluctuation term is scaled by the root mean square velocity fluctuations which is known as the correlation coefficient of the Reynolds shear stress term. When this term is unity, it signifies that the axial and tangential velocity fluctuations are correlated while a value of zero indicates uncorrelated fluctuations. Negative values imply anti-correlation. In the structural parameter a_1 , the fluctuating term is now scaled by the summation of the Reynolds normal stress terms. Since in both cases the denominator is always positive, the resulting curves follow the same trends as seen in panel (a) with higher magnitudes since they are divided by the RMS fluctuations which are of smaller magnitude than the centerline axial velocity. The fluctuating velocity profiles show an increasing trend toward correlation (and anti-correlation) for increasing distance downstream which matches with the analysis of Morris. [273] It is important to note that the first downstream location has been changed from 2.3 diameters to 5.0 diameters. The RMS fluctuations are so low at the jet exit, that division by such a small number results in wild variations that provide only confusion to the graph, therefore the line was moved further downstream to improve clarity.[107, 224, 289]

Panel (d) of Figure 4.16 is of turbulent kinetic energy (TKE) $k = (\sigma_u^2 + \sigma_v^2)/2$, scaled by the kinetic energy of the jet centerline $U_o^2/2$. The TKE is a summation of the Reynolds normal stresses and represents the relative energy in the fluctuations. At 2.3 diameters downstream the profile is similar to the RMS fluctuations, showing spikes in the thin shear layer. The centerline TKE increases as the quiet core of the jet is replaced by more turbulent shear layers. At 11.3 diameters, the profile is beginning to take on the Gaussian shape, an indicator of self-preserving flow structure which is then independent of axial location. Turbulent kinetic energy will become a useful analysis tool as this section progresses.[103, 107, 224, 289]

The third moments of velocity fluctuations are examined in Figure 4.17 on page 116. Panels (a) and (b) show the normal components $\overline{u^3}/U_o^3$ and $\overline{v^3}/U_o^3$, respectively. Note in this figure, the initial line is removed completely to improve clarity. The jet core is still visible in panel (a) at a location of 7 diameters, but quickly vanishes at 9 and 11 diameters. Panel (b) shows the tangential component of third moment fluctuations with similar trends as were observed in σ_v earlier, however now with a smaller magnitude. The cross-coupled third moment fluctuations of panels (c) and (d) show trends in growth as the jet progresses downstream, with some interesting features. The $\overline{u^2v}/U_o^3$ term is marked by an anti-symmetry which crosses zero at the jet centerline and then reverses abruptly in the shear layer, while the $\overline{uv^2}/U_o^3$ term shows symmetry in the core with a polarity reversal in the shear as well. Both of these plots highlight the importance of the distribution of tangential velocity fluctuations. In the first term, the switch in sign of tangential velocity

at the centerline is passed through the correlation factor and results in the anti-symmetry while the second term eliminates that factor through the square of tangential velocity.[107, 224, 289]

Finally, Figure 4.18 on page 117 is a plot of the downstream progression of skewness and kurtosis of axial velocity fluctuations. Skewness, $\overline{u^3}/\sigma_u^3$, is a measure of symmetry in the probability density function describing the distribution of axial velocity fluctuations. A skewness of zero represents a symmetric distribution of velocity fluctuations. Positive skewness indicates that the right tail is longer, while negative skewness indicates the opposite trend. A review article by List reported for self-similar turbulent jets that probability density functions of axial velocity fluctuations tended toward positive skewness. As this jet under investigation here is still developing, panel (a) shows some interesting features. First, at 7 diameters downstream, the core of the jet is still visible near the centerline. Further outboard, the deceleration of the shear layer is present in the trend toward negative tailed distributions marked by the two negative lobes. The immediate reversal on the outside of the shear layer appears to be a function of compressibility as the jet becomes subsonic at about the point of reversal. At 9 diameters downstream, the core of the jet is gone, yet the reversal remains where the jet transitions from supersonic speeds to subsonic speeds. Finally, at 11 diameters, the jet is completely subsonic and the self-similar profile described by List [224] begins to develop.[107, 133, 273, 289]

Panel (b) of Figure 4.18 shows the kurtosis, $\overline{u^4}/\sigma_u^4$, of the axial velocity fluctuations. Kurtosis is a measure of the peakedness of the probability density function. A Gaussian distribution has kurtosis of 3, indicated by the red line in the figure. Values higher than three indicate distributions which are flatter than a Gaussian, while smaller values indicate sharper velocity distributions. Davies [107] found that for a developing jet, kurtosis is Gaussian in the core and peaks to 6 in the transition between the core and the encroaching shear layers, falling to 2.5 in the mixing region before reaching an asymptote as the velocity approaches zero at the edge of the outer shear layer. The results measured here agree well with those findings. [273]

In summary, the measurements taken for the perfectly expanded jet exhausting into a 5 torr chamber match very well to the isentropic predictions at the exit and compare well to the atmospheric jet of Mosedale et. al.[275] in both mean and RMS fluctuations of axial velocity. This comparison is further indication of adequate particle tracking in the rarefied flow after the uncertainty estimates provided by modeling. In the next section, the effect of plasma-on this jet will be examined.

4.2.2 Mach 1.4, 5 Torr Converging-Diverging Axisymmetric Jet

Figure 4.19 begins the investigation into the influence of a plasma field on mean and turbulent jet features. Note that to eliminate the effect of the tolerance on pressure matching between tests, the plasma-off/plasma-

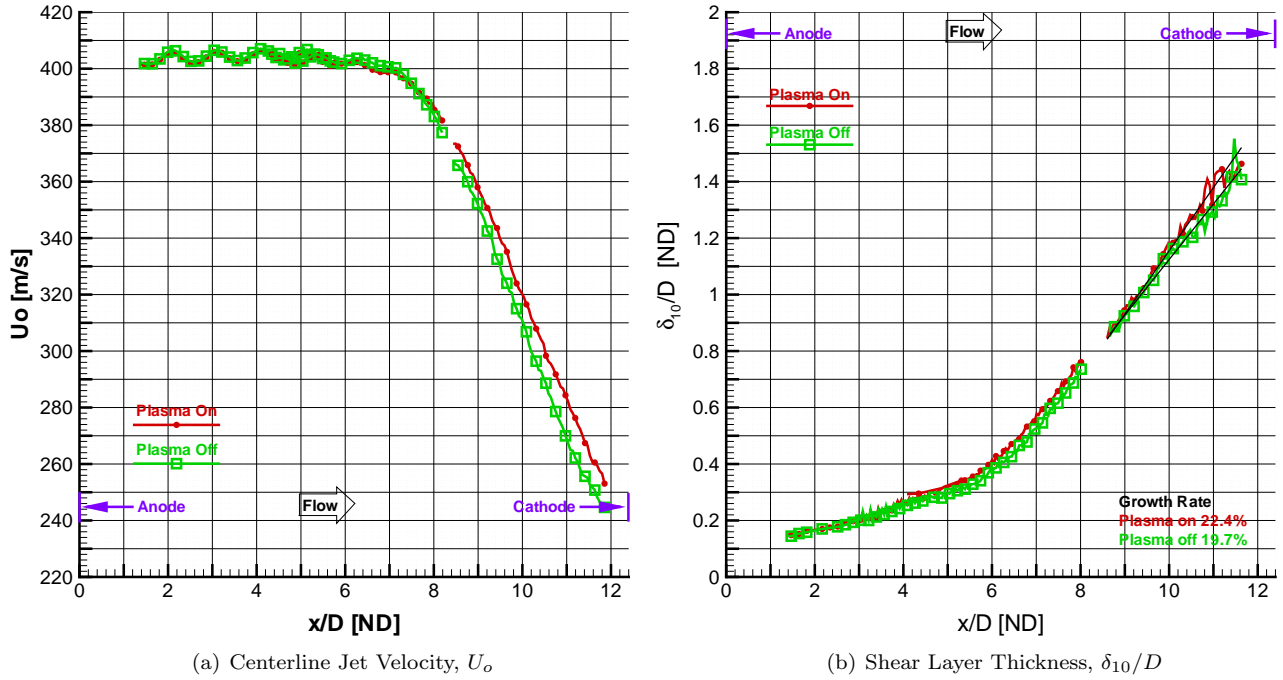


Figure 4.19: Plasma Effects on Downstream Progression of Centerline Jet Velocity and Shear Layer Thickness for a Mach 1.4 Axisymmetric Jet at 5 Torr

on runs were conducted in one block and were interleaved. The mean centerline axial jet velocity U_o is shown in panel (a) and is a composition of three separate PIV runs, as was shown in the contours of Figure 4.13. Note that variations in pressure matching and minor nozzle imperfections combine to form weak waves which show up as oscillations in the core flow of the jet. As the jet transitions through core breakdown, the decay in velocity picks up the common linear slope. The influence of plasma is seen here, where the green line indicating plasma-off overlays the red plasma-on line in the core, but the plasma-on centerline velocity becomes visible with a slower decay rate. This is initially postulated as a thermal effect based on the heating of the quiescent region which allows the core of the jet to break down more slowly in the lower density chamber when the plasma is on, versus the plasma-off case.[193, 251, 255, 308]

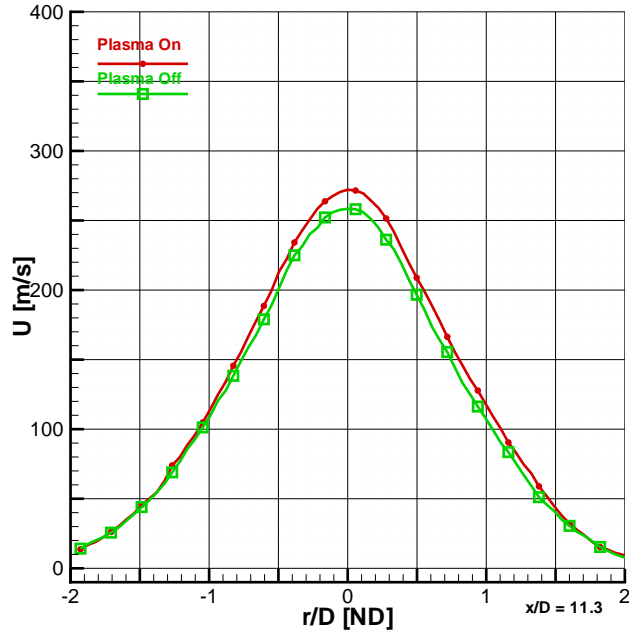
In panel (b), the shear layer thickness δ_{10} , was measured as the difference in radial position of the axial velocity between 10% and 90% of the maximum velocity. Maximum velocity was used to avoid the possibility of minor shocks in the jet which could lower the centerline velocity below the core velocity at a particular location. The maximum comprised of an average of the 4 highest values of axial velocity at this station, to minimize the potential of a spurious data point. Again the jet shows the transition between developing jet and self-similar flow at a location between 6 and 7 jet diameters, picking up a linear growth rate. The growth rate is measured only in this linear region and presented as a percentage in panel (b). The shear layer growth rate is increased for the plasma-on by 2.7% over the plasma-off case. The increase in growth

rate also seems to point to the heating of the shear layer by the plasma field with the subsequent increase in viscosity and speed of sound.[216, 251, 376]

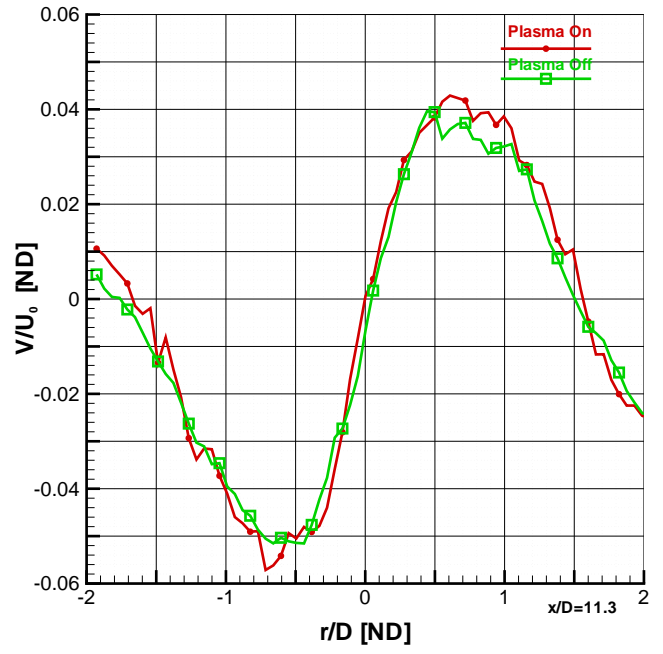
In the first look at cross-sections of the jet, plots were presented as a series of lines, beginning at the jet exit and progressing downstream. In the pages which follow, only the furthest downstream case will be displayed. As can be seen in in Figure 4.19 (a) the mean centerline axial velocity of the jet consists initially of a core region which breaks down at about 7 diameters from the anode face. The plasma does not begin to influence the flow until after core break down. The relative weakness of the plasma field near the anode, coupled with the strong shear created at the core interface results in negligible plasma influence on mean and turbulent velocity fluctuations at upstream locations. Therefore for clarity, only the profiles furthest downstream will be presented to determine the effects of plasma-on the flow measurements.[216, 251, 376]

Figure 4.20 on the following page contains plots of mean axial and tangential velocity, as well as their RMS fluctuations 11.3 jet diameters downstream of the anode face for the perfectly expanded Mach 1.4 jet into a chamber at a pressure of 5 torr. Panel (a) indicates an increase in centerline axial velocity of 5.1% for the plasma-on case over the plasma-off case. This increase is consistent with the decrease in centerline decay for plasma-on discussed in Figure 4.19. In the tangential velocity, shown in panel (b) the plasma-on case increases in magnitude slightly over the plasma-off case at the center of the shear layer and crosses to lower magnitudes, which indicate a slightly stronger shear when the plasma is on. The turbulent velocity fluctuations in the axial and tangential directions are shown in panels (c) and (d), respectively. The plasma-on trend for both panels is similar - fluctuations increase in the shear layer (3.1% for the axial case) and decrease on the centerline. These trends support the theory of delayed core breakdown caused by shear layer heating from the plasma.[251, 273]

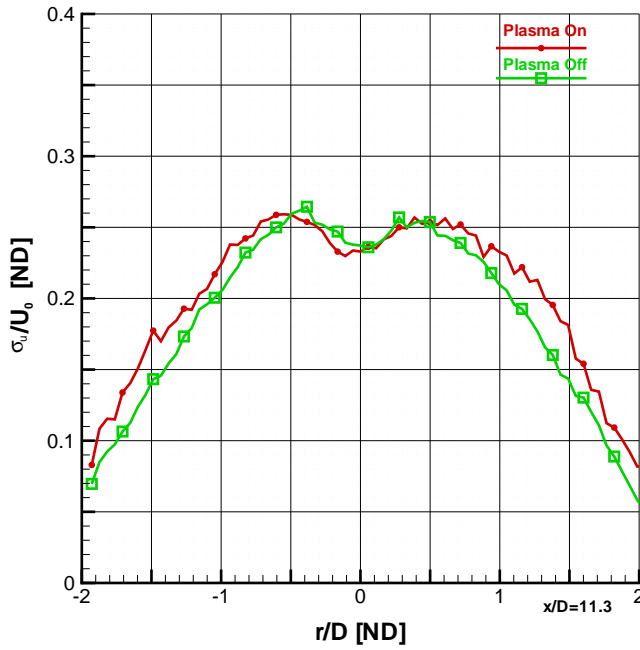
Next, the second moment fluctuations of turbulence are examined in Figure 4.21 on page 123. Panel (a) shows the Reynolds shear stress term, scaled by the centerline velocity. While there is a difference visible in the figure, it is masked somewhat by the fact that the scaling parameter U_o had a corresponding increase. Better scalings of Reynolds shear stress appear in the correlation coefficient and the structural parameter, shown in panels (b) and (c) respectively. Given that $\sigma_u \sigma_v$ and $\sigma_u^2 + \sigma_v^2$ are positive semi-definite, the trend both of these parameters show is almost identical, differing only in the magnitude on the ordinate. The increase in RMS turbulence in the shear layer region with plasma-on decreases both the correlation coefficient and the structural parameter. The final panel of Figure 4.21 is of turbulent kinetic energy $k = (\sigma_u^2 + \sigma_v^2)/2$, scaled by $U_o^2/2$. This term takes both variances of velocity fluctuations and combine them to show an increase of 3.1% of TKE in the shear layer and a decrease of 5.1% along the centerline for the plasma-on case, when compared to the plasma-off condition.[103, 109, 273]



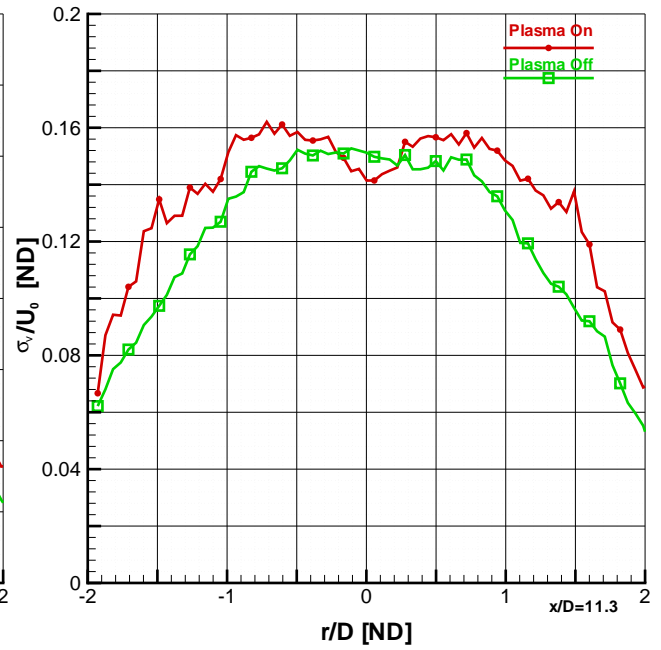
(a) Mean Axial Velocity, U



(b) Mean Tangential Velocity, V/U_o

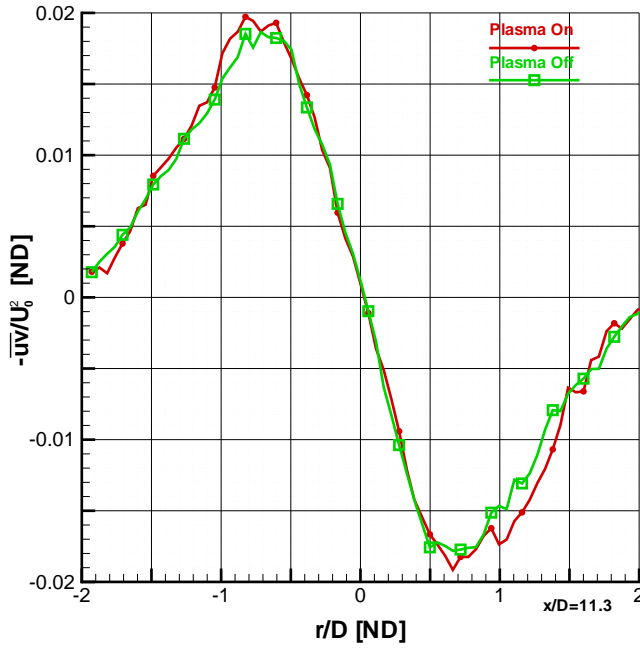


(c) Turbulent Axial Velocity Fluctuations, σ_u/U_o

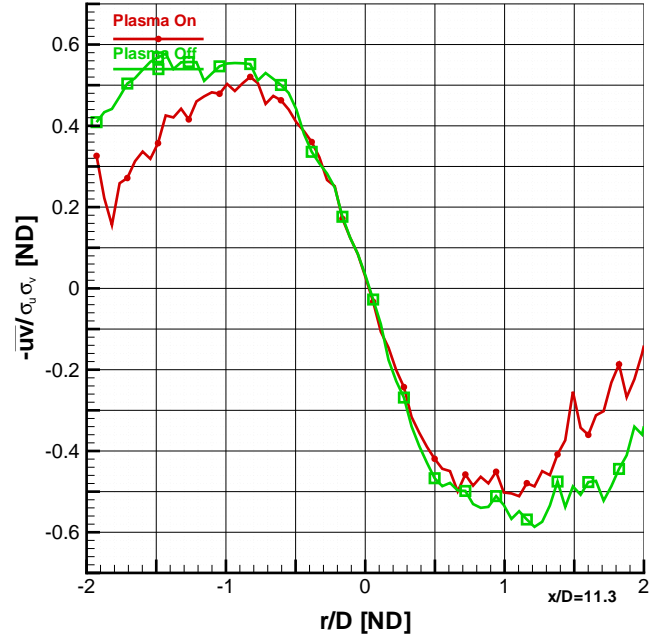


(d) Turbulent Tangential Velocity Fluctuations, σ_v/U_o

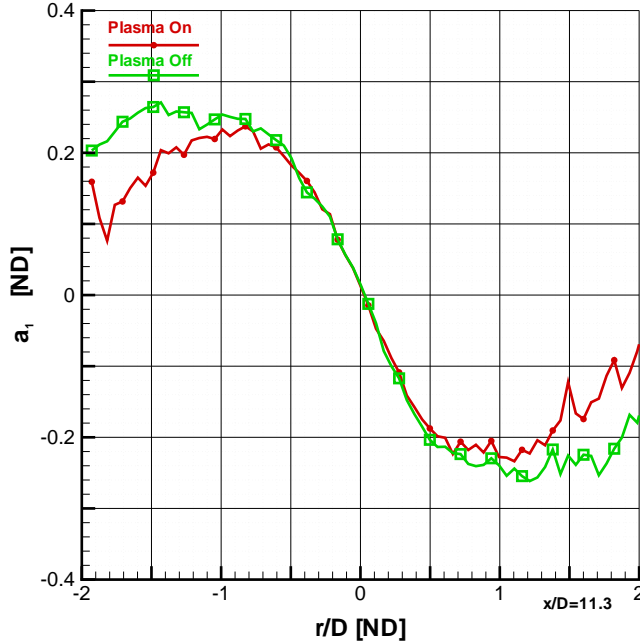
Figure 4.20: Plasma Effects on Mean and Turbulent Axial Velocities for a Mach 1.4 Axisymmetric Jet at 5 Torr



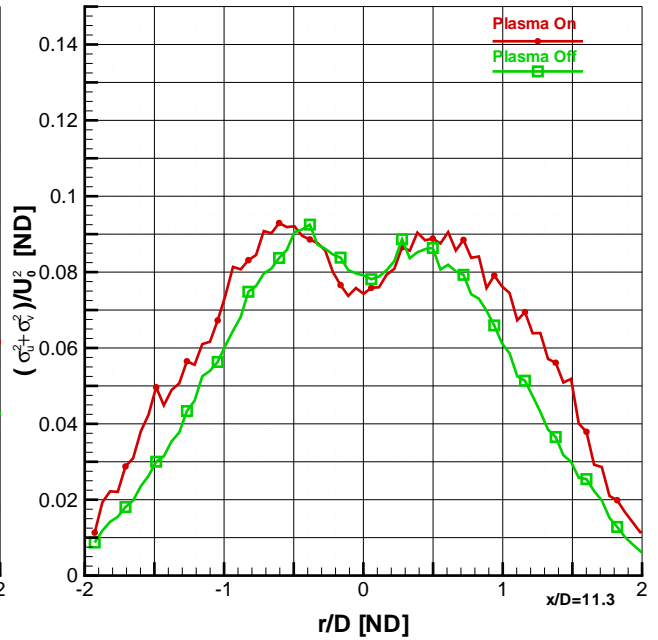
(a) Reynolds Shear Stress Term, $-\overline{uv}/U_o^2$



(b) Correlation Coefficient of Reynolds Shear Stress, $-\overline{uv}/\sigma_u\sigma_v$

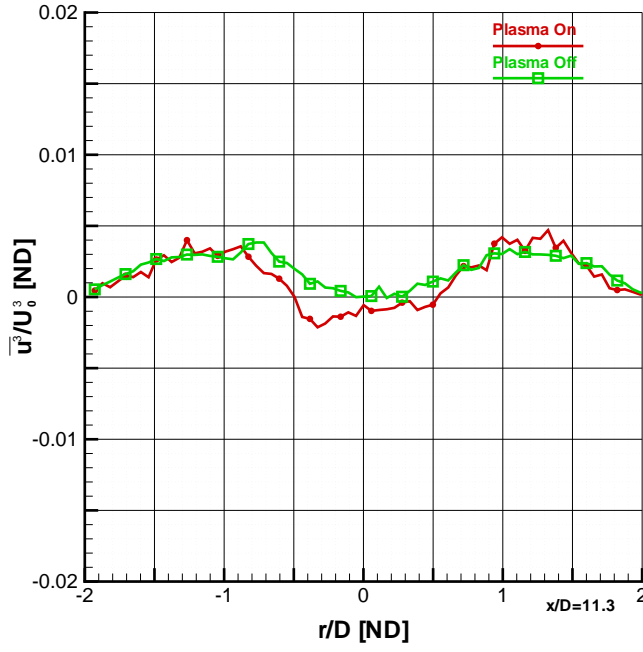


(c) Structural Parameter, $a_1 = -\overline{uv}/(\sigma_u^2 + \sigma_v^2)$

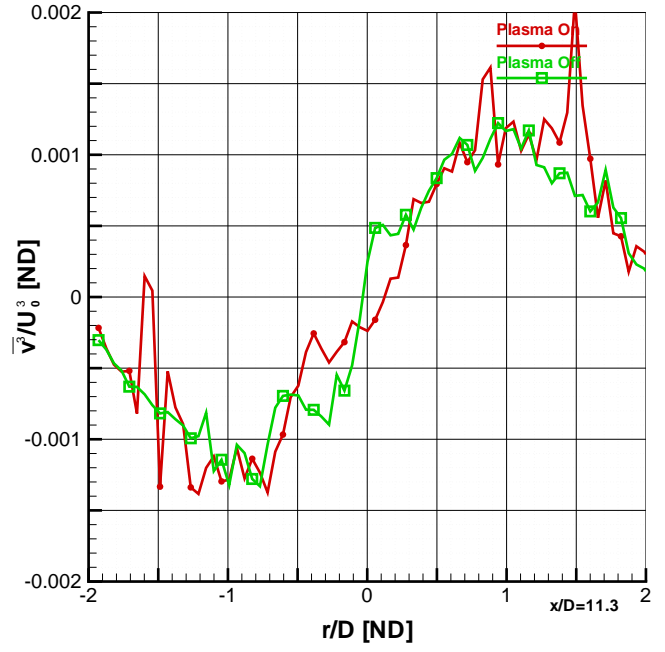


(d) Turbulent Kinetic Energy, $(\sigma_u^2 + \sigma_v^2)/U_o^2$

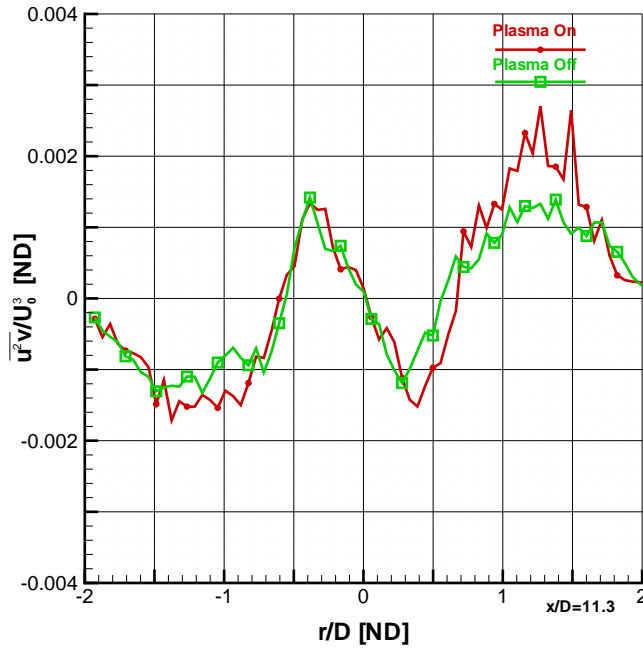
Figure 4.21: Plasma Effects on Second Moment Turbulent Fluctuations for a Mach 1.4 Axisymmetric Jet at 5 Torr



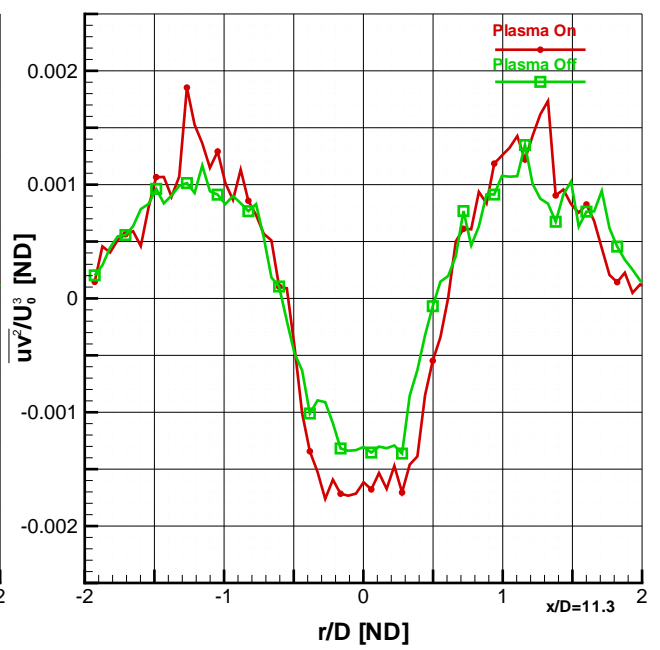
(a) Third Moment Axial Velocity Fluctuations, $\overline{u^3}/U_0^3$



(b) Third Moment Tangential Velocity Fluctuations, $\overline{v^3}/U_0^3$



(c) Third Moment Crossed Velocity Fluctuations, $\overline{u^2 v}/U_0^3$



(d) Third Moment Crossed Velocity Fluctuations, $\overline{u v^2}/U_0^3$

Figure 4.22: Plasma Effects on Third Moment Turbulent Fluctuations for a Mach 1.4 Axisymmetric Jet at 5 Torr

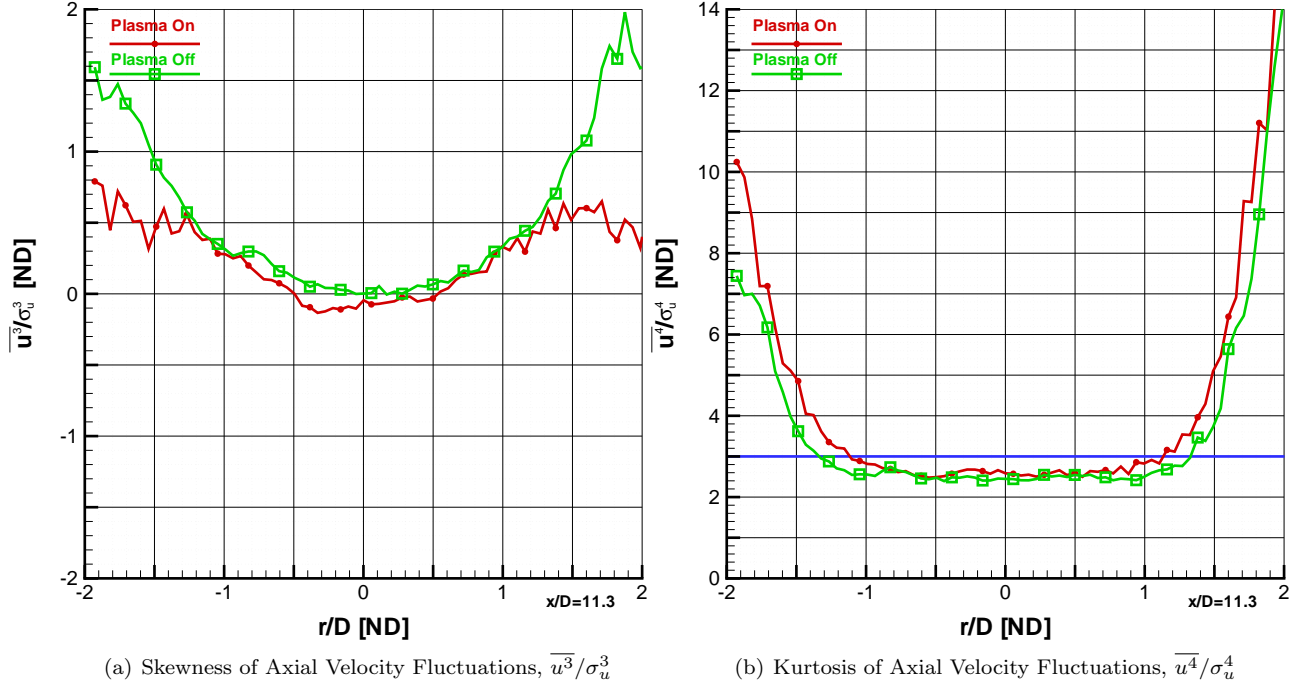


Figure 4.23: Plasma Effects on Skewness and Kurtosis of Axial Velocity Fluctuations for a Mach 1.4 Axisymmetric Jet at 5 Torr

Continuing onto the third-moment terms shown in Figure 4.22, panels (a) through (d) show the four combinations of third order fluctuations. Panel (a) shows the axial normal term $\overline{u^3}/U_o^3$. The plasma-on condition decreases slightly along the centerline when compared to the plasma off case. The tangential normal component in panel (b) $\overline{v^3}/U_o^3$ is an order of magnitude smaller and shows increased fluctuations for plasma-on, but generally tracking the same as for plasma-off. The cross-coupled terms $\overline{u^2v}/U_o^3$ and $\overline{uv^2}/U_o^3$ in panels (c) and (d) respectively, show an increased magnitude in the shear layer, while $\overline{uv^2}/U_o^3$ shows a decrease (larger negative value) along the centerline as well. These trends agree with the previous postulation that warmer air in the shear layer, caused by plasma heating, allow the jet core to penetrate further downstream. Note in all cases, while there are discernable differences, care should be taken in interpreting the results as the ordinate axes each reveal that these values are only 1% of the centerline axial velocity cubed, or less. The effects of propagated uncertainty are present here as well as witnessed by the wild fluctuations entering into the data as a result of manipulation by small numbers.[107, 224, 352]

Looking at skewness and kurtosis in Figure 4.23, both show that the probability density functions which describe the distribution of velocity fluctuations remain near their expected values of 0 and 2.5, respectively, in the core region for both plasma-on and plasma-off. In contrast, the outer portion shear layer performance shows a change for plasma-on versus plasma-off. In skewness (panel (a)), the distribution of axial fluctuations becomes more Gaussian as indicated by the decrease for plasma-on. Increased viscosity caused by shear layer

heating could be responsible for this shift toward symmetry. Panel (d) shows that kurtosis begins to increase in the outer shear layer when the plasma is turned on. This is further evidence supporting the jet penetration supposition - as the region at kurtosis of 2.5 decreases 20% when the plasma is engaged. A narrower jet region indicates less core breakdown and therefore further penetration of the jet into the plasma heated flow.[107, 273, 289]

4.2.3 The Effect of Plasma for Increasing Pressure Ratios in Perfectly Expanded Axisymmetric Jets

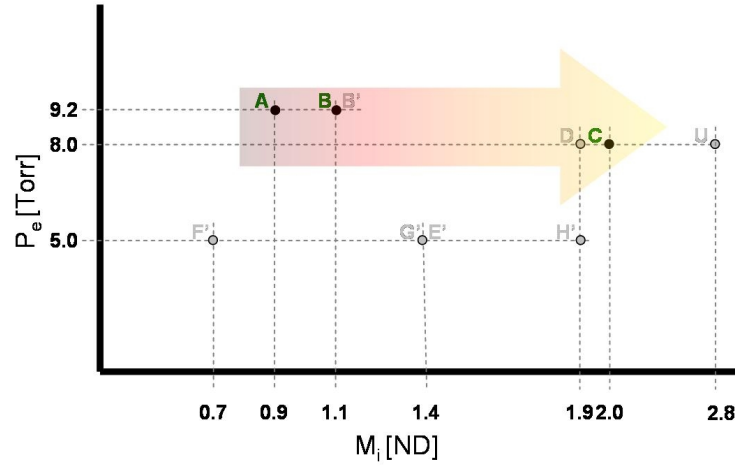


Figure 4.24: A Path Showing The Progression Through the Experiment Space to Investigate Compressibility on Perfectly Expanded Axisymmetric Jets

This section looks at three perfectly expanded jets which provide increasing Mach numbers to look into the effect of plasma influence of mean and turbulent velocities with varying compressibility. Figure 4.24 shows the path taken through the experiment space of chamber pressure and equivalent Mach number. Note the Mach 2.0 case occurred at a lower chamber pressure due to pressure matching considerations. The cases are summarized in Table 4.10 by case identifier and followed by the pertinent measured and calculated parameters described in detail at the beginning of this chapter. The first case to be examined will be the Mach 0.7 jet. Then in increasing Mach number, the Mach 1.1 and Mach 2.0 cases will be examined.

Table 4.10: Estimation of Jet Exit Conditions for the 8-9 Torr Converging-Diverging Axisymmetric Jets

Case	P_o [torr]	P_e [torr]	T_o [K]	M_e [ND]	U_e [m/s]	T_e [K]	D^* [mm]	D_e [mm]	Re_D [ND]
A	12.7	9.15	289	0.69	229	264	20.3	20.8	4470
B	20.5	9.15	293	1.13	350	233	15.2	15.7	8501
C	71.0	8.00	292	2.03	523	160	8.0	11.3	22430

Mach 0.6, 9 Torr Converging-Diverging Axisymmetric Jet

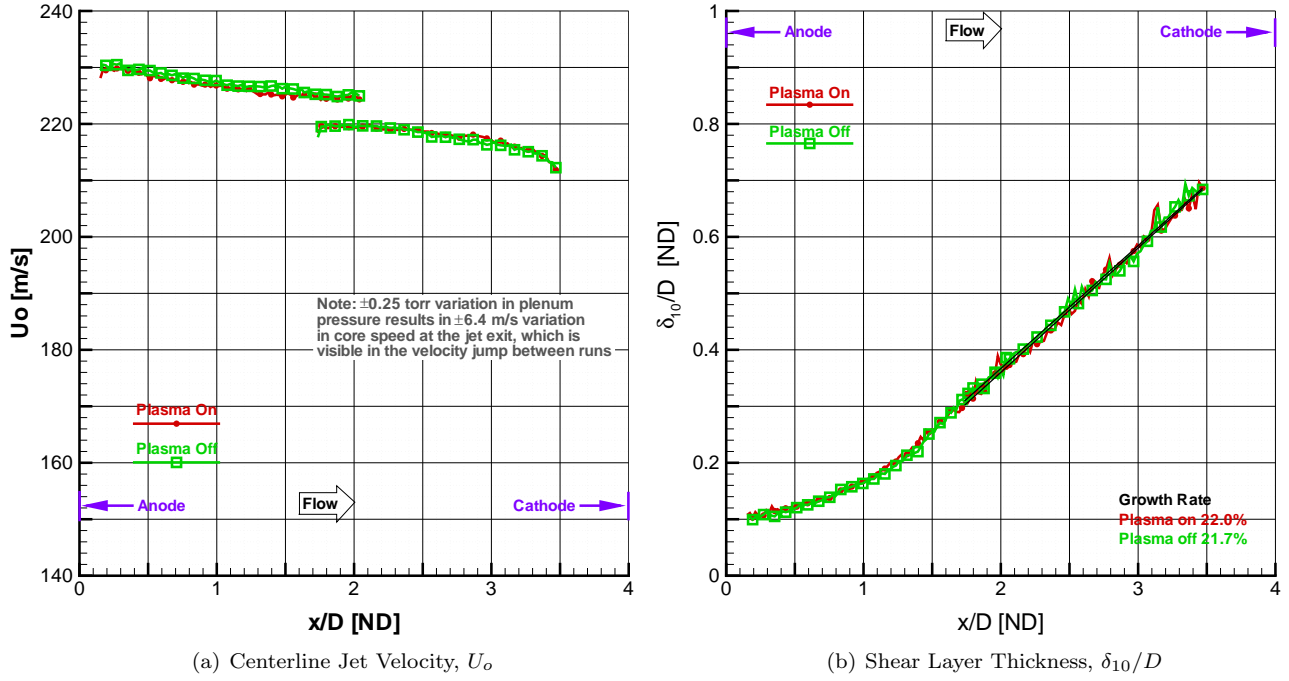


Figure 4.25: Plasma Effects on Downstream Progression of Centerline Jet Velocity and Shear Layer Thickness for a Mach 0.7 Axisymmetric Jet at 9 Torr

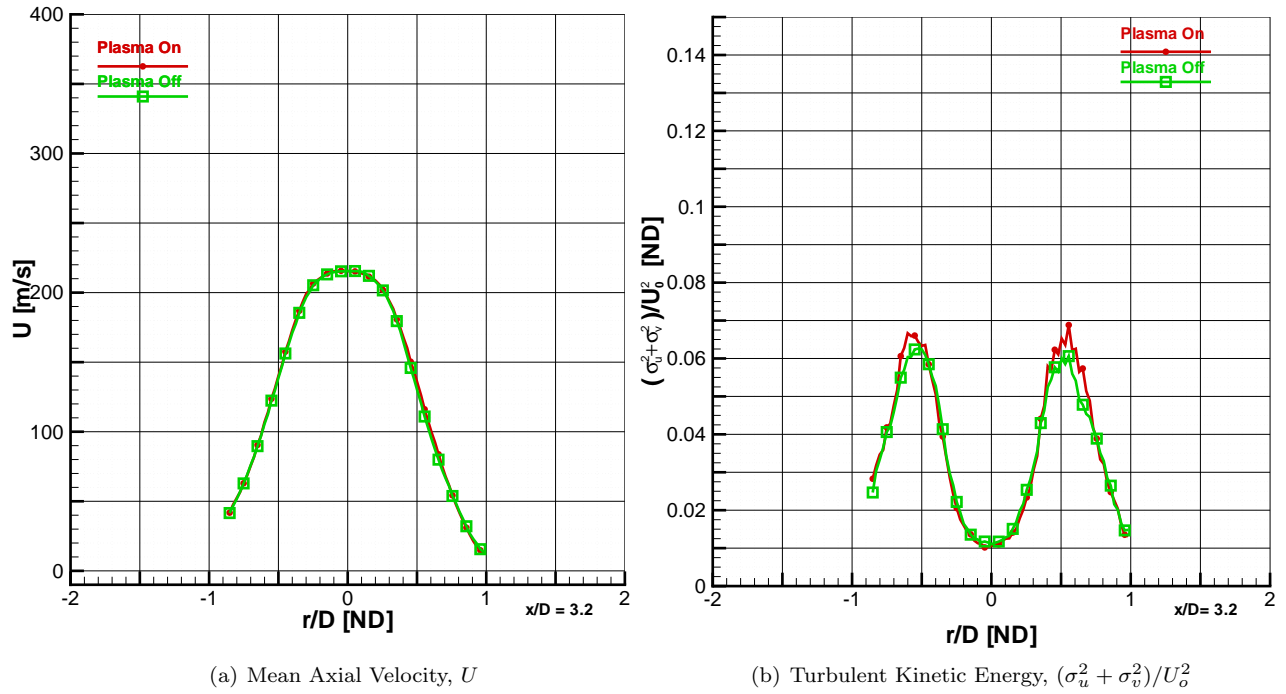


Figure 4.26: Plasma Effects on Mean Axial Velocity and Turbulent Kinetic Energy for a Mach 0.7 Axisymmetric Jet at 9 Torr, 3.2 Diameters from the Anode Face

The investigation reported here looks at the changes along the centerline of the jet, and proceeds to look in greater detail at transverse slice across the jet 3.2 jet diameters downstream of the anode - or roughly 10 mm in front of the cathode. To investigate the effect of plasma-on this particular case, first the centerline axial velocity (U_o) and shear layer thickness (δ_{10}) are examined in the gap between electrodes in Figure 4.25. The data to form these lines were a composite of two separate PIV runs. Note the vertical mismatch in centerline velocity in panel (a). Even with the tightest monitoring of plenum pressure and chamber pressure, the jet conditions for this case were very difficult to repeat exactly. The difference in centerline velocity between these two runs is 5 m/s. The tolerance in chamber pressure allowed for a variation of ± 6.4 m/s. Tighter monitoring was not possible given the dependant nature of chamber pressure and plenum pressure for subsonic nozzle flow, therefore the runs were combined with the caveat that there was a 2% variation in core velocity between each of the runs forming the composite.

There is no measurable difference between the centerline axial velocity or shear layer thickness for the entire region examinable in the electrode gap. The shear layer thickness δ_{10} , was measured as the difference in radial position of the axial velocity between 10% and 90% of the maximum velocity. Maximum velocity was used to avoid the possibility of minor shocks in the jet which could lower the centerline velocity below the core velocity at that location. The maximum comprised of an average of the 4 highest values of axial velocity at this station, to minimize the potential of a spurious data point.[\[103, 216\]](#)

Next, Figure 4.26 examines the mean axial velocity and turbulent kinetic energy at the last downstream station before the cathode. No appreciable difference in mean axial velocity is present - the plasma-off line is drawn last in the figure to highlight changes in the flow due to the influence of plasma. If there is no change between plasma-off and plasma-on conditions, then the green line lies directly on top of the red line and thus no red is observed. In panel (b) of Figure 4.26 a small increase (5.6%) in peak TKE is observed in the shear layer.

Mach 1.1, 9 Torr Converging-Diverging Axisymmetric Jet

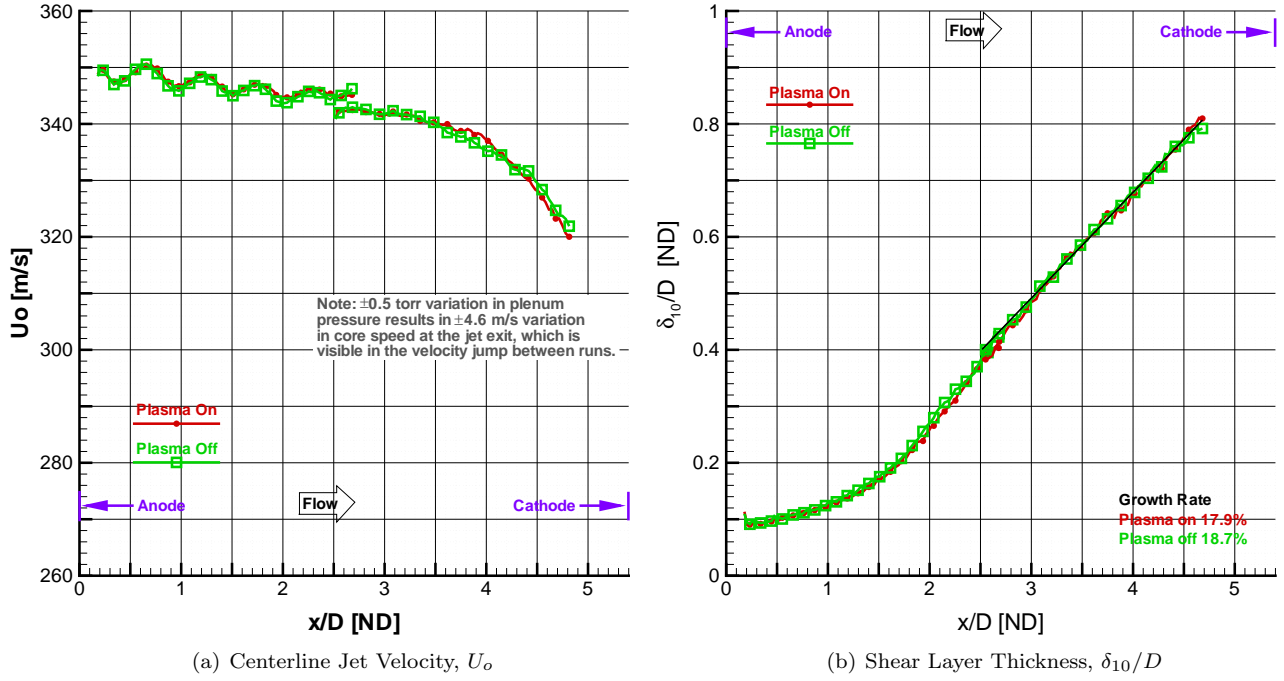


Figure 4.27: Plasma Effects on Downstream Progression of Centerline Jet Velocity and Shear Layer Thickness for a Mach 1.1 Axisymmetric Jet at 9 Torr

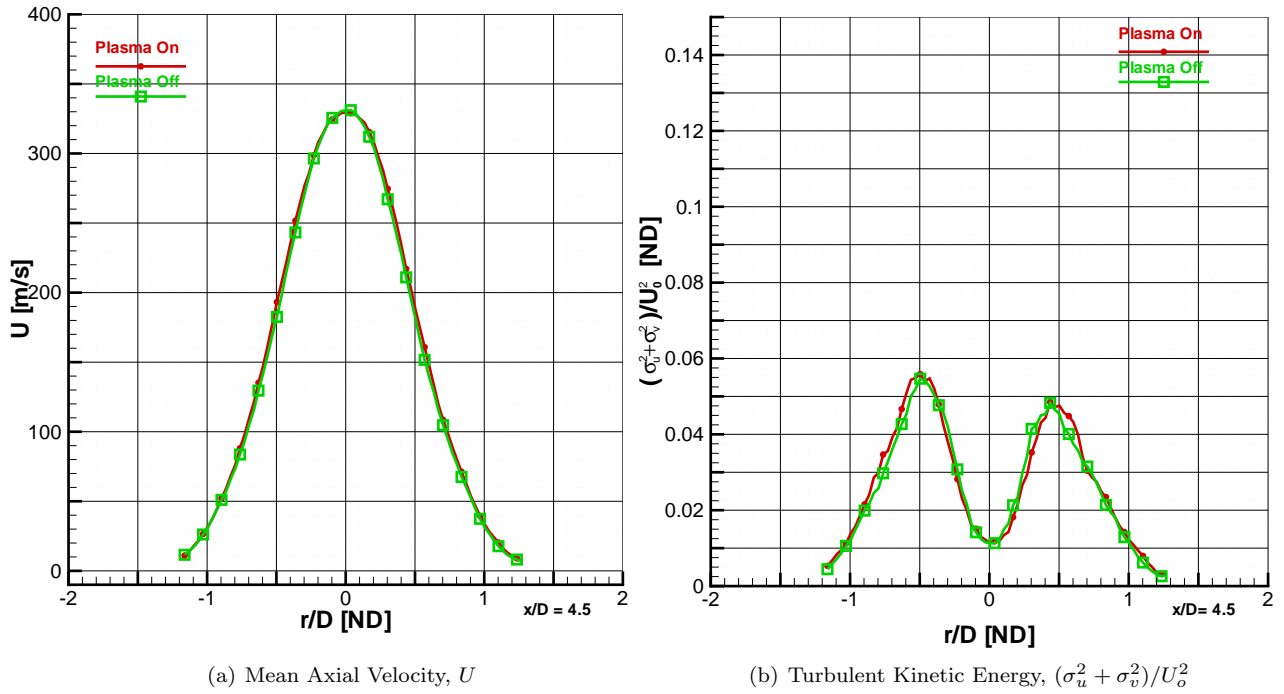


Figure 4.28: Plasma Effects on Mean Axial Velocity and Turbulent Kinetic Energy for a Mach 1.1 Axisymmetric Jet at 9 Torr, 4.5 Diameters from the Anode Face

This jet transitions into supersonic core velocities in comparison to the previous jet. Figure 4.27 (a) shows mean axial velocity along the centerline for this Mach 1.1 jet. Note that the measurements were made by PIV at two separate locations in order to cover the electrode gap region with adequate resolution. The two runs were combined here to form a composite curve. One of the effects of the composite curve was highlighting the variation in plenum pressure from run to run. In this case, the tolerance in plenum pressure results in a variation in core speed of ± 4.6 m/s.

Any changes visible between the plasma-off and plasma-on cases were below the measurement uncertainty, which in this case was 1.4% because this line was formed from averaging 1000 samples. Only cross-sectional comparisons were a compilation of four rows of data to create the larger 4000 sample sets. Panel (b) of Figure 4.27 also shows no significant change in shear layer thickness or shear layer growth rate. Similarly in Figure 4.28, changes in mean axial velocity and turbulent kinetic energy are well below measurement uncertainties for these parameters. The increase in jet exit velocity appears to have eliminated the small change in TKE which was noticed at Mach 0.7 (case A).

Mach 2.0, 8 Torr Converging-Diverging Axisymmetric Jet

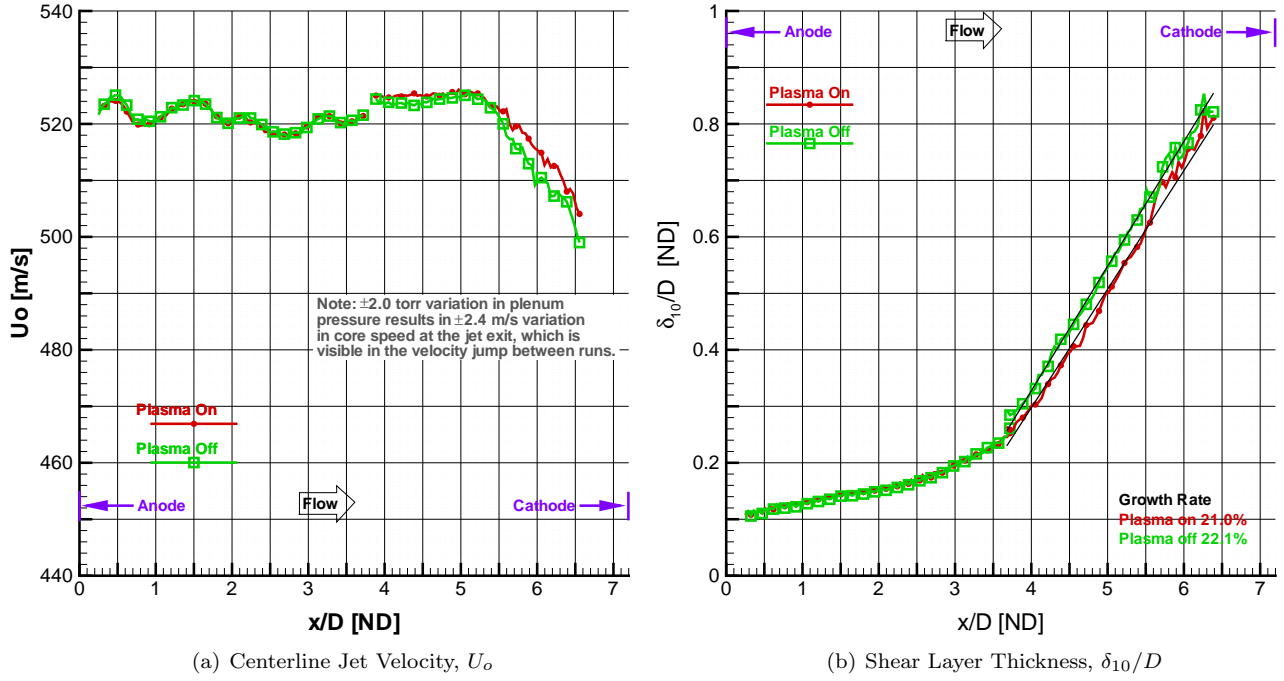


Figure 4.29: Plasma Effects on Downstream Progression of Centerline Jet Velocity and Shear Layer Thickness for a Mach 2.0 Axisymmetric Jet at 8 Torr

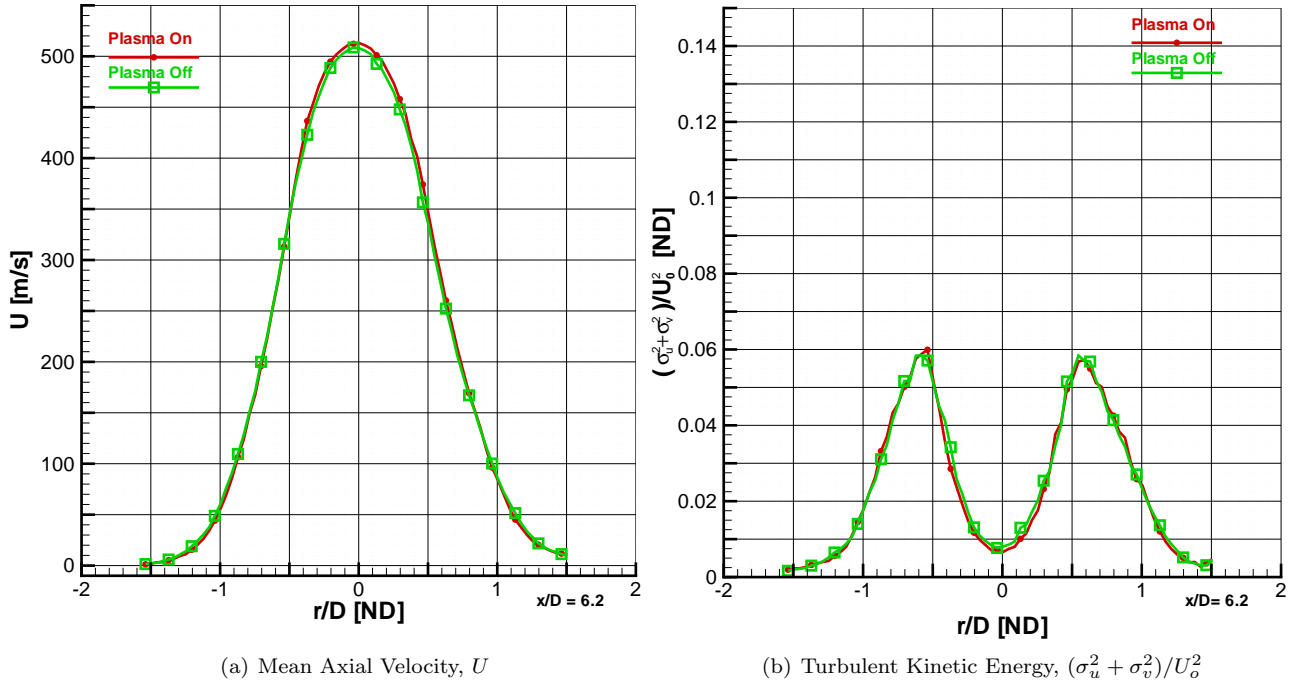


Figure 4.30: Plasma Effects on Mean Axial Velocity and Turbulent Kinetic Energy for a Mach 2.0 Axisymmetric Jet at 8 Torr, 6.2 Diameters from the Anode Face

A change in centerline axial velocity is visible in Figure 4.29 (a), and is increasing as the flow progresses downstream. The plasma-on case has higher centerline velocity than the plasma-off case. This is not attributed to an error in setting plenum or chamber pressures - as each PIV run comprised of interleaved cases - alternating between plasma-off and plasma-on. The chamber and plenum pressures were set at the beginning of the test block and were unaltered between the interleaved sequence. There is a slight increase in shear layer thickness in Figure 4.29 (b) with a difference of 0.2 mm at 4 jet diameters, which grows to 0.6 mm at 6 jet diameters from the anode face. The change in growth rate however is less than 1%.

Further evidence of change is visible in the mean axial velocity is present in Figure 4.30 (a). At this station, the plasma-on case is 5.1 m/s higher than plasma-off. Due to the high core velocity, this represents a 1% change. Figure 4.30 (b), interestingly shows a 14% change in turbulent kinetic energy along the centerline with the plasma-on case dropping below the baseline plasma-off case. Note that the percent change in TKE can be somewhat misleading, given that the baseline TKE along the centerline is still rather low for this developing jet. No measurable change is present in TKE in the shear layer however.

Summary of Important Findings in Perfectly Expanded Jet Flows

Here is a summary of the significant conclusions obtained in the comparison of mean and turbulent fluctuations measured by particle image velocimetry of perfectly expanded jets with plasma-on and plasma-off.

- At a chamber pressure of 5 torr, the Mach 1.4 jet was most influenced by the plasma field. Measurements 11.3 diameters downstream of the anode face revealed a 5.1% change in mean axial velocity at the centerline. A coincidental decrease in TKE of 5.1% also occurred on the jet centerline, with a 3.1% increase in TKE in the shear layer. These measurements support a supposition that the primary influence this plasma field has over the coaxial jet is through heating the shear layer, thus decreasing the density and increasing the speed of sound locally. The jet core remains relatively undisturbed by the plasma field and therefore results in an delay in core breakdown until further downstream.
- The Mach 0.7 jet at a chamber pressure of 9 torr showed no change in mean axial velocity between plasma-on and plasma-off. Turbulent kinetic energy however showed a 5.6% increase in the shear layer.
- The Mach 1.1 jet exhausting into a chamber pressure of 9 torr showed no change in mean axial velocity or fluctuating velocity measurements when comparing the plasma-on and plasma-off cases.
- The Mach 2.0 jet at 8 torr however, showed minor changes. The TKE along the centerline decreased by 14% noting that k along the centerline was small and therefore changes were magnified in percentage

analysis. The centerline mean axial flow also saw a change, the plasma-on case was 1% larger than the plasma-off case.

Two factors contribute to the changes discovered so far. First, the largest driver in change appears to be chamber pressure when considering the effect of plasma-on mean and turbulent velocities. The optimal distance between electrodes increases for decreasing chamber pressure. This increase in distance provides longer plasma volumes along the shear layer of the jet which in turn produces longer jet resident times in the plasma field and therefore increases the potential for plasma to influence the flow. The second factor appears to be related to jet diameter. Jet diameter influences the location where the core breakdown of the jet occurs. Core breakdown typically begins before 8 jet diameters downstream and self similar flow conditions are typically reported for jets beyond 15 diameters. Therefore in a fixed gap space, the jet with smaller exit diameter will experience core breakdown first - for a given pressure ratio. The reduction of chamber pressure from 8-9 torr to 5 torr combines those effects. The lower chamber pressure has an optimal electrode spacing increase of 50%. The chamber pressure is set by the mass flow of gas passing through the vacuum pump. At 5 torr the mass flow rate through the pump is reduced 40% from 8 torr - requiring less mass flow to pass through the nozzle. The requirement for lower mass flow through the nozzle then drives a smaller throat diameter which then allows the jet to reach near self-similar conditions. The almost self-similar is marked by ever increasing turbulent fluctuations in the jet core and shear layer. Therefore it is possible to conclude from these experiments that the plasma field shows the most influence on flows which have higher concentrations of turbulence.[308, 376]

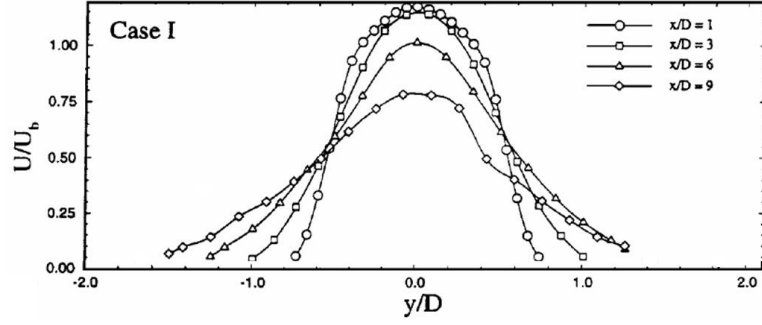
4.2.4 Mean and Turbulent Characteristics of Constant-Diameter Axisymmetric Jets

The goal of the next sequence of experiments look to capitalize on the lessons learned in perfectly matched jets. The desire was to provide a flow which was more easily influenced by the plasma field. Therefore, the next sequence of experiments was accomplished at 5 torr to use increased gap spacing and smaller jet exit diameter. To accomplish this, a nozzle was formed out of a constant-diameter tube, 9.5 mm in diameter and 12.7 cm long. The flow speed could be adjusted by variation of the plenum pressure to include supersonic speeds - which were achieved through choking provided an aerodynamic throat formed at the tube entrance. The tube created developing pipe flow at its exit into the test chamber, which had further desirable properties of increased turbulence in the jet core.[130, 133]

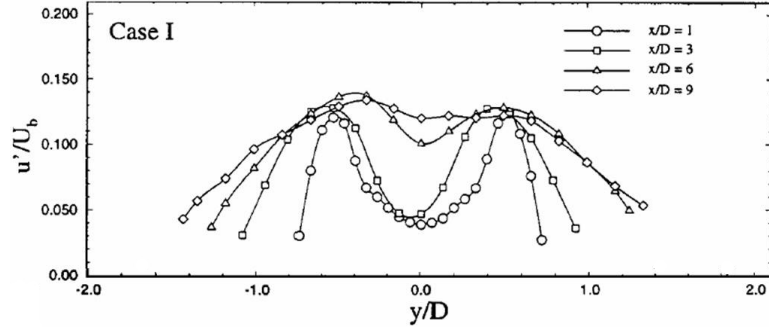
This section will begin with a comparison to the results of an experiment by Ferdman, Otugen and Kim [133] which shows mean and turbulent fluctuations of axial velocity for a fully developed pipe flow from

a straight tube exiting into atmospheric air. Next, the equivalent Mach 1.4 constant-diameter jet results will be compared to the perfectly expanded Mach 1.4 jet. Finally, the section will examine the effect of plasma-on the mean and turbulent kinetic energy 11.4 diameters downstream of the anode face for three equivalent Mach numbers to observe the influence of compressibility.

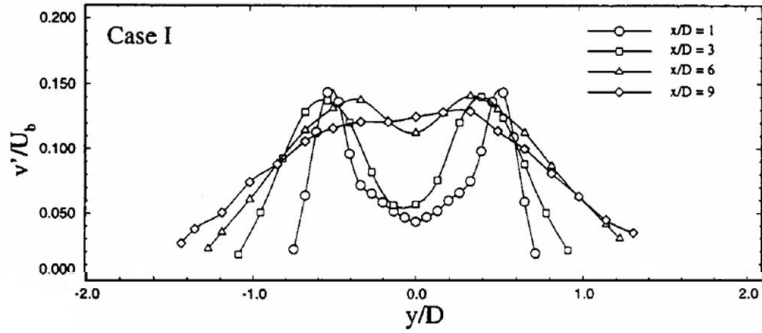
Figure 4.31 on the next page are the results of Ferdman, Otugen and Kim.[133] The baseline jet shown here was a long straight pipe of constant diameter. The Reynolds number based on a mass flux exit velocity U_b was 24,000. Although the jet of Ferdman, Otugen and Kim was subsonic and higher Reynolds number than the jet used in this research, the trends found there are expected to be valid for comparison with the higher Mach numbers in this effort. Panel (a) shows the progression of axial velocity at 1, 3, 6 and 9 jet diameters downstream from the jet exit, scaled by U_b so that near the exit the centerline velocities exceed unity. In contrast to the perfectly expanded jets shown in the previous section, the core breakdown here has occurred before an x/D of 6. The top-hat profile present in jets formed from converging-diverging nozzles is absent here as well since the flow is fully-developed pipe flow at its exit. The turbulent fluctuations in panels (b) and (c) show peaks in the shear layer near the jet exit which merge and broaden as they progress downstream. Note here that near the jet exit, the turbulence intensities are not approaching zero, but are rather decreasing smoothly to the centerline and approach 5% of the bulk velocity. The Reynolds shear stress term in panel (c) shows lobes in the shear layer as seen in perfectly expanded near-field nozzle flows. However, the peak magnitude is half of that found in conventional nozzles and the peaks broaden but do not increase as they progress downstream.[133, 399]



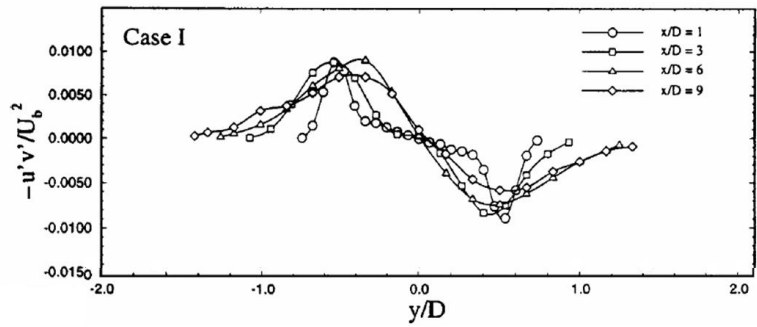
(a) Mean Axial Velocity, U/U_b



(b) Axial Velocity Fluctuations, σ_u/U_b



(c) Tangential Velocity Fluctuations, σ_v/U_b



(d) Reynolds Shear Stress Term, $-\overline{u'v'}/U_b^2$

Figure 4.31: Downstream Progression of Mean Axial Velocity and Velocity Fluctuations for an Incompressible Axisymmetric Straight Pipe at Atmospheric Pressure Where U_b is the Exit Bulk Velocity Based on Mass Flux, From Ferdman, Otugen and Kim (with Permission) [133]

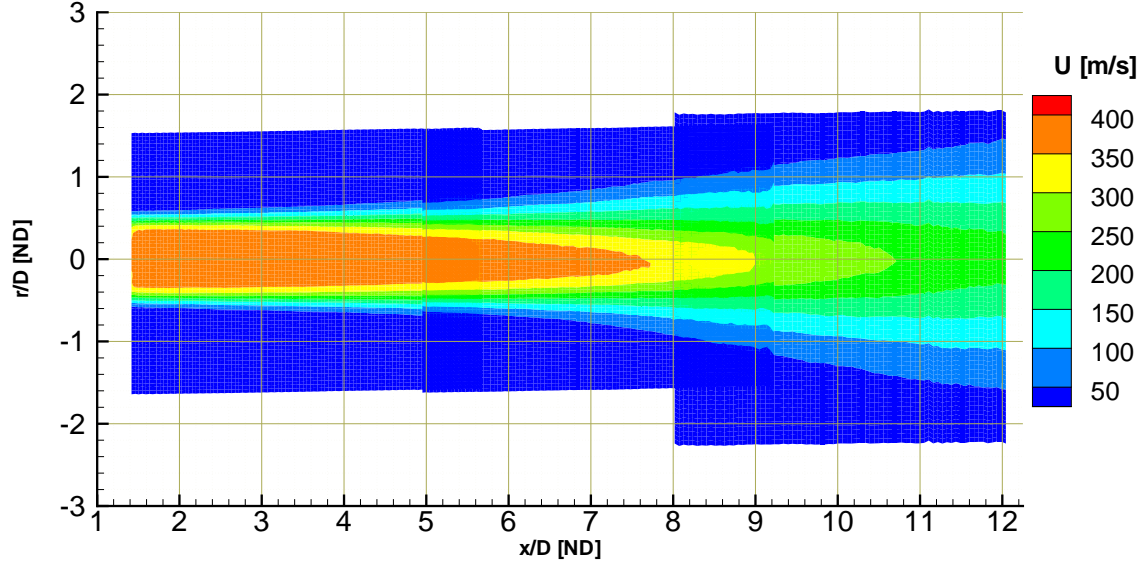


Figure 4.32: Mean Axial Velocity Contours of the Equivalent Mach 1.4 Axisymmetric Constant-Diameter Jet

Figure 4.32 is a patchwork plot of axial velocity contours from three separate PIV measurement stations of the equivalent Mach 1.4 jet created by developing flow from a constant diameter pipe 9.5 mm in diameter and 12.7 cm long. In comparison with Figure 4.13, the jet looks similar in shape and spreading but with a lower core velocity. Figure 4.33 shows mean and turbulent velocity fluctuations at a series of downstream locations. The lines show the progression of the jet from near the exit ($x/D = 2.4$) to near the cathode face ($x/D = 11.4$). First the mean axial velocity is presented in panel (a) to compare with Figure 4.31 (a). In the case measured here, the pipe flow is not fully developed as the pipe is only 13 diameters long. Other experiments indicate that pipe flow is considered fully developed after 50 diameters of travel. Therefore the developing nature of the pipe flow at the jet exit shows up as a rounded top-hat profile at 2.4 diameters. The core of the jet breaks down soon after that however, and the remaining profiles resemble the findings of Ferdman, Otugen and Kim.[133, 328, 399]

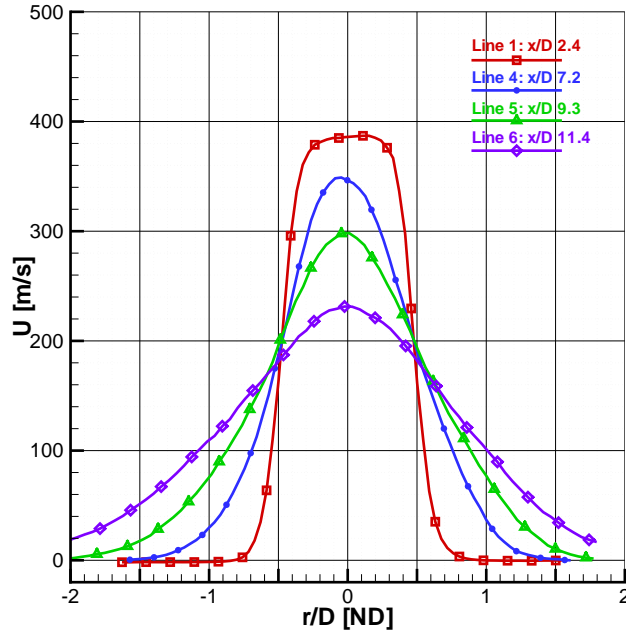
Panel (b) of Figure 4.33 shows axial velocity fluctuations to compare with the Ferdman, Otugen and Kim results of Figure 4.31 (b). The key differences focus on the first profile, 2.4 diameters from the anode face where the turbulence intensity forms sharper peaks and is lower than the fully developed counterpart. Note that although the pipe flow of this experiment has not matured in turbulence prior to the exit, it quickly approaches the more rounded characteristics of the fully developed structure.

Note that Figure 4.33 (b) shows a trend of increasing RMS for increasing downstream location, while Figure 4.31 (b) shows no such increase. The increase in RMS fluctuations is explained by the differences in

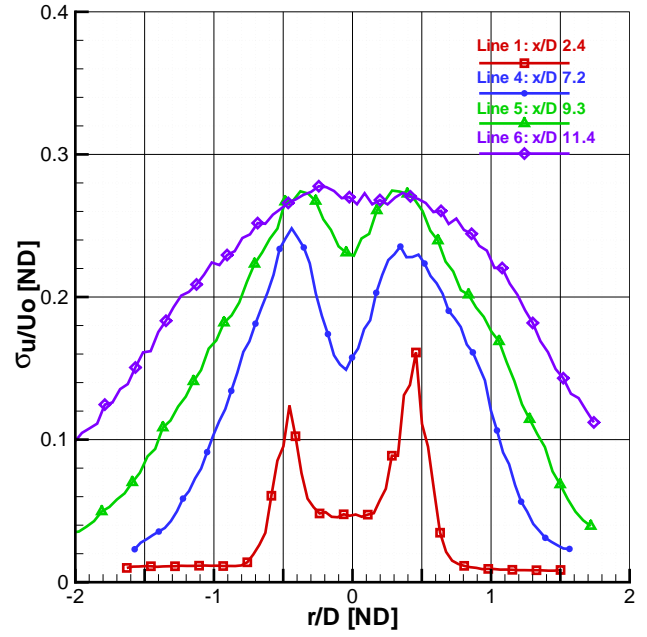
scaling parameters. For Ferdman, Otugen and Kim, the scaling velocity U_b was a constant factor based on mass flux and also subsonic. In this research the scaling velocity is the centerline velocity which decreases as the jet progresses further downstream, thus causing the relatively constant peak magnitudes to increase as flow progresses downstream. U_o was chosen as a scaling velocity for consistency in comparison with conventional matched nozzle jets. Panel (c) is the progression of tangential velocity fluctuations. The results found in this effort are much smoother than the results of Ferdman, Otugen and Kim and are believed also to be based on the developing structure found here versus the fully-developed structure of Ferdman, Otugen and Kim.[133, 399]

The final panel of Figure 4.33 is the Reynolds shear stress term scaled by centerline velocity. The increase in magnitude as flow progresses downstream is again explained by the choice in scaling factor. Note that immediately downstream of the jet exit, the line at x/D of 2.4 is unresponsive. This is believed to be another function of developing flow, vice the fully developed counterpart of Ferdman, Otugen and Kim. When compared to Figure 4.16, the pipe flow case appears more rounded at 7 diameters downstream, but begins to resemble the conventional jet only with slightly higher magnitudes.[133, 399]

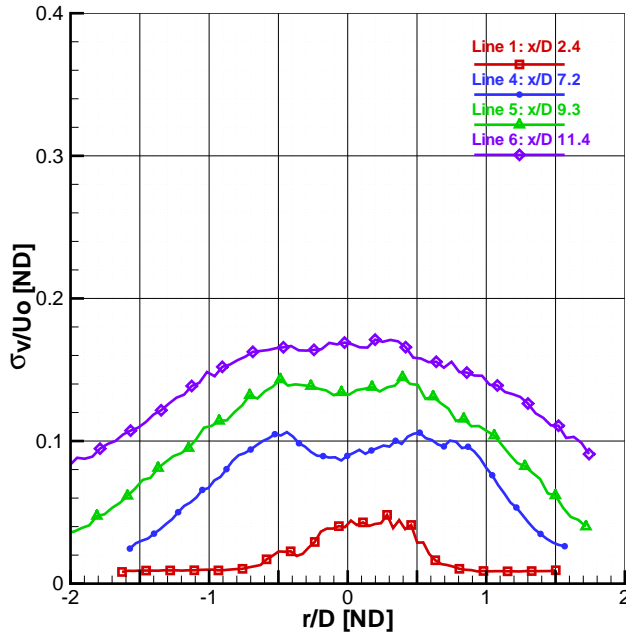
The next section will make some direct comparisons between the conventional Mach 1.4 jet and the equivalent Mach 1.4 jet borne out of developing pipe flow. After that comparison the effect of plasma on this jet will be examined in detail.



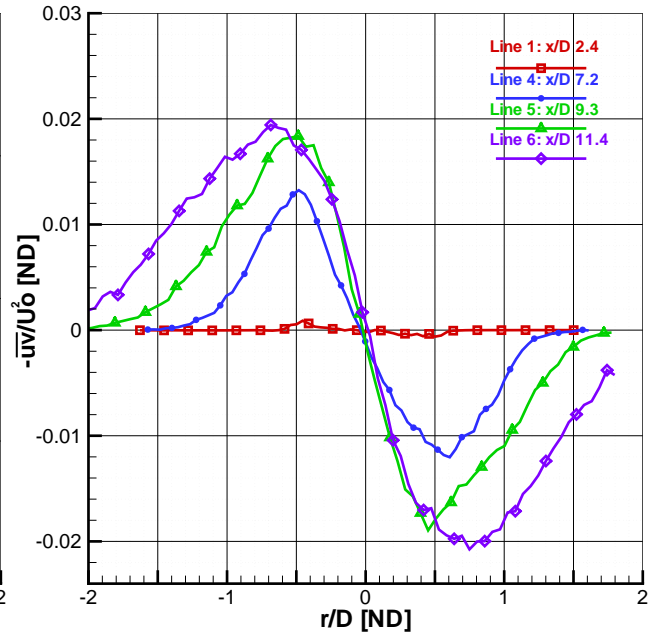
(a) Mean Axial Velocity, U



(b) Turbulent Axial Velocity Fluctuations, σ_u/U_o



(c) Turbulent Tangential Velocity Fluctuations, σ_v/U_o



(d) Reynolds Shear Stress Term, $-\overline{uv}/U_o^2$

Figure 4.33: Plasma Effects on Mean and Turbulent Axial Velocities for a Mach 1.4 Axisymmetric Jet at 5 Torr

Mach 1.4, 5 Torr Converging-Diverging and Constant-Diameter Axisymmetric Jets

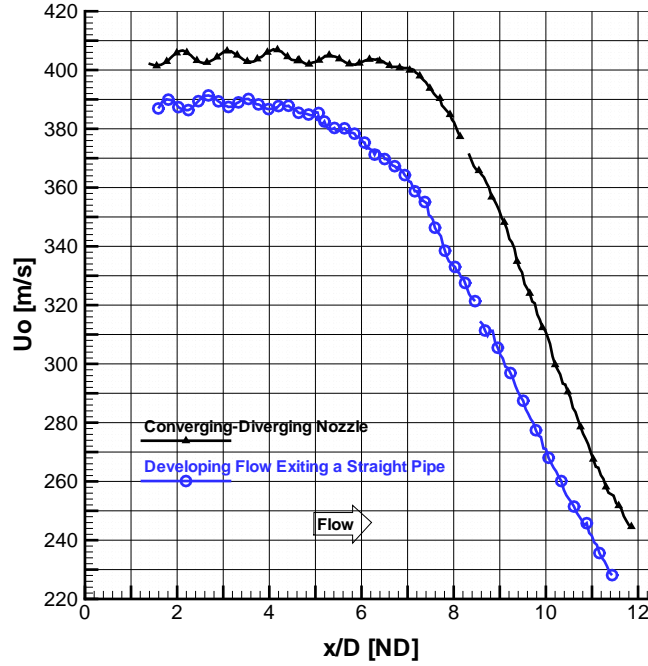


Figure 4.34: Comparison of Centerline jet Velocity Between a Mach 1.4 Axisymmetric Jet and a Jet Created by Developing Flow Exiting from a Constant-Diameter Tube Driven at a Mach 1.4 Isentropic Pressure Ratio

Figure 4.34 shows the centerline velocity between two jets with identical exit diameters, driven by identical pressure ratios as indicated in Table 4.11. The conventional jet, indicated by the black line reaches near isentropic exit conditions. The jet formed by a constant-diameter tube reaches 95.8% of the isentropic conditions based on pressure ratio and indicated by the blue line in the figure. The difference is accounted for by pressure losses associated with developing pipe flow. Table 4.11 shows the measured pressures and temperatures of the plenum (P_o, T_o) and the plenum (P_e). Then a Mach number and static temperature are calculated based on the measured exit velocity and assuming that the total temperature in the plenum is unchanged at the jet exit. The throat diameter D^* , is shown in order to distinguish between the constant-diameter pipe and the converging-diverging nozzle.

Reynolds number is calculated using the length scale of exit diameter, measured exit velocity, and density and viscosity based on the estimated for exit temperature using the ideal gas law and Sutherland's law, respectively.[14, 328, 383]

Figure 4.35 compares the conventional nozzle to the constant-diameter nozzle in both mean axial velocity and turbulent kinetic energy 2.3 diameters from the anode face for the plasma-off baseline cases. The core velocity decreases 4.2% in panel (a). In panel (b), the centerline turbulent kinetic energy increases

Table 4.11: Estimation of Jet Exit Conditions for the Mach 1.4, 5 Torr Converging-Diverging and Constant-Diameter Axisymmetric Jet

Case	P_o (1) [torr]	P_e (1) [torr]	T_o (1) [K]	M_e (2) [ND]	U_e (1) [m/s]	T_e (2) [K]	D^* (1) [mm]	D_e (1) [mm]	Re_D (2) [ND]
E	16.5	5.00	296	1.35	404	217	8.9	9.5	6133
G	16.5	5.00	295	1.27	387	222	9.5	9.5	5605

(1) Measured Quantity
(2) Estimated From Plenum Temperature and Measured Exit Velocity

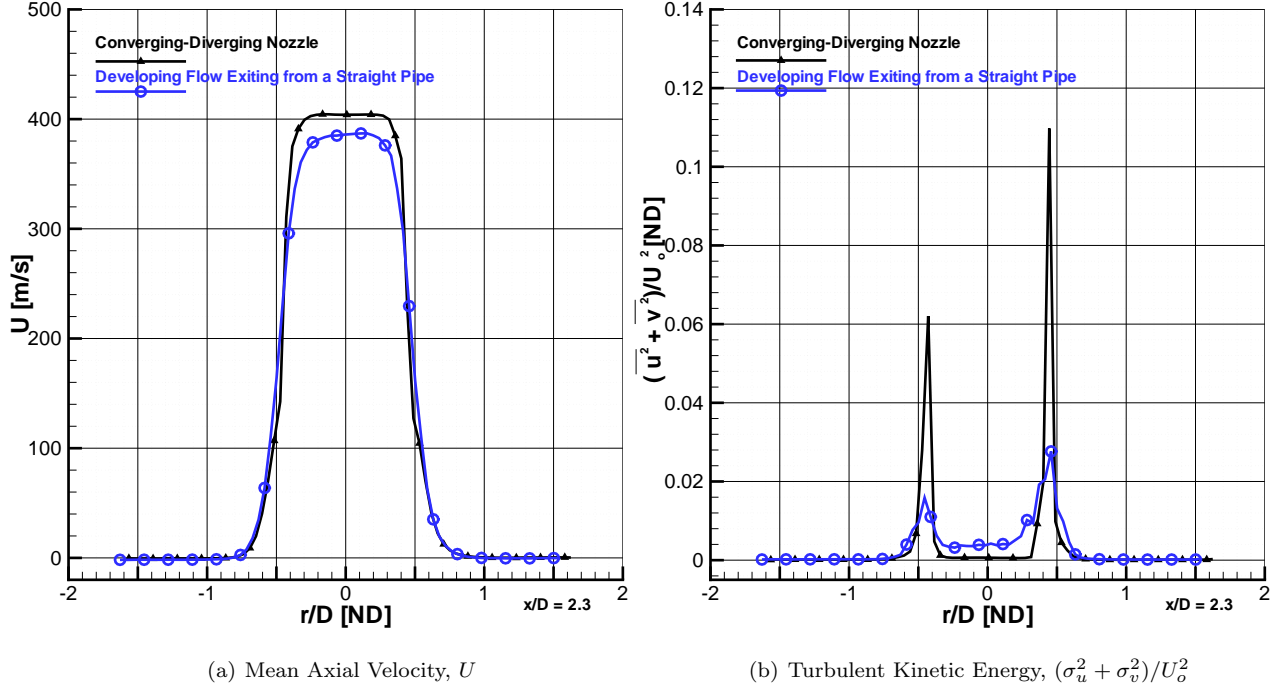


Figure 4.35: Comparison of Mean Axial Velocity and Turbulent Kinetic Energy between a Mach 1.4 Axisymmetric Jet and Flow Created from a Tube Driven at a Mach 1.4 Pressure Ratio at 5 Torr, Near the Jet Exit ($x/D = 2.3$)

significantly (533%) for the constant-diameter nozzle over the conventional nozzle. It can be argued, that 3% of the energy lost in decreasing core velocity is transferred into increased turbulent kinetic energy in the core of the jet. The decrease in TKE in the shear layer is 42%. The increase TKE in the jet core was one of the reasons behind choosing this case to test in the plasma field. Additionally, nozzle manufacturing was relatively simple, when compared to the converging-diverging nozzles and all three pressure ratios were tested in this sequence using the same nozzle. Pressure ratios were varied by using a ball valve upstream of the plenum choke to provide additional regulation, while still allowing for adequate seeding for PIV measurements.[103, 133]

At 11.3 jet diameters, Figure 4.36 shows the remarkable differences between the jet features. The jet formed by developing pipe flow is 10.8% lower in centerline velocity than the conventional nozzle in panel

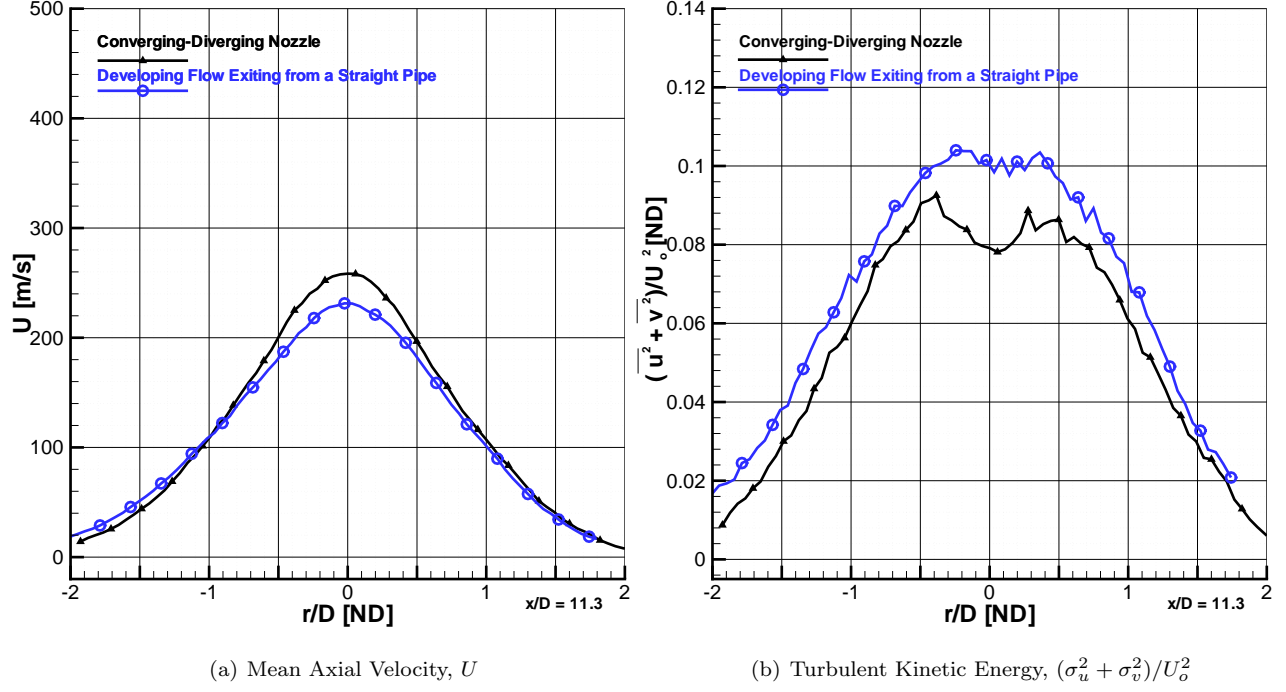


Figure 4.36: Comparison of Mean Axial Velocity and Turbulent Kinetic Energy between a Mach 1.4 Axisymmetric Jet and Flow Created from a Tube Driven at a Mach 1.4 Pressure Ratio at 5 Torr, Much Further Downstream ($x/D = 11.3$)

(a). While in panel (b), TKE is 26.6% higher on the centerline and 14.9% higher in the shear layer for the pipe flow nozzle when compared to the converging-diverging nozzle with identical exit diameters. The next three cases investigate the influence of increasing pressure ratio on the plasma field by examining mean and turbulent kinetic energy measured by particle image velocimetry.

4.2.5 The Effect of Plasma for Increasing Pressure Ratios in Jets Formed out of Developing Pipe Flows

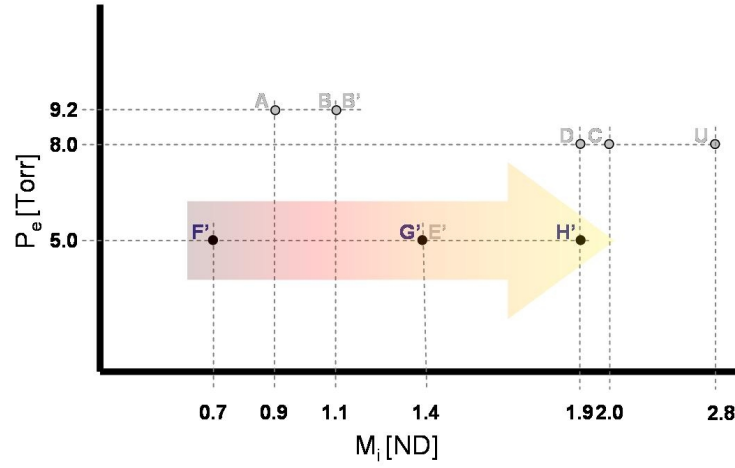


Figure 4.37: A Path Showing The Progression Through the Experiment Space to Investigate Compressibility on Developing Pipe Flow From Constant-Diameter Nozzles

This section looks at three constant-diameter nozzle flow fields which provide increasing equivalent Mach numbers to look into the effect of plasma influence of mean and turbulent velocities with varying compressibility. Figure 4.37 shows the path taken through the experiment space of chamber pressure and equivalent Mach number. The cases are summarized in Table 4.12 by case identifier and followed by the pertinent measured and calculated parameters described in detail at the beginning of this chapter. The first case to be examined is the equivalent Mach 0.9 jet. Then in increasing equivalent Mach number, the equivalent Mach 1.4 and equivalent Mach 1.9 cases will be examined.

Table 4.12: Estimation of Jet Exit Conditions for the 8-9 Torr Converging-Diverging Axisymmetric Jets

Case	P_o (1) [torr]	P_e (1) [torr]	T_o (1) [K]	M_e (2) [ND]	U_e (1) [m/s]	T_e (2) [K]	D^* (1) [mm]	D_e (1) [mm]	Re_D (2) [ND]
F'	8.2	5.00	293	0.75	247	263	9.5	9.5	2637
G'	16.5	5.00	295	1.27	387	222	9.5	9.5	5605
H'	34.0	5.00	294	1.63	460	192	9.5	9.5	8733
(1) Measured Quantity									
(2) Estimated From Plenum Temperature and Measured Exit Velocity									

Equivalent Mach 0.9, 5 Torr Constant-Diameter Axisymmetric Jet

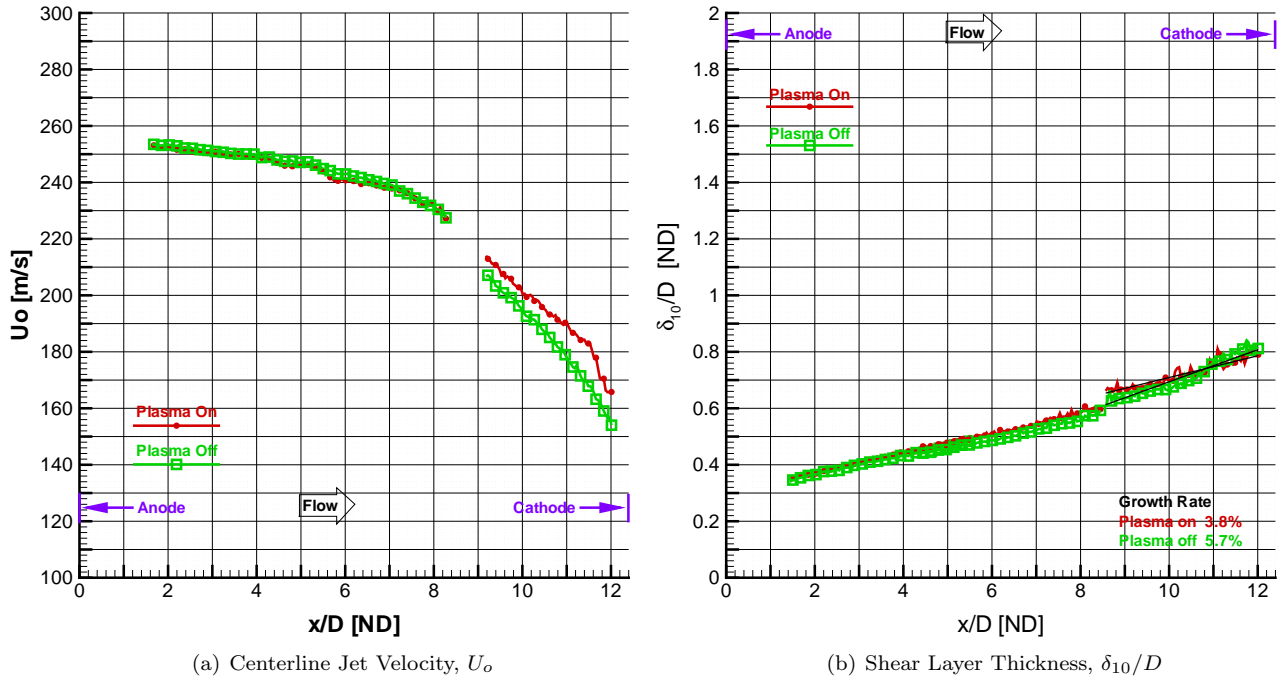


Figure 4.38: Plasma Effects on Downstream Progression of Centerline Jet Velocity and Shear Layer Thickness for a Flow Created from a Tube Driven at a Mach 0.9 Pressure Ratio at 5 Torr

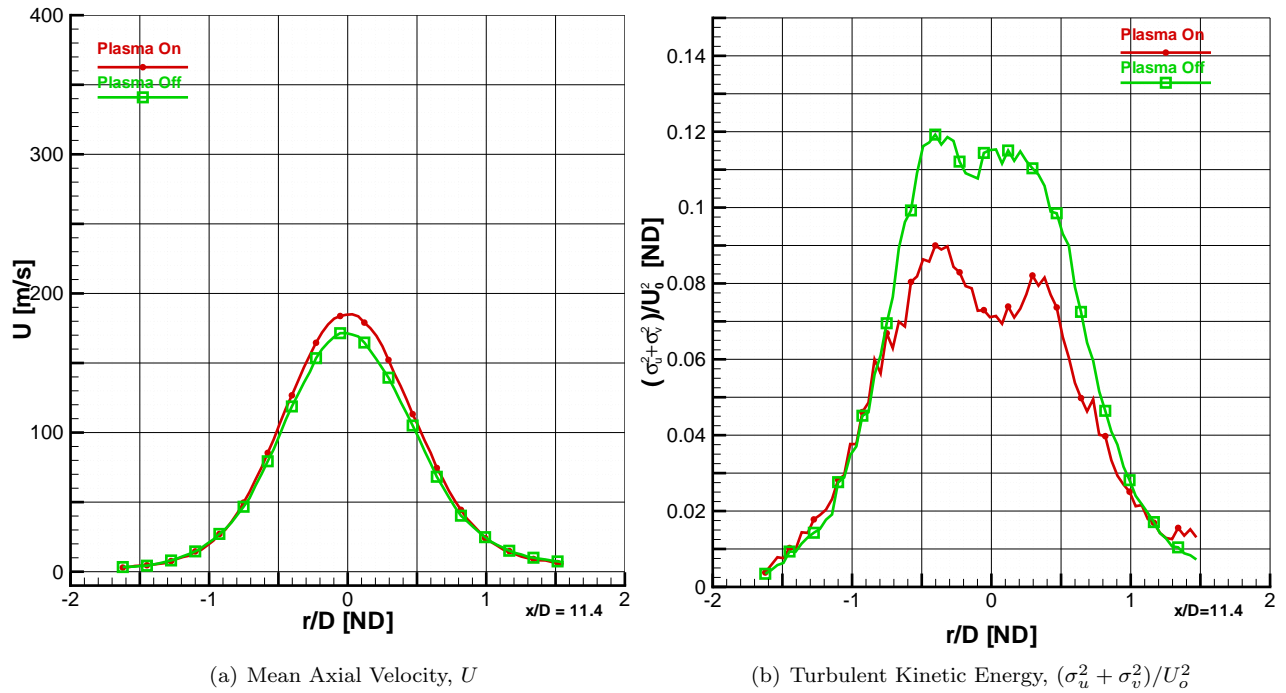


Figure 4.39: Plasma Effects on Mean Axial Velocity and Turbulent Kinetic Energy for a Flow Created from a Tube Driven at a Mach 0.9 Pressure Ratio at 5 Torr

In continuing variations in pressure ratio and nozzle type, this begins the sequence of plasma influence on constant-diameter tube measurements. Figure 4.38 shows the centerline axial velocity and shear layer thickness along the electrode gap in panels (a) and (b), respectively. It is surprising the change in centerline velocity visible in panel (a) given the relatively weak visible light emission seen in Section 4.5. Shear layer growth rate changes are considered insignificant here given the small overall growth rate reported and the still developing nature of the jet even at 11.4 jet diameters.

Figure 4.39 reports an 8% increase in axial velocity for the plasma-on case over the baseline case at the centerline of the jet, 11.4 jet diameters downstream of the anode face. Panel (b) shows an astounding 36% decrease in turbulent kinetic energy along the centerline with a 29% decrease in TKE in the shear layer. From the axial velocity and TKE plots, it appears as if the plasma-on case is taken at a location much closer to the anode face, than the baseline case. This is indeed not the case, just an observation that the jet shows signs of less decay with the plasma field active when compared to the baseline case at the same location.^[133]

Equivalent Mach 1.4, 5 Torr Constant-Diameter Axisymmetric Jet

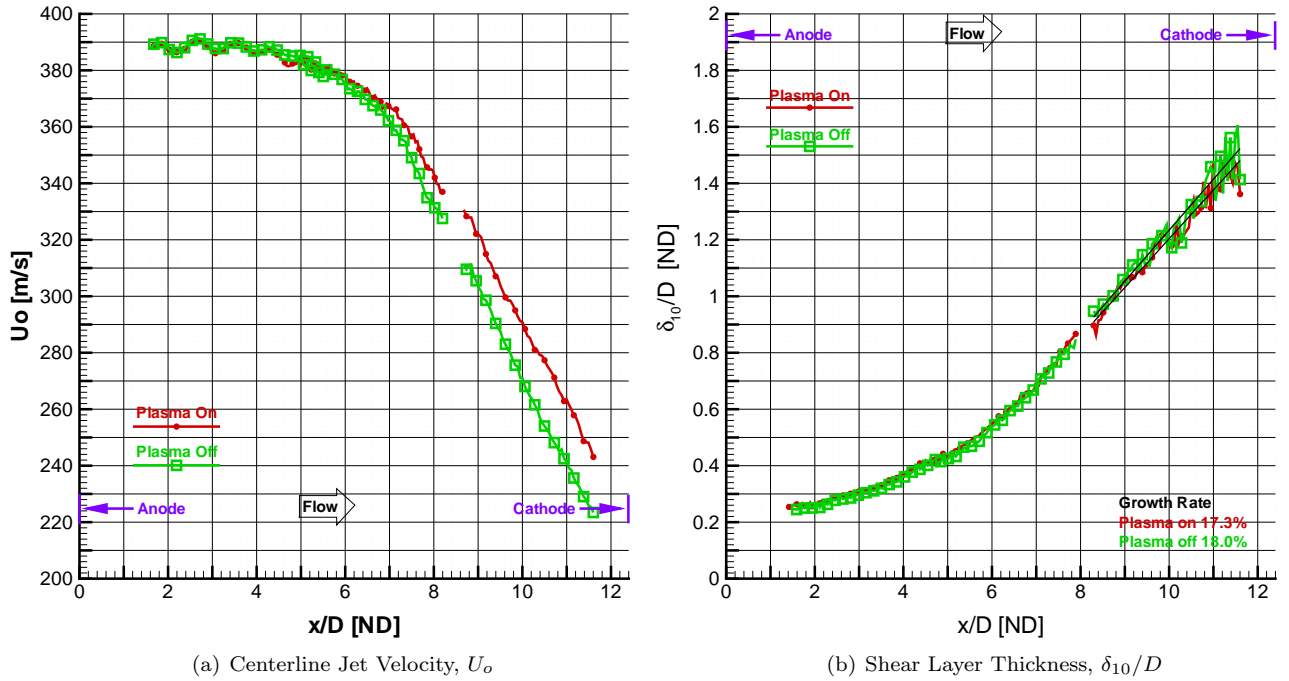


Figure 4.40: Plasma Effects on Downstream Progression of Centerline Jet Velocity and Shear Layer Thickness for a Flow Created from a Tube Driven at a Mach 1.4 Pressure Ratio at 5 Torr

Again, Figure 4.40 continues to show visible change in the axial velocity when compared to the other cases examined so far. And as in the subsonic case previous to this one, the shear layer growth rate reports changes which are below the uncertainty threshold in Figure 4.40 (b). Figure 4.41 (a) and (b) show a cross-

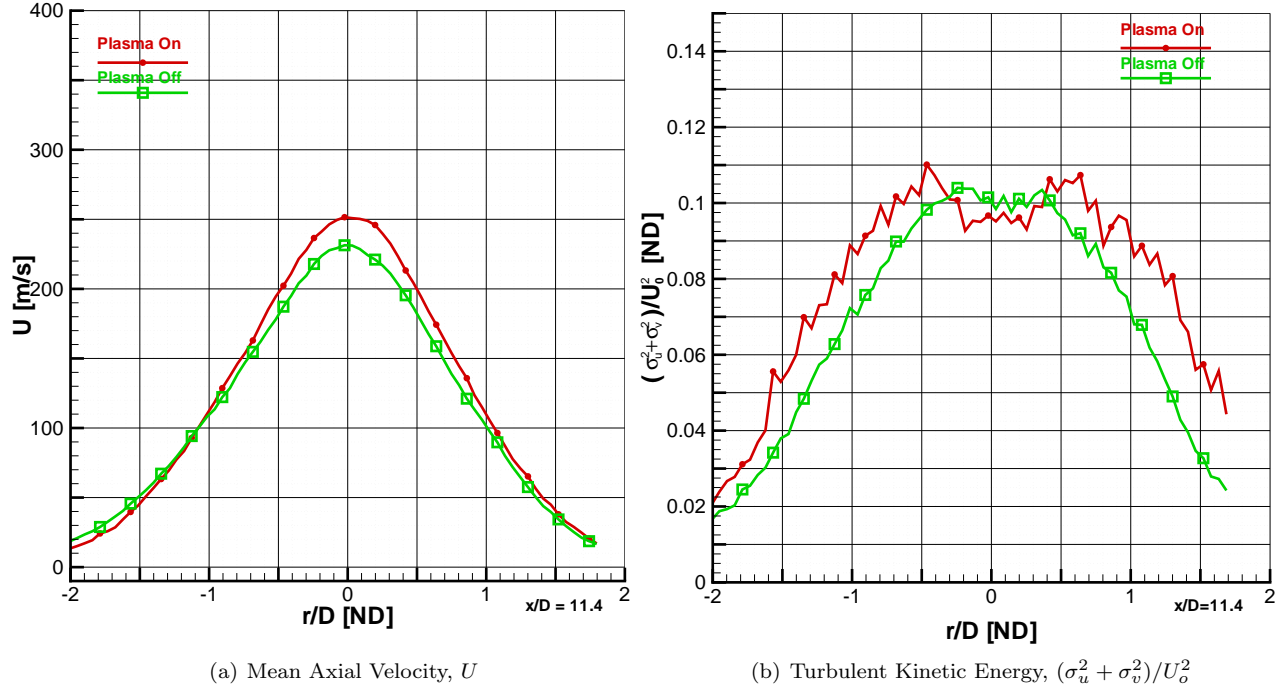
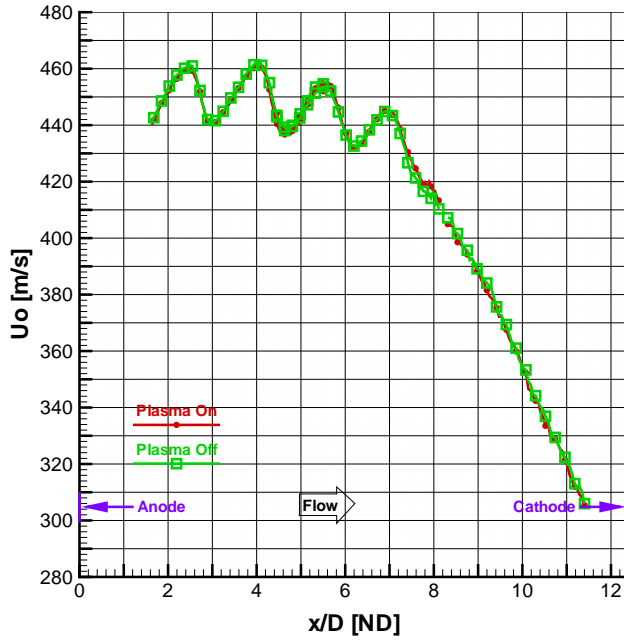


Figure 4.41: Plasma Effects on Mean Axial Velocity and Turbulent Kinetic Energy for a Flow Created from a Tube Driven at a Mach 1.4 Pressure Ratio at 5 Torr

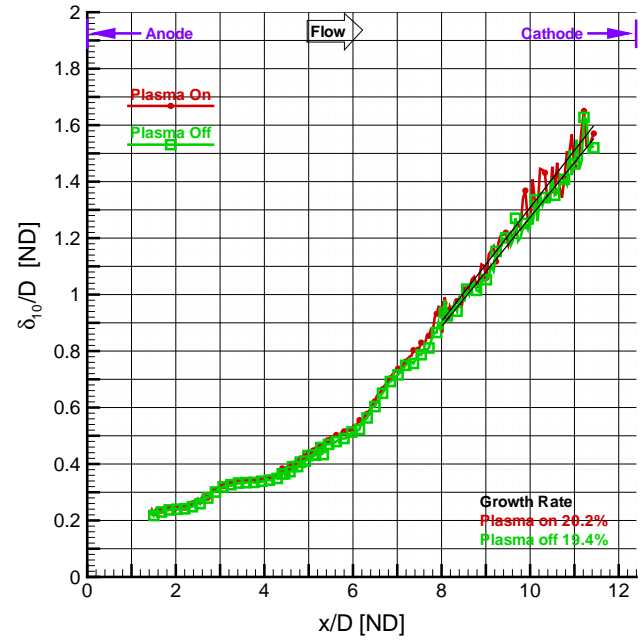
section of mean axial velocity and turbulent kinetic energy at a station located 11.4 jet diameters from the anode face. In similar fashion to the subsonic case of the previous section, a 9% increase in mean axial velocity occurs at the centerline, when the plasma is turned on. However, the TKE decreases by 5% on the centerline and increases by 3% in the shear layer. This is in contrast to the subsonic pressure ratio case F, but is still consistent with the observation that the plasma-on case looks very similar to the plasma off case, but at a station closer to the anode face.^[133]

Equivalent Mach 1.9, 5 Torr Constant-Diameter Axisymmetric Jet

The final pressure ratio in this sequence results in an equivalent Mach number of 1.9. From Figure 4.42, no noticeable changes in centerline axial velocity or shear layer thickness, or growth rate are observed. In Figure 4.43, panel (a) similarly shows no change in the axial velocity profile. However, TKE (panel (b)) increases for the plasma-on case, when compared to the baseline case 11% along the centerline and 14% in the shear layer.

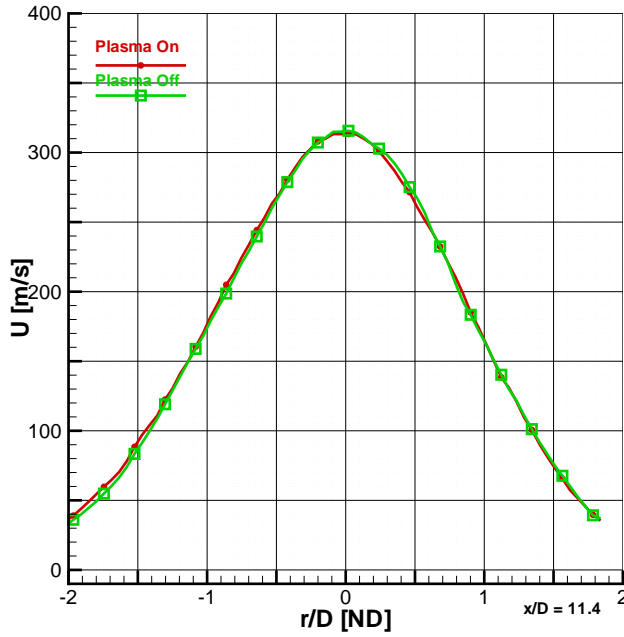


(a) Centerline Jet Velocity, U_o

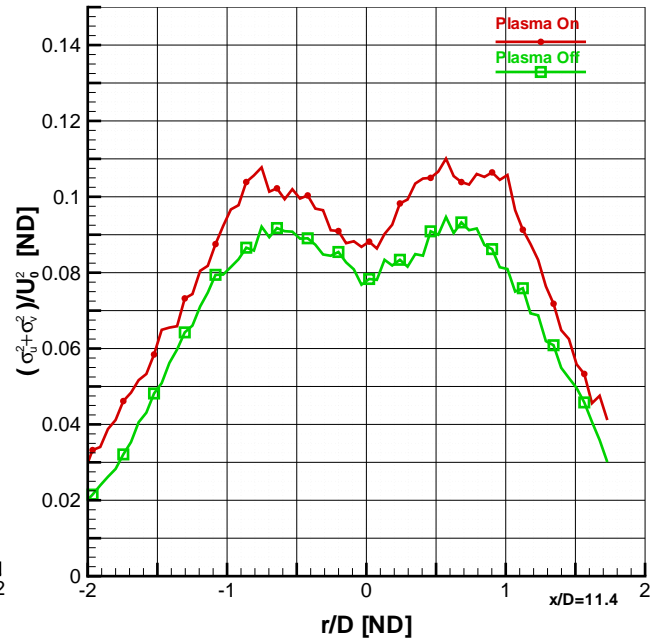


(b) Shear Layer Thickness, δ_{10}/D

Figure 4.42: Plasma Effects on Downstream Progression of Centerline Jet Velocity and Shear Layer Thickness for a Flow Created from a Tube Driven at a Mach 1.9 Pressure Ratio at 5 Torr



(a) Mean Axial Velocity, U



(b) Turbulent Kinetic Energy, $(\sigma_u^2 + \sigma_v^2)/U_o^2$

Figure 4.43: Plasma Effects on Mean Axial Velocity and Turbulent Kinetic Energy for a Flow Created from a Tube Driven at a Mach 1.9 Pressure Ratio at 5 Torr

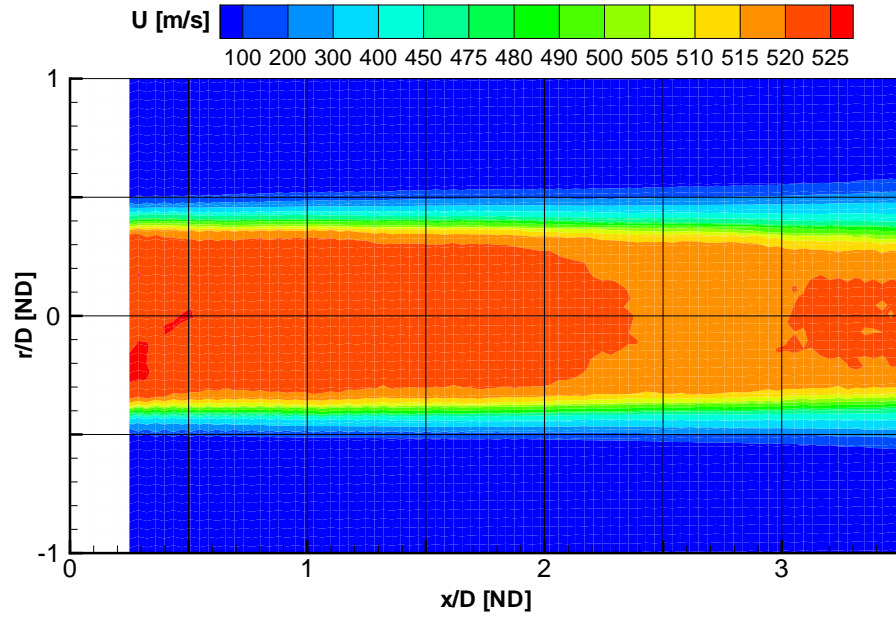
Summary of Important Findings in Jets From Developing Pipe Flows

Here is a summary of the significant conclusions obtained in the comparison of mean and turbulent fluctuations measured by particle image velocimetry of developing pipe flow jets with plasma-on and plasma-off.

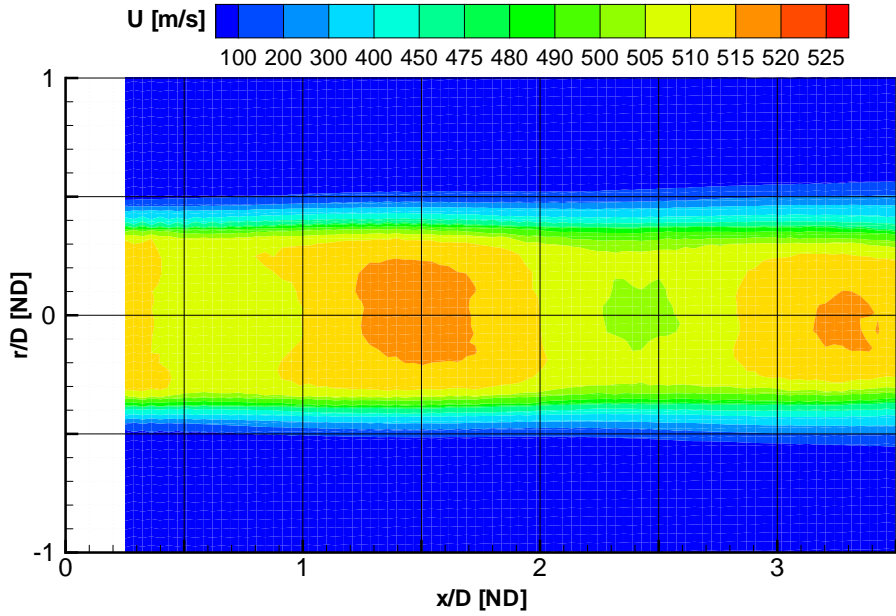
- The jet created by the constant-diameter nozzle was effective in increasing turbulence intensities in the core of the jet which translated into higher turbulent kinetic energy further downstream.
- The equivalent Mach 0.9 jet is influenced by the plasma considerably, given the relative weakness of the plasma field which will be discussed more in Section 4.5. The plasma-on case had a centerline velocity which was 8% higher than the plasma-off case at 11.4 diameters from the anode face. The turbulent kinetic energy was 29 to 36% lower for the plasma-on case when compared to the plasma-off case at this location.
- The equivalent Mach 1.4 jet showed a 9% increase in centerline axial velocity and a 5% decrease in centerline TKE. In the shear layer however, the turbulent kinetic energy increased by 3%.
- For the high speed, equivalent Mach 1.9 case the axial velocity profiles looked the same, but turbulent kinetic energy increased 11% on the centerline and 14% in the shear layer when the plasma was initiated. This case shows shock and expansion phenomena in the jet core region from overexpansion in the tube.

Given the trend for centerline velocity to rise when the plasma is turned on, the influence of plasma appears to support the theory of the jet core penetrating further into a shear layer when it is heated by the plasma field. The turbulent kinetic energy shows an interesting trend that appears to be related to the variation in compressibility. For the subsonic pressure ratio the TKE dropped. At an equivalent Mach 1.4 the value of k was lower in the center and slightly higher in the shear and at equivalent Mach 1.9, the TKE was higher. Possible causes for this are the change in convective velocity due to plasma heating, or the plasma field interacting with the weak shocks in the core region to influence the flow downstream. The next section will investigate the influence the plasma effects on an overexpanded converging-diverging jet.[\[11, 193, 251\]](#)

4.2.6 Mach 1.9 (Overexpanded), 8 Torr Converging-Diverging Axisymmetric Jet

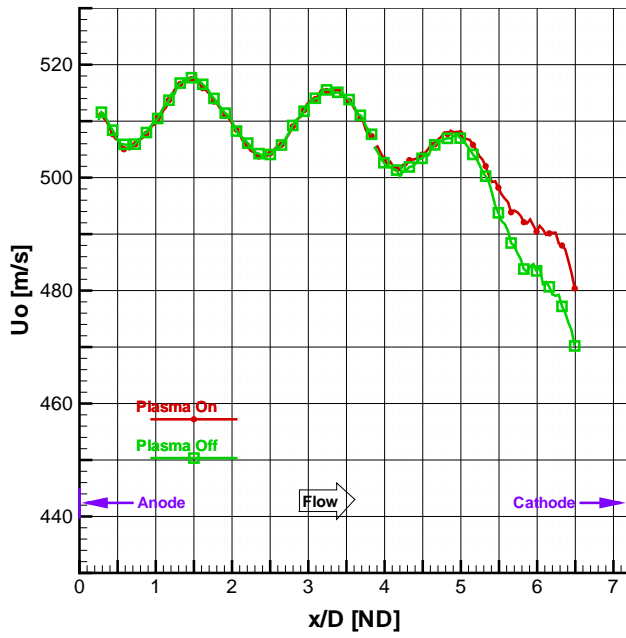


(a) Nominal Mach 2.0 Case

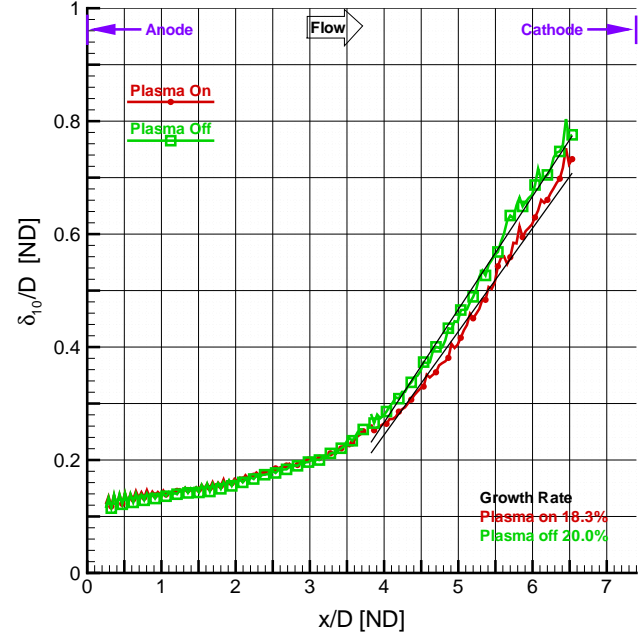


(b) Overexpanded Case

Figure 4.44: Contours of Mean Axial Velocity, U [m/s] Comparing the Nominal Mach 2.0 Jet to the Overexpanded Jet, Driven at Mach 1.9 Isentropic Pressure Ratio

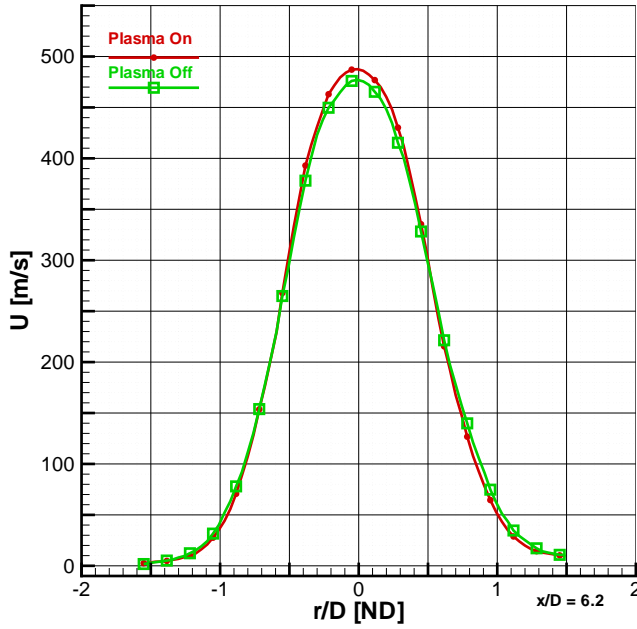


(a) Centerline Jet Velocity, U_o

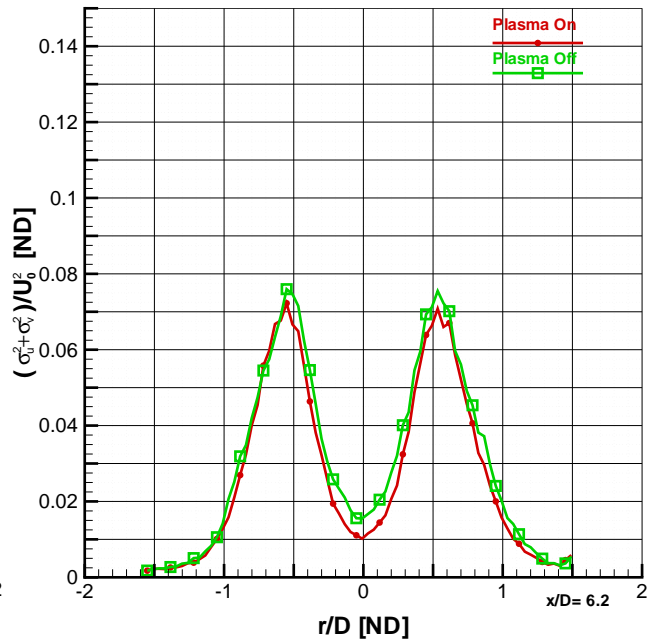


(b) Shear Layer Thickness, δ_{10}/D

Figure 4.45: Plasma Effects on Downstream Progression of Centerline Jet Velocity and Shear Layer Thickness in an Overexpanded Jet Driven at a Mach 1.9 Pressure Ratio at 8 Torr



(a) Mean Axial Velocity, U



(b) Turbulent Kinetic Energy, $(\sigma_u^2 + \sigma_v^2)/U_o^2$

Figure 4.46: Plasma Effects on Mean Axial Velocity and Turbulent Kinetic Energy in an Overexpanded Jet Driven at a Mach 1.9 Pressure Ratio at 8 Torr

Table 4.13: Estimation of Jet Exit Conditions for the Mach 1.9, 8 Torr Converging-Diverging Axisymmetric Jet

Case	P_o (1) [torr]	P_e (1) [torr]	T_o (1) [K]	M_e (2) [ND]	U_e (1) [m/s]	T_e (2) [K]	D^* (1) [mm]	D_e (1) [mm]	Re_D (2) [ND]
D	62.0	8.00	293	1.94	510	167	8.0	11.3	20208
(1) Measured Quantity									
(2) Estimated From Plenum Temperature and Measured Exit Velocity									

Figure 4.44 describes this off-nominal case where the baseline flow is a converging-diverging jet at Mach 2.0. The influence of plasma-on a weakly over-expanded jet is investigated here. The baseline Mach 2.0 jet is driven at a pressure ratio equivalent to a Mach number of 1.9, details of jet exit conditions are found in Table 4.13. The diamond shock-expansion structure is visible in panel (b) of Figure 4.44. Note that near the jet exit, Section 4.2 showed that PIV results tend to smear shock structures and particle lag produces errors in mean axial velocity. The reader is cautioned as to the accuracy of these results near the jet exit. Further downstream, the flow becomes subsonic and allows the particles to effectively track the flow. See Table 4.7 details the decrease in measurement uncertainty in turbulent fluctuations for this case (case D).[\[76, 193, 219, 251\]](#)

Figure 4.45 shows the axial trends of centerline velocity and shear layer thickness for this overexpanded off-nominal condition. When compared to section 4.4.4 (the baseline nominal case), the influence of the plasma field is more pronounced. The centerline velocity decreases for the plasma-on case again, as well as the plasma-on case shows a decrease in shear layer thickness and growth rate. In the off nominal case, the growth rate decreases by 1.7% for the equivalent Mach 1.9 case, and only 1.1% for the nominal Mach 2.0 case.

Figure 4.46 shows the mean axial velocity and turbulent kinetic energy at 6.2 jet diameters from the anode face. In this case, the axial velocity along the centerline increases 11 m/s for a 2.4% change in the plasma-on case over the plasma-off condition. Recall, for the nominal jet, the increase was 5 m/s or a 1% change. TKE decreases 31% along the centerline and 5% in the shear layer for the overexpanded plasma-on condition over the corresponding plasma-off baseline. For the nominal Mach 2.0 jet, the centerline decrease was 14% and an increase of 1% was noticed for the plasma-on case, when compared to its baseline plasma-off case. From these remarkable changes in plasma for the slightly overexpanded condition, it is concluded that the plasma field may have an impact on weak shocks. It has been hypothesized that a plasma field may interact electrically with the dissociation which occurs in shock waves to weaken them thermally resulting in a higher downstream fluid velocity in the presence of a plasma. Conversely, the convective Mach number is lower in this case, when compared to the Mach 2.0 nominal case and that may be the driver for the change

noticed here.[194, 193, 251]

4.2.7 Influence of Anode Design on Mean Flow and Turbulence

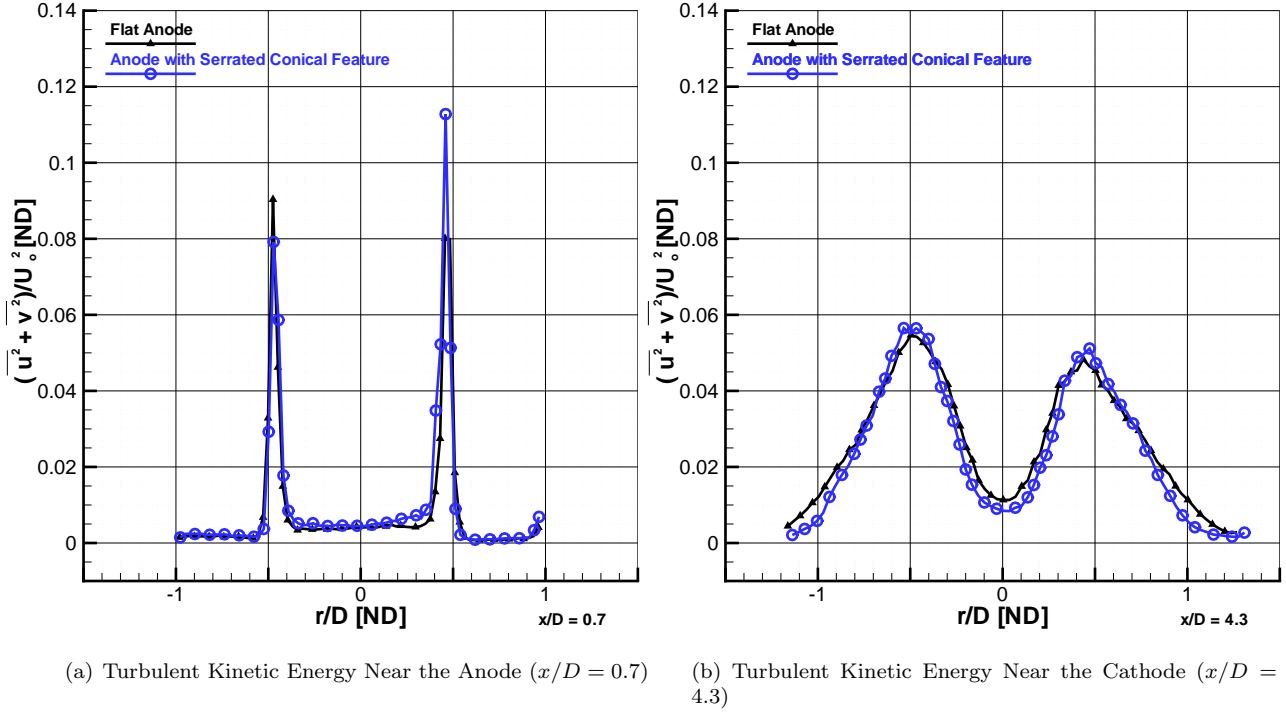
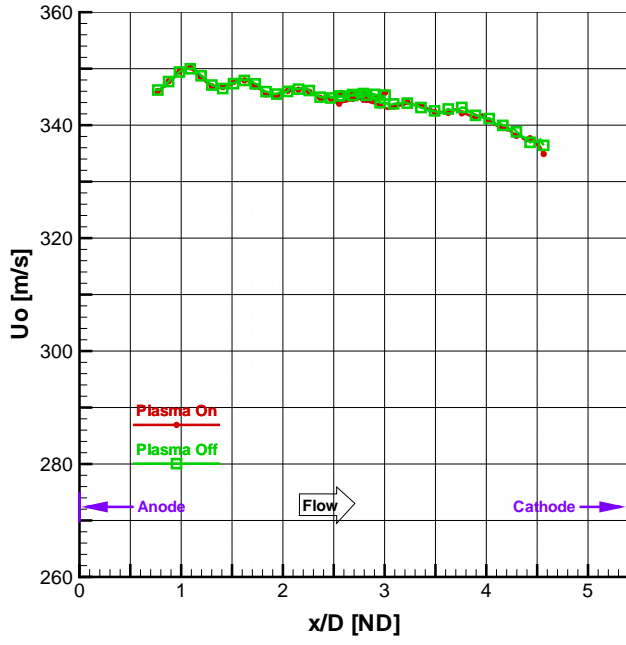
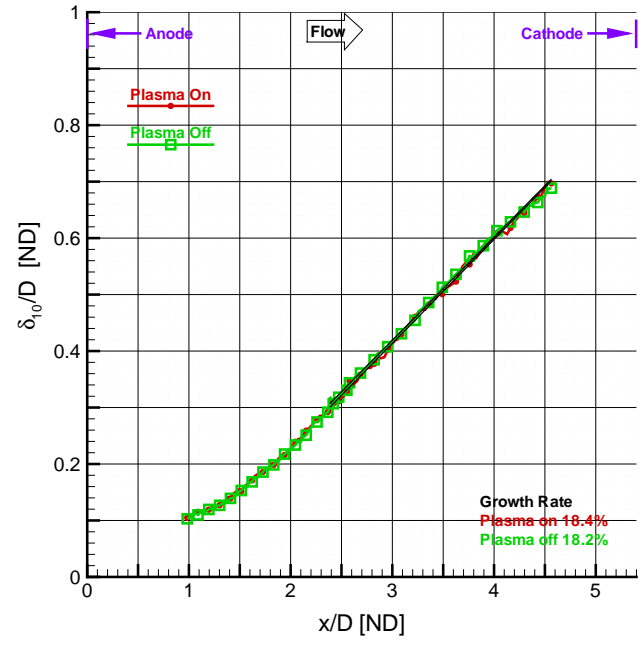


Figure 4.47: Comparison of Turbulent Kinetic Energy between a Flat Anode and an Anode with Serrated Conical Feature for a Mach 1.1 Axisymmetric Jet at 9 Torr - Plasma-Off

The last off-nominal case examined in this section is the influence of anode design on the mean and turbulent structure of the jet. The baseline anode was a flat faced anode with rounded edges. Preliminary investigations concluded that sharp edges, particularly from cap screws used to assemble older nozzles, were sources of plasma instability at higher chamber pressures. However, the rough edges were advantages in increasing the plasma field strength near the anode. Therefore, to investigate the effect of a stronger plasma field near the jet exit an anode with serrated conical feature was examined. To insure a consistent evaluation, first look at Figure 4.50. In this figure, the turbulent kinetic energy is shown for the plasma-off cases where the only difference is the anode. Virtually no difference is noticed at the anode face in TKE, while minor variations in TKE further downstream are attributed to minor differences in pressure ratio between the two cases. Axial velocity is not shown here, as there was no noticeable difference at either location.[76]

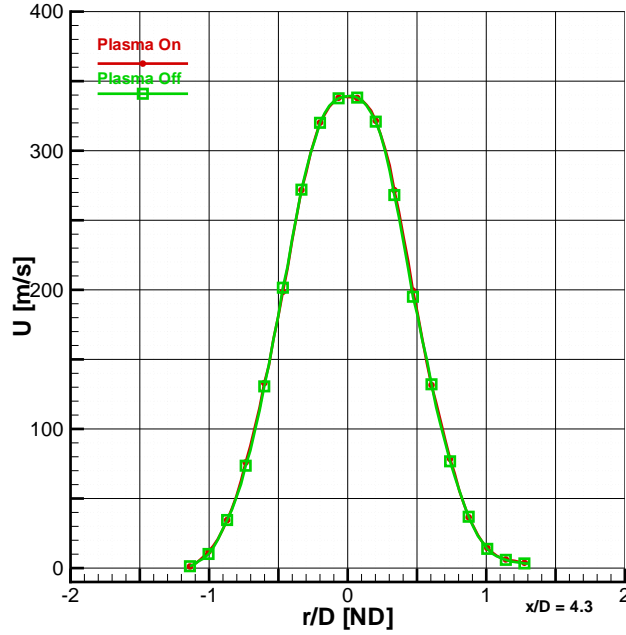


(a) Centerline Jet Velocity, U_o

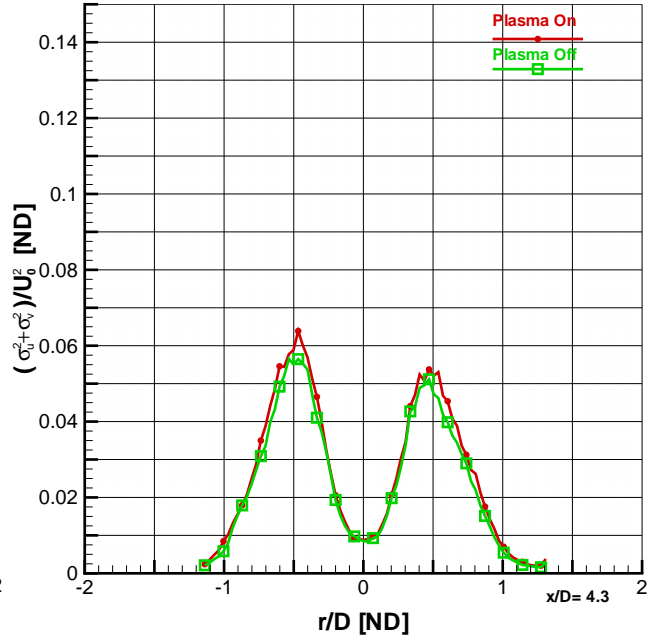


(b) Shear Layer Thickness, δ_{10}/D

Figure 4.48: Plasma Effects on Downstream Progression of Centerline Jet Velocity and Shear Layer Thickness for a Mach 1.1 Axisymmetric Jet at 9 Torr for an Anode with Serrated Conical Feature



(a) Mean Axial Velocity, U



(b) Turbulent Kinetic Energy, $(\sigma_u^2 + \sigma_v^2)/U_o^2$

Figure 4.49: Plasma Effects on Mean Axial Velocity and Turbulent Kinetic Energy for a Mach 1.1 Axisymmetric Jet at 9 Torr for an Anode with Serrated Conical Feature

Table 4.14: Estimation of Jet Exit Conditions for the Mach 1.1, 9 Torr Converging-Diverging Axisymmetric Jet

Case	P_o (1) [torr]	P_e (1) [torr]	T_o (1) [K]	M_e (2) [ND]	U_e (1) [m/s]	T_e (2) [K]	D^* (1) [mm]	D_e (1) [mm]	Re_D (2) [ND]
B	20.5	9.15	293	1.13	350	233	15.2	15.7	8501
(1) Measured Quantity									
(2) Estimated From Plenum Temperature and Measured Exit Velocity									

Table 4.14 shows the exit conditions for this jet, case B. Figure 4.48 shows the difference between plasma-off and plasma-on for the case where the anode is modified with serrated conical feature. No noticeable difference is visible between centerline axial velocity, shear layer thickness or shear layer growth rate. Figure 4.49 shows a cross-section of mean axial velocity and non-dimensional turbulent kinetic energy at a location 4.3 diameters from the anode face. No changes are noted in axial velocity, while an 8% increase in TKE in the shear layer is reported in the plasma-on case over the plasma off case. In the baseline flat anode, it was previously reported that the shear layer increase in TKE was 3% for plasma-on over plasma-off.

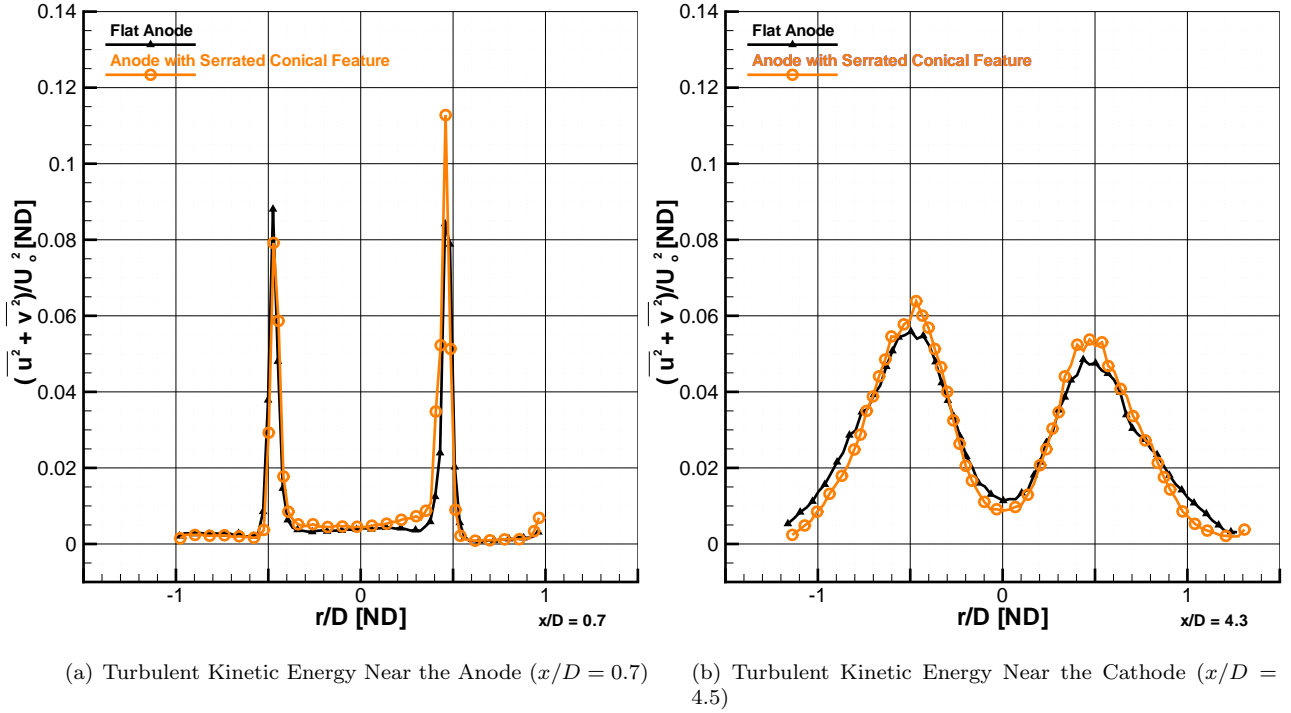


Figure 4.50: Comparison of Turbulent Kinetic Energy between a Flat Anode and an Anode with Serrated Conical Feature for a Mach 1.1 Axisymmetric Jet at 9 Torr - plasma-on

Figure 4.50 compares the turbulent kinetic energy for plasma-on conditions between flat anode face and anode face with serrated conical feature. There is no noticeable difference in TKE at the anode face, however the increase in TKE near the cathode face is visible in the shear layer. The serrated conical feature

is concluded to improve the influence of the plasma field on turbulent structure, without significant impact on the mean flow. Note that mean flow features could be influenced by the plasma field more significantly by the modified anode design if the gap distance were able to be increased, or for smaller diameter jets. Additionally, the modified anode is not recommended for use at higher chamber pressures as arcs form easily in the non-linear electric field created near the serrated cone. The modified anode design was used exclusively for the 5 torr plasmas tested, while the 8-9 torr plasmas used the flat anode (with case B repeated with both anodes for this section). More testing would have been done with the modified anode, however some of the 8-9 torr jets had larger exit diameters than the one available modified anode. Therefore, all the tests done at the higher chamber pressure used flat anodes for consistency.

4.2.8 Summary of Important Findings from Particle Image Velocimetry Measurements

The first cases examined by PIV looked at the influence of increasing pressure ratios for the conventional converging-diverging nozzles. Here is a synopsis of the findings.

- At a chamber pressure of 5 torr, the Mach 1.4 jet was most influenced by the plasma field in terms of mean axial velocity change. Measurements 11.3 diameters downstream of the anode face revealed a 5.1% change in mean axial velocity at the centerline. A coincidental decrease in TKE of 5.1% also occurred on the jet centerline, with a 3.1% increase in TKE in the shear layer.
- The Mach 0.7 jet at a chamber pressure of 9 torr showed no change in mean axial velocity between plasma-on and plasma-off. Turbulent kinetic energy however showed a 7.1% increase in the shear layer. There is a 6.7% change in k on the centerline, however the fact that TKE on the centerline of this jet is so low makes this change negligible.
- The Mach 1.1 jet exhausting into a chamber pressure of 9 torr showed small changes in mean axial velocity or fluctuating velocity measurements when comparing the plasma-on and plasma-off cases.
- The Mach 2.0 jet at 8 torr however, showed minor changes. The TKE along the centerline decreased by 14% noting that k along the centerline was small and therefore changes were magnified in percentage analysis. The centerline mean axial flow also saw a change, the plasma-on case was 1% larger than the plasma-off case which was a change of 5 m/s.
- These measurements support a supposition that the primary influence this plasma field has over the coaxial jet is through heating the shear layer, thus decreasing the density and increasing the speed of

sound locally. The jet core remains relatively undisturbed by the plasma field and therefore results in an delay in core breakdown until further downstream.

Two factors contributed to the changes discovered so far. First, the largest driver in change appeared to be chamber pressure when considering the effect of plasma, on mean and turbulent velocities. The optimal distance between electrodes increased for decreasing chamber pressure. This increase in distance provided longer plasma volumes along the shear layer of the jet which in turn produced longer jet resident times in the plasma field and therefore increased the potential for plasma to influence the flow. The second factor appeared to be related to jet diameter. Jet diameter influenced the location where the core breakdown of the jet occurred. Core breakdown typically began before 8 jet diameters downstream of the anode. Therefore in a fixed gap space, the jet with smaller exit diameter experienced core breakdown first - for a given pressure ratio. The reduction of chamber pressure from 8-9 torr to 5 torr combined those effects. The lower chamber pressure had an optimal electrode spacing increase of 50%. The chamber pressure was set by the mass flow of gas passing through the vacuum pump. At 5 torr the mass flow rate through the pump was reduced 40% from 8 torr - requiring less mass flow to pass through the nozzle. The requirement for lower mass flow through the nozzle then drove a smaller throat diameter which then allowed the jet to reach near self-similar conditions. This nearly self-similar flow was marked by ever increasing turbulent fluctuations in the jet core and shear layer. Therefore it was possible to conclude from these experiments that the plasma field shows the most influence on flows which have higher concentrations of turbulence.[145, 224, 273]

Table 4.15: Effect of Increasing Mach Number on Converging-Diverging Nozzles

	P_o	P_e	U_e	M_e	x/D	ΔU_o	$\Delta[(\sigma_u^2 + \sigma_v^2)/U_o^2]$ <i>Centerline</i>
	[torr]	[torr]	[m/s]	[ND]	[ND]	[%]	[%]
A	12.7	9.15	229	0.7	3.2	0.0	-6.7
B	20.5	9.15	350	1.1	3.2	0.0	-13.5
C	71.0	8.00	523	2.0	2.7	0.0	-9.3

Table 4.15 summarizes the results of the three perfectly-expanded nozzles at chamber pressures of 8-9 torr. The table begins on the left with the familiar case identifier for cross-reference. Next, the jet conditions namely: plenum and chamber pressure, measured exit velocity and Mach number derived from U_e and the plenum temperature are listed. To make a similar comparison, these results are all made roughly 3 diameters from the jet face as indicated by the station location. Then the change in centerline velocity is listed, followed by the percent change in scaled turbulent kinetic energy along the centerline, $(\sigma_u^2 + \sigma_v^2)/U_o^2 = 2k/U_o^2$.

At this location, the centerline velocity is 96% of the measured exit velocity, indicating that core breakdown has not yet occurred which is revealed in this comparison as no change between the plasma-on and plasma-off centerline velocities. However, in all three cases, the centerline turbulent kinetic energy decreases when the plasma is initiated. At this axial location in the jet flow, centerline turbulent kinetic energy decreases if the core is allowed to penetrate further downstream. Given the uncertainty of this measurement is 6.7%, there is no trend versus Mach number - only a consistent decrease in centerline TKE for all cases. Therefore it is concluded that the plasma effect on perfectly expanded jets is not dependent upon Mach number in the developing jet, but that overall the plasma allows the jet core to penetrate further downstream. It is believed that this penetration is an effect a bias of convective velocity to higher values towards the jet core velocity - due to heating of the shear layer by the plasma field.[145, 224, 273]

The next three flow conditions examined the influence plasma for increasing equivalent Mach number on mean and turbulent fluctuations for developing pipe flow jets.

- The jet created by the constant-diameter nozzle was effective in increasing turbulence intensities in the core of the jet which translated into higher turbulent kinetic energy further downstream.
- The equivalent Mach 0.9 jet was influenced by the plasma considerably, especially given the relative weakness of the plasma field. The plasma-on case had a centerline velocity which was 8% higher than the plasma-off case at 11.4 diameters from the anode face. The turbulent kinetic energy was 28 to 36% lower for the plasma-on case when compared to the plasma-off case at this location.
- The equivalent Mach 1.4 jet showed a 9% increase in centerline axial velocity and a 5% decrease in centerline TKE. In the shear layer however, the turbulent kinetic energy increased by 3%.
- For the high-speed, equivalent Mach 1.9 case, the axial velocity profiles looked the same, but turbulent kinetic energy increased 11% on the centerline and 14% in the shear layer when the plasma was initiated. This case shows shock and expansion phenomena in the jet core region from pressure mismatches in the tube nozzle.

Figure 4.51 shows the change in scaled turbulent kinetic energy $(\sigma_u^2 + \sigma_v^2)/U_o^2 = 2k/U_o^2$ as a function of downstream location for all three equivalent Mach numbers tested. The centerline change in scaled TKE is based on an average of the four points closest to the centerline and then calculated as the difference between the plasma-off case and the plasma-on case at that location. The shear layer location was determined as the location of the peak in axial turbulence intensity, σ_u . From this peak location, the four nearest points were averaged.

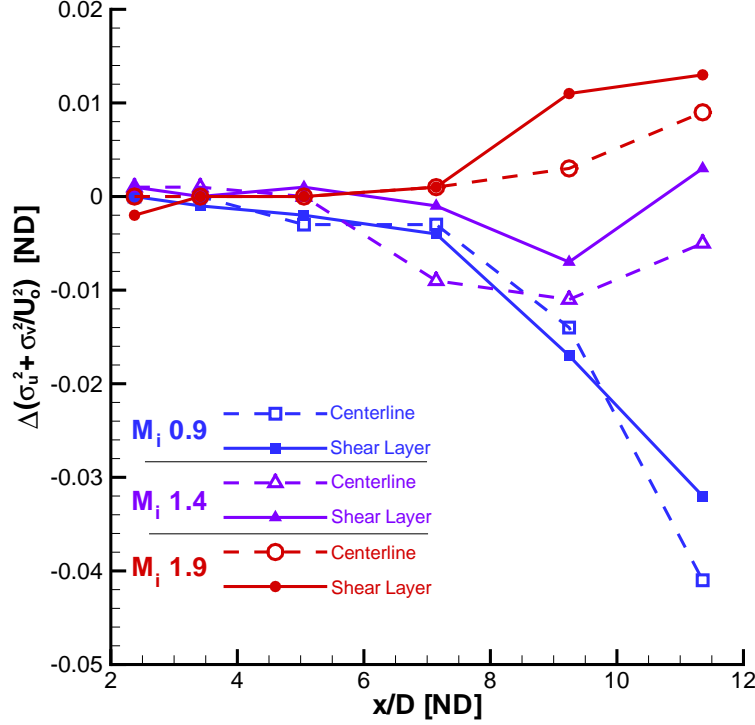


Figure 4.51: Effect of Increasing Equivalent Mach Number on Constant-Diameter Tube Nozzles

There is a trend present in scaled turbulent kinetic energy with increasing effective Mach number. Initially, the $M_i = 0.9$ jet sees a reduction in TKE as the flow progresses downstream. At an effective Mach number of 1.4, the trend stagnates and then begins to reverse. At $M_i = 1.9$ the effect is reversed, with plasma beginning to increase TKE as the flow travels downstream. Reynolds number effects were investigated, by computing a *local* Reynolds number, based on the jet diameter, local centerline velocity U_o , an estimate for density based on chamber pressure and estimated jet temperature T_1 , and viscosity based on measured shear layer temperatures from spectroscopy (presented later in this chapter). The Reynolds number calculations showed a general decrease of 8 to 16% with plasma-on and did not show any trends with Figure 4.51. Therefore, it is concluded that the trend in turbulence is for an initial decrease, switching to an increase in TKE as the effective Mach number progresses from subsonic to supersonic values. The developing pipe flow which generated this flow is a complicated jet structure with many rich features for the plasma field to interact with. The supersonic flow begins smoothly, but then develops a pattern of reflected shocks and expansions from observation of the velocity fluctuations in the centerline velocity near the jet exit. It is possible that the plasma field is interacting with the shock structures in the jet. Weakened shocks would allow for increased jet turbulence through higher core velocities passing downstream. Evidence of the

higher core velocities was absent from these measurements, however the increase in TKE for the $M_i = 1.9$ jet could be a precursor to higher plasma-on core velocities further downstream. A computational study on the developing pipe flow jet and influences from shear layer heating by a simulated plasma field are recommended for further research.[133, 193, 194, 251]

Table 4.16: Comparison Between Perfectly-Expanded and Overexpanded Jets

	P_o	P_e	U_e	M_e	x/D	ΔU_o	$\Delta[(\sigma_u^2 + \sigma_v^2)/U_o^2]$ <i>Centerline</i>
	[torr]	[torr]	[m/s]	[ND]	[ND]	[%]	[%]
C	71.0	8.00	523	2.0	6.2	1.0	-13.9
D	62.0	8.00	510	1.9	6.2	2.4	-31.2

The next comparison shown in Table 4.16 is of an off-nominal case, where the baseline flow is a converging-diverging jet at Mach 2.0 (case C). The influence of plasma on a weakly overexpanded jet is investigated here. The baseline Mach 2.0 nozzle is driven at a pressure ratio equivalent to a Mach number of 1.9 (case D). When compared to the baseline nominal case, the influence of the plasma field is more pronounced on the overexpanded jet.

- In case D, the axial velocity along the centerline increases 11 m/s for a 2.4% change in the plasma-on case over the plasma-off condition. For the nominal jet (case C), the increase was 5 m/s or a 1% change.
- TKE decreases 31% along the centerline and 5% in the shear layer for the overexpanded plasma-on condition compared to plasma-off. For the nominal Mach 2.0 jet, the corresponding centerline decrease was 14% with no detectable change in the shear layer.

From these changes in plasma for the slightly overexpanded condition, it is concluded that the plasma field may have an impact on weak shocks. It has been hypothesized that a plasma field may interact with the shock waves to weaken them thermally resulting in a higher downstream fluid velocity in the presence of a plasma. Conversely, the convective Mach number is lower in this case, when compared to the Mach 2.0 nominal case and that may be another driver for the change noticed here. In either case, the effect of the plasma-on was more pronounced in the overexpanded jet than in the perfectly expanded jet.[133, 193, 194, 251]

The final comparison, shown in Table 4.17, was to examine the effect of anode design on the plasma field and the resulting impact on mean velocity and velocity fluctuations. On the left, the table begins with the case identifier for cross-reference. Next, the jet conditions namely: plenum and chamber pressure, measured exit velocity were listed. Then the Mach number derived from U_e and the plenum temperature is listed

Table 4.17: Comparison Between Flat Anode and Anode with Serrated Conical Tip Feature

	P_o	P_e	U_e	Anode Design	M_e	x/D	$\Delta[(\sigma_u^2 + \sigma_v^2)/U_o^2]$	
	[torr]	[torr]	[m/s]		[ND]	[ND]	<i>Centerline</i>	<i>Shear Layer</i>
							[%]	[%]
B	20.5	9.15	350	flat	1.1	4.5	1.9	2.7
B'	20.5	9.15	347	ser-cone	1.1	4.3	2.8	7.7

next to the measurement location x/D . Finally, the percent change in scaled turbulent kinetic energy , $(\sigma_u^2 + \sigma_v^2)/U_o^2 = 2k/U_o^2$ were presented for locations along the centerline and in the shear layer, respectively.

- The shape modified anode was a significant feature which had the potential to change the jet structure without the influence of plasma. However, the modified anode tip was near the jet exit with supersonic speeds and the orifice for the jet to exit through was larger than the jet exit to minimize the potential for influence.
- The mean flow and turbulent kinetic energy did not change when comparing the plasma-off flow with the flat anode to the plasma-off flow with the modified anode. Therefore it is concluded that the presence of the modified anode had no significant impact on the measurements being taken.
- In comparing plasma-on cases between the anode designs, the mean centerline velocity was unchanged.
- Turbulent kinetic energy increased on the centerline by 2% for the flat anode, and by 3% for the modified anode. In the shear layer, the increases were 3% and 8% respectively.

From these measurements it was concluded that the modified anode design improved the influence of the plasma field on turbulent structure, but did not significantly impact on the mean flow in this case. Note that mean flow features could be influenced more significantly by the plasma field if the gap distance were increased, or for smaller diameter jets. The modified anode was not recommended for use at higher chamber pressures as arcs form easily in the non-linear electric field created near the serrated cone. The modified anode design was used exclusively for the 5 torr plasmas tested, while the 8-9 torr plasmas used the flat anode (with the exception of case B repeated with both anodes for this comparison). The modified anode could have been used on cases C and D, however case A had a larger exit diameter than the modified anode. Therefore, all the tests done at the higher chamber pressure used flat anodes for consistency.[145]

4.3 Large Scale Structure Tracking by Means of Laser Energy Deposition

The tracking of large scale structures in the shear layer is an excellent technique for measuring the convective velocity of the shear layer. This section is important because the influence of plasma-on the speed of sound in the shear layer could provide significant insight into the mechanism of influence on mean flow and turbulent fluctuations presented in the previous section. This section will provide some illustrative plots to better describe how the process of tracking structures in the shear layer was accomplished. Next the large scale structure tracking effort is reduced into convective velocity measurement, which is reported for each case tested.

To track structures in the shear layer, the use of large scale structures by laser energy deposition is employed. Pulsed laser energy is focused to a point at the exit of the nozzle, in this case on the lip of the anode. This focused energy creates a large disturbance in the shear layer which quickly forms a vortex roller structure that moves downstream at the convective velocity U_c . This large scale structure is visualized by phase-locked particle image velocimetry in a sequence of increasing time delays, allowing the structure to travel downstream through the measurement window carried by the convective velocity. The structure is tracked by means of a centroid tracker of a contour of tangential velocity, scaled by the convective velocity U_{ci} . In actuality, the tangential velocity contour which is tracked corresponds to the wave formed in the core attached to the large scale structure.[11]

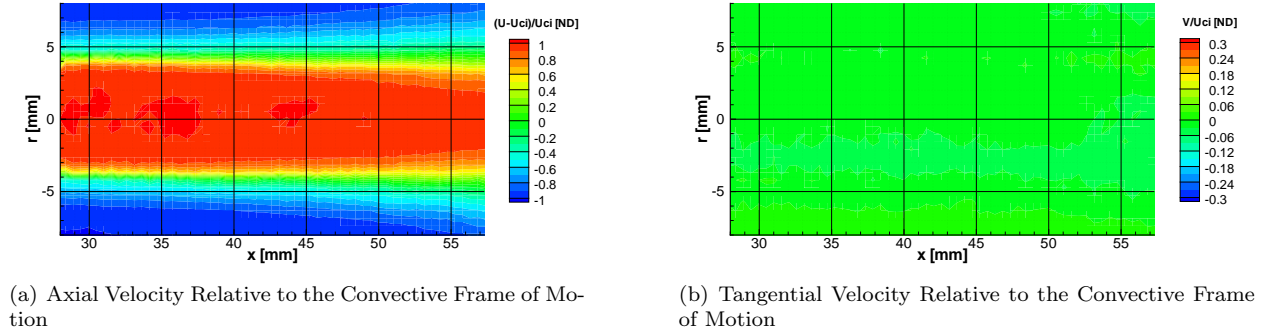


Figure 4.52: Baseline Flow Undisturbed by Laser Energy Deposition

Figure 4.52 shows a baseline jet (case E') in a shifted reference frame. The reference frame is shifted by the convective velocity, $U_c = (a_1 U_2 + a_2 U_1)/(a_1 + a_2)$ where U_1 is the high speed flow velocity, U_2 is the low speed flow velocity, a_1 and a_2 are the speed of sound in the high and low speed flow, respectively. In this case, U_1 is the core exit velocity and U_2 is zero. The speeds of sound are calculated with temperatures

estimated from the plenum temperature. Note in this reference frame, the axial velocity is negative for the quiescent fluid at the top and bottom of panel (a). The tangential velocity scaled by U_{ci} in panel (b) was found by Adelgren [11] to be the best variable to track the large scale structure and was confirmed in this investigation as well. Note that for undisturbed axisymmetric jets, the tangential velocity is under 10% of the incompressible convective velocity and therefore shows up as green in the contours in panel (b) of Figure 4.52.

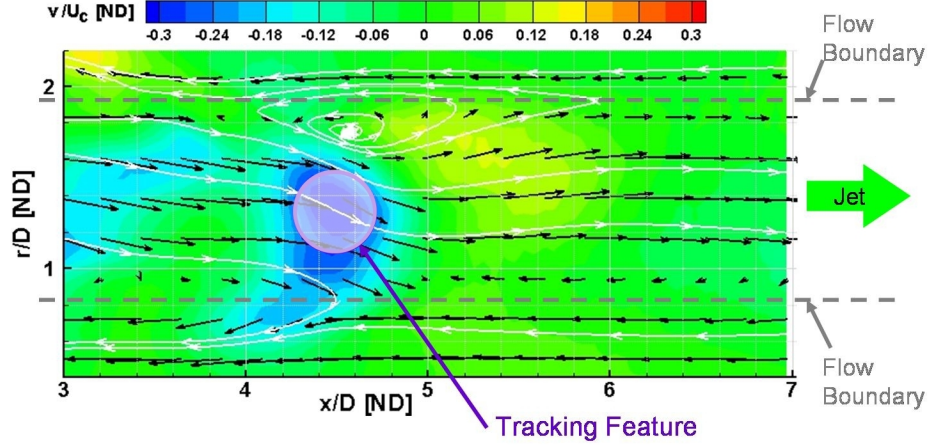


Figure 4.53: Schematic of Large Scale Structure Pointing Out the Tracking Feature

Figure 4.53 shows contours of mean velocity in the tangential direction scaled by the convective velocity. Overlayed on the contour are vectors in the convective frame with streamlines integrated from the velocity field in that same frame. The jet boundaries are roughly indicated by the grey dashed lines, where the jet is proceeding through the frame from left to right. In the convective reference frame the quiescent air appears to be traveling to the left at the convective speed. The location highlighted as the tracking feature marks the outer region of the vortex structure with rotational motion in that region directed towards the jet core. This is the feature which will be tracked to measure convective velocity. Next, laser energy deposition will be used to see the formation of the large scale structure.

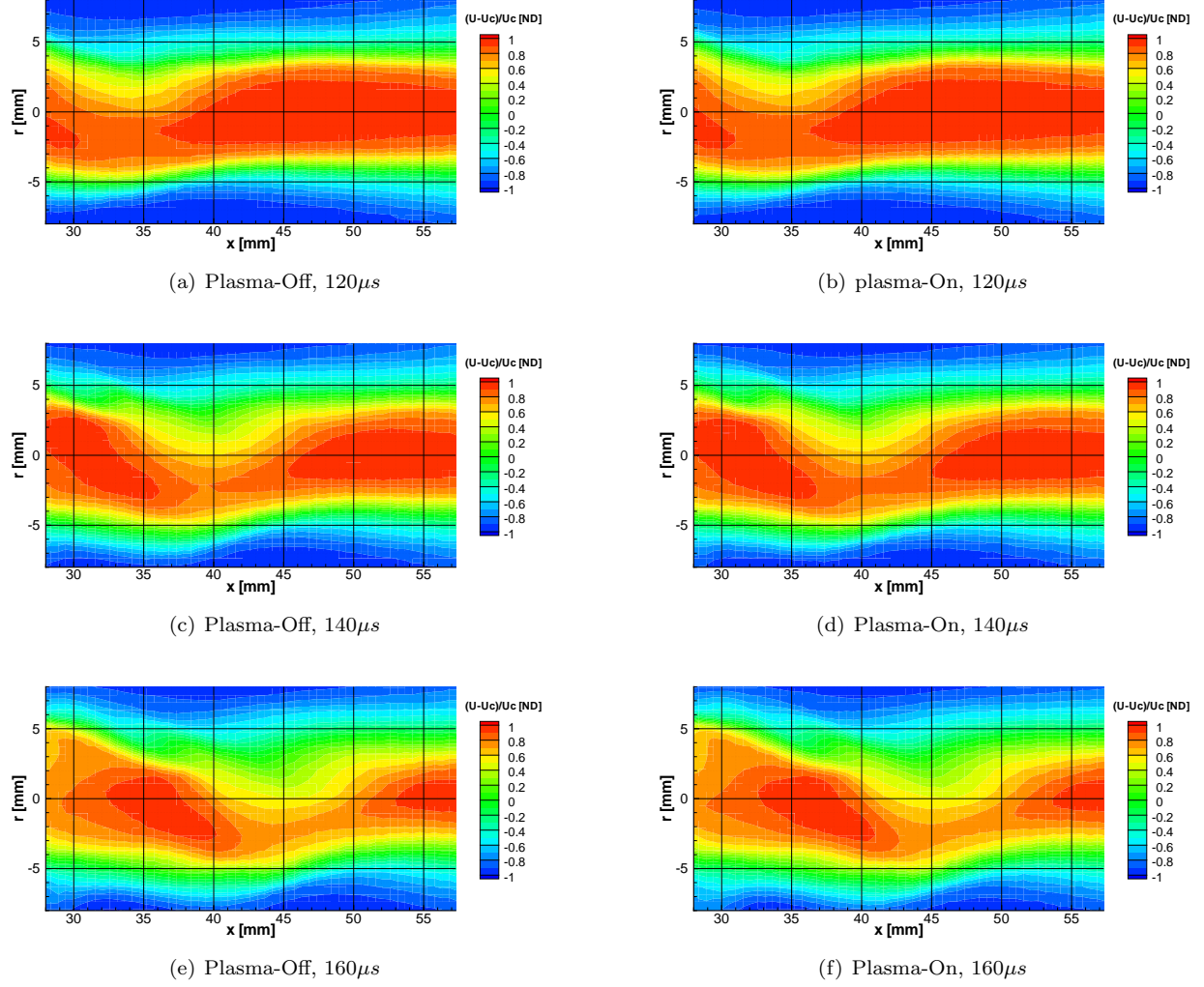


Figure 4.54: Influence of Plasma on Large Scale Structure Motion Using Time Phased Framing of Axial Velocity Relative to the Convective Frame of Motion

To give an idea of the level of disturbance injected into the flow from laser energy deposition (LED), Figure 4.54 shows contours of axial velocity for the jet driven at the conditions of case H - now disturbed by laser energy deposition. On the left are contours for the plasma-off cases at three different phase-locked time steps. The plasma is on for the cases on the right and show the results for the same time steps. Note the progression of the disturbance downstream for increasing delay times. The LED system was measured to deposit 20 mJ of energy to the lip of the anode which created this structure. The amount of energy deposited was optimized based on the findings of Adelgren [11]. Different levels of energy deposition were investigated for this experiment as well and confirmed the 20 mJ level as best. Higher energy deposition levels resulted in a structure which dominated the flow field enough to alter the convective velocity being measured, while lower energy levels produced structures which were hard to track. The energy levels were

set by use of neutral density filters placed in the beam path upstream of the focal point and measured throughout testing by periodic spot checks with a laser power meter and realtime by boxcar integration of the photodiode response of each pulse.

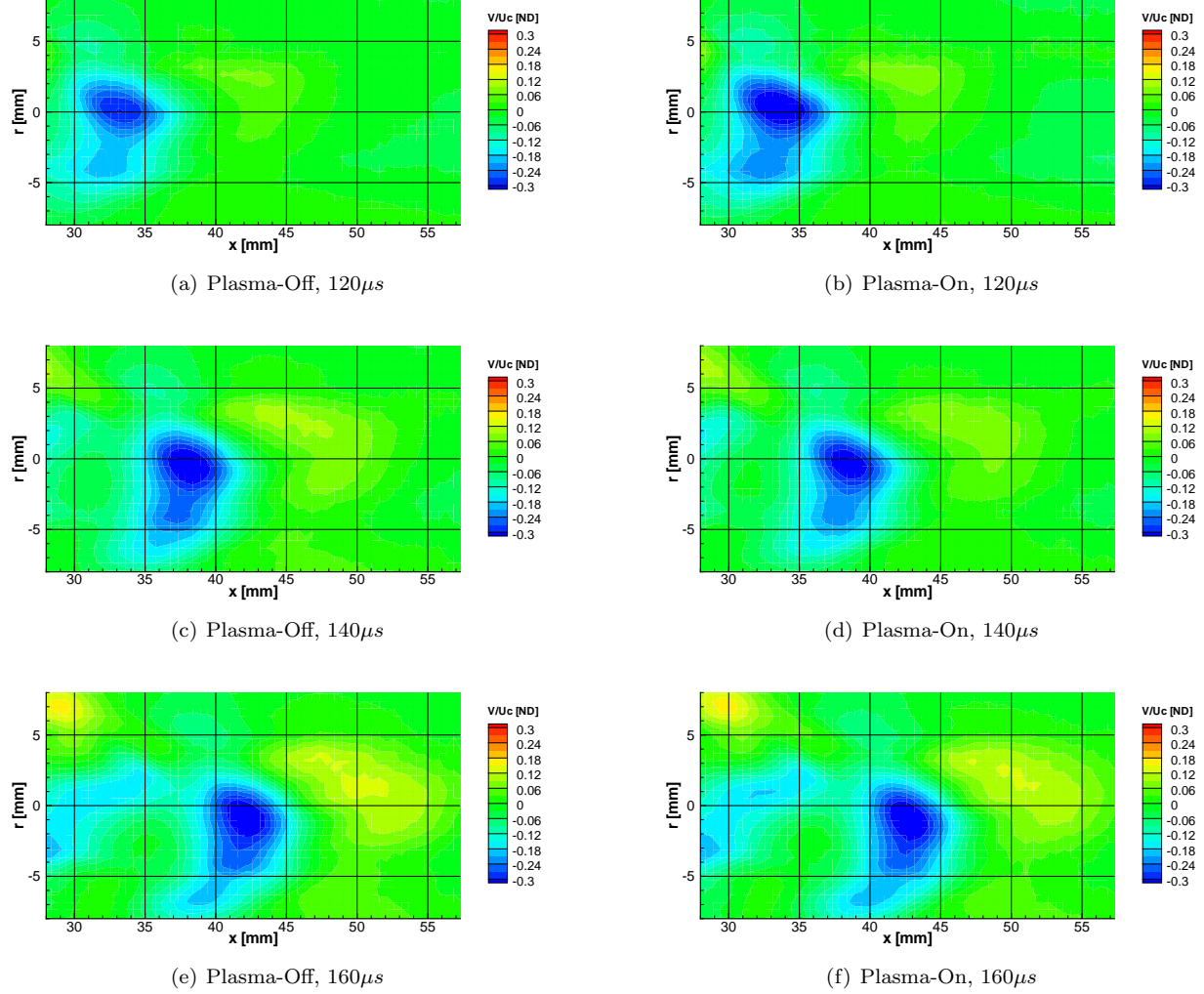


Figure 4.55: Influence of Plasma on Large Scale Structure Motion Using Time Phased Framing of Tangential Velocity Relative to the Convective Frame of Motion

Figure 4.55 shows contours of tangential velocity scaled by U_{ci} to highlight the ease of tracking the large scale structure. Note here that the contours of Figure 4.55 are the same as Figure 4.52 (b). The disturbance created by laser energy deposition produces a large scale structure with velocities that are more than 30% of the convective velocity. Plasma-off conditions again are on the left and plasma-on are on the right, in a progression of phase-locked time steps. The circular region of negative tangential velocity provides a consistently circular region, easily tracked by integration of a specific contour to determine the centroid position.

Based on a worst case variation in contour level choice, the uncertainty of centroid position was estimated at 0.2 mm for this measurements technique. To determine the uncertainty in convective velocity measurement, two independent position measurements are required. Therefore the contribution of centroid position uncertainty to convective velocity measurements is 0.28 mm. The uncertainty in timing measurement is 8 ns. Given the relatively small contribution of timing error in the calculation of convective velocity, it is neglected in the uncertainty analysis.[92]

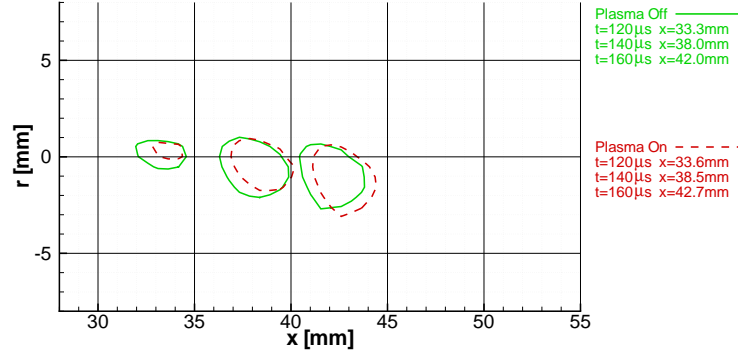


Figure 4.56: Comparison of Large Scale Structure Motion by Centroid Tracking

Figure 4.56 shows the progression of contours in tangential velocity which were used in the centroid tracking analysis. These contours were a compilation of the images found in Figure 4.55. The green contours represent the plasma-off cases for all three time delays to show the progression of the structure. The dashed red lines are the plasma-on contours at the corresponding time delays. From the progression of contours for each time step, there is visible evidence of differences in convective velocity when the LED flow is influenced by the plasma field.

In each case more than 800 PIV image pairs were examined at every time step for both the plasma-off and plasma-on conditions. From the mean velocity fields in a reference frame traveling downstream with the incompressible convective velocity, contours of tangential velocity were created for each jet, time delay and plasma state. These contours were examined to determine the best contour to use for tracking, based on the shape of the contour and the quality with which it represented the location of the large scale structure. Care was taken in order to keep the selected contour to remain at the same level ($\pm 5\%$) relative to other time delays and plasma states for that jet. The chosen contours were then subjected to centroidal analysis. From the time of flight of the centroid, the convective velocity was calculated. Table 4.18 summarizes the results of the centroid tracking analysis.[11]

Table 4.18 is broken into sections based on nozzle type and anode design in order to highlight trends. The

Table 4.18: Summary of Large Scale Structure Tracking Analysis

Case	M_i	U_c	U_c Measured		ΔU_c		Δt	ΔU_c
	Predicted		Plasma Off	Plasma On			Uncertainty	
	[ND]	[m/s]	[m/s]	[m/s]	[m/s]	[%]	[μs]	[%]
8-9 Torr Converging-Diverging Nozzle Series with Flat Anode								
A	0.8	91.4	100.4	108.0	7.6	7.6	100	2.8
B	1.1	156.8	177.6	185.4	7.9	4.4	90	1.8
C	2.0	285.8	324.3	329.0	4.8	1.5	40	2.2
8-9 Torr Converging-Diverging Nozzle Using Anode with Serrated Conical Feature								
B'	1.1	156.8	187.7	198.7	11.0	5.9	30	5.0
5 Torr Constant-Diameter Nozzle Series Using Anode with Serrated Conical Feature								
F'	0.9	77.8	96.3	96.7	0.4	0.4	150	2.0
G'	1.4	175.5	202.3	205.5	3.3	1.6	40	3.5
H'	1.9	237.9	268.6	275.0	6.4	2.4	50	2.1
5 Torr Converging-Diverging Nozzle Using Anode with Serrated Conical Feature								
E'	1.4	204.2	218.3	225.8	7.5	3.4	40	3.2

cross-reference case identifiers lead off the table, with prime marks (') indicating the modified anode. The equivalent Mach number M_i is based on measured pressure ratio, while the predicted convective velocity is based on an assumed isentropic flow. Next the convective velocity measurements are presented for plasma-off and plasma-on. Note that the convective velocity measured by tracking contours of radial velocity picks up the wave attached to the large scale structure in the jet core and as such is biased toward the high side velocity. The change in convective velocity and percent change are listed next. Next, the difference in delay time used to calculate time of flight is presented as it is the most variable factor in calculating the measurement uncertainty. The uncertainty in measuring a change in convective velocity finishes the table.[\[11, 92\]](#)

Overall, all convective velocity measurements in Table 4.18 show an increase when the plasma is turned on. The first sequence is of the perfectly expanded jets showing the change with increasing Mach number. The clear trend in this sequence is decreasing effectiveness for increasing Mach number. The plasma could be less effective for increasing Mach number do to an increased convection of the heated plasma gases out of the plasma field by the higher jet speeds and mass flows represented with increasing Mach number. Next the effect of anode design and resulting change in plasma field is investigated by convective velocity measurements. From this measurement, it appears that the modified anode design produces a more effective plasma field which is able to increase the convective velocity 1.5% over the flat anode plasma.[\[193, 194, 251\]](#)

Next, using the modified anode, the series of jets created by developing pipe flow from a constant-diameter nozzle are studied. For increasing pressure ratio, the trend is for the plasma field to be more effective on convective velocity. In this case, the increased mixing caused by increased shear layer turbulence of a constant-diameter nozzle may provide more thermal interaction in the shear layer. This thermal interaction

could raise the speed of sound and the convective velocity. This trend is opposite what was found for perfectly expanded nozzles and appears to be a function of a difference in nozzle design. Case E' in the last row is a direct comparison of nozzle design with the same pressure ratio as Case G'. The converging-diverging nozzle of E' shows a 3.4% change with the plasma-on, a 1% increase when compared to the constant-diameter nozzle at the same pressure ratio. From this result, it appears that the convective velocity of perfectly expanded nozzles are more influenced by the plasma than developing pipe flow nozzles. Constant-diameter nozzles may be less susceptible to changes in convective velocity due to the increase in turbulence associated with the developing pipe flow.[133, 194, 193, 251, 399]

Some observations surface in review of the information in Table 4.18. Note that in each case, the plasma-on convective velocity is higher than the baseline plasma-off measurement. From the worst-case uncertainty evaluation, some of the cases fall below the threshold of measurement uncertainty. In general, 3 to 4 different time steps were measured. Each time step includes between 828 and 1104 image pairs processed through particle image velocimetry. To achieve the lowest uncertainty measurement, the longest difference in time step, Δt , was chosen. In some cases, time steps were discarded when the contour was partially out of the field of view. Therefore, in cases C, F' and G', the uncertainty is unfortunately higher than desired in order to conclusively measure change.

Summary of Important Findings from Large Scale Structure Tracking

It is postulated here that the reason for the increase in convective velocity with the plasma-on can be attributed entirely to the increase in gas temperature in the shear layer as a result heating by the plasma field. The compressible convective velocity, U_c can be related to the temperature of the jet and of the chamber through $U_c = (a_2 U_1 + a_1 U_2)/(a_1 + a_2)$ - where U_1 is the core velocity of the jet and U_2 is zero in these cases. Therefore an increase in the the chamber temperature surrounding the jet, T_2 from 300 K to 400 K would result in an increase in convective velocity of 7% for all the cases in Table 4.18. In an effort to quantify the T_2 required to produce the measured change in convective velocity, the equation above is manipulated into a more convenient form in Equation 4.14.

$$T_{2-\text{plasma}} = \frac{(U_{c-\text{plasma}}/U_c)^2 T_1 T_2}{(\sqrt{T_1} + \sqrt{T_2}(1 - U_{c-\text{plasma}}/U_c))^2} \quad (4.14)$$

The result ($T_{2-\text{plasma}}$) is the shear layer temperature required to bring about the measured change in convective velocities $U_{c-\text{plasma}}/U_c$. The plasma-off shear layer temperature is assumed to be near the measured plenum temperature, which averaged at 294 K. Based on the measured core and convective velocities, shear layer temperatures between 315 K and 378 K would produce the measured change in convective velocity.

4.4 Plasma Imagery of Visible Light Emission

As an assessment of the plasma field, visible light from plasma emission was collected for each case studied. Visible light emission from the plasma field is an easily observable phenomena which indicates the presence of a strong plasma field. Figure 4.57 is a drawing of a collisionally excited molecule releasing a photon and dropping from an excited electronic state E_2 , to a lower state E_1 . The plasma works on the both the radicals and molecules, pumping them into electronic states much higher than ground. One of the readily apparent indicators of the presence of molecules in elevated electronic states is photon emission. And therefore in locations where there are high concentrations of molecules and radicals emitting photons, it can be deduced that the field performing the work on those molecules is high. By capturing light on a charge-coupled device with constant exposure settings, the relative grayscale intensity of the light can be compared to provide a figure of merit on the plasma strength for each case.[229, 308]

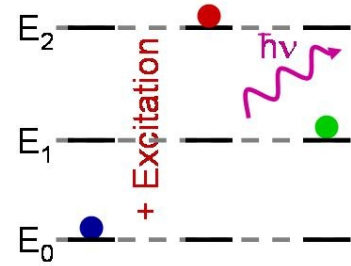


Figure 4.57: Schematic of Photon Emission from a Collisionally Excited Molecule

To begin, the series of jets created by converging-diverging nozzles at 8-9 Torr were investigated which comprised of cases A, B and C. Then the effect of anode design was compared between case B and B'. Then the series of jets created by developing flow from constant-diameter axisymmetric nozzles at 5 Torr (cases F, G and H) are described by their light emission and compared to plasmas fields at 8 Torr (between case C and case E). Finally, an examination of a barrel shock structure is investigated (case U)- showing the location of the normal shock disk.

4.4.1 Effect of Compressibility on Plasma Fields for Perfectly Expanded Jets

Table 4.19: Plasma and Jet Configuration for the Series of Converging-Diverging Nozzles with Flat Anodes at a Chamber Pressure of 8-9 Torr

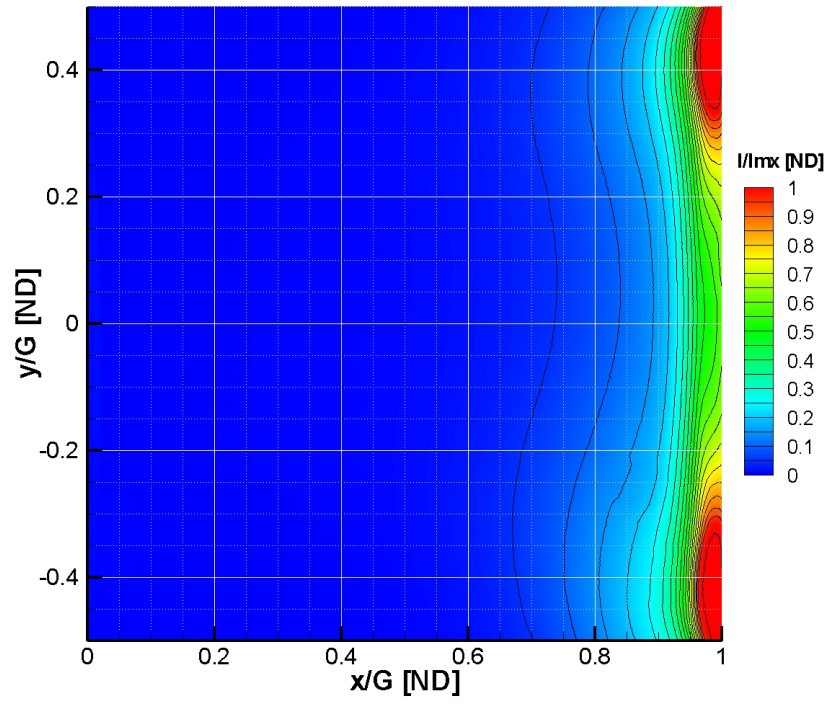
	M_i [ND]	P_o [torr]	P_e [torr]	U_e [m/s]	D_e [mm]	D_a [mm]	G [mm]	P_f [W]	P_r [W]	V_{bias} [V]	C_T [%]	C_L [%]
A	0.7	12.5	9.15	229	20.8	21.4	75.8	95	0	6-16	19.1	50.3
B	1.1	20.5	9.15	348	11.3	11.5	79.1	110	0	11-30	18.8	48.0
C	2.1	71.0	8.00	523	15.7	17.0	75.8	94	0	5-21	19.1	52.2

Table 4.19 lists the settings used to create the plasma fields which were imaged on the next three pages. Tables with these parameters appear throughout this section. Great detail will be provided on the meaning of each of the parameters here, and the remaining tables will serve as a reference with discussion focused on

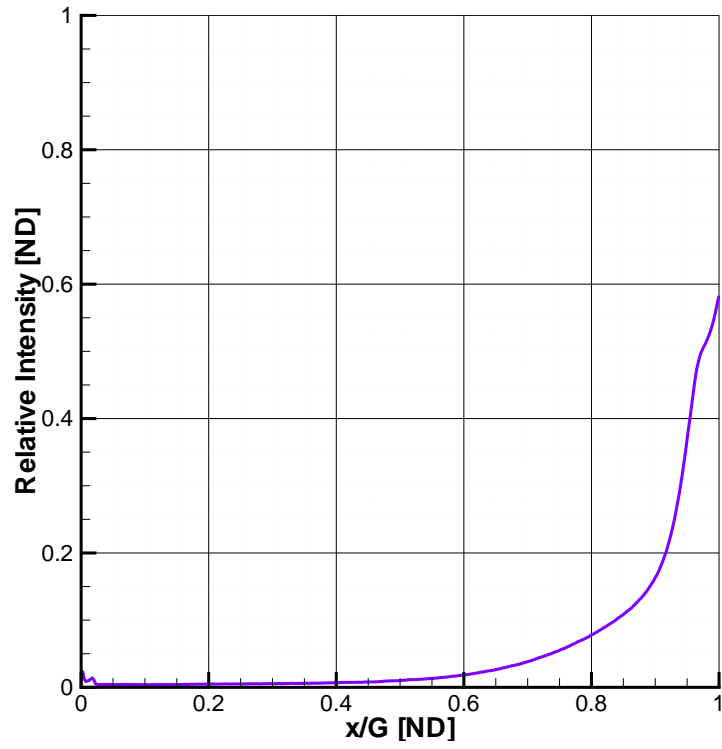
the most salient features. The case identifier again leads off the table for cross-reference purposes, followed by the jet conditions. The equivalent Mach number M_i is calculated based on the ratio of pressures between the chamber (P_e) and plenum (P_o) and assumes isentropic flow through the nozzle. Next, the physical features of the jet and electrodes are presented. The exit diameter of the jet D_e is found in column 6 from the left and is useful in converting the scaling downstream and tangential positions (x and r , respectively) between the electrode gap space G and jet exit diameter. All of the charts which follow scale the coordinates by gap spacing for the convenience of making comparisons between plasmas with different gap spacings. Gap spacing is a strong factor in plasma strength and therefore G becomes an important length scale regarding the plasma field, while the most important length scale for the jet is the exit diameter. The parameter D_a is the diameter of the hole bored through the anode. The jet exhausts into the test chamber and plasma through the hole in the anode. The anode diameter is larger than the jet exit diameter to prevent weak shocks from occurring in the jet from a seam or lip at the junction between the nozzle and anode.[14, 145]

The far right section of the table contains the plasma parameters set on the Dressler Cesar RF plasma generator. The forward power P_f was the power level controlled by the plasma generator. It was set about 5% below the level at which the plasma field showed signs of instability (the indicators of transition into an arc plasma). Next, tuning was performed to drop the reflected power P_r to zero. Reflected power was a sign of impedance mismatch between the plasma generator and the rest of the circuit. Following the initial optimization procedure, only minor variations in the tuning (C_T) and load (C_L) capacitors were needed (under 5%) in order to maintain impedance balance and drive the reflected power to zero. The bias voltage V_{bias} , was an indicator of good plasma quality. For these experiments, the best bias voltages hovered around 20 V. The bias voltage was a DC potential applied to the RF power signal and was automatically controlled by the plasma generator and compensated for the electric field created by the plasma volume. A higher bias voltage corresponded to a stronger electric field (for a given chamber pressure and gap space) which therefore implied a stronger plasma field or larger plasma volume as the electric field in the gap was caused by the potential created from increasing distances between the radicals and free electrons and the number of ions in the plasma volume.[33, 145, 308]

In Table 4.19 note that the gap distance, G , was held relatively constant and that the forward power, W_f increased with increasing Mach number and decreased for decreasing chamber pressure. In each case the power was increased to the point of plasma instability, and then reduced to roughly 95% of the instability threshold. The tune (C_T) and load (C_L) capacitors were manually adjusted to maximize bias voltage. The bias voltage fluctuated throughout each test. The plasma generator controlled V_{bias} to maintain plasma stability. The limits of fluctuation were recorded in the table.[33, 145, 308]

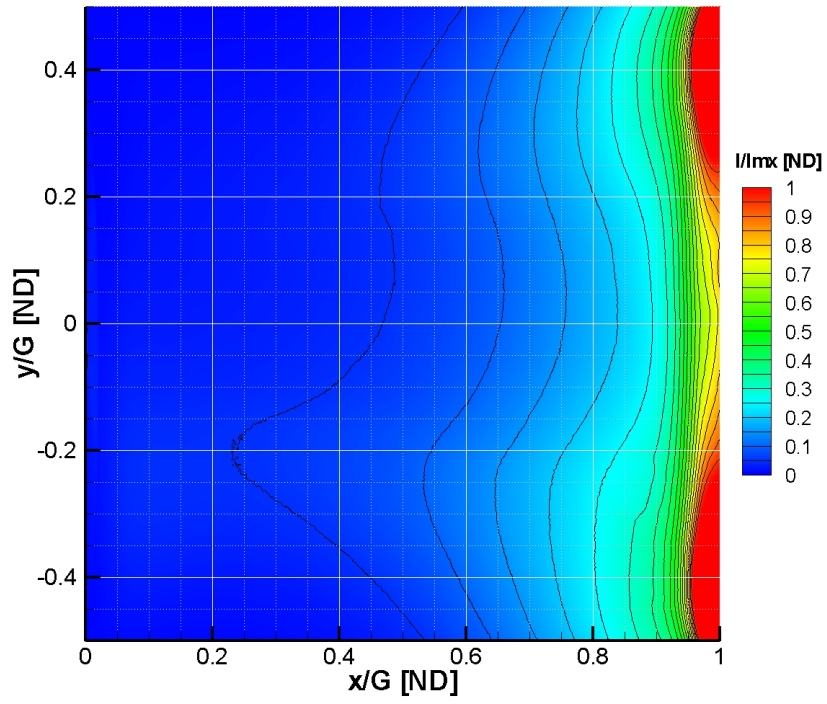


(a) Contours of Relative Intensity

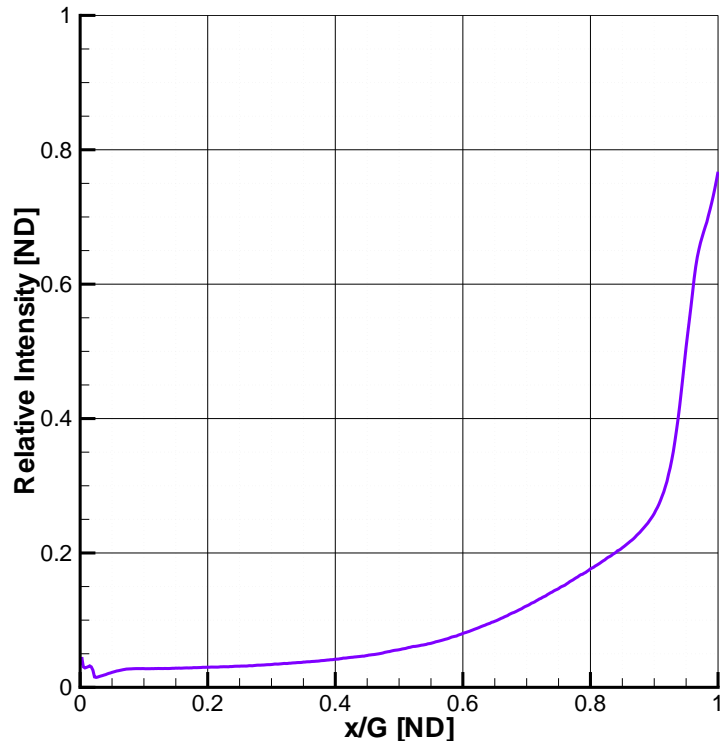


(b) Relative Intensity along the Centerline

Figure 4.58: Relative Intensity of Visible Emission from the Plasma Field for a Flat Anode Around a Mach 0.6 Axisymmetric Jet at 9 Torr

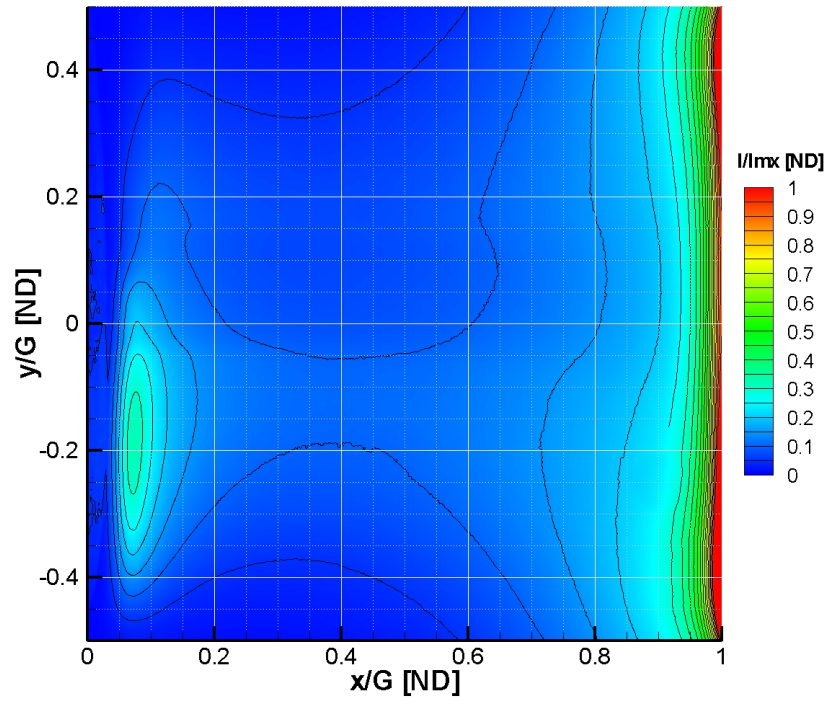


(a) Contours of Relative Intensity

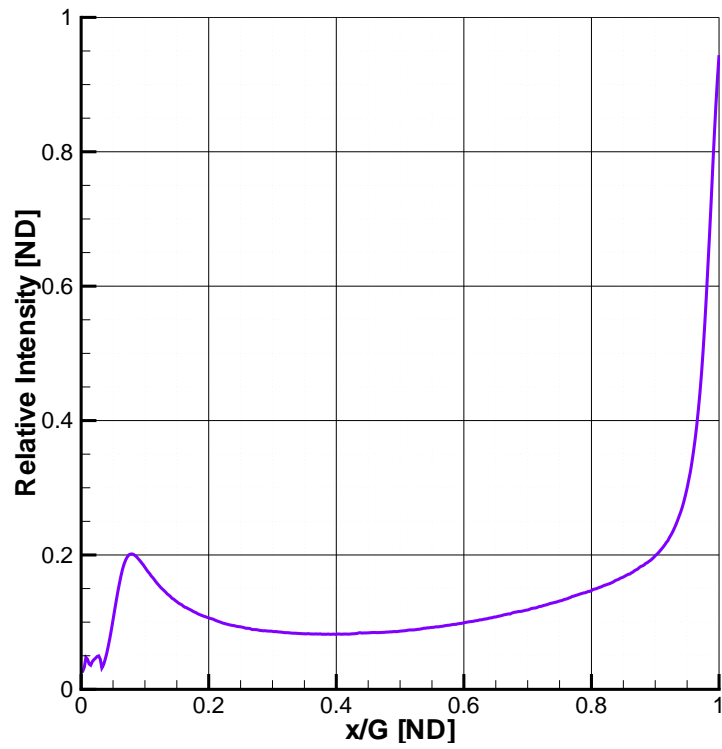


(b) Relative Intensity along the Centerline

Figure 4.59: Relative Intensity of Visible Emission from the Plasma Field for a Flat Anode Around a Mach 1.1 Axisymmetric Jet at 9 Torr



(a) Contours of Relative Intensity



(b) Relative Intensity along the Centerline

Figure 4.60: Relative Intensity of Visible Emission from the Plasma Field for a Flat Anode around a Mach 2.0 Axisymmetric Jet at 8 Torr

The goal in plasma tuning was to produce a uniform and symmetric (about the centerline of the jet) visible emission between the cathode and the anode. The plasma could not transition into an unstable thermal mode such as an arc discharge. If the plasma emission did not reach the entire distance from the cathode to the anode, the power was incrementally adjusted to achieve the maximum plasma volume in the electrode gap. Typical behavior of the plasma was to begin as a cathode layer and grow with a positive column towards the anode with increasing forward power. Forward power was increased until hints of instability appeared, the first signs of instability were typically asymmetries on the cathode which grew into visible waves which traveled toward the anode. At this point, the power was reduced slightly to eliminate the plasma waves. If the waves were left uncountered, they would transition to an arc later during testing. When creating a plasma for increasing Mach numbers, the forward power was not able to be fixed at one value. The highest power settings used at Mach 2.0 would have transitioned immediately to an arc at the lower jet speeds, while the low power setting used in the subsonic case would not have ignited a plasma for the faster jets.[33, 145, 229, 251, 308]

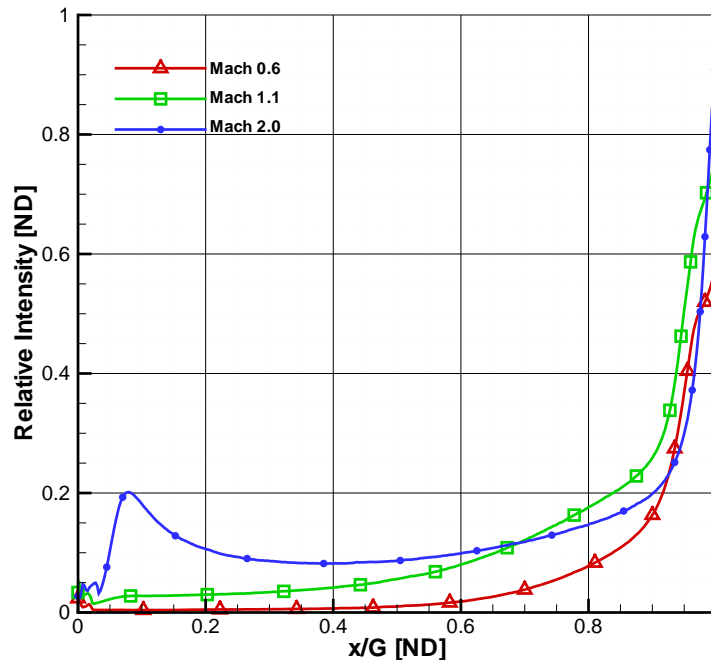


Figure 4.61: Comparison Between Increasing Pressure Ratios of Relative Intensity of Visible Emission Along the Centerline of the Plasma Field for a Flat Anode around Axisymmetric Jets at Mach 0.6, 1.1 and 2.0 at 8-9 Torr

Figures 4.58 through 4.60 indicate the relative intensity of visible light emitted by the plasma field, with flow going across the contour from left to right. There was a clear increase in visible light emitted with increasing Mach number. The increase in photon emission was an indicator of increased plasma strength.

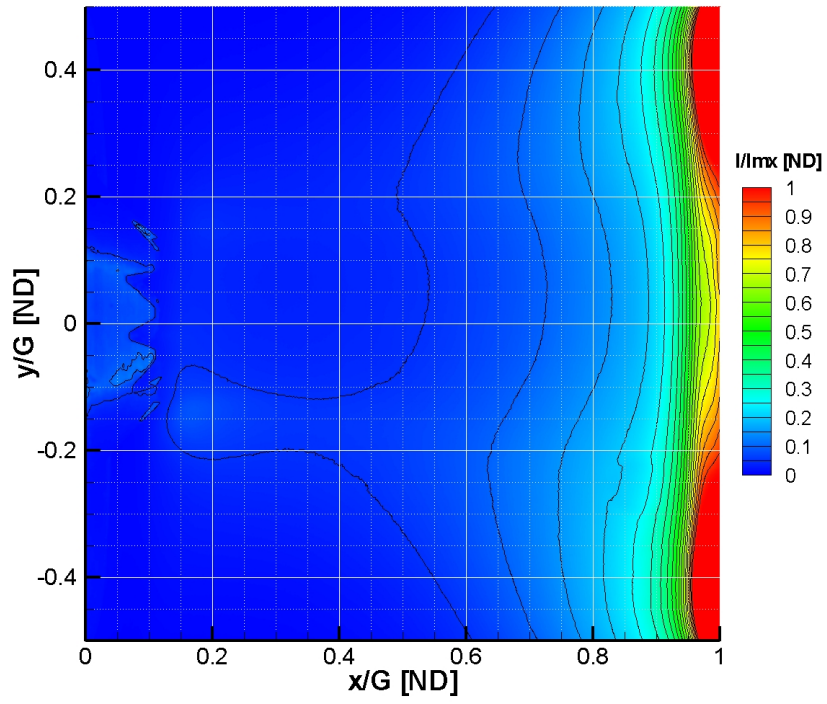
The higher Mach number flows were better at carrying heat away from the plasma field through convection, which allowed for higher forward power settings and produced larger plasma volumes. The larger plasma volumes radiated more visible light. Table 4.19 indicated that the Mach 2.1 jet did not follow the trend of increasing forward power for increasing Mach number. The Mach 2.1 jet exhausted into a chamber pressure of 8 torr, required for matched flow conditions. The lower chamber pressure required less forward power for a given electrode gap and therefore it was difficult to compare plasma fields based solely on forward power and bias voltage. Figure 4.61 provides a summary of the increasing illumination for Mach number along the centerline across the electrode gap. The cathode glow region was marked by the increased intensity at the right of the figure. In the center of the electrode gap, the light intensity was caused by the positive column structure and was highest for the Mach 2.0 case near the anode. Also note that there is a clear anode glow region for the Mach 2.0 case. Both of these features were caused by the plasma field reaching across the electrode gap with the most uniformity for the Mach 2.0 case versus the Mach 0.7 and 1.1 cases. For the slower speed cases, their strongest intensity occurs at the cathode glow and then drops monotonically until reaching the anode. The Mach 1.1 case shows measurable intensity all of the way to the anode, while the Mach 0.7 case drops to zero at 40% of the distance from the anode.[33, 145, 308]

4.4.2 Effect of Anode Design on Visible Light Emissions from the Plasma Field

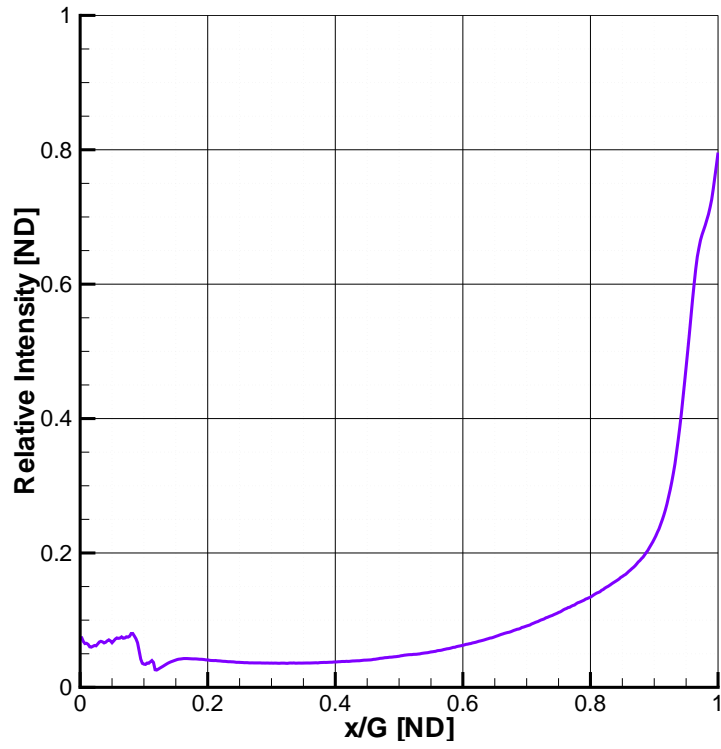
The influence of anode design will be examined next by comparing cases B and B'. These plasmas were created using the same nozzle, and pressure ratio as are indicated in Table 4.20.

Table 4.20: Plasma and Jet Configuration Comparing Anode Design for the Mach 1.1 Converging-Diverging Nozzle at a Chamber Pressure of 9 Torr

	M_i [ND]	P_o [torr]	P_e [torr]	U_e [m/s]	D_e [mm]	D_a [mm]	G [mm]	P_f [W]	P_r [W]	V_{bias} [V]	C_T [%]	C_L [%]
B	1.1	20.5	9.15	348	11.3	11.5	79.1	110	0	11-30	18.8	48.0
B'	1.1	20.5	9.15	348	11.3	15.9★	76.7	100	0	6-17	19.8	60.0
★ This anode includes a serrated conical feature which extends into the electrode gap 5.8mm.												



(a) Contours of Relative Intensity



(b) Relative Intensity along the Centerline

Figure 4.62: Relative Intensity of Visible Emission from the Plasma Field for an Anode with Serrated Conical Feature Around a Mach 1.1 Axisymmetric Jet at 9 Torr

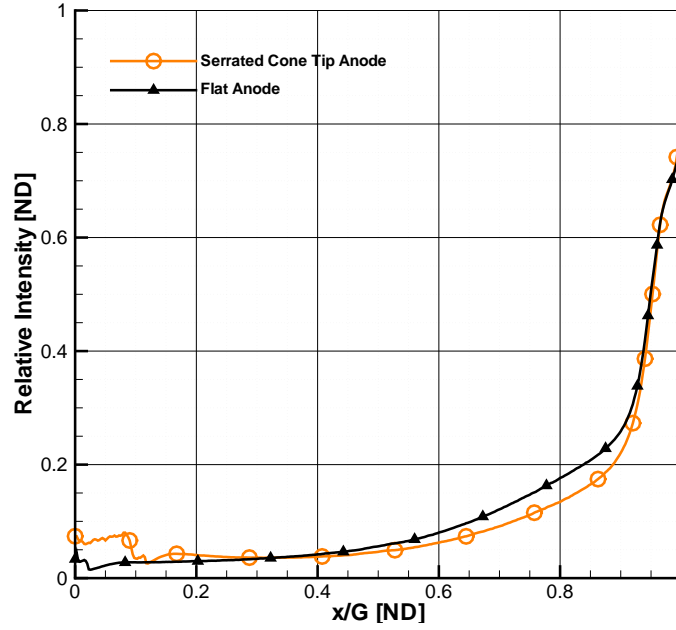


Figure 4.63: Comparison Between Anode Designs of Relative Intensity of Visible Emission Along the Centerline of the Plasma Field for an Anode with Serrated Conical Feature and a Flat Anode Around a Mach 1.1 Axisymmetric Jet at 9 Torr

Figure 4.62 shows the light emitted from the plasma field for the Mach 1.1 converging-diverging nozzle at 9 torr with the anode modified with a serrated conical feature. The advantage of the modified anode over a flat-faced anode was the creation of a small corona discharge in the serrations similar to a flame holder, which then had the effect of drawing the plasma field towards the anode. The feature was created by the addition of a cone segment which forms a sharp lip. The lip was further altered by eight serrated grooves cut into the circumference of the lip. A comparison between the flat anode and the modified anode is made in Figure 4.63. Note that the plasma illumination drops near the cathode (right) when the modified anode is employed. The effect at the anode face is not clear from Figure 4.63 - as only illumination along the centerline is described. However in comparing Figure 4.59 to Figure 4.62 there is clear evidence that the plasma field is drawn toward the anode. Table 4.20 indicates that forward power and bias voltage are decreased for the modified anode. Note here that the electrode gap is measured from the flat face of the anode to the face of the cathode and that the serrated conical feature extends into the gap by 5.8mm. This effectively decreases the electrode distance and therefore less forward power is required before plasma instabilities occur. Additionally, the sharp features of the serrated cone were a source of plasma instability as corona discharges formed in the serrations and quickly transitioned to arc discharges - requiring extra margin in forward power to maintain stable plasma fields.[33, 145, 308]

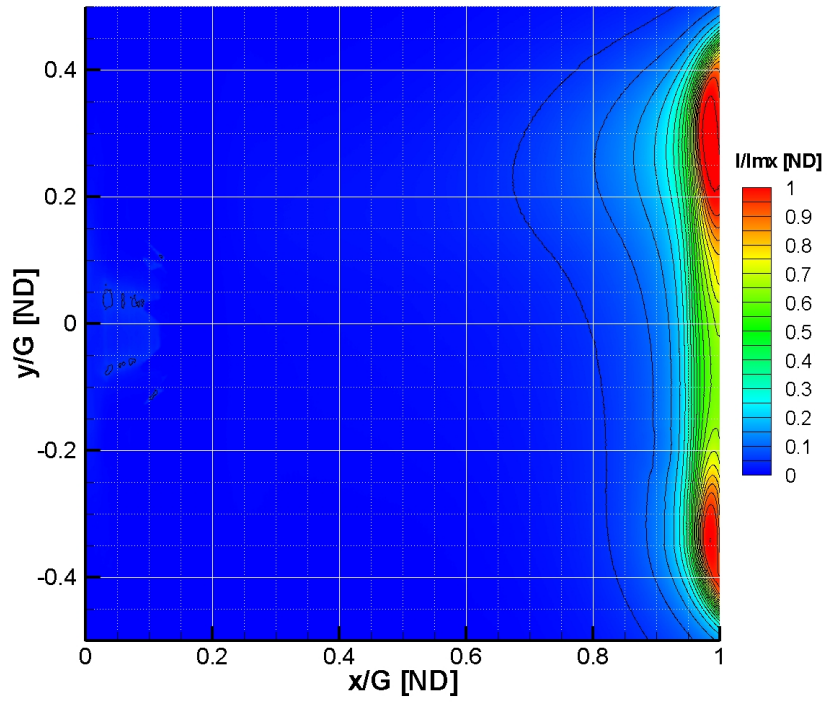
4.4.3 Effect of Compressibility on Plasma Fields for Developing Pipe Flow Jets

Since the improvement on the plasma field by the modified anode design was desired to influence more of the jet shear layer, the modified anode was used for all of the 9.5 mm diameter nozzles. Given the complexity of building this anode, only one of them was constructed. Next the visible light emissions for plasma fields around developing pipe flow jets will be examined for increasing equivalent Mach numbers.

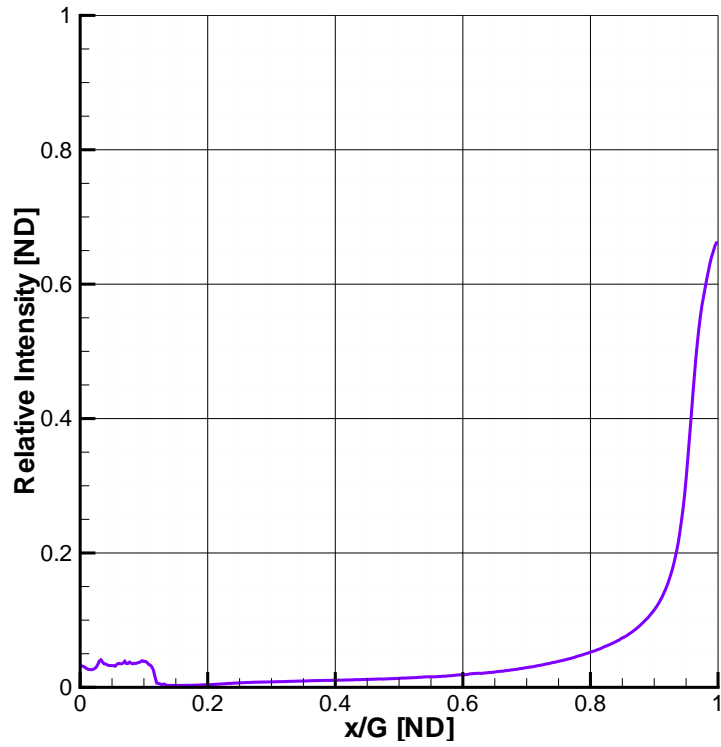
Table 4.21: Plasma and Jet Configuration for the Series of Constant-Diameter Nozzles for an Anode with Serrated Conical Feature at a Chamber Pressure of 5 Torr

	M_i [ND]	P_o [torr]	P_e [torr]	U_e [m/s]	D_e [mm]	D_a [mm]	G [mm]	P_f [W]	P_r [W]	V_{bias} [V]	C_T [%]	C_L [%]
F'	0.9	8.0	5.00	279	9.5	15.9★	77.4	19	0	2-5	19.7	71.1
G'	1.4	16.5	5.00	412	9.5	15.9★	76.5	47	0	6-13	19.6	69.7
H'	1.9	34.0	5.00	498	9.5	15.9★	76.5	100	0	8-18	19.7	69.6
★ This anode includes a serrated conical feature which extends into the electrode gap 5.8mm.												

Figures 4.64 through 4.66 step through the visible light emitted from the plasma field for increasing pressure ratios exiting into a chamber at a pressure of 5 torr. The jet was created by a constant-diameter tube, 9.5mm in diameter and 12.7 cm long. The jet exit speed was varied by changing the plenum pressure, and while the flow conditions achieved were not isentropic, a large range of Mach numbers were investigated. The constant-diameter nozzle was used to increase the turbulence in the jet core from the developing pipe flow which was created through this nozzle.

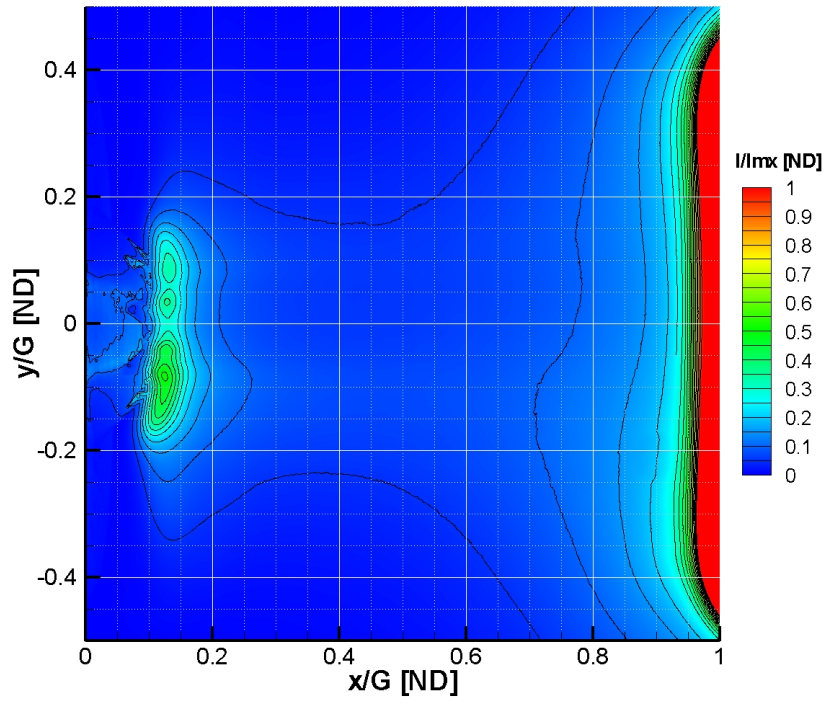


(a) Contours of Relative Intensity

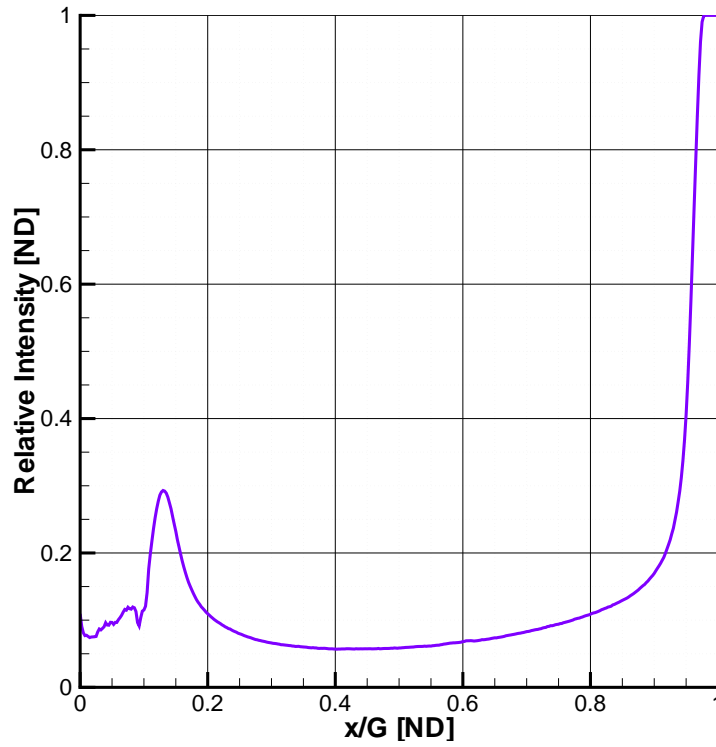


(b) Relative Intensity along the Centerline

Figure 4.64: Relative Intensity of Visible Emission from the Plasma Field for an Anode with Serrated Conical Feature Around an Axisymmetric Jet of Developing Pipe Flow Driven at a Pressure Ratio Corresponding Isentropically to Mach 0.9

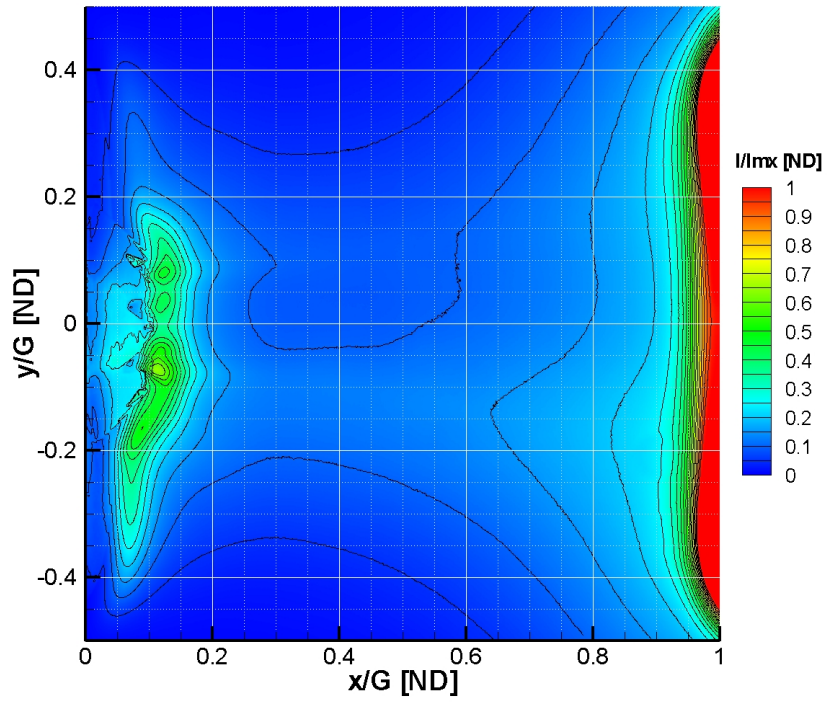


(a) Contours of Relative Intensity

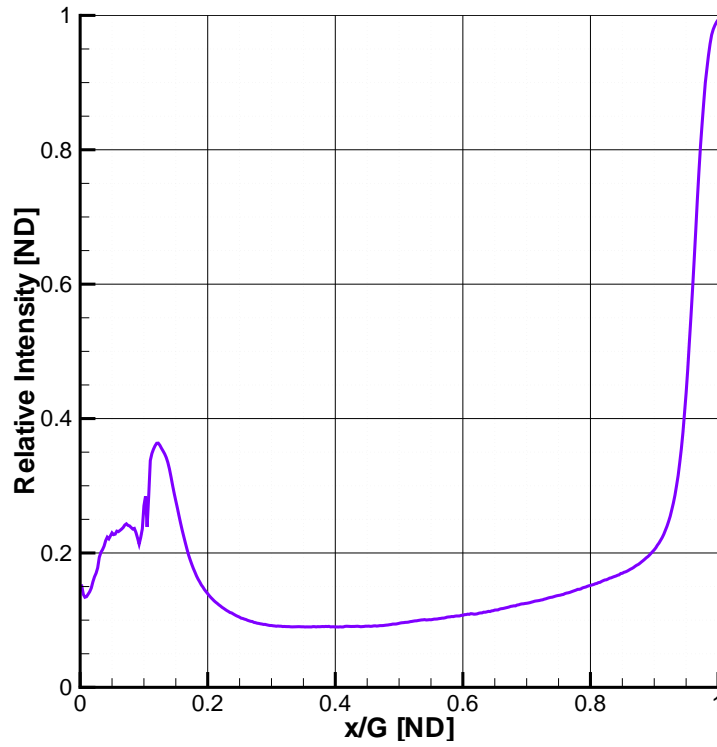


(b) Relative Intensity along the Centerline

Figure 4.65: Relative Intensity of Visible Emission from the Plasma Field for an Anode with Serrated Conical Feature Around an Axisymmetric Jet of Developing Pipe Flow Driven at a Pressure Ratio Corresponding Isentropically to Mach 1.4



(a) Contours of Relative Intensity



(b) Relative Intensity along the Centerline

Figure 4.66: Relative Intensity of Visible Emission from the Plasma Field for an Anode with Serrated Conical Feature Around an Axisymmetric Jet of Developing Pipe Flow Driven at a Pressure Ratio Corresponding Isentropically to Mach 1.9

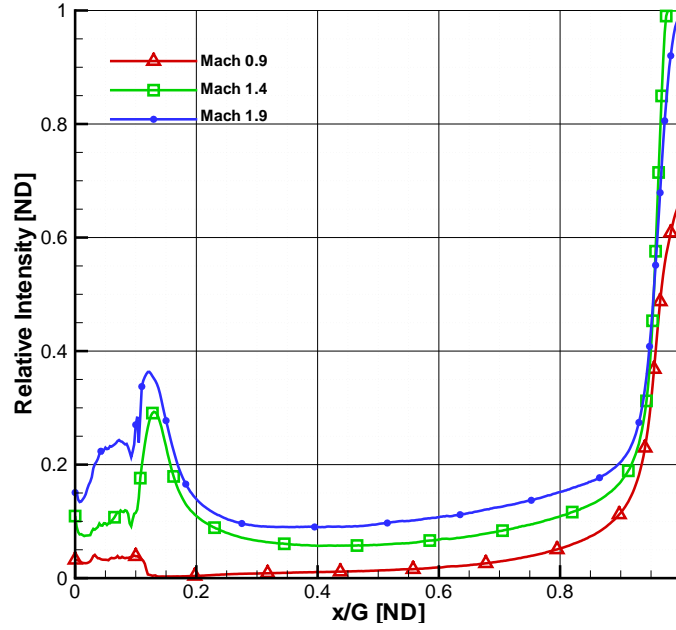


Figure 4.67: Comparison Between Increasing Pressure Ratios of Relative Intensity of Visible Emission Along the Centerline of the Plasma Field for an Anode with Serrated Conical Feature Around an Axisymmetric Jet of Developing Pipe Flow Driven at Pressure Ratios Corresponding Isentropically to Mach 0.9, 1.4 and 1.9

Table 4.21 summarizes the settings used in creating these plasma fields and clearly show the increase in forward power and bias voltage with increasing equivalent Mach number, M_i (based on the isentropic relation to pressure ratio). The extent of the plasma field is summarized in Figure 4.67 and shows a clear increase in emission intensity with the increasing pressure ratio. This increase in illumination is directly related to the increase in forward power and the resulting increase in plasma field. Increasing pressure ratios, provide increasing convection of the heat generated by the plasma field and therefore prevent the plasma from transitioning to an arc due to thermal instability until much higher forward power levels. These results are consistent with what was found earlier in this section at higher chamber pressures. [33, 145, 308]

4.4.4 Comparison of Visible Light Emitted Between Plasmas at 8 Torr and 5 Torr

Figure 4.68 compares the centerline visible relative light intensity between plasma fields at 5 and 8 torr. Both fields are the highest forward power settings achieved in each sequence - to provide the best comparison between intensity levels across the electrode gap. There is a significant increase in light emission near the anode, which is attributed to the difference in anode design between the two cases. In the center of the

Table 4.22: Comparison of Plasma and Jet Configuration for Increasing Chamber Pressure

	M_i [ND]	P_o [torr]	P_e [torr]	U_e [m/s]	D_e [mm]	D_a [mm]	G [mm]	P_f [W]	P_r [W]	V_{bias} [V]	C_T [%]	C_L [%]
C	2.1	71.0	8.00	523	15.7	17.0	75.8	94	0	5-21	19.1	52.2
H	1.9	34.0	5.00	498	9.5	15.9★	76.5	100	0	8-18	19.7	69.6
★ This anode includes a serrated conical feature which extends into the electrode gap 5.8mm.												

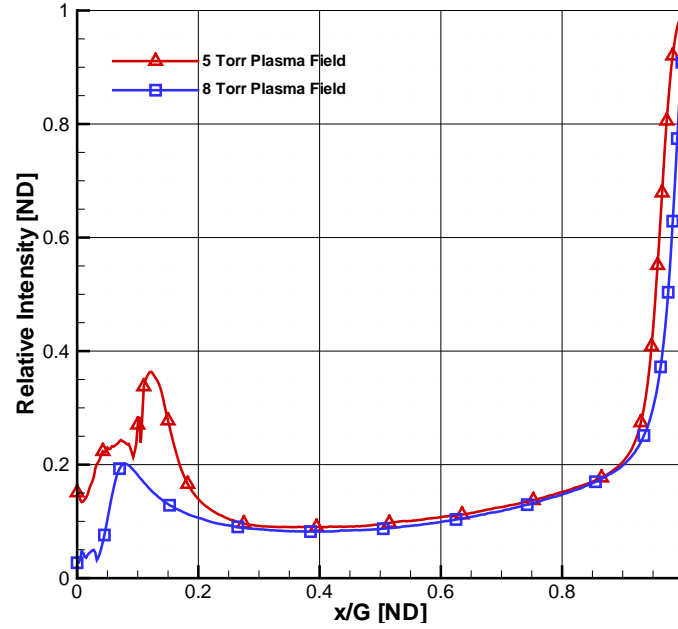


Figure 4.68: Comparison Between Chamber Pressures of 5 Torr and 8 Torr of Relative Intensity of Visible Emission Along the Centerline of the Plasma Field

plasma field, intensity levels increased 11% when the chamber pressure was lowered from 8 torr down to 5 torr, suggesting a stronger pressure field at lower chamber pressure. Table 4.22 indicates forward power showed an increase of 6% while mean bias voltage remained unchanged. Differences were encountered in creating plasmas at the two chamber pressures. It was significantly easier to start a plasma at 5 torr than at 8-9 torr and lower chamber pressures were also found to be less sensitive to electrode gap changes. However, when tuned, the plasma fields appear to be similar in terms of light emitted.

4.4.5 Visible Light Emissions from a Highly Underexpanded Jet at 8 Torr

The next case to be investigated was the highly underexpanded jet created by flow exiting a sonic orifice. The sonic orifice is aptly named because the flow chokes at the nozzle exit. The resulting near field flow is left to form its own nozzle with strong reflected shocks and expansions in order to equalize the pressure differential. The near field flow is described generally in Figure 4.69. The barrel shock and Mach disk shown

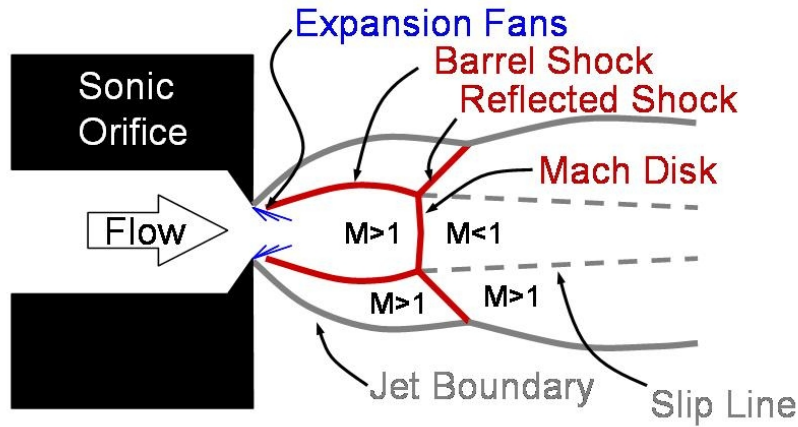


Figure 4.69: Schematic of a Flow Created by a Sonic Orifice

have been studied extensively and reasonably accurate empirical formulas exist to describe the location and diameter of the Mach disk based on the pressure ratio used to drive the jet and the diameter of the sonic orifice.[37, 100, 221, 228, 283]

This case was studied for four reasons. First, reports have indicated that plasma may weaken shock structures and this case provided an excellent method to test that hypothesis. If the shock was weakened by the plasma, the shock location should change. Next, while examining this theory, it was determined that the plasma visibly interacted with the barrel shock because the shock structure was clearly illuminated in the presence of the plasma. Thirdly, the sudden decrease in jet velocity in the transition through the Mach disk provided an extreme example for investigating seed particle tracking errors. Finally, the region near the Mach disk is a location with good illumination and temperature predictions which provides validation of rotational temperature measurements taken by spectroscopy, reported in the next section.[193, 219, 229, 251]

The conditions which created this underexpanded jet are listed in Table 4.23. The pressure ratio was chosen to be the lowest possible to create the barrel shock structure from the sonic orifice created by an upstream lip forming a 60° angle. Lower pressure ratios produce smaller Mach Disks closer to the jet exit and significantly more difficult to reach with particle image velocimetry due to the inset of the jet exit 3.2 mm from the anode face. Higher pressure ratios accelerated the flow to more than 700 m/s, which left the seed particles with more latency and was unnecessary.[8]

The highly underexpanded jet, created by flow exiting a sonic orifice was photographed in Figure 4.70. The influence of plasma-on strong shocks was studied here. The barrel shock formed as the jet matched pressure conditions is highlighted by plasma emission. Figure 4.71 documented the relative intensity of this

Table 4.23: Plasma and Jet Configuration for the Highly Underexpanded Jet Created by a Sonic Orifice with a Flat Anode

	M_i [ND]	P_o [torr]	P_e [torr]	D_e [mm]	D_a [mm]	G [mm]	P_f [W]	P_r [W]	V_{bias} [V]	C_T [%]	C_L [%]
U	2.8	76.0	8.00	8.2	15.7	68.0	92	0	8-28	19.1	45.9

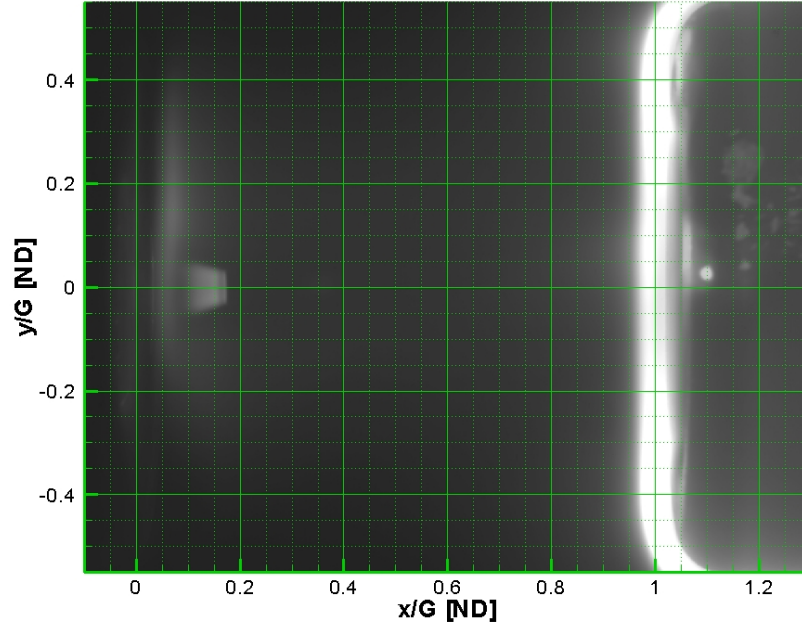
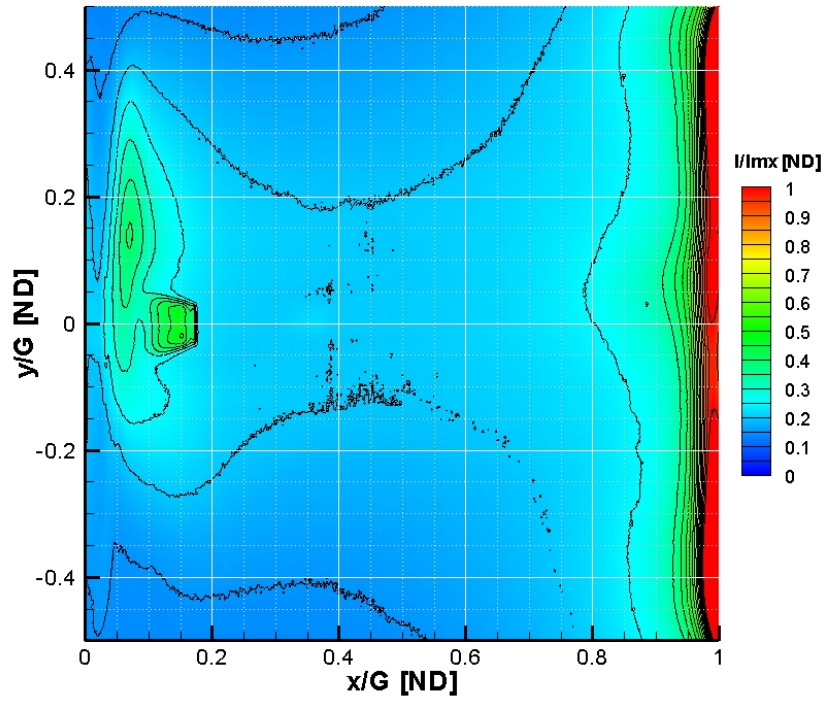
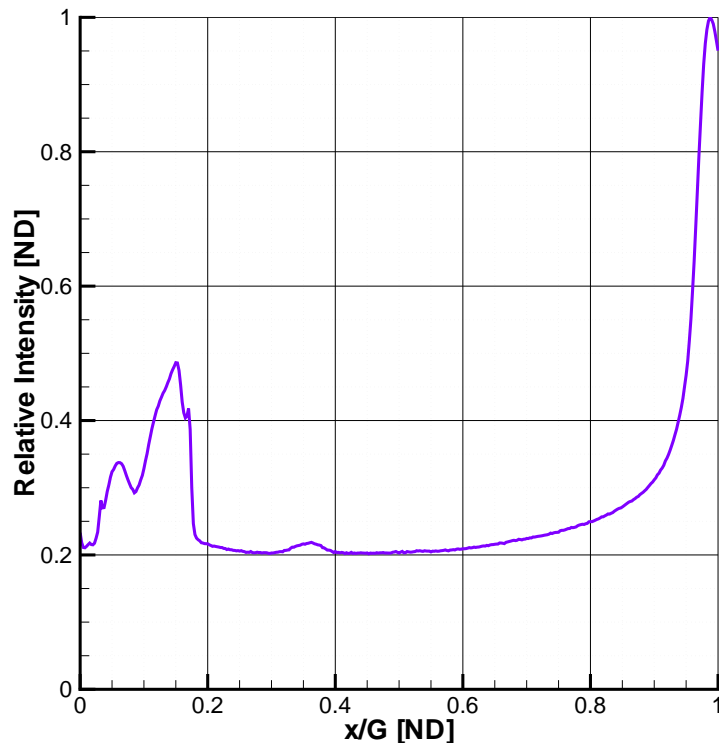


Figure 4.70: Image of Visible Emission from the Plasma Field at 8 Torr for a Flat Anode Around a Flow Created by a Sonic Orifice Which Generated a Visible Barrel Shock Wave

plasma field and indicates that for the plasma-on case, the normal shock location is 15.3 mm or 1.9 ± 0.1 jet diameters downstream of the jet exit. The empirical model of Crist [100] ($x/D_e = \sqrt{P_o/2.4P_e}$) places the location of the Mach disk at 2.0 jet diameters. Therefore it is concluded that the effect of the plasma-on the strong shocks of a highly underexpanded jet did not influence the location of the Mach disk.



(a) Contours of Relative Intensity



(b) Relative Intensity along the Centerline

Figure 4.71: Relative Intensity of Visible Emission from the Plasma Field at 8 Torr for a Flat Anode Around a Flow Created by a Sonic Orifice Which Generated a Visible Barrel Shock Wave

4.4.6 Summary of Important Findings from Visible Light Emission Imagery

Here is a summary of the significant conclusions obtained by investigating the plasma fields by photography of visible light emission.

- The intensity of visible light increased in intensity and stretched further from the cathode towards the anode across the electrode gap for increasing jet pressure ratios. The increased emission intensity and plasma volume, coupled with comparable increases in forward power and bias voltage all indicated stronger plasma fields with increasing jet Mach number.
- Increases in visible light emission were measured with a decrease in chamber pressure. Large increases occurred in the anode and cathode glow regions, however the glow regions provide little influence to the jet flow field. An increase in the center of electrode gap of 11% was found in the comparison between a chamber pressure of 8 torr with a decrease to 5 torr. This increase indicated a stronger plasma field existed at the lower chamber pressure.
- The modified anode design with the serrated conical feature enhanced the performance of the plasma field in the electrode gap, bringing more plasma volume toward the anode, as measured by light emissions. The modified anode was noted as slightly less stable which required slightly lower forward power settings.
- The location of the Mach disk of a highly underexpanded jet appeared to be unaffected by an RF capacitively-coupled plasma field. The plasma field provided a good technique for flow visualization of the strong shock structure of the barrel shock.

4.5 Temperature Measurement with Spectroscopy of the Second Positive System of Diatomic Nitrogen

Spectroscopy is a non-intrusive diagnostic in which light emitted by the plasma field was captured and analyzed. The light was separated by frequency and then recorded on an intensified CCD. Focusing on a narrow bandwidth of light between 364 and 384 nm, the emission of stimulated diatomic Nitrogen was observed. By matching the recorded spectra to a model of molecular Nitrogen emissions, the rotational and vibrational temperatures were determined. The rotational temperatures are considered an accurate method of measuring gas temperature in most cases, as the conversion of rotational and vibrational energy between molecules occurs very quickly. This rapid conversion means that rotational and vibrational temperatures are usually in equilibrium. From the rotational and vibrational temperatures of the test gas, taken across the electrode gap, the plasma field effects on the jet are quantified here. These temperatures aid in explaining the measured effects on mean and turbulent velocity fluctuations reported earlier in this section.[80, 113, 125, 131, 172, 250]

This section will detail each of the spectroscopy measurements made of the plasma fields. In all cases, spectra were obtained along a vertical line oriented across the radial direction of the jet. Baseline spectroscopy measurements for all plasma fields were made about 10 mm in front of the cathode face - a point far from the jet exit and just in front of the cathode glow region. Some distance was required from the cathode to avoid the plasma created at the cathode face, the so-called cathode glow. Since the cathode surface was so far from the jet core, its glow region did not influence the jet and light emitted from the glow would saturate the signal received, overpowering the light emitted from the shear layer of the jet.[145, 308]

Spectra were collected in a vertical line ranging from -24 mm to +27 mm from the jet centerline. The spectrometer could be traversed in the streamwise direction in 20 mm increments from the baseline location 10 mm in front of the cathode face. This obtained rotational and vibrational temperatures along the vertical line at multiple streamwise locations. In some cases a full plane of data was assembled across the entire electrode gap. In other cases, emission intensity decreased to the point it was impractical to continue and therefore the measurement was truncated.

Figure 4.72 is a schematic showing the collection plane for spectroscopy data. It should be noted that spectroscopy is a line of sight technique, collecting emissions through the entire plasma volume. However, the focusing of the light on the entrance slit to the spectrometer acts like a field stop and heavily biases the measurements toward the focal plane along the jet centerline. Also, note that the spectroscopy data was imaged in a plane perpendicular to the PIV data. And while the jet and plasma field are relatively

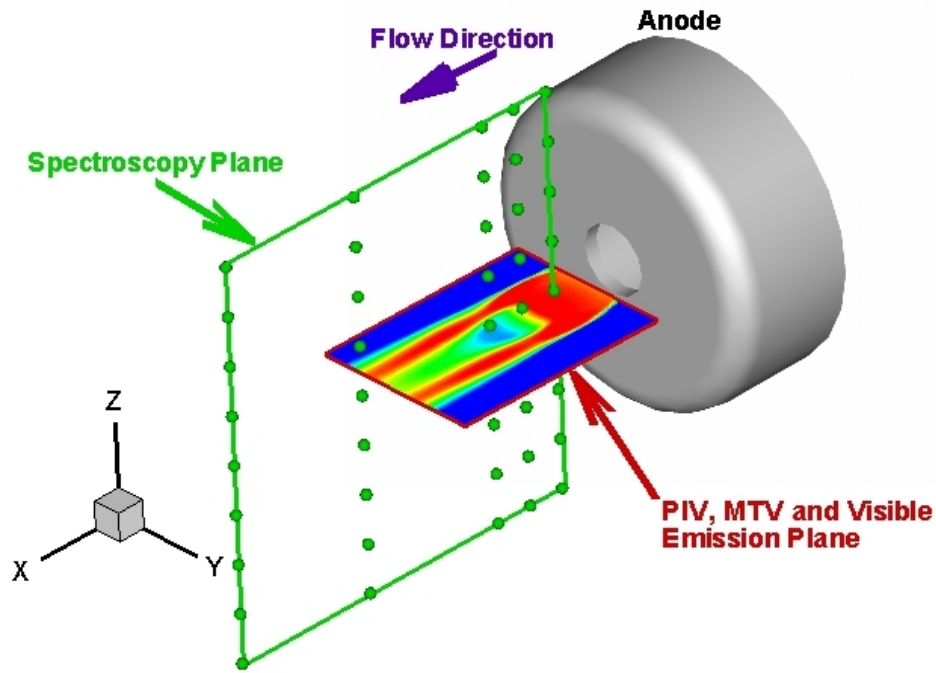


Figure 4.72: Schematic Showing the Imaging Focal Planes for Spectroscopy Orthogonal to the PIV, MTV and Visible Imagery Plane

axisymmetric, slight differences between the two planes were noticed while acquiring the data. For example, it was noted that the cathode leaned forward slightly due to a bending moment placed on it from the electrical connection. This caused the top of the cathode to be slightly closer to the anode than the bottom. Visibly, more light was observed on the top-half of the plasma field due to the closer gap distance there. However, as the data will show in this section, the temperature differences between top and bottom are relatively small. This same asymmetry appears in the visible emissions captured in the horizontal plane, as reported in Section 4.4. Under vacuum, the jet would flex slightly in its frame and would bring one side of the anode closer to the cathode than the other side. The result was increased visible emission on one side of the jet. However, the PIV data showed symmetry in mean and turbulent measurements in the same plane. Therefore, by analogy it is believed that these differences are relatively small and provide little influence to the results.^[145]

The first field to be examined is the highly underexpanded jet used in the particle tracking study. The barrel shock is illuminated by the plasma field and provides some interesting insights of a known flow field aiding in the interpretation of the results that follow. The next fields to be examined are the 8-9 torr plasmas created with the flat anode for increasing pressure ratios (cases A, B and C). Then, to ascertain

the influence of the anode modified with serrated conical feature, the modified anode field will be presented for comparison with the baseline field (case B'). Next, the 5 torr plasmas with the modified anode will be examined for increasing pressure ratios (cases F', G' and H').

The 5 torr plasma fields were mapped with PIV by using two gap spacings. In order to map the velocity field near the anode, the gap space was reduced by 30%, in order to bring the flow into the field of view of the PIV system. To determine the change in plasma field for this decreased gap space, a comparison is made. Then, the plasma field is examined for differences between cases C and D - where a pressure ratio was changed to produce an overexpanded jet from the baseline Mach 2.0 nozzle. Finally, the 10 torr plasma spectroscopy measurements are documented to provide some direction for future experiments.

4.5.1 Spectroscopy of the Highly Underexpanded Jet at 8 Torr

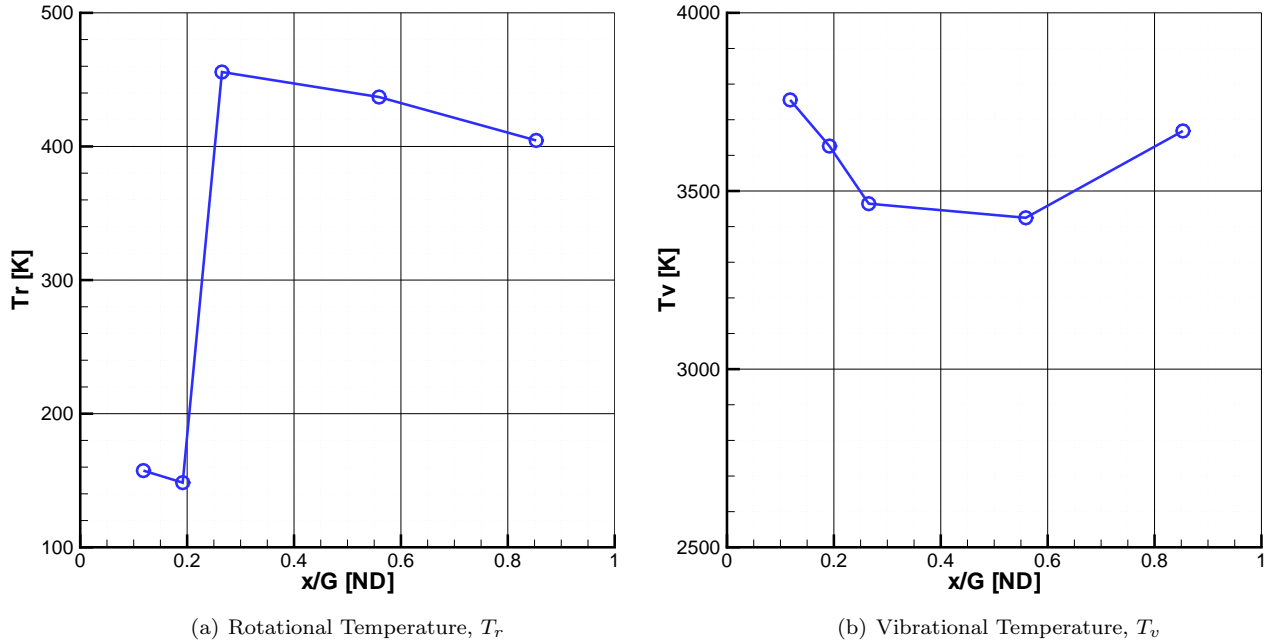


Figure 4.73: Rotational and Vibrational Temperature of Flow Exiting from a Sonic Orifice from Spectra of Diatomic Nitrogen, Along the Centerline of the Jet

Figure 4.73 shows the rotational (T_r) and vibrational (T_v) temperatures measured by line spectroscopy of the emissions captured from the second positive system of diatomic Nitrogen. In this case, only the reading taken near the centerline of the jet is presented along the gap space between the cathode and electrode. The barrel shock is marked by the sharp decrease in rotational temperature at gap locations below x/G of 0.2, where G is the gap distance of 68.0 mm. Just prior to the Mach disk, the jet flow accelerates to over 600 m/s when measured by molecular tagging velocimetry (MTV). At 1.2 jet diameters from the nozzle

Table 4.24: Rotational and Vibrational Temperatures Taken by Line Spectroscopy of the Highly Underexpanded Jet at 8 Torr

T_r [K]	r/D								
x/D	-3.0	-2.2	-1.4	-0.6	0.2	1.0	1.8	2.6	3.4
1.0	299	388	292	168	157	382	454	432	368
1.6	257	384	283	173	148	387	449	349	351
				Normal Shock					
2.2	307	384	279	424	456	372	368	434	368
4.6	304	387	334	417	437	368	364	429	368
7.1	405	426	307	396	405	332	394	410	345
T_v [K]	r/D								
x/D	-3.0	-2.2	-1.4	-0.6	0.2	1.0	1.8	2.6	3.4
1.0	3126	3176	3313	3660	3756	3573	3296	3192	3059
1.6	2986	3056	3189	3595	3626	3447	3193	3100	2935
2.2	2986	2999	3144	3268	3464	3386	3190	3015	2911
4.6	2958	2979	3108	3213	3425	3337	3164	3016	2972
7.1	3065	3227	3405	3532	3669	3644	3368	3133	3145
Note: Jet Exit Diameter D is 8.2 mm and Gap Distance G is 68.0 mm.									

exit, MTV data indicated a centerline flow speed of 590 m/s. For an assumed isentropic flow, based on the measured plenum temperature of 293 K - the predicted static temperature is 125K for a flow speed of 590 m/s. The measured rotational temperature is 148 K 1.2 jet diameters from the exit of the jet, which is consistent with the predicted uncertainty of ± 25 K. A prediction of static temperature downstream of the Mach disk from normal shock relations estimates the rotational temperature downstream of the shock to be 286 K. A measurement of 440 K indicates that the plasma emission captured is in the heated shear layer and not the core of the jet. The jet core was visible in the plasma field as a dark region, where it was difficult to ascertain if the plasma illuminated into the jet core. Panel (b) shows T_v near 3,500 K which increases approaching the electrodes from the center of the gap. In the barrel shock region, energy appears to be trapped in the vibrational state of molecular Nitrogen, marked by the increase in vibrational temperature there. This increase in T_v is consistent with frozen flow which is associated with quickly expanding supersonic jets.[100, 14, 283]

Table 4.24 shows the rotational and vibrational temperatures measured in a grid across the electrode gap, G . The top portion of the table is devoted to rotational temperature, T_r , while the bottom section reports T_v , vibrational temperature. The position from left to right corresponds to jet diameters of vertical displacement from the centerline of the jet. The radial positions are negative for the positions measured vertically below the centerline and positive above the jet center. Each row in the table corresponds to a different location along the gap, beginning near the anode face and progressing downstream towards the cathode. The distance from the electrode (x/D) for each row of temperature measurements is the far left hand column.

In order to clear up confusion, jet exit diameter is used as much as possible to give physical meaning relative to comparable experiments involving axisymmetric jets. However, when different plasma fields are compared the critical parameter is the spacing of the electrode gap. Therefore all of the plots in this section are scaled by the gap distance for consistency and to aid in plasma field comparisons, but this table is scaled by jet exit diameter for use in comparison with other experiments.[100, 145, 221]

With regards to rotational temperature, three trends can be observed in Table 4.24. First, the location of the barrel shock is marked by low rotational temperatures at x/D locations of 1.0 and 1.6 and at r/D positions nearest the centerline (-0.6 and 0.2, respectively). Next, the rotational temperature downstream of the shock is significantly higher and reflects the light being emitted primarily from the shear layer, as the core of the jet is observed to be visibly darker. Therefore, from observations of the light emitted in the visible spectrum, it is assumed that light emitted in the near UV range is also decreased in the jet core, meaning the spectroscopy measurements made are based on the information received from the plasma regions emitting light. In Table 4.24, the rotational temperature peaks at the center of the jet, and then drops for the measurements taken about one exit diameter from the centerline radially. Further outboard of the jet centerline, T_r rises again at the furthest outboard radial stations. It is believed that the centerline peak corresponds to measurements of the visibly brightest portions of the plasma field in the shear layer. Menart et. al. [251] made a similar observation of plasma strength growing in the shear layer region. The centerline measurements capture emissions from the shear layer closest to the spectrometer. The rise in rotational temperature at the outboard stations corresponds to a decrease in vibrational temperature at the same location and is attributed to a quenching of the vibrational temperature through collisional energy transfers in the shear layer. There is a region of decreased rotational temperature between the centerline and the outboard stations. The temperature here is attributed to the cool core gas of the jet, mixing with the excited gas in the plasma field and thereby lowering the temperature.[145, 308]

No trend is observed in rotational temperature as the flow travels from anode to cathode. The only conclusion that can be drawn is that the rotational gas temperature in the shear layer appears to be about 400 K but is lower in the core mixing region, and also near the edge of the plasma field. There are some hot spots observed near the anode and cathode and these are believed to be from the anode and cathode glow regions, respectively.[131, 145, 308]

Two trends are observed in the vibrational temperatures of this plasma field. First, the the vibrational temperatures are about 10% higher near the cathode and the anode than in the center of the gap. Secondly, the vibrational temperatures are highest along the centerline of the jet and decrease radially outward from the center. This corresponds to the centerline of the plasma field as well. The vibrational temperatures

suggest a symmetry of the plasma field. Higher vibrational temperatures are expected near the electrodes as the gas is exposed to stronger excitation from the electrode glow regions. Higher vibrational energy along the centerline tracks with previously mentioned expectations as well. The vibrational energy is somewhat trapped, but achieves balance by radiation, convection and diffusion to the chamber walls - therefore as the plasma reaches outward from the electrodes towards the plasma walls, the vibrational energy tapers off and manifests itself as lower measured vibrational temperatures, and subsequently higher measured rotational temperatures.[145]

4.5.2 Effect of Compressibility on Plasma Field Temperatures for Perfectly Expanded Jets

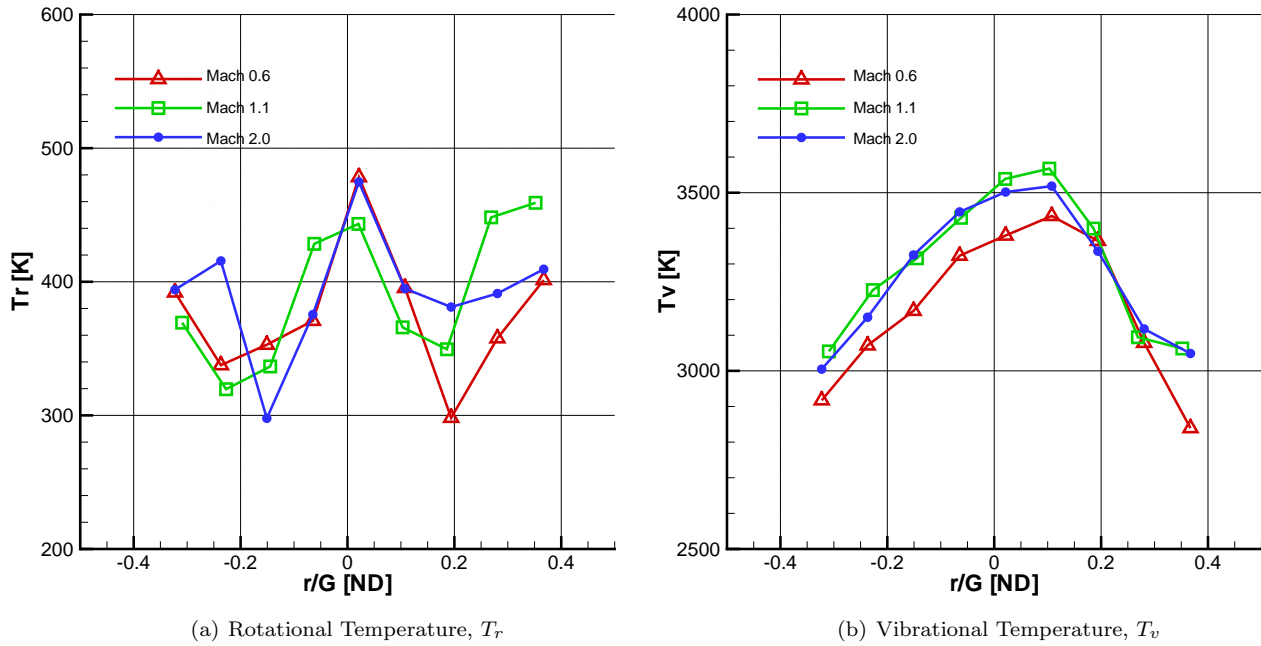


Figure 4.74: Summary of Temperature Comparisons for Increasing Mach Numbers from Spectra of Diatomic Nitrogen for Axisymmetric Jets at 8-9 Torr, Taken 10 mm Away from the Cathode

Figure 4.74 is a compilation of temperature measurements for increasing pressure ratios to examine the effects of compressibility on the plasma field temperatures. Each of the lines represent a measurement taken 10 mm upstream of the cathode, the point furthest from the jet exit and are points which extend outward from the centerline of the jet. Three pressure ratios are examined, all with matched converging-diverging nozzles and are for Mach numbers of 0.7, 1.1 and 2.0. The rotational temperature measurements show similar trends as found in the underexpanded jet measured previously. Namely, the rotational temperature peaks along the centerline and decreases in the region where visibility occurs through the outer plasma region into

the shear-core interaction. The temperature peaks again along the edge and matches the corresponding decrease in vibrational temperature - again suggesting a vibrational quenching.[308]

Vibrationally, the plasma field looks very similar to the previous example of the underexpanded jet. The vibrational temperature increases toward the center of the jet, and decreases radially outward. The only influence of compressibility can be seen here as well. The Mach 0.7 case shows a 100 K decrease in vibrational temperature when compared to the Mach 1.1 and 2.0 cases. This tracks with the trend observed in the visible emission spectrum where the subsonic plasma fields were notably weaker than the supersonic cases both in terms of light emitted and in power transmitted. Note however that a change of 100 K is within the uncertainty bounds for this measurement technique.[145, 251]

4.5.3 Effect of Anode Design on Plasma Field Temperatures

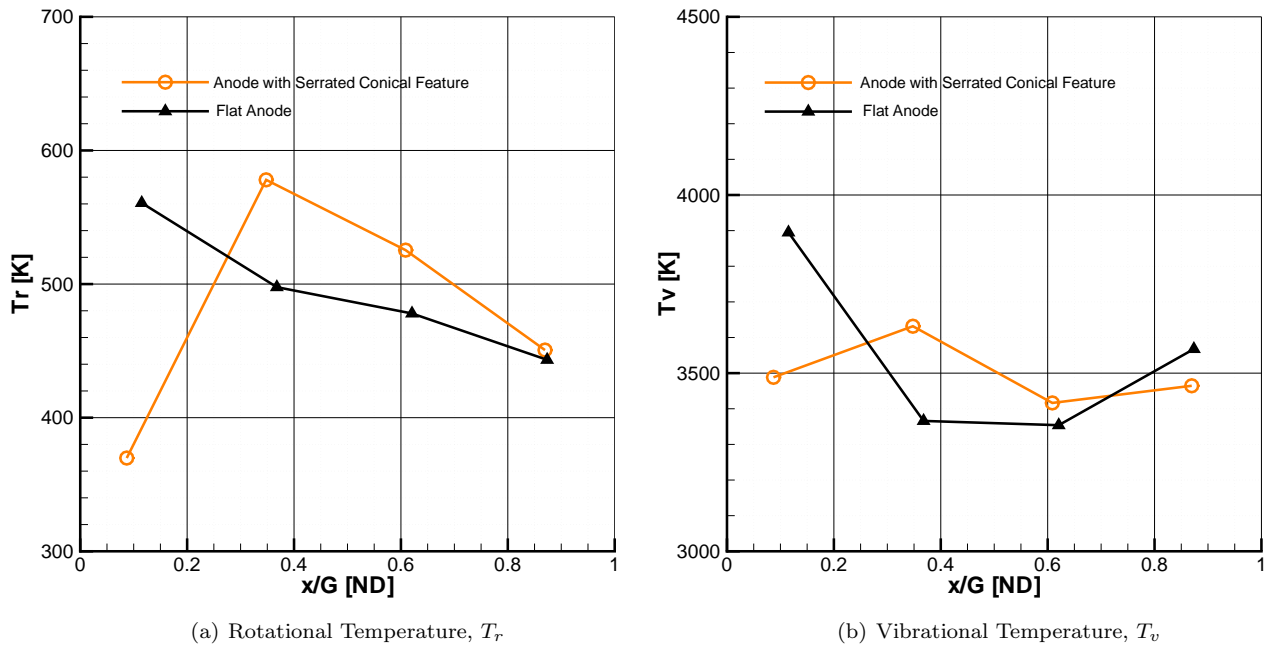


Figure 4.75: Temperature Comparisons Between Anode Designs from Spectra of Diatomic Nitrogen for a Mach 1.1 Axisymmetric Jet at 9 Torr, Along the Centerline of the Jet

Here is the investigation into the difference in plasma field based on anode design. Figure 4.75 compares the Mach 1.1 axisymmetric jet at 9 torr for two anodes. The first anode was the baseline flat anode. The new anode was based on the flat anode design, but modified with a serrated conical tip at the exit of the jet. The modified anode was chosen to create weak corona discharges to modify the plasma field and bring stronger intensity plasma towards the exit of the jet. To compare the influence of anode design, the rotational and vibrational temperatures are shown along the centerline of the jet between the electrodes. Rotational and

vibrational temperatures show the same trends. First, T_r and T_v are markedly higher in the center of the electrode gap for the modified anode. Also of interest is the sharp decline in both rotational and vibrational temperatures at the anode face. This measurement was made intentionally near the corona discharge of the conical tip, which extends 7% into the electrode gap. Therefore it is believed that the anode dark space contributes most to this reading and to the low temperatures measured. It is concluded that the modified anode does improve the plasma field. The flat anodes were used for all of the 8-9 torr plasma fields due to the larger jet exit diameters and potential for plasma instabilities at higher pressures. Only one modified anode existed, it was used consistently for all of the 5 torr plasma fields. One of the 9 torr nozzles had an exit diameter which was at or larger than the exit of the modified anode. For consistencies sake, all three nozzles were matched to flat anodes for that sequence of testing. [145, 308]

4.5.4 Effect of Compressibility on Plasma Field Temperatures for Developing Pipe Flow Jets

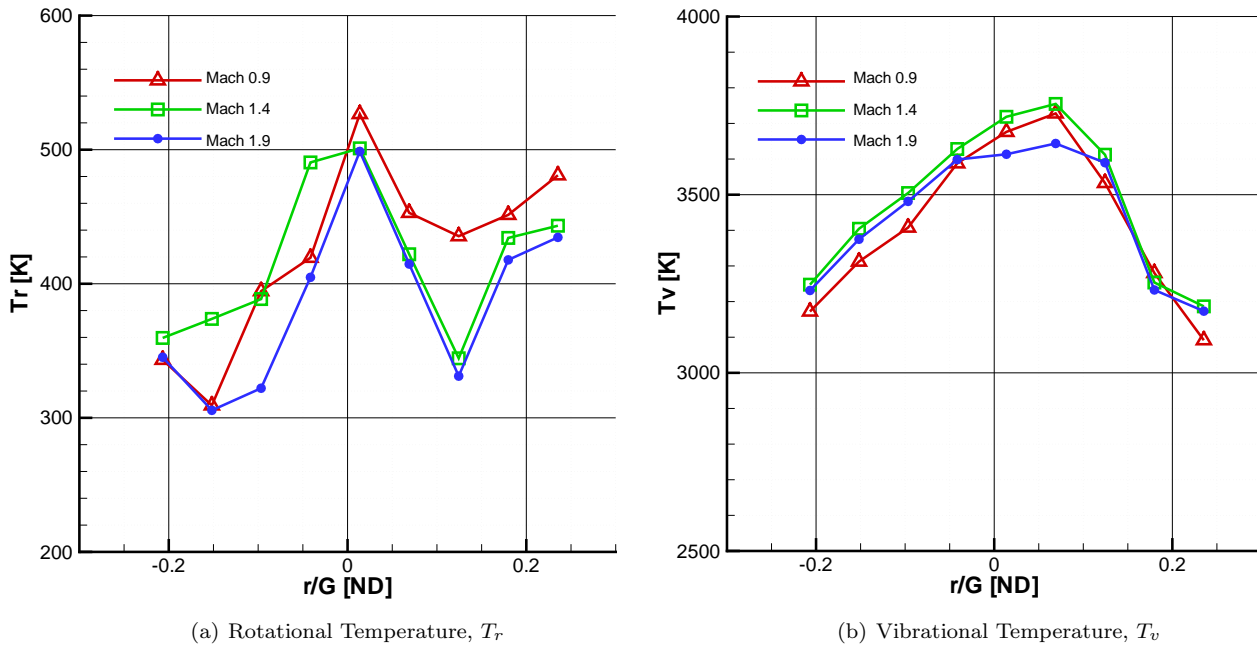


Figure 4.76: Summary of Temperature Comparisons for Increasing Mach Numbers from Spectra of Diatomic Nitrogen for Developing Flow Exiting from a Constant-Diameter Pipe at 5 Torr, Taken 10 mm Away from the Cathode

Examined in Figure 4.76 are the plasma fields generated around a constant-diameter tube. The variation of compressibility is investigated by increasing the pressure ratio applied across the nozzle. Supersonic exit conditions are achieved with the constant-diameter pipe through an aerodynamic throat caused by a separation at the tube entrance. Looking at the rotational temperatures in panel (a), the peak at the

centerline is seen here, as was noted earlier. Also, the decrease in T_r seen previously is apparent here as well at r/G of 0.1, which is attributed to the mixing of the cold jet with the warm shear layer and results in a decrease in temperature from the shear layer measurement from light emitted just outboard of the centerline. Note here that there is a difference between the positive radial positions and the negative radial positions. The rotational temperature is higher on the positive side. In these cases there was a difference in gap spacing between the top of the cathode and the bottom of the cathode of about 1 mm. The top side was closer to the anode and the plasma field was observed to be brighter on the top side in the visible spectrum. Therefore since the plasma field is believed to be stronger there, the rotational asymmetry is attributed to the slight lean of the cathode and corresponding shift in the plasma field.[130]

Vibrational temperatures, show a continuing trend of peaking in the center and decreasing toward the radial edges. The decrease in T_v again tracks with an increased T_r and is believed to be a combination of energy transfer to rotational and translational temperatures, as well as radiation and diffusion to the chamber walls. Note that in both rotational and vibrational temperatures, no significant change is observed for the variation of pressure ratios. This is a change from the plasmas at higher pressures, where the subsonic case showed slightly lower vibrational temperatures. The trend in subsonic plasma being weaker in terms of visible light emitted and in power transmitted is noted - but does not translate into a reduced vibrational temperature.

4.5.5 Summary of Important Findings from Temperature Measurement by Spectroscopy

It was postulated previously that the reason for the increase in convective velocity with the plasma on can be attributed entirely to the increase in gas temperature in the shear layer as a result heating by the plasma field. The compressible convective velocity, U_c can be related to the temperature of the jet and of the chamber through $U_c = (a_2 U_1 + a_1 U_2)/(a_1 + a_2)$ - where U_1 is the core velocity of the jet and U_2 is zero for these jets. To quantify the T_2 required to produce the measured change in convective velocity, the equation above can be manipulated into the more convenient form found in Equation 4.14. The resulting $(T_{2-\text{plasma}})$ is the shear layer temperature required to bring about the measured change in convective velocities $U_{c-\text{plasma}}/U_c$. The plasma-off shear layer temperature is assumed to be near the measured plenum temperature, which is averaged to be 294 K. This calculation was performed based on the measured core and convective velocities to compare to measured the rotational gas temperatures in the shear layer. The convective velocity analysis indicated that shear layer temperatures between 315 K and 378 K would produce the measured change in convective velocity. The measured rotational temperatures in the area believed to be emissions from the

shear layer do indicate that those temperatures are between 326 and 372 K. Therefore, given the overlap of measured shear layer temperatures and the estimate of required shear layer temperatures, the change in convective velocity due to an increased speed of sound associated with the increased temperature of the shear layer from the plasma field is most plausible.

Chapter 5

Conclusions

5.1 Test Objectives

This research set out generally to find the influence of plasma on compressible turbulence. Compressible turbulence in plasma touches many fields of interest. Vehicles such as the space shuttle experience the combined effects of plasma and compressible turbulence on re-entry into the earth's atmosphere. As we learned in the space race of the 1960s, the stresses placed on a re-entry vehicle during the return to earth are severe and miscalculations carry devastating consequences. Plasmas are being used also in space applications, such as hall-effect thrusters on orbiting satellites. In order to achieve an understanding of the underlying features of plasmas and to predict the impact of those features on future designs, modeling is required. And therein lies the strongest influence for this research - that this work provides data which will validate modeling of this rather complicated juncture of interwoven phenomena.

The main goal of the research presented here was to determine the differences between a plasma field and neutral field flow structure (both mean and turbulent effects) for varying Mach number. The overall objective was to describe the effect of Radio Frequency Capacitively Coupled Plasma (RF-CCP) on the flow features of compressible axisymmetric jets. This objective was examined through three specific sub-objectives.

- Confirm the Measurement Technique Accurately Describes the Flow Field
- Define a Measure for Plasma Quality
- Measure the Effect of Plasma on the Flow Field

The first sub-objective was to confirm the measurement technique accurately describes the flow field. Research indicates that atomized liquid seed particles were small enough to accurately track the flow dynamics of these nozzles. However, the accuracy of the particle tracking must be quantified. Measurements taken with seed particle based tracking techniques were compared to molecular tracer techniques to confirm the particles accurately tracked the flow. Good theoretical models exist which were used for comparison. One aspect of this sub-objective was the concern that the plasma may induce motion in the seed particles.

However, through observation prior to testing, the seed particles in these experiments were noted not to be disturbed electrically or thermophoretically by the plasma field. This sub objective was considered successful when two conditions were met. First, particles based velocity measurements tracked the mean flow features to within 5% of the molecular tracer based velocimetry technique. Second, the model based approach to estimating uncertainty in turbulent fluctuations determined that uncertainty was below 10%.

The next sub-objective was to define a measure for plasma quality. The goal of this sub objective was to quantify a factor which can be measured independent of the flow structure to determine the influence of the plasma on the flow structure. Success in this category was based on documenting plasma quality for all plasma fields tested.

Measuring the effect of plasma on the flow field was the final sub-objective. This sub-objective was the primary path to answering the test objective. Both mean and turbulent fluctuating velocity fields were acquired for plasma and neutral fields at the same test conditions and flow locations. Success here was in acquiring these sets at at least two different Mach numbers for: a free shear flow, the same free shear flow with an induced large scale structure, and an oblique shock structure.

This document began with a review of axisymmetric jet flow structures. Next, to gain a better understanding of plasmas, the mechanics of the fourth state of matter and the techniques used in generating sustained plasma in the laboratory were reported. The plasma fields described there were important because many of them were encountered in testing, and phenomena encountered in one type of plasma field are often used to describe features of other plasmas.

Then, the equipment used and developed for this research effort were described. First the facilities which deliver high pressure air and evacuate the test chamber were detailed. Next, the test section was described. The nozzle design procedure was then reported along with descriptions of all the nozzle contours as an aid to modeling with computational fluid dynamics. Next, the equipment used to generate seed particles was over-viewed. Finally, the plasma generation system is detailed, along with tuning philosophy and electrode design methodology.

The non-intrusive diagnostics described next were used in determining the flow properties of interest in this research effort. Each of the diagnostics was based on the measurement of light. The measurement techniques used, the test procedures and the measurement uncertainties were reported for each diagnostic.

Finally, the measurements conducted to characterize the plasma and its effect on the mean and turbulence quantities of the jet were documented. The results were divided into the specific test techniques used to investigate the jet flow fields. First, verification results were reported to investigate how well the seed particles track the flow. Then, with adequate tracking characterized, particle based velocimetry techniques were used

for the quantitative measurement effort. The bulk of the results then focused on the velocimetry data, examining the effect plasma had on mean and turbulent measurements of the velocity field for various jet conditions. Four different axisymmetric jets and their resulting shear layers were investigated to determine the influence of a plasma field on them: perfectly expanded subsonic and supersonic jets, jets created by developing pipe flow exhausting from a constant-diameter tube, and large scale structures created by forced laser energy deposition into jet flows. The plasma field was documented next by examining the intensity of light emitted in the visible spectrum. Finally, the plasma field was defined quantitatively by examining the rotational and vibrational temperatures of diatomic nitrogen through spectroscopy of the emission of near ultraviolet light from second positive system of diatomic nitrogen.

5.2 Findings

Characterizing the ability of particles to adequately track the mean and turbulent velocities was accomplished first, in order that tested could proceed with confidence in the measurements. It was found near the exit (1.1 diameters downstream of the anode), the effects of particle latency on mean flow determination resulted in up to a 5% error in PIV measurements of centerline axial velocity for the 100 nm seed particles. In general, the 100 nm seed particles showed excellent tracking ability of the mean flow of the jet, which was expected to improve as the flow gradients shallow and the jet core is dissolved. Mean flow tracking was not acceptable in the presence of strong shocks. Flow test conditions under evaluation in the remainder of this effort minimized the effect of shocks through pressure matching jet conditions and focusing on flow features much further downstream than the expected location of shock structures. Then using a model based approach, the effect of particle latency on turbulence measurements of axial and tangential velocity produced a propagated uncertainty of between 2.3% and 2.6% using sample sizes of 4000 velocity vectors. Additionally, particle tracking was found to have negligible effect on determining shear layer thickness. Measurement comparisons were made and found errors of between 1% and 3% 1.1 diameters downstream of the anode face. Further downstream it was reasoned that this measurement error should decrease as particle tracking improves in the growing shear layer.

Particle Image Velocimetry (PIV) was used to quantify the mean and turbulent velocities of three perfectly expanded jets. A comparison was made three jet diameters downstream of the anode face. At this location, the centerline velocity is 96% of the measured exit velocity, indicating that core breakdown has not yet occurred and therefore the velocity is unaffected by the plasma field. However, in all three cases, the centerline Turbulent Kinetic Energy (TKE) decreases when the plasma is initiated. At this axial loca-

tion in the jet flow, centerline turbulent kinetic energy decreases if the core is allowed to penetrate further downstream. Given the uncertainty of this measurement is 6.7%, there is no trend versus Mach number - only a consistent decrease in centerline TKE for all cases. Therefore it is concluded that the plasma effect on perfectly expanded jets is not dependent upon Mach number in the developing jet, but that overall the plasma allows the jet core to penetrate further downstream. It is believed that this penetration is an effect a bias of convective velocity to higher values towards the jet core velocity - due to heating of the shear layer by the plasma field.

Next, PIV was used to examine the influence plasma for increasing equivalent Mach number on mean and turbulent fluctuations for developing pipe flow jets. In general, the jet created by the constant-diameter nozzle was effective in increasing turbulence intensities in the core of the jet which translated into higher turbulent kinetic energy further downstream. A comparison was made between all three equivalent Mach numbers at a station 11.4 diameters downstream of the jet anode. The equivalent Mach 0.9 jet was influenced by the plasma considerably, especially given the relative weakness of the plasma field. The plasma-on case had a centerline velocity which was 8% higher than the plasma-off case at 11.4 diameters from the anode face. The TKE was 28 to 36% lower for the plasma-on case when compared to the plasma-off case at this location. The turbulent kinetic energy was 28 to 36% lower for the plasma-on case when compared to the plasma-off case at this location. For the high-speed, equivalent Mach 1.9 case, the axial velocity profiles looked the same, but turbulent kinetic energy increased 11% on the centerline and 14% in the shear layer when the plasma was initiated. This case exhibited shock and expansion phenomena in the jet core region from pressure mismatches in the tube nozzle.

There was a trend present in scaled turbulent kinetic energy with increasing effective Mach number for the progression of the jet from the anode face downstream. Initially, the $M_i = 0.9$ jet saw a reduction in TKE as the flow progresses downstream. At an effective Mach number of 1.4, the trend stagnated and then began to reverse. At $M_i = 1.9$ the effect was reversed, with plasma beginning to increase TKE as the flow travels downstream. Reynolds number effects were investigated, by computing a *local* Reynolds number, based on the jet diameter, local centerline velocity U_o , an estimate for density based on chamber pressure and estimated jet temperature T_1 , and viscosity based on measured shear layer temperatures from spectroscopy (presented later in this chapter). The Reynolds number calculations showed a general decrease of 8 to 16% with plasma-on and did not match any trends of TKE progression. Therefore, it was concluded that the trend in turbulence was for an initial decrease, switching to an increase in TKE as the effective Mach number progresses from subsonic to supersonic values. The developing pipe flow which generated this flow was a complicated jet structure with many rich features for the plasma field to interact with.

The supersonic flow began smoothly, but then developed a pattern of reflected shocks and expansions from observation of the velocity fluctuations in the centerline velocity near the jet exit. It was possible that the plasma field was interacting with the shock structures in the jet. Weakened shocks would allow for increased jet turbulence through higher core velocities passing downstream. Evidence of the higher core velocities was absent from these measurements, however the increase in TKE for the $M_i = 1.9$ jet could be a precursor to higher plasma-on core velocities further downstream.

The next comparison was of an off-nominal case, where the baseline flow is a converging-diverging jet at Mach 2.0. The influence of plasma on a weakly overexpanded jet was then investigated. The baseline Mach 2.0 nozzle was driven at a pressure ratio equivalent to a Mach number of 1.9 . When compared to the baseline nominal case, the influence of the plasma field is more pronounced on the overexpanded jet. In the overexpanded case, the axial velocity along the centerline increases 11 m/s for a 2.4% change in the plasma-on case over the plasma-off condition. For the nominal jet, the increase was 5 m/s or a 1% change. TKE decreases 31% along the centerline and 5% in the shear layer for the overexpanded plasma-on condition compared to plasma-off. For the nominal Mach 2.0 jet, the corresponding centerline decrease was 14% with no detectable change in the shear layer. From these changes in velocity measurements for the slightly overexpanded condition, it was concluded that the plasma field may have an impact on weak shocks. It has been hypothesized that a plasma field may interact with the shock waves to weaken them thermally, resulting in a higher downstream fluid velocity in the presence of a plasma. Conversely, the convective Mach number was lower in the overexpanded case, when compared to the Mach 2.0 nominal case and that may be another driver for the change noticed here. In either case, the effect of the plasma-on was more pronounced in the overexpanded jet than in the perfectly expanded jet.

The final comparison in PIV measurements was to examine the effect of anode design on the plasma field and the resulting impact on mean velocity and velocity fluctuations. The mean flow and turbulent kinetic energy did not change when comparing the plasma-off flow with the flat anode to the plasma-off flow with the modified anode. Therefore it was concluded that the presence of the modified anode had no significant impact on the measurements being taken. In comparing plasma-on cases between the anode designs, the mean centerline velocity was unchanged. Turbulent kinetic energy increased on the centerline by 2% for the flat anode, and by 3% for the modified anode. In the shear layer, the increases were 3% and 8% respectively. From these measurements it was concluded that the modified anode design improved the influence of the plasma field on turbulent structure, but did not significantly impact on the mean flow in this case. The modified anode was not recommended for use at higher chamber pressures as arcs form easily in the non-linear electric field created near the serrated cone.

It is postulated here that the reason for the increase in convective velocity with the plasma-on can be attributed entirely to the increase in gas temperature in the shear layer as a result heating by the plasma field. An increase in the the chamber temperature surrounding the jet, T_2 from 300 K to 400 K would result in an increase in convective velocity of 7% for all the cases examined. In an effort to quantify the T_2 required to produce the measured change in convective velocity, an estimated shear layer temperature needed to make the measured change in convective velocity was calculated. Shear layer temperatures between 315 K and 378 K would produce the measured change in convective velocity. The measured rotational temperatures in the area believed to be emissions from the shear layer do indicate that those temperatures are between 326 and 372 K. Therefore, given the overlap of measured shear layer temperatures and the estimate of required shear layer temperatures, the change in convective velocity due to an increased speed of sound associated with the increased temperature of the shear layer from the plasma field was the most plausible explanation.

5.3 Recommendations

This field has many avenues for further research. Here are some of the author's ideas to answer the question 'where do we go from here?' It is hoped that the experiments performed will be both an encouragement and a challenge to continue research in this area.

- Employ numerical modeling of the perfectly expanded jet in a simulated plasma field, where the plasma is approximated as heat addition in the shear layer of the jet to investigate if heating is the only source of change
- Employ numerical modeling of the developing pipe flow jet in a simulated plasma field, where the plasma is approximated as heat addition in the shear layer of the jet to investigate if heating is the only source of change
- Construct a larger test section which will allow for investigations of the jet flow after it has traveled through the plasma field to investigate whether the plasma influence on the jet is diminished upon exiting the plasma field.
- Use other plasma generation schemes to investigate if the effects observed here are related only to radio-frequency capacitively coupled plasmas or if their are universal effects.
- Construct other nozzles which further increase the core turbulence to investigate the plasma influence on these jet structures.

- Construct an impinging nozzle with variable impingement angle in the flow field to further quantify the effect of plasma fields on strong and weak shocks. This could be a precursor to using this plasma field to simulate re-entry conditions.

Appendix A

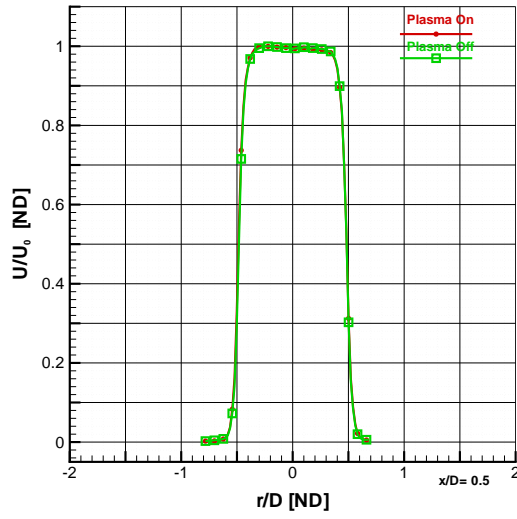
Archival of Particle Image Velocimetry Statistical Data

This Appendix contains a compilation of statistical data taken by particle image velocimetry (PIV). Each of the data presented here are the result of statistical analysis of over 4000 two dimensional velocity vectors. The vectors analyzed are from the combination of four rows of PIV data which were separated by less than 1 mm (less than one-tenth of a jet diameter in all cases). Each of the PIV data sets are a vector field of either 1032 or 1150 image pairs. Two to three overlapping PIV regions were measured and processed. Lines were investigated at roughly 20 mm intervals across the electrode gap, starting at the exit of the jet (anode) and progressing towards the cathode. Each of those lines are presented as a series of ten figures, covering three pages. The first three sequences cover the converging-diverging jets at 9 and 8 torr in increasing Mach numbers. Next, the overexpanded case where the Mach 2.0 jet was run with a pressure ratio of mach 1.9 is presented. Then the Mach 1.4 converging-diverging jet at 5 torr is detailed. The next three sequences cover a series of runs using the developing flow exiting from a nozzle formed from a constant diameter tube in order of increasing pressure ratios with subsonic and supersonic conditions achieved. The final sequence is a modification to the Mach 1.1, 9 torr case to investigate the effects of a modified anode. The normal flat faced anode cap was replaced with one with a serrated conical feature protruding from it. For reference, Table A.1 lists the case identifier, followed by downstream location in jet diameters, the Mach number based on measured centerline velocity and plenum temperature, and the beginning figure number and page for that sequence.

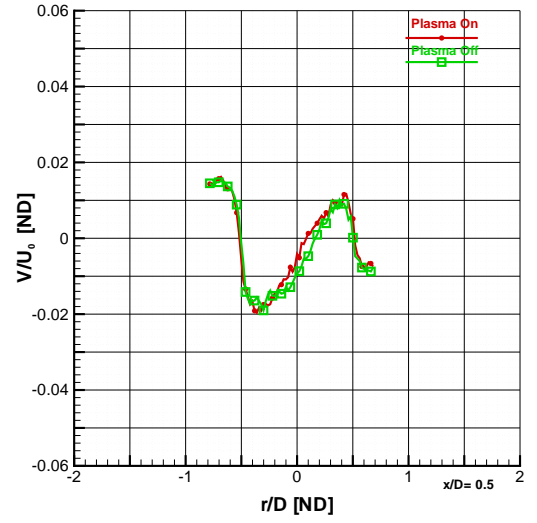
Table A.1: Test Conditions Reference

Case	x/D_e	M_1	Beginning Figure
A	0.5	0.69	A.1 on the next page
	1.5	0.68	A.4 on page 209
	2.3	0.66	A.7 on page 212
	3.2	0.65	A.10 on page 215
B	0.7	1.13	A.13 on page 218
	1.9	1.11	A.16 on page 221
	3.2	1.10	A.19 on page 224
	4.5	1.05	A.22 on page 227
C	0.9	2.04	A.25 on page 230
	2.7	2.02	A.28 on page 233
	4.4	2.05	A.31 on page 236
	6.2	1.93	A.34 on page 239
D	0.9	1.96	A.37 on page 242
	2.7	1.94	A.40 on page 245
	4.4	1.92	A.43 on page 248
	6.2	1.74	A.46 on page 251
E'	2.3	1.37	A.49 on page 254
	3.4	1.37	A.52 on page 257
	5.0	1.36	A.55 on page 260
	7.1	1.35	A.58 on page 263
	9.2	1.10	A.61 on page 266
	11.3	0.79	A.64 on page 269
F'	2.4	0.75	A.67 on page 272
	3.4	0.75	A.70 on page 275
	5.1	0.73	A.73 on page 278
	7.1	0.71	A.76 on page 281
	9.2	0.62	A.79 on page 284
	11.4	0.50	A.82 on page 287
G'	2.3	1.29	A.85 on page 290
	3.4	1.30	A.88 on page 293
	5.0	1.26	A.91 on page 296
	7.1	1.12	A.94 on page 299
	9.3	0.92	A.97 on page 302
	11.3	0.70	A.100 on page 305
H'	2.3	1.65	A.103 on page 308
	3.4	1.59	A.106 on page 311
	5.0	1.54	A.109 on page 314
	7.1	1.57	A.112 on page 317
	9.3	1.29	A.115 on page 320
	11.3	0.99	A.118 on page 323
B'	0.7	1.13	A.121 on page 326
	1.9	1.11	A.124 on page 329
	3.2	1.10	A.127 on page 332
	4.5	1.05	A.130 on page 335

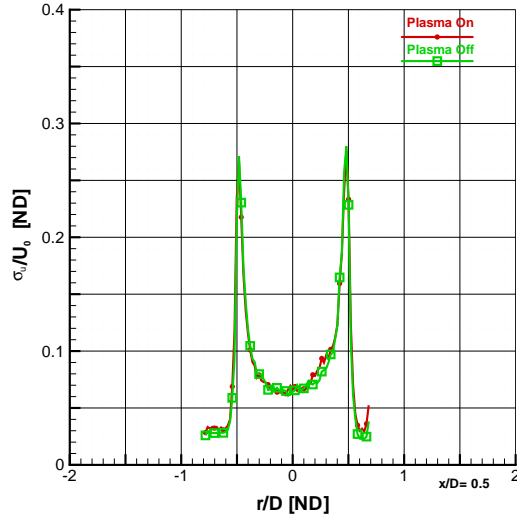
A.1 Mach 0.6 Converging-Diverging Nozzle at 9 Torr



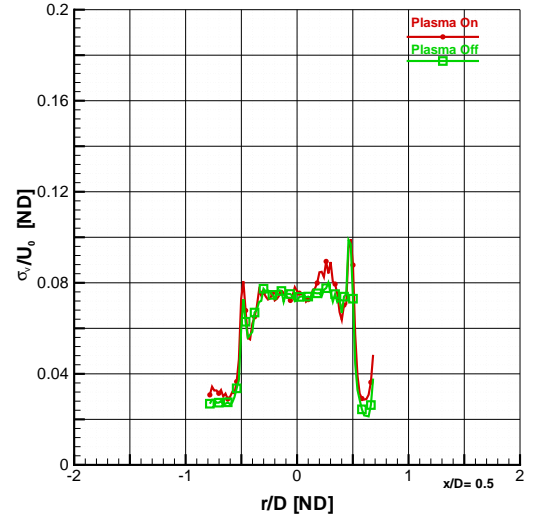
(a) Mean Axial Velocity, U/U_o



(b) Mean Tangential Velocity, V/U_o



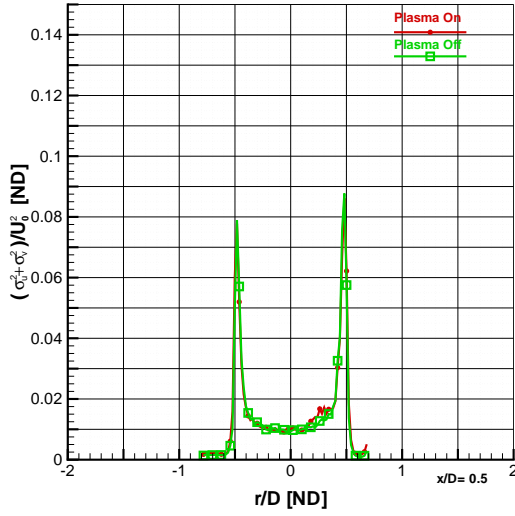
(c) Fluctuating Axial Velocity, σ_u/U_o



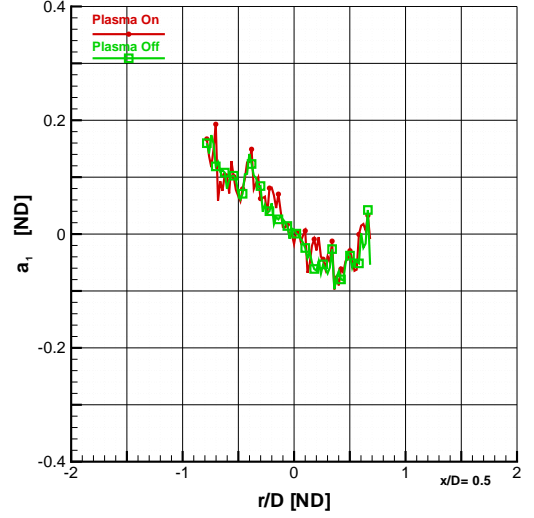
(d) Fluctuating Tangential Velocity, σ_v/U_o

Figure A.1: Comparison of Plasma Effects on Mean Velocity and Fluctuations: Case 613LINE1024

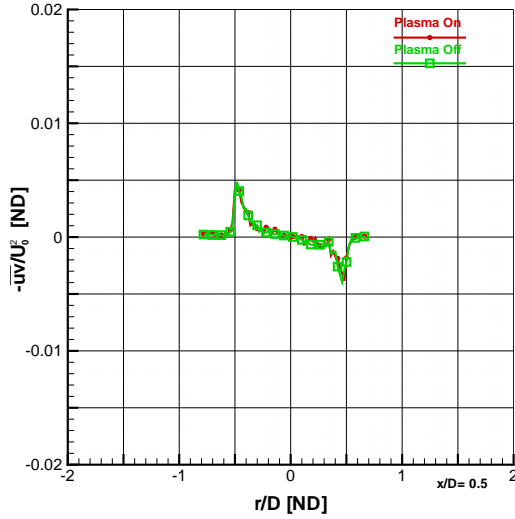
This is an investigation into the effect of plasma on a Mach 0.7 jet, 0.5 diameters from the anode face. The jet diameter is 20.8 mm. The four plots represented above are a comparison between plasma on in red versus plasma off in green. Figure A.1 (a) is non-dimensionalized axial velocity. For these figures, U_o is 229.3 m/s for the plasma off case and 228.4 m/s for the plasma on case. Figure A.1 (b) is the mean tangential component of the velocity. Figures A.1 (c) and (d) show the Reynolds normal stresses in the axial and tangential directions, respectively.



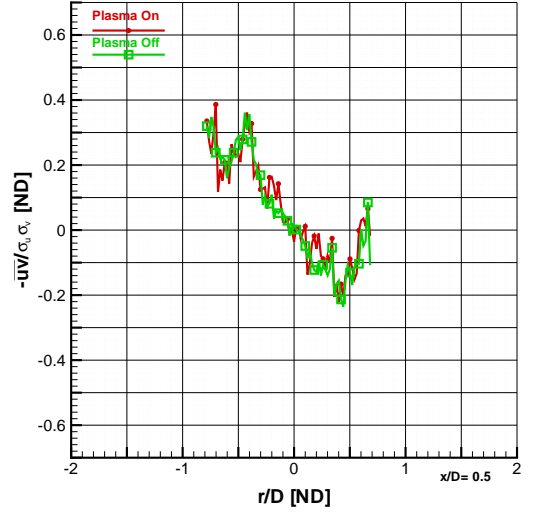
(a) Turbulent Kinetic Energy, $(\sigma_u^2 + \sigma_v^2)/U_o^2$



(b) Structural Parameter, $a_1 = -\overline{uv}/(\sigma_u^2 + \sigma_v^2)$



(c) Reynolds Shear Stress, \overline{uv}/U_o^2



(d) Correlation Coefficient of Reynolds Shear Stress, $-\overline{uv}/(\sigma_u \sigma_v)$

Figure A.2: Comparison of Plasma Effects on Second Moment Fluctuations: Case 613LINE1024

This is a continuing investigation into the effect of plasma on a Mach 0.7 jet, 0.5 diameters from the anode face. The jet diameter is 20.8 mm. The four plots represented above are a comparison between plasma on in red versus plasma off in green. Figure A.2 (a) is non-dimensionalized turbulent kinetic energy and panel (b) is the structural parameter a_1 . At this station, U_o is 229.3 m/s for the plasma off case and 228.4 m/s for the plasma on case. Figures A.2 (c) and (d) show the Reynolds shear stress and the correlation coefficient of Reynolds shear stress, respectively. The case identifiers for this comparison were 613cn-LINE1024 for plasma off and 613pn-LINE1024 for plasma on.

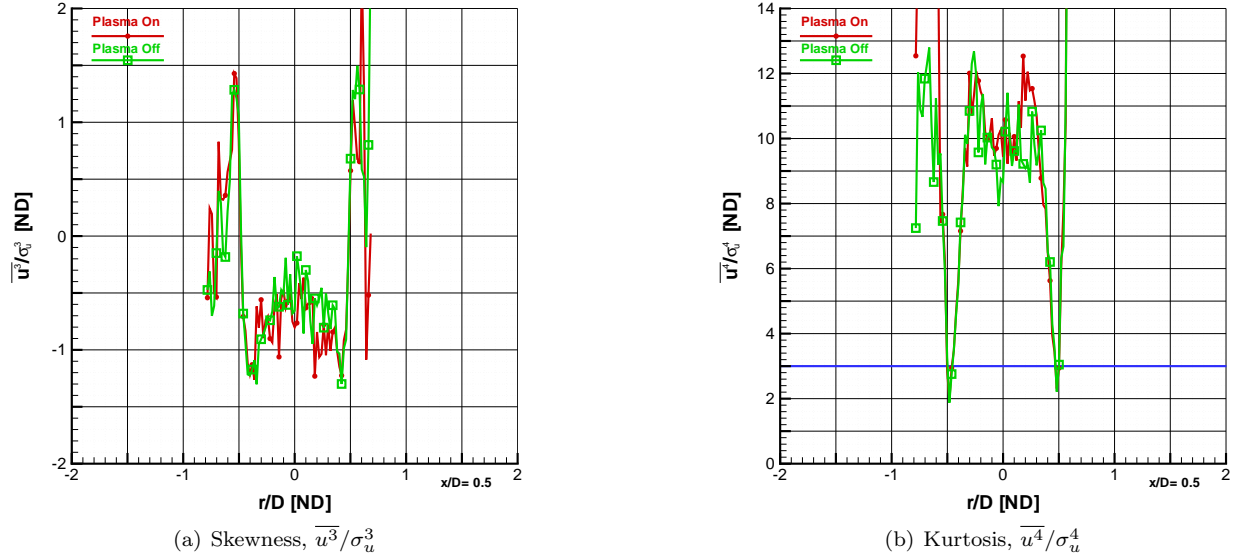
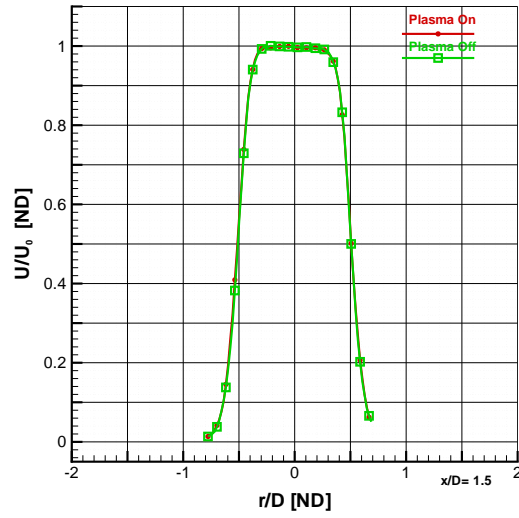
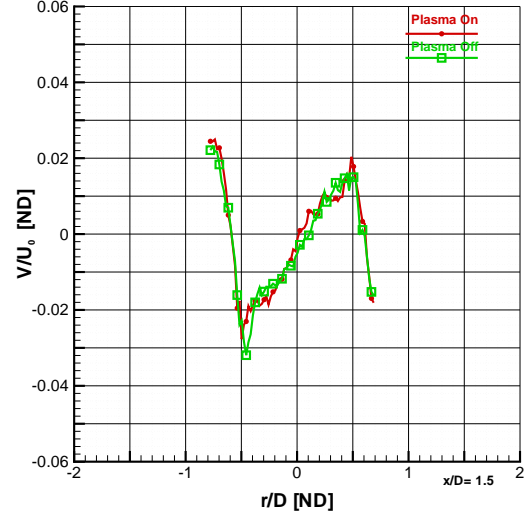


Figure A.3: Comparison of Plasma Effects on Skewness and Kurtosis: Case 613LINE1024

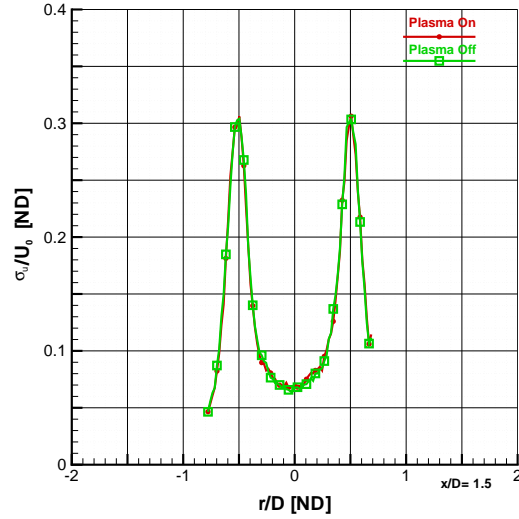
This is the final series of figures on the investigation into the effect of plasma on a Mach 0.7 jet, 0.5 diameters from the anode face. The jet diameter is 20.8 mm. The two plots represented above are a comparison between plasma on in red versus plasma off in green. The plasma off case is placed on top of the plasma on case, therefore making it easier to notice small changes between the two cases. Figure A.3 (a) (b) are the measurements of skewness and kurtosis (or flatness), respectively. A Gaussian distribution has skewness of zero, which indicates a distribution of fluctuations is symmetric about the mean. Positive skewness represents a shift toward the right tail (positive fluctuations), while negative skewness is shifted toward negative fluctuations. A Gaussian distribution has kurtosis of three, represented by the blue line. Values lower than three represent a distribution of velocity with higher peakedness than a Gaussian distribution. Conversely, values above three represent flatter distributions. The case identifiers for this comparison were 613cn-LINE1024 for plasma off and 613pn-LINE1024 for plasma on.



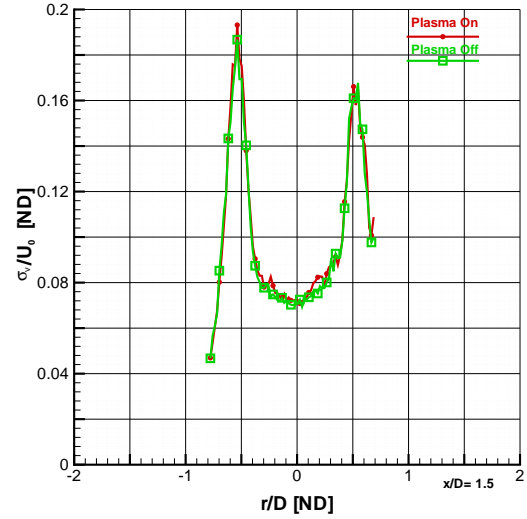
(a) Mean Axial Velocity, U/U_o



(b) Mean Tangential Velocity, V/U_o



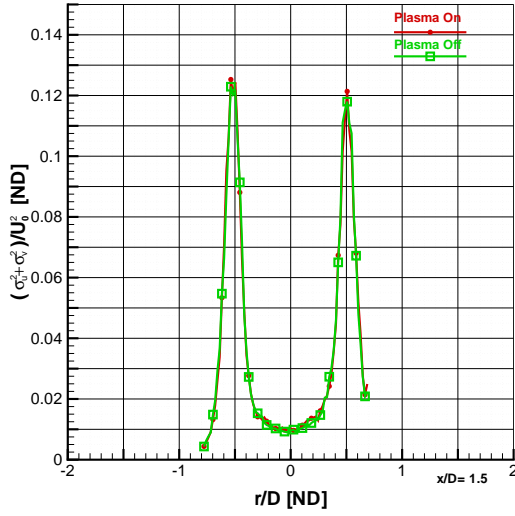
(c) Fluctuating Axial Velocity, σ_u/U_o



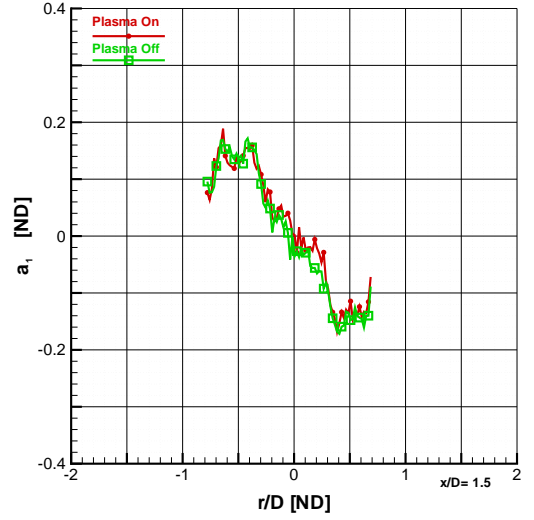
(d) Fluctuating Tangential Velocity, σ_v/U_o

Figure A.4: Comparison of Plasma Effects on Mean Velocity and Fluctuations: Case 613LINE3024

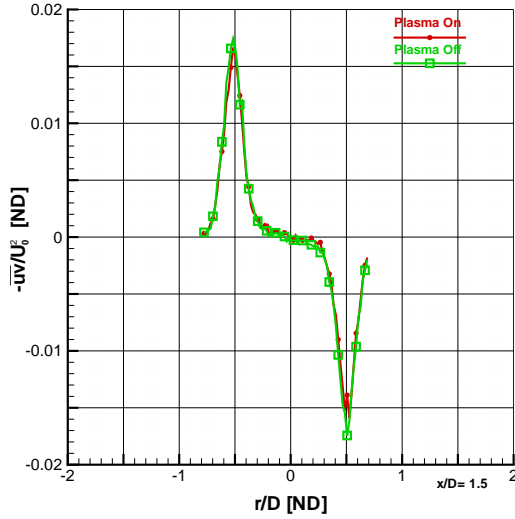
This is an investigation into the effect of plasma on a Mach 0.7 jet, 1.5 diameters from the anode face. The jet diameter is 20.8 mm. The four plots represented above are a comparison between plasma on in red versus plasma off in green. Figure A.4 (a) is non-dimensionalized axial velocity. For these figures, U_o is 226.4 m/s for the plasma off case and 224.9 m/s for the plasma on case. Figure A.4 (b) is the mean tangential component of the velocity. Figures A.4 (c) and (d) show the Reynolds normal stresses in the axial and tangential directions, respectively. The case identifiers for this comparison were 613cn-LINE3024 for plasma off and 613pn-LINE3024 for plasma on.



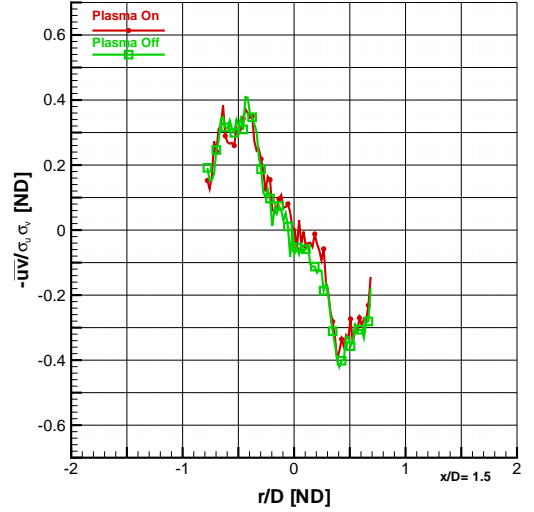
(a) Turbulent Kinetic Energy, $(\sigma_u^2 + \sigma_v^2)/U_o^2$



(b) Structural Parameter, $a_1 = -\overline{uv}/(\sigma_u^2 + \sigma_v^2)$



(c) Reynolds Shear Stress, \overline{uv}/U_o^2



(d) Correlation Coefficient of Reynolds Shear Stress, $-\overline{uv}/(\sigma_u \sigma_v)$

Figure A.5: Comparison of Plasma Effects on Second Moment Fluctuations: Case 613LINE3024

This is a continuing investigation into the effect of plasma on a Mach 0.7 jet, 1.5 diameters from the anode face. The jet diameter is 20.8 mm. The four plots represented above are a comparison between plasma on in red versus plasma off in green. Figure A.5 (a) is non-dimensionalized turbulent kinetic energy and panel (b) is the structural parameter a_1 . At this station, U_o is 226.4 m/s for the plasma off case and 224.9 m/s for the plasma on case. Figures A.5 (c) and (d) show the Reynolds shear stress and the correlation coefficient of Reynolds shear stress, respectively. The case identifiers for this comparison were 613cn-LINE3024 for plasma off and 613pn-LINE3024 for plasma on.

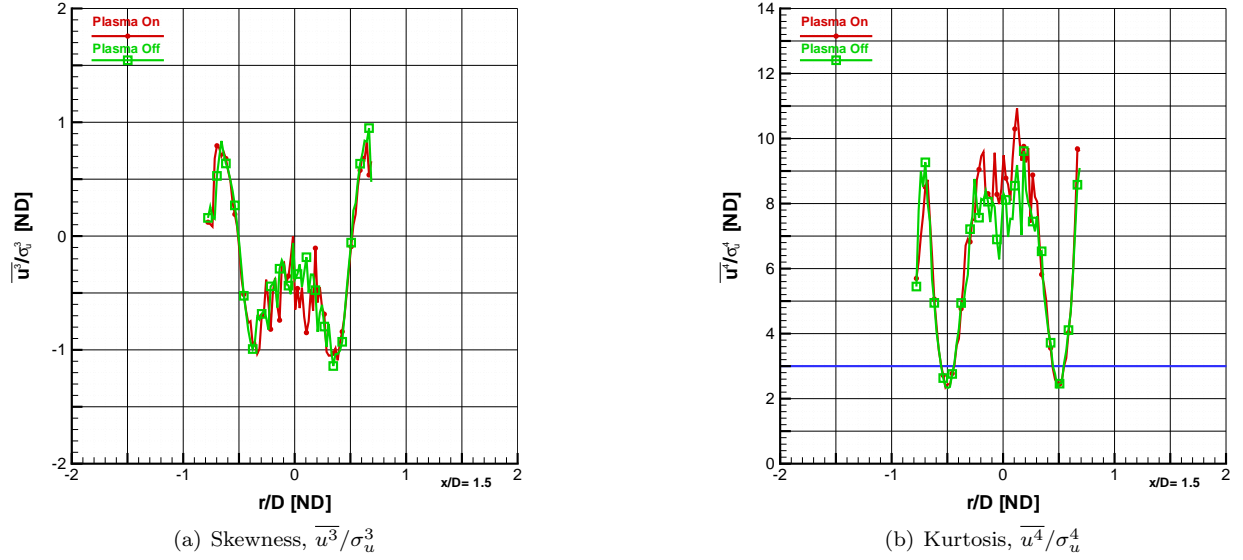
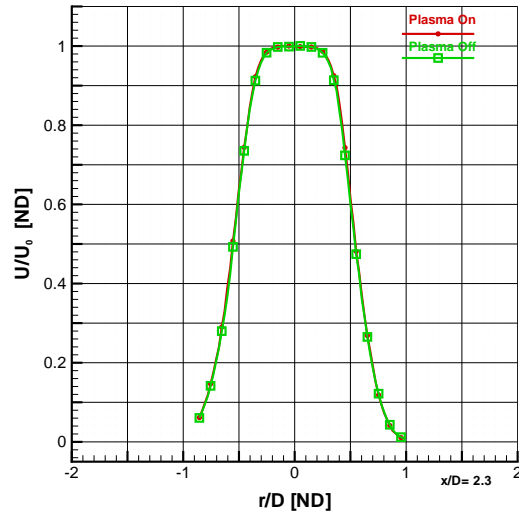
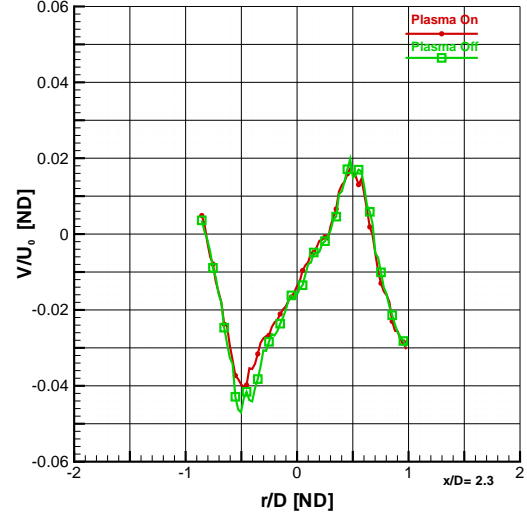


Figure A.6: Comparison of Plasma Effects on Skewness and Kurtosis: Case 613LINE3024

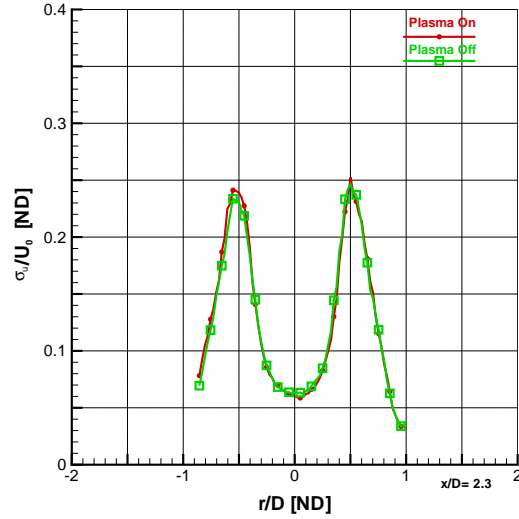
This is the final series of figures on the investigation into the effect of plasma on a Mach 0.7 jet, 1.5 diameters from the anode face. The jet diameter is 20.8 mm. The two plots represented above are a comparison between plasma on in red versus plasma off in green. The plasma off case is placed on top of the plasma on case, therefore making it easier to notice small changes between the two cases. Figure A.6 (a) (b) are the measurements of skewness and kurtosis (or flatness), respectively. A Gaussian distribution has skewness of zero, which indicates a distribution of fluctuations is symmetric about the mean. Positive skewness represents a shift toward the right tail (positive fluctuations), while negative skewness is shifted toward negative fluctuations. A Gaussian distribution has kurtosis of three, represented by the blue line. Values lower than three represent a distribution of velocity with higher peakedness than a Gaussian distribution. Conversely, values above three represent flatter distributions. The case identifiers for this comparison were 613cn-LINE3024 for plasma off and 613pn-LINE3024 for plasma on.



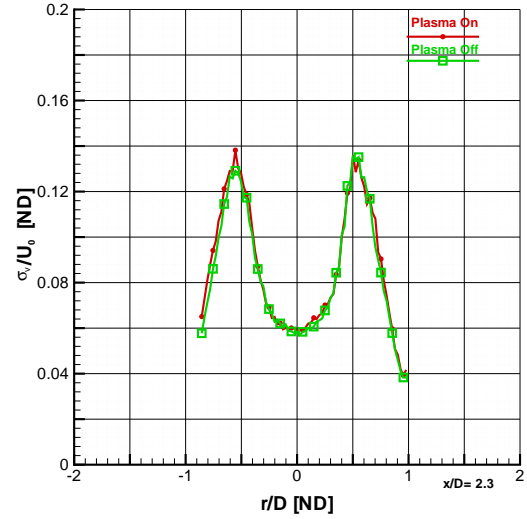
(a) Mean Axial Velocity, U/U_o



(b) Mean Tangential Velocity, V/U_o



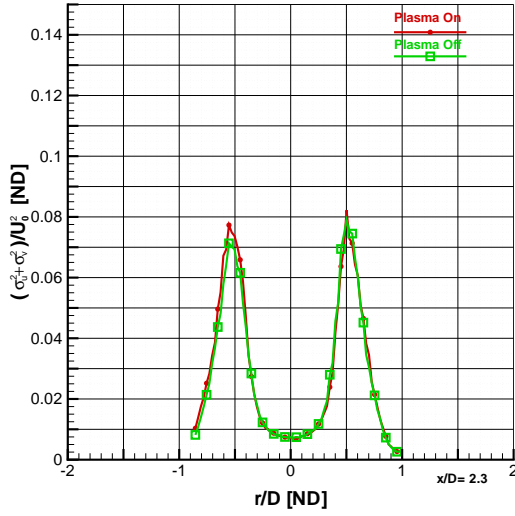
(c) Fluctuating Axial Velocity, σ_u/U_o



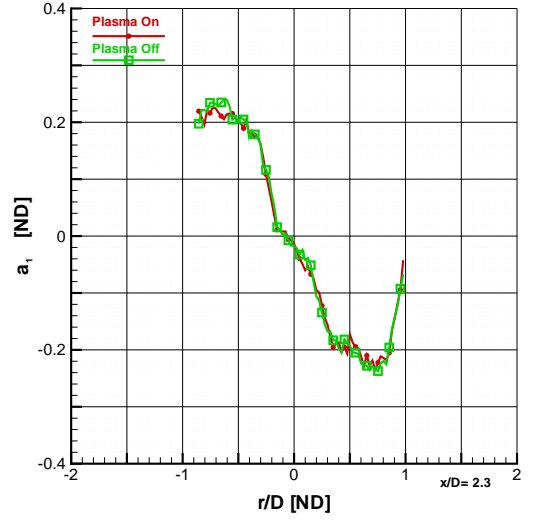
(d) Fluctuating Tangential Velocity, σ_v/U_o

Figure A.7: Comparison of Plasma Effects on Mean Velocity and Fluctuations: Case 604LINE4673

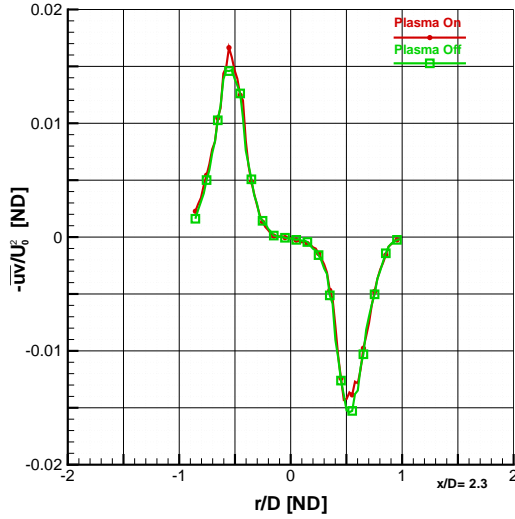
This is an investigation into the effect of plasma on a Mach 0.7 jet, 2.3 diameters from the anode face. The jet diameter is 20.8 mm. The four plots represented above are a comparison between plasma on in red versus plasma off in green. Figure A.7 (a) is non-dimensionalized axial velocity. For these figures, U_o is 219.3 m/s for the plasma off case and 219.0 m/s for the plasma on case. Figure A.7 (b) is the mean tangential component of the velocity. Figures A.7 (c) and (d) show the Reynolds normal stresses in the axial and tangential directions, respectively. The case identifiers for this comparison were 604cnc-LINE4673 for plasma off and 604pnc-LINE4673 for plasma on.



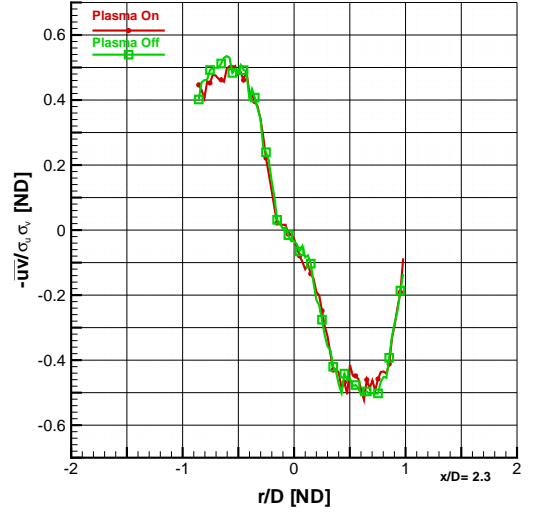
(a) Turbulent Kinetic Energy, $(\sigma_u^2 + \sigma_v^2)/U_o^2$



(b) Structural Parameter, $a_1 = -\overline{uv}/(\sigma_u^2 + \sigma_v^2)$



(c) Reynolds Shear Stress, \overline{uv}/U_o^2



(d) Correlation Coefficient of Reynolds Shear Stress, $-\overline{uv}/(\sigma_u \sigma_v)$

Figure A.8: Comparison of Plasma Effects on Second Moment Fluctuations: Case 604LINE4673

This is a continuing investigation into the effect of plasma on a Mach 0.7 jet, 2.3 diameters from the anode face. The jet diameter is 20.8 mm. The four plots represented above are a comparison between plasma on in red versus plasma off in green. Figure A.8 (a) is non-dimensionalized turbulent kinetic energy and panel (b) is the structural parameter a_1 . At this station, U_o is 219.3 m/s for the plasma off case and 219.0 m/s for the plasma on case. Figures A.8 (c) and (d) show the Reynolds shear stress and the correlation coefficient of Reynolds shear stress, respectively. The case identifiers for this comparison were 604cnc-LINE4673 for plasma off and 604pnc-LINE4673 for plasma on.

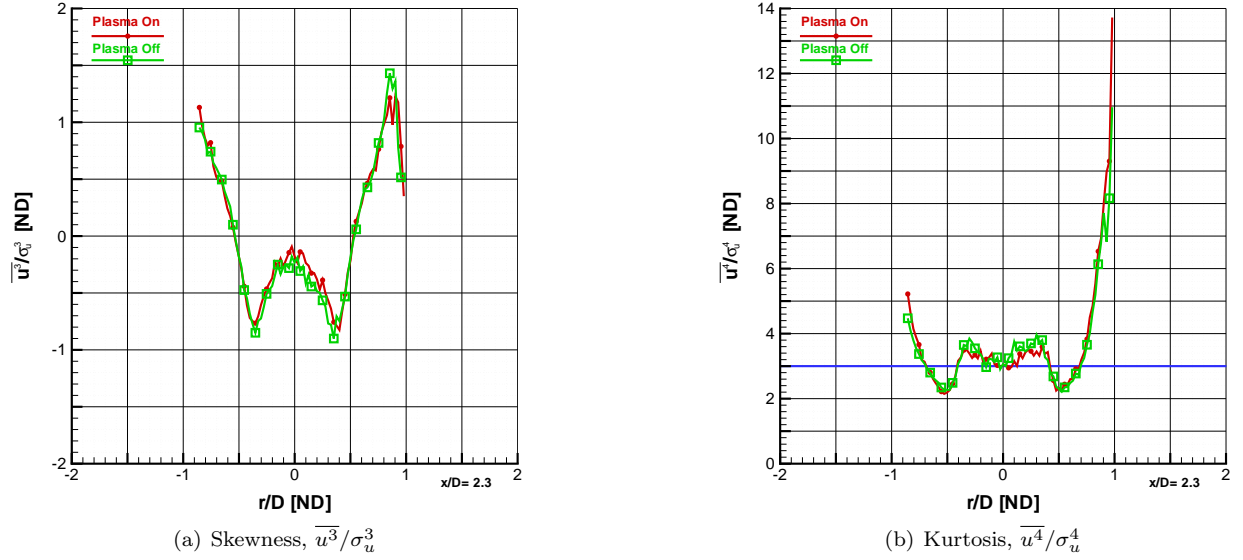
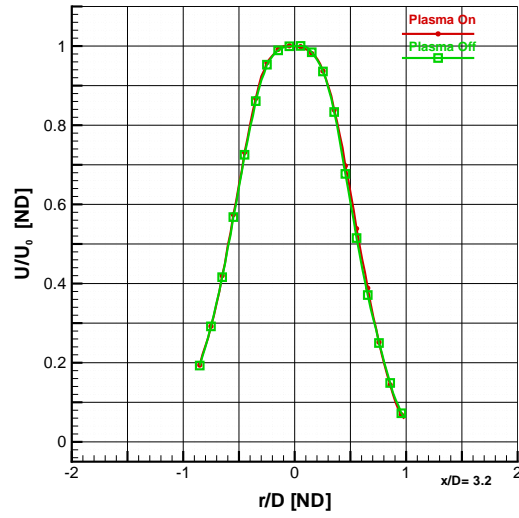
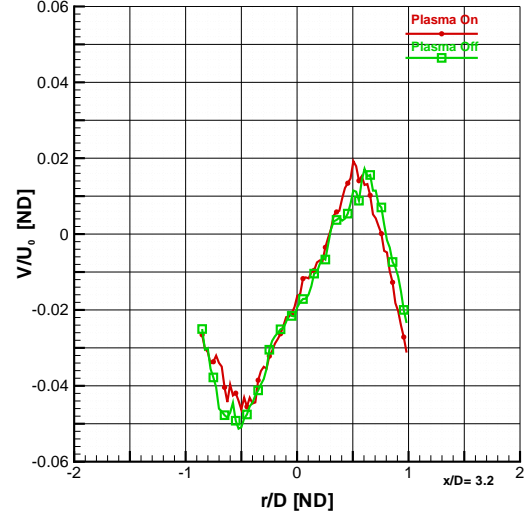


Figure A.9: Comparison of Plasma Effects on Skewness and Kurtosis: Case 604LINE4673

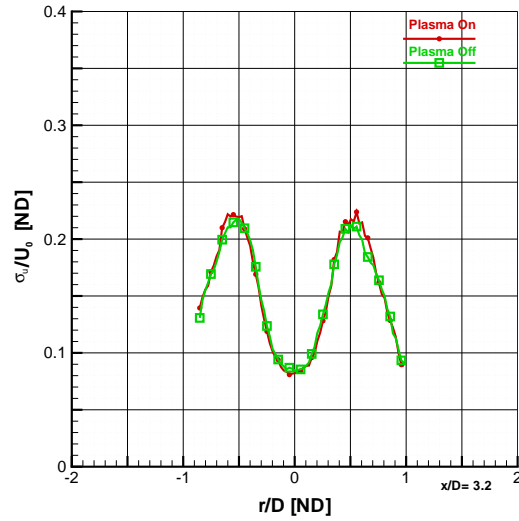
This is the final series of figures on the investigation into the effect of plasma on a Mach 0.7 jet, 2.3 diameters from the anode face. The jet diameter is 20.8 mm. The two plots represented above are a comparison between plasma on in red versus plasma off in green. The plasma off case is placed on top of the plasma on case, therefore making it easier to notice small changes between the two cases. Figure A.9 (a) (b) are the measurements of skewness and kurtosis (or flatness), respectively. A Gaussian distribution has skewness of zero, which indicates a distribution of fluctuations is symmetric about the mean. Positive skewness represents a shift toward the right tail (positive fluctuations), while negative skewness is shifted toward negative fluctuations. A Gaussian distribution has kurtosis of three, represented by the blue line. Values lower than three represent a distribution of velocity with higher peakedness than a Gaussian distribution. Conversely, values above three represent flatter distributions. The case identifiers for this comparison were 604cnc-LINE4673 for plasma off and 604pnc-LINE4673 for plasma on.



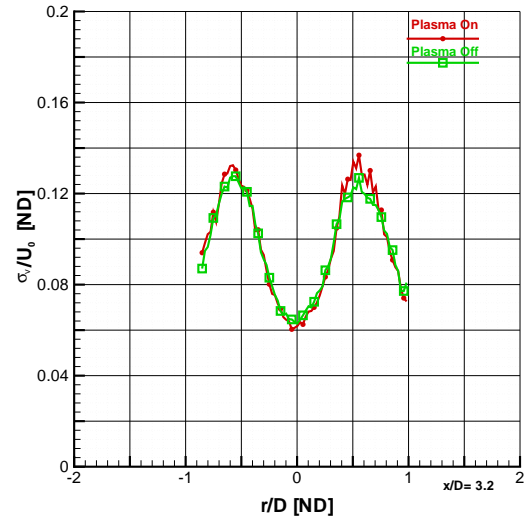
(a) Mean Axial Velocity, U/U_o



(b) Mean Tangential Velocity, V/U_o



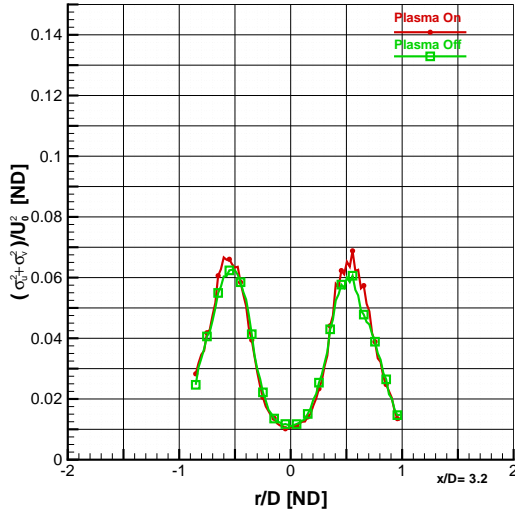
(c) Fluctuating Axial Velocity, σ_u/U_o



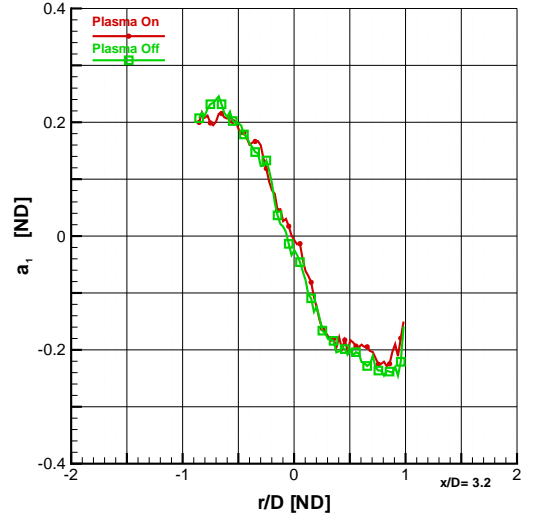
(d) Fluctuating Tangential Velocity, σ_v/U_o

Figure A.10: Comparison of Plasma Effects on Mean Velocity and Fluctuations: Case 604LINE6655

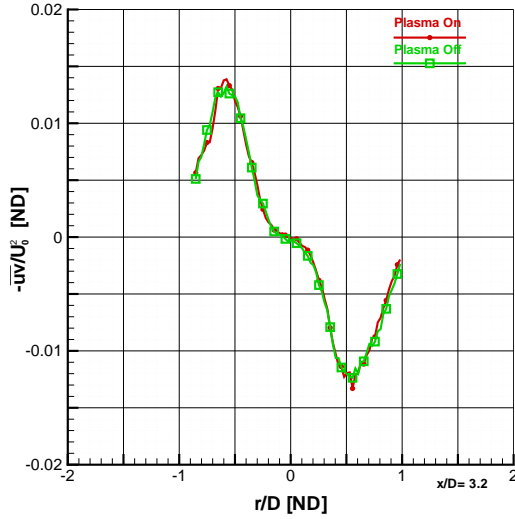
This is an investigation into the effect of plasma on a Mach 0.7 jet, 3.2 diameters from the anode face. The jet diameter is 20.8 mm. The four plots represented above are a comparison between plasma on in red versus plasma off in green. Figure A.10 (a) is non-dimensionalized axial velocity. For these figures, U_o is 215.4 m/s for the plasma off case and 215.5 m/s for the plasma on case. Figure A.10 (b) is the mean tangential component of the velocity. Figures A.10 (c) and (d) show the Reynolds normal stresses in the axial and tangential directions, respectively. The case identifiers for this comparison were 604cnc-LINE6655 for plasma off and 604pnc-LINE6655 for plasma on.



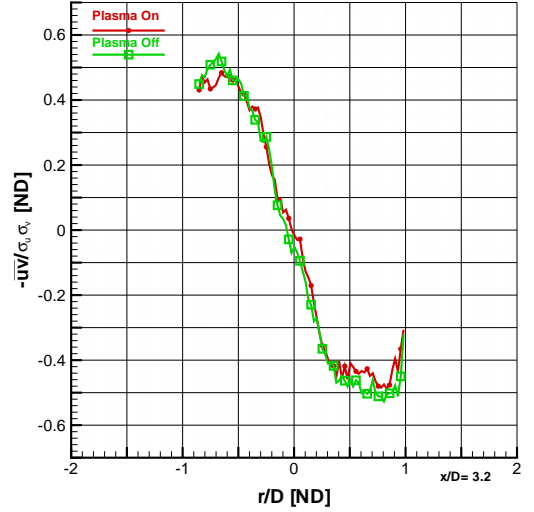
(a) Turbulent Kinetic Energy, $(\sigma_u^2 + \sigma_v^2)/U_o^2$



(b) Structural Parameter, $a_1 = -\overline{uv}/(\sigma_u^2 + \sigma_v^2)$



(c) Reynolds Shear Stress, \overline{uv}/U_o^2



(d) Correlation Coefficient of Reynolds Shear Stress, $-\overline{uv}/(\sigma_u \sigma_v)$

Figure A.11: Comparison of Plasma Effects on Second Moment Fluctuations: Case 604LINE6655

This is a continuing investigation into the effect of plasma on a Mach 0.7 jet, 3.2 diameters from the anode face. The jet diameter is 20.8 mm. The four plots represented above are a comparison between plasma on in red versus plasma off in green. Figure A.11 (a) is non-dimensionalized turbulent kinetic energy and panel (b) is the structural parameter a_1 . At this station, U_o is 215.4 m/s for the plasma off case and 215.5 m/s for the plasma on case. Figures A.11 (c) and (d) show the Reynolds shear stress and the correlation coefficient of Reynolds shear stress, respectively. The case identifiers for this comparison were 604cnc-LINE6655 for plasma off and 604pnc-LINE6655 for plasma on.

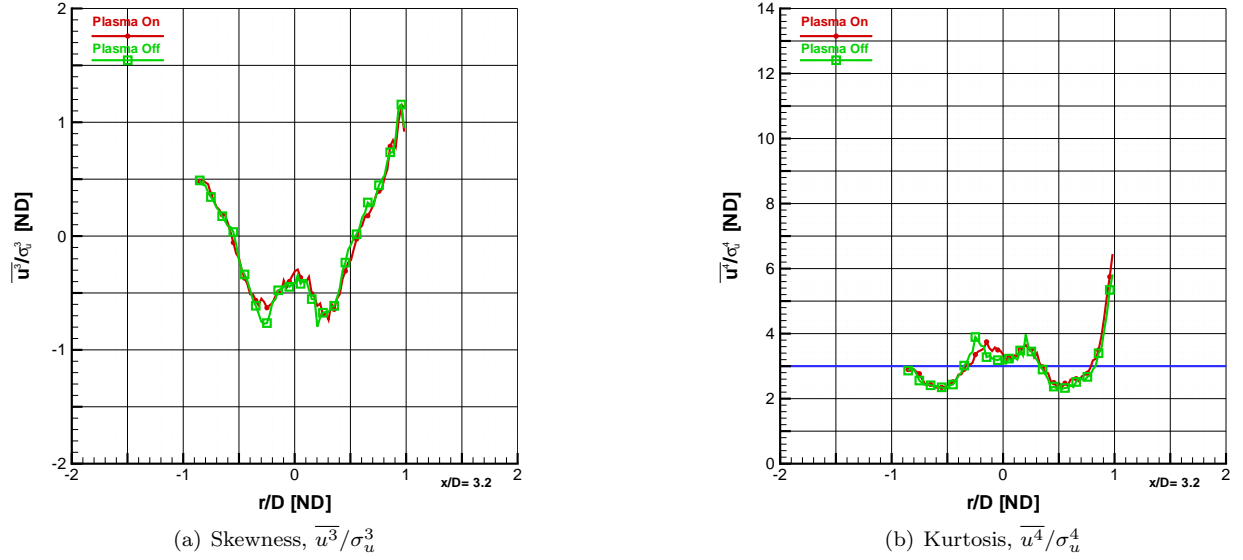
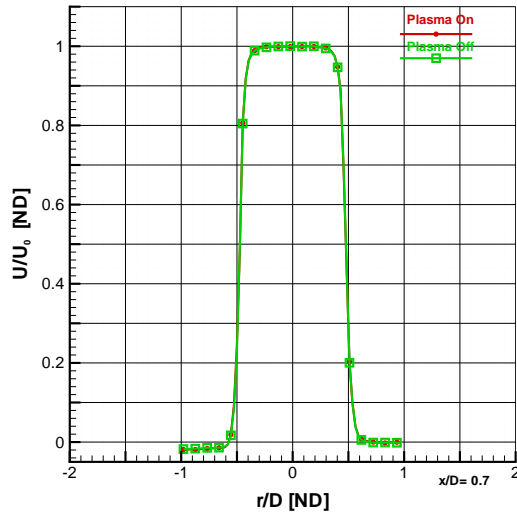


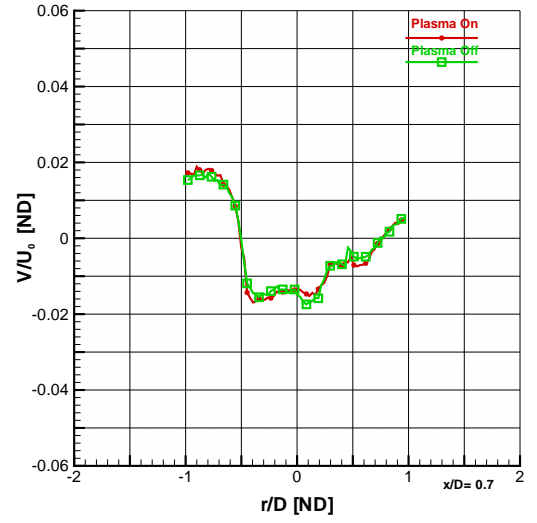
Figure A.12: Comparison of Plasma Effects on Skewness and Kurtosis: Case 604LINE6655

This is the final series of figures on the investigation into the effect of plasma on a Mach 0.7 jet, 3.2 diameters from the anode face. The jet diameter is 20.8 mm. The two plots represented above are a comparison between plasma on in red versus plasma off in green. The plasma off case is placed on top of the plasma on case, therefore making it easier to notice small changes between the two cases. Figure A.12 (a) (b) are the measurements of skewness and kurtosis (or flatness), respectively. A Gaussian distribution has skewness of zero, which indicates a distribution of fluctuations is symmetric about the mean. Positive skewness represents a shift toward the right tail (positive fluctuations), while negative skewness is shifted toward negative fluctuations. A Gaussian distribution has kurtosis of three, represented by the blue line. Values lower than three represent a distribution of velocity with higher peakedness than a Gaussian distribution. Conversely, values above three represent flatter distributions. The case identifiers for this comparison were 604cnc-LINE6655 for plasma off and 604pnc-LINE6655 for plasma on.

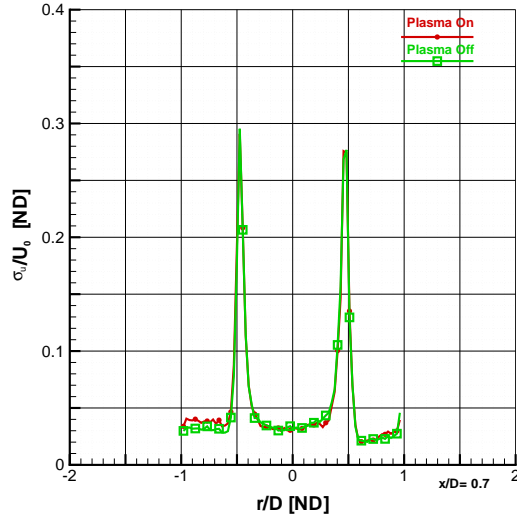
A.2 Mach 1.1 Converging-Diverging Nozzle at 9 Torr



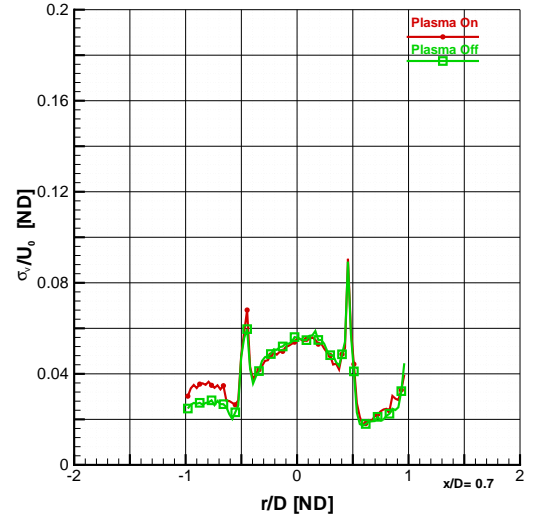
(a) Mean Axial Velocity, U/U_o



(b) Mean Tangential Velocity, V/U_o



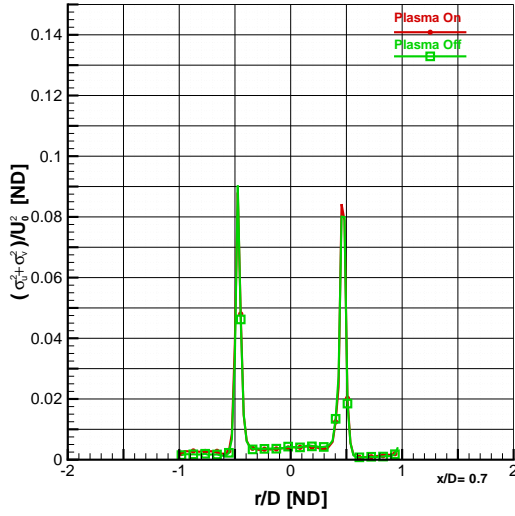
(c) Fluctuating Axial Velocity, σ_u/U_o



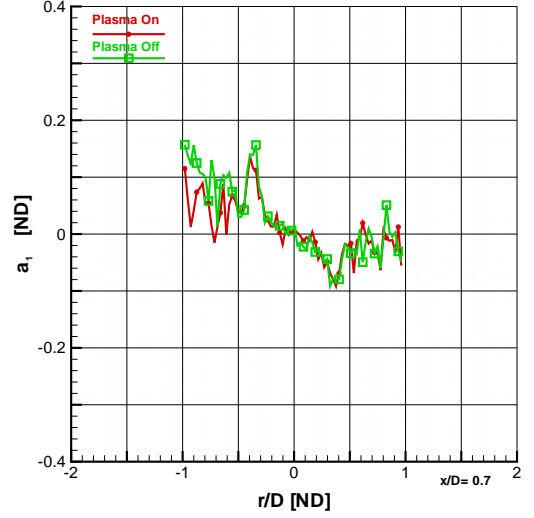
(d) Fluctuating Tangential Velocity, σ_v/U_o

Figure A.13: Comparison of Plasma Effects on Mean Velocity and Fluctuations: Case 611LINE1051

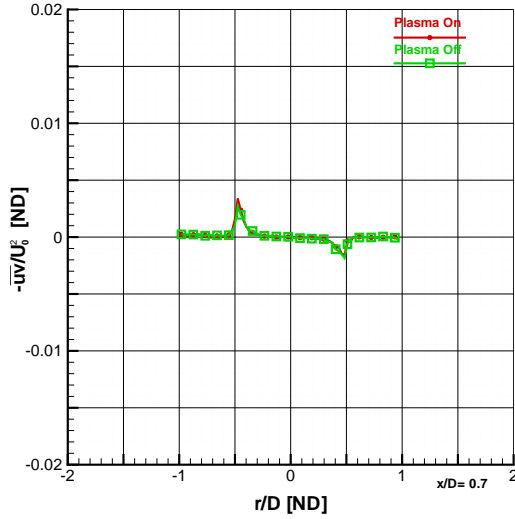
This is an investigation into the effect of plasma on a Mach 1.1 jet, 0.7 diameters from the anode face. The jet diameter is 15.7 mm. The four plots represented above are a comparison between plasma on in red versus plasma off in green. Figure A.13 (a) is non-dimensionalized axial velocity. For these figures, U_o is 350.1 m/s for the plasma off case and 350.2 m/s for the plasma on case. Figure A.13 (b) is the mean tangential component of the velocity. Figures A.13 (c) and (d) show the Reynolds normal stresses in the axial and tangential directions, respectively.



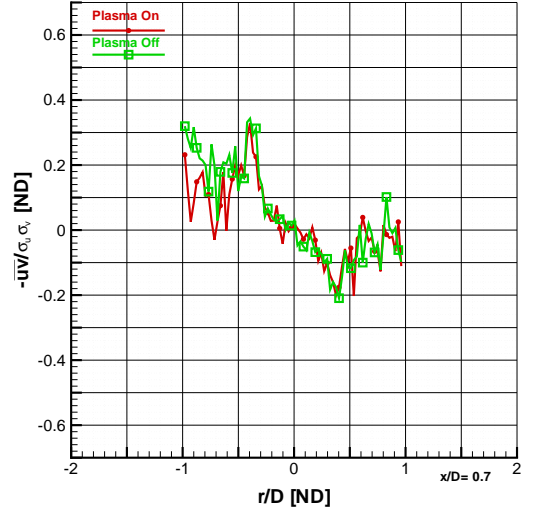
(a) Turbulent Kinetic Energy, $(\sigma_u^2 + \sigma_v^2)/U_o^2$



(b) Structural Parameter, $a_1 = -\overline{uv}/(\sigma_u^2 + \sigma_v^2)$



(c) Reynolds Shear Stress, \overline{uv}/U_o^2



(d) Correlation Coefficient of Reynolds Shear Stress, $-\overline{uv}/(\sigma_u \sigma_v)$

Figure A.14: Comparison of Plasma Effects on Second Moment Fluctuations: Case 611LINE1051

This is a continuing investigation into the effect of plasma on a Mach 1.1 jet, 0.7 diameters from the anode face. The jet diameter is 15.7 mm. The four plots represented above are a comparison between plasma on in red versus plasma off in green. Figure A.14 (a) is non-dimensionalized turbulent kinetic energy and panel (b) is the structural parameter a_1 . At this station, U_o is 350.1 m/s for the plasma off case and 350.2 m/s for the plasma on case. Figures A.14 (c) and (d) show the Reynolds shear stress and the correlation coefficient of Reynolds shear stress, respectively. The case identifiers for this comparison were 611cn-LINE1051 for plasma off and 611pn-LINE1051 for plasma on.

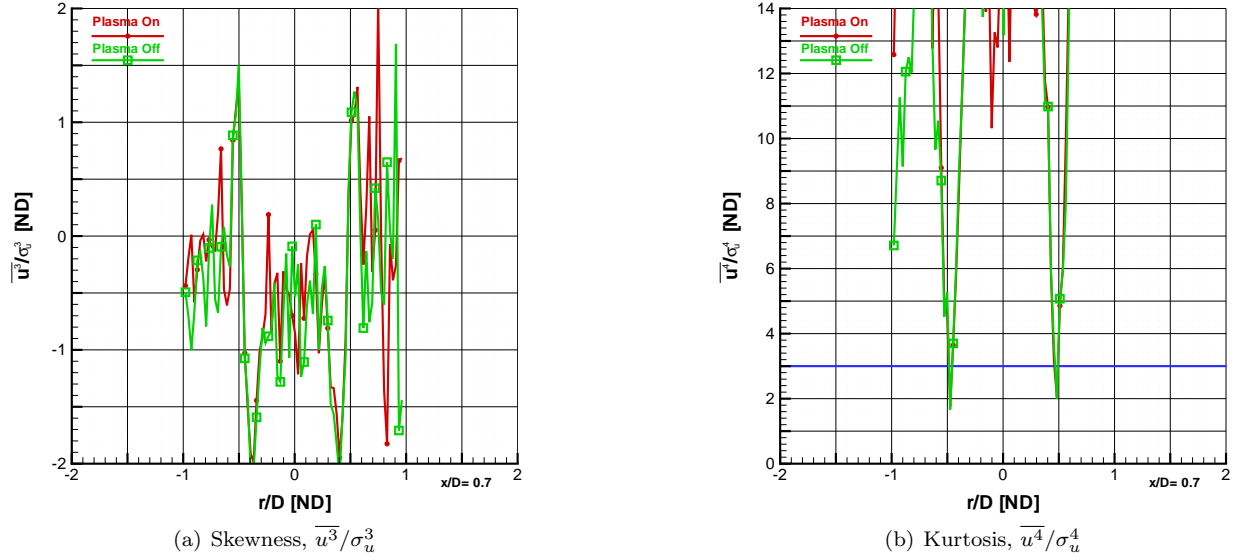
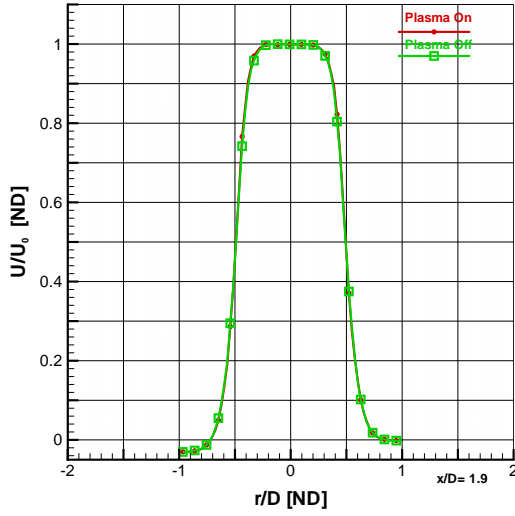
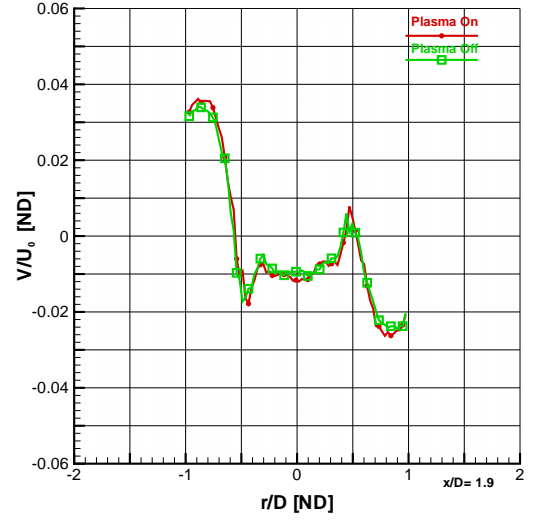


Figure A.15: Comparison of Plasma Effects on Skewness and Kurtosis: Case 611LINE1051

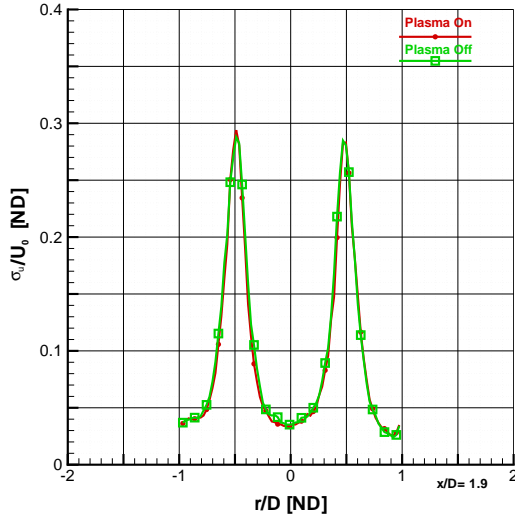
This is the final series of figures on the investigation into the effect of plasma on a Mach 1.1 jet, 0.7 diameters from the anode face. The jet diameter is 15.7 mm. The two plots represented above are a comparison between plasma on in red versus plasma off in green. The plasma off case is placed on top of the plasma on case, therefore making it easier to notice small changes between the two cases. Figure A.15 (a) (b) are the measurements of skewness and kurtosis (or flatness), respectively. A Gaussian distribution has skewness of zero, which indicates a distribution of fluctuations is symmetric about the mean. Positive skewness represents a shift toward the right tail (positive fluctuations), while negative skewness is shifted toward negative fluctuations. A Gaussian distribution has kurtosis of three, represented by the blue line. Values lower than three represent a distribution of velocity with higher peakedness than a Gaussian distribution. Conversely, values above three represent flatter distributions. The case identifiers for this comparison were 611cn-LINE1051 for plasma off and 611pn-LINE1051 for plasma on.



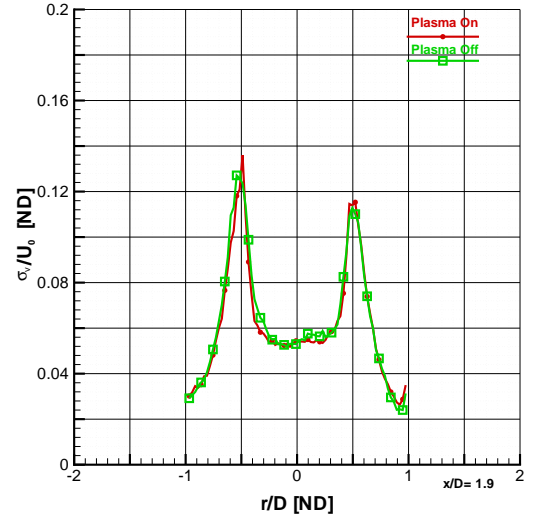
(a) Mean Axial Velocity, U/U_o



(b) Mean Tangential Velocity, V/U_o



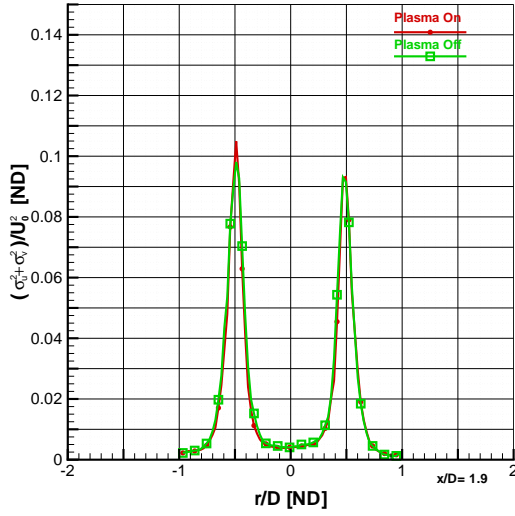
(c) Fluctuating Axial Velocity, σ_u/U_o



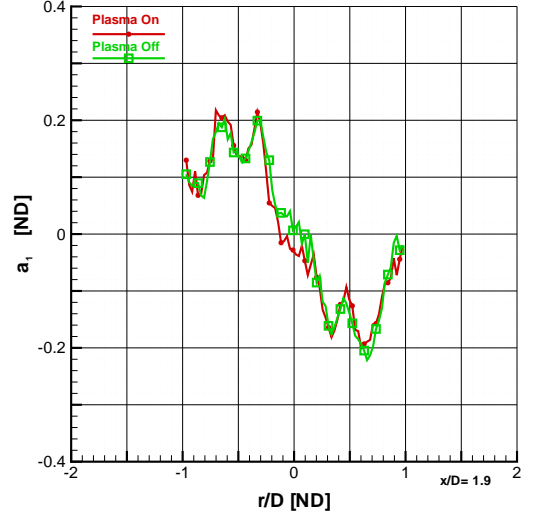
(d) Fluctuating Tangential Velocity, σ_v/U_o

Figure A.16: Comparison of Plasma Effects on Mean Velocity and Fluctuations: Case 611LINE3051

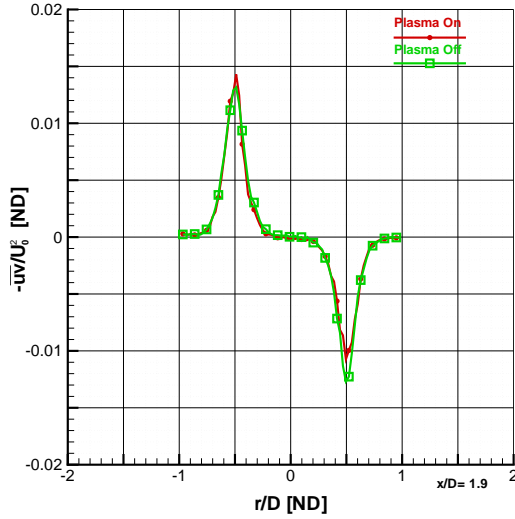
This is an investigation into the effect of plasma on a Mach 1.1 jet, 1.9 diameters from the anode face. The jet diameter is 15.7 mm. The four plots represented above are a comparison between plasma on in red versus plasma off in green. Figure A.16 (a) is non-dimensionalized axial velocity. For these figures, U_o is 343.9 m/s for the plasma off case and 344.9 m/s for the plasma on case. Figure A.16 (b) is the mean tangential component of the velocity. Figures A.16 (c) and (d) show the Reynolds normal stresses in the axial and tangential directions, respectively. The case identifiers for this comparison were 611cn-LINE3051 for plasma off and 611pn-LINE3051 for plasma on.



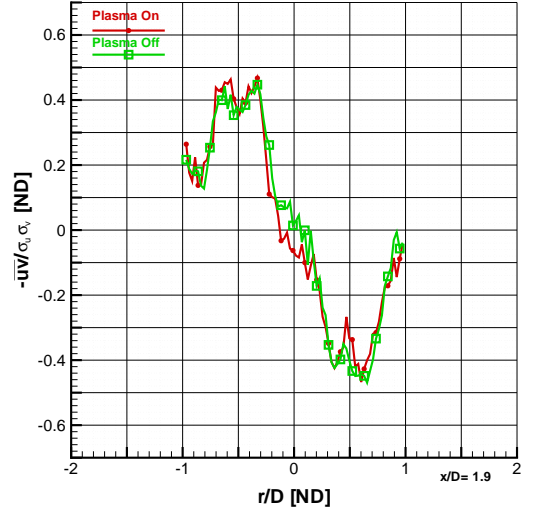
(a) Turbulent Kinetic Energy, $(\sigma_u^2 + \sigma_v^2)/U_o^2$



(b) Structural Parameter, $a_1 = -\overline{uv}/(\sigma_u^2 + \sigma_v^2)$



(c) Reynolds Shear Stress, \overline{uv}/U_o^2



(d) Correlation Coefficient of Reynolds Shear Stress, $-\overline{uv}/(\sigma_u \sigma_v)$

Figure A.17: Comparison of Plasma Effects on Second Moment Fluctuations: Case 611LINE3051

This is a continuing investigation into the effect of plasma on a Mach 1.1 jet, 1.9 diameters from the anode face. The jet diameter is 15.7 mm. The four plots represented above are a comparison between plasma on in red versus plasma off in green. Figure A.17 (a) is non-dimensionalized turbulent kinetic energy and panel (b) is the structural parameter a_1 . At this station, U_o is 343.9 m/s for the plasma off case and 344.9 m/s for the plasma on case. Figures A.17 (c) and (d) show the Reynolds shear stress and the correlation coefficient of Reynolds shear stress, respectively. The case identifiers for this comparison were 611cn-LINE3051 for plasma off and 611pn-LINE3051 for plasma on.

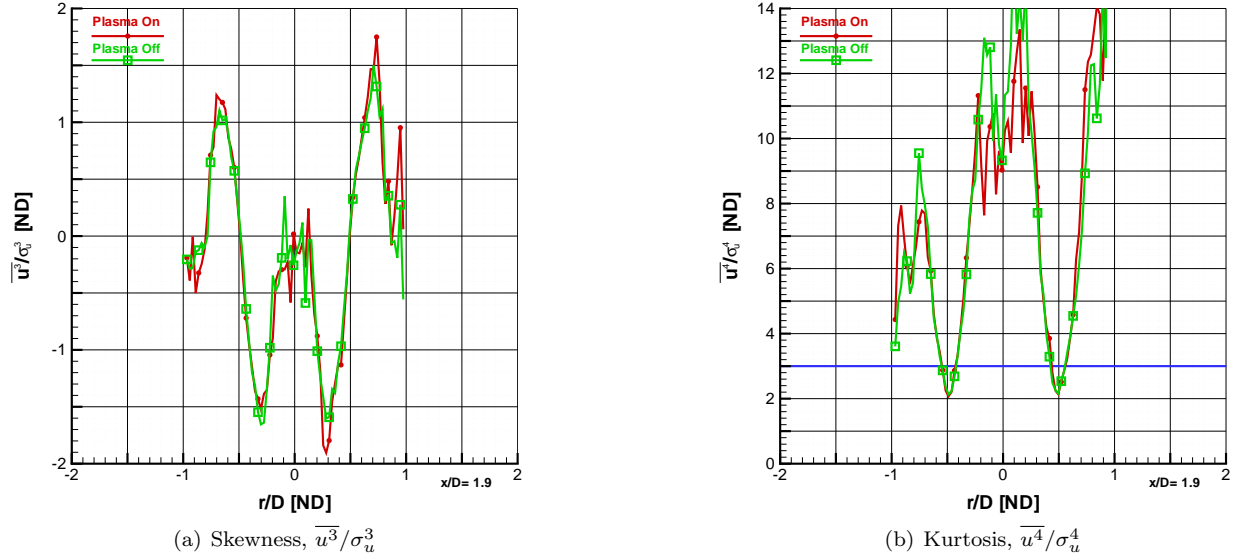
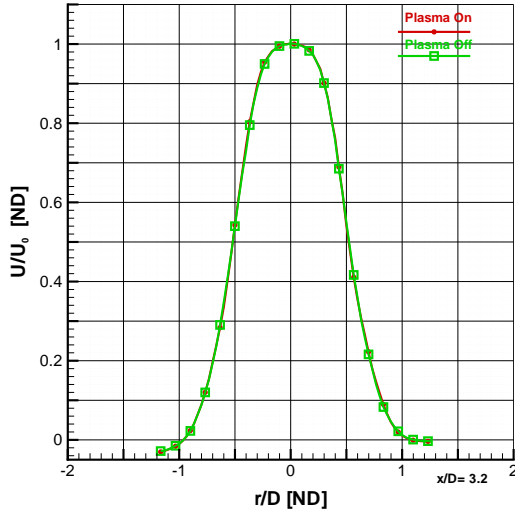
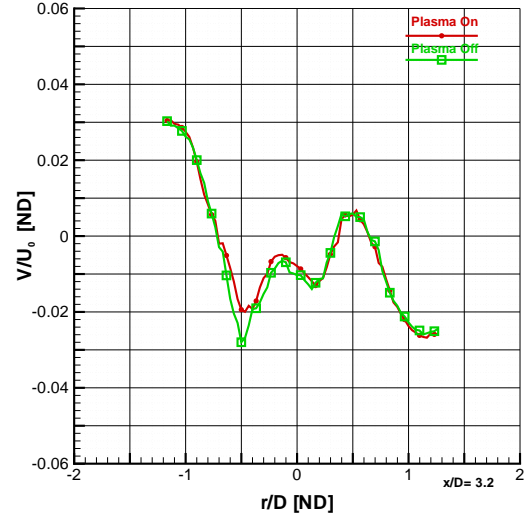


Figure A.18: Comparison of Plasma Effects on Skewness and Kurtosis: Case 611LINE3051

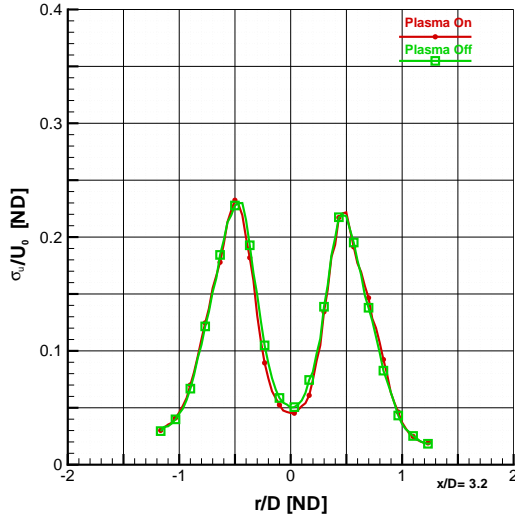
This is the final series of figures on the investigation into the effect of plasma on a Mach 1.1 jet, 1.9 diameters from the anode face. The jet diameter is 15.7 mm. The two plots represented above are a comparison between plasma on in red versus plasma off in green. The plasma off case is placed on top of the plasma on case, therefore making it easier to notice small changes between the two cases. Figure A.18 (a) (b) are the measurements of skewness and kurtosis (or flatness), respectively. A Gaussian distribution has skewness of zero, which indicates a distribution of fluctuations is symmetric about the mean. Positive skewness represents a shift toward the right tail (positive fluctuations), while negative skewness is shifted toward negative fluctuations. A Gaussian distribution has kurtosis of three, represented by the blue line. Values lower than three represent a distribution of velocity with higher peakedness than a Gaussian distribution. Conversely, values above three represent flatter distributions. The case identifiers for this comparison were 611cn-LINE3051 for plasma off and 611pn-LINE3051 for plasma on.



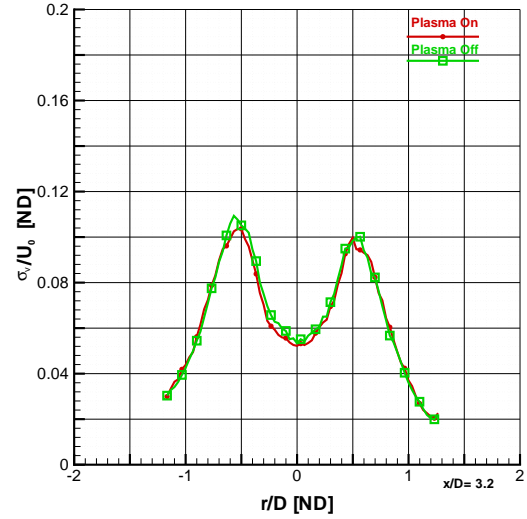
(a) Mean Axial Velocity, U/U_o



(b) Mean Tangential Velocity, V/U_o



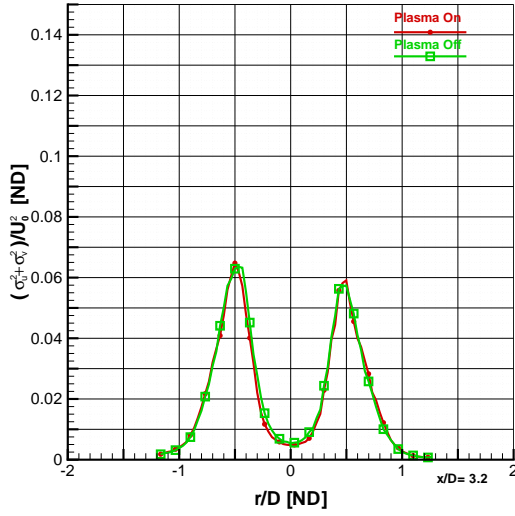
(c) Fluctuating Axial Velocity, σ_u/U_o



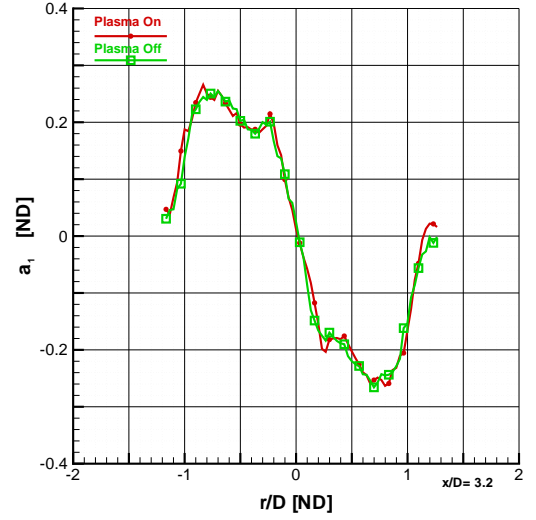
(d) Fluctuating Tangential Velocity, σ_v/U_o

Figure A.19: Comparison of Plasma Effects on Mean Velocity and Fluctuations: Case 603LINE5011

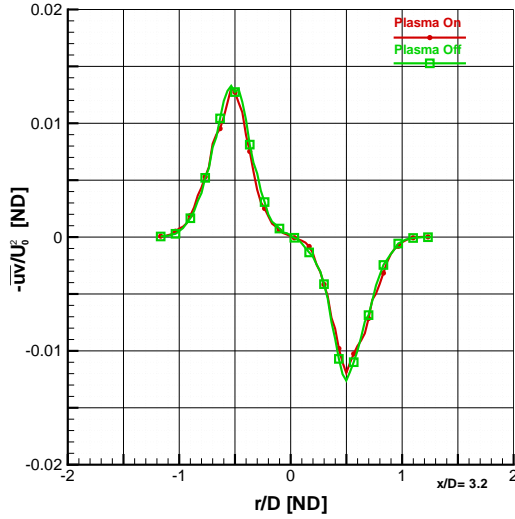
This is an investigation into the effect of plasma on a Mach 1.1 jet, 3.2 diameters from the anode face. The jet diameter is 15.7 mm. The four plots represented above are a comparison between plasma on in red versus plasma off in green. Figure A.19 (a) is non-dimensionalized axial velocity. For these figures, U_o is 341.5 m/s for the plasma off case and 341.5 m/s for the plasma on case. Figure A.19 (b) is the mean tangential component of the velocity. Figures A.19 (c) and (d) show the Reynolds normal stresses in the axial and tangential directions, respectively. The case identifiers for this comparison were 603cnc-LINE5011 for plasma off and 603pnc-LINE5011 for plasma on.



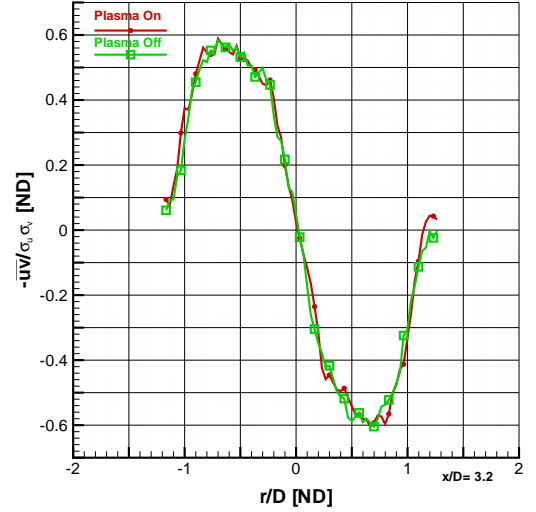
(a) Turbulent Kinetic Energy, $(\sigma_u^2 + \sigma_v^2)/U_o^2$



(b) Structural Parameter, $a_1 = -\overline{uv}/(\sigma_u^2 + \sigma_v^2)$



(c) Reynolds Shear Stress, \overline{uv}/U_o^2



(d) Correlation Coefficient of Reynolds Shear Stress, $-\overline{uv}/(\sigma_u \sigma_v)$

Figure A.20: Comparison of Plasma Effects on Second Moment Fluctuations: Case 603LINE5011

This is a continuing investigation into the effect of plasma on a Mach 1.1 jet, 3.2 diameters from the anode face. The jet diameter is 15.7 mm. The four plots represented above are a comparison between plasma on in red versus plasma off in green. Figure A.20 (a) is non-dimensionalized turbulent kinetic energy and panel (b) is the structural parameter a_1 . At this station, U_o is 341.5 m/s for the plasma off case and 341.5 m/s for the plasma on case. Figures A.20 (c) and (d) show the Reynolds shear stress and the correlation coefficient of Reynolds shear stress, respectively. The case identifiers for this comparison were 603cnc-LINE5011 for plasma off and 603pnc-LINE5011 for plasma on.

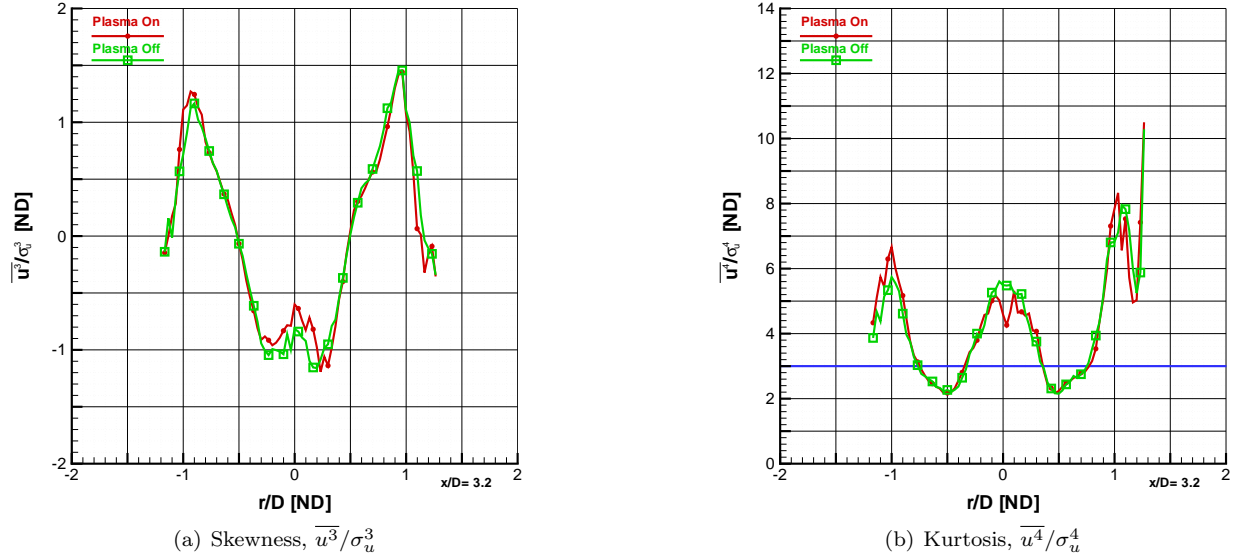
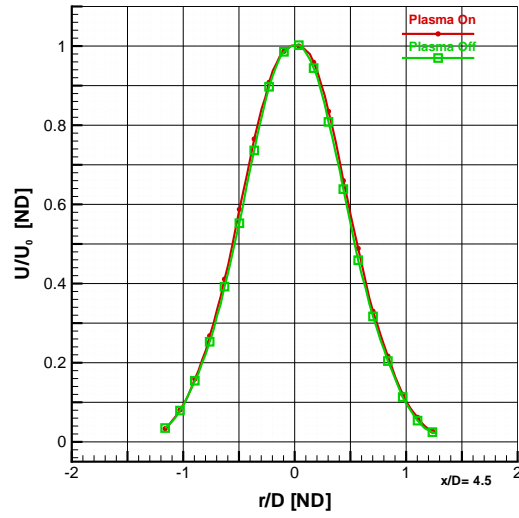
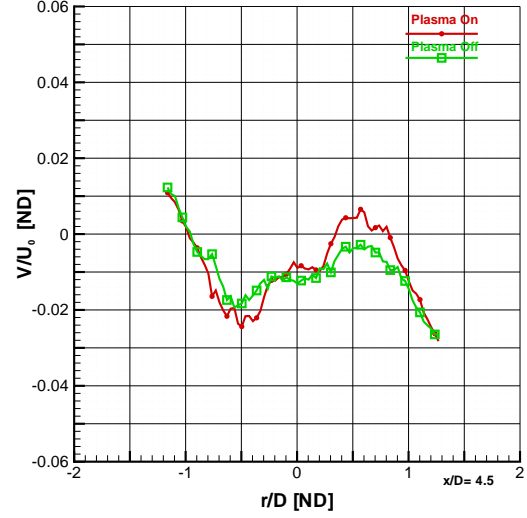


Figure A.21: Comparison of Plasma Effects on Skewness and Kurtosis: Case 603LINE5011

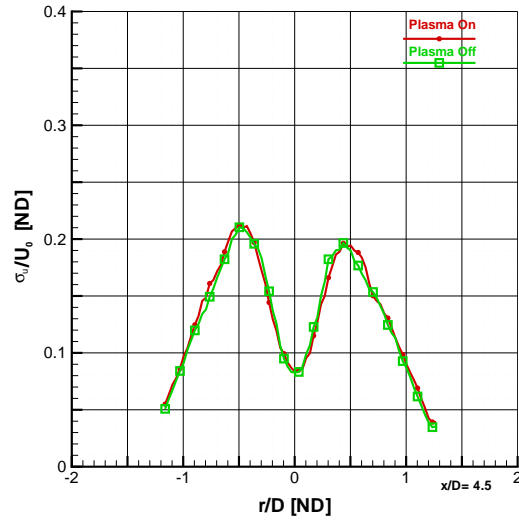
This is the final series of figures on the investigation into the effect of plasma on a Mach 1.1 jet, 3.2 diameters from the anode face. The jet diameter is 15.7 mm. The two plots represented above are a comparison between plasma on in red versus plasma off in green. The plasma off case is placed on top of the plasma on case, therefore making it easier to notice small changes between the two cases. Figure A.21 (a) (b) are the measurements of skewness and kurtosis (or flatness), respectively. A Gaussian distribution has skewness of zero, which indicates a distribution of fluctuations is symmetric about the mean. Positive skewness represents a shift toward the right tail (positive fluctuations), while negative skewness is shifted toward negative fluctuations. A Gaussian distribution has kurtosis of three, represented by the blue line. Values lower than three represent a distribution of velocity with higher peakedness than a Gaussian distribution. Conversely, values above three represent flatter distributions. The case identifiers for this comparison were 603cnc-LINE5011 for plasma off and 603pnc-LINE5011 for plasma on.



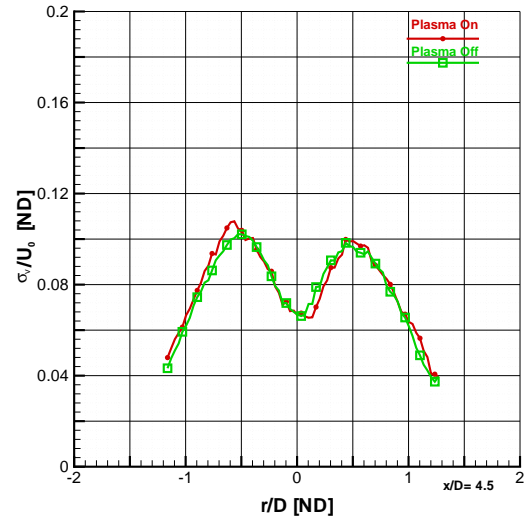
(a) Mean Axial Velocity, U/U_o



(b) Mean Tangential Velocity, V/U_o



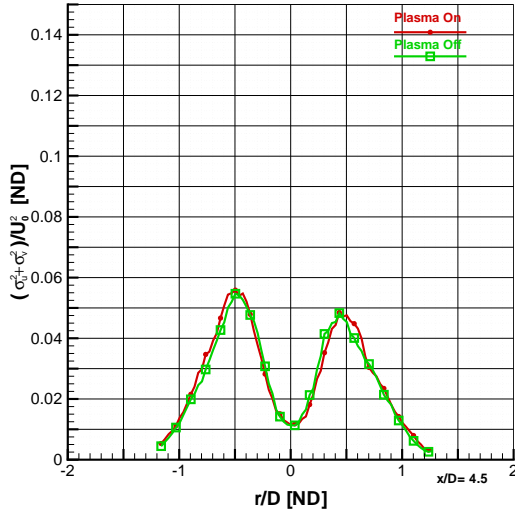
(c) Fluctuating Axial Velocity, σ_u/U_o



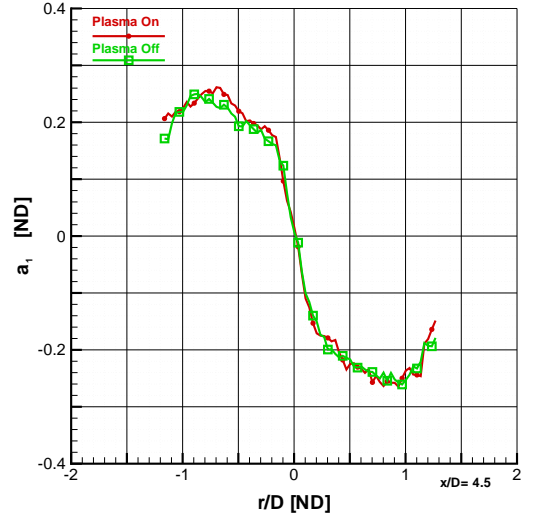
(d) Fluctuating Tangential Velocity, σ_v/U_o

Figure A.22: Comparison of Plasma Effects on Mean Velocity and Fluctuations: Case 603LINE6993

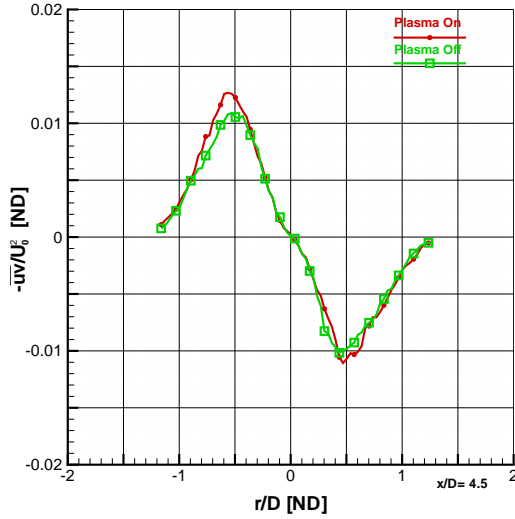
This is an investigation into the effect of plasma on a Mach 1.1 jet, 4.5 diameters from the anode face. The jet diameter is 15.7 mm. The four plots represented above are a comparison between plasma on in red versus plasma off in green. Figure A.22 (a) is non-dimensionalized axial velocity. For these figures, U_o is 330.4 m/s for the plasma off case and 328.9 m/s for the plasma on case. Figure A.22 (b) is the mean tangential component of the velocity. Figures A.22 (c) and (d) show the Reynolds normal stresses in the axial and tangential directions, respectively. The case identifiers for this comparison were 603cnc-LINE6993 for plasma off and 603pnc-LINE6993 for plasma on.



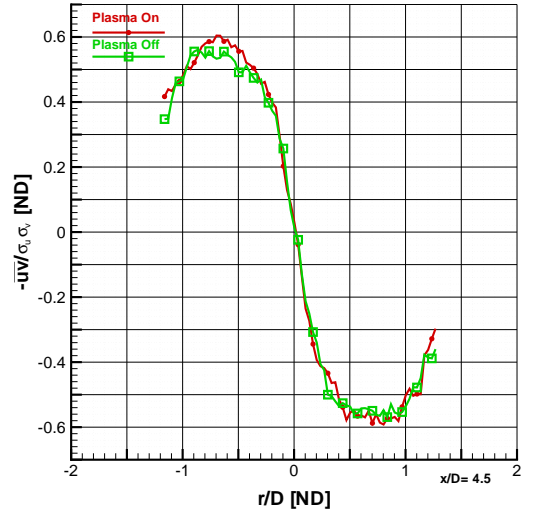
(a) Turbulent Kinetic Energy, $(\sigma_u^2 + \sigma_v^2)/U_o^2$



(b) Structural Parameter, $a_1 = -\overline{uv}/(\sigma_u^2 + \sigma_v^2)$



(c) Reynolds Shear Stress, \overline{uv}/U_o^2



(d) Correlation Coefficient of Reynolds Shear Stress, $-\overline{uv}/(\sigma_u \sigma_v)$

Figure A.23: Comparison of Plasma Effects on Second Moment Fluctuations: Case 603LINE6993

This is a continuing investigation into the effect of plasma on a Mach 1.1 jet, 4.5 diameters from the anode face. The jet diameter is 15.7 mm. The four plots represented above are a comparison between plasma on in red versus plasma off in green. Figure A.23 (a) is non-dimensionalized turbulent kinetic energy and panel (b) is the structural parameter a_1 . At this station, U_o is 330.4 m/s for the plasma off case and 328.9 m/s for the plasma on case. Figures A.23 (c) and (d) show the Reynolds shear stress and the correlation coefficient of Reynolds shear stress, respectively. The case identifiers for this comparison were 603cnc-LINE6993 for plasma off and 603pnc-LINE6993 for plasma on.

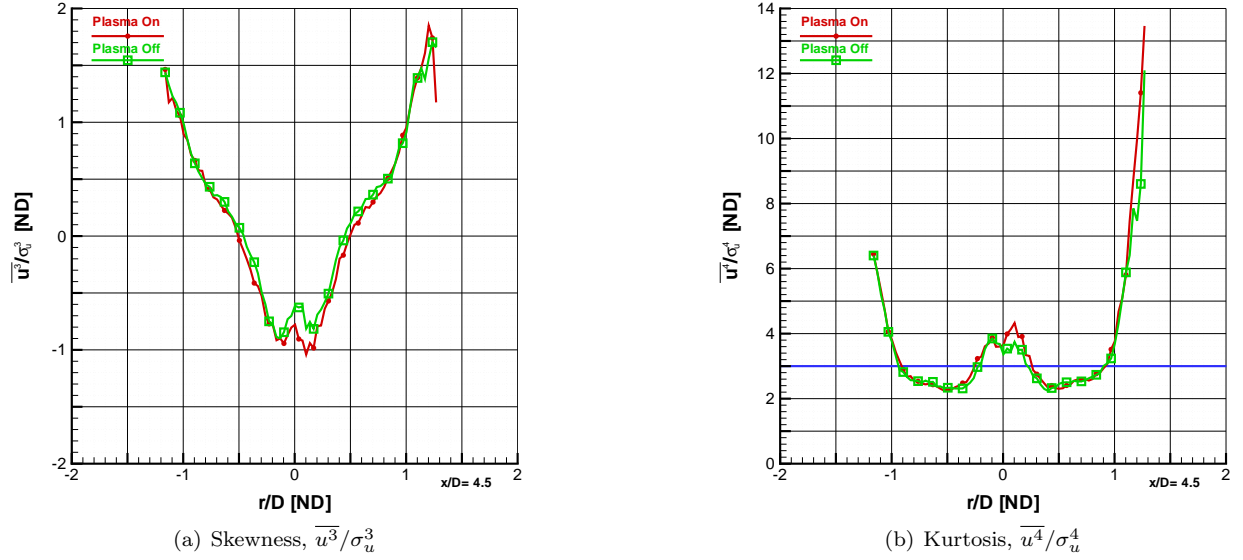
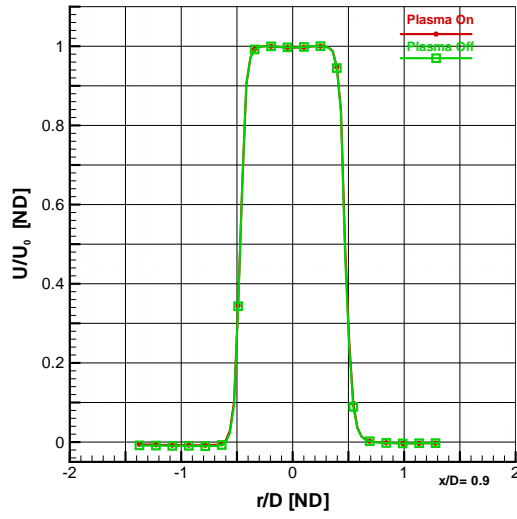


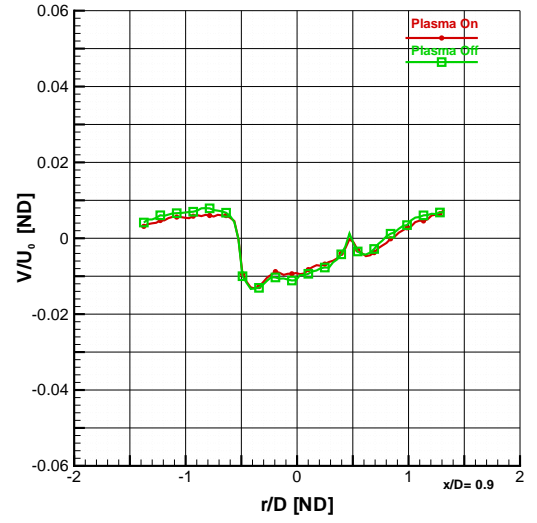
Figure A.24: Comparison of Plasma Effects on Skewness and Kurtosis: Case 603LINE6993

This is the final series of figures on the investigation into the effect of plasma on a Mach 1.1 jet, 4.5 diameters from the anode face. The jet diameter is 15.7 mm. The two plots represented above are a comparison between plasma on in red versus plasma off in green. The plasma off case is placed on top of the plasma on case, therefore making it easier to notice small changes between the two cases. Figure A.24 (a) (b) are the measurements of skewness and kurtosis (or flatness), respectively. A Gaussian distribution has skewness of zero, which indicates a distribution of fluctuations is symmetric about the mean. Positive skewness represents a shift toward the right tail (positive fluctuations), while negative skewness is shifted toward negative fluctuations. A Gaussian distribution has kurtosis of three, represented by the blue line. Values lower than three represent a distribution of velocity with higher peakedness than a Gaussian distribution. Conversely, values above three represent flatter distributions. The case identifiers for this comparison were 603cnc-LINE6993 for plasma off and 603pnc-LINE6993 for plasma on.

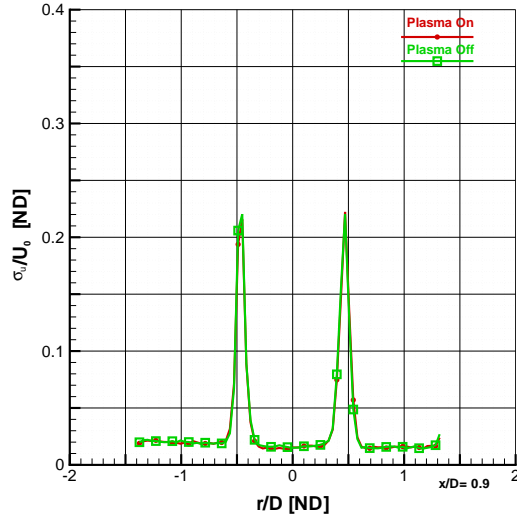
A.3 Mach 2.0 Converging-Diverging Nozzle at 8 Torr



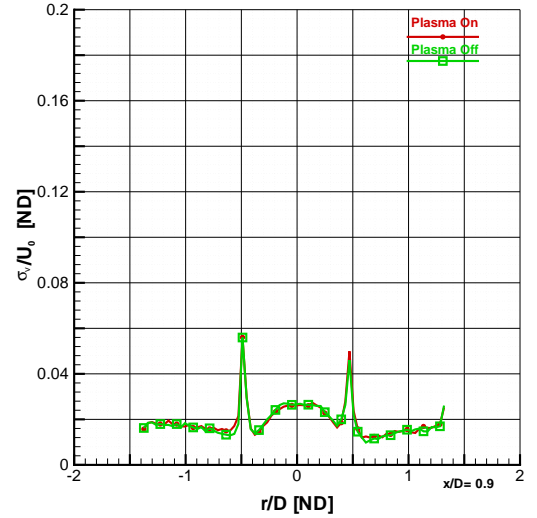
(a) Mean Axial Velocity, U/U_o



(b) Mean Tangential Velocity, V/U_o



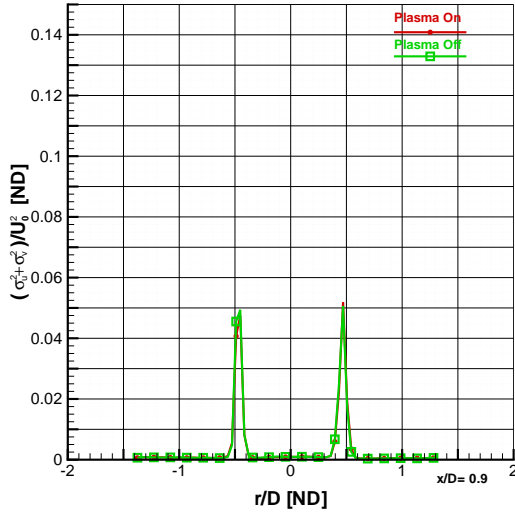
(c) Fluctuating Axial Velocity, σ_u/U_o



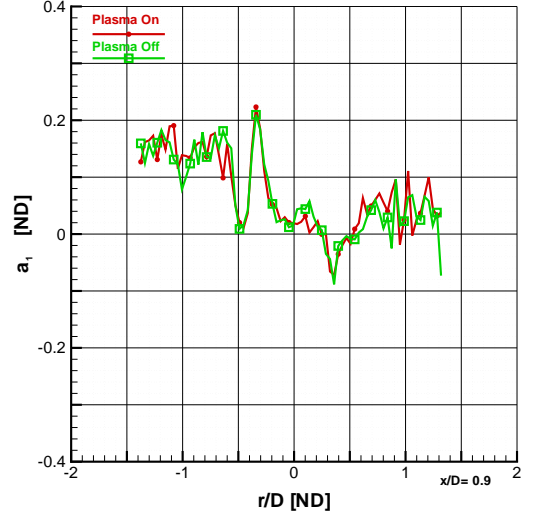
(d) Fluctuating Tangential Velocity, σ_v/U_o

Figure A.25: Comparison of Plasma Effects on Mean Velocity and Fluctuations: Case 609LINE1012

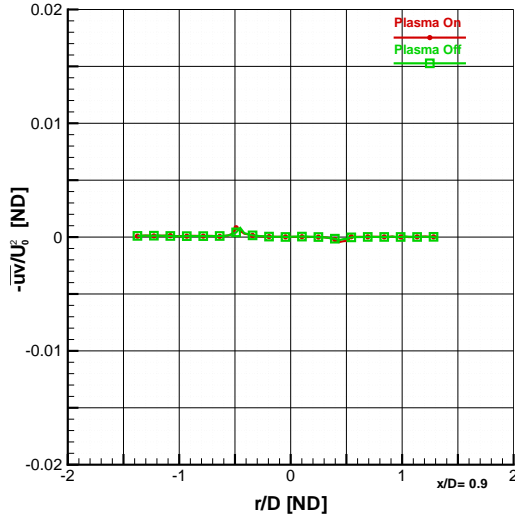
This is an investigation into the effect of plasma on a Mach 2.0 jet, 0.9 diameters from the anode face. The jet diameter is 11.3 mm. The four plots represented above are a comparison between plasma on in red versus plasma off in green. Figure A.25 (a) is non-dimensionalized axial velocity. For these figures, U_o is 522.2 m/s for the plasma off case and 521.8 m/s for the plasma on case. Figure A.25 (b) is the mean tangential component of the velocity. Figures A.25 (c) and (d) show the Reynolds normal stresses in the axial and tangential directions, respectively.



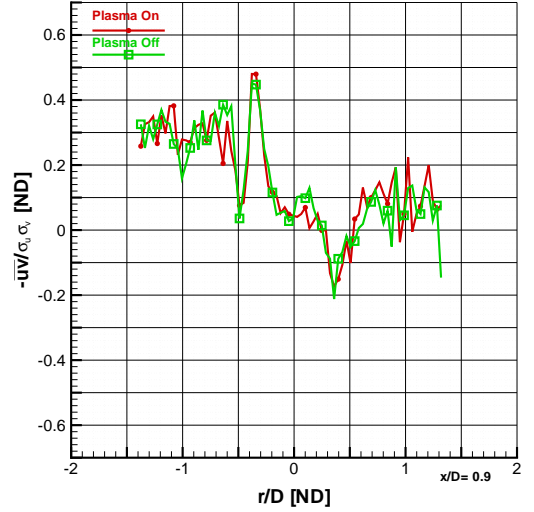
(a) Turbulent Kinetic Energy, $(\sigma_u^2 + \sigma_v^2)/U_o^2$



(b) Structural Parameter, $a_1 = -\overline{uv}/(\sigma_u^2 + \sigma_v^2)$



(c) Reynolds Shear Stress, \overline{uv}/U_o^2



(d) Correlation Coefficient of Reynolds Shear Stress, $-\overline{uv}/(\sigma_u \sigma_v)$

Figure A.26: Comparison of Plasma Effects on Second Moment Fluctuations: Case 609LINE1012

This is a continuing investigation into the effect of plasma on a Mach 2.0 jet, 0.9 diameters from the anode face. The jet diameter is 11.3 mm. The four plots represented above are a comparison between plasma on in red versus plasma off in green. Figure A.26 (a) is non-dimensionalized turbulent kinetic energy and panel (b) is the structural parameter a_1 . At this station, U_o is 522.2 m/s for the plasma off case and 521.8 m/s for the plasma on case. Figures A.26 (c) and (d) show the Reynolds shear stress and the correlation coefficient of Reynolds shear stress, respectively. The case identifiers for this comparison were 609cn-LINE1012 for plasma off and 609pn-LINE1012 for plasma on.

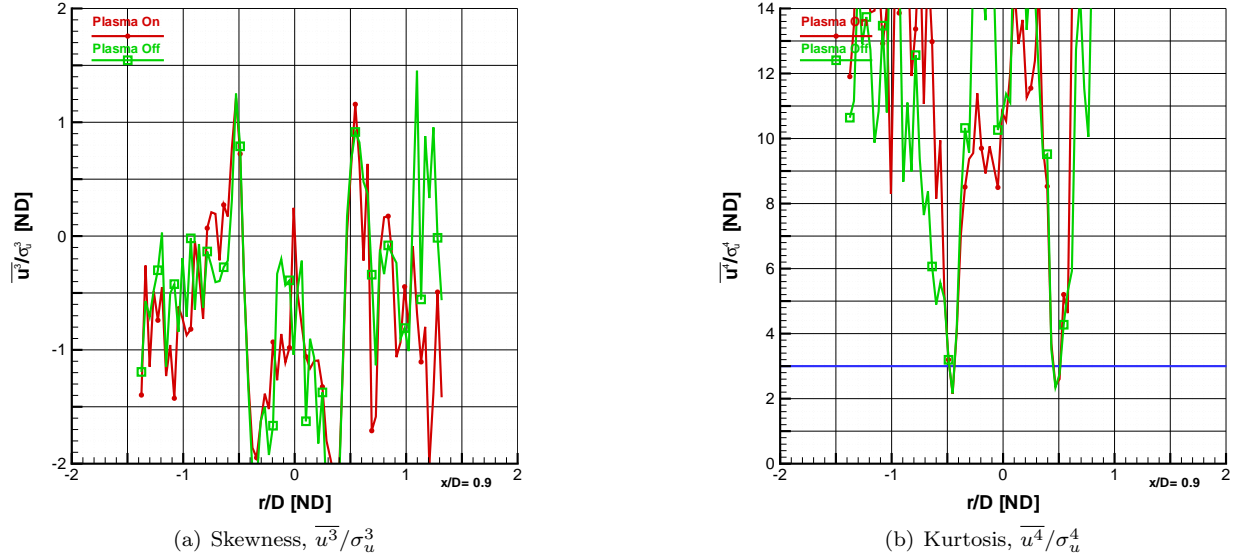
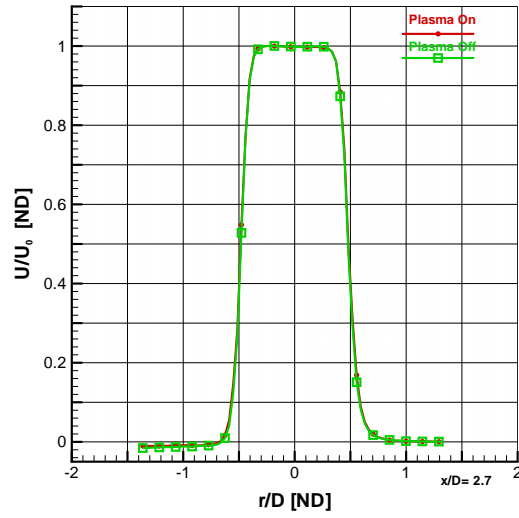
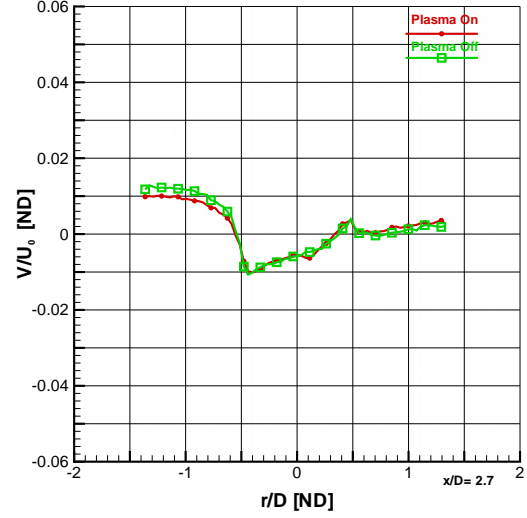


Figure A.27: Comparison of Plasma Effects on Skewness and Kurtosis: Case 609LINE1012

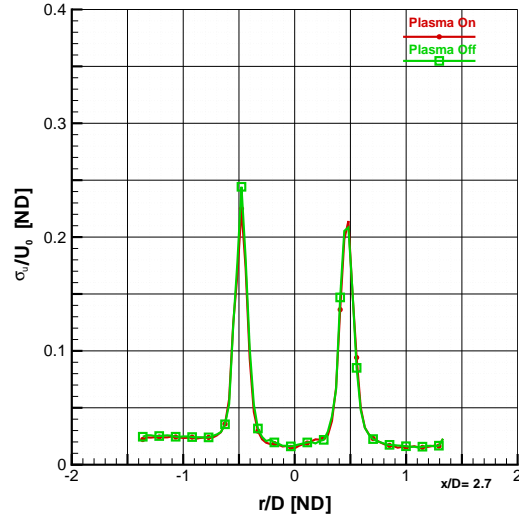
This is the final series of figures on the investigation into the effect of plasma on a Mach 2.0 jet, 0.9 diameters from the anode face. The jet diameter is 11.3 mm. The two plots represented above are a comparison between plasma on in red versus plasma off in green. The plasma off case is placed on top of the plasma on case, therefore making it easier to notice small changes between the two cases. Figure A.27 (a) (b) are the measurements of skewness and kurtosis (or flatness), respectively. A Gaussian distribution has skewness of zero, which indicates a distribution of fluctuations is symmetric about the mean. Positive skewness represents a shift toward the right tail (positive fluctuations), while negative skewness is shifted toward negative fluctuations. A Gaussian distribution has kurtosis of three, represented by the blue line. Values lower than three represent a distribution of velocity with higher peakedness than a Gaussian distribution. Conversely, values above three represent flatter distributions. The case identifiers for this comparison were 609cn-LINE1012 for plasma off and 609pn-LINE1012 for plasma on.



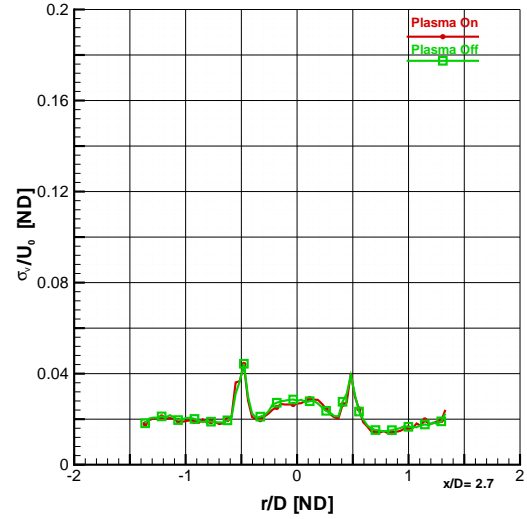
(a) Mean Axial Velocity, U/U_o



(b) Mean Tangential Velocity, V/U_o



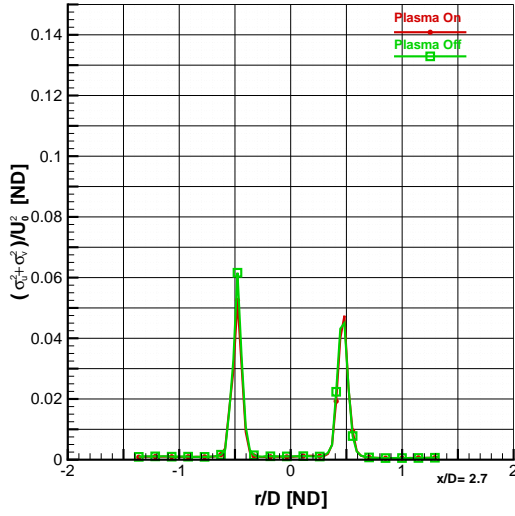
(c) Fluctuating Axial Velocity, σ_u/U_o



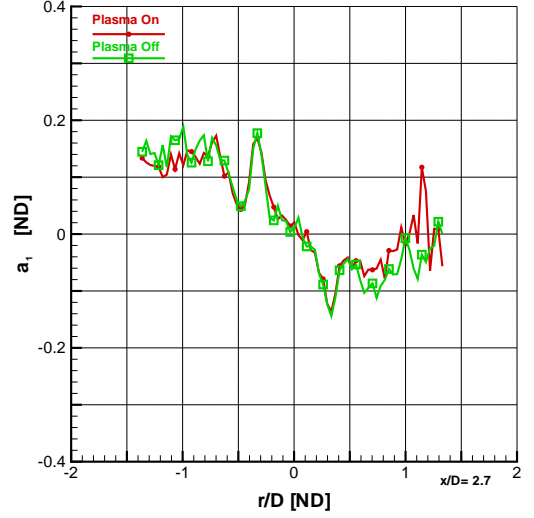
(d) Fluctuating Tangential Velocity, σ_v/U_o

Figure A.28: Comparison of Plasma Effects on Mean Velocity and Fluctuations: Case 609LINE3011

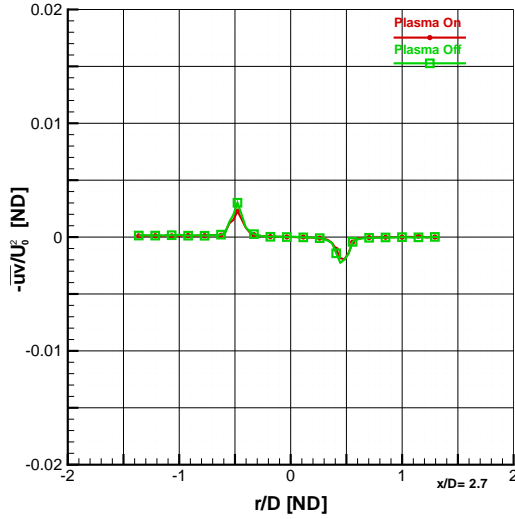
This is an investigation into the effect of plasma on a Mach 2.0 jet, 2.7 diameters from the anode face. The jet diameter is 11.3 mm. The four plots represented above are a comparison between plasma on in red versus plasma off in green. Figure A.28 (a) is non-dimensionalized axial velocity. For these figures, U_o is 519.1 m/s for the plasma off case and 519.0 m/s for the plasma on case. Figure A.28 (b) is the mean tangential component of the velocity. Figures A.28 (c) and (d) show the Reynolds normal stresses in the axial and tangential directions, respectively. The case identifiers for this comparison were 609cn-LINE3011 for plasma off and 609pn-LINE3011 for plasma on.



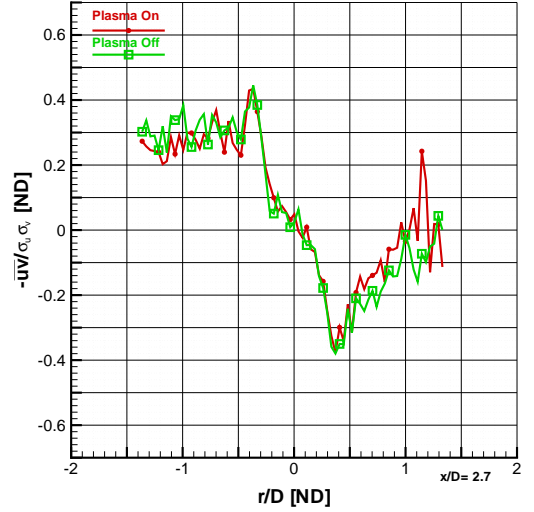
(a) Turbulent Kinetic Energy, $(\sigma_u^2 + \sigma_v^2)/U_o^2$



(b) Structural Parameter, $a_1 = -\overline{uv}/(\sigma_u^2 + \sigma_v^2)$



(c) Reynolds Shear Stress, \overline{uv}/U_o^2



(d) Correlation Coefficient of Reynolds Shear Stress, $-\overline{uv}/(\sigma_u \sigma_v)$

Figure A.29: Comparison of Plasma Effects on Second Moment Fluctuations: Case 609LINE3011

This is a continuing investigation into the effect of plasma on a Mach 2.0 jet, 2.7 diameters from the anode face. The jet diameter is 11.3 mm. The four plots represented above are a comparison between plasma on in red versus plasma off in green. Figure A.29 (a) is non-dimensionalized turbulent kinetic energy and panel (b) is the structural parameter a_1 . At this station, U_o is 519.1 m/s for the plasma off case and 519.0 m/s for the plasma on case. Figures A.29 (c) and (d) show the Reynolds shear stress and the correlation coefficient of Reynolds shear stress, respectively. The case identifiers for this comparison were 609cn-LINE3011 for plasma off and 609pn-LINE3011 for plasma on.

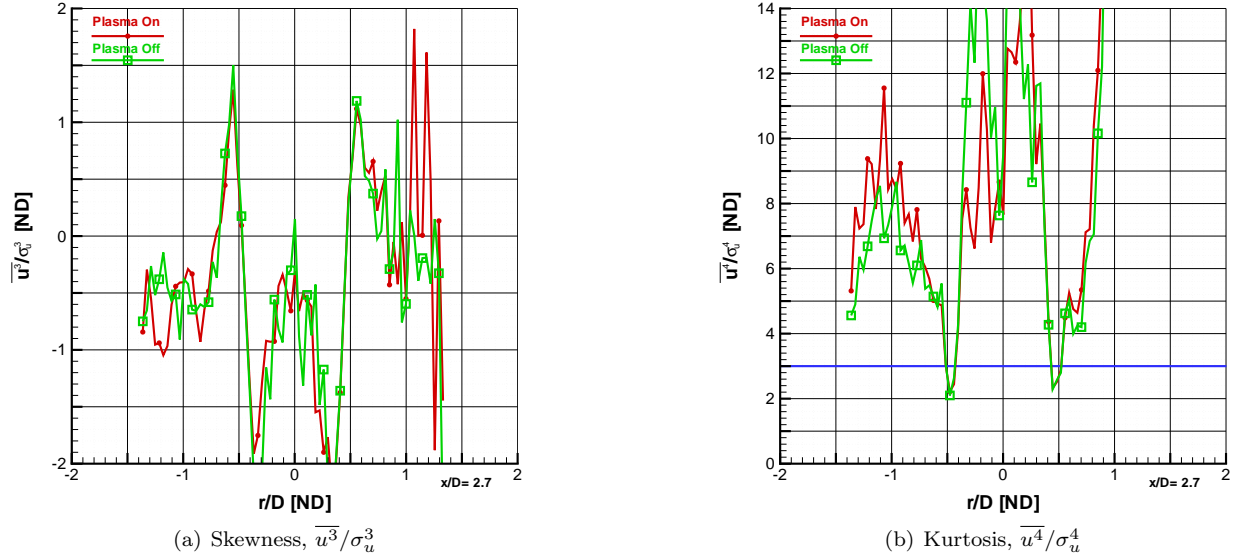
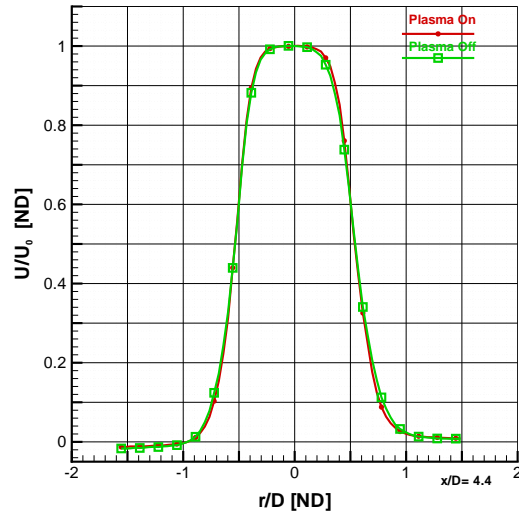
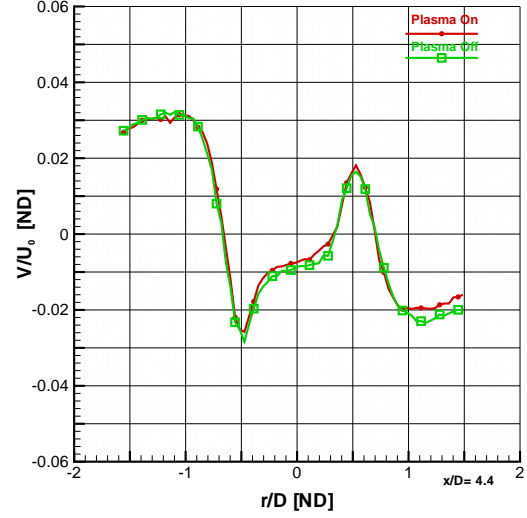


Figure A.30: Comparison of Plasma Effects on Skewness and Kurtosis: Case 609LINE3011

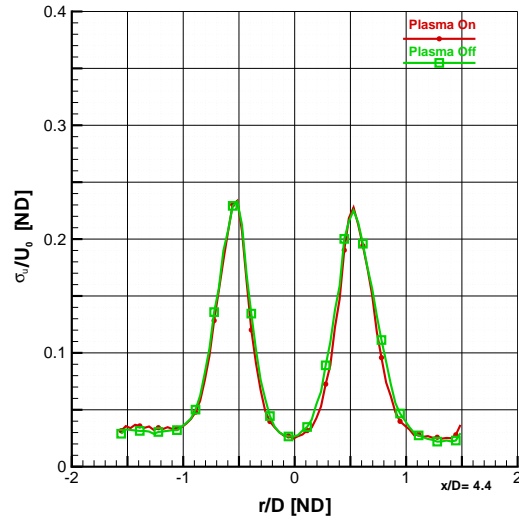
This is the final series of figures on the investigation into the effect of plasma on a Mach 2.0 jet, 2.7 diameters from the anode face. The jet diameter is 11.3 mm. The two plots represented above are a comparison between plasma on in red versus plasma off in green. The plasma off case is placed on top of the plasma on case, therefore making it easier to notice small changes between the two cases. Figure A.30 (a) (b) are the measurements of skewness and kurtosis (or flatness), respectively. A Gaussian distribution has skewness of zero, which indicates a distribution of fluctuations is symmetric about the mean. Positive skewness represents a shift toward the right tail (positive fluctuations), while negative skewness is shifted toward negative fluctuations. A Gaussian distribution has kurtosis of three, represented by the blue line. Values lower than three represent a distribution of velocity with higher peakedness than a Gaussian distribution. Conversely, values above three represent flatter distributions. The case identifiers for this comparison were 609cn-LINE3011 for plasma off and 609pn-LINE3011 for plasma on.



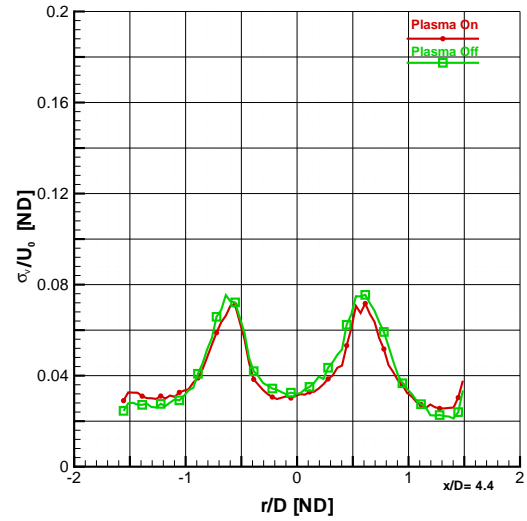
(a) Mean Axial Velocity, U/U_o



(b) Mean Tangential Velocity, V/U_o



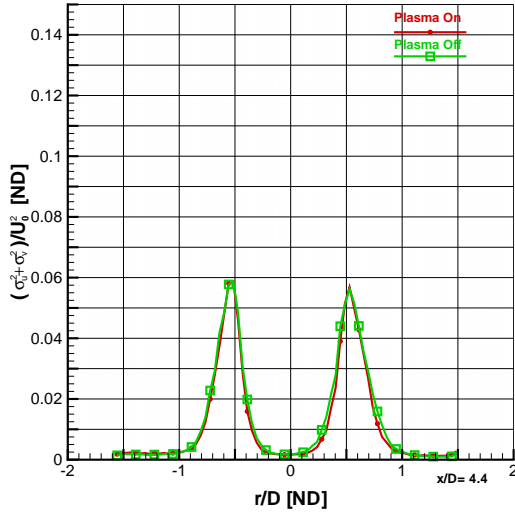
(c) Fluctuating Axial Velocity, σ_u/U_o



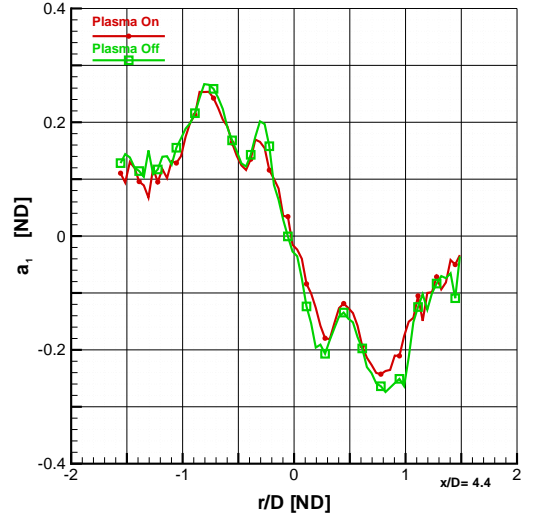
(d) Fluctuating Tangential Velocity, σ_v/U_o

Figure A.31: Comparison of Plasma Effects on Mean Velocity and Fluctuations: Case 607LINE5024

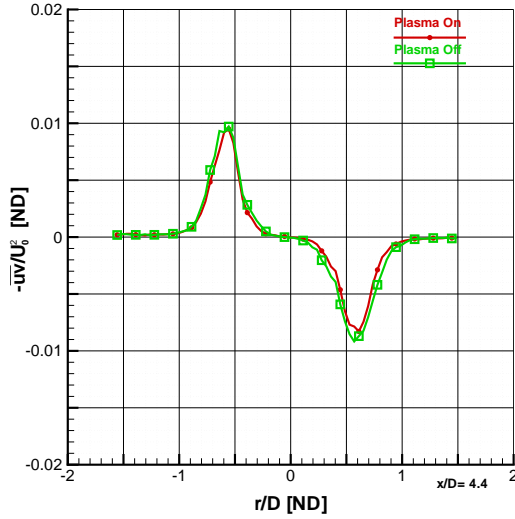
This is an investigation into the effect of plasma on a Mach 2.0 jet, 4.4 diameters from the anode face. The jet diameter is 11.3 mm. The four plots represented above are a comparison between plasma on in red versus plasma off in green. Figure A.31 (a) is non-dimensionalized axial velocity. For these figures, U_o is 523.6 m/s for the plasma off case and 525.0 m/s for the plasma on case. Figure A.31 (b) is the mean tangential component of the velocity. Figures A.31 (c) and (d) show the Reynolds normal stresses in the axial and tangential directions, respectively. The case identifiers for this comparison were 607cnc-LINE5024 for plasma off and 607pnc-LINE5024 for plasma on.



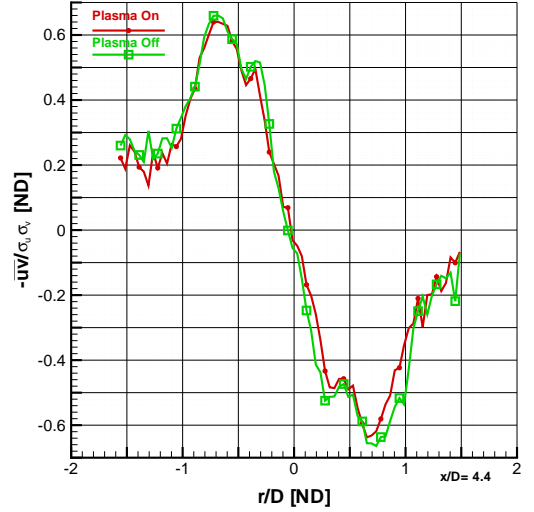
(a) Turbulent Kinetic Energy, $(\sigma_u^2 + \sigma_v^2)/U_o^2$



(b) Structural Parameter, $a_1 = -\overline{uv}/(\sigma_u^2 + \sigma_v^2)$



(c) Reynolds Shear Stress, \overline{uv}/U_o^2



(d) Correlation Coefficient of Reynolds Shear Stress, $-\overline{uv}/(\sigma_u \sigma_v)$

Figure A.32: Comparison of Plasma Effects on Second Moment Fluctuations: Case 607LINE5024

This is a continuing investigation into the effect of plasma on a Mach 2.0 jet, 4.4 diameters from the anode face. The jet diameter is 11.3 mm. The four plots represented above are a comparison between plasma on in red versus plasma off in green. Figure A.32 (a) is non-dimensionalized turbulent kinetic energy and panel (b) is the structural parameter a_1 . At this station, U_o is 523.6 m/s for the plasma off case and 525.0 m/s for the plasma on case. Figures A.32 (c) and (d) show the Reynolds shear stress and the correlation coefficient of Reynolds shear stress, respectively. The case identifiers for this comparison were 607cnc-LINE5024 for plasma off and 607pnc-LINE5024 for plasma on.

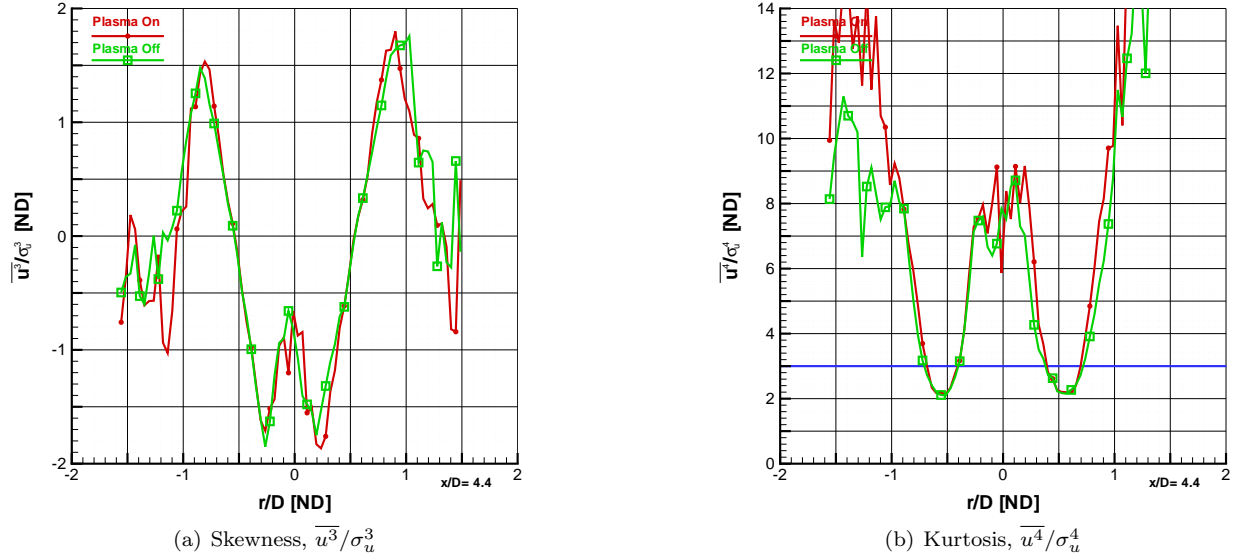
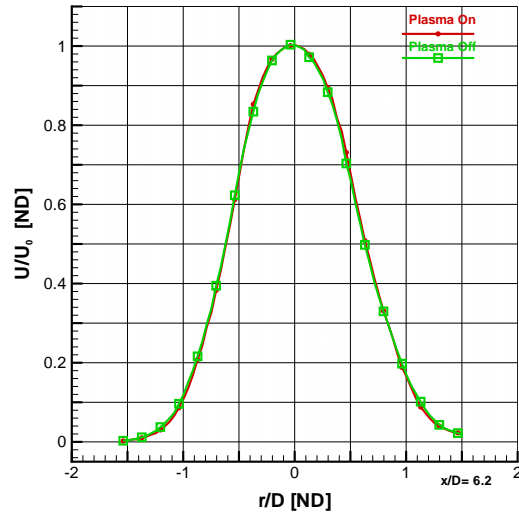
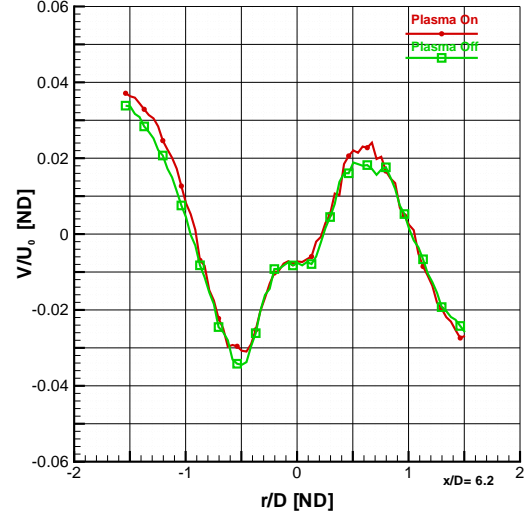


Figure A.33: Comparison of Plasma Effects on Skewness and Kurtosis: Case 607LINE5024

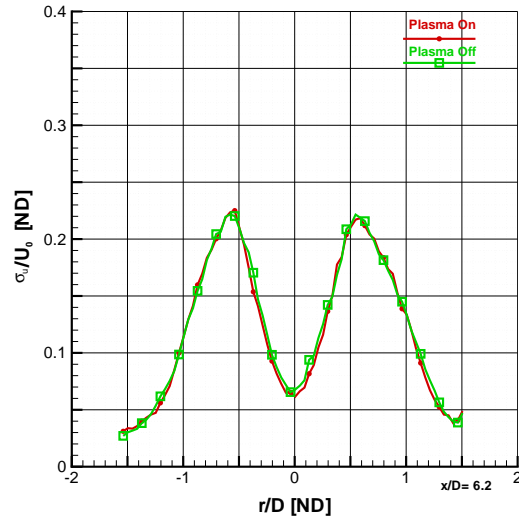
This is the final series of figures on the investigation into the effect of plasma on a Mach 2.0 jet, 4.4 diameters from the anode face. The jet diameter is 11.3 mm. The two plots represented above are a comparison between plasma on in red versus plasma off in green. The plasma off case is placed on top of the plasma on case, therefore making it easier to notice small changes between the two cases. Figure A.33 (a) (b) are the measurements of skewness and kurtosis (or flatness), respectively. A Gaussian distribution has skewness of zero, which indicates a distribution of fluctuations is symmetric about the mean. Positive skewness represents a shift toward the right tail (positive fluctuations), while negative skewness is shifted toward negative fluctuations. A Gaussian distribution has kurtosis of three, represented by the blue line. Values lower than three represent a distribution of velocity with higher peakedness than a Gaussian distribution. Conversely, values above three represent flatter distributions. The case identifiers for this comparison were 607cnc-LINE5024 for plasma off and 607pnc-LINE5024 for plasma on.



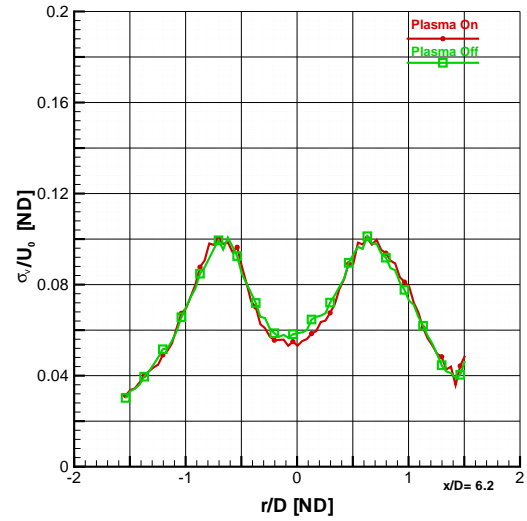
(a) Mean Axial Velocity, U/U_o



(b) Mean Tangential Velocity, V/U_o



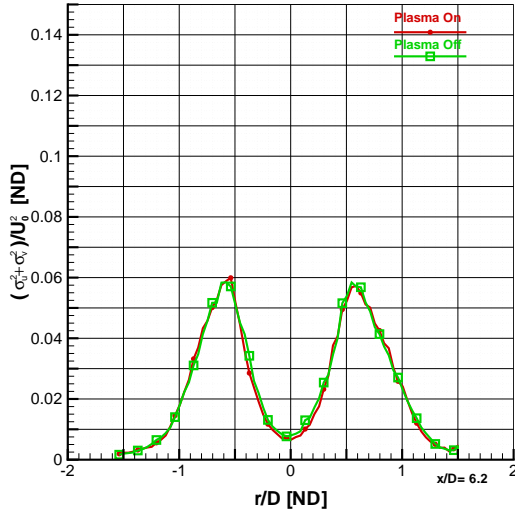
(c) Fluctuating Axial Velocity, σ_u/U_o



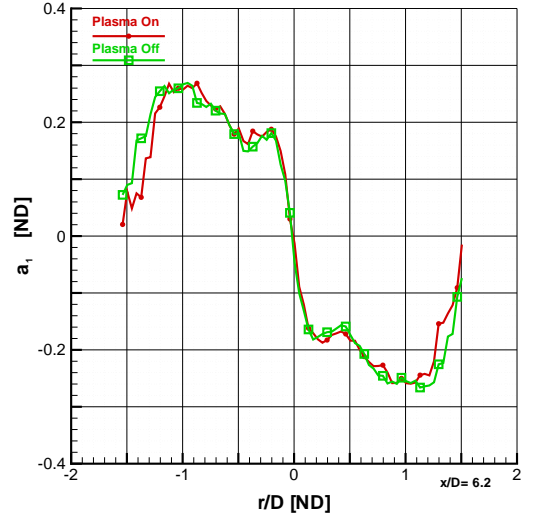
(d) Fluctuating Tangential Velocity, σ_v/U_o

Figure A.34: Comparison of Plasma Effects on Mean Velocity and Fluctuations: Case 607LINE7001

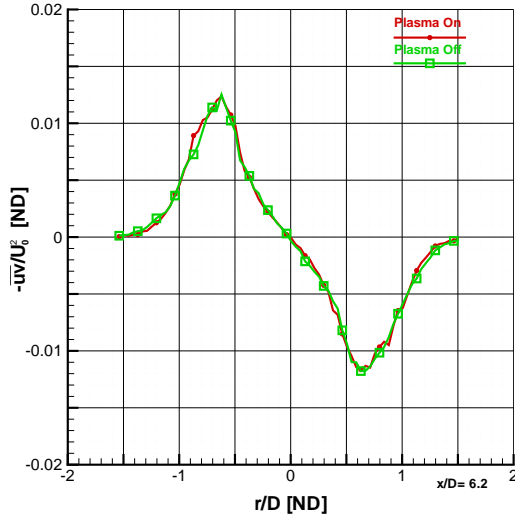
This is an investigation into the effect of plasma on a Mach 2.0 jet, 6.2 diameters from the anode face. The jet diameter is 11.3 mm. The four plots represented above are a comparison between plasma on in red versus plasma off in green. Figure A.34 (a) is non-dimensionalized axial velocity. For these figures, U_o is 506.9 m/s for the plasma off case and 511.7 m/s for the plasma on case. Figure A.34 (b) is the mean tangential component of the velocity. Figures A.34 (c) and (d) show the Reynolds normal stresses in the axial and tangential directions, respectively. The case identifiers for this comparison were 607cnc-LINE7001 for plasma off and 607pnc-LINE7001 for plasma on.



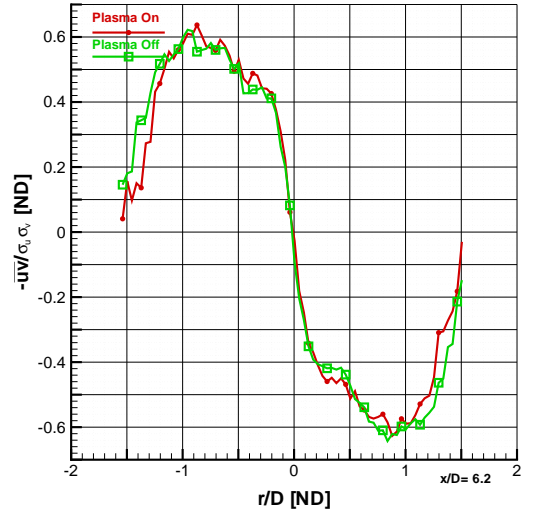
(a) Turbulent Kinetic Energy, $(\sigma_u^2 + \sigma_v^2)/U_o^2$



(b) Structural Parameter, $a_1 = -\overline{uv}/(\sigma_u^2 + \sigma_v^2)$



(c) Reynolds Shear Stress, \overline{uv}/U_o^2



(d) Correlation Coefficient of Reynolds Shear Stress, $-\overline{uv}/(\sigma_u \sigma_v)$

Figure A.35: Comparison of Plasma Effects on Second Moment Fluctuations: Case 607LINE7001

This is a continuing investigation into the effect of plasma on a Mach 2.0 jet, 6.2 diameters from the anode face. The jet diameter is 11.3 mm. The four plots represented above are a comparison between plasma on in red versus plasma off in green. Figure A.35 (a) is non-dimensionalized turbulent kinetic energy and panel (b) is the structural parameter a_1 . At this station, U_o is 506.9 m/s for the plasma off case and 511.7 m/s for the plasma on case. Figures A.35 (c) and (d) show the Reynolds shear stress and the correlation coefficient of Reynolds shear stress, respectively. The case identifiers for this comparison were 607cnc-LINE7001 for plasma off and 607pnc-LINE7001 for plasma on.

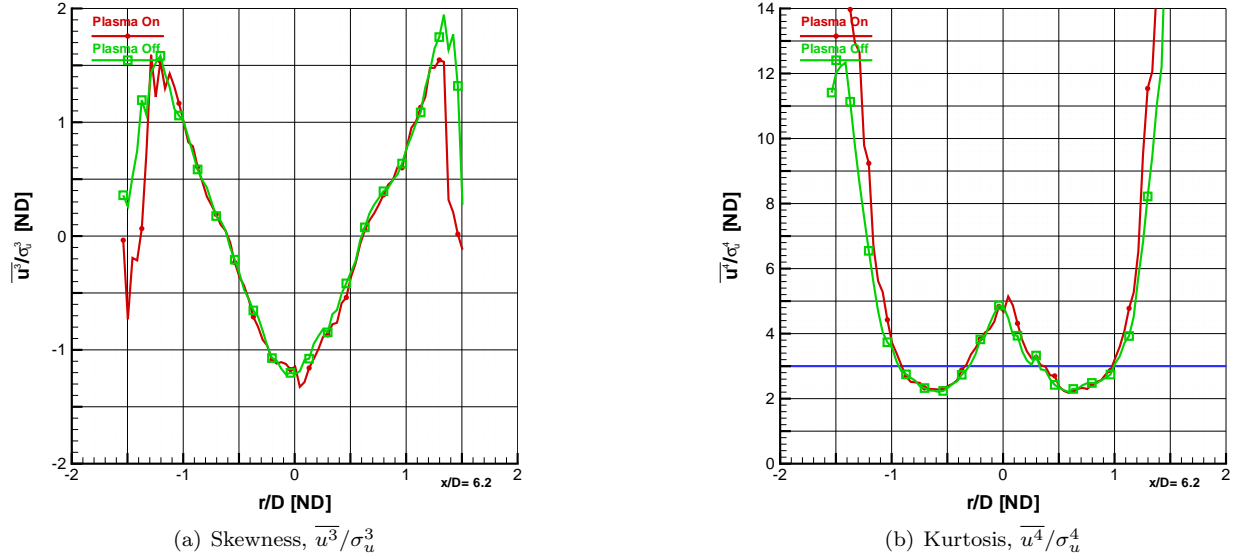


Figure A.36: Comparison of Plasma Effects on Skewness and Kurtosis: Case 607LINE7001

This is the final series of figures on the investigation into the effect of plasma on a Mach 2.0 jet, 6.2 diameters from the anode face. The jet diameter is 11.3 mm. The two plots represented above are a comparison between plasma on in red versus plasma off in green. The plasma off case is placed on top of the plasma on case, therefore making it easier to notice small changes between the two cases. Figure A.36 (a) (b) are the measurements of skewness and kurtosis (or flatness), respectively. A Gaussian distribution has skewness of zero, which indicates a distribution of fluctuations is symmetric about the mean. Positive skewness represents a shift toward the right tail (positive fluctuations), while negative skewness is shifted toward negative fluctuations. A Gaussian distribution has kurtosis of three, represented by the blue line. Values lower than three represent a distribution of velocity with higher peakedness than a Gaussian distribution. Conversely, values above three represent flatter distributions. The case identifiers for this comparison were 607cnc-LINE7001 for plasma off and 607pnc-LINE7001 for plasma on.

A.4 Overexpanded Converging-Diverging Nozzle at 8 Torr

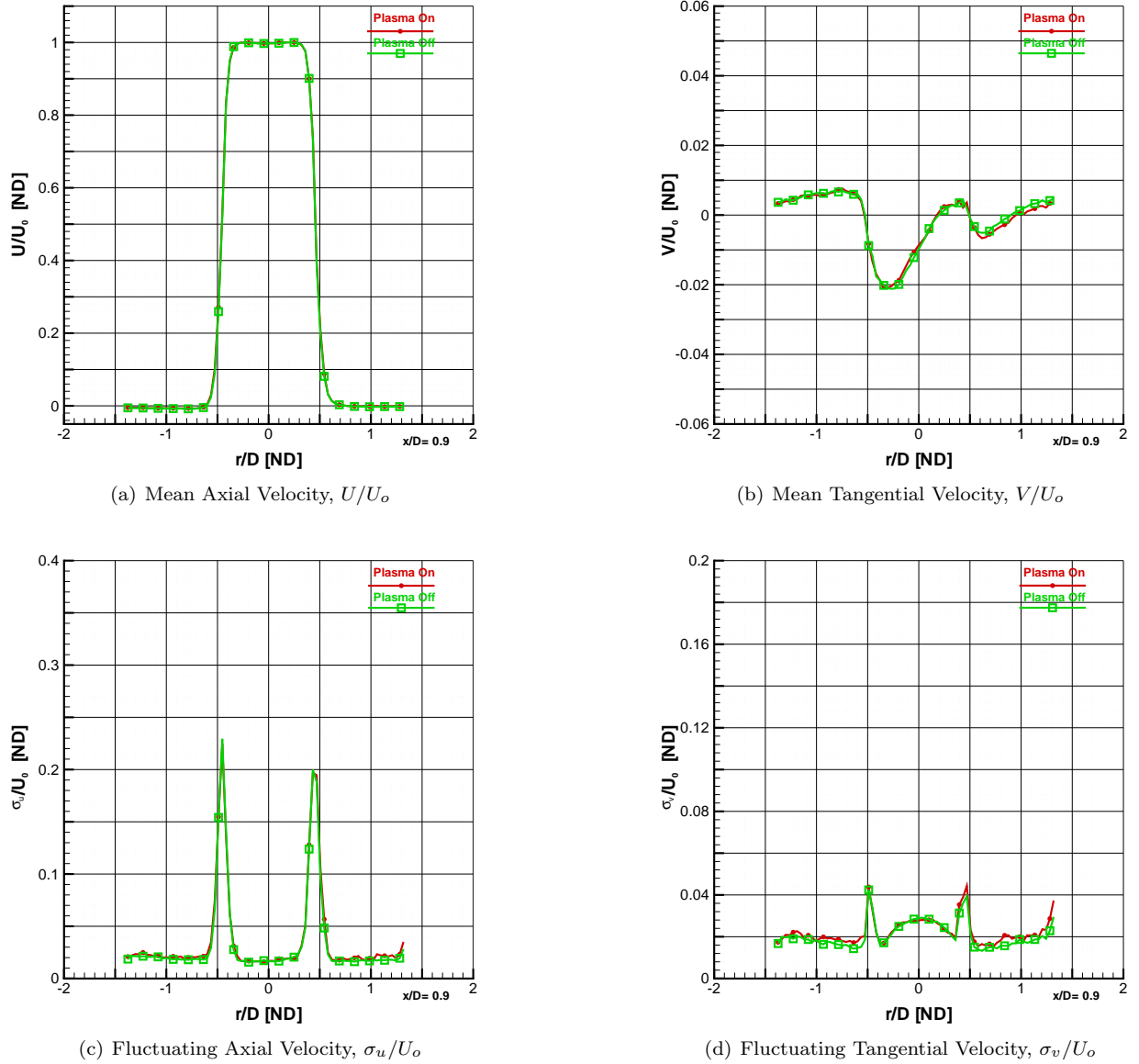
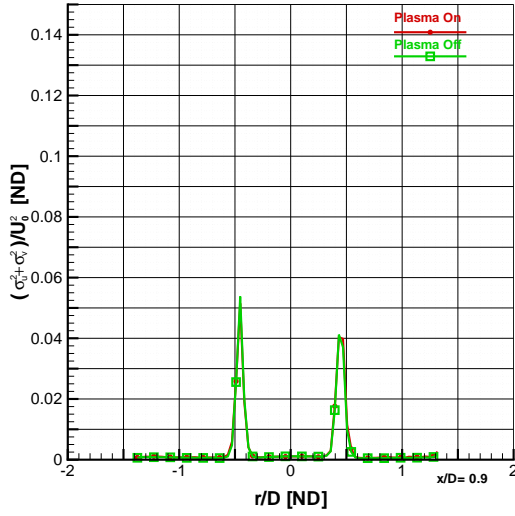
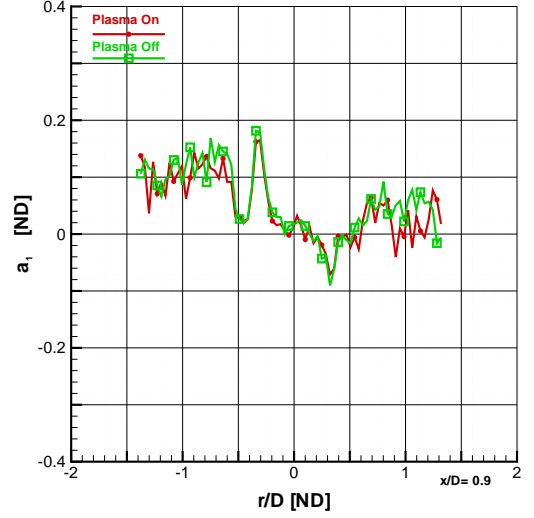


Figure A.37: Comparison of Plasma Effects on Mean Velocity and Fluctuations: Case 610LINE1033

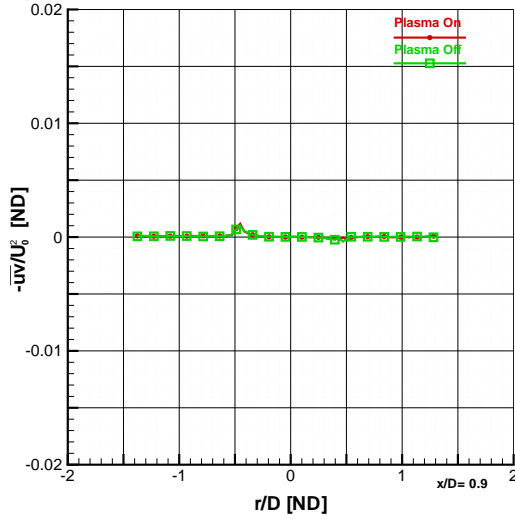
This is an investigation into the effect of plasma on an overexpanded jet (Mach 2.0 jet driven with a Mach 1.9 pressure ratio), 0.9 diameters from the anode face. The jet diameter is 11.3 mm. The four plots represented above are a comparison between plasma on in red versus plasma off in green. Figure A.37 (a) is non-dimensionalized axial velocity. For these figures, U_o is 510.2 m/s for the plasma off case and 509.8 m/s for the plasma on case. Figure A.37 (b) is the mean tangential component of the velocity. Figures A.37 (c) and (d) show the Reynolds normal stresses in the axial and tangential directions, respectively.



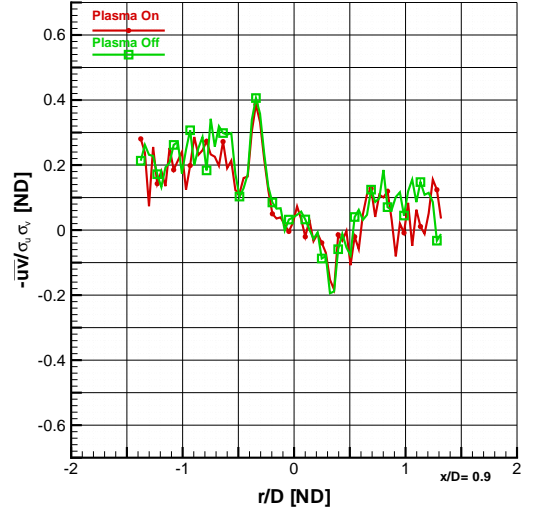
(a) Turbulent Kinetic Energy, $(\sigma_u^2 + \sigma_v^2)/U_o^2$



(b) Structural Parameter, $a_1 = -\overline{uv}/(\sigma_u^2 + \sigma_v^2)$



(c) Reynolds Shear Stress, \overline{uv}/U_o^2



(d) Correlation Coefficient of Reynolds Shear Stress, $-\overline{uv}/(\sigma_u \sigma_v)$

Figure A.38: Comparison of Plasma Effects on Second Moment Fluctuations: Case 610LINE1033

This is a continuing investigation into the effect of plasma on an overexpanded jet (Mach 2.0 jet driven with a Mach 1.9 pressure ratio), 0.9 diameters from the anode face. The jet diameter is 11.3 mm. The four plots represented above are a comparison between plasma on in red versus plasma off in green. Figure A.38 (a) is non-dimensionalized turbulent kinetic energy and panel (b) is the structural parameter a_1 . At this station, U_o is 510.2 m/s for the plasma off case and 509.8 m/s for the plasma on case. Figures A.38 (c) and (d) show the Reynolds shear stress and the correlation coefficient of Reynolds shear stress, respectively. The case identifiers for this comparison were 610cn-LINE1033 for plasma off and 610pn-LINE1033 for plasma on.

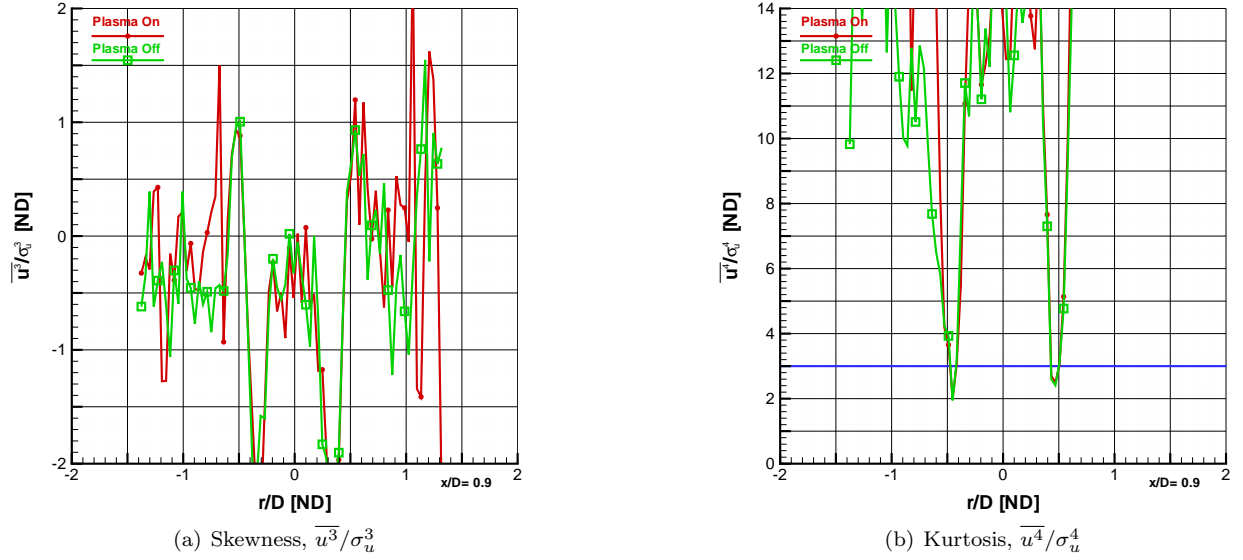
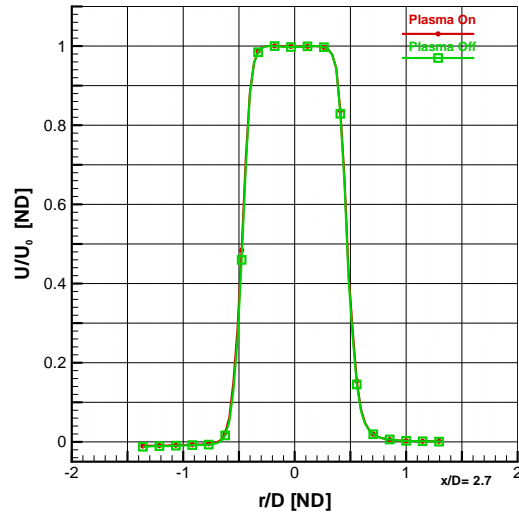
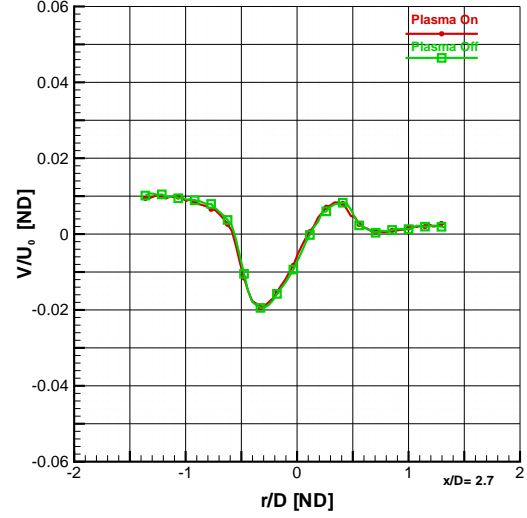


Figure A.39: Comparison of Plasma Effects on Skewness and Kurtosis: Case 610LINE1033

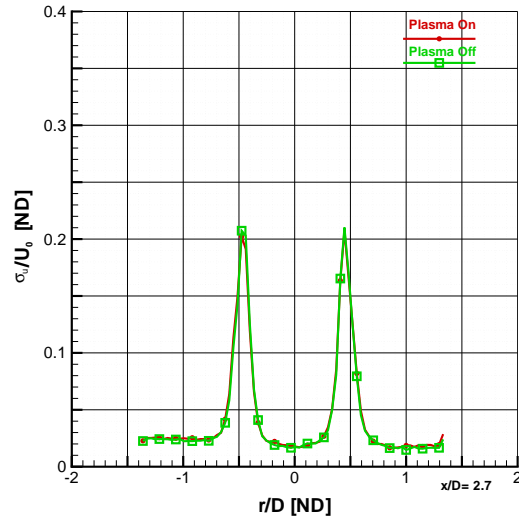
This is the final series of figures on the investigation into the effect of plasma on an overexpanded jet (Mach 2.0 jet driven with a Mach 1.9 pressure ratio), 0.9 diameters from the anode face. The jet diameter is 11.3 mm. The two plots represented above are a comparison between plasma on in red versus plasma off in green. The plasma off case is placed on top of the plasma on case, therefore making it easier to notice small changes between the two cases. Figure A.39 (a) (b) are the measurements of skewness and kurtosis (or flatness), respectively. A Gaussian distribution has skewness of zero, which indicates a distribution of fluctuations is symmetric about the mean. Positive skewness represents a shift toward the right tail (positive fluctuations), while negative skewness is shifted toward negative fluctuations. A Gaussian distribution has kurtosis of three, represented by the blue line. Values lower than three represent a distribution of velocity with higher peakedness than a Gaussian distribution. Conversely, values above three represent flatter distributions. The case identifiers for this comparison were 610cn-LINE1033 for plasma off and 610pn-LINE1033 for plasma on.



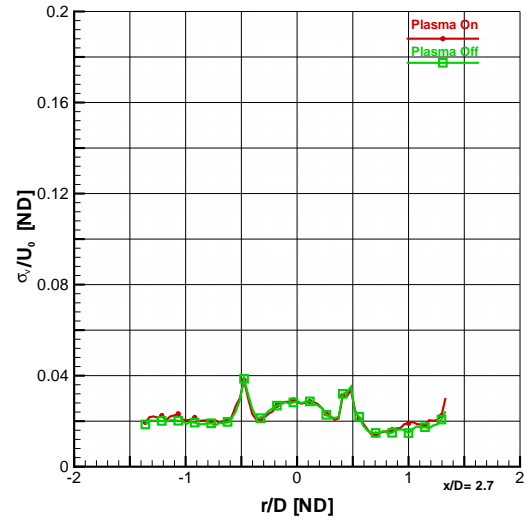
(a) Mean Axial Velocity, U/U_o



(b) Mean Tangential Velocity, V/U_o



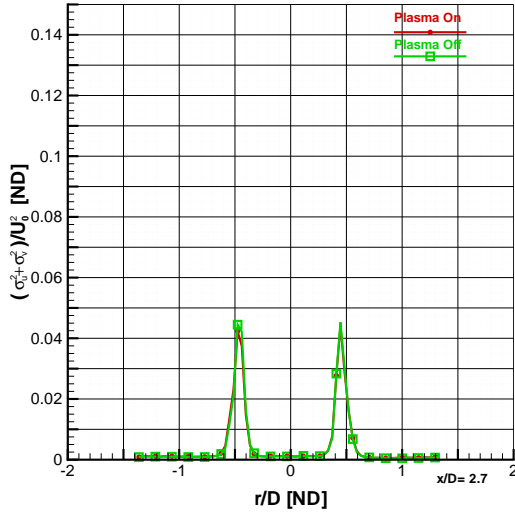
(c) Fluctuating Axial Velocity, σ_u/U_o



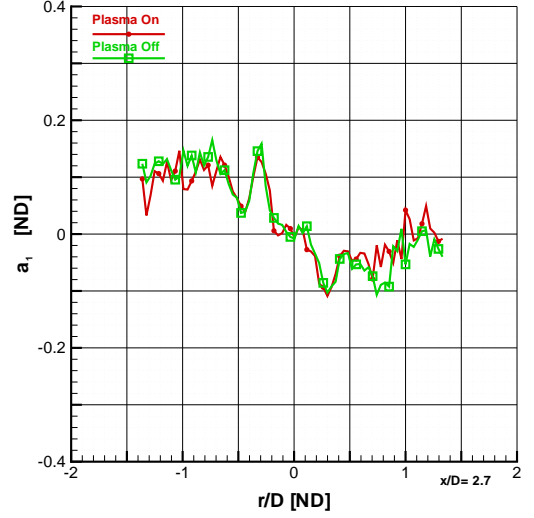
(d) Fluctuating Tangential Velocity, σ_v/U_o

Figure A.40: Comparison of Plasma Effects on Mean Velocity and Fluctuations: Case 610LINE3032

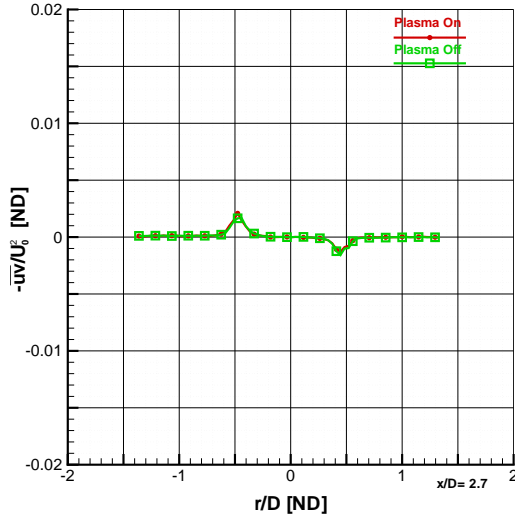
This is an investigation into the effect of plasma on an overexpanded jet (Mach 2.0 jet driven with a Mach 1.9 pressure ratio), 2.7 diameters from the anode face. The jet diameter is 11.3 mm. The four plots represented above are a comparison between plasma on in red versus plasma off in green. Figure A.40 (a) is non-dimensionalized axial velocity. For these figures, U_o is 507.9 m/s for the plasma off case and 507.4 m/s for the plasma on case. Figure A.40 (b) is the mean tangential component of the velocity. Figures A.40 (c) and (d) show the Reynolds normal stresses in the axial and tangential directions, respectively. The case identifiers for this comparison were 610cn-LINE3032 for plasma off and 610pn-LINE3032 for plasma on.



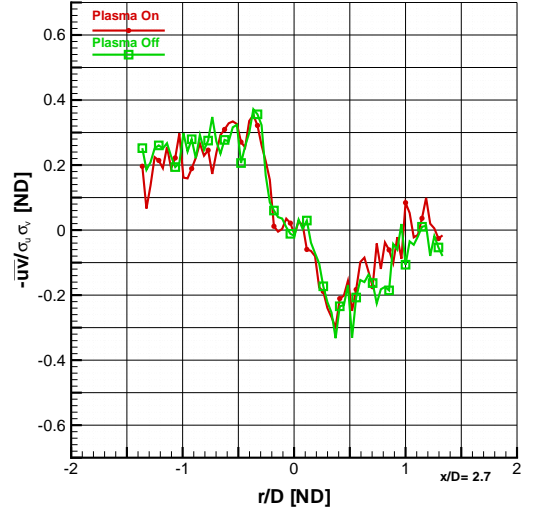
(a) Turbulent Kinetic Energy, $(\sigma_u^2 + \sigma_v^2)/U_o^2$



(b) Structural Parameter, $a_1 = -\overline{uv}/(\sigma_u^2 + \sigma_v^2)$



(c) Reynolds Shear Stress, \overline{uv}/U_o^2



(d) Correlation Coefficient of Reynolds Shear Stress, $-\overline{uv}/(\sigma_u \sigma_v)$

Figure A.41: Comparison of Plasma Effects on Second Moment Fluctuations: Case 610LINE3032

This is a continuing investigation into the effect of plasma on an overexpanded jet (Mach 2.0 jet driven with a Mach 1.9 pressure ratio), 2.7 diameters from the anode face. The jet diameter is 11.3 mm. The four plots represented above are a comparison between plasma on in red versus plasma off in green. Figure A.41 (a) is non-dimensionalized turbulent kinetic energy and panel (b) is the structural parameter a_1 . At this station, U_o is 507.9 m/s for the plasma off case and 507.4 m/s for the plasma on case. Figures A.41 (c) and (d) show the Reynolds shear stress and the correlation coefficient of Reynolds shear stress, respectively. The case identifiers for this comparison were 610cn-LINE3032 for plasma off and 610pn-LINE3032 for plasma on.

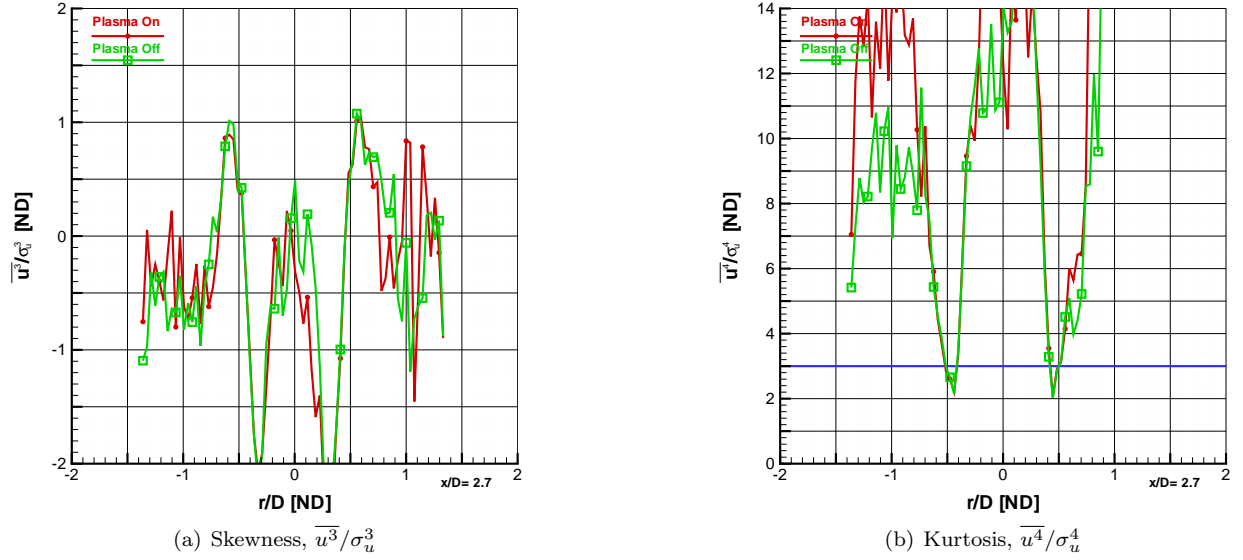
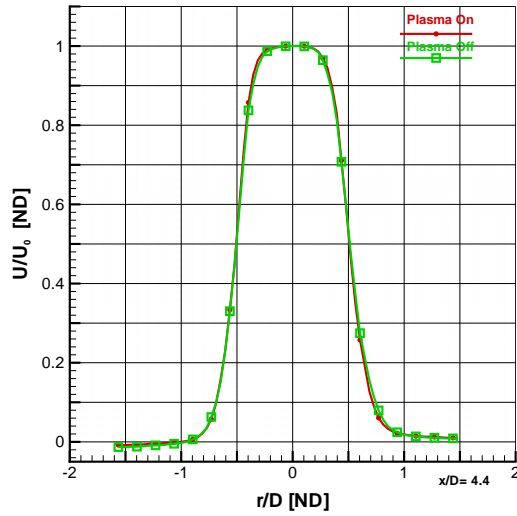
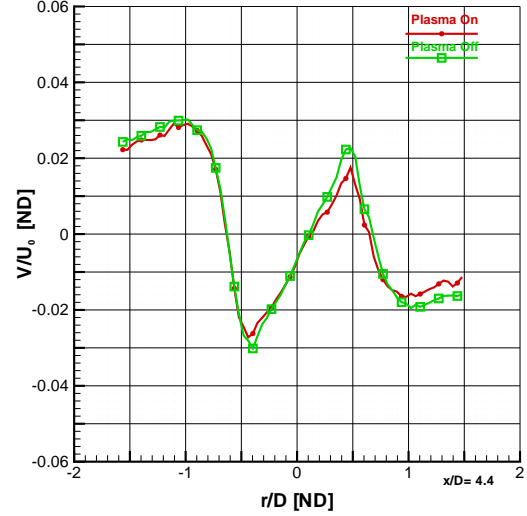


Figure A.42: Comparison of Plasma Effects on Skewness and Kurtosis: Case 610LINE3032

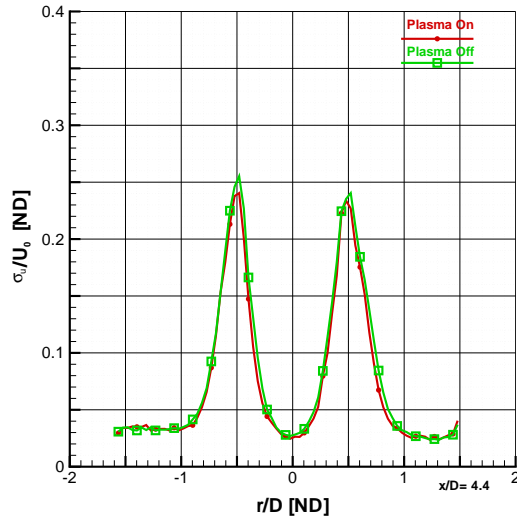
This is the final series of figures on the investigation into the effect of plasma on an overexpanded jet (Mach 2.0 jet driven with a Mach 1.9 pressure ratio), 2.7 diameters from the anode face. The jet diameter is 11.3 mm. The two plots represented above are a comparison between plasma on in red versus plasma off in green. The plasma off case is placed on top of the plasma on case, therefore making it easier to notice small changes between the two cases. Figure A.42 (a) (b) are the measurements of skewness and kurtosis (or flatness), respectively. A Gaussian distribution has skewness of zero, which indicates a distribution of fluctuations is symmetric about the mean. Positive skewness represents a shift toward the right tail (positive fluctuations), while negative skewness is shifted toward negative fluctuations. A Gaussian distribution has kurtosis of three, represented by the blue line. Values lower than three represent a distribution of velocity with higher peakedness than a Gaussian distribution. Conversely, values above three represent flatter distributions. The case identifiers for this comparison were 610cn-LINE3032 for plasma off and 610pn-LINE3032 for plasma on.



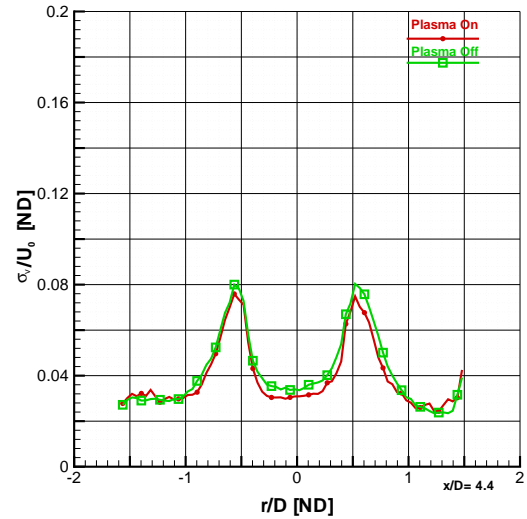
(a) Mean Axial Velocity, U/U_o



(b) Mean Tangential Velocity, V/U_o



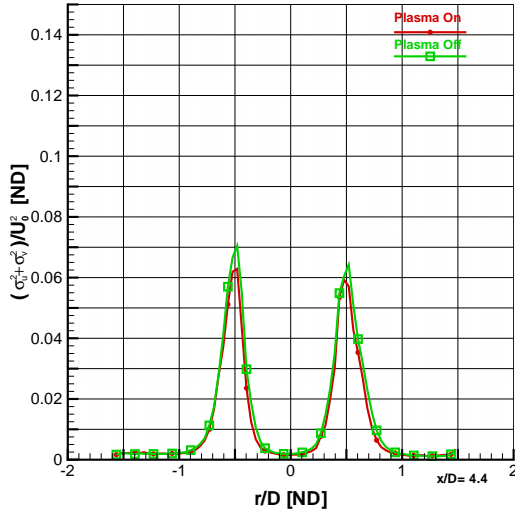
(c) Fluctuating Axial Velocity, σ_u/U_o



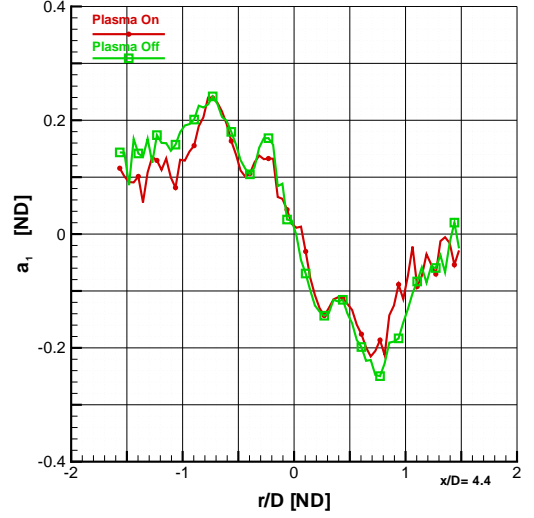
(d) Fluctuating Tangential Velocity, σ_v/U_o

Figure A.43: Comparison of Plasma Effects on Mean Velocity and Fluctuations: Case 608LINE5018

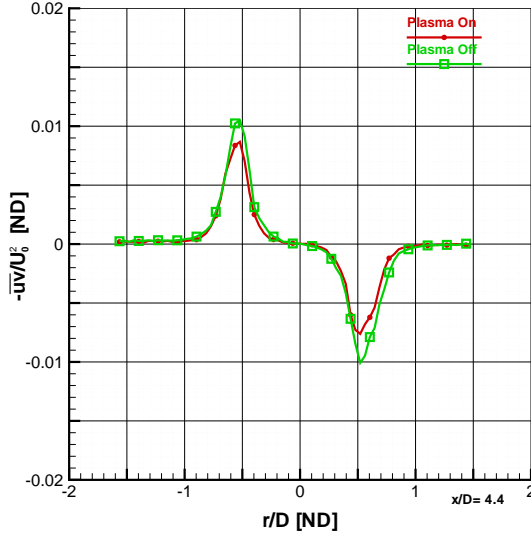
This is an investigation into the effect of plasma on an overexpanded jet (Mach 2.0 jet driven with a Mach 1.9 pressure ratio), 4.4 diameters from the anode face. The jet diameter is 11.3 mm. The four plots represented above are a comparison between plasma on in red versus plasma off in green. Figure A.43 (a) is non-dimensionalized axial velocity. For these figures, U_o is 504.7 m/s for the plasma off case and 505.3 m/s for the plasma on case. Figure A.43 (b) is the mean tangential component of the velocity. Figures A.43 (c) and (d) show the Reynolds normal stresses in the axial and tangential directions, respectively. The case identifiers for this comparison were 608cnc-LINE5018 for plasma off and 608pnc-LINE5018 for plasma on.



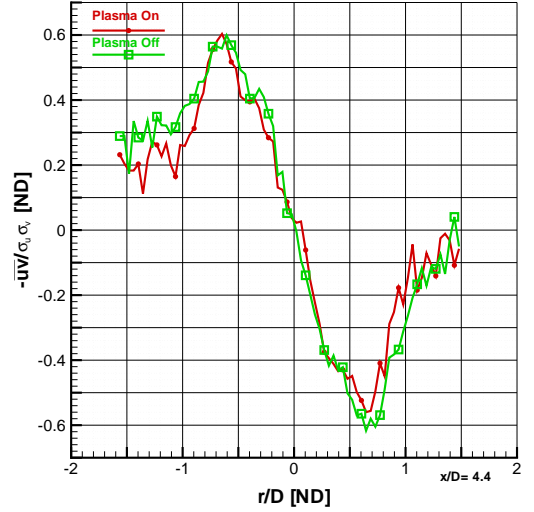
(a) Turbulent Kinetic Energy, $(\sigma_u^2 + \sigma_v^2)/U_o^2$



(b) Structural Parameter, $a_1 = -\overline{uv}/(\sigma_u^2 + \sigma_v^2)$



(c) Reynolds Shear Stress, \overline{uv}/U_o^2



(d) Correlation Coefficient of Reynolds Shear Stress, $-\overline{uv}/(\sigma_u \sigma_v)$

Figure A.44: Comparison of Plasma Effects on Second Moment Fluctuations: Case 608LINE5018

This is a continuing investigation into the effect of plasma on an overexpanded jet (Mach 2.0 jet driven with a Mach 1.9 pressure ratio), 4.4 diameters from the anode. The jet diameter is 11.3 mm. The four plots represented above are a comparison between plasma on in red versus plasma off in green. Figure A.44 (a) is non-dimensionalized turbulent kinetic energy and panel (b) is the structural parameter a_1 . At this station, U_o is 504.7 m/s for the plasma off case and 505.3 m/s for the plasma on case. Figures A.44 (c) and (d) show the Reynolds shear stress and the correlation coefficient of Reynolds shear stress, respectively. The case identifiers were 608cnc-LINE5018 for plasma off and 608pnc-LINE5018 for plasma on.

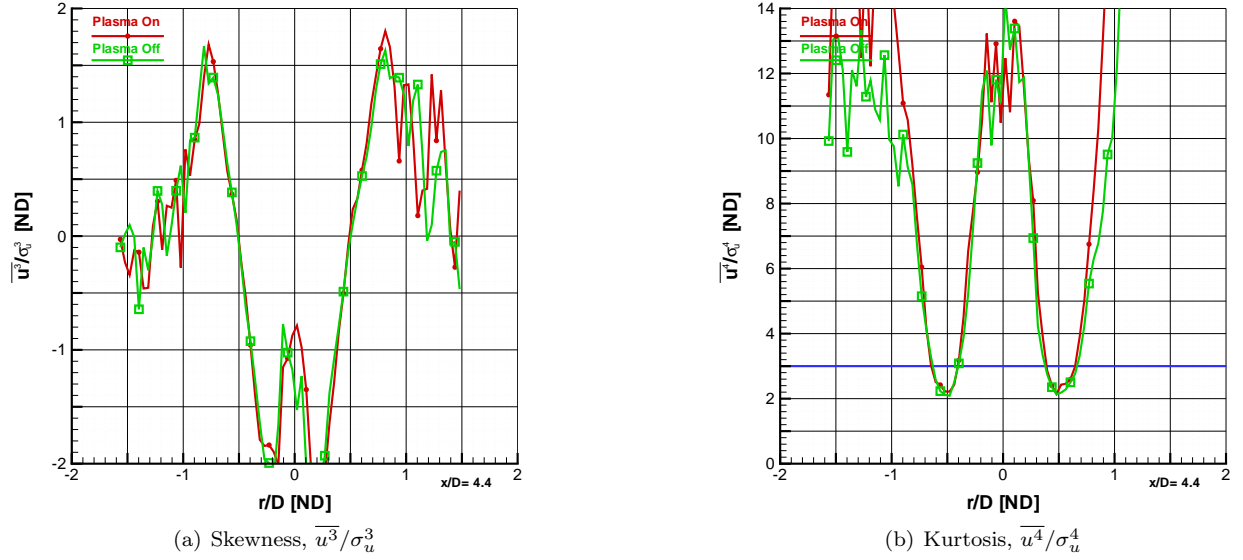
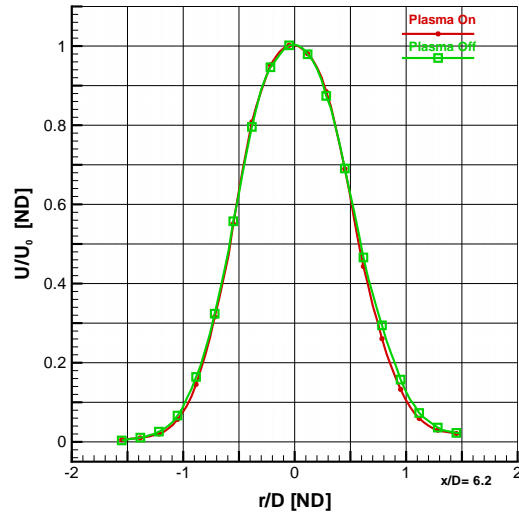
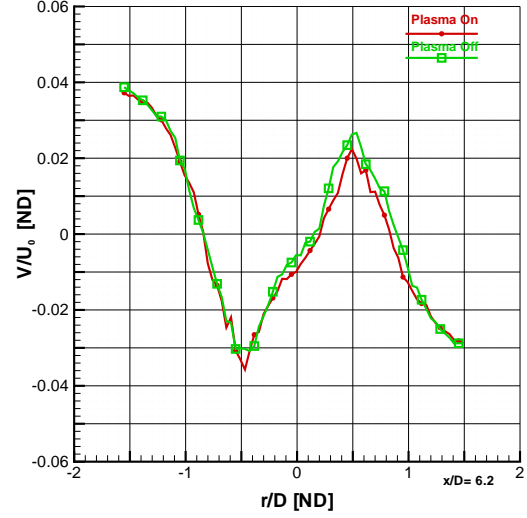


Figure A.45: Comparison of Plasma Effects on Skewness and Kurtosis: Case 608LINE5018

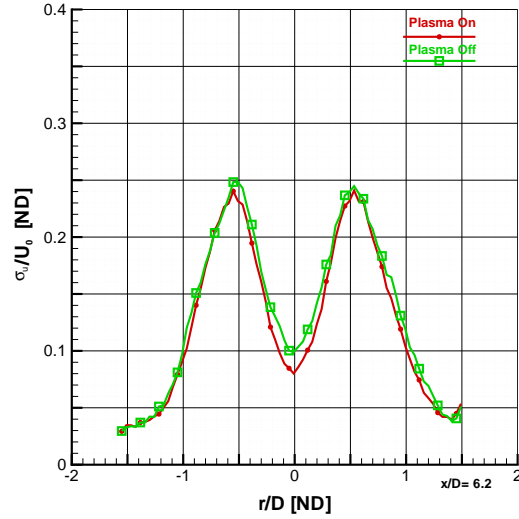
This is the final series of figures on the investigation into the effect of plasma on an overexpanded jet (Mach 2.0 jet driven with a Mach 1.9 pressure ratio), 4.4 diameters from the anode face. The jet diameter is 11.3 mm. The two plots represented above are a comparison between plasma on in red versus plasma off in green. The plasma off case is placed on top of the plasma on case, therefore making it easier to notice small changes between the two cases. Figure A.45 (a) (b) are the measurements of skewness and kurtosis (or flatness), respectively. A Gaussian distribution has skewness of zero, which indicates a distribution of fluctuations is symmetric about the mean. Positive skewness represents a shift toward the right tail (positive fluctuations), while negative skewness is shifted toward negative fluctuations. A Gaussian distribution has kurtosis of three, represented by the blue line. Values lower than three represent a distribution of velocity with higher peakedness than a Gaussian distribution. Conversely, values above three represent flatter distributions. The case identifiers for this comparison were 608cnc-LINE5018 for plasma off and 608pnc-LINE5018 for plasma on.



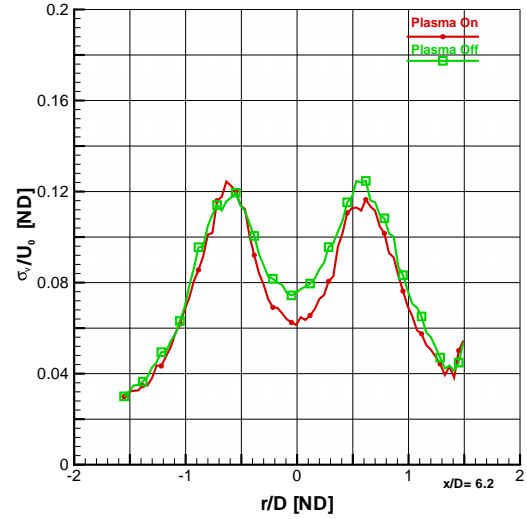
(a) Mean Axial Velocity, U/U_o



(b) Mean Tangential Velocity, V/U_o



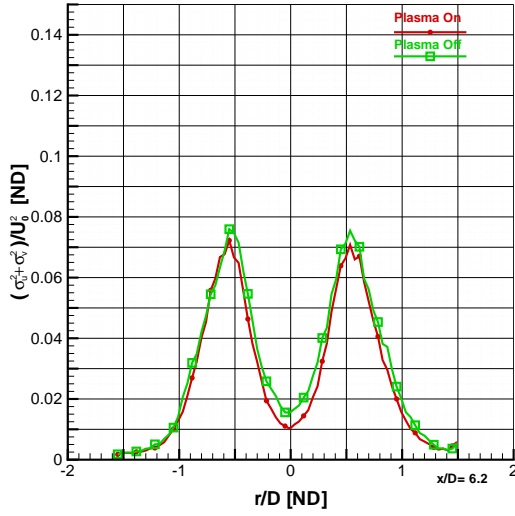
(c) Fluctuating Axial Velocity, σ_u/U_o



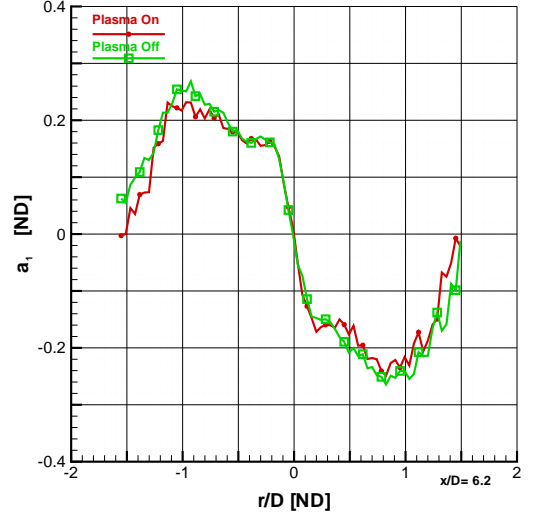
(d) Fluctuating Tangential Velocity, σ_v/U_o

Figure A.46: Comparison of Plasma Effects on Mean Velocity and Fluctuations: Case 608LINE6996

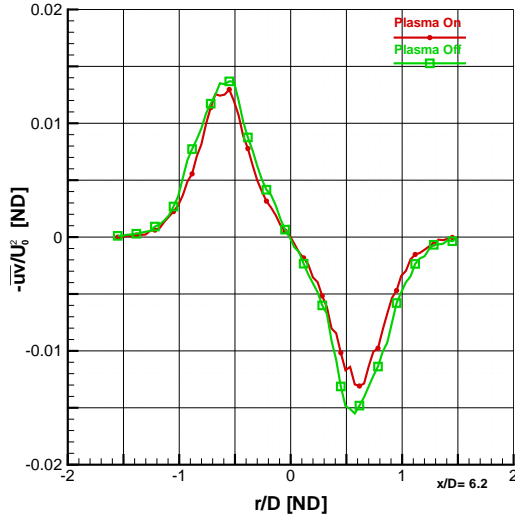
This is an investigation into the effect of plasma on an overexpanded jet (Mach 2.0 jet driven with a Mach 1.9 pressure ratio), 6.2 diameters from the anode face. The jet diameter is 11.3 mm. The four plots represented above are a comparison between plasma on in red versus plasma off in green. Figure A.46 (a) is non-dimensionalized axial velocity. For these figures, U_o is 475.2 m/s for the plasma off case and 486.2 m/s for the plasma on case. Figure A.46 (b) is the mean tangential component of the velocity. Figures A.46 (c) and (d) show the Reynolds normal stresses in the axial and tangential directions, respectively. The case identifiers for this comparison were 608cnc-LINE6996 for plasma off and 608pnc-LINE6996 for plasma on.



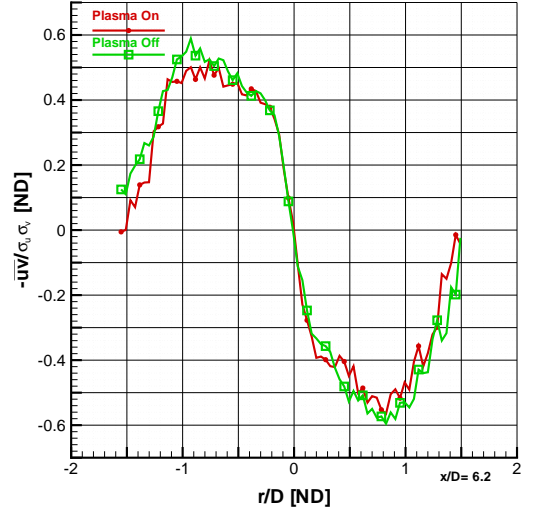
(a) Turbulent Kinetic Energy, $(\sigma_u^2 + \sigma_v^2)/U_o^2$



(b) Structural Parameter, $a_1 = -\overline{uv}/(\sigma_u^2 + \sigma_v^2)$



(c) Reynolds Shear Stress, \overline{uv}/U_o^2



(d) Correlation Coefficient of Reynolds Shear Stress, $-\overline{uv}/(\sigma_u \sigma_v)$

Figure A.47: Comparison of Plasma Effects on Second Moment Fluctuations: Case 608LINE6996

This is a continuing investigation into the effect of plasma on an overexpanded jet (Mach 2.0 jet driven with a Mach 1.9 pressure ratio), 6.2 diameters from the anode. The jet diameter is 11.3 mm. The four plots represented above are a comparison between plasma on in red versus plasma off in green. Figure A.47 (a) is non-dimensionalized turbulent kinetic energy and panel (b) is the structural parameter a_1 . At this station, U_o is 475.2 m/s for the plasma off case and 486.2 m/s for the plasma on case. Figures A.47 (c) and (d) show the Reynolds shear stress and the correlation coefficient of Reynolds shear stress, respectively. The case identifiers were 608cnc-LINE6996 for plasma off and 608pnc-LINE6996 for plasma on.

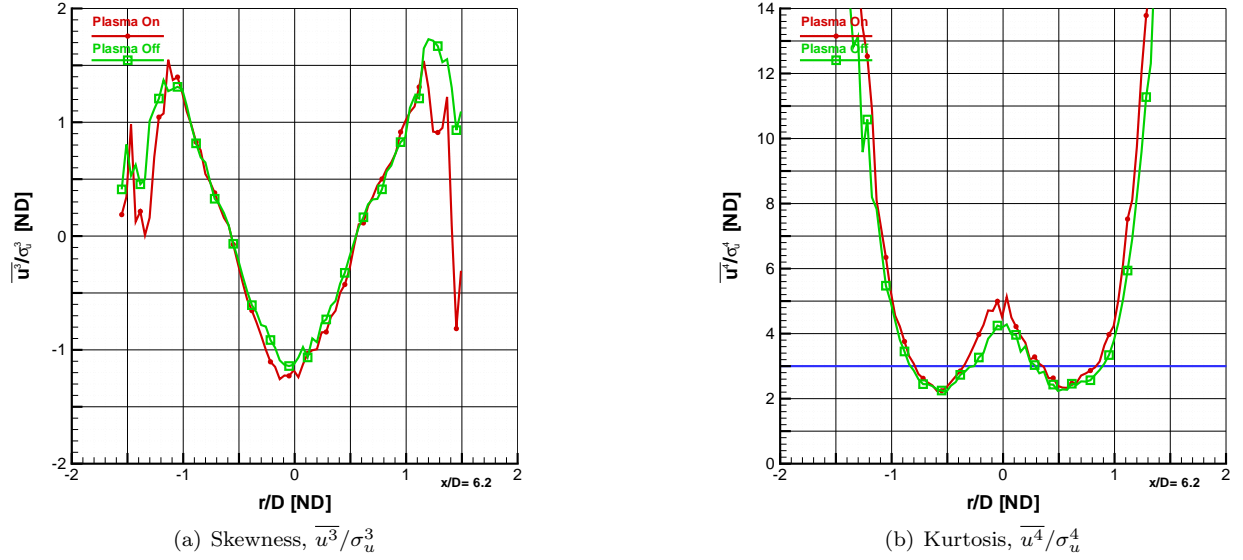


Figure A.48: Comparison of Plasma Effects on Skewness and Kurtosis: Case 608LINE6996

This is the final series of figures on the investigation into the effect of plasma on an overexpanded jet (Mach 2.0 jet driven with a Mach 1.9 pressure ratio), 6.2 diameters from the anode face. The jet diameter is 11.3 mm. The two plots represented above are a comparison between plasma on in red versus plasma off in green. The plasma off case is placed on top of the plasma on case, therefore making it easier to notice small changes between the two cases. Figure A.48 (a) (b) are the measurements of skewness and kurtosis (or flatness), respectively. A Gaussian distribution has skewness of zero, which indicates a distribution of fluctuations is symmetric about the mean. Positive skewness represents a shift toward the right tail (positive fluctuations), while negative skewness is shifted toward negative fluctuations. A Gaussian distribution has kurtosis of three, represented by the blue line. Values lower than three represent a distribution of velocity with higher peakedness than a Gaussian distribution. Conversely, values above three represent flatter distributions. The case identifiers for this comparison were 608cnc-LINE6996 for plasma off and 608pnc-LINE6996 for plasma on.

A.5 Mach 1.4 Converging-Diverging Nozzle at 5 Torr Using Anode with Serrated Conical Feature

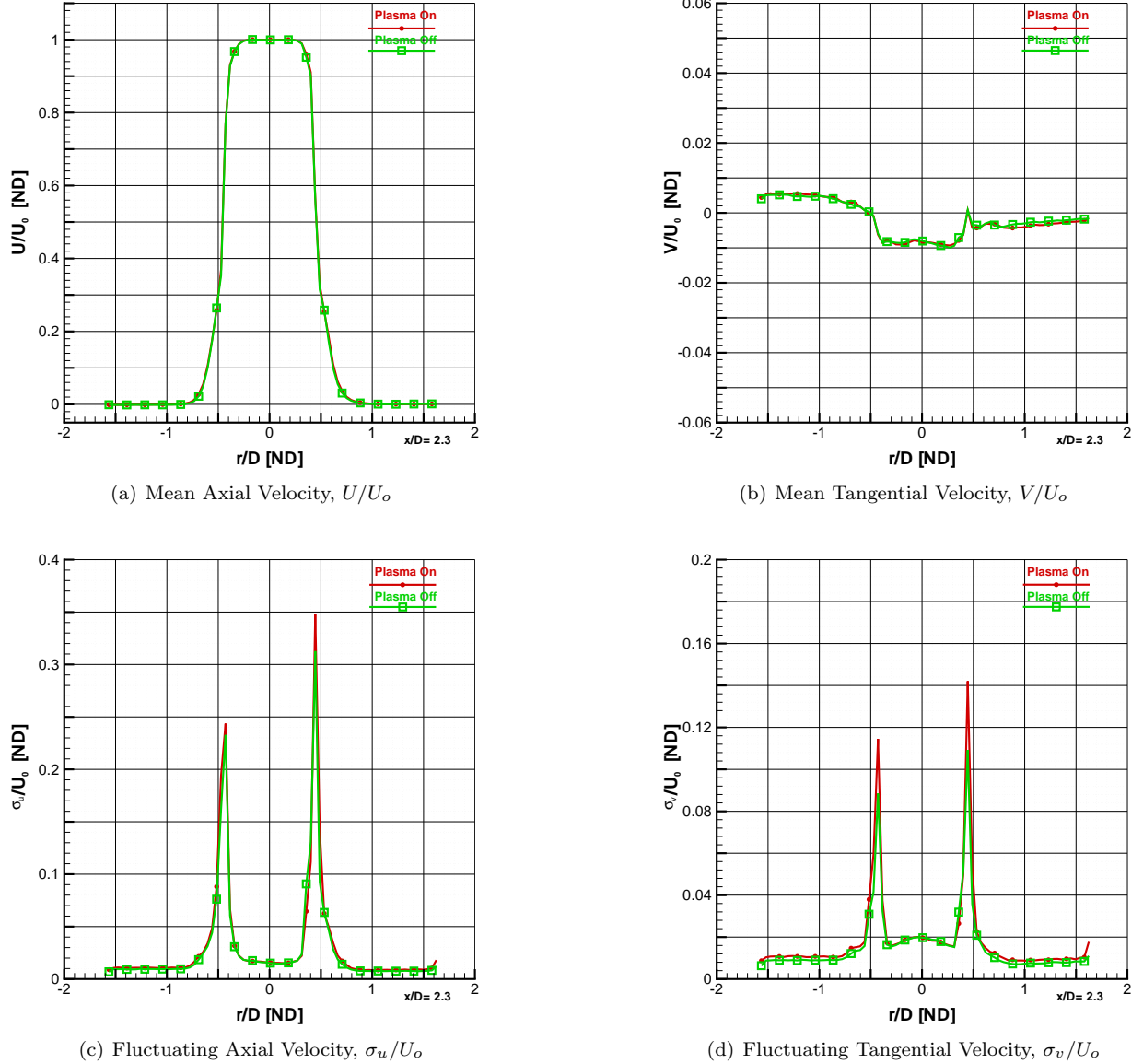
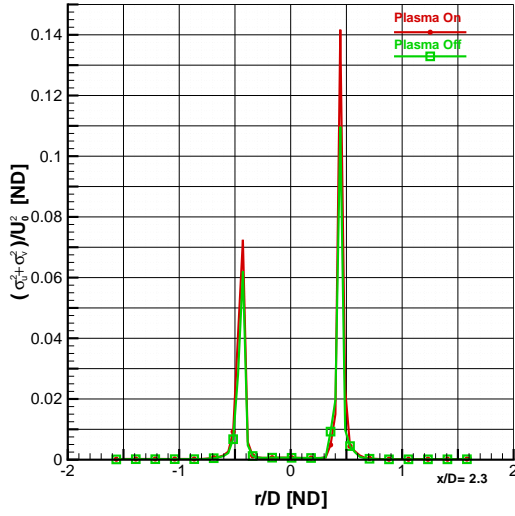
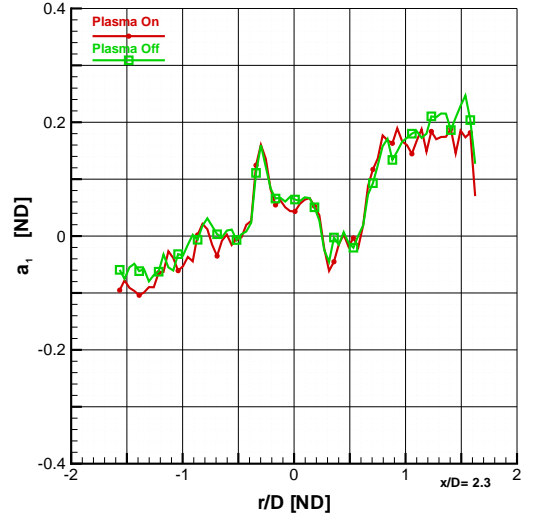


Figure A.49: Comparison of Plasma Effects on Mean Velocity and Fluctuations: Case 633LINE2229

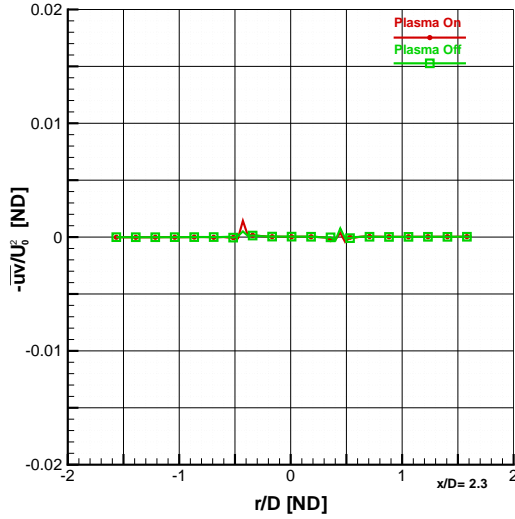
This is an investigation into the effect of plasma on a Mach 1.4 jet, 2.3 diameters from the anode face. The jet diameter is 9.5 mm. The four plots represented above are a comparison between plasma on in red versus plasma off in green. Figure A.49 (a) is non-dimensionalized axial velocity. For these figures, U_o is 404.3 m/s for the plasma off case and 403.4 m/s for the plasma on case. Figure A.49 (b) is the mean tangential component of the velocity. Figures A.49 (c) and (d) show the Reynolds normal stresses.



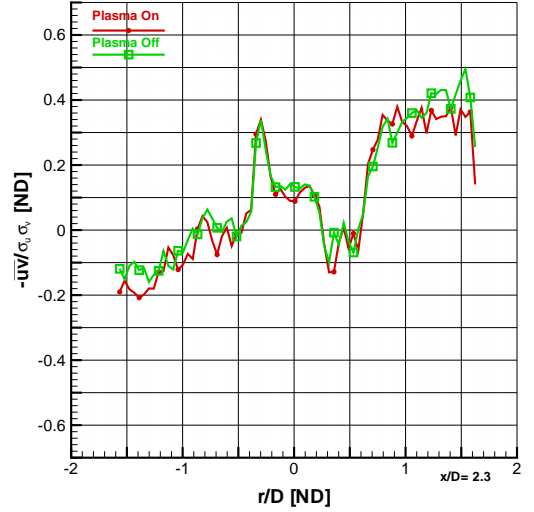
(a) Turbulent Kinetic Energy, $(\sigma_u^2 + \sigma_v^2)/U_o^2$



(b) Structural Parameter, $a_1 = -\overline{uv}/(\sigma_u^2 + \sigma_v^2)$



(c) Reynolds Shear Stress, \overline{uv}/U_o^2



(d) Correlation Coefficient of Reynolds Shear Stress, $-\overline{uv}/(\sigma_u \sigma_v)$

Figure A.50: Comparison of Plasma Effects on Second Moment Fluctuations: Case 633LINE2229

This is a continuing investigation into the effect of plasma on a Mach 1.4 jet, 2.3 diameters from the anode face. The jet diameter is 9.5 mm. The four plots represented above are a comparison between plasma on in red versus plasma off in green. Figure A.50 (a) is non-dimensionalized turbulent kinetic energy and panel (b) is the structural parameter a_1 . At this station, U_o is 404.3 m/s for the plasma off case and 403.4 m/s for the plasma on case. Figures A.50 (c) and (d) show the Reynolds shear stress and the correlation coefficient of Reynolds shear stress, respectively. The case identifiers for this comparison were 633cn-LINE2229 for plasma off and 633pn-LINE2229 for plasma on.

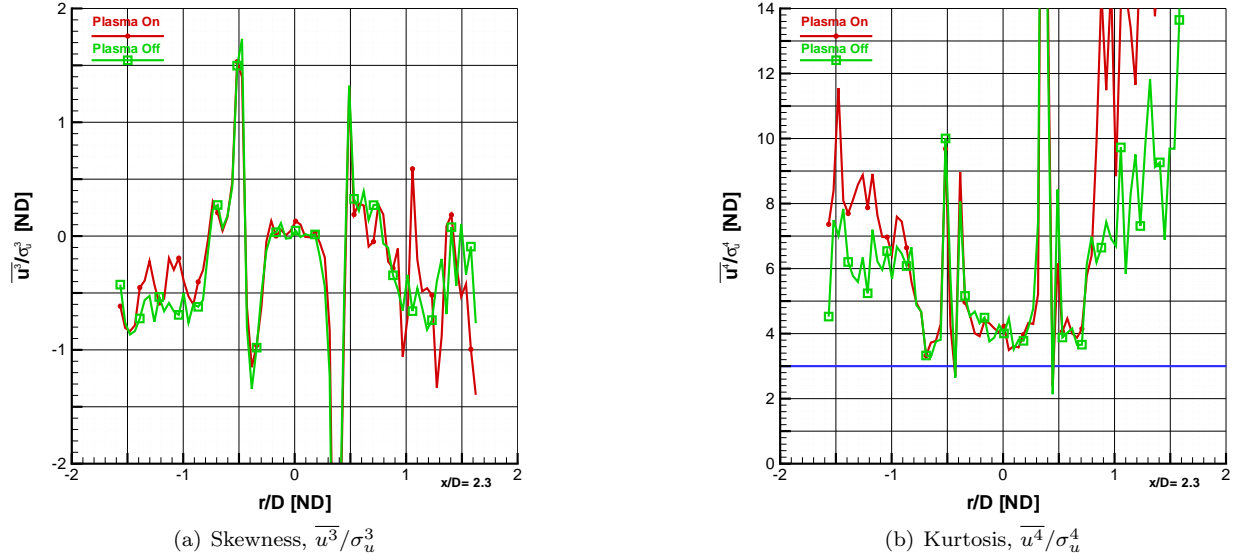
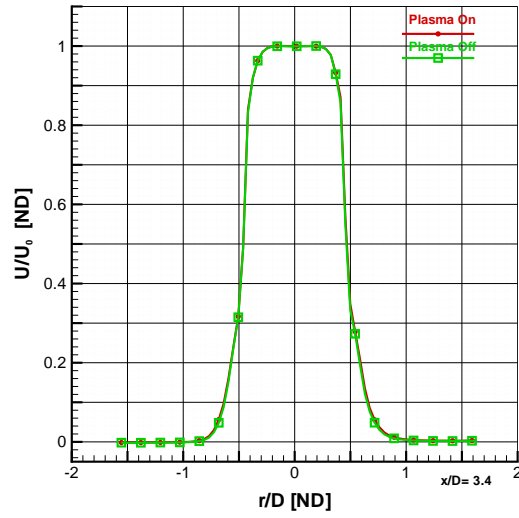
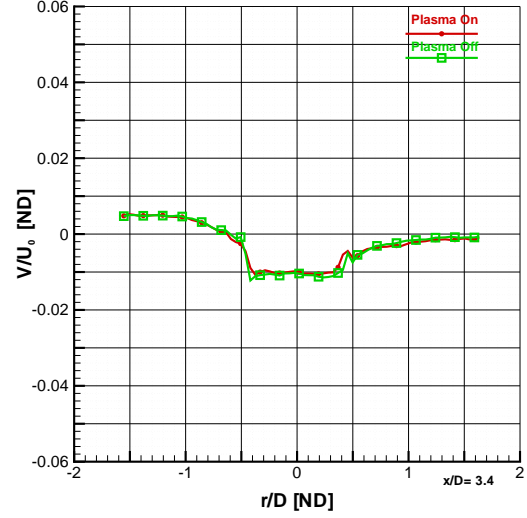


Figure A.51: Comparison of Plasma Effects on Skewness and Kurtosis: Case 633LINE2229

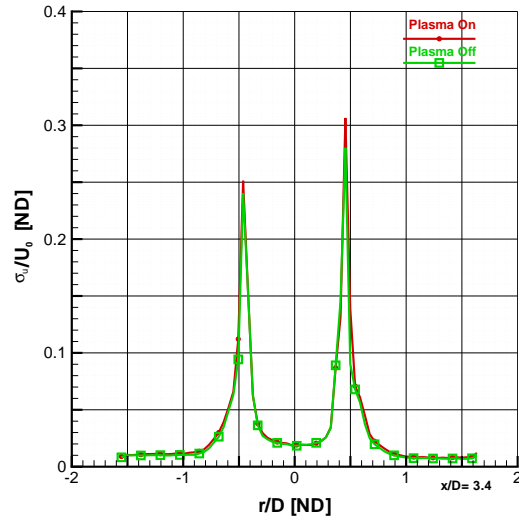
This is the final series of figures on the investigation into the effect of plasma on a Mach 1.4 jet, 2.3 diameters from the anode face. The jet diameter is 9.5 mm. The two plots represented above are a comparison between plasma on in red versus plasma off in green. The plasma off case is placed on top of the plasma on case, therefore making it easier to notice small changes between the two cases. Figure A.51 (a) (b) are the measurements of skewness and kurtosis (or flatness), respectively. A Gaussian distribution has skewness of zero, which indicates a distribution of fluctuations is symmetric about the mean. Positive skewness represents a shift toward the right tail (positive fluctuations), while negative skewness is shifted toward negative fluctuations. A Gaussian distribution has kurtosis of three, represented by the blue line. Values lower than three represent a distribution of velocity with higher peakedness than a Gaussian distribution. Conversely, values above three represent flatter distributions. The case identifiers for this comparison were 633cn-LINE2229 for plasma off and 633pn-LINE2229 for plasma on.



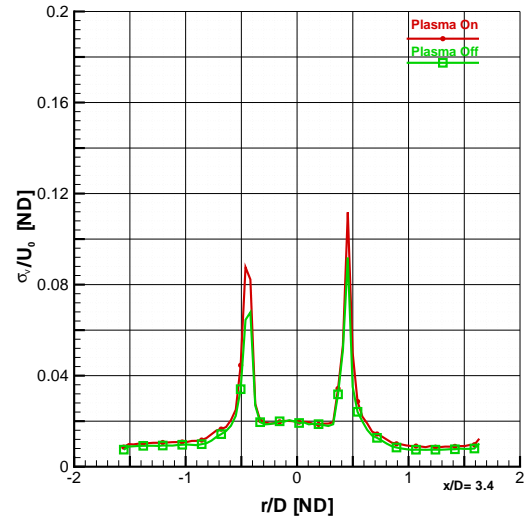
(a) Mean Axial Velocity, U/U_o



(b) Mean Tangential Velocity, V/U_o



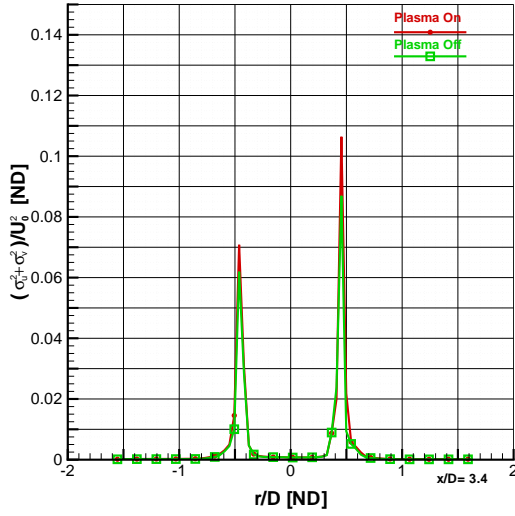
(c) Fluctuating Axial Velocity, σ_u/U_o



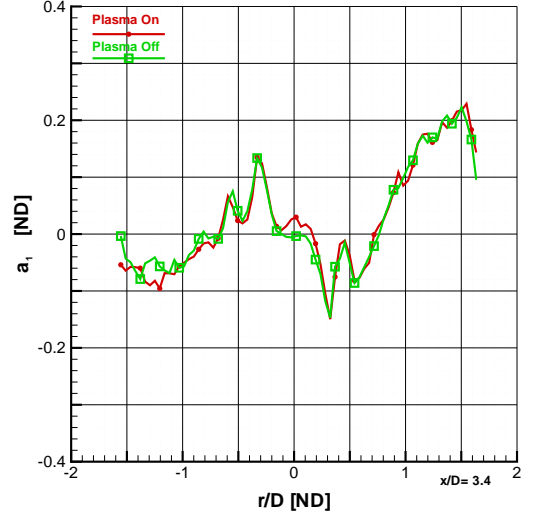
(d) Fluctuating Tangential Velocity, σ_v/U_o

Figure A.52: Comparison of Plasma Effects on Mean Velocity and Fluctuations: Case 633LINE3227

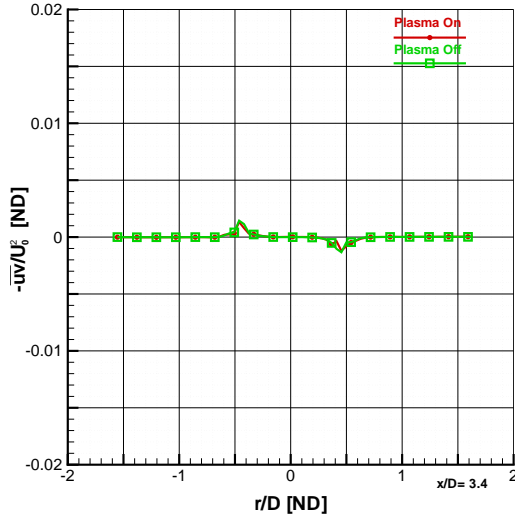
This is an investigation into the effect of plasma on a Mach 1.4 jet, 3.4 diameters from the anode face. The jet diameter is 9.5 mm. The four plots represented above are a comparison between plasma on in red versus plasma off in green. Figure A.52 (a) is non-dimensionalized axial velocity. For these figures, U_o is 404.1 m/s for the plasma off case and 403.7 m/s for the plasma on case. Figure A.52 (b) is the mean tangential component of the velocity. Figures A.52 (c) and (d) show the Reynolds normal stresses in the axial and tangential directions, respectively. The case identifiers for this comparison were 633cn-LINE3227 for plasma off and 633pn-LINE3227 for plasma on.



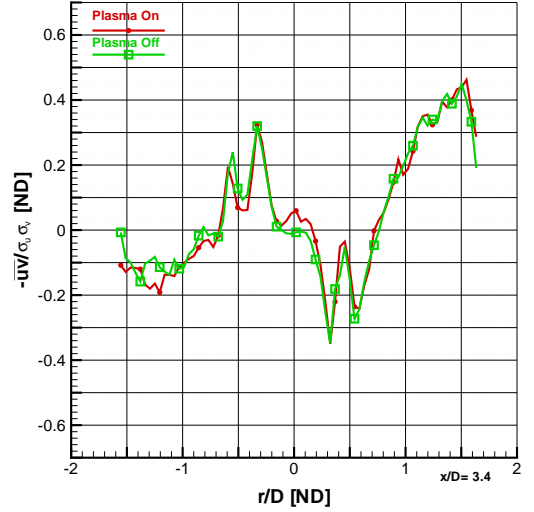
(a) Turbulent Kinetic Energy, $(\sigma_u^2 + \sigma_v^2)/U_o^2$



(b) Structural Parameter, $a_1 = -\overline{uv}/(\sigma_u^2 + \sigma_v^2)$



(c) Reynolds Shear Stress, \overline{uv}/U_o^2



(d) Correlation Coefficient of Reynolds Shear Stress, $-\overline{uv}/(\sigma_u \sigma_v)$

Figure A.53: Comparison of Plasma Effects on Second Moment Fluctuations: Case 633LINE3227

This is a continuing investigation into the effect of plasma on a Mach 1.4 jet, 3.4 diameters from the anode face. The jet diameter is 9.5 mm. The four plots represented above are a comparison between plasma on in red versus plasma off in green. Figure A.53 (a) is non-dimensionalized turbulent kinetic energy and panel (b) is the structural parameter a_1 . At this station, U_o is 404.1 m/s for the plasma off case and 403.7 m/s for the plasma on case. Figures A.53 (c) and (d) show the Reynolds shear stress and the correlation coefficient of Reynolds shear stress, respectively. The case identifiers for this comparison were 633cn-LINE3227 for plasma off and 633pn-LINE3227 for plasma on.

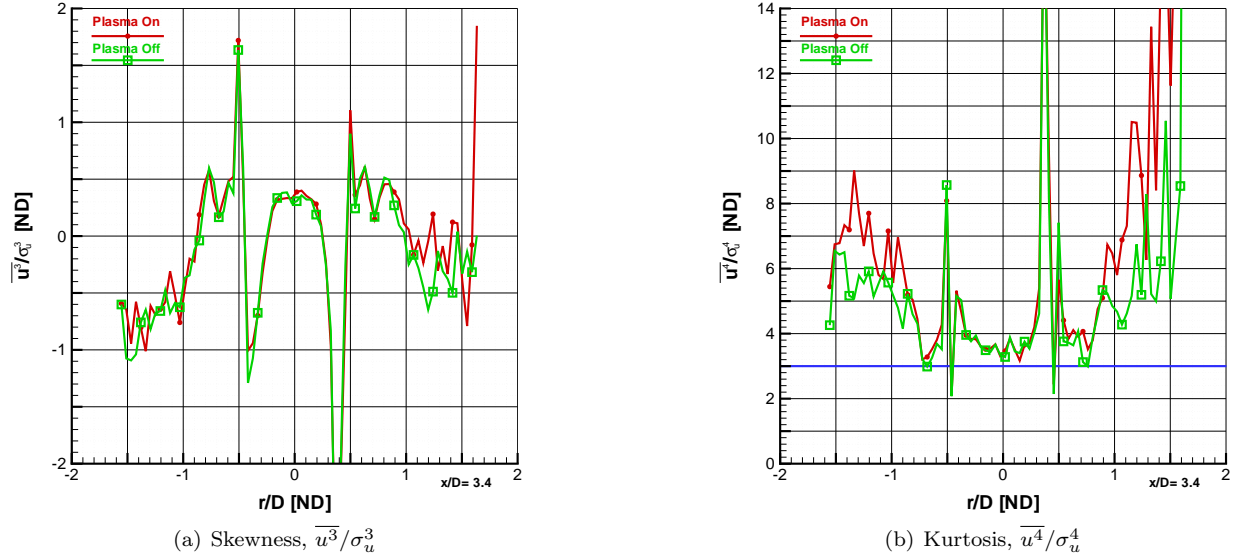
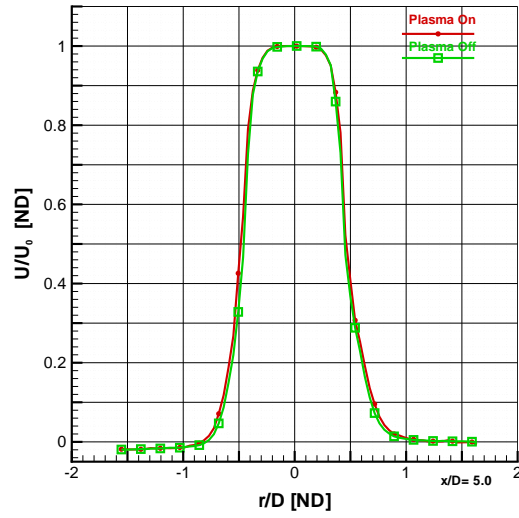
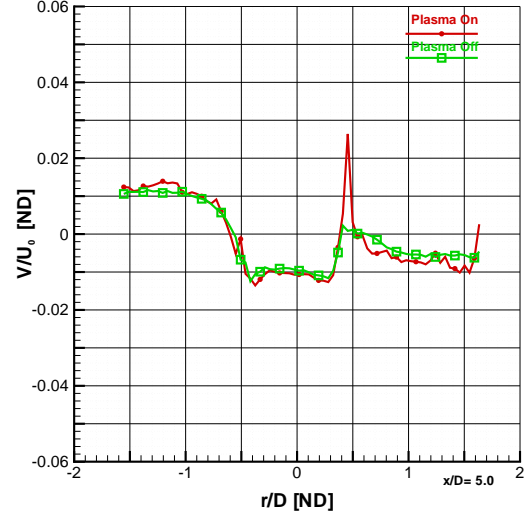


Figure A.54: Comparison of Plasma Effects on Skewness and Kurtosis: Case 633LINE3227

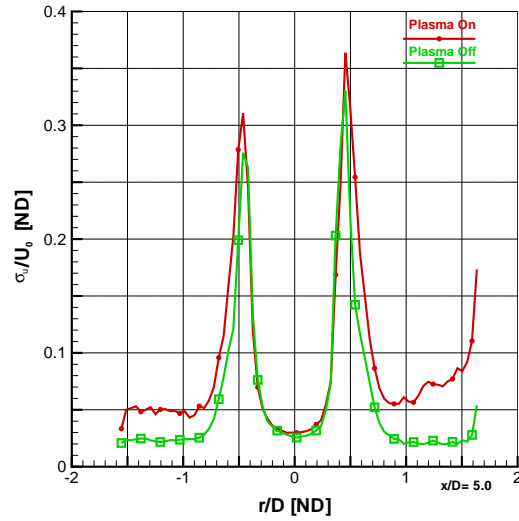
This is the final series of figures on the investigation into the effect of plasma on a Mach 1.4 jet, 3.4 diameters from the anode face. The jet diameter is 9.5 mm. The two plots represented above are a comparison between plasma on in red versus plasma off in green. The plasma off case is placed on top of the plasma on case, therefore making it easier to notice small changes between the two cases. Figure A.54 (a) (b) are the measurements of skewness and kurtosis (or flatness), respectively. A Gaussian distribution has skewness of zero, which indicates a distribution of fluctuations is symmetric about the mean. Positive skewness represents a shift toward the right tail (positive fluctuations), while negative skewness is shifted toward negative fluctuations. A Gaussian distribution has kurtosis of three, represented by the blue line. Values lower than three represent a distribution of velocity with higher peakedness than a Gaussian distribution. Conversely, values above three represent flatter distributions. The case identifiers for this comparison were 633cn-LINE3227 for plasma off and 633pn-LINE3227 for plasma on.



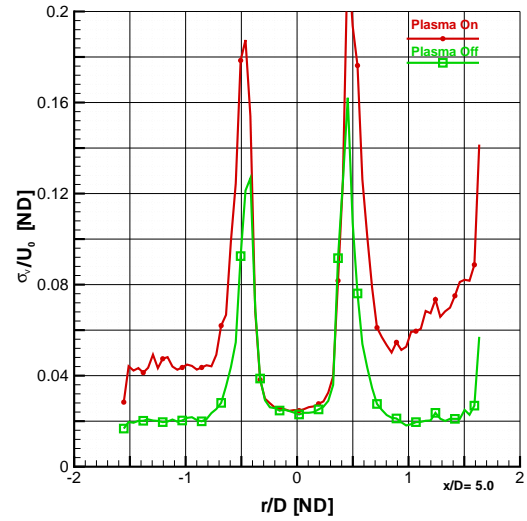
(a) Mean Axial Velocity, U/U_o



(b) Mean Tangential Velocity, V/U_o



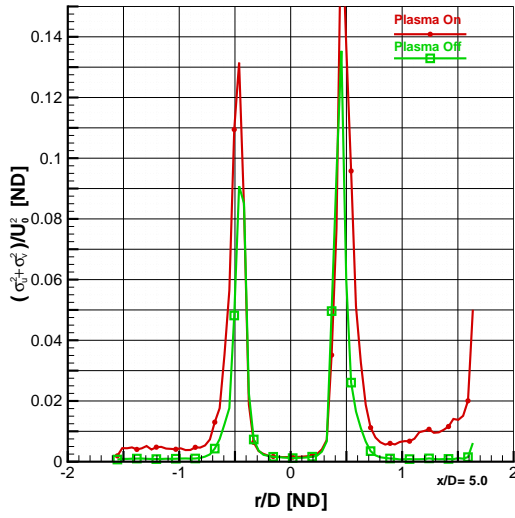
(c) Fluctuating Axial Velocity, σ_u/U_o



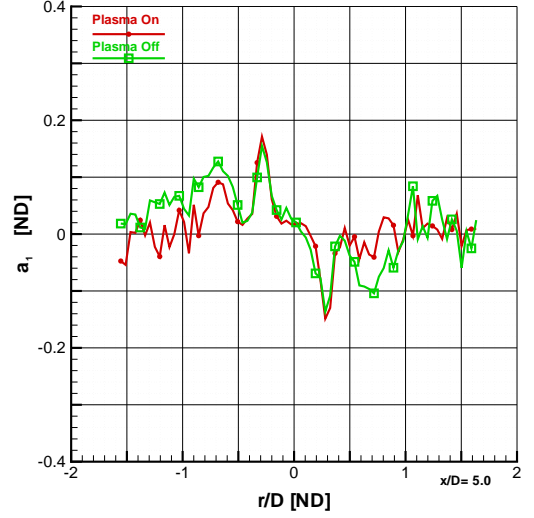
(d) Fluctuating Tangential Velocity, σ_v/U_o

Figure A.55: Comparison of Plasma Effects on Mean Velocity and Fluctuations: Case 634LINE4789

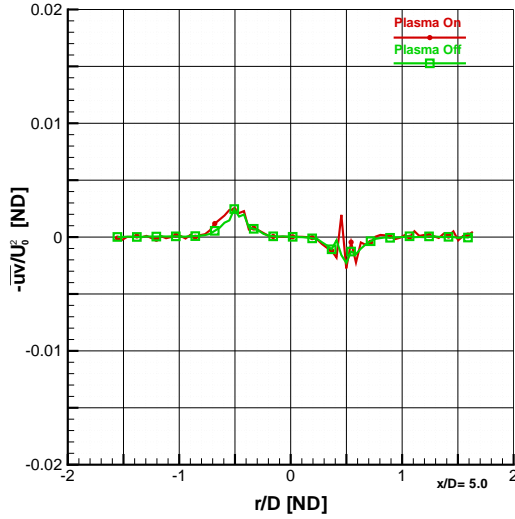
This is an investigation into the effect of plasma on a Mach 1.4 jet, 5.0 diameters from the anode face. The jet diameter is 9.5 mm. The four plots represented above are a comparison between plasma on in red versus plasma off in green. Figure A.55 (a) is non-dimensionalized axial velocity. For these figures, U_o is 402.6 m/s for the plasma off case and 401.6 m/s for the plasma on case. Figure A.55 (b) is the mean tangential component of the velocity. Figures A.55 (c) and (d) show the Reynolds normal stresses in the axial and tangential directions, respectively. The case identifiers for this comparison were 634cn-LINE4789 for plasma off and 634pn-LINE4789 for plasma on.



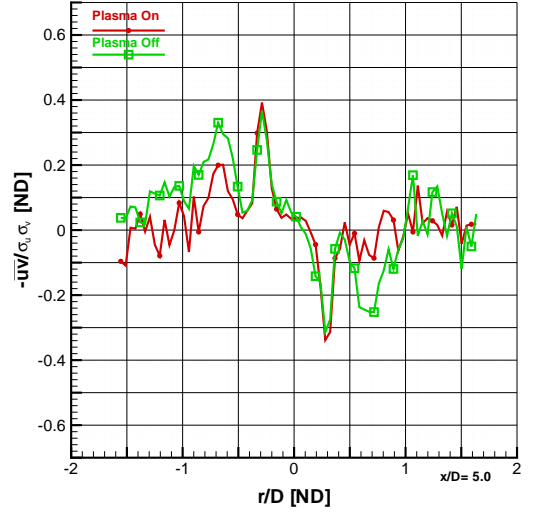
(a) Turbulent Kinetic Energy, $(\sigma_u^2 + \sigma_v^2)/U_o^2$



(b) Structural Parameter, $a_1 = -\overline{uv}/(\sigma_u^2 + \sigma_v^2)$



(c) Reynolds Shear Stress, \overline{uv}/U_o^2



(d) Correlation Coefficient of Reynolds Shear Stress, $-\overline{uv}/(\sigma_u \sigma_v)$

Figure A.56: Comparison of Plasma Effects on Second Moment Fluctuations: Case 634LINE4789

This is a continuing investigation into the effect of plasma on a Mach 1.4 jet, 5.0 diameters from the anode face. The jet diameter is 9.5 mm. The four plots represented above are a comparison between plasma on in red versus plasma off in green. Figure A.56 (a) is non-dimensionalized turbulent kinetic energy and panel (b) is the structural parameter a_1 . At this station, U_o is 402.6 m/s for the plasma off case and 401.6 m/s for the plasma on case. Figures A.56 (c) and (d) show the Reynolds shear stress and the correlation coefficient of Reynolds shear stress, respectively. The case identifiers for this comparison were 634cn-LINE4789 for plasma off and 634pn-LINE4789 for plasma on.

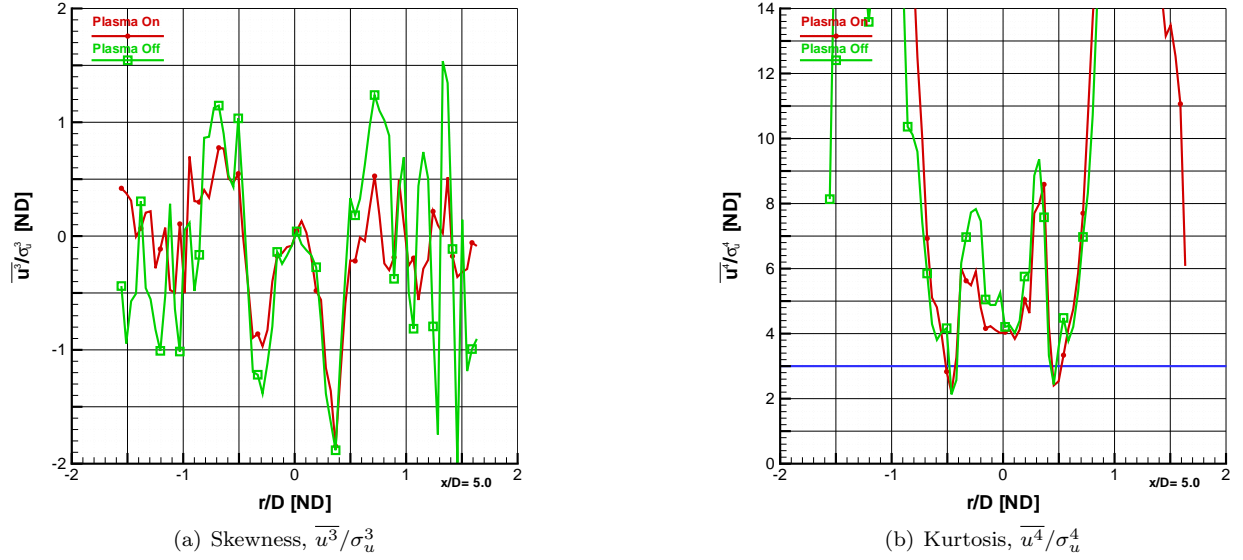
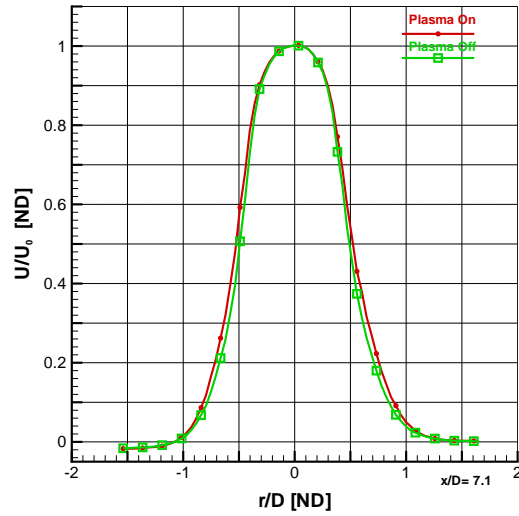
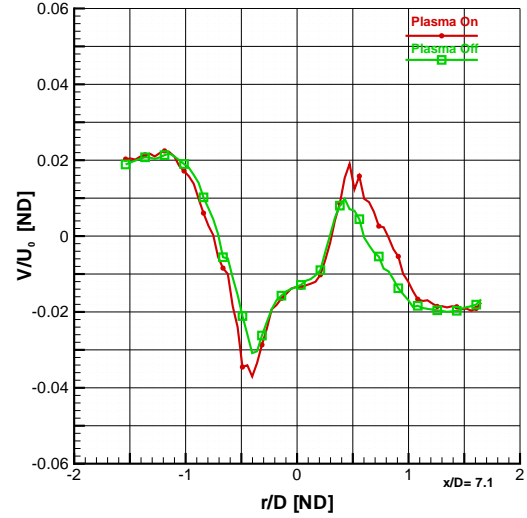


Figure A.57: Comparison of Plasma Effects on Skewness and Kurtosis: Case 634LINE4789

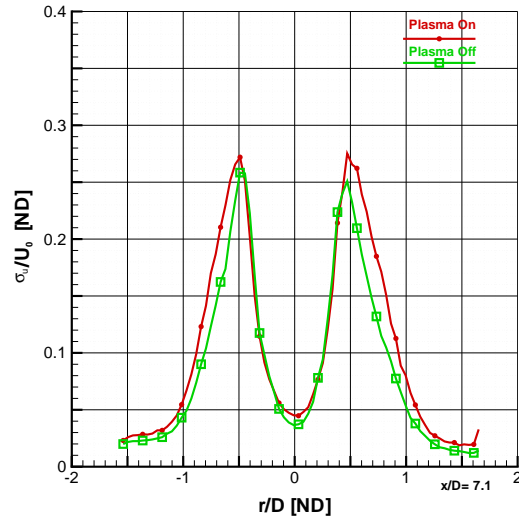
This is the final series of figures on the investigation into the effect of plasma on a Mach 1.4 jet, 5.0 diameters from the anode face. The jet diameter is 9.5 mm. The two plots represented above are a comparison between plasma on in red versus plasma off in green. The plasma off case is placed on top of the plasma on case, therefore making it easier to notice small changes between the two cases. Figure A.57 (a) (b) are the measurements of skewness and kurtosis (or flatness), respectively. A Gaussian distribution has skewness of zero, which indicates a distribution of fluctuations is symmetric about the mean. Positive skewness represents a shift toward the right tail (positive fluctuations), while negative skewness is shifted toward negative fluctuations. A Gaussian distribution has kurtosis of three, represented by the blue line. Values lower than three represent a distribution of velocity with higher peakedness than a Gaussian distribution. Conversely, values above three represent flatter distributions. The case identifiers for this comparison were 634cn-LINE4789 for plasma off and 634pn-LINE4789 for plasma on.



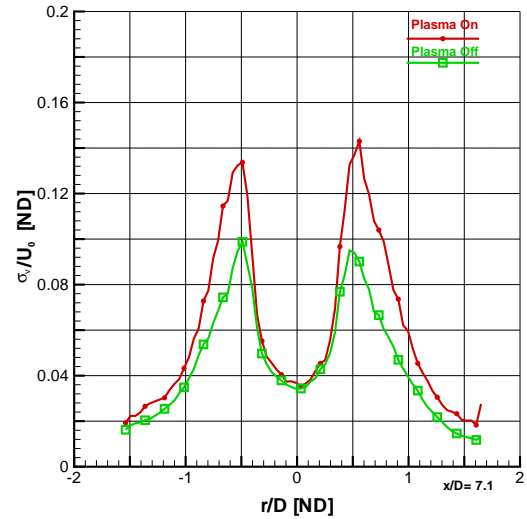
(a) Mean Axial Velocity, U/U_o



(b) Mean Tangential Velocity, V/U_o



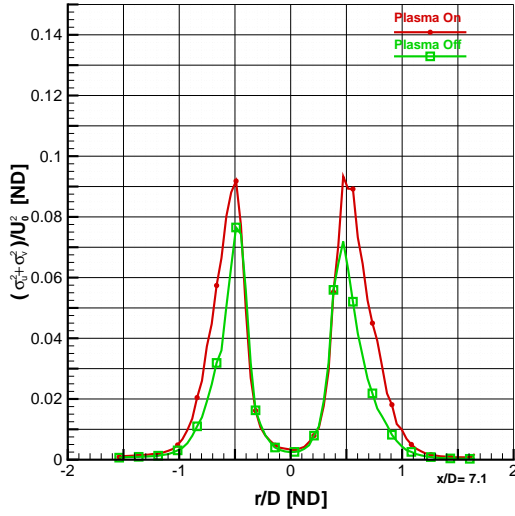
(c) Fluctuating Axial Velocity, σ_u/U_o



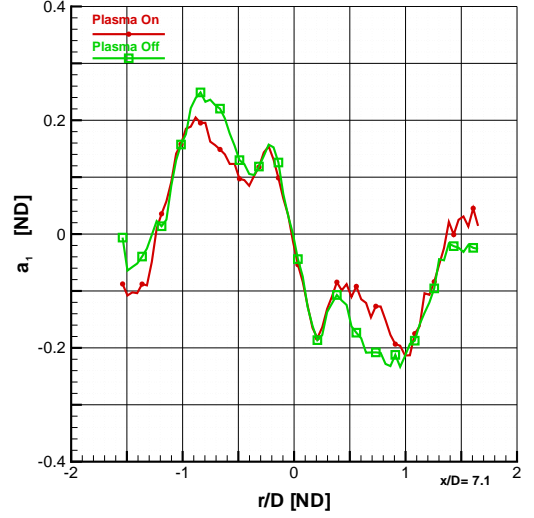
(d) Fluctuating Tangential Velocity, σ_v/U_o

Figure A.58: Comparison of Plasma Effects on Mean Velocity and Fluctuations: Case 634LINE6785

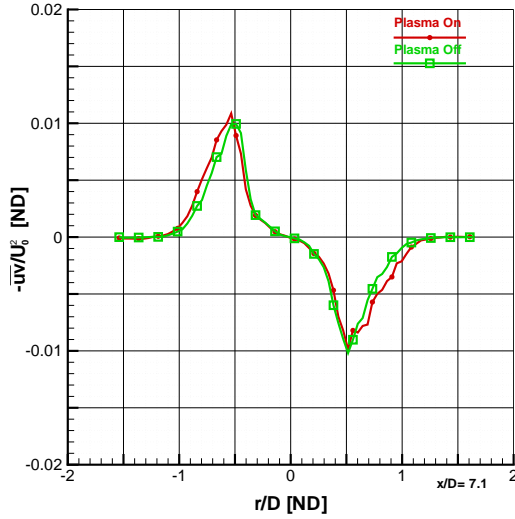
This is an investigation into the effect of plasma on a Mach 1.4 jet, 7.1 diameters from the anode face. The jet diameter is 9.5 mm. The four plots represented above are a comparison between plasma on in red versus plasma off in green. Figure A.58 (a) is non-dimensionalized axial velocity. For these figures, U_o is 400.9 m/s for the plasma off case and 398.6 m/s for the plasma on case. Figure A.58 (b) is the mean tangential component of the velocity. Figures A.58 (c) and (d) show the Reynolds normal stresses in the axial and tangential directions, respectively. The case identifiers for this comparison were 634cn-LINE6785 for plasma off and 634pn-LINE6785 for plasma on.



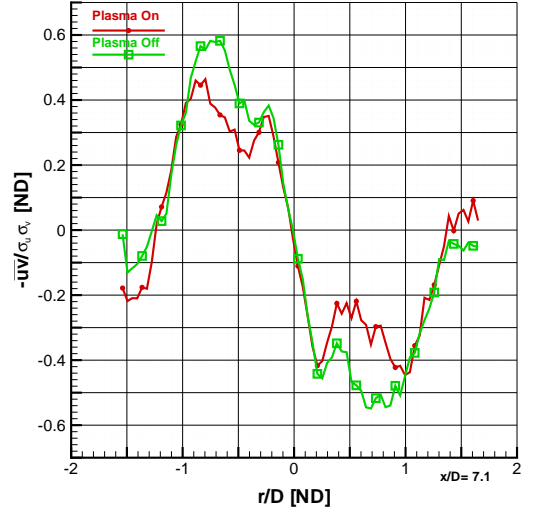
(a) Turbulent Kinetic Energy, $(\sigma_u^2 + \sigma_v^2)/U_o^2$



(b) Structural Parameter, $a_1 = -\overline{uv}/(\sigma_u^2 + \sigma_v^2)$



(c) Reynolds Shear Stress, \overline{uv}/U_o^2



(d) Correlation Coefficient of Reynolds Shear Stress, $-\overline{uv}/(\sigma_u \sigma_v)$

Figure A.59: Comparison of Plasma Effects on Second Moment Fluctuations: Case 634LINE6785

This is a continuing investigation into the effect of plasma on a Mach 1.4 jet, 7.1 diameters from the anode face. The jet diameter is 9.5 mm. The four plots represented above are a comparison between plasma on in red versus plasma off in green. Figure A.59 (a) is non-dimensionalized turbulent kinetic energy and panel (b) is the structural parameter a_1 . At this station, U_o is 400.9 m/s for the plasma off case and 398.6 m/s for the plasma on case. Figures A.59 (c) and (d) show the Reynolds shear stress and the correlation coefficient of Reynolds shear stress, respectively. The case identifiers for this comparison were 634cn-LINE6785 for plasma off and 634pn-LINE6785 for plasma on.

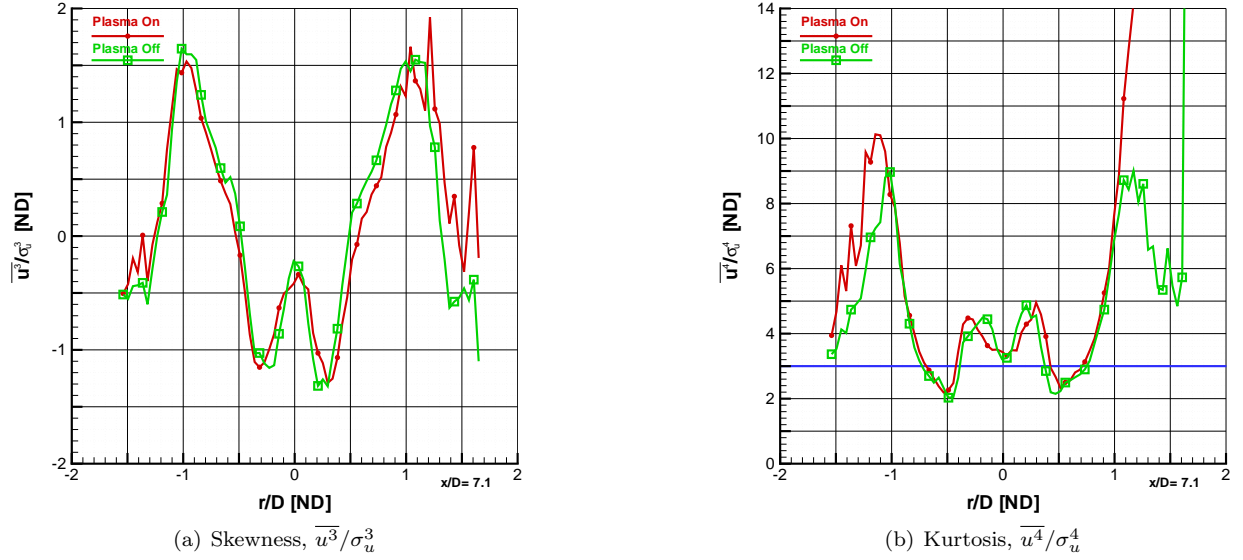
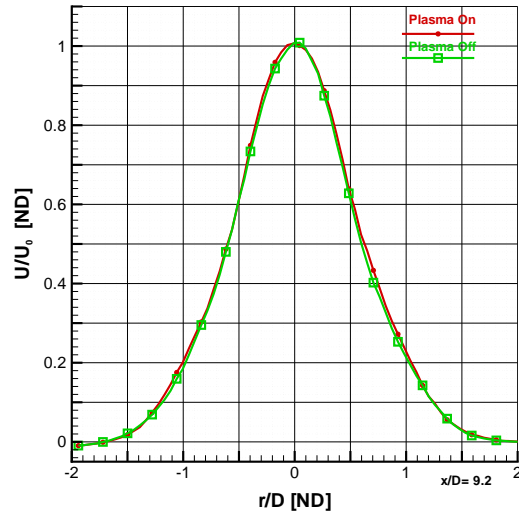
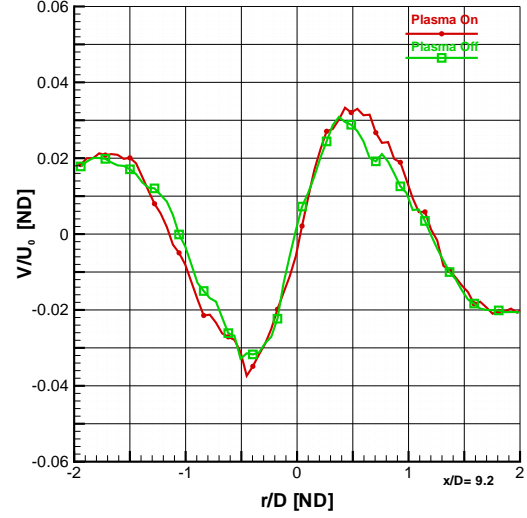


Figure A.60: Comparison of Plasma Effects on Skewness and Kurtosis: Case 634LINE6785

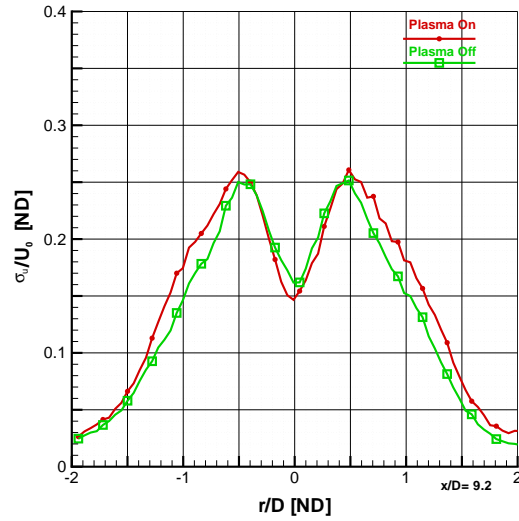
This is the final series of figures on the investigation into the effect of plasma on a Mach 1.4 jet, 7.1 diameters from the anode face. The jet diameter is 9.5 mm. The two plots represented above are a comparison between plasma on in red versus plasma off in green. The plasma off case is placed on top of the plasma on case, therefore making it easier to notice small changes between the two cases. Figure A.60 (a) (b) are the measurements of skewness and kurtosis (or flatness), respectively. A Gaussian distribution has skewness of zero, which indicates a distribution of fluctuations is symmetric about the mean. Positive skewness represents a shift toward the right tail (positive fluctuations), while negative skewness is shifted toward negative fluctuations. A Gaussian distribution has kurtosis of three, represented by the blue line. Values lower than three represent a distribution of velocity with higher peakedness than a Gaussian distribution. Conversely, values above three represent flatter distributions. The case identifiers for this comparison were 634cn-LINE6785 for plasma off and 634pn-LINE6785 for plasma on.



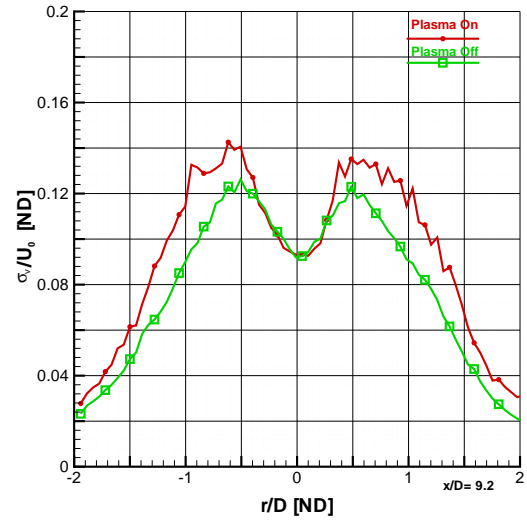
(a) Mean Axial Velocity, U/U_o



(b) Mean Tangential Velocity, V/U_o



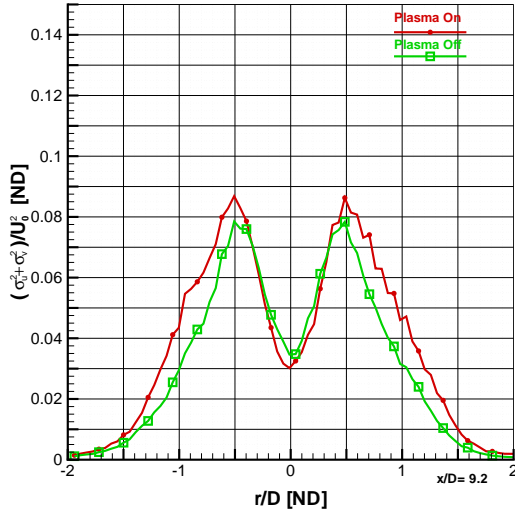
(c) Fluctuating Axial Velocity, σ_u/U_o



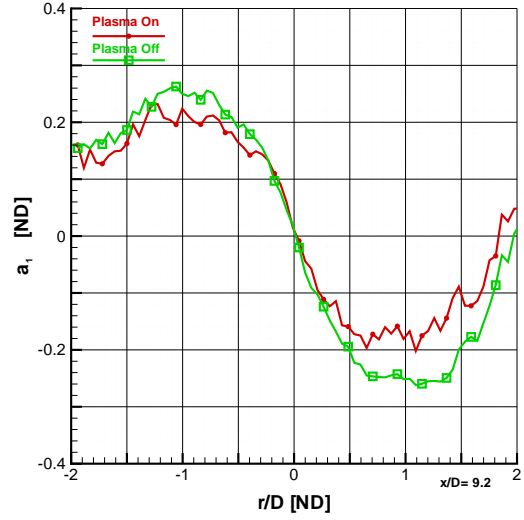
(d) Fluctuating Tangential Velocity, σ_v/U_o

Figure A.61: Comparison of Plasma Effects on Mean Velocity and Fluctuations: Case 635LINE8792

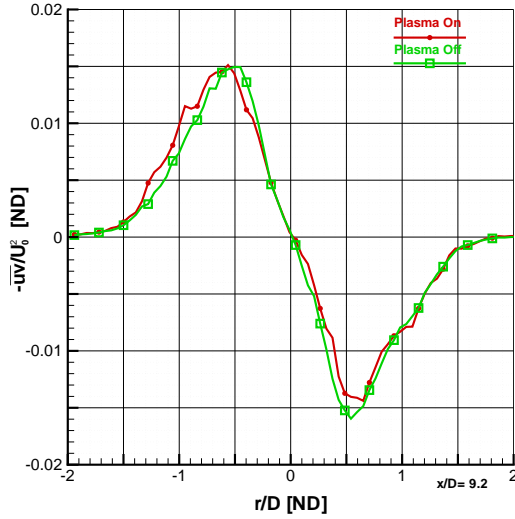
This is an investigation into the effect of plasma on a Mach 1.4 jet, 9.2 diameters from the anode face. The jet diameter is 9.5 mm. The four plots represented above are a comparison between plasma on in red versus plasma off in green. Figure A.61 (a) is non-dimensionalized axial velocity. For these figures, U_o is 342.1 m/s for the plasma off case and 349.6 m/s for the plasma on case. Figure A.61 (b) is the mean tangential component of the velocity. Figures A.61 (c) and (d) show the Reynolds normal stresses in the axial and tangential directions, respectively. The case identifiers for this comparison were 635cnc-LINE8792 for plasma off and 635pnc-LINE8792 for plasma on.



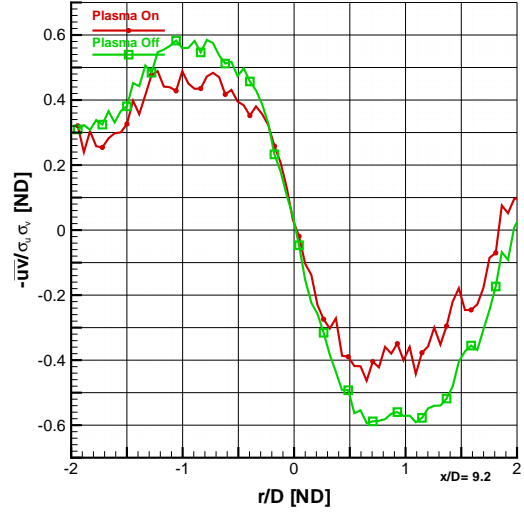
(a) Turbulent Kinetic Energy, $(\sigma_u^2 + \sigma_v^2)/U_o^2$



(b) Structural Parameter, $a_1 = -\overline{uv}/(\sigma_u^2 + \sigma_v^2)$



(c) Reynolds Shear Stress, \overline{uv}/U_o^2



(d) Correlation Coefficient of Reynolds Shear Stress, $-\overline{uv}/(\sigma_u \sigma_v)$

Figure A.62: Comparison of Plasma Effects on Second Moment Fluctuations: Case 635LINE8792

This is a continuing investigation into the effect of plasma on a Mach 1.4 jet, 9.2 diameters from the anode face. The jet diameter is 9.5 mm. The four plots represented above are a comparison between plasma on in red versus plasma off in green. Figure A.62 (a) is non-dimensionalized turbulent kinetic energy and panel (b) is the structural parameter a_1 . At this station, U_o is 342.1 m/s for the plasma off case and 349.6 m/s for the plasma on case. Figures A.62 (c) and (d) show the Reynolds shear stress and the correlation coefficient of Reynolds shear stress, respectively. The case identifiers for this comparison were 635cnc-LINE8792 for plasma off and 635pnc-LINE8792 for plasma on.

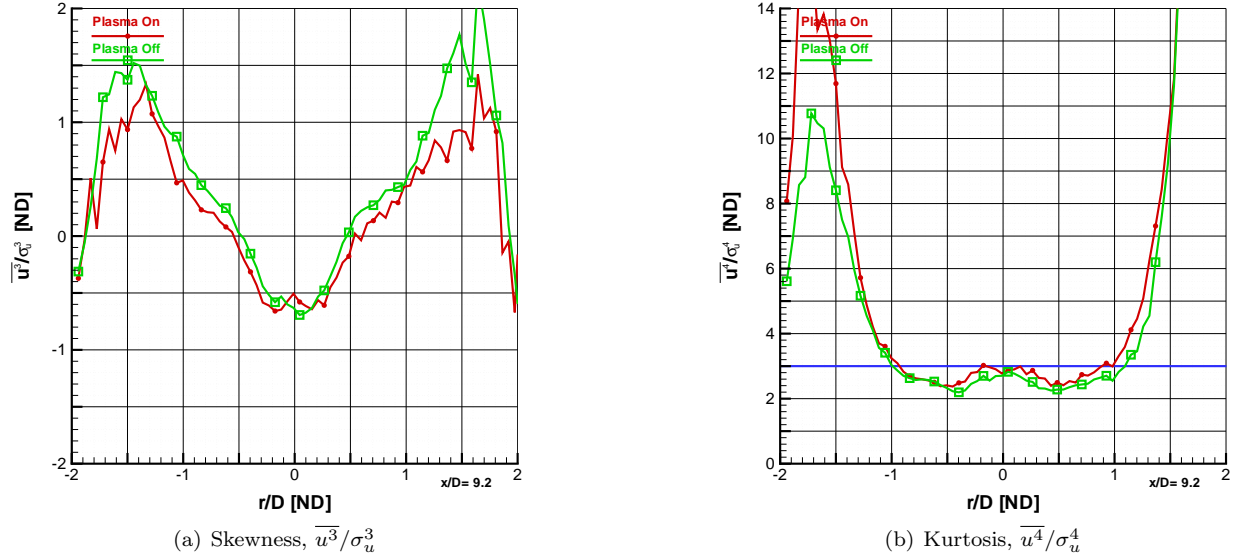
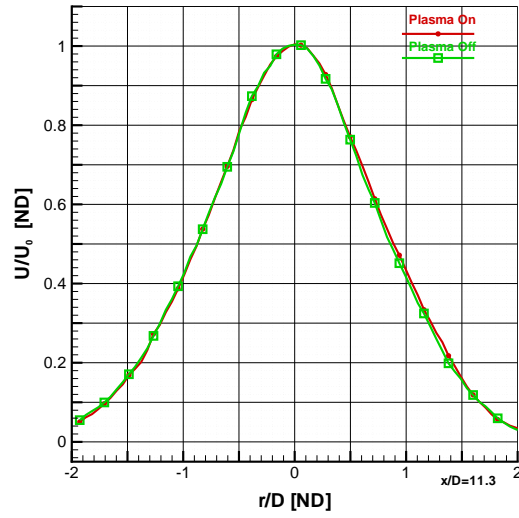
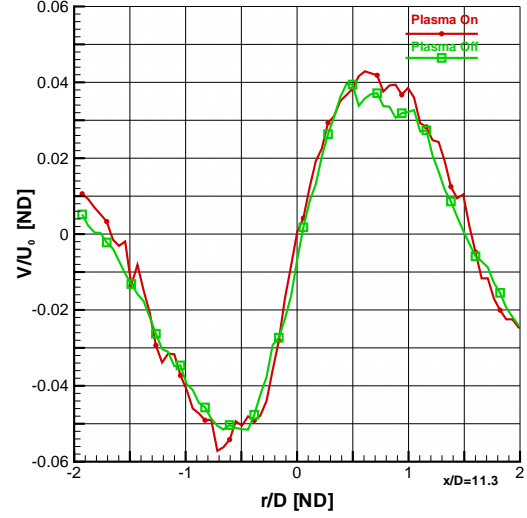


Figure A.63: Comparison of Plasma Effects on Skewness and Kurtosis: Case 635LINE8792

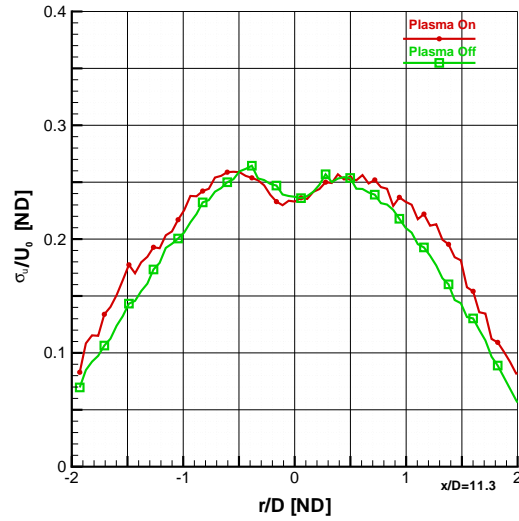
This is the final series of figures on the investigation into the effect of plasma on a Mach 1.4 jet, 9.2 diameters from the anode face. The jet diameter is 9.5 mm. The two plots represented above are a comparison between plasma on in red versus plasma off in green. The plasma off case is placed on top of the plasma on case, therefore making it easier to notice small changes between the two cases. Figure A.63 (a) (b) are the measurements of skewness and kurtosis (or flatness), respectively. A Gaussian distribution has skewness of zero, which indicates a distribution of fluctuations is symmetric about the mean. Positive skewness represents a shift toward the right tail (positive fluctuations), while negative skewness is shifted toward negative fluctuations. A Gaussian distribution has kurtosis of three, represented by the blue line. Values lower than three represent a distribution of velocity with higher peakedness than a Gaussian distribution. Conversely, values above three represent flatter distributions. The case identifiers for this comparison were 635cnc-LINE8792 for plasma off and 635pnc-LINE8792 for plasma on.



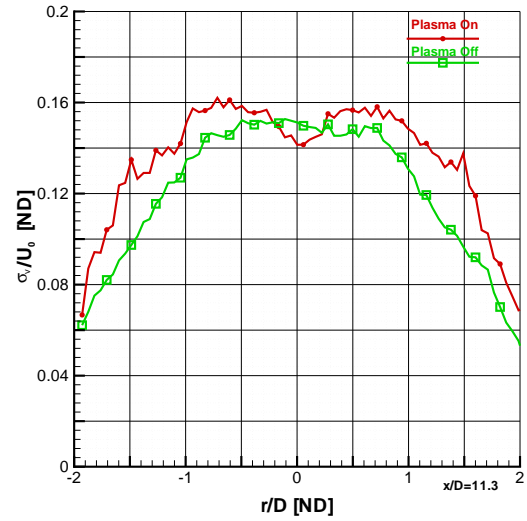
(a) Mean Axial Velocity, U/U_o



(b) Mean Tangential Velocity, V/U_o



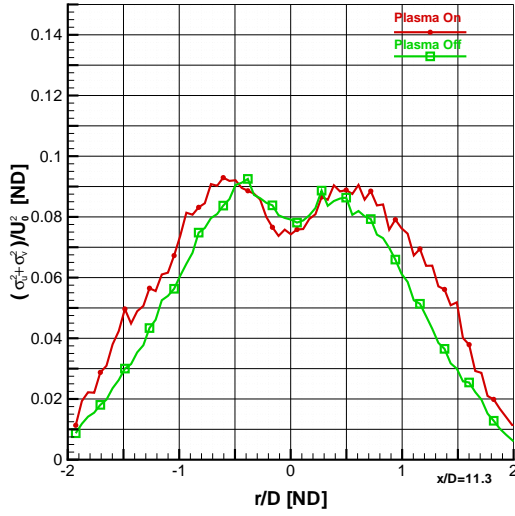
(c) Fluctuating Axial Velocity, σ_u/U_o



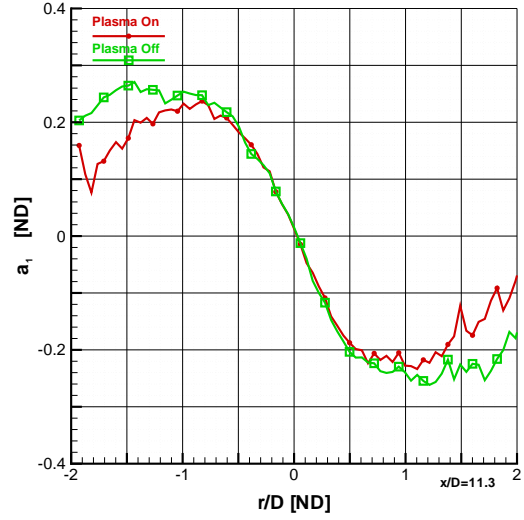
(d) Fluctuating Tangential Velocity, σ_v/U_o

Figure A.64: Comparison of Plasma Effects on Mean Velocity and Fluctuations: Case 635LINE10787

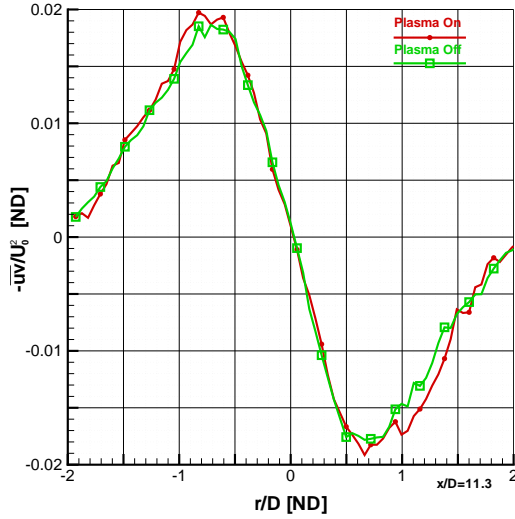
This is an investigation into the effect of plasma on a Mach 1.4 jet, 11.3 diameters from the anode face. The jet diameter is 9.5 mm. The four plots represented above are a comparison between plasma on in red versus plasma off in green. Figure A.64 (a) is non-dimensionalized axial velocity. For these figures, U_o is 257.5 m/s for the plasma off case and 270.9 m/s for the plasma on case. Figure A.64 (b) is the mean tangential component of the velocity. Figures A.64 (c) and (d) show the Reynolds normal stresses in the axial and tangential directions, respectively. The case identifiers for this comparison were 635cnc-LINE10787 for plasma off and 635pnc-LINE10787 for plasma on.



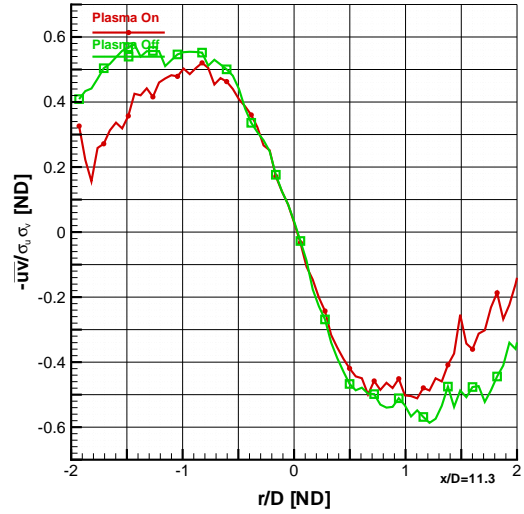
(a) Turbulent Kinetic Energy, $(\sigma_u^2 + \sigma_v^2)/U_o^2$



(b) Structural Parameter, $a_1 = -\overline{uv}/(\sigma_u^2 + \sigma_v^2)$



(c) Reynolds Shear Stress, \overline{uv}/U_o^2



(d) Correlation Coefficient of Reynolds Shear Stress, $-\overline{uv}/(\sigma_u \sigma_v)$

Figure A.65: Comparison of Plasma Effects on Second Moment Fluctuations: Case 635LINE10787

This is a continuing investigation into the effect of plasma on a Mach 1.4 jet, 11.3 diameters from the anode face. The jet diameter is 9.5 mm. The four plots represented above are a comparison between plasma on in red versus plasma off in green. Figure A.65 (a) is non-dimensionalized turbulent kinetic energy and panel (b) is the structural parameter a_1 . At this station, U_o is 257.5 m/s for the plasma off case and 270.9 m/s for the plasma on case. Figures A.65 (c) and (d) show the Reynolds shear stress and the correlation coefficient of Reynolds shear stress, respectively. The case identifiers for this comparison were 635cnc-LINE10787 for plasma off and 635pnc-LINE10787 for plasma on.

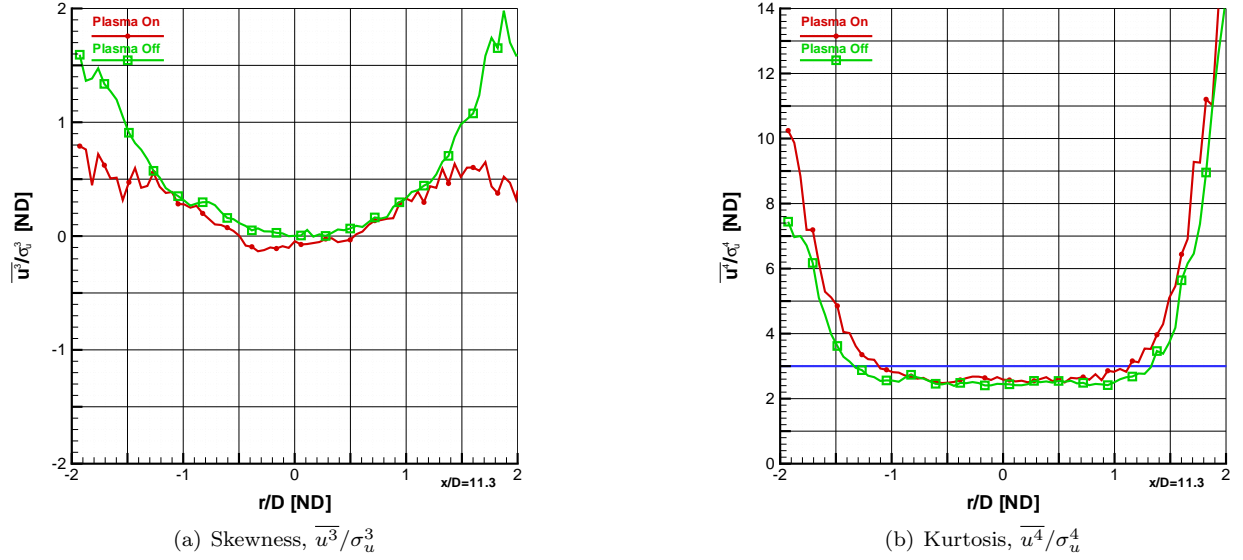


Figure A.66: Comparison of Plasma Effects on Skewness and Kurtosis: Case 635LINE10787

This is the final series of figures on the investigation into the effect of plasma on a Mach 1.4 jet, 11.3 diameters from the anode face. The jet diameter is 9.5 mm. The two plots represented above are a comparison between plasma on in red versus plasma off in green. The plasma off case is placed on top of the plasma on case, therefore making it easier to notice small changes between the two cases. Figure A.66 (a) (b) are the measurements of skewness and kurtosis (or flatness), respectively. A Gaussian distribution has skewness of zero, which indicates a distribution of fluctuations is symmetric about the mean. Positive skewness represents a shift toward the right tail (positive fluctuations), while negative skewness is shifted toward negative fluctuations. A Gaussian distribution has kurtosis of three, represented by the blue line. Values lower than three represent a distribution of velocity with higher peakedness than a Gaussian distribution. Conversely, values above three represent flatter distributions. The case identifiers for this comparison were 635cnc-LINE10787 for plasma off and 635pnc-LINE10787 for plasma on.

A.6 Flow from a Tube Driven at a Mach 0.9 Pressure Ratio at 5 Torr Using Anode with Serrated Conical Feature

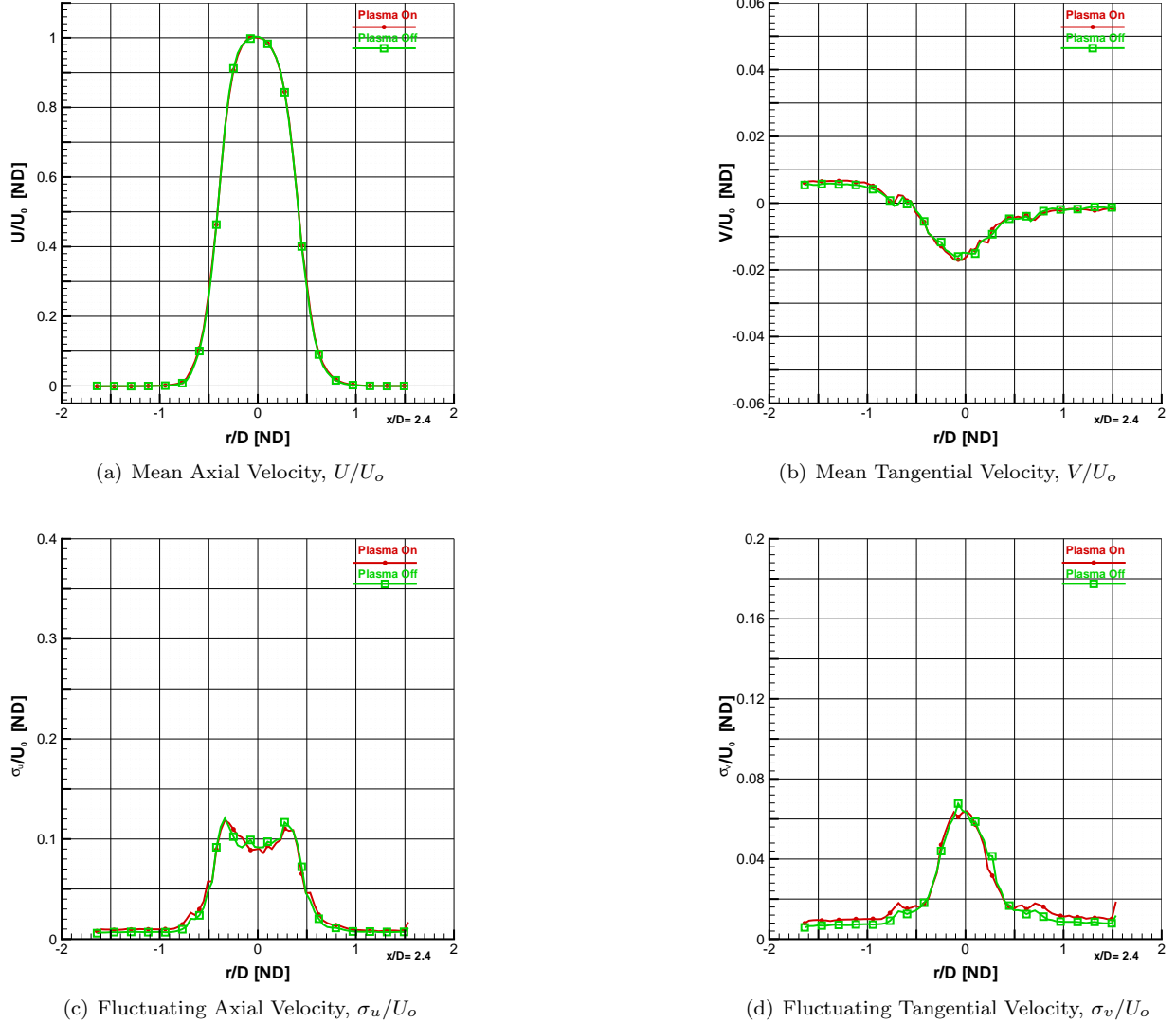
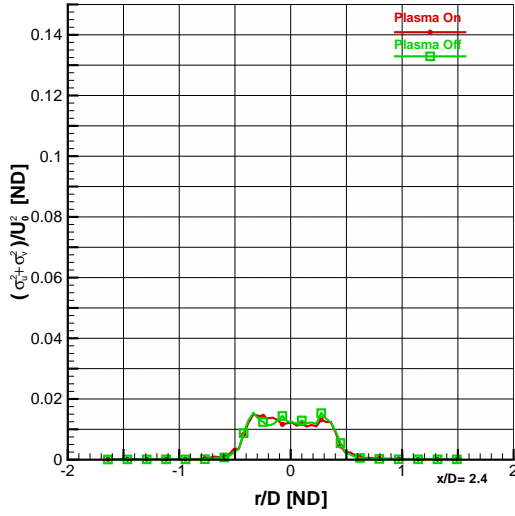
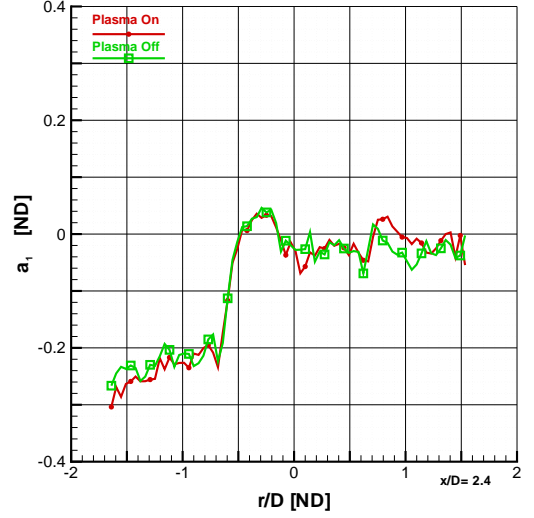


Figure A.67: Comparison of Plasma Effects on Mean Velocity and Fluctuations: Case 624LINE2260

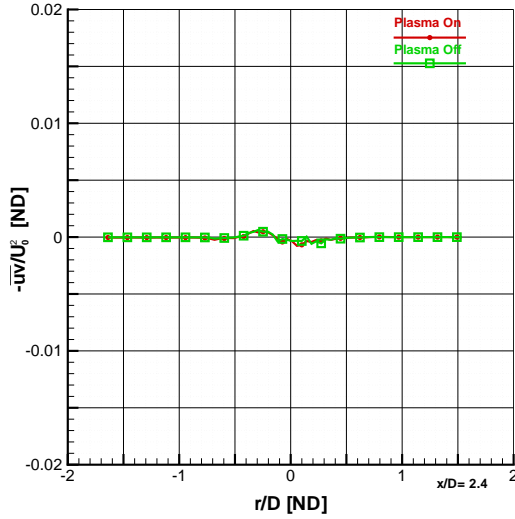
This is an investigation into the effect of plasma on jet created by developing flow in a constant-diameter tube driven at a Mach 0.9 isentropic pressure ratio, 2.4 diameters from the anode face. The jet diameter is 9.5 mm. The four plots represented above are a comparison between plasma on in red versus plasma off in green. Figure A.67 (a) is non-dimensionalized axial velocity. For these figures, U_o is 247.3 m/s for the plasma off case and 247.4 m/s for the plasma on case. Figure A.67 (b) is the mean tangential component of the velocity. Figures A.67 (c) and (d) show the Reynolds normal stresses.



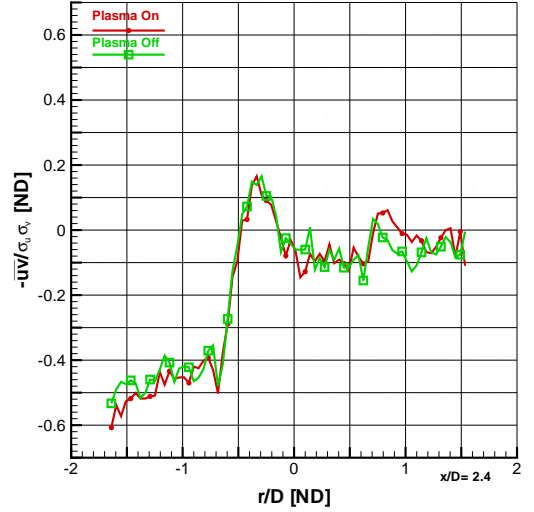
(a) Turbulent Kinetic Energy, $(\sigma_u^2 + \sigma_v^2)/U_o^2$



(b) Structural Parameter, $a_1 = -\overline{uv}/(\sigma_u^2 + \sigma_v^2)$



(c) Reynolds Shear Stress, \overline{uv}/U_o^2



(d) Correlation Coefficient of Reynolds Shear Stress, $-\overline{uv}/(\sigma_u \sigma_v)$

Figure A.68: Comparison of Plasma Effects on Second Moment Fluctuations: Case 624LINE2260

This is a continuing investigation into the effect of plasma on a Mach 0.9 isentropic pressure ratio, 2.4 diameters from the anode face. The jet diameter is 9.5 mm. The four plots represented above are a comparison between plasma on in red versus plasma off in green. Figure A.68 (a) is non-dimensionalized turbulent kinetic energy and panel (b) is the structural parameter a_1 . At this station, U_o is 247.3 m/s for the plasma off case and 247.4 m/s for the plasma on case. Figures A.68 (c) and (d) show the Reynolds shear stress and the correlation coefficient of Reynolds shear stress, respectively. The case identifiers for this comparison were 624cn-LINE2260 for plasma off and 624pn-LINE2260 for plasma on.

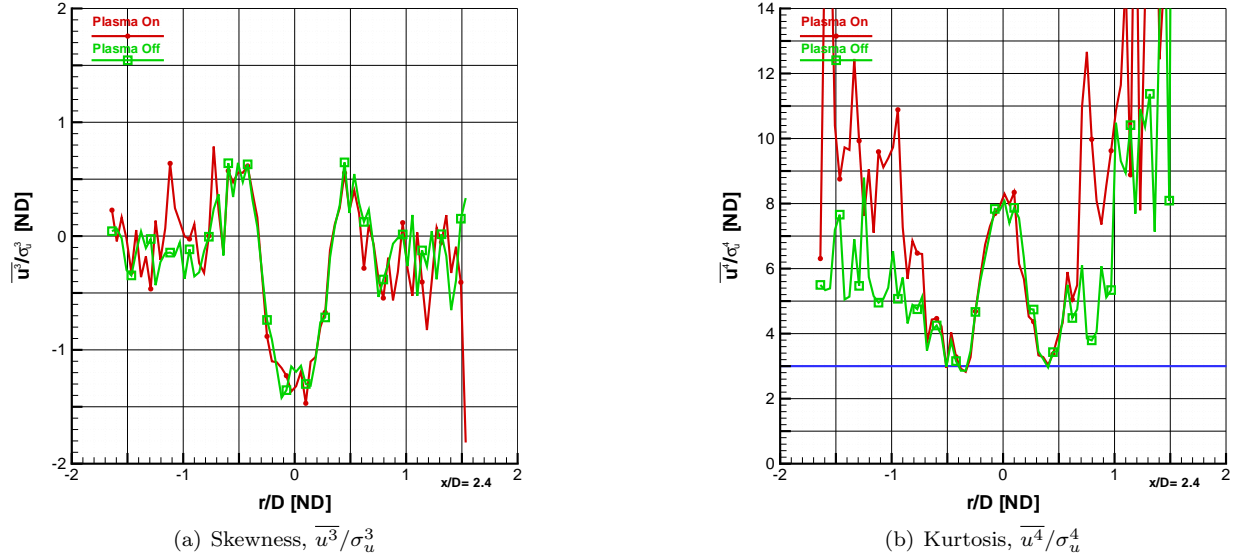
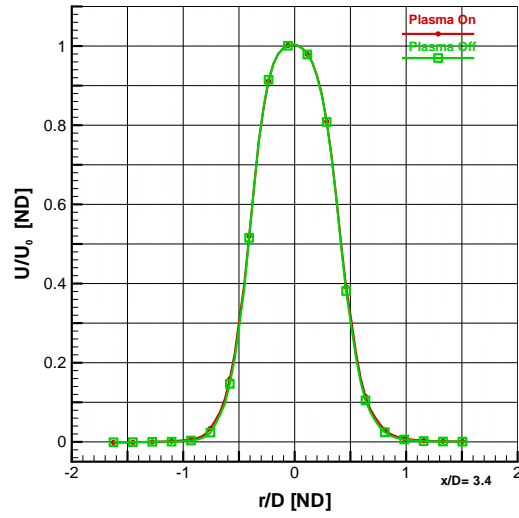
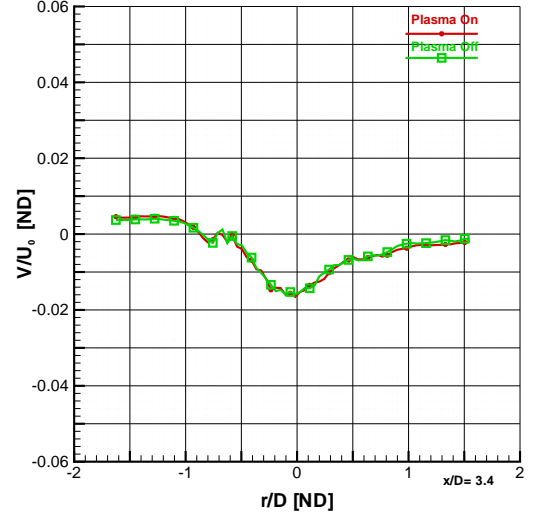


Figure A.69: Comparison of Plasma Effects on Skewness and Kurtosis: Case 624LINE2260

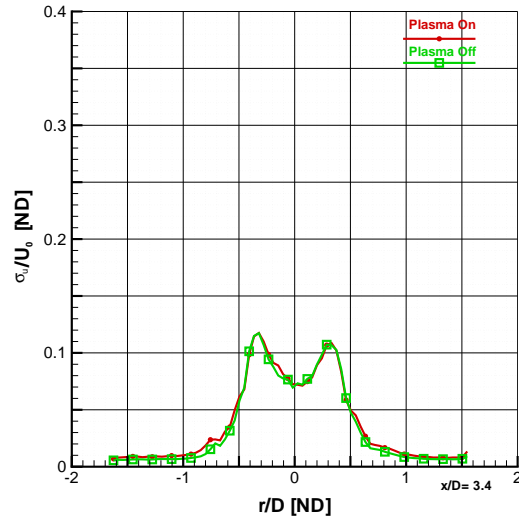
This is the final series of figures on the investigation into the effect of plasma on jet created by developing flow in a constant-diameter tube driven at a Mach 0.9 isentropic pressure ratio, 2.4 diameters from the anode face. The jet diameter is 9.5 mm. The two plots represented above are a comparison between plasma on in red versus plasma off in green. The plasma off case is placed on top of the plasma on case, therefore making it easier to notice small changes between the two cases. Figure A.69 (a) (b) are the measurements of skewness and kurtosis (or flatness), respectively. A Gaussian distribution has skewness of zero, which indicates a distribution of fluctuations is symmetric about the mean. Positive skewness represents a shift toward the right tail (positive fluctuations), while negative skewness is shifted toward negative fluctuations. A Gaussian distribution has kurtosis of three, represented by the blue line. Values lower than three represent a distribution of velocity with higher peakedness than a Gaussian distribution. Conversely, values above three represent flatter distributions. The case identifiers for this comparison were 624cn-LINE2260 for plasma off and 624pn-LINE2260 for plasma on.



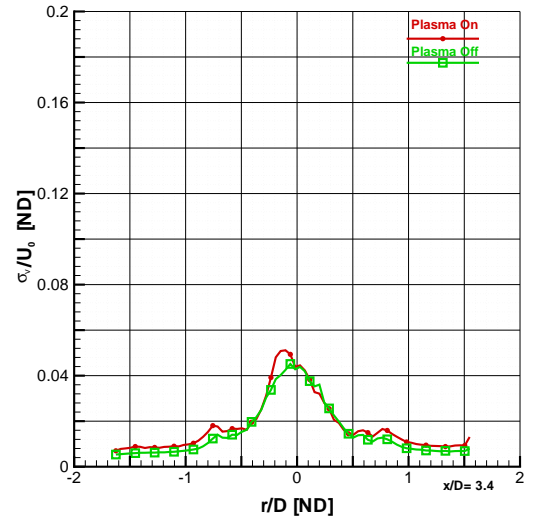
(a) Mean Axial Velocity, U/U_o



(b) Mean Tangential Velocity, V/U_o



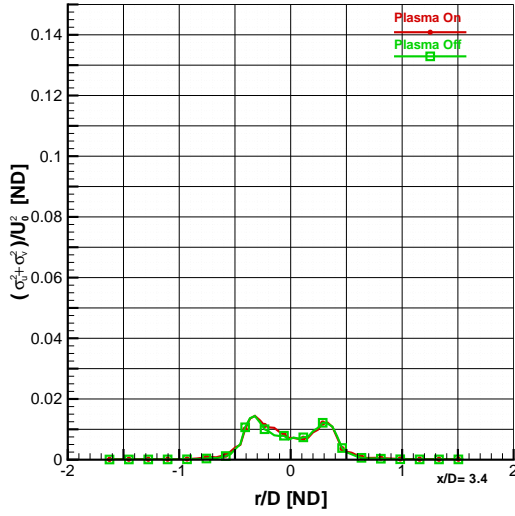
(c) Fluctuating Axial Velocity, σ_u/U_o



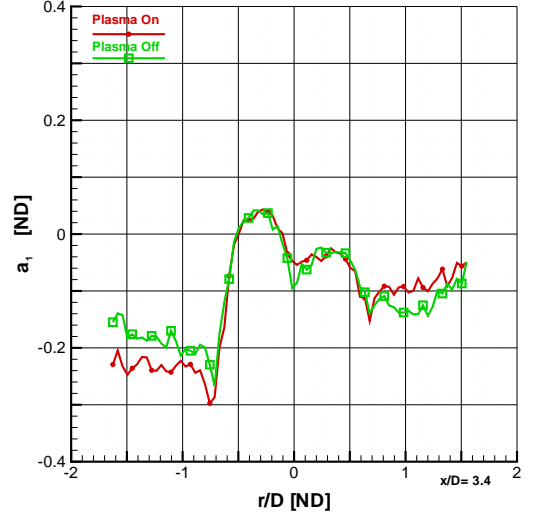
(d) Fluctuating Tangential Velocity, σ_v/U_o

Figure A.70: Comparison of Plasma Effects on Mean Velocity and Fluctuations: Case 624LINE3253

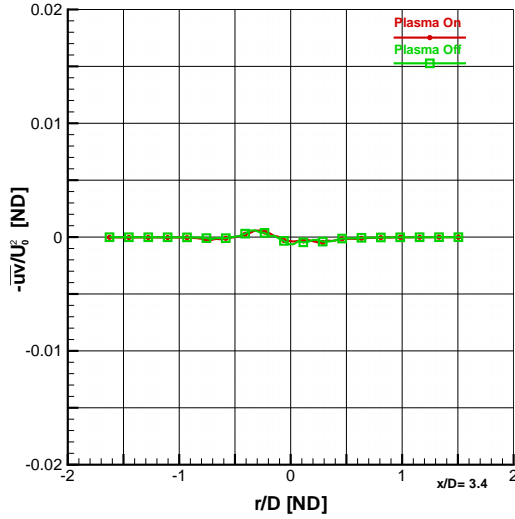
This is an investigation into the effect of plasma on jet created by developing flow in a constant-diameter tube driven at a Mach 0.9 isentropic pressure ratio, 3.4 diameters from the anode face. The jet diameter is 9.5 mm. The four plots represented above are a comparison between plasma on in red versus plasma off in green. Figure A.70 (a) is non-dimensionalized axial velocity. For these figures, U_o is 247.3 m/s for the plasma off case and 247.1 m/s for the plasma on case. Figure A.70 (b) is the mean tangential component of the velocity. Figures A.70 (c) and (d) show the Reynolds normal stresses in the axial and tangential directions, respectively. The case identifiers for this comparison were 624cn-LINE3253 for plasma off and 624pn-LINE3253 for plasma on.



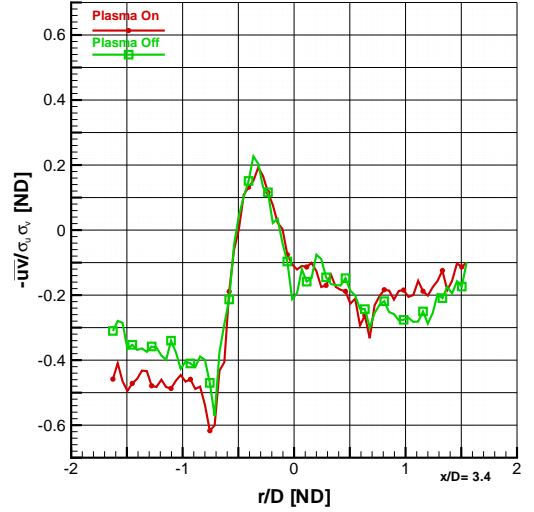
(a) Turbulent Kinetic Energy, $(\sigma_u^2 + \sigma_v^2)/U_o^2$



(b) Structural Parameter, $a_1 = -\overline{uv}/(\sigma_u^2 + \sigma_v^2)$



(c) Reynolds Shear Stress, \overline{uv}/U_o^2



(d) Correlation Coefficient of Reynolds Shear Stress, $-\overline{uv}/(\sigma_u \sigma_v)$

Figure A.71: Comparison of Plasma Effects on Second Moment Fluctuations: Case 624LINE3253

This is a continuing investigation into the effect of plasma on a Mach 0.9 isentropic pressure ratio, 3.4 diameters from the anode face. The jet diameter is 9.5 mm. The four plots represented above are a comparison between plasma on in red versus plasma off in green. Figure A.71 (a) is non-dimensionalized turbulent kinetic energy and panel (b) is the structural parameter a_1 . At this station, U_o is 247.3 m/s for the plasma off case and 247.1 m/s for the plasma on case. Figures A.71 (c) and (d) show the Reynolds shear stress and the correlation coefficient of Reynolds shear stress, respectively. The case identifiers for this comparison were 624cn-LINE3253 for plasma off and 624pn-LINE3253 for plasma on.

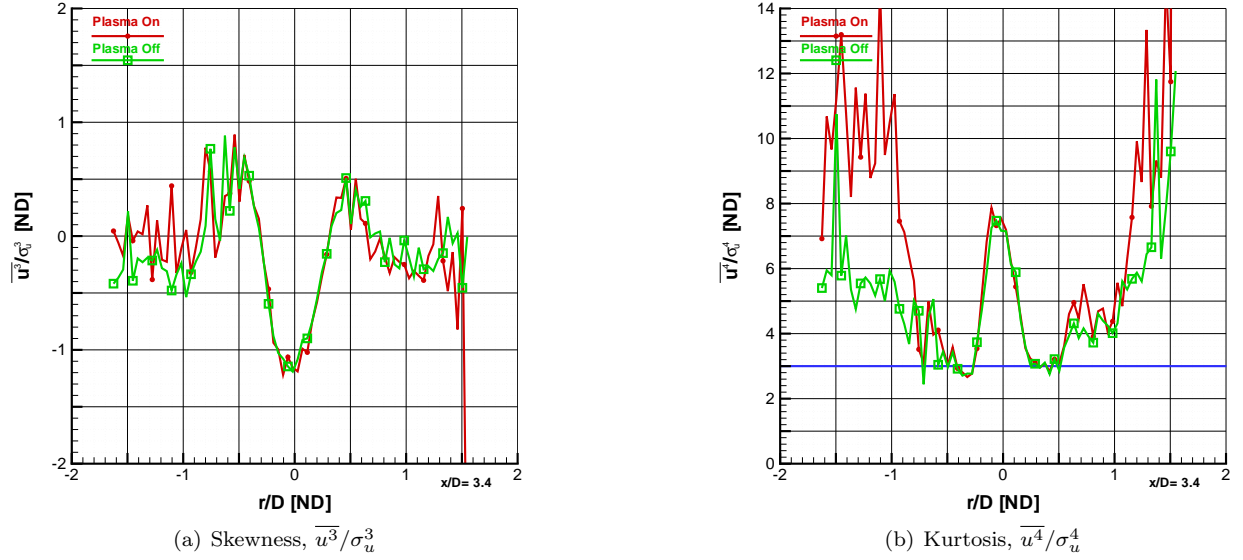
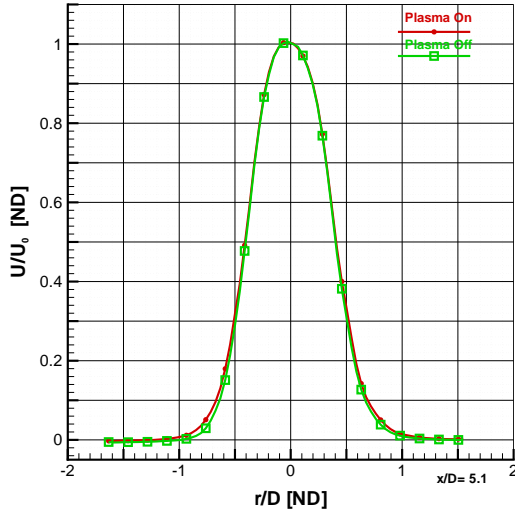
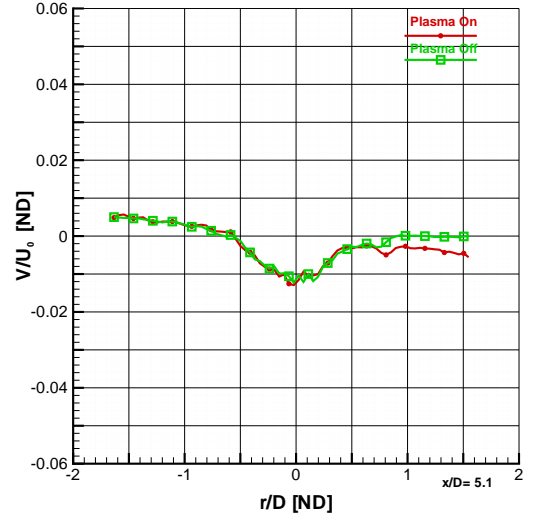


Figure A.72: Comparison of Plasma Effects on Skewness and Kurtosis: Case 624LINE3253

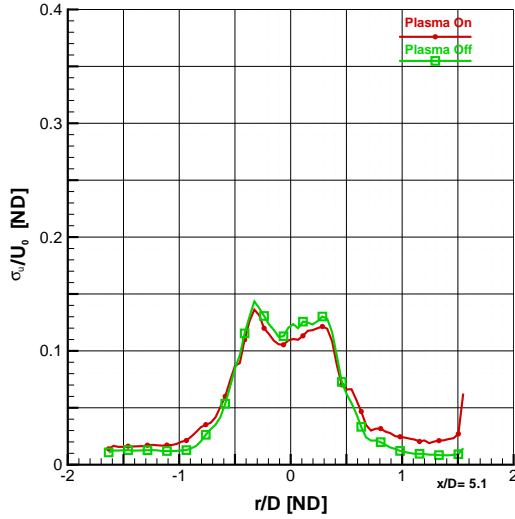
This is the final series of figures on the investigation into the effect of plasma on jet created by developing flow in a constant-diameter tube driven at a Mach 0.9 isentropic pressure ratio, 3.4 diameters from the anode face. The jet diameter is 9.5 mm. The two plots represented above are a comparison between plasma on in red versus plasma off in green. The plasma off case is placed on top of the plasma on case, therefore making it easier to notice small changes between the two cases. Figure A.72 (a) (b) are the measurements of skewness and kurtosis (or flatness), respectively. A Gaussian distribution has skewness of zero, which indicates a distribution of fluctuations is symmetric about the mean. Positive skewness represents a shift toward the right tail (positive fluctuations), while negative skewness is shifted toward negative fluctuations. A Gaussian distribution has kurtosis of three, represented by the blue line. Values lower than three represent a distribution of velocity with higher peakedness than a Gaussian distribution. Conversely, values above three represent flatter distributions. The case identifiers for this comparison were 624cn-LINE3253 for plasma off and 624pn-LINE3253 for plasma on.



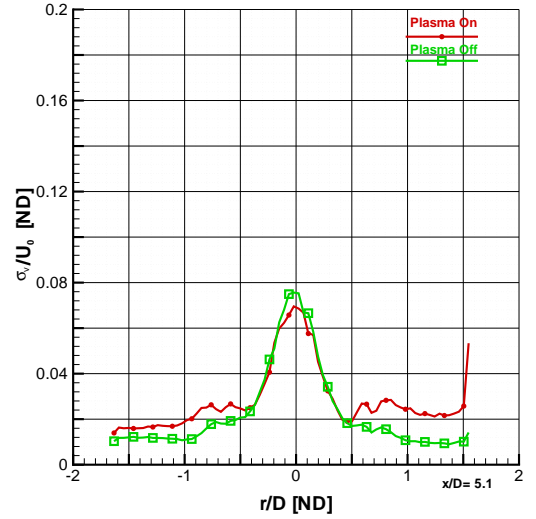
(a) Mean Axial Velocity, U/U_o



(b) Mean Tangential Velocity, V/U_o



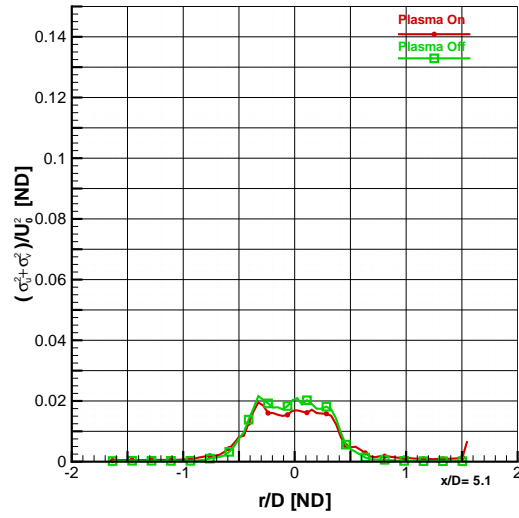
(c) Fluctuating Axial Velocity, σ_u/U_o



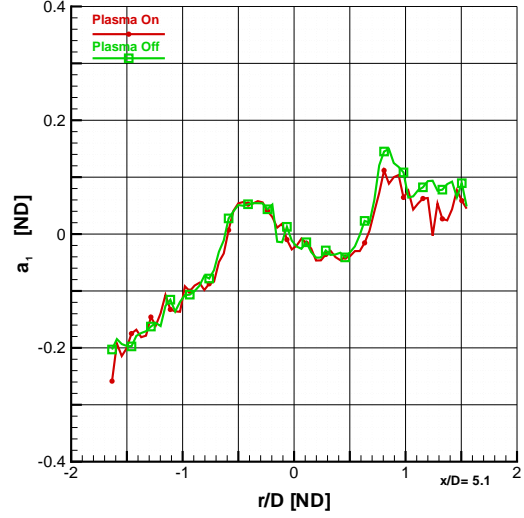
(d) Fluctuating Tangential Velocity, σ_v/U_o

Figure A.73: Comparison of Plasma Effects on Mean Velocity and Fluctuations: Case 623LINE4808

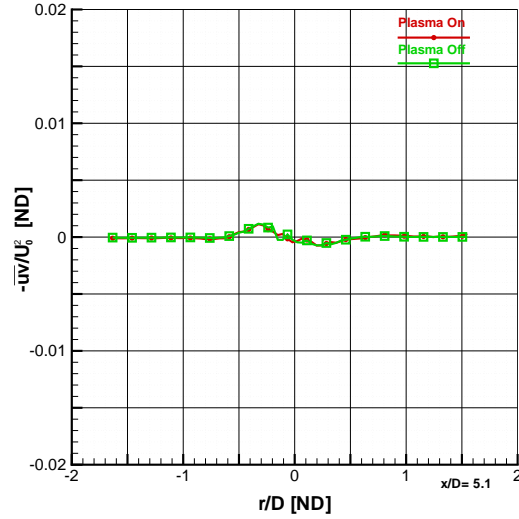
This is an investigation into the effect of plasma on jet created by developing flow in a constant-diameter tube driven at a Mach 0.9 isentropic pressure ratio, 5.1 diameters from the anode face. The jet diameter is 9.5 mm. The four plots represented above are a comparison between plasma on in red versus plasma off in green. Figure A.73 (a) is non-dimensionalized axial velocity. For these figures, U_o is 240.9 m/s for the plasma off case and 241.8 m/s for the plasma on case. Figure A.73 (b) is the mean tangential component of the velocity. Figures A.73 (c) and (d) show the Reynolds normal stresses in the axial and tangential directions, respectively. The case identifiers for this comparison were 623cn-LINE4808 for plasma off and 623pn-LINE4808 for plasma on.



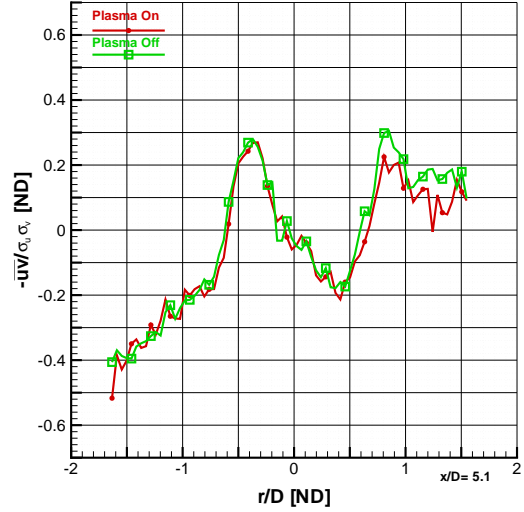
(a) Turbulent Kinetic Energy, $(\sigma_u^2 + \sigma_v^2)/U_o^2$



(b) Structural Parameter, $a_1 = -\overline{uv}/(\sigma_u^2 + \sigma_v^2)$



(c) Reynolds Shear Stress, \overline{uv}/U_o^2



(d) Correlation Coefficient of Reynolds Shear Stress, $-\overline{uv}/(\sigma_u \sigma_v)$

Figure A.74: Comparison of Plasma Effects on Second Moment Fluctuations: Case 623LINE4808

This is a continuing investigation into the effect of plasma on a Mach 0.9 isentropic pressure ratio, 5.1 diameters from the anode face. The jet diameter is 9.5 mm. The four plots represented above are a comparison between plasma on in red versus plasma off in green. Figure A.74 (a) is non-dimensionalized turbulent kinetic energy and panel (b) is the structural parameter a_1 . At this station, U_o is 240.9 m/s for the plasma off case and 241.8 m/s for the plasma on case. Figures A.74 (c) and (d) show the Reynolds shear stress and the correlation coefficient of Reynolds shear stress, respectively. The case identifiers for this comparison were 623cn-LINE4808 for plasma off and 623pn-LINE4808 for plasma on.

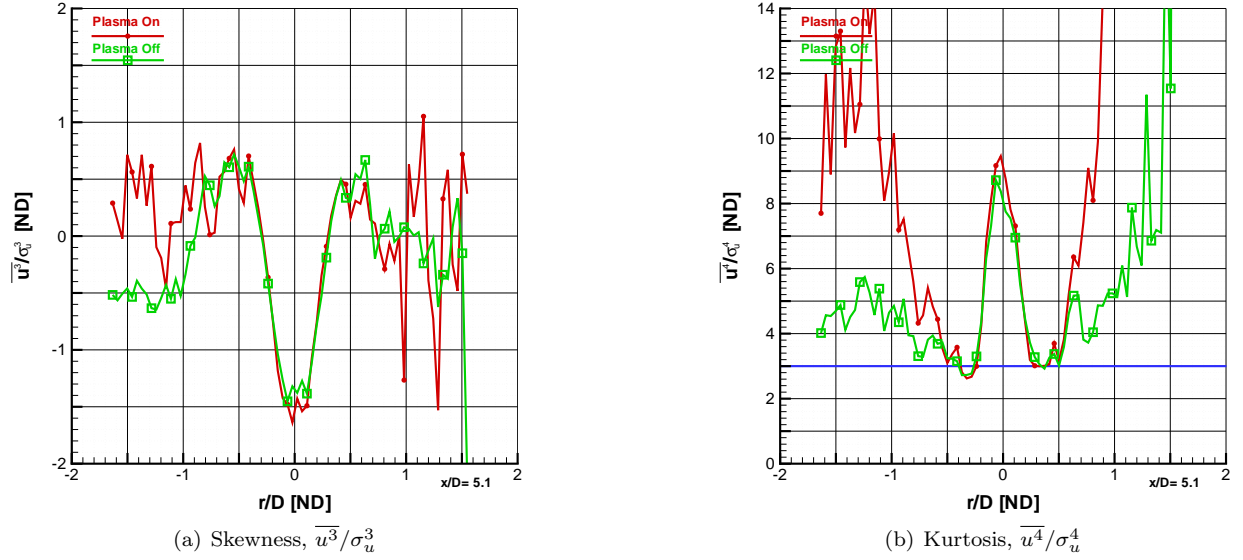
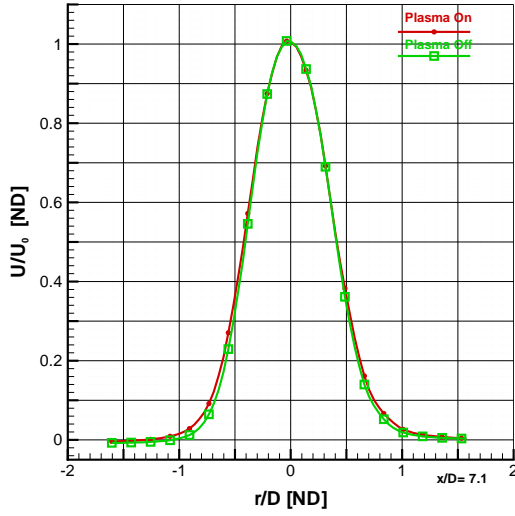
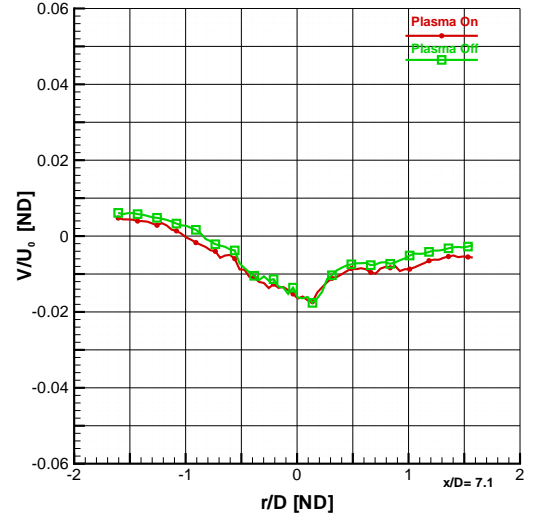


Figure A.75: Comparison of Plasma Effects on Skewness and Kurtosis: Case 623LINE4808

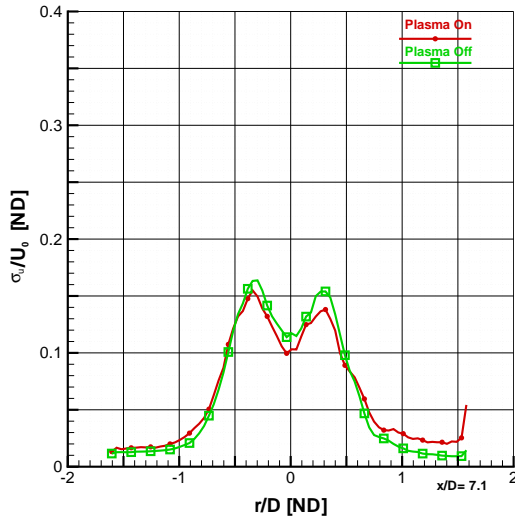
This is the final series of figures on the investigation into the effect of plasma on jet created by developing flow in a constant-diameter tube driven at a Mach 0.9 isentropic pressure ratio, 5.1 diameters from the anode face. The jet diameter is 9.5 mm. The two plots represented above are a comparison between plasma on in red versus plasma off in green. The plasma off case is placed on top of the plasma on case, therefore making it easier to notice small changes between the two cases. Figure A.75 (a) (b) are the measurements of skewness and kurtosis (or flatness), respectively. A Gaussian distribution has skewness of zero, which indicates a distribution of fluctuations is symmetric about the mean. Positive skewness represents a shift toward the right tail (positive fluctuations), while negative skewness is shifted toward negative fluctuations. A Gaussian distribution has kurtosis of three, represented by the blue line. Values lower than three represent a distribution of velocity with higher peakedness than a Gaussian distribution. Conversely, values above three represent flatter distributions. The case identifiers for this comparison were 623cn-LINE4808 for plasma off and 623pn-LINE4808 for plasma on.



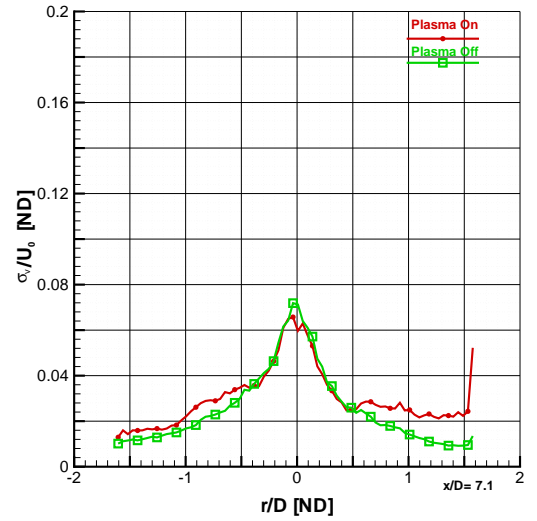
(a) Mean Axial Velocity, U/U_o



(b) Mean Tangential Velocity, V/U_o



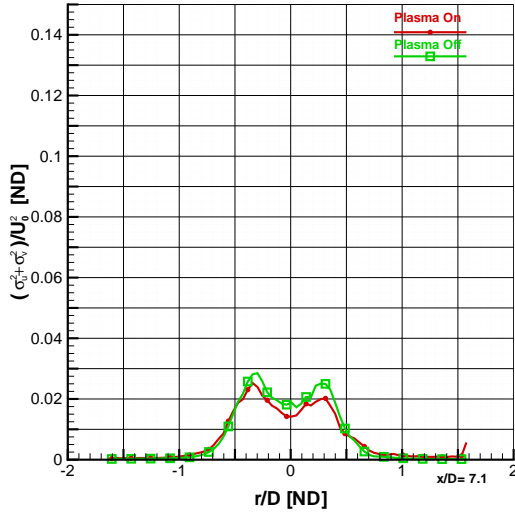
(c) Fluctuating Axial Velocity, σ_u/U_o



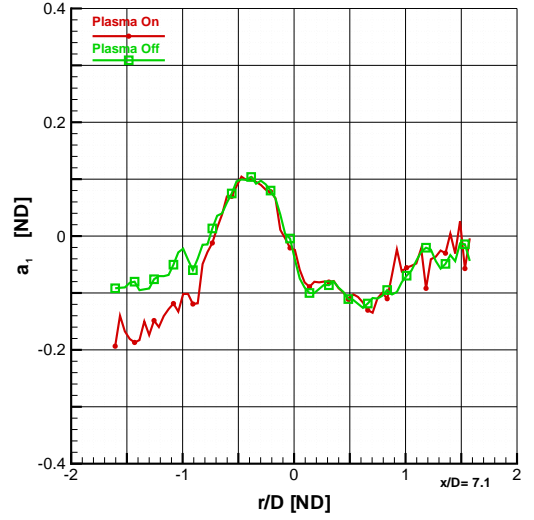
(d) Fluctuating Tangential Velocity, σ_v/U_o

Figure A.76: Comparison of Plasma Effects on Mean Velocity and Fluctuations: Case 623LINE6799

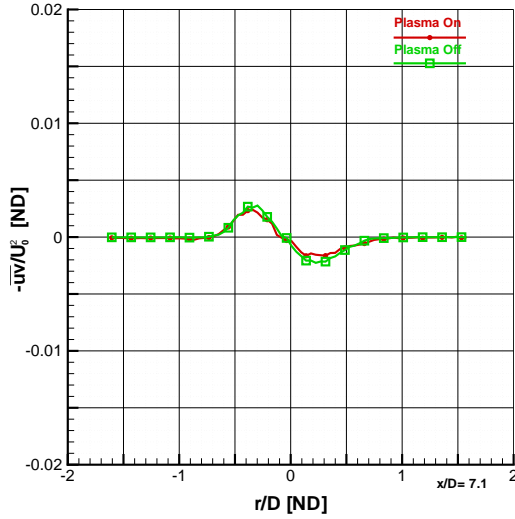
This is an investigation into the effect of plasma on jet created by developing flow in a constant-diameter tube driven at a Mach 0.9 isentropic pressure ratio, 7.1 diameters from the anode face. The jet diameter is 9.5 mm. The four plots represented above are a comparison between plasma on in red versus plasma off in green. Figure A.76 (a) is non-dimensionalized axial velocity. For these figures, U_o is 234.6 m/s for the plasma off case and 237.4 m/s for the plasma on case. Figure A.76 (b) is the mean tangential component of the velocity. Figures A.76 (c) and (d) show the Reynolds normal stresses in the axial and tangential directions, respectively. The case identifiers for this comparison were 623cn-LINE6799 for plasma off and 623pn-LINE6799 for plasma on.



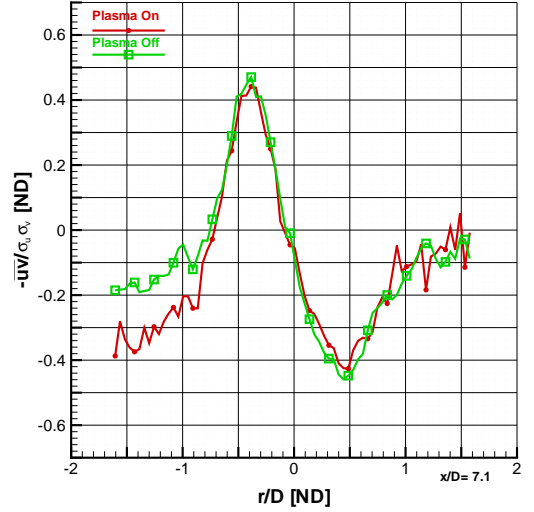
(a) Turbulent Kinetic Energy, $(\sigma_u^2 + \sigma_v^2)/U_o^2$



(b) Structural Parameter, $a_1 = -\overline{uv}/(\sigma_u^2 + \sigma_v^2)$



(c) Reynolds Shear Stress, \overline{uv}/U_o^2



(d) Correlation Coefficient of Reynolds Shear Stress, $-\overline{uv}/(\sigma_u \sigma_v)$

Figure A.77: Comparison of Plasma Effects on Second Moment Fluctuations: Case 623LINE6799

This is a continuing investigation into the effect of plasma on a Mach 0.9 isentropic pressure ratio, 7.1 diameters from the anode face. The jet diameter is 9.5 mm. The four plots represented above are a comparison between plasma on in red versus plasma off in green. Figure A.77 (a) is non-dimensionalized turbulent kinetic energy and panel (b) is the structural parameter a_1 . At this station, U_o is 234.6 m/s for the plasma off case and 237.4 m/s for the plasma on case. Figures A.77 (c) and (d) show the Reynolds shear stress and the correlation coefficient of Reynolds shear stress, respectively. The case identifiers for this comparison were 623cn-LINE6799 for plasma off and 623pn-LINE6799 for plasma on.

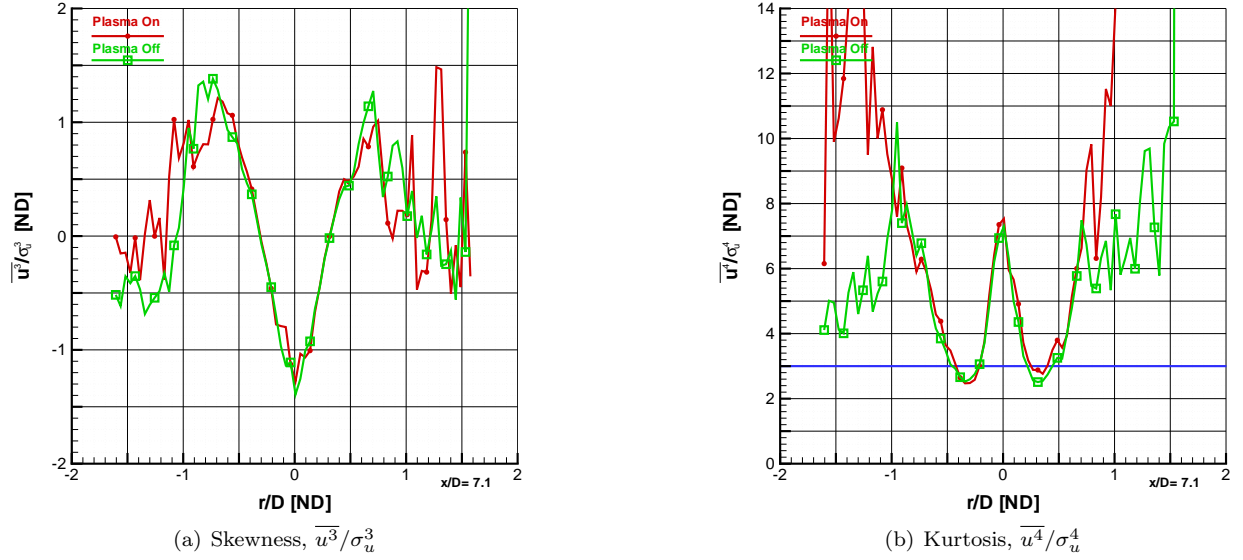
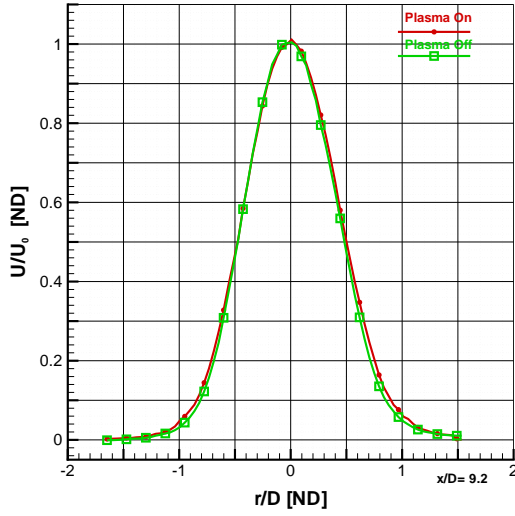
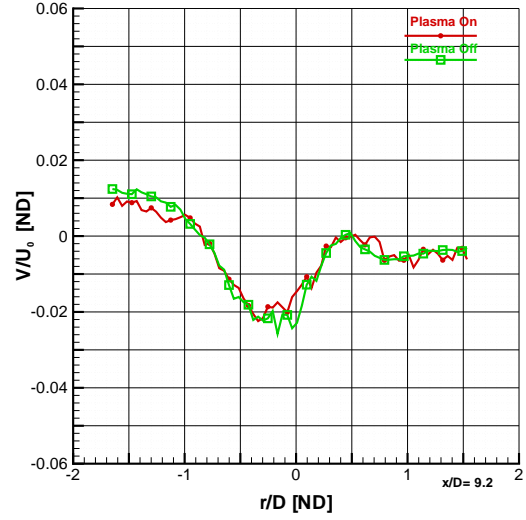


Figure A.78: Comparison of Plasma Effects on Skewness and Kurtosis: Case 623LINE6799

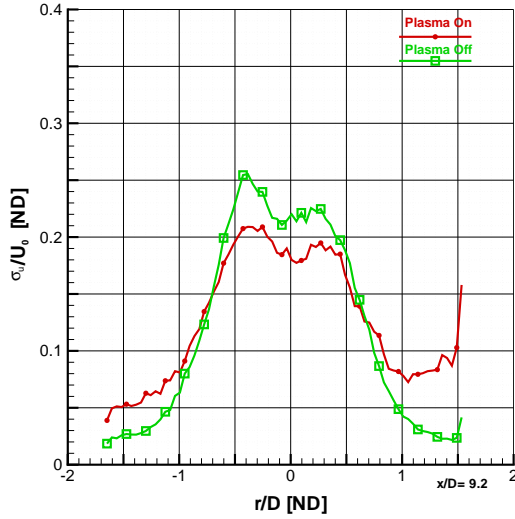
This is the final series of figures on the investigation into the effect of plasma on jet created by developing flow in a constant-diameter tube driven at a Mach 0.9 isentropic pressure ratio, 7.1 diameters from the anode face. The jet diameter is 9.5 mm. The two plots represented above are a comparison between plasma on in red versus plasma off in green. The plasma off case is placed on top of the plasma on case, therefore making it easier to notice small changes between the two cases. Figure A.78 (a) (b) are the measurements of skewness and kurtosis (or flatness), respectively. A Gaussian distribution has skewness of zero, which indicates a distribution of fluctuations is symmetric about the mean. Positive skewness represents a shift toward the right tail (positive fluctuations), while negative skewness is shifted toward negative fluctuations. A Gaussian distribution has kurtosis of three, represented by the blue line. Values lower than three represent a distribution of velocity with higher peakedness than a Gaussian distribution. Conversely, values above three represent flatter distributions. The case identifiers for this comparison were 623cn-LINE6799 for plasma off and 623pn-LINE6799 for plasma on.



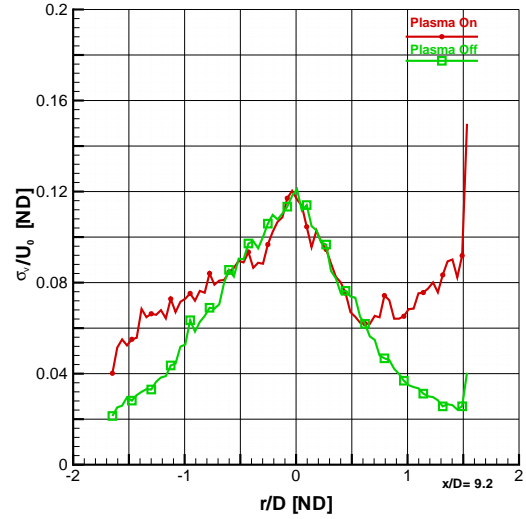
(a) Mean Axial Velocity, U/U_o



(b) Mean Tangential Velocity, V/U_o



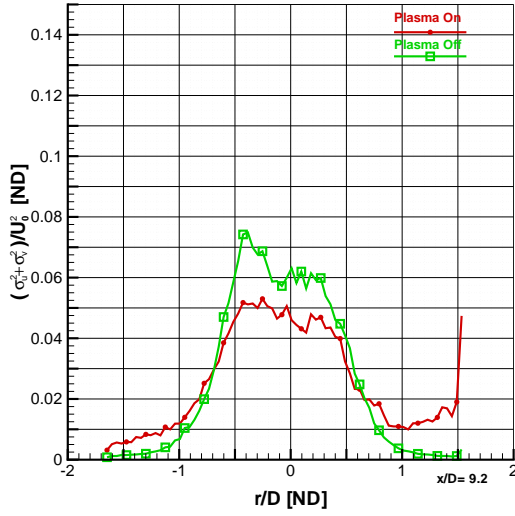
(c) Fluctuating Axial Velocity, σ_u/U_o



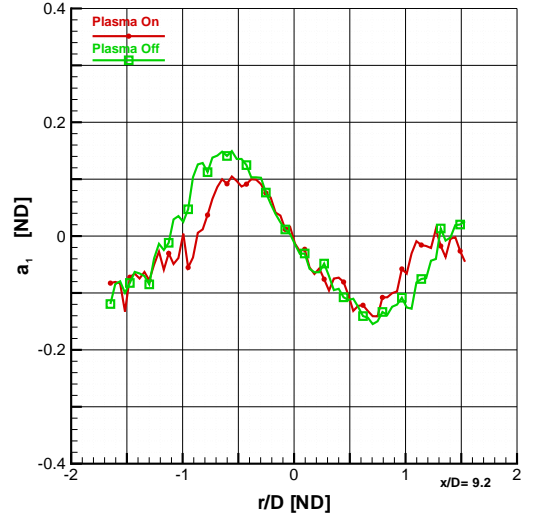
(d) Fluctuating Tangential Velocity, σ_v/U_o

Figure A.79: Comparison of Plasma Effects on Mean Velocity and Fluctuations: Case 618LINE8800

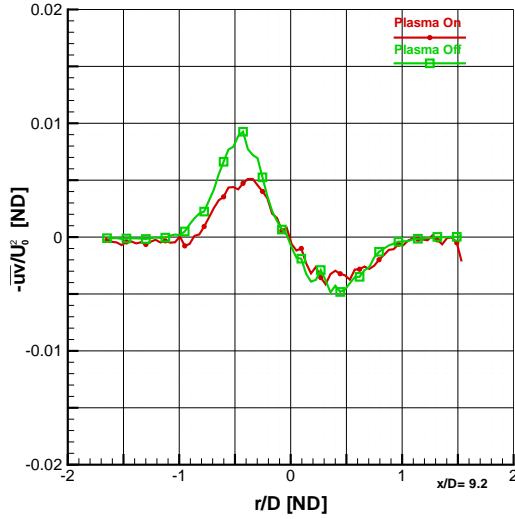
This is an investigation into the effect of plasma on jet created by developing flow in a constant-diameter tube driven at a Mach 0.9 isentropic pressure ratio, 9.2 diameters from the anode face. The jet diameter is 9.5 mm. The four plots represented above are a comparison between plasma on in red versus plasma off in green. Figure A.79 (a) is non-dimensionalized axial velocity. For these figures, U_o is 206.5 m/s for the plasma off case and 212.6 m/s for the plasma on case. Figure A.79 (b) is the mean tangential component of the velocity. Figures A.79 (c) and (d) show the Reynolds normal stresses in the axial and tangential directions, respectively. The case identifiers for this comparison were 618cnc-LINE8800 for plasma off and 618pnc-LINE8800 for plasma on.



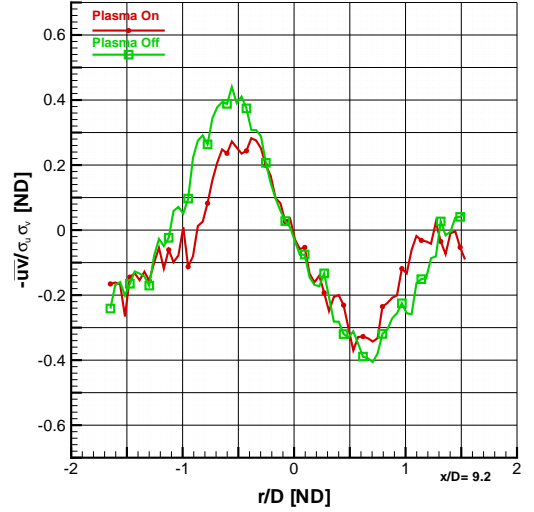
(a) Turbulent Kinetic Energy, $(\sigma_u^2 + \sigma_v^2)/U_o^2$



(b) Structural Parameter, $a_1 = -\overline{u'v'} / (\sigma_u^2 + \sigma_v^2)$



(c) Reynolds Shear Stress, $\overline{u'v'} / U_o^2$



(d) Correlation Coefficient of Reynolds Shear Stress, $-\overline{u'v'} / (\sigma_u \sigma_v)$

Figure A.80: Comparison of Plasma Effects on Second Moment Fluctuations: Case 618LINE8800

This is a continuing investigation into the effect of plasma on a Mach 0.9 isentropic pressure ratio, 9.2 diameters from the anode face. The jet diameter is 9.5 mm. The four plots represented above are a comparison between plasma on in red versus plasma off in green. Figure A.80 (a) is non-dimensionalized turbulent kinetic energy and panel (b) is the structural parameter a_1 . At this station, U_o is 206.5 m/s for the plasma off case and 212.6 m/s for the plasma on case. Figures A.80 (c) and (d) show the Reynolds shear stress and the correlation coefficient of Reynolds shear stress, respectively. The case identifiers for this comparison were 618cnc-LINE8800 for plasma off and 618pnc-LINE8800 for plasma on.

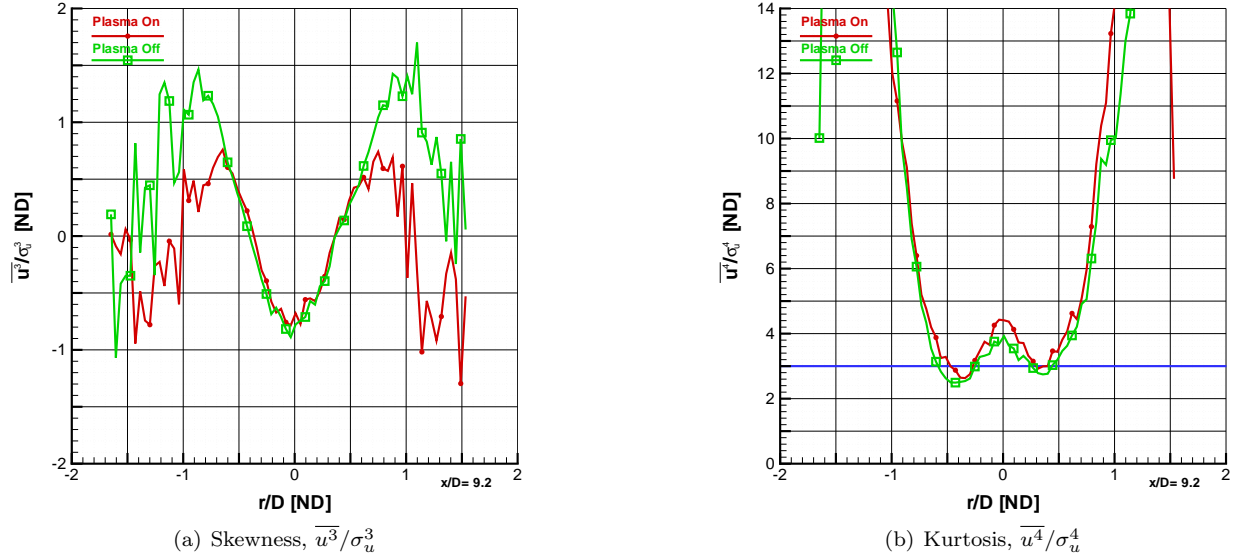
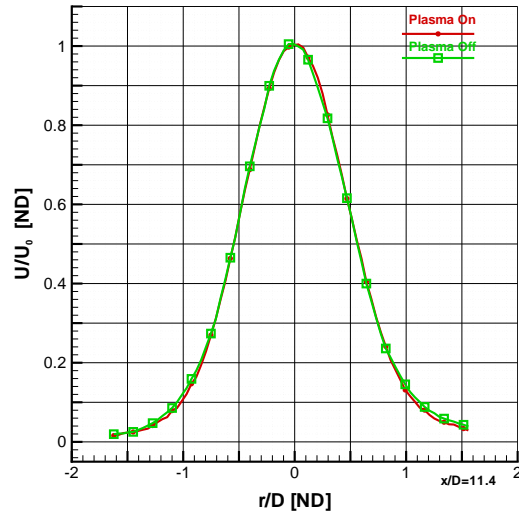
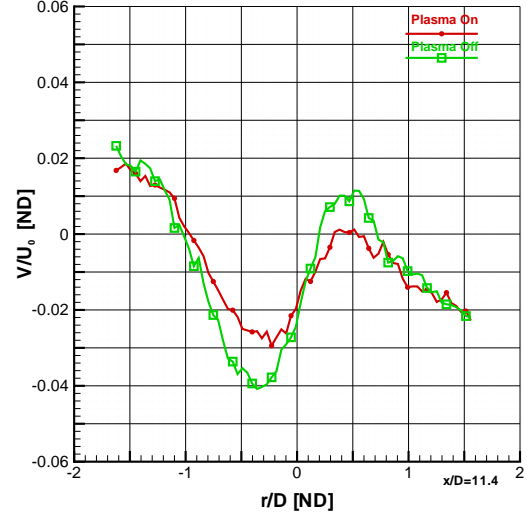


Figure A.81: Comparison of Plasma Effects on Skewness and Kurtosis: Case 618LINE8800

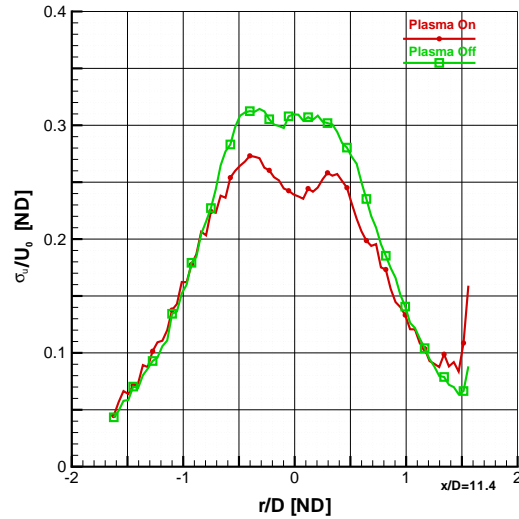
This is the final series of figures on the investigation into the effect of plasma on jet created by developing flow in a constant-diameter tube driven at a Mach 0.9 isentropic pressure ratio, 9.2 diameters from the anode face. The jet diameter is 9.5 mm. The two plots represented above are a comparison between plasma on in red versus plasma off in green. The plasma off case is placed on top of the plasma on case, therefore making it easier to notice small changes between the two cases. Figure A.81 (a) (b) are the measurements of skewness and kurtosis (or flatness), respectively. A Gaussian distribution has skewness of zero, which indicates a distribution of fluctuations is symmetric about the mean. Positive skewness represents a shift toward the right tail (positive fluctuations), while negative skewness is shifted toward negative fluctuations. A Gaussian distribution has kurtosis of three, represented by the blue line. Values lower than three represent a distribution of velocity with higher peakedness than a Gaussian distribution. Conversely, values above three represent flatter distributions. The case identifiers for this comparison were 618cnc-LINE8800 for plasma off and 618pnc-LINE8800 for plasma on.



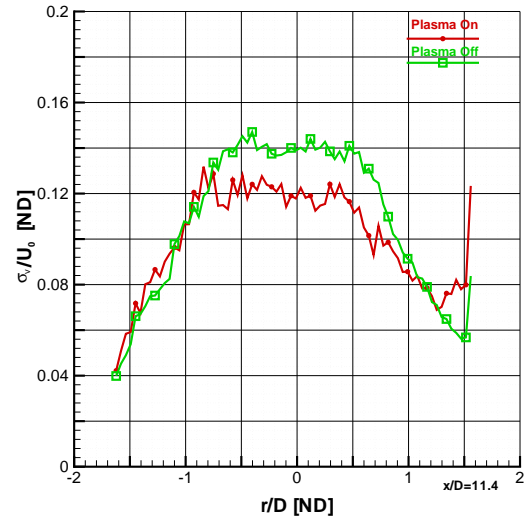
(a) Mean Axial Velocity, U/U_o



(b) Mean Tangential Velocity, V/U_o



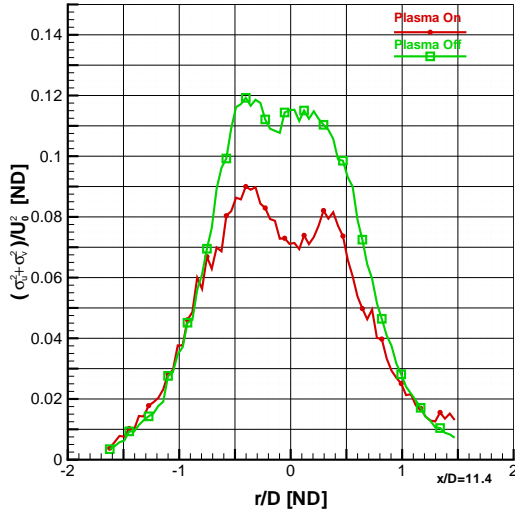
(c) Fluctuating Axial Velocity, σ_u/U_o



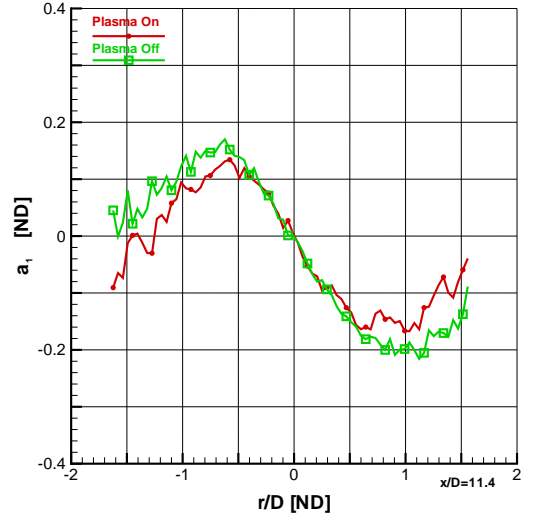
(d) Fluctuating Tangential Velocity, σ_v/U_o

Figure A.82: Comparison of Plasma Effects on Mean Velocity and Fluctuations: Case 618LINE10812

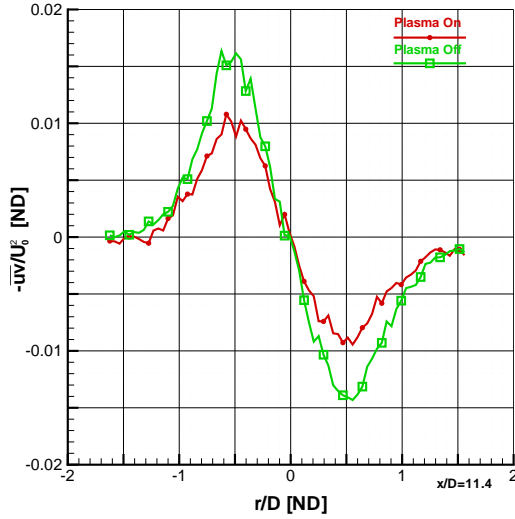
This is an investigation into the effect of plasma on jet created by developing flow in a constant-diameter tube driven at a Mach 0.9 isentropic pressure ratio, 11.4 diameters from the anode face. The jet diameter is 9.5 mm. The four plots represented above are a comparison between plasma on in red versus plasma off in green. Figure A.82 (a) is non-dimensionalized axial velocity. For these figures, U_o is 170.6 m/s for the plasma off case and 184.3 m/s for the plasma on case. Figure A.82 (b) is the mean tangential component of the velocity. Figures A.82 (c) and (d) show the Reynolds normal stresses in the axial and tangential directions, respectively. The case identifiers for this comparison were 618cnc-LINE10812 for plasma off and 618pnc-LINE10812 for plasma on.



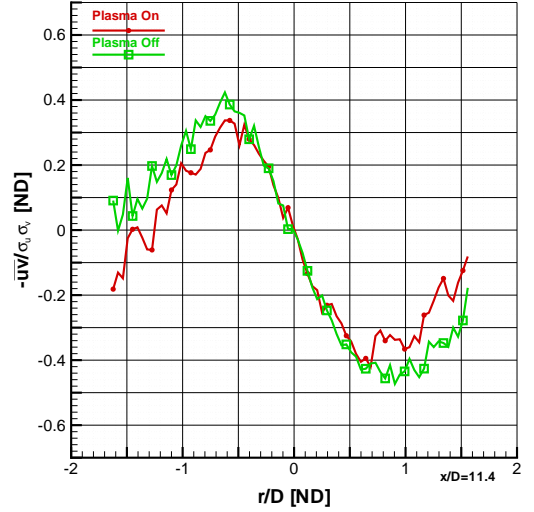
(a) Turbulent Kinetic Energy, $(\sigma_u^2 + \sigma_v^2)/U_o^2$



(b) Structural Parameter, $a_1 = -\overline{uv}/(\sigma_u^2 + \sigma_v^2)$



(c) Reynolds Shear Stress, \overline{uv}/U_o^2



(d) Correlation Coefficient of Reynolds Shear Stress, $-\overline{uv}/(\sigma_u \sigma_v)$

Figure A.83: Comparison of Plasma Effects on Second Moment Fluctuations: Case 618LINE10812

This is a continuing investigation into the effect of plasma on a Mach 0.9 isentropic pressure ratio, 11.4 diameters from the anode face. The jet diameter is 9.5 mm. The four plots represented above are a comparison between plasma on in red versus plasma off in green. Figure A.83 (a) is non-dimensionalized turbulent kinetic energy and panel (b) is the structural parameter a_1 . At this station, U_o is 170.6 m/s for the plasma off case and 184.3 m/s for the plasma on case. Figures A.83 (c) and (d) show the Reynolds shear stress and the correlation coefficient of Reynolds shear stress, respectively. The case identifiers for this comparison were 618cnc-LINE10812 for plasma off and 618pnc-LINE10812 for plasma on.

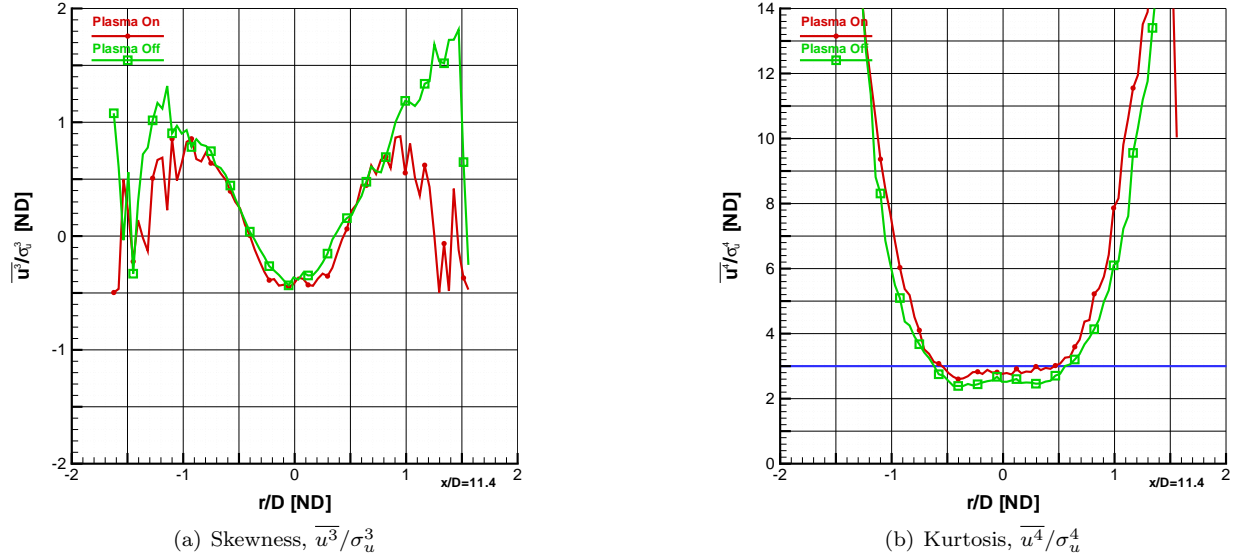


Figure A.84: Comparison of Plasma Effects on Skewness and Kurtosis: Case 618LINE10812

This is the final series of figures on the investigation into the effect of plasma on jet created by developing flow in a constant-diameter tube driven at a Mach 0.9 isentropic pressure ratio, 11.4 diameters from the anode face. The jet diameter is 9.5 mm. The two plots represented above are a comparison between plasma on in red versus plasma off in green. The plasma off case is placed on top of the plasma on case, therefore making it easier to notice small changes between the two cases. Figure A.84 (a) (b) are the measurements of skewness and kurtosis (or flatness), respectively. A Gaussian distribution has skewness of zero, which indicates a distribution of fluctuations is symmetric about the mean. Positive skewness represents a shift toward the right tail (positive fluctuations), while negative skewness is shifted toward negative fluctuations. A Gaussian distribution has kurtosis of three, represented by the blue line. Values lower than three represent a distribution of velocity with higher peakedness than a Gaussian distribution. Conversely, values above three represent flatter distributions. The case identifiers for this comparison were 618cnc-LINE10812 for plasma off and 618pnc-LINE10812 for plasma on.

A.7 Flow from a Tube Driven at a Mach 1.4 Pressure Ratio at 5 Torr Using Anode with Serrated Conical Feature

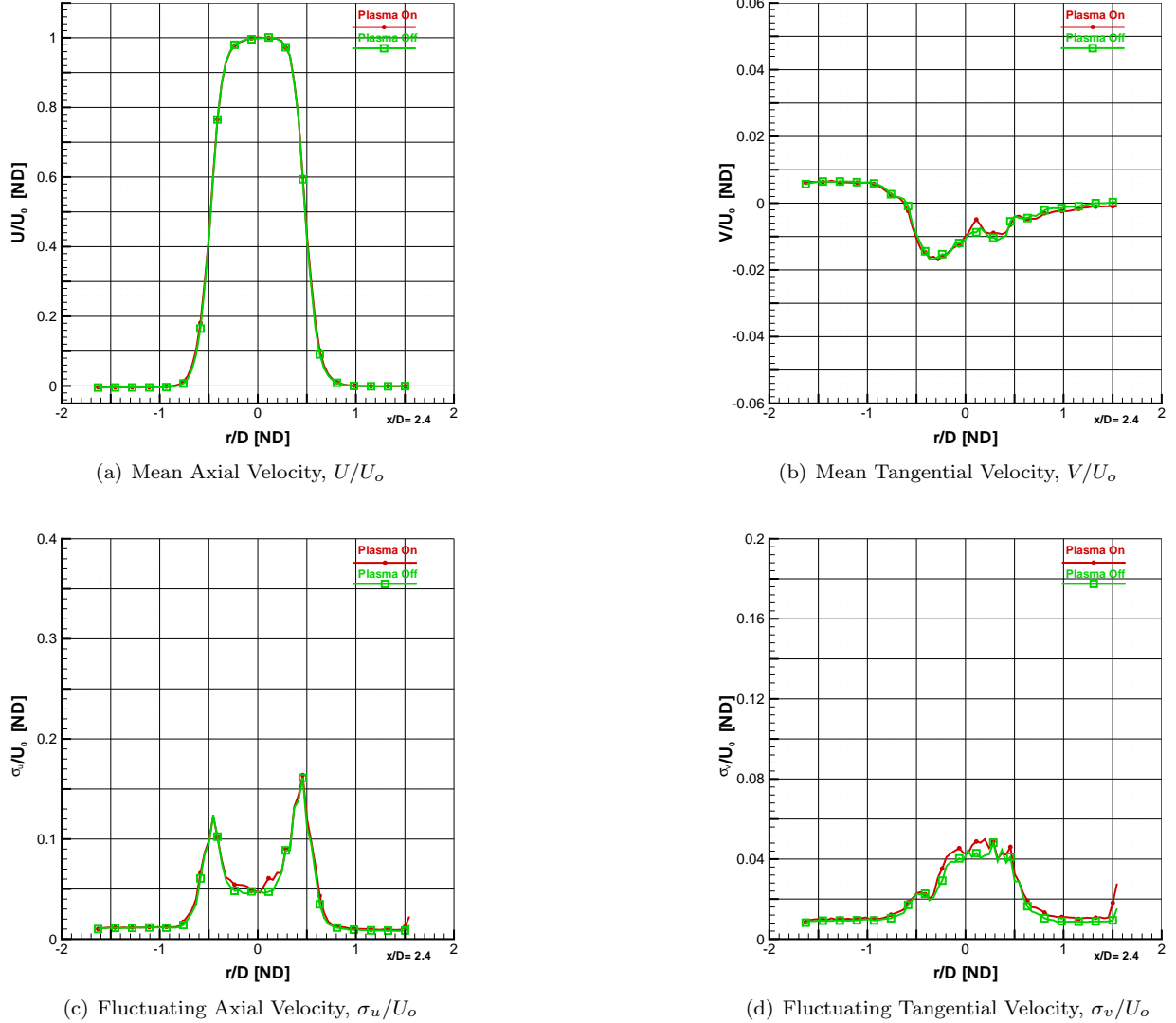
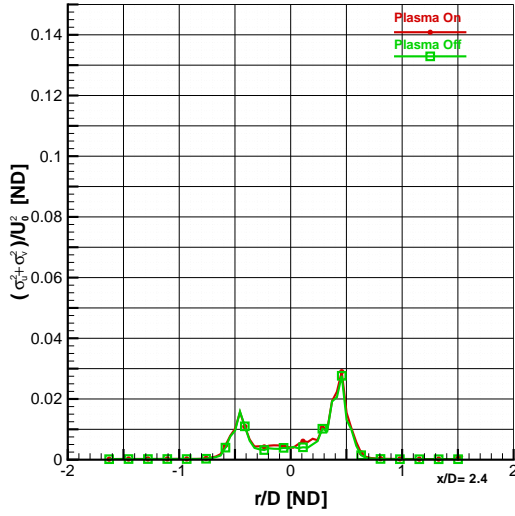
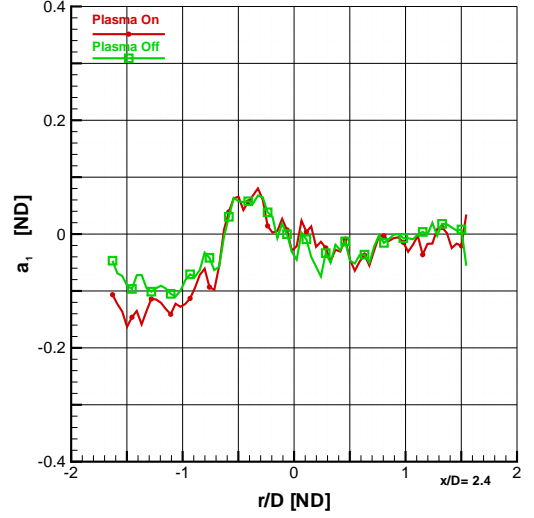


Figure A.85: Comparison of Plasma Effects on Mean Velocity and Fluctuations: Case 626LINE2260

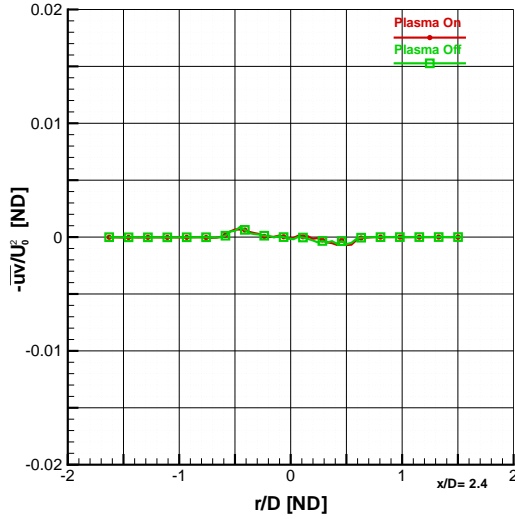
This is an investigation into the effect of plasma on jet created by developing flow in a constant-diameter tube driven at a Mach 1.4 isentropic pressure ratio, 2.4 diameters from the anode face. The jet diameter is 9.5 mm. The four plots represented above are a comparison between plasma on in red versus plasma off in green. Figure A.85 (a) is non-dimensionalized axial velocity. For these figures, U_o is 386.7 m/s for the plasma off case and 386.0 m/s for the plasma on case. Figure A.85 (b) is the mean tangential component of the velocity. Figures A.85 (c) and (d) show the Reynolds normal stresses.



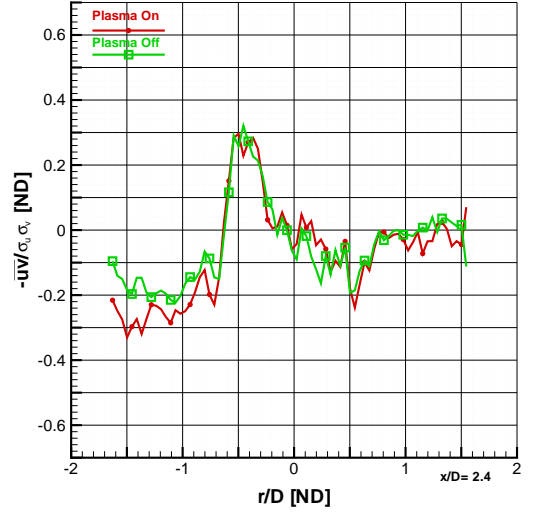
(a) Turbulent Kinetic Energy, $(\sigma_u^2 + \sigma_v^2)/U_o^2$



(b) Structural Parameter, $a_1 = -\overline{uv}/(\sigma_u^2 + \sigma_v^2)$



(c) Reynolds Shear Stress, \overline{uv}/U_o^2



(d) Correlation Coefficient of Reynolds Shear Stress, $-\overline{uv}/(\sigma_u \sigma_v)$

Figure A.86: Comparison of Plasma Effects on Second Moment Fluctuations: Case 626LINE2260

This is a continuing investigation into the effect of plasma on a Mach 1.4 isentropic pressure ratio, 2.4 diameters from the anode face. The jet diameter is 9.5 mm. The four plots represented above are a comparison between plasma on in red versus plasma off in green. Figure A.86 (a) is non-dimensionalized turbulent kinetic energy and panel (b) is the structural parameter a_1 . At this station, U_o is 386.7 m/s for the plasma off case and 386.0 m/s for the plasma on case. Figures A.86 (c) and (d) show the Reynolds shear stress and the correlation coefficient of Reynolds shear stress, respectively. The case identifiers for this comparison were 626cn-LINE2260 for plasma off and 626pn-LINE2260 for plasma on.

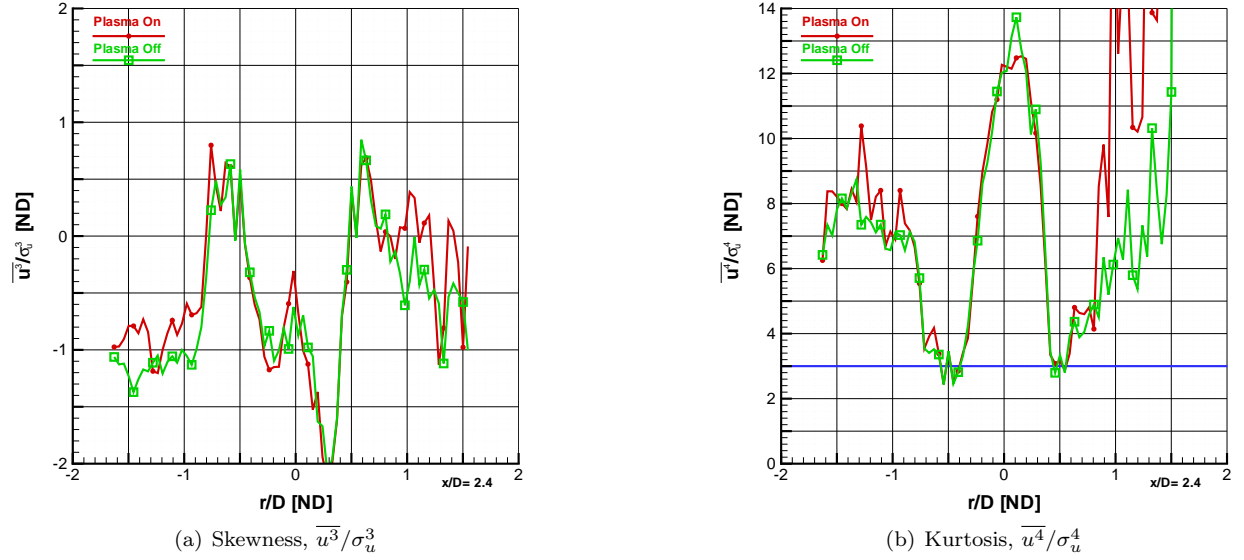
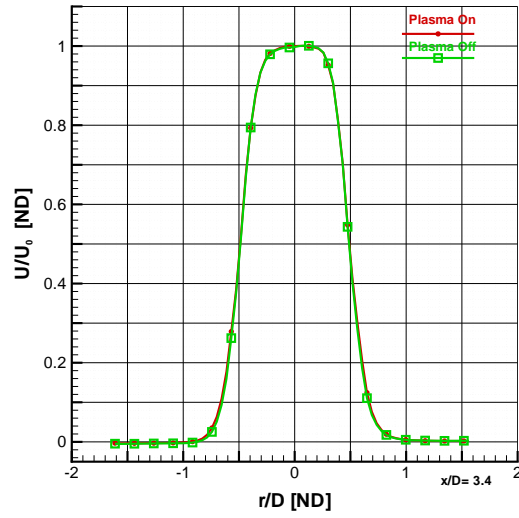
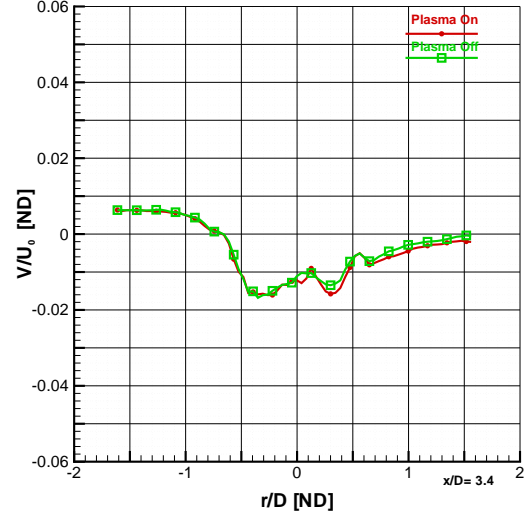


Figure A.87: Comparison of Plasma Effects on Skewness and Kurtosis: Case 626LINE2260

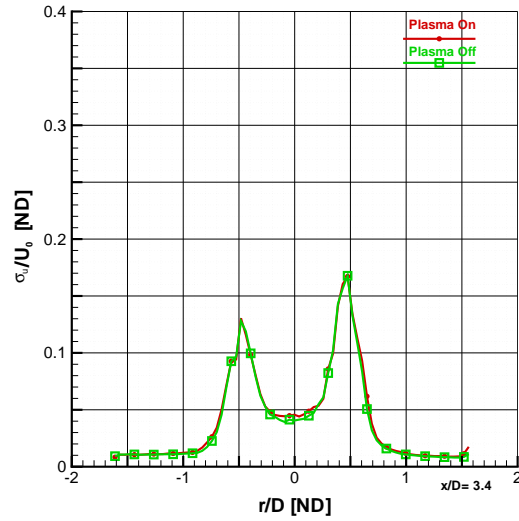
This is the final series of figures on the investigation into the effect of plasma on jet created by developing flow in a constant-diameter tube driven at a Mach 1.4 isentropic pressure ratio, 2.4 diameters from the anode face. The jet diameter is 9.5 mm. The two plots represented above are a comparison between plasma on in red versus plasma off in green. The plasma off case is placed on top of the plasma on case, therefore making it easier to notice small changes between the two cases. Figure A.87 (a) (b) are the measurements of skewness and kurtosis (or flatness), respectively. A Gaussian distribution has skewness of zero, which indicates a distribution of fluctuations is symmetric about the mean. Positive skewness represents a shift toward the right tail (positive fluctuations), while negative skewness is shifted toward negative fluctuations. A Gaussian distribution has kurtosis of three, represented by the blue line. Values lower than three represent a distribution of velocity with higher peakedness than a Gaussian distribution. Conversely, values above three represent flatter distributions. The case identifiers for this comparison were 626cn-LINE2260 for plasma off and 626pn-LINE2260 for plasma on.



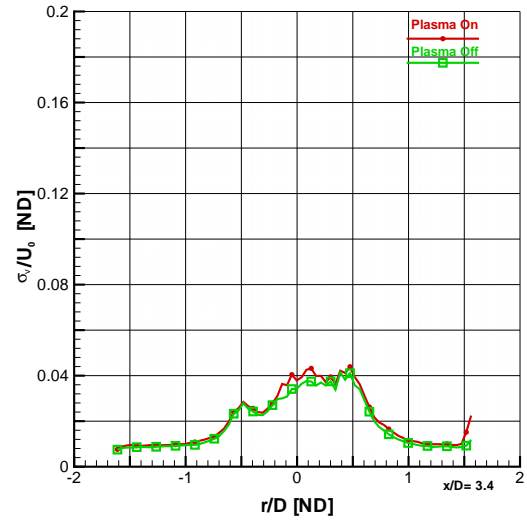
(a) Mean Axial Velocity, U/U_o



(b) Mean Tangential Velocity, V/U_o



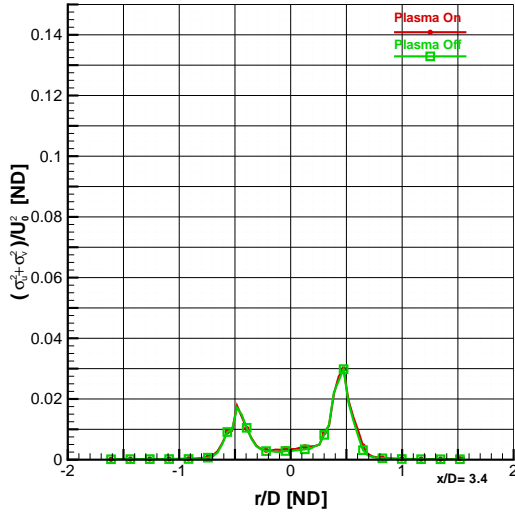
(c) Fluctuating Axial Velocity, σ_u/U_o



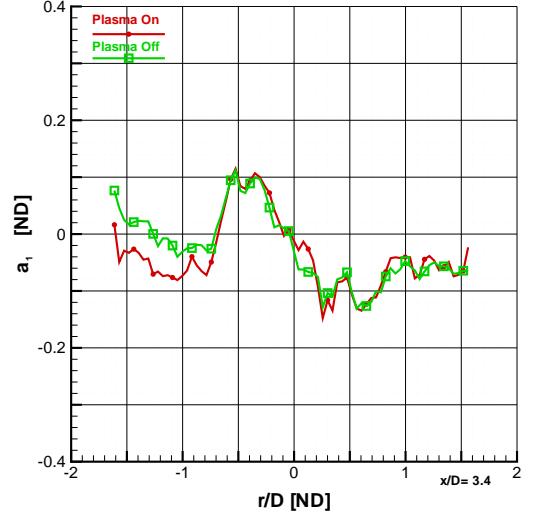
(d) Fluctuating Tangential Velocity, σ_v/U_o

Figure A.88: Comparison of Plasma Effects on Mean Velocity and Fluctuations: Case 626LINE3253

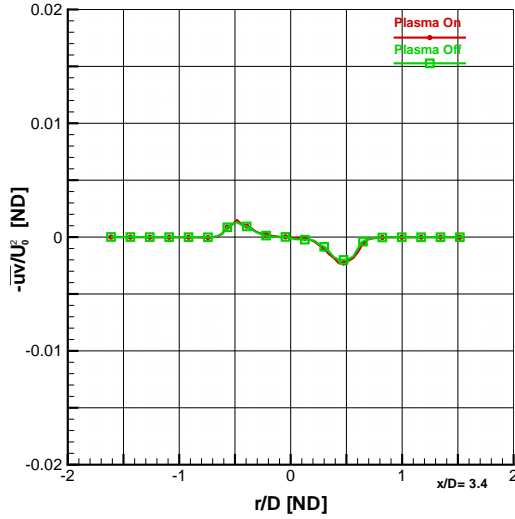
This is an investigation into the effect of plasma on jet created by developing flow in a constant-diameter tube driven at a Mach 1.4 isentropic pressure ratio, 3.4 diameters from the anode face. The jet diameter is 9.5 mm. The four plots represented above are a comparison between plasma on in red versus plasma off in green. Figure A.88 (a) is non-dimensionalized axial velocity. For these figures, U_o is 388.6 m/s for the plasma off case and 388.2 m/s for the plasma on case. Figure A.88 (b) is the mean tangential component of the velocity. Figures A.88 (c) and (d) show the Reynolds normal stresses in the axial and tangential directions, respectively. The case identifiers for this comparison were 626cn-LINE3253 for plasma off and 626pn-LINE3253 for plasma on.



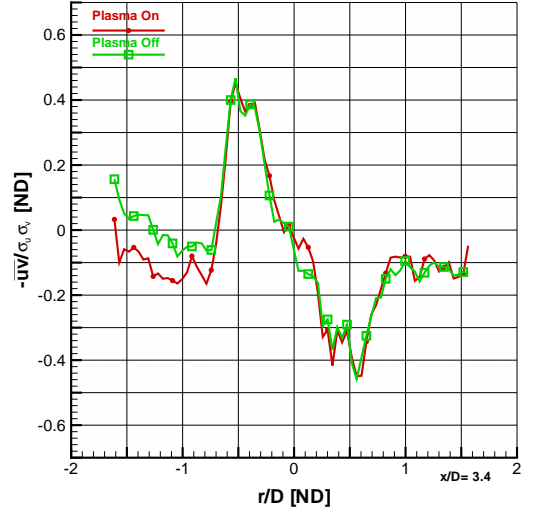
(a) Turbulent Kinetic Energy, $(\sigma_u^2 + \sigma_v^2)/U_o^2$



(b) Structural Parameter, $a_1 = -\overline{uv}/(\sigma_u^2 + \sigma_v^2)$



(c) Reynolds Shear Stress, \overline{uv}/U_o^2



(d) Correlation Coefficient of Reynolds Shear Stress, $-\overline{uv}/(\sigma_u \sigma_v)$

Figure A.89: Comparison of Plasma Effects on Second Moment Fluctuations: Case 626LINE3253

This is a continuing investigation into the effect of plasma on a Mach 1.4 isentropic pressure ratio, 3.4 diameters from the anode face. The jet diameter is 9.5 mm. The four plots represented above are a comparison between plasma on in red versus plasma off in green. Figure A.89 (a) is non-dimensionalized turbulent kinetic energy and panel (b) is the structural parameter a_1 . At this station, U_o is 388.6 m/s for the plasma off case and 388.2 m/s for the plasma on case. Figures A.89 (c) and (d) show the Reynolds shear stress and the correlation coefficient of Reynolds shear stress, respectively. The case identifiers for this comparison were 626cn-LINE3253 for plasma off and 626pn-LINE3253 for plasma on.

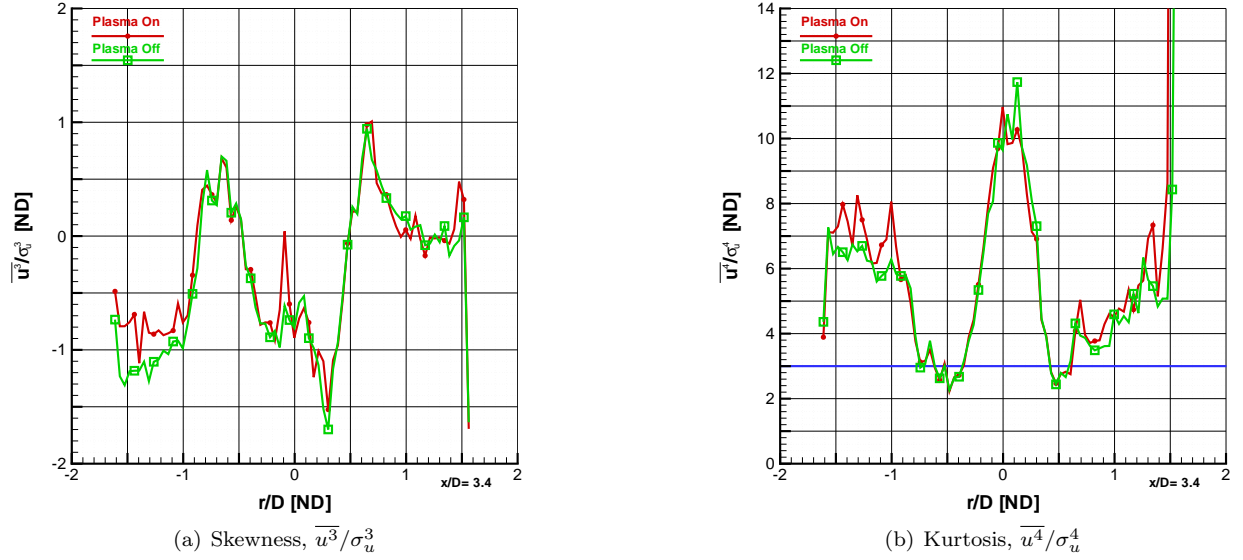
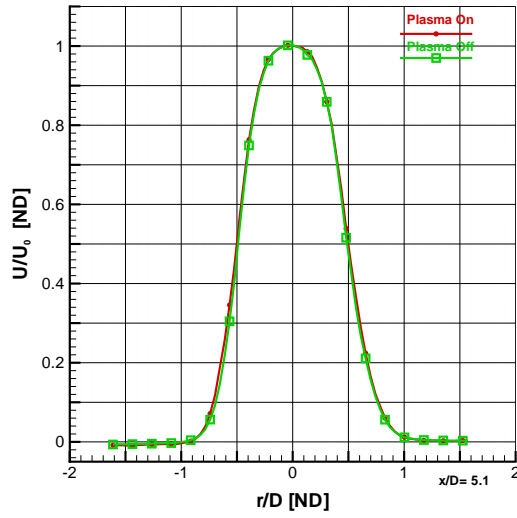
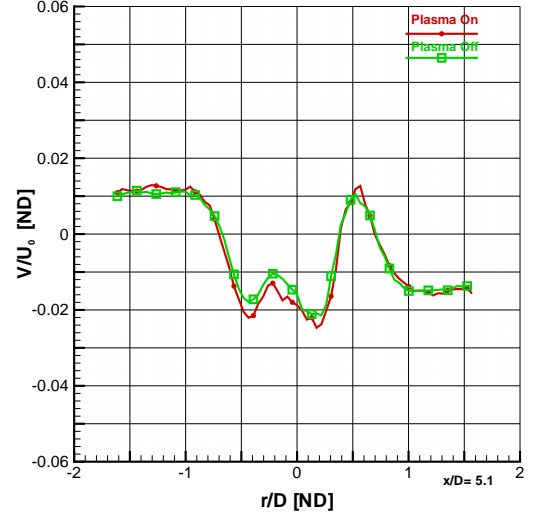


Figure A.90: Comparison of Plasma Effects on Skewness and Kurtosis: Case 626LINE3253

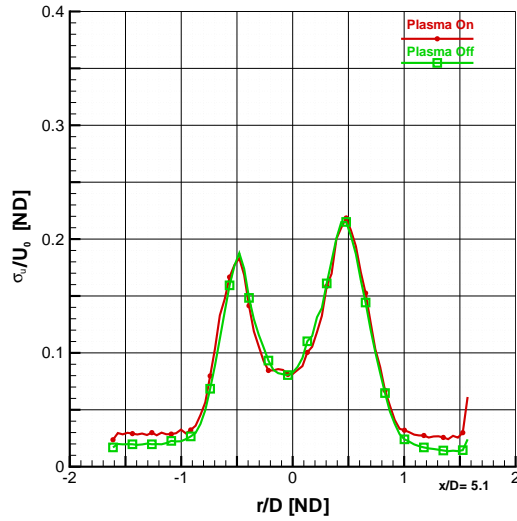
This is the final series of figures on the investigation into the effect of plasma on jet created by developing flow in a constant-diameter tube driven at a Mach 1.4 isentropic pressure ratio, 3.4 diameters from the anode face. The jet diameter is 9.5 mm. The two plots represented above are a comparison between plasma on in red versus plasma off in green. The plasma off case is placed on top of the plasma on case, therefore making it easier to notice small changes between the two cases. Figure A.90 (a) (b) are the measurements of skewness and kurtosis (or flatness), respectively. A Gaussian distribution has skewness of zero, which indicates a distribution of fluctuations is symmetric about the mean. Positive skewness represents a shift toward the right tail (positive fluctuations), while negative skewness is shifted toward negative fluctuations. A Gaussian distribution has kurtosis of three, represented by the blue line. Values lower than three represent a distribution of velocity with higher peakedness than a Gaussian distribution. Conversely, values above three represent flatter distributions. The case identifiers for this comparison were 626cn-LINE3253 for plasma off and 626pn-LINE3253 for plasma on.



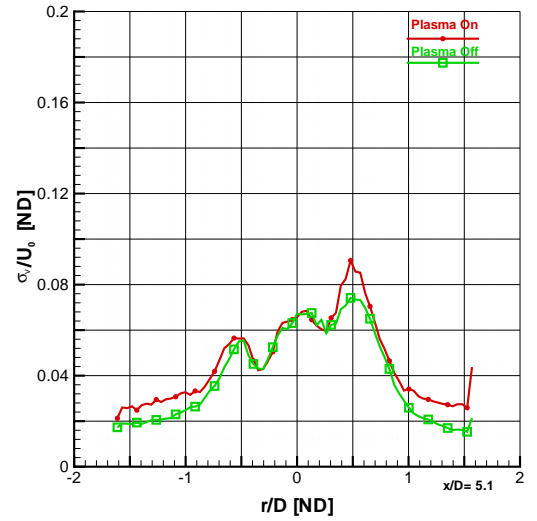
(a) Mean Axial Velocity, U/U_o



(b) Mean Tangential Velocity, V/U_o



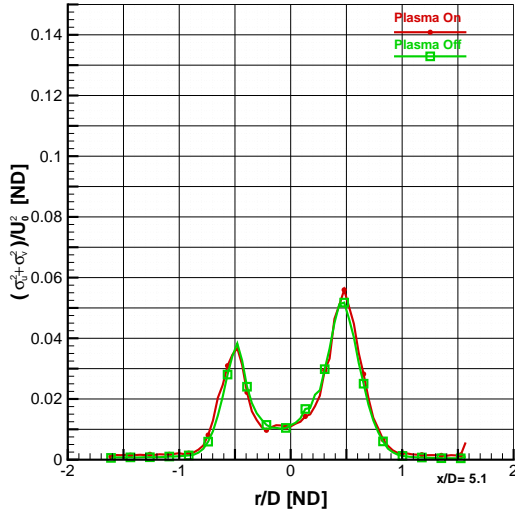
(c) Fluctuating Axial Velocity, σ_u/U_o



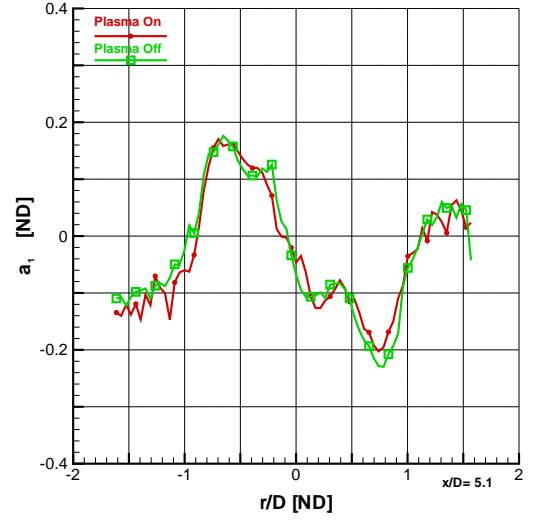
(d) Fluctuating Tangential Velocity, σ_v/U_o

Figure A.91: Comparison of Plasma Effects on Mean Velocity and Fluctuations: Case 621LINE4808

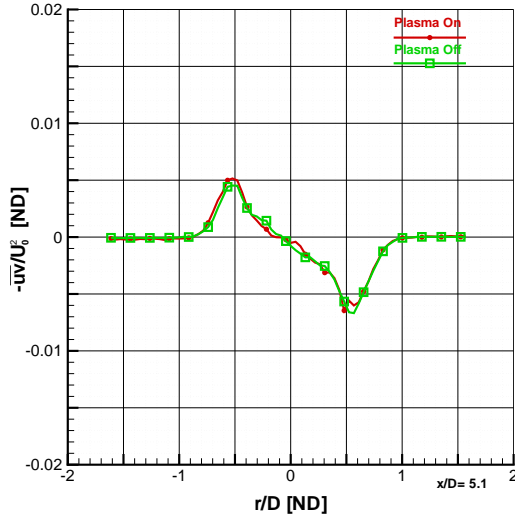
This is an investigation into the effect of plasma on jet created by developing flow in a constant-diameter tube driven at a Mach 1.4 isentropic pressure ratio, 5.1 diameters from the anode face. The jet diameter is 9.5 mm. The four plots represented above are a comparison between plasma on in red versus plasma off in green. Figure A.91 (a) is non-dimensionalized axial velocity. For these figures, U_o is 379.9 m/s for the plasma off case and 380.3 m/s for the plasma on case. Figure A.91 (b) is the mean tangential component of the velocity. Figures A.91 (c) and (d) show the Reynolds normal stresses in the axial and tangential directions, respectively. The case identifiers for this comparison were 621cn-LINE4808 for plasma off and 621pn-LINE4808 for plasma on.



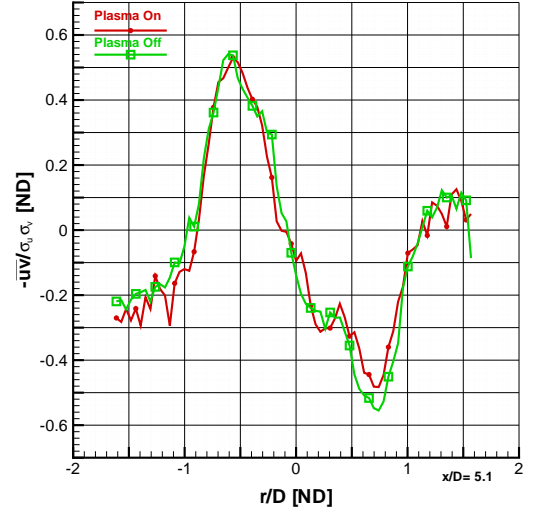
(a) Turbulent Kinetic Energy, $(\sigma_u^2 + \sigma_v^2)/U_o^2$



(b) Structural Parameter, $a_1 = -\overline{u'v'} / (\sigma_u^2 + \sigma_v^2)$



(c) Reynolds Shear Stress, $\overline{u'v'} / U_o^2$



(d) Correlation Coefficient of Reynolds Shear Stress, $-\overline{u'v'} / (\sigma_u \sigma_v)$

Figure A.92: Comparison of Plasma Effects on Second Moment Fluctuations: Case 621LINE4808

This is a continuing investigation into the effect of plasma on a Mach 1.4 isentropic pressure ratio, 5.1 diameters from the anode face. The jet diameter is 9.5 mm. The four plots represented above are a comparison between plasma on in red versus plasma off in green. Figure A.92 (a) is non-dimensionalized turbulent kinetic energy and panel (b) is the structural parameter a_1 . At this station, U_o is 379.9 m/s for the plasma off case and 380.3 m/s for the plasma on case. Figures A.92 (c) and (d) show the Reynolds shear stress and the correlation coefficient of Reynolds shear stress, respectively. The case identifiers for this comparison were 621cn-LINE4808 for plasma off and 621pn-LINE4808 for plasma on.

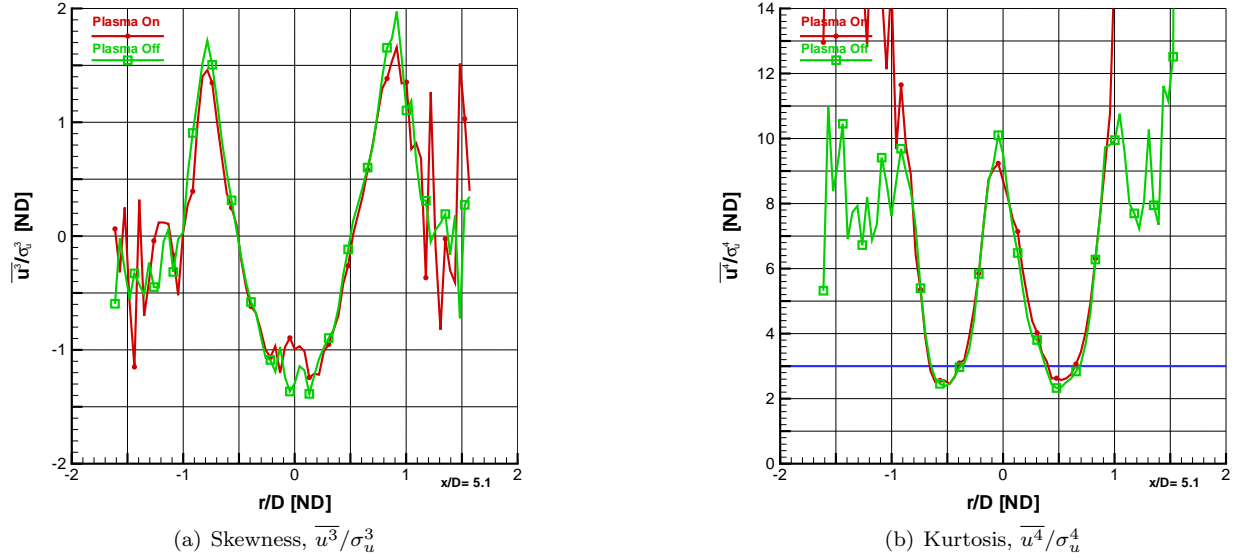
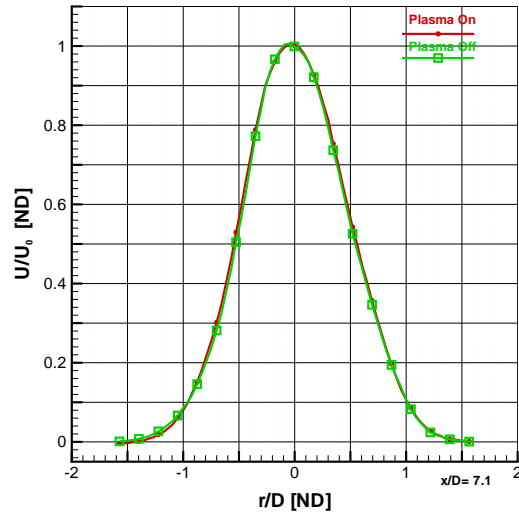
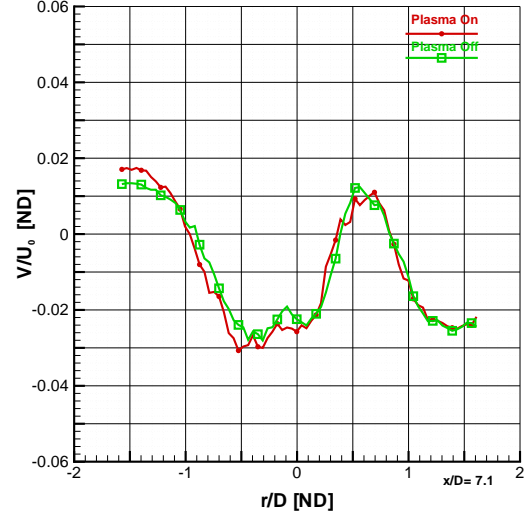


Figure A.93: Comparison of Plasma Effects on Skewness and Kurtosis: Case 621LINE4808

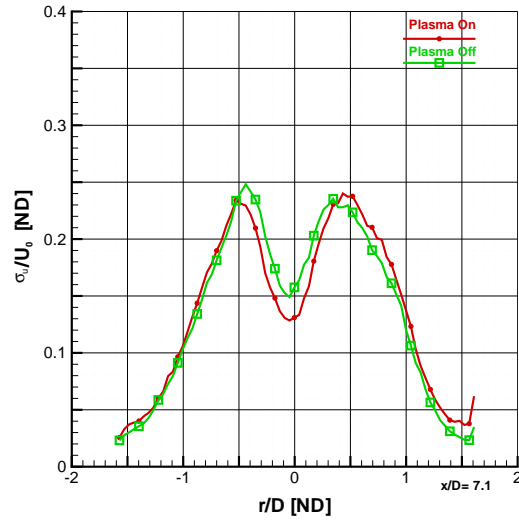
This is the final series of figures on the investigation into the effect of plasma on jet created by developing flow in a constant-diameter tube driven at a Mach 1.4 isentropic pressure ratio, 5.1 diameters from the anode face. The jet diameter is 9.5 mm. The two plots represented above are a comparison between plasma on in red versus plasma off in green. The plasma off case is placed on top of the plasma on case, therefore making it easier to notice small changes between the two cases. Figure A.93 (a) (b) are the measurements of skewness and kurtosis (or flatness), respectively. A Gaussian distribution has skewness of zero, which indicates a distribution of fluctuations is symmetric about the mean. Positive skewness represents a shift toward the right tail (positive fluctuations), while negative skewness is shifted toward negative fluctuations. A Gaussian distribution has kurtosis of three, represented by the blue line. Values lower than three represent a distribution of velocity with higher peakedness than a Gaussian distribution. Conversely, values above three represent flatter distributions. The case identifiers for this comparison were 621cn-LINE4808 for plasma off and 621pn-LINE4808 for plasma on.



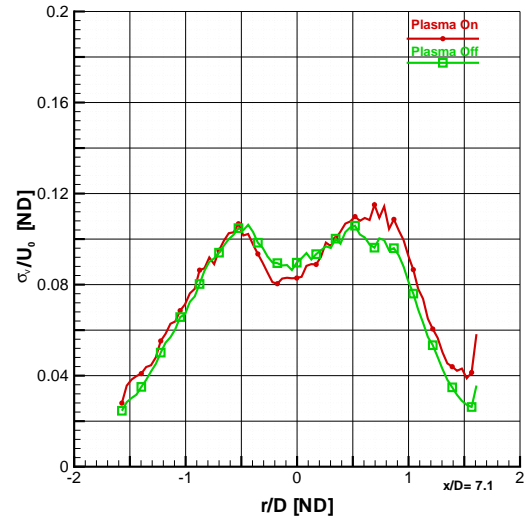
(a) Mean Axial Velocity, U/U_o



(b) Mean Tangential Velocity, V/U_o



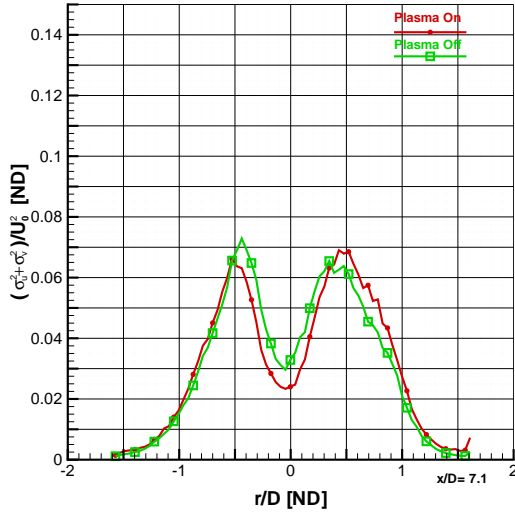
(c) Fluctuating Axial Velocity, σ_u/U_o



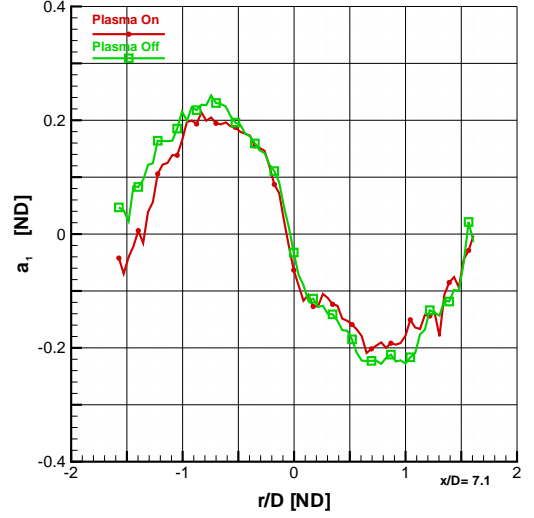
(d) Fluctuating Tangential Velocity, σ_v/U_o

Figure A.94: Comparison of Plasma Effects on Mean Velocity and Fluctuations: Case 621LINE6799

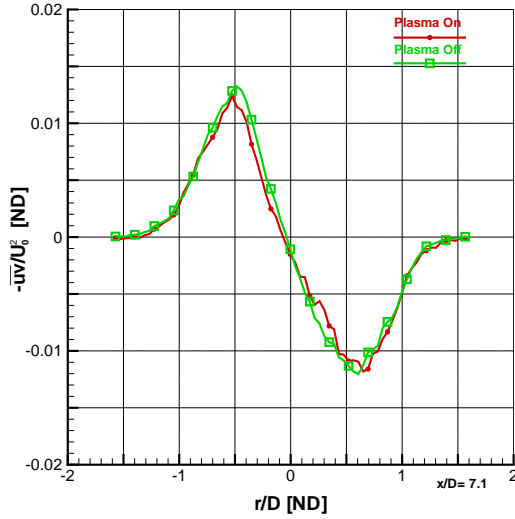
This is an investigation into the effect of plasma on jet created by developing flow in a constant-diameter tube driven at a Mach 1.4 isentropic pressure ratio, 7.1 diameters from the anode face. The jet diameter is 9.5 mm. The four plots represented above are a comparison between plasma on in red versus plasma off in green. Figure A.94 (a) is non-dimensionalized axial velocity. For these figures, U_o is 346.8 m/s for the plasma off case and 356.2 m/s for the plasma on case. Figure A.94 (b) is the mean tangential component of the velocity. Figures A.94 (c) and (d) show the Reynolds normal stresses in the axial and tangential directions, respectively. The case identifiers for this comparison were 621cn-LINE6799 for plasma off and 621pn-LINE6799 for plasma on.



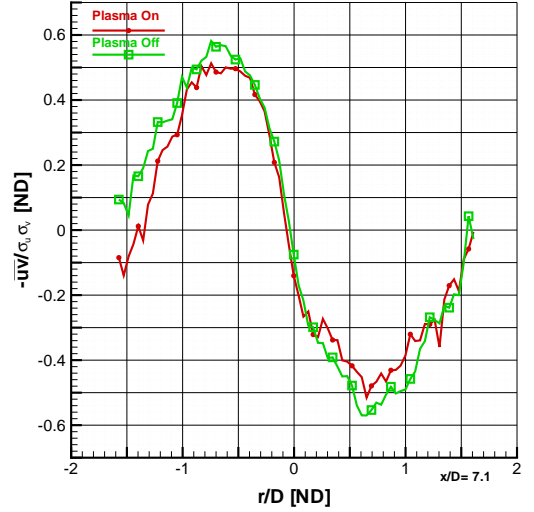
(a) Turbulent Kinetic Energy, $(\sigma_u^2 + \sigma_v^2)/U_o^2$



(b) Structural Parameter, $a_1 = -\overline{uv}/(\sigma_u^2 + \sigma_v^2)$



(c) Reynolds Shear Stress, \overline{uv}/U_o^2



(d) Correlation Coefficient of Reynolds Shear Stress, $-\overline{uv}/(\sigma_u \sigma_v)$

Figure A.95: Comparison of Plasma Effects on Second Moment Fluctuations: Case 621LINE6799

This is a continuing investigation into the effect of plasma on a Mach 1.4 isentropic pressure ratio, 7.1 diameters from the anode face. The jet diameter is 9.5 mm. The four plots represented above are a comparison between plasma on in red versus plasma off in green. Figure A.95 (a) is non-dimensionalized turbulent kinetic energy and panel (b) is the structural parameter a_1 . At this station, U_o is 346.8 m/s for the plasma off case and 356.2 m/s for the plasma on case. Figures A.95 (c) and (d) show the Reynolds shear stress and the correlation coefficient of Reynolds shear stress, respectively. The case identifiers for this comparison were 621cn-LINE6799 for plasma off and 621pn-LINE6799 for plasma on.

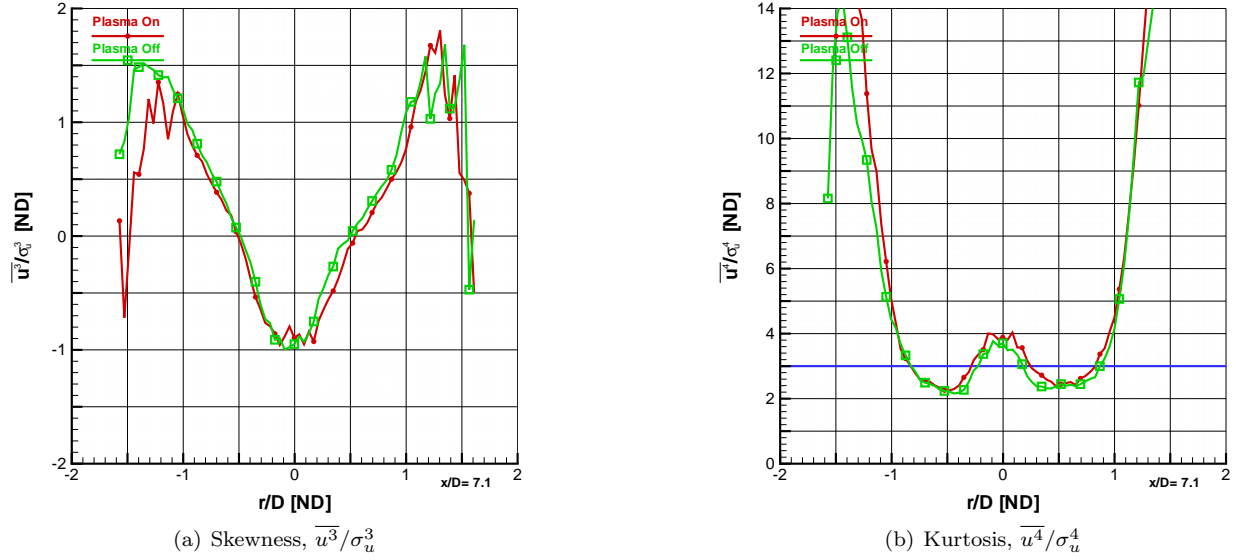
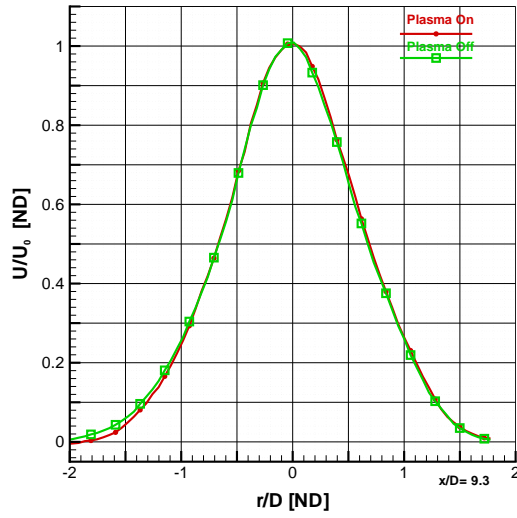
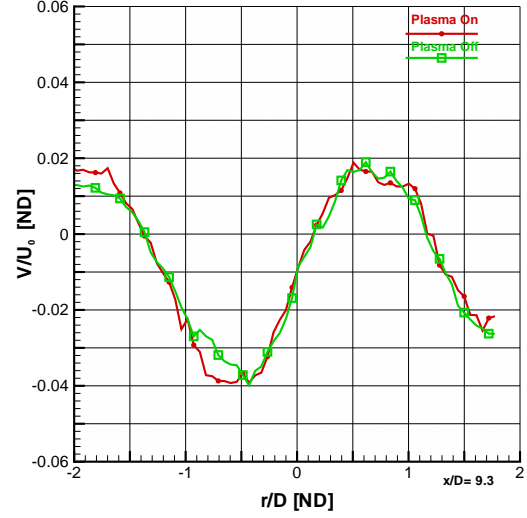


Figure A.96: Comparison of Plasma Effects on Skewness and Kurtosis: Case 621LINE6799

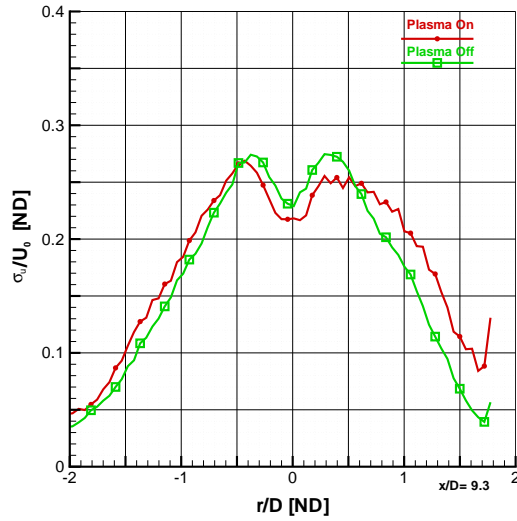
This is the final series of figures on the investigation into the effect of plasma on jet created by developing flow in a constant-diameter tube driven at a Mach 1.4 isentropic pressure ratio, 7.1 diameters from the anode face. The jet diameter is 9.5 mm. The two plots represented above are a comparison between plasma on in red versus plasma off in green. The plasma off case is placed on top of the plasma on case, therefore making it easier to notice small changes between the two cases. Figure A.96 (a) (b) are the measurements of skewness and kurtosis (or flatness), respectively. A Gaussian distribution has skewness of zero, which indicates a distribution of fluctuations is symmetric about the mean. Positive skewness represents a shift toward the right tail (positive fluctuations), while negative skewness is shifted toward negative fluctuations. A Gaussian distribution has kurtosis of three, represented by the blue line. Values lower than three represent a distribution of velocity with higher peakedness than a Gaussian distribution. Conversely, values above three represent flatter distributions. The case identifiers for this comparison were 621cn-LINE6799 for plasma off and 621pn-LINE6799 for plasma on.



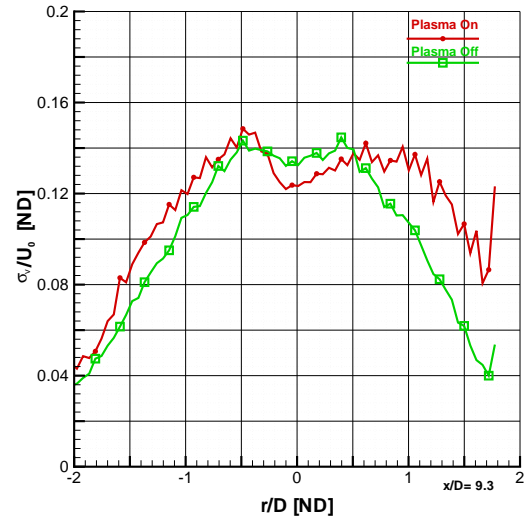
(a) Mean Axial Velocity, U/U_o



(b) Mean Tangential Velocity, V/U_o



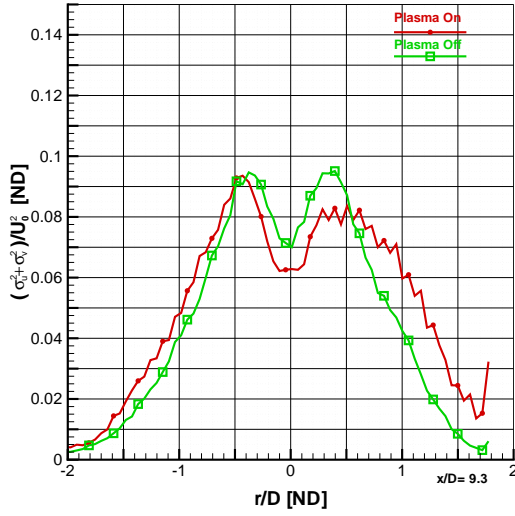
(c) Fluctuating Axial Velocity, σ_u/U_o



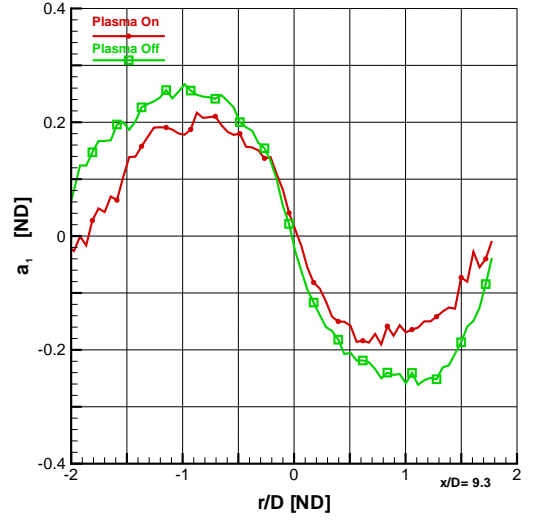
(d) Fluctuating Tangential Velocity, σ_v/U_o

Figure A.97: Comparison of Plasma Effects on Mean Velocity and Fluctuations: Case 617LINE8814

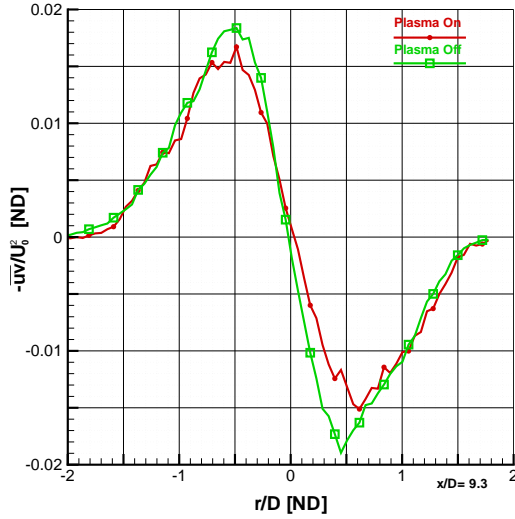
This is an investigation into the effect of plasma on jet created by developing flow in a constant-diameter tube driven at a Mach 1.4 isentropic pressure ratio, 9.3 diameters from the anode face. The jet diameter is 9.5 mm. The four plots represented above are a comparison between plasma on in red versus plasma off in green. Figure A.97 (a) is non-dimensionalized axial velocity. For these figures, U_o is 295.7 m/s for the plasma off case and 312.1 m/s for the plasma on case. Figure A.97 (b) is the mean tangential component of the velocity. Figures A.97 (c) and (d) show the Reynolds normal stresses in the axial and tangential directions, respectively. The case identifiers for this comparison were 617cnc-LINE8814 for plasma off and 617pnc-LINE8814 for plasma on.



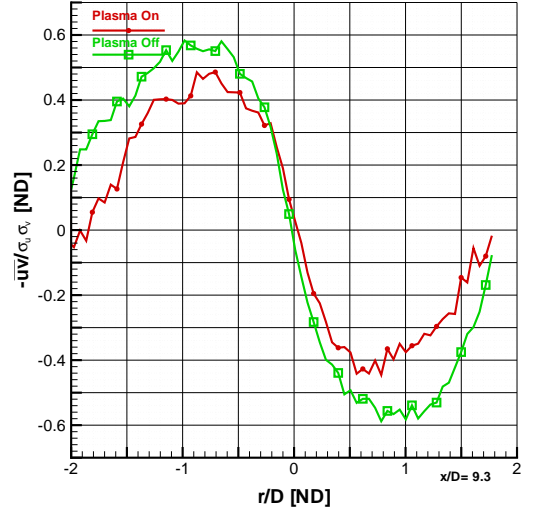
(a) Turbulent Kinetic Energy, $(\sigma_u^2 + \sigma_v^2)/U_o^2$



(b) Structural Parameter, $a_1 = -\overline{uv}/(\sigma_u^2 + \sigma_v^2)$



(c) Reynolds Shear Stress, \overline{uv}/U_o^2



(d) Correlation Coefficient of Reynolds Shear Stress, $-\overline{uv}/(\sigma_u \sigma_v)$

Figure A.98: Comparison of Plasma Effects on Second Moment Fluctuations: Case 617LINE8814

This is a continuing investigation into the effect of plasma on a Mach 1.4 isentropic pressure ratio, 9.3 diameters from the anode face. The jet diameter is 9.5 mm. The four plots represented above are a comparison between plasma on in red versus plasma off in green. Figure A.98 (a) is non-dimensionalized turbulent kinetic energy and panel (b) is the structural parameter a_1 . At this station, U_o is 295.7 m/s for the plasma off case and 312.1 m/s for the plasma on case. Figures A.98 (c) and (d) show the Reynolds shear stress and the correlation coefficient of Reynolds shear stress, respectively. The case identifiers for this comparison were 617cnc-LINE8814 for plasma off and 617pnc-LINE8814 for plasma on.

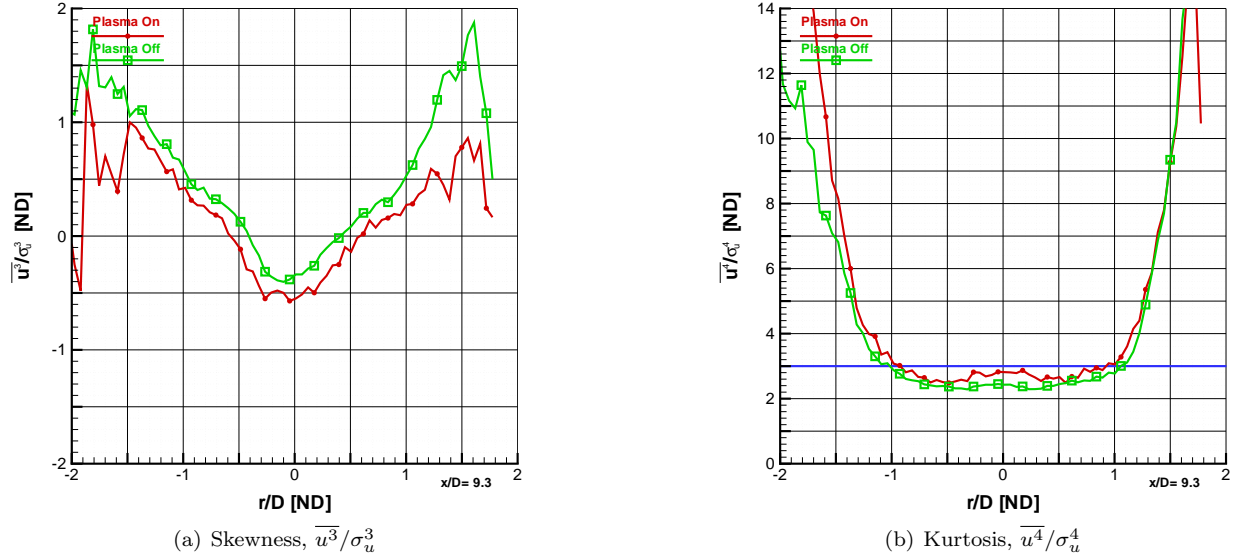
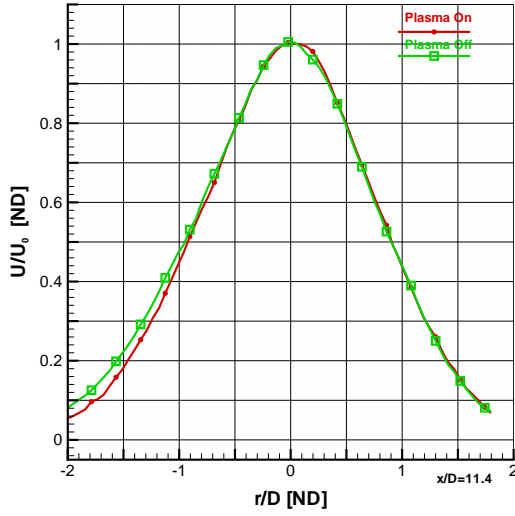
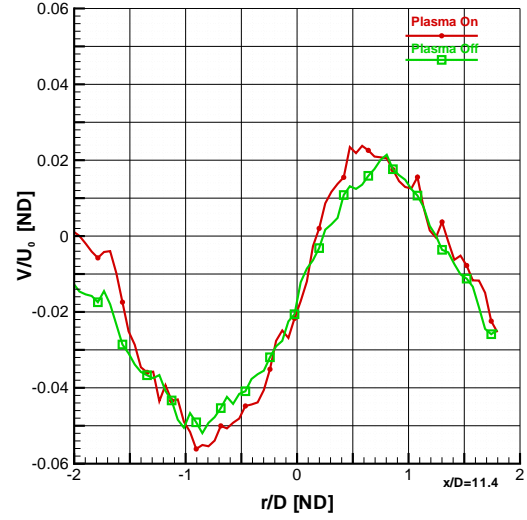


Figure A.99: Comparison of Plasma Effects on Skewness and Kurtosis: Case 617LINE8814

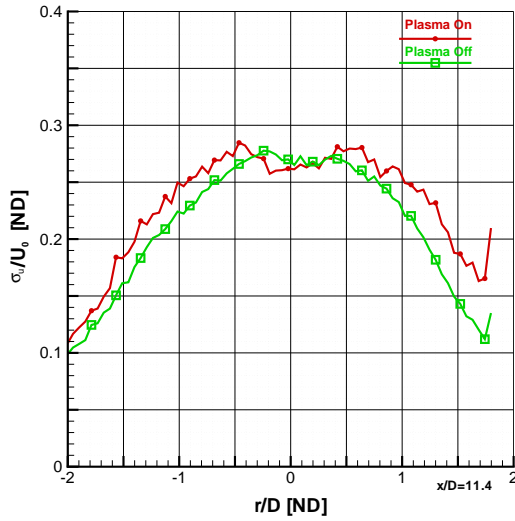
This is the final series of figures on the investigation into the effect of plasma on jet created by developing flow in a constant-diameter tube driven at a Mach 1.4 isentropic pressure ratio, 9.3 diameters from the anode face. The jet diameter is 9.5 mm. The two plots represented above are a comparison between plasma on in red versus plasma off in green. The plasma off case is placed on top of the plasma on case, therefore making it easier to notice small changes between the two cases. Figure A.99 (a) (b) are the measurements of skewness and kurtosis (or flatness), respectively. A Gaussian distribution has skewness of zero, which indicates a distribution of fluctuations is symmetric about the mean. Positive skewness represents a shift toward the right tail (positive fluctuations), while negative skewness is shifted toward negative fluctuations. A Gaussian distribution has kurtosis of three, represented by the blue line. Values lower than three represent a distribution of velocity with higher peakedness than a Gaussian distribution. Conversely, values above three represent flatter distributions. The case identifiers for this comparison were 617cnc-LINE8814 for plasma off and 617pnc-LINE8814 for plasma on.



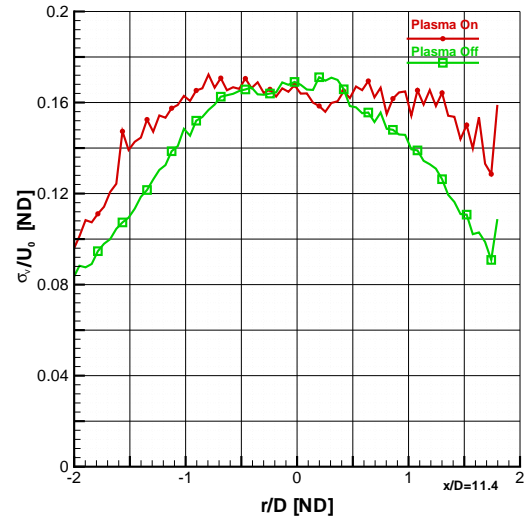
(a) Mean Axial Velocity, U/U_o



(b) Mean Tangential Velocity, V/U_o



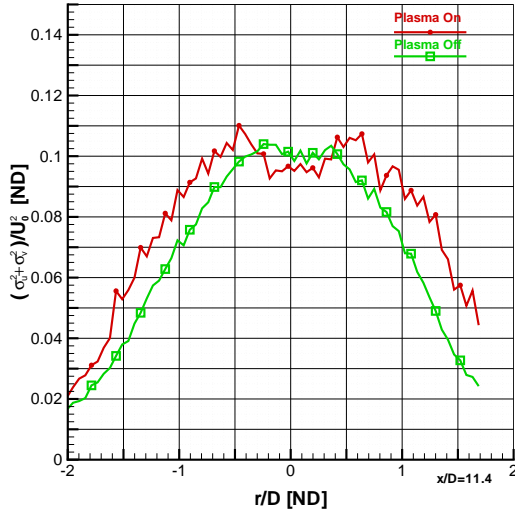
(c) Fluctuating Axial Velocity, σ_u/U_o



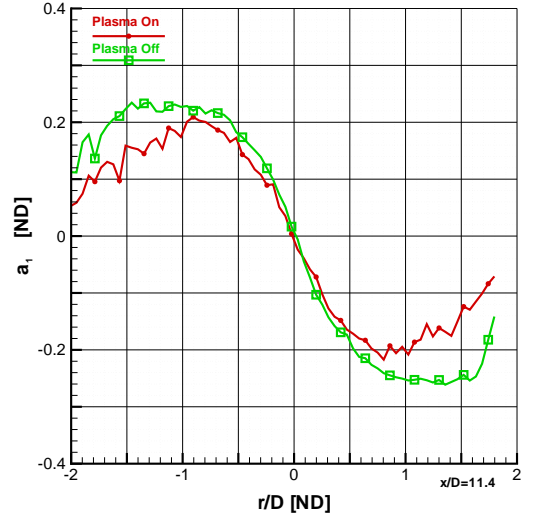
(d) Fluctuating Tangential Velocity, σ_v/U_o

Figure A.100: Comparison of Plasma Effects on Mean Velocity and Fluctuations: Case 617LINE10809

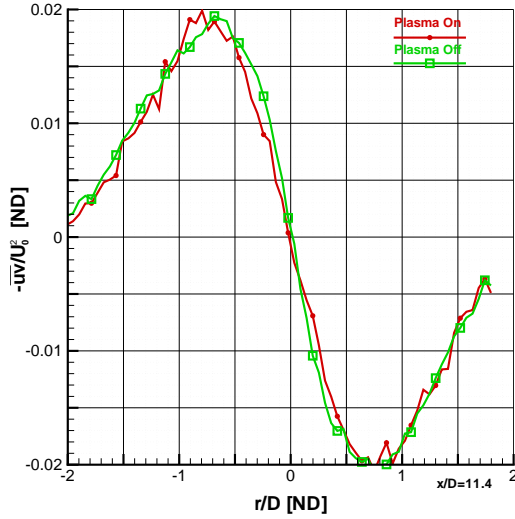
This is an investigation into the effect of plasma on jet created by developing flow in a constant-diameter tube driven at a Mach 1.4 isentropic pressure ratio, 11.4 diameters from the anode face. The jet diameter is 9.5 mm. The four plots represented above are a comparison between plasma on in red versus plasma off in green. Figure A.100 (a) is non-dimensionalized axial velocity. For these figures, U_o is 230.1 m/s for the plasma off case and 250.5 m/s for the plasma on case. Figure A.100 (b) is the mean tangential component of the velocity. Figures A.100 (c) and (d) show the Reynolds normal stresses in the axial and tangential directions, respectively. The case identifiers for this comparison were 617cnc-LINE10809 for plasma off and 617pnc-LINE10809 for plasma on.



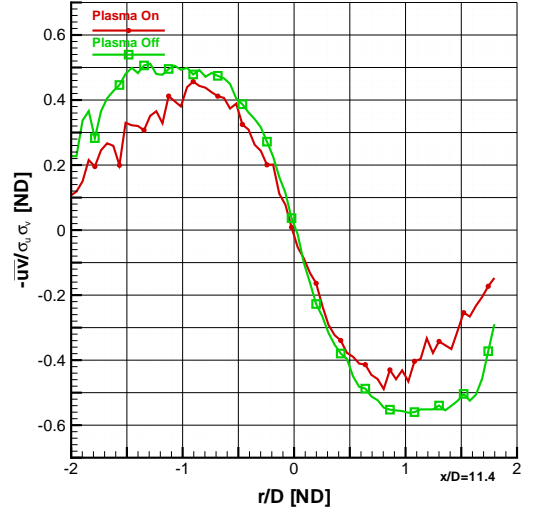
(a) Turbulent Kinetic Energy, $(\sigma_u^2 + \sigma_v^2)/U_o^2$



(b) Structural Parameter, $a_1 = -\overline{uv}/(\sigma_u^2 + \sigma_v^2)$



(c) Reynolds Shear Stress, \overline{uv}/U_o^2



(d) Correlation Coefficient of Reynolds Shear Stress, $-\overline{uv}/(\sigma_u \sigma_v)$

Figure A.101: Comparison of Plasma Effects on Second Moment Fluctuations: Case 617LINE10809

This is a continuing investigation into the effect of plasma on a Mach 1.4 isentropic pressure ratio, 11.4 diameters from the anode face. The jet diameter is 9.5 mm. The four plots represented above are a comparison between plasma on in red versus plasma off in green. Figure A.101 (a) is non-dimensionalized turbulent kinetic energy and panel (b) is the structural parameter a_1 . At this station, U_o is 230.1 m/s for the plasma off case and 250.5 m/s for the plasma on case. Figures A.101 (c) and (d) show the Reynolds shear stress and the correlation coefficient of Reynolds shear stress, respectively. The case identifiers for this comparison were 617cnc-LINE10809 for plasma off and 617pnc-LINE10809 for plasma on.

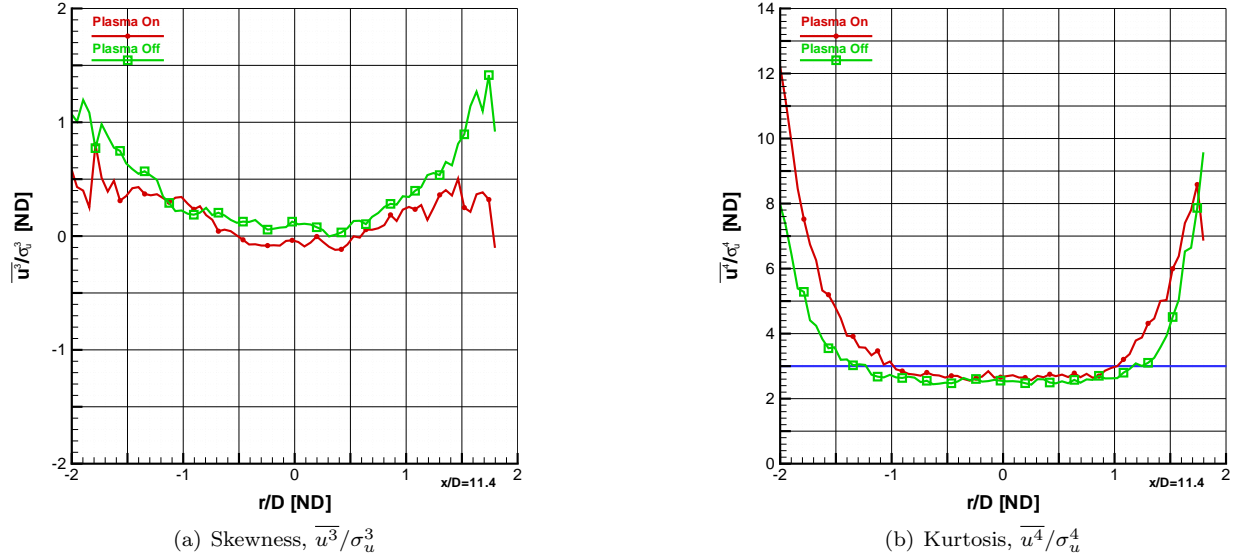


Figure A.102: Comparison of Plasma Effects on Skewness and Kurtosis: Case 617LINE10809

This is the final series of figures on the investigation into the effect of plasma on jet created by developing flow in a constant-diameter tube driven at a Mach 1.4 isentropic pressure ratio, 11.4 diameters from the anode face. The jet diameter is 9.5 mm. The two plots represented above are a comparison between plasma on in red versus plasma off in green. The plasma off case is placed on top of the plasma on case, therefore making it easier to notice small changes between the two cases. Figure A.102 (a) (b) are the measurements of skewness and kurtosis (or flatness), respectively. A Gaussian distribution has skewness of zero, which indicates a distribution of fluctuations is symmetric about the mean. Positive skewness represents a shift toward the right tail (positive fluctuations), while negative skewness is shifted toward negative fluctuations. A Gaussian distribution has kurtosis of three, represented by the blue line. Values lower than three represent a distribution of velocity with higher peakedness than a Gaussian distribution. Conversely, values above three represent flatter distributions. The case identifiers for this comparison were 617cnc-LINE10809 for plasma off and 617pnc-LINE10809 for plasma on.

A.8 Flow from a Tube Driven at a Mach 1.9 Pressure Ratio at 5 Torr Using Anode with Serrated Conical Feature

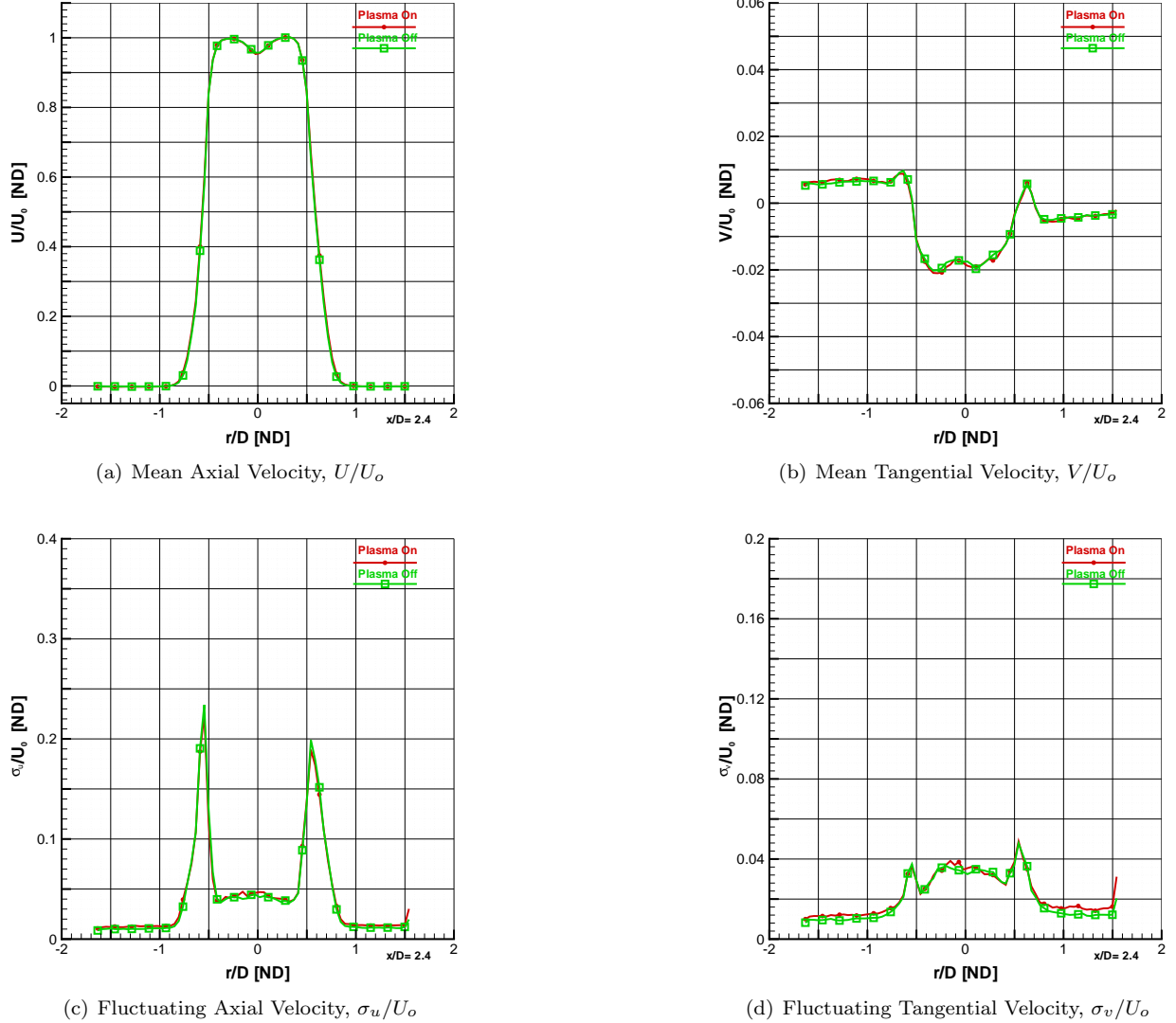
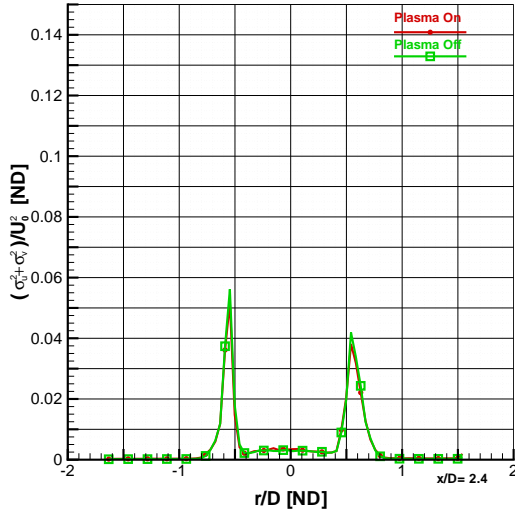
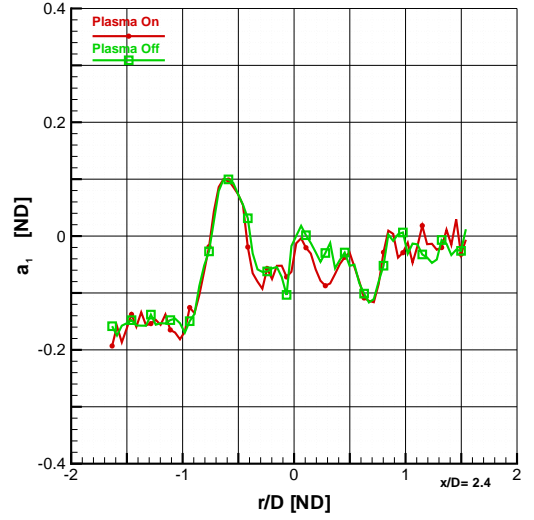


Figure A.103: Comparison of Plasma Effects on Mean Velocity and Fluctuations: Case 627LINE2260

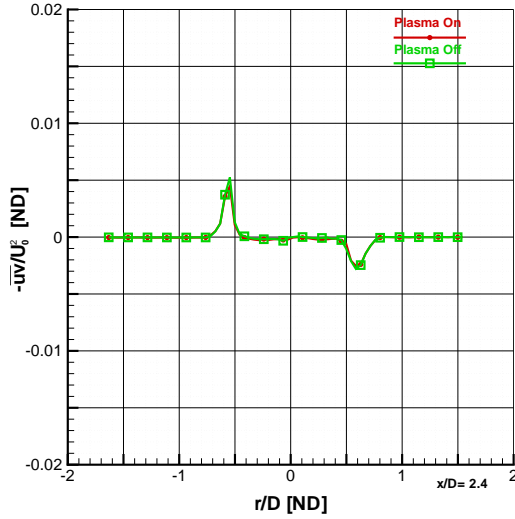
This is an investigation into the effect of plasma on jet created by developing flow in a constant-diameter tube driven at a Mach 1.9 isentropic pressure ratio, 2.4 diameters from the anode face. The jet diameter is 9.5 mm. The four plots represented above are a comparison between plasma on in red versus plasma off in green. Figure A.103 (a) is non-dimensionalized axial velocity. For these figures, U_o is 459.6 m/s for the plasma off case and 459.1 m/s for the plasma on case. Figure A.103 (b) is the mean tangential component of the velocity. Figures A.103 (c) and (d) show the Reynolds normal stresses.



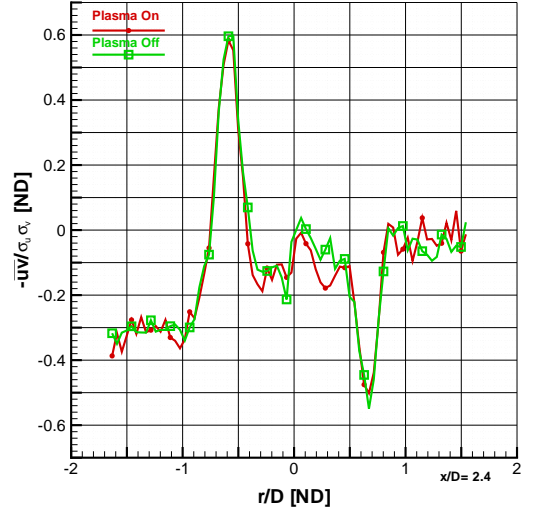
(a) Turbulent Kinetic Energy, $(\sigma_u^2 + \sigma_v^2)/U_o^2$



(b) Structural Parameter, $a_1 = -\overline{uv}/(\sigma_u^2 + \sigma_v^2)$



(c) Reynolds Shear Stress, \overline{uv}/U_o^2



(d) Correlation Coefficient of Reynolds Shear Stress, $-\overline{uv}/(\sigma_u \sigma_v)$

Figure A.104: Comparison of Plasma Effects on Second Moment Fluctuations: Case 627LINE2260

This is a continuing investigation into the effect of plasma on a Mach 1.9 isentropic pressure ratio, 2.4 diameters from the anode face. The jet diameter is 9.5 mm. The four plots represented above are a comparison between plasma on in red versus plasma off in green. Figure A.104 (a) is non-dimensionalized turbulent kinetic energy and panel (b) is the structural parameter a_1 . At this station, U_o is 459.6 m/s for the plasma off case and 459.1 m/s for the plasma on case. Figures A.104 (c) and (d) show the Reynolds shear stress and the correlation coefficient of Reynolds shear stress, respectively. The case identifiers for this comparison were 627cn-LINE2260 for plasma off and 627pn-LINE2260 for plasma on.

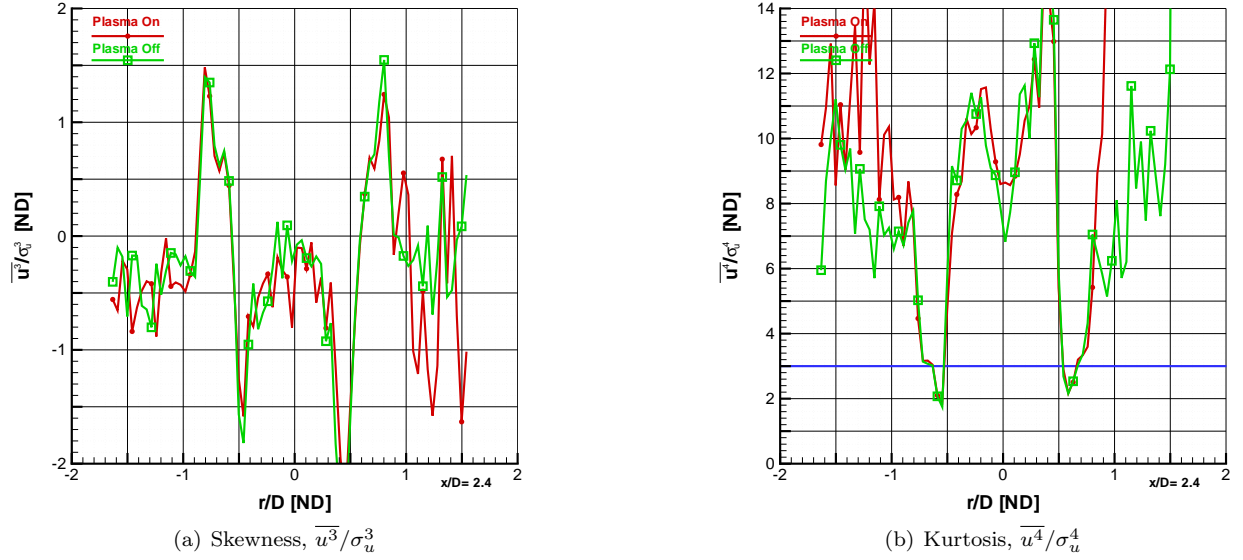
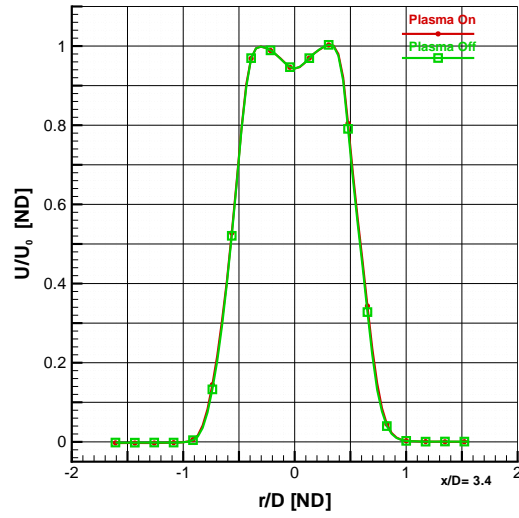
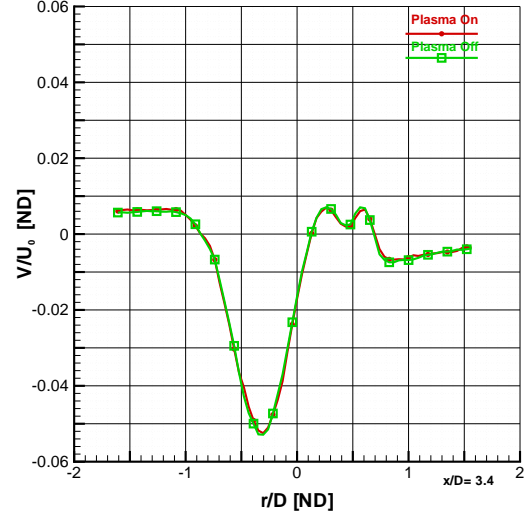


Figure A.105: Comparison of Plasma Effects on Skewness and Kurtosis: Case 627LINE2260

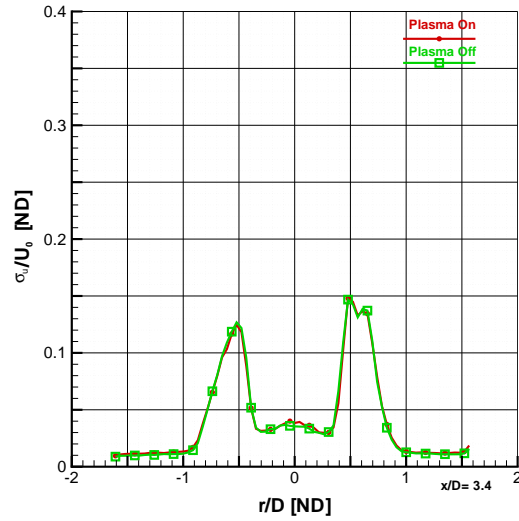
This is the final series of figures on the investigation into the effect of plasma on jet created by developing flow in a constant-diameter tube driven at a Mach 1.9 isentropic pressure ratio, 2.4 diameters from the anode face. The jet diameter is 9.5 mm. The two plots represented above are a comparison between plasma on in red versus plasma off in green. The plasma off case is placed on top of the plasma on case, therefore making it easier to notice small changes between the two cases. Figure A.105 (a) (b) are the measurements of skewness and kurtosis (or flatness), respectively. A Gaussian distribution has skewness of zero, which indicates a distribution of fluctuations is symmetric about the mean. Positive skewness represents a shift toward the right tail (positive fluctuations), while negative skewness is shifted toward negative fluctuations. A Gaussian distribution has kurtosis of three, represented by the blue line. Values lower than three represent a distribution of velocity with higher peakedness than a Gaussian distribution. Conversely, values above three represent flatter distributions. The case identifiers for this comparison were 627cn-LINE2260 for plasma off and 627pn-LINE2260 for plasma on.



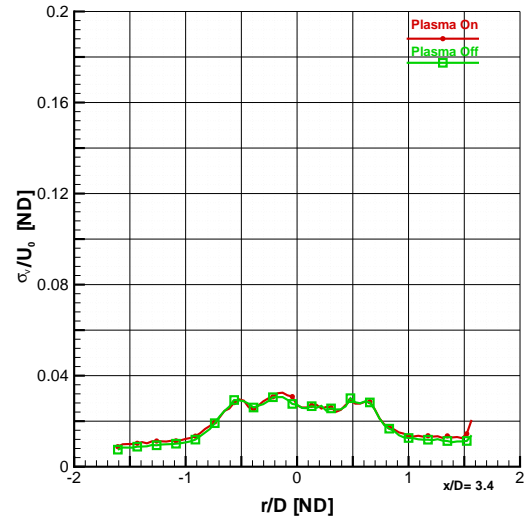
(a) Mean Axial Velocity, U/U_o



(b) Mean Tangential Velocity, V/U_o



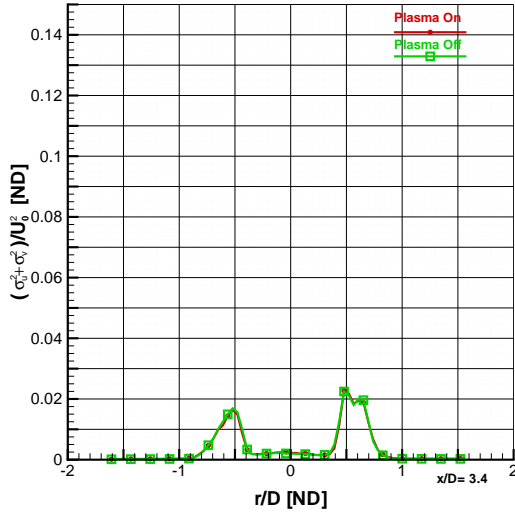
(c) Fluctuating Axial Velocity, σ_u/U_o



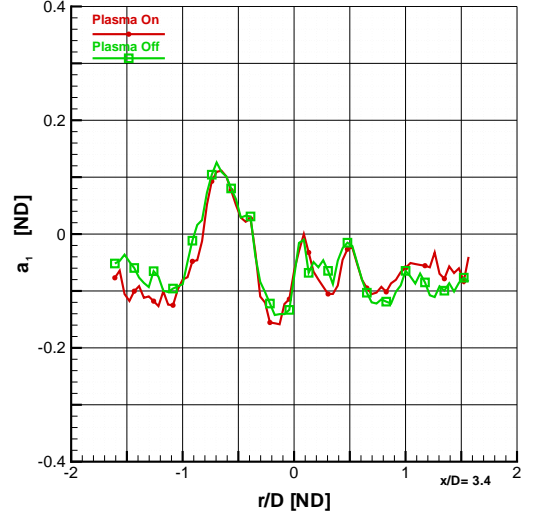
(d) Fluctuating Tangential Velocity, σ_v/U_o

Figure A.106: Comparison of Plasma Effects on Mean Velocity and Fluctuations: Case 627LINE3253

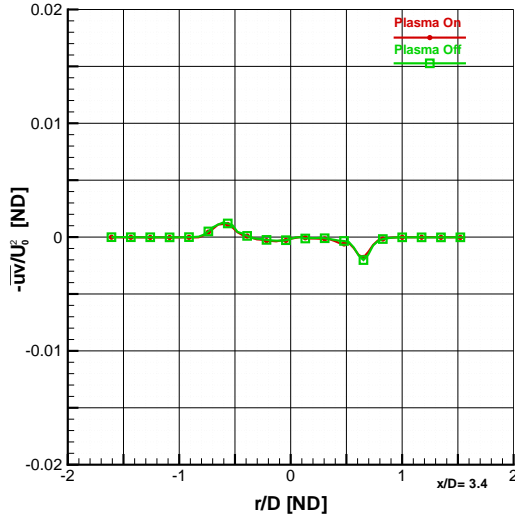
This is an investigation into the effect of plasma on jet created by developing flow in a constant-diameter tube driven at a Mach 1.9 isentropic pressure ratio, 3.4 diameters from the anode face. The jet diameter is 9.5 mm. The four plots represented above are a comparison between plasma on in red versus plasma off in green. Figure A.106 (a) is non-dimensionalized axial velocity. For these figures, U_o is 449.0 m/s for the plasma off case and 448.6 m/s for the plasma on case. Figure A.106 (b) is the mean tangential component of the velocity. Figures A.106 (c) and (d) show the Reynolds normal stresses in the axial and tangential directions, respectively. The case identifiers for this comparison were 627cn-LINE3253 for plasma off and 627pn-LINE3253 for plasma on.



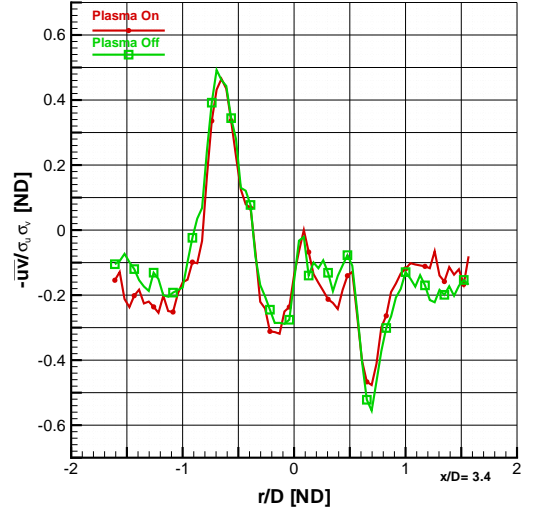
(a) Turbulent Kinetic Energy, $(\sigma_u^2 + \sigma_v^2)/U_o^2$



(b) Structural Parameter, $a_1 = -\overline{uv}/(\sigma_u^2 + \sigma_v^2)$



(c) Reynolds Shear Stress, \overline{uv}/U_o^2



(d) Correlation Coefficient of Reynolds Shear Stress, $-\overline{uv}/(\sigma_u \sigma_v)$

Figure A.107: Comparison of Plasma Effects on Second Moment Fluctuations: Case 627LINE3253

This is a continuing investigation into the effect of plasma on a Mach 1.9 isentropic pressure ratio, 3.4 diameters from the anode face. The jet diameter is 9.5 mm. The four plots represented above are a comparison between plasma on in red versus plasma off in green. Figure A.107 (a) is non-dimensionalized turbulent kinetic energy and panel (b) is the structural parameter a_1 . At this station, U_o is 449.0 m/s for the plasma off case and 448.6 m/s for the plasma on case. Figures A.107 (c) and (d) show the Reynolds shear stress and the correlation coefficient of Reynolds shear stress, respectively. The case identifiers for this comparison were 627cn-LINE3253 for plasma off and 627pn-LINE3253 for plasma on.

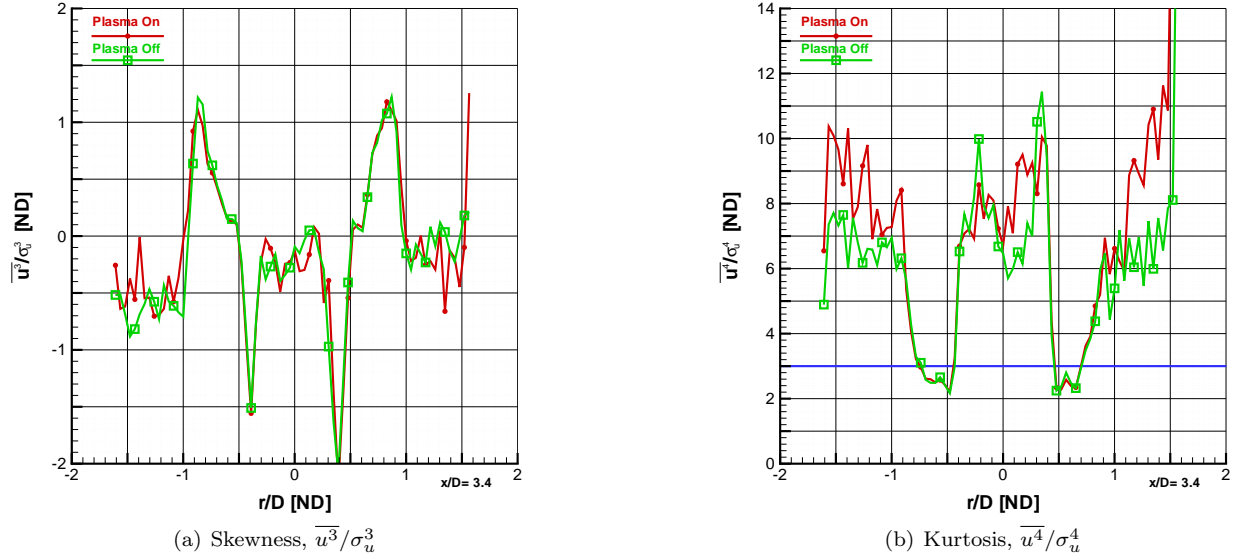
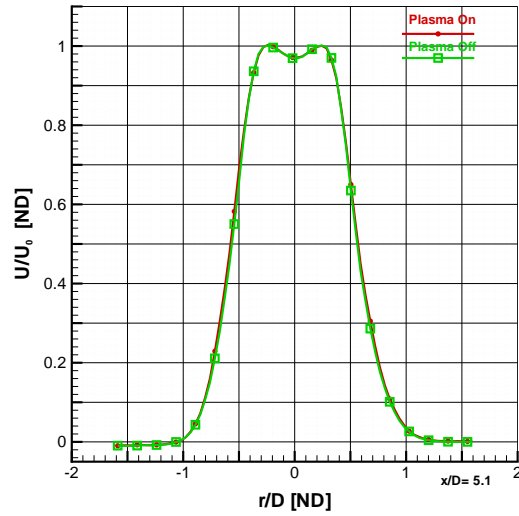
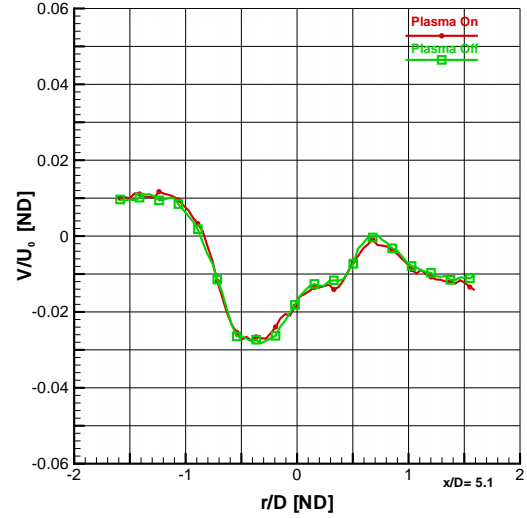


Figure A.108: Comparison of Plasma Effects on Skewness and Kurtosis: Case 627LINE3253

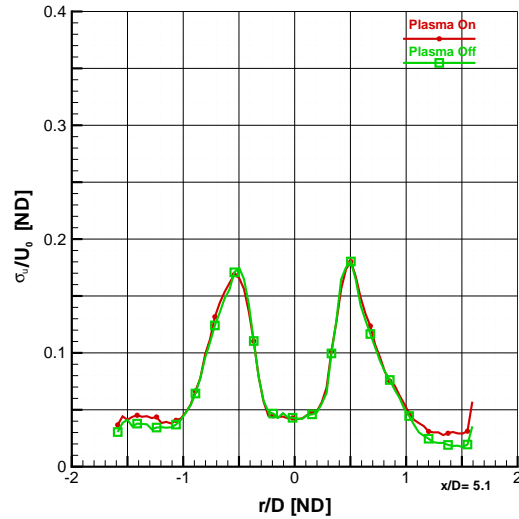
This is the final series of figures on the investigation into the effect of plasma on jet created by developing flow in a constant-diameter tube driven at a Mach 1.9 isentropic pressure ratio, 3.4 diameters from the anode face. The jet diameter is 9.5 mm. The two plots represented above are a comparison between plasma on in red versus plasma off in green. The plasma off case is placed on top of the plasma on case, therefore making it easier to notice small changes between the two cases. Figure A.108 (a) (b) are the measurements of skewness and kurtosis (or flatness), respectively. A Gaussian distribution has skewness of zero, which indicates a distribution of fluctuations is symmetric about the mean. Positive skewness represents a shift toward the right tail (positive fluctuations), while negative skewness is shifted toward negative fluctuations. A Gaussian distribution has kurtosis of three, represented by the blue line. Values lower than three represent a distribution of velocity with higher peakedness than a Gaussian distribution. Conversely, values above three represent flatter distributions. The case identifiers for this comparison were 627cn-LINE3253 for plasma off and 627pn-LINE3253 for plasma on.



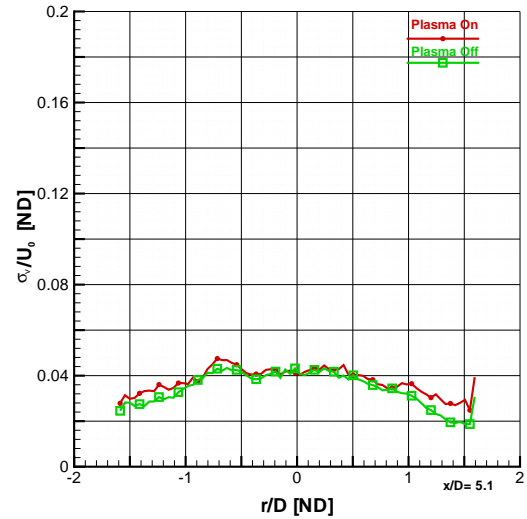
(a) Mean Axial Velocity, U/U_o



(b) Mean Tangential Velocity, V/U_o



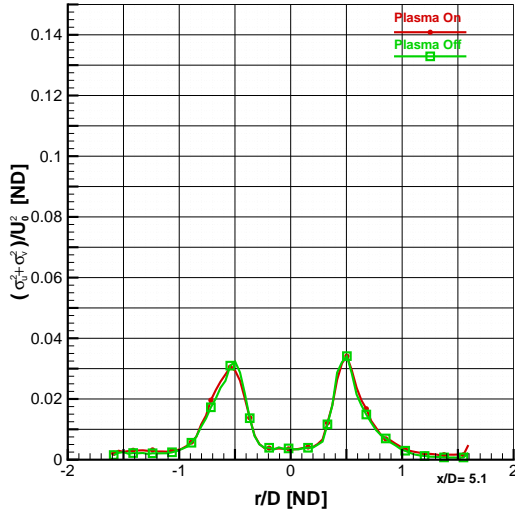
(c) Fluctuating Axial Velocity, σ_u/U_o



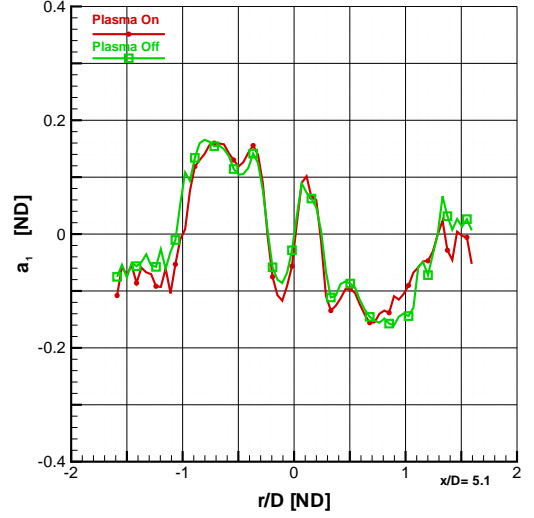
(d) Fluctuating Tangential Velocity, σ_v/U_o

Figure A.109: Comparison of Plasma Effects on Mean Velocity and Fluctuations: Case 620LINE4808

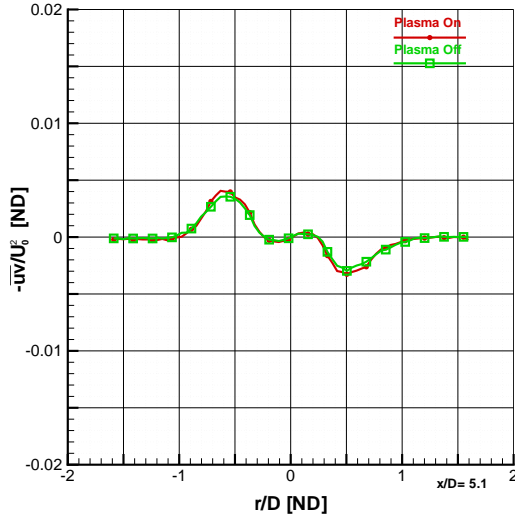
This is an investigation into the effect of plasma on jet created by developing flow in a constant-diameter tube driven at a Mach 1.9 isentropic pressure ratio, 5.1 diameters from the anode face. The jet diameter is 9.5 mm. The four plots represented above are a comparison between plasma on in red versus plasma off in green. Figure A.109 (a) is non-dimensionalized axial velocity. For these figures, U_o is 439.6 m/s for the plasma off case and 438.8 m/s for the plasma on case. Figure A.109 (b) is the mean tangential component of the velocity. Figures A.109 (c) and (d) show the Reynolds normal stresses in the axial and tangential directions, respectively. The case identifiers for this comparison were 620cn-LINE4808 for plasma off and 620pn-LINE4808 for plasma on.



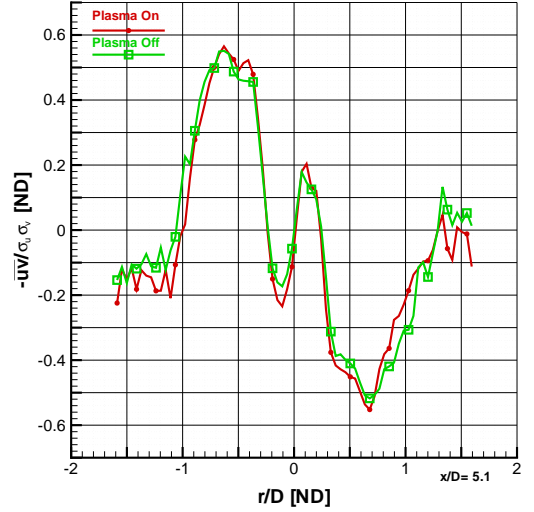
(a) Turbulent Kinetic Energy, $(\sigma_u^2 + \sigma_v^2)/U_o^2$



(b) Structural Parameter, $a_1 = -\overline{uv}/(\sigma_u^2 + \sigma_v^2)$



(c) Reynolds Shear Stress, \overline{uv}/U_o^2



(d) Correlation Coefficient of Reynolds Shear Stress, $-\overline{uv}/(\sigma_u \sigma_v)$

Figure A.110: Comparison of Plasma Effects on Second Moment Fluctuations: Case 620LINE4808

This is a continuing investigation into the effect of plasma on a Mach 1.9 isentropic pressure ratio, 5.1 diameters from the anode face. The jet diameter is 9.5 mm. The four plots represented above are a comparison between plasma on in red versus plasma off in green. Figure A.110 (a) is non-dimensionalized turbulent kinetic energy and panel (b) is the structural parameter a_1 . At this station, U_o is 439.6 m/s for the plasma off case and 438.8 m/s for the plasma on case. Figures A.110 (c) and (d) show the Reynolds shear stress and the correlation coefficient of Reynolds shear stress, respectively. The case identifiers for this comparison were 620cn-LINE4808 for plasma off and 620pn-LINE4808 for plasma on.

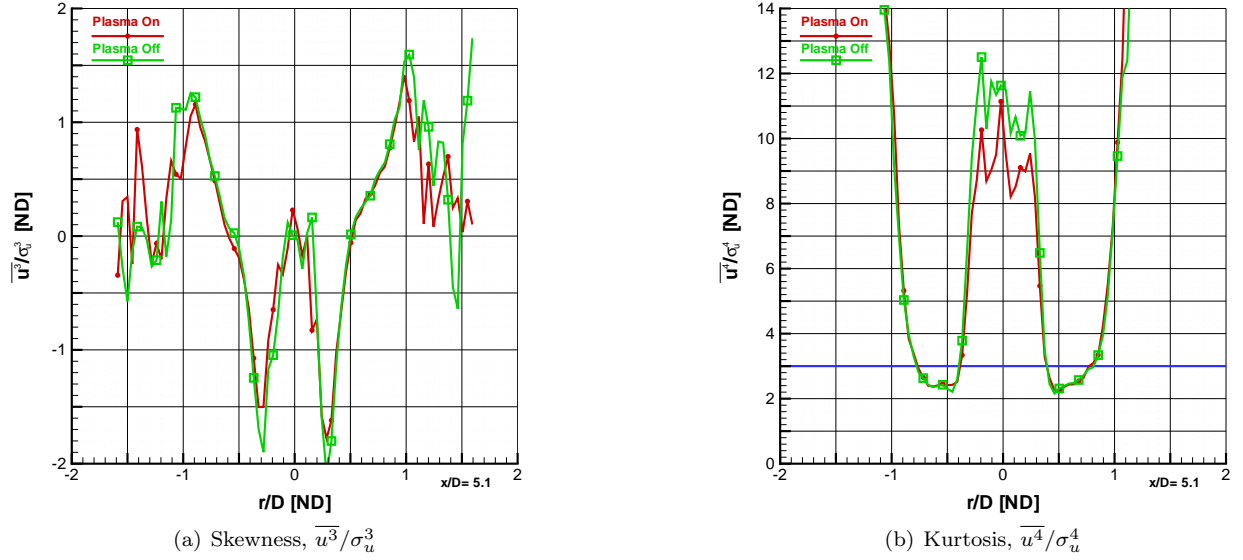
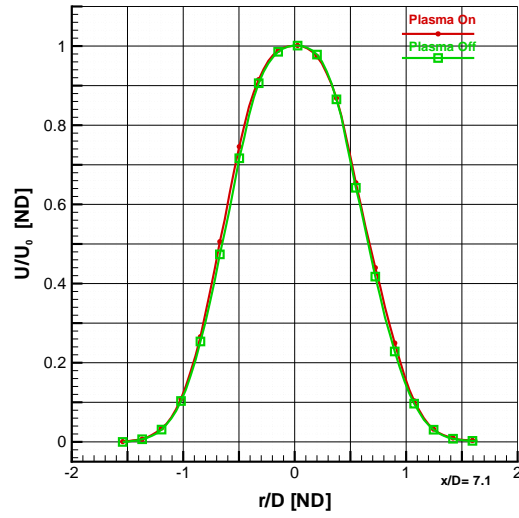
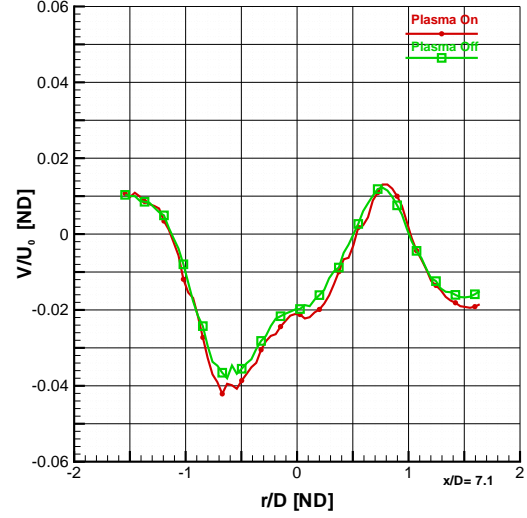


Figure A.111: Comparison of Plasma Effects on Skewness and Kurtosis: Case 620LINE4808

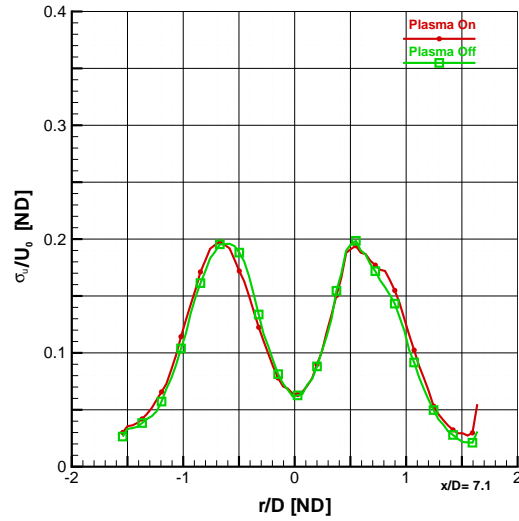
This is the final series of figures on the investigation into the effect of plasma on jet created by developing flow in a constant-diameter tube driven at a Mach 1.9 isentropic pressure ratio, 5.1 diameters from the anode face. The jet diameter is 9.5 mm. The two plots represented above are a comparison between plasma on in red versus plasma off in green. The plasma off case is placed on top of the plasma on case, therefore making it easier to notice small changes between the two cases. Figure A.111 (a) (b) are the measurements of skewness and kurtosis (or flatness), respectively. A Gaussian distribution has skewness of zero, which indicates a distribution of fluctuations is symmetric about the mean. Positive skewness represents a shift toward the right tail (positive fluctuations), while negative skewness is shifted toward negative fluctuations. A Gaussian distribution has kurtosis of three, represented by the blue line. Values lower than three represent a distribution of velocity with higher peakedness than a Gaussian distribution. Conversely, values above three represent flatter distributions. The case identifiers for this comparison were 620cn-LINE4808 for plasma off and 620pn-LINE4808 for plasma on.



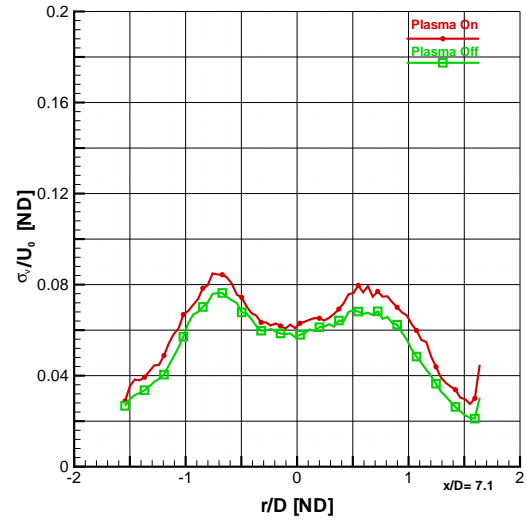
(a) Mean Axial Velocity, U/U_o



(b) Mean Tangential Velocity, V/U_o



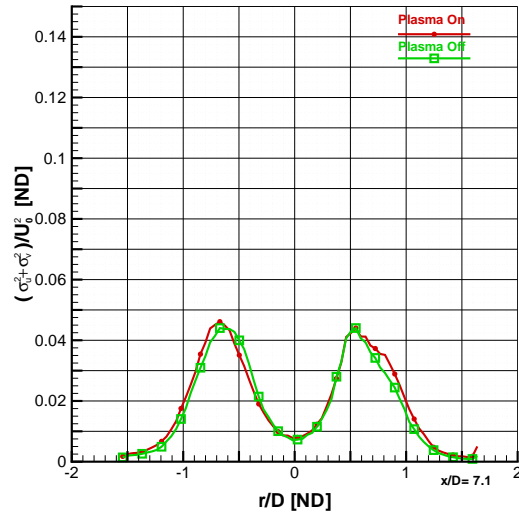
(c) Fluctuating Axial Velocity, σ_u/U_o



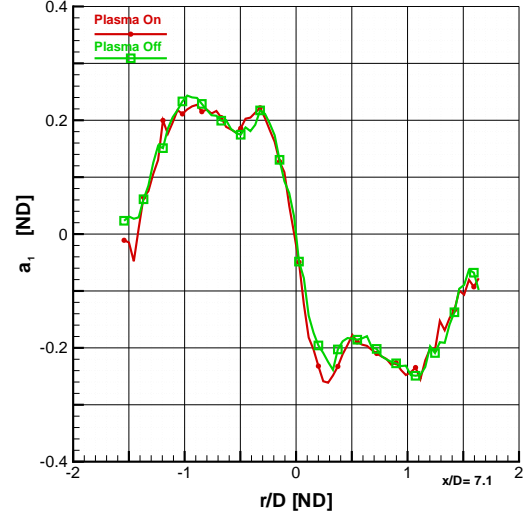
(d) Fluctuating Tangential Velocity, σ_v/U_o

Figure A.112: Comparison of Plasma Effects on Mean Velocity and Fluctuations: Case 620LINE6799

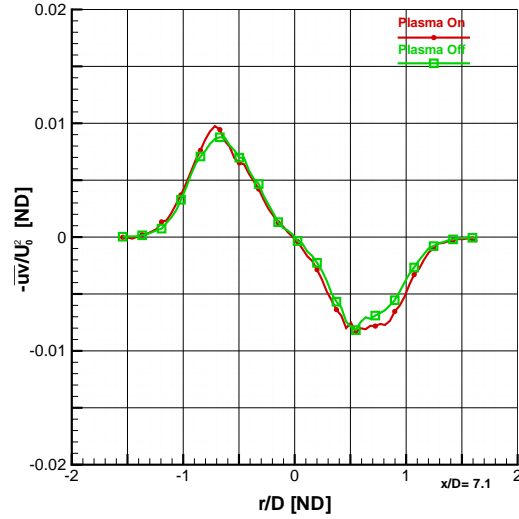
This is an investigation into the effect of plasma on jet created by developing flow in a constant-diameter tube driven at a Mach 1.9 isentropic pressure ratio, 7.1 diameters from the anode face. The jet diameter is 9.5 mm. The four plots represented above are a comparison between plasma on in red versus plasma off in green. Figure A.112 (a) is non-dimensionalized axial velocity. For these figures, U_o is 444.5 m/s for the plasma off case and 444.4 m/s for the plasma on case. Figure A.112 (b) is the mean tangential component of the velocity. Figures A.112 (c) and (d) show the Reynolds normal stresses in the axial and tangential directions, respectively. The case identifiers for this comparison were 620cn-LINE6799 for plasma off and 620pn-LINE6799 for plasma on.



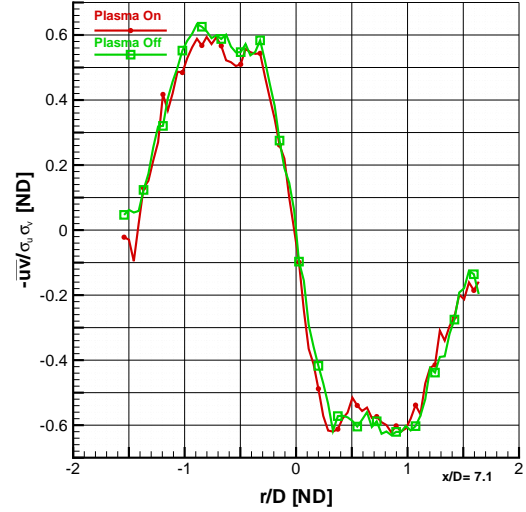
(a) Turbulent Kinetic Energy, $(\sigma_u^2 + \sigma_v^2)/U_o^2$



(b) Structural Parameter, $a_1 = -\overline{uv}/(\sigma_u^2 + \sigma_v^2)$



(c) Reynolds Shear Stress, \overline{uv}/U_o^2



(d) Correlation Coefficient of Reynolds Shear Stress, $-\overline{uv}/(\sigma_u \sigma_v)$

Figure A.113: Comparison of Plasma Effects on Second Moment Fluctuations: Case 620LINE6799

This is a continuing investigation into the effect of plasma on a Mach 1.9 isentropic pressure ratio, 7.1 diameters from the anode face. The jet diameter is 9.5 mm. The four plots represented above are a comparison between plasma on in red versus plasma off in green. Figure A.113 (a) is non-dimensionalized turbulent kinetic energy and panel (b) is the structural parameter a_1 . At this station, U_o is 444.5 m/s for the plasma off case and 444.4 m/s for the plasma on case. Figures A.113 (c) and (d) show the Reynolds shear stress and the correlation coefficient of Reynolds shear stress, respectively. The case identifiers for this comparison were 620cn-LINE6799 for plasma off and 620pn-LINE6799 for plasma on.

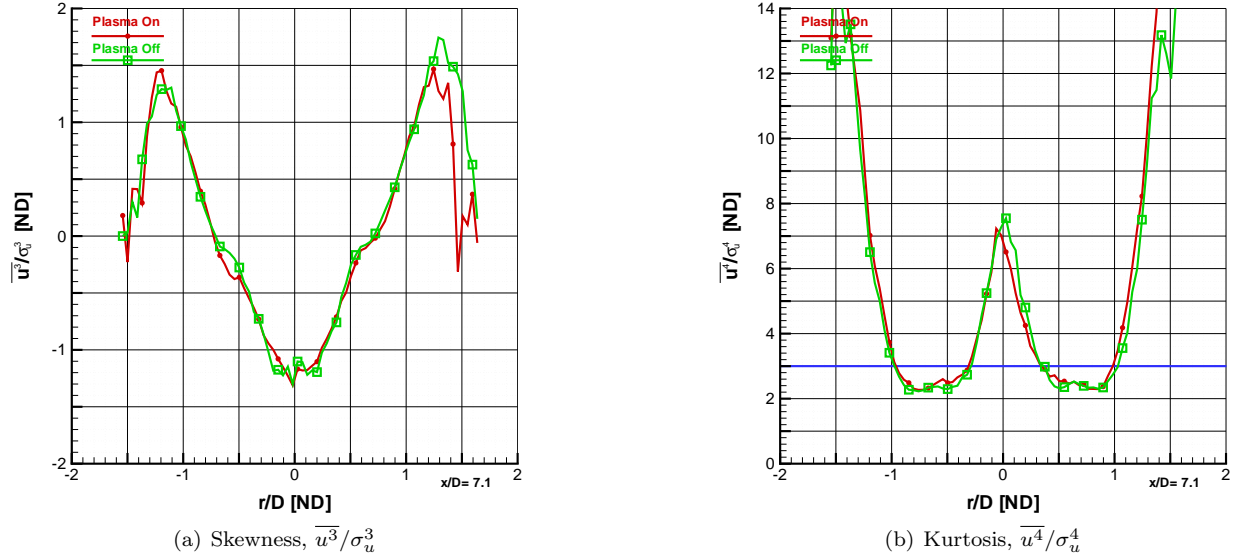
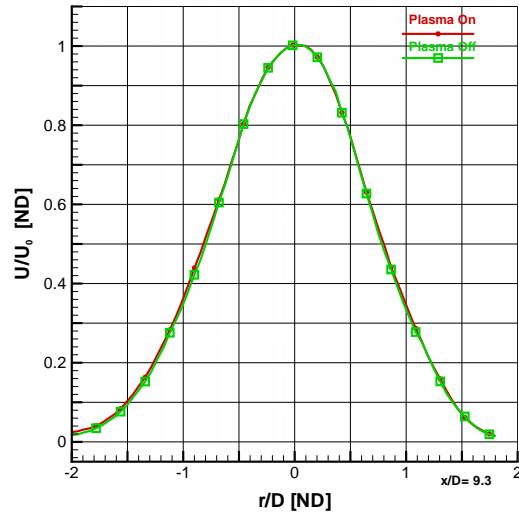
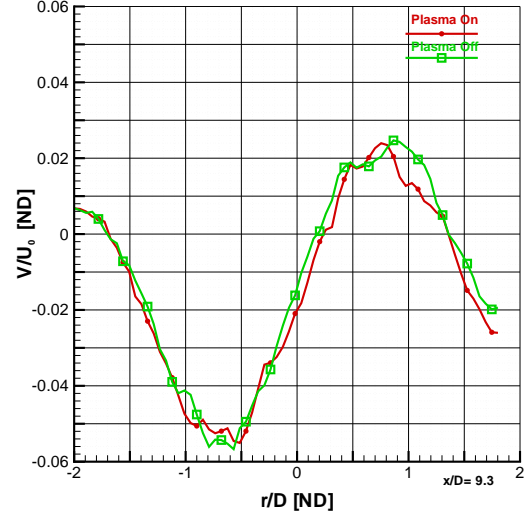


Figure A.114: Comparison of Plasma Effects on Skewness and Kurtosis: Case 620LINE6799

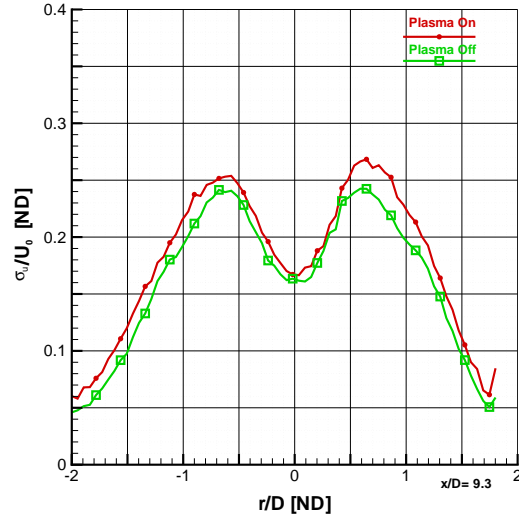
This is the final series of figures on the investigation into the effect of plasma on jet created by developing flow in a constant-diameter tube driven at a Mach 1.9 isentropic pressure ratio, 7.1 diameters from the anode face. The jet diameter is 9.5 mm. The two plots represented above are a comparison between plasma on in red versus plasma off in green. The plasma off case is placed on top of the plasma on case, therefore making it easier to notice small changes between the two cases. Figure A.114 (a) (b) are the measurements of skewness and kurtosis (or flatness), respectively. A Gaussian distribution has skewness of zero, which indicates a distribution of fluctuations is symmetric about the mean. Positive skewness represents a shift toward the right tail (positive fluctuations), while negative skewness is shifted toward negative fluctuations. A Gaussian distribution has kurtosis of three, represented by the blue line. Values lower than three represent a distribution of velocity with higher peakedness than a Gaussian distribution. Conversely, values above three represent flatter distributions. The case identifiers for this comparison were 620cn-LINE6799 for plasma off and 620pn-LINE6799 for plasma on.



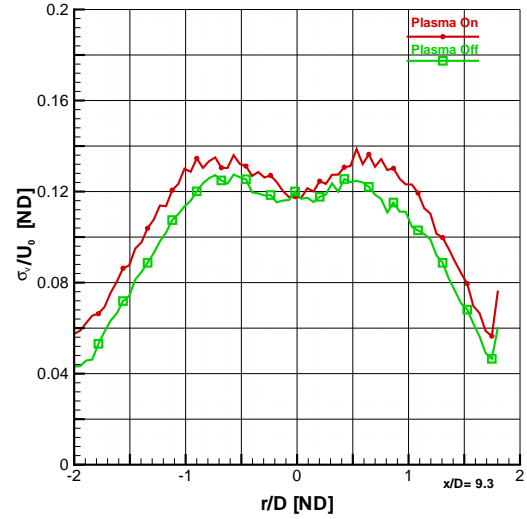
(a) Mean Axial Velocity, U/U_o



(b) Mean Tangential Velocity, V/U_o



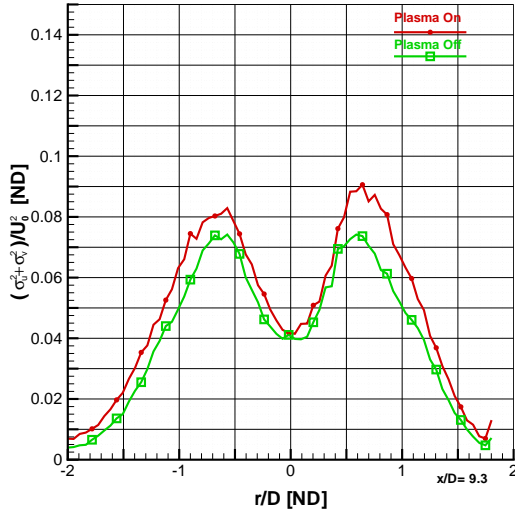
(c) Fluctuating Axial Velocity, σ_u/U_o



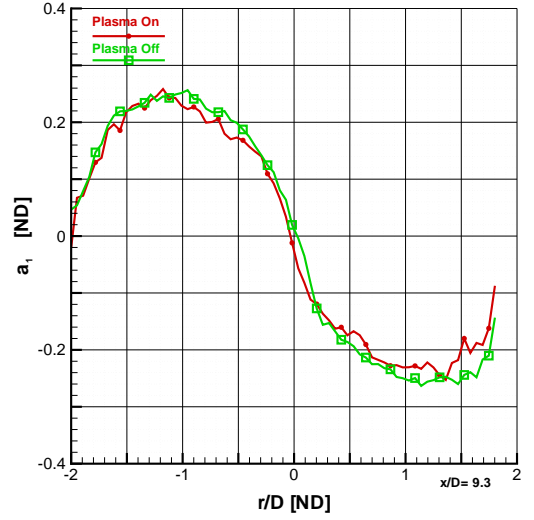
(d) Fluctuating Tangential Velocity, σ_v/U_o

Figure A.115: Comparison of Plasma Effects on Mean Velocity and Fluctuations: Case 616LINE8814

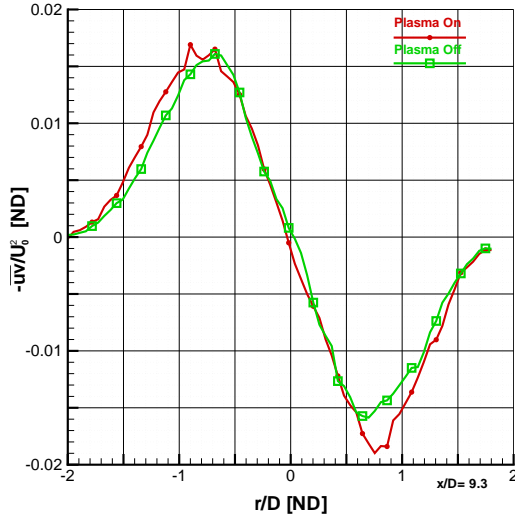
This is an investigation into the effect of plasma on jet created by developing flow in a constant-diameter tube driven at a Mach 1.9 isentropic pressure ratio, 9.3 diameters from the anode face. The jet diameter is 9.5 mm. The four plots represented above are a comparison between plasma on in red versus plasma off in green. Figure A.115 (a) is non-dimensionalized axial velocity. For these figures, U_o is 387.2 m/s for the plasma off case and 385.9 m/s for the plasma on case. Figure A.115 (b) is the mean tangential component of the velocity. Figures A.115 (c) and (d) show the Reynolds normal stresses in the axial and tangential directions, respectively. The case identifiers for this comparison were 616cnc-LINE8814 for plasma off and 616pnc-LINE8814 for plasma on.



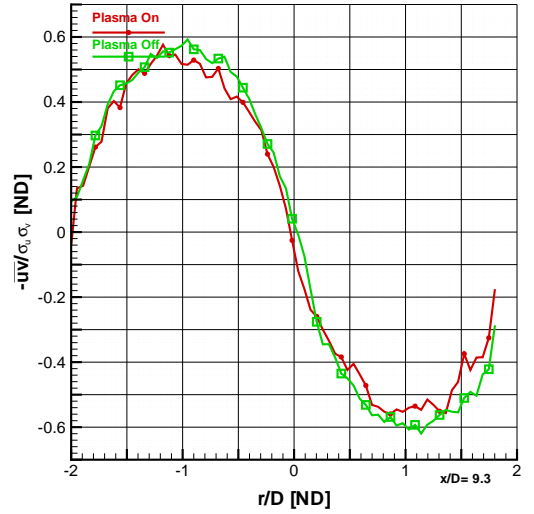
(a) Turbulent Kinetic Energy, $(\sigma_u^2 + \sigma_v^2)/U_o^2$



(b) Structural Parameter, $a_1 = -\overline{uv}/(\sigma_u^2 + \sigma_v^2)$



(c) Reynolds Shear Stress, \overline{uv}/U_o^2



(d) Correlation Coefficient of Reynolds Shear Stress, $-\overline{uv}/(\sigma_u \sigma_v)$

Figure A.116: Comparison of Plasma Effects on Second Moment Fluctuations: Case 616LINE8814

This is a continuing investigation into the effect of plasma on a Mach 1.9 isentropic pressure ratio, 9.3 diameters from the anode face. The jet diameter is 9.5 mm. The four plots represented above are a comparison between plasma on in red versus plasma off in green. Figure A.116 (a) is non-dimensionalized turbulent kinetic energy and panel (b) is the structural parameter a_1 . At this station, U_o is 387.2 m/s for the plasma off case and 385.9 m/s for the plasma on case. Figures A.116 (c) and (d) show the Reynolds shear stress and the correlation coefficient of Reynolds shear stress, respectively. The case identifiers for this comparison were 616cnc-LINE8814 for plasma off and 616pnc-LINE8814 for plasma on.

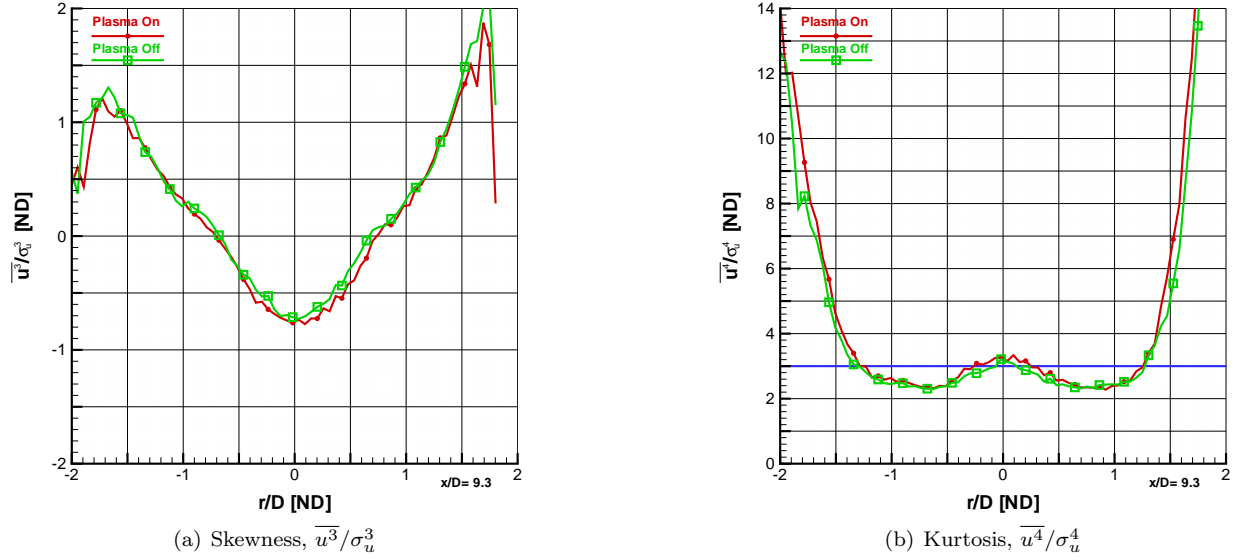
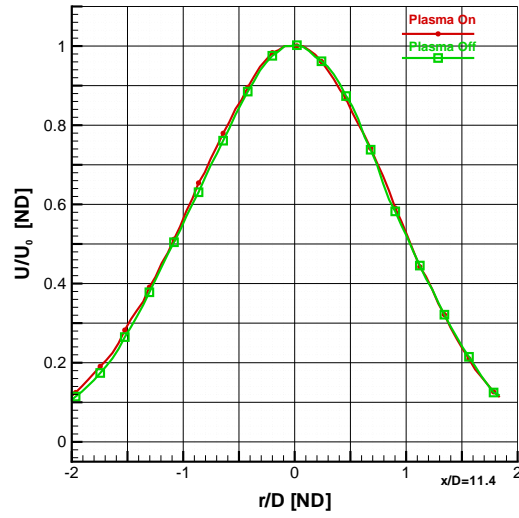
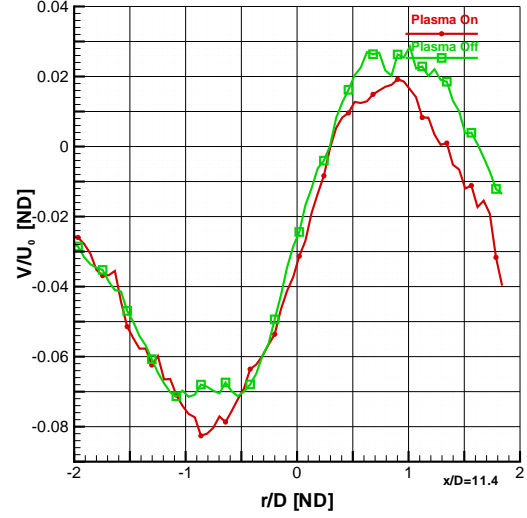


Figure A.117: Comparison of Plasma Effects on Skewness and Kurtosis: Case 616LINE8814

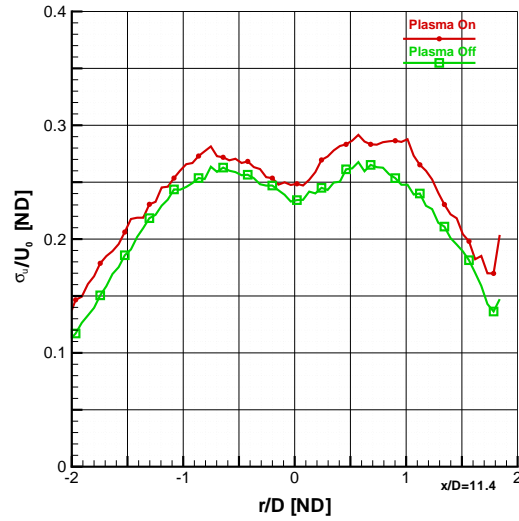
This is the final series of figures on the investigation into the effect of plasma on jet created by developing flow in a constant-diameter tube driven at a Mach 1.9 isentropic pressure ratio, 9.3 diameters from the anode face. The jet diameter is 9.5 mm. The two plots represented above are a comparison between plasma on in red versus plasma off in green. The plasma off case is placed on top of the plasma on case, therefore making it easier to notice small changes between the two cases. Figure A.117 (a) (b) are the measurements of skewness and kurtosis (or flatness), respectively. A Gaussian distribution has skewness of zero, which indicates a distribution of fluctuations is symmetric about the mean. Positive skewness represents a shift toward the right tail (positive fluctuations), while negative skewness is shifted toward negative fluctuations. A Gaussian distribution has kurtosis of three, represented by the blue line. Values lower than three represent a distribution of velocity with higher peakedness than a Gaussian distribution. Conversely, values above three represent flatter distributions. The case identifiers for this comparison were 616cnc-LINE8814 for plasma off and 616pnc-LINE8814 for plasma on.



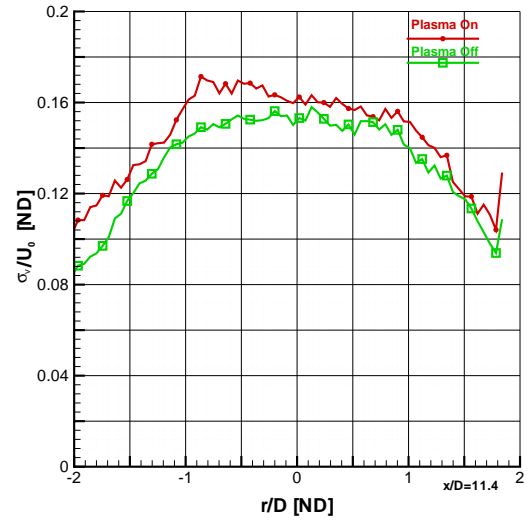
(a) Mean Axial Velocity, U/U_o



(b) Mean Tangential Velocity, V/U_o



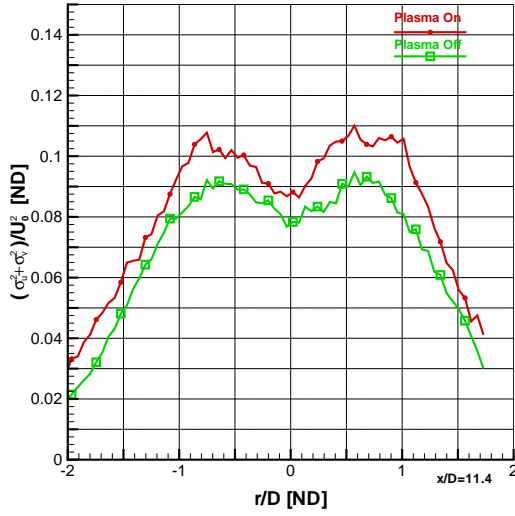
(c) Fluctuating Axial Velocity, σ_u/U_o



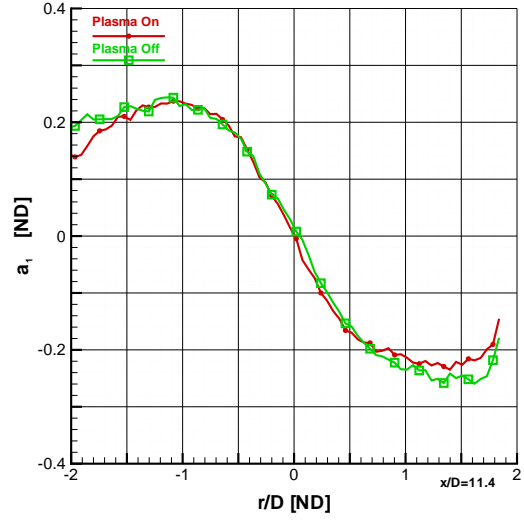
(d) Fluctuating Tangential Velocity, σ_v/U_o

Figure A.118: Comparison of Plasma Effects on Mean Velocity and Fluctuations: Case 616LINE10809

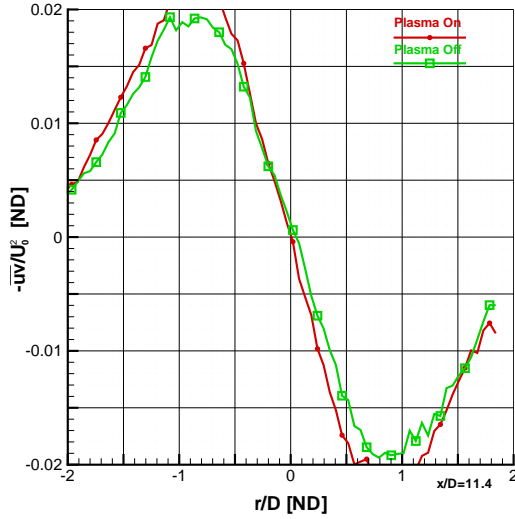
This is an investigation into the effect of plasma on jet created by developing flow in a constant-diameter tube driven at a Mach 1.9 isentropic pressure ratio, 11.4 diameters from the anode face. The jet diameter is 9.5 mm. The four plots represented above are a comparison between plasma on in red versus plasma off in green. Figure A.118 (a) is non-dimensionalized axial velocity. For these figures, U_o is 314.9 m/s for the plasma off case and 313.2 m/s for the plasma on case. Figure A.118 (b) is the mean tangential component of the velocity. Figures A.118 (c) and (d) show the Reynolds normal stresses in the axial and tangential directions, respectively. The case identifiers for this comparison were 616cnc-LINE10809 for plasma off and 616pnc-LINE10809 for plasma on.



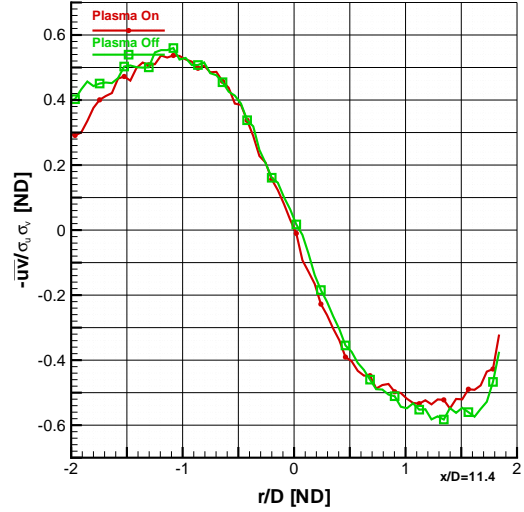
(a) Turbulent Kinetic Energy, $(\sigma_u^2 + \sigma_v^2)/U_o^2$



(b) Structural Parameter, $a_1 = -\overline{uv}/(\sigma_u^2 + \sigma_v^2)$



(c) Reynolds Shear Stress, \overline{uv}/U_o^2



(d) Correlation Coefficient of Reynolds Shear Stress, $-\overline{uv}/(\sigma_u \sigma_v)$

Figure A.119: Comparison of Plasma Effects on Second Moment Fluctuations: Case 616LINE10809

This is a continuing investigation into the effect of plasma on a Mach 1.9 isentropic pressure ratio, 11.4 diameters from the anode face. The jet diameter is 9.5 mm. The four plots represented above are a comparison between plasma on in red versus plasma off in green. Figure A.119 (a) is non-dimensionalized turbulent kinetic energy and panel (b) is the structural parameter a_1 . At this station, U_o is 314.9 m/s for the plasma off case and 313.2 m/s for the plasma on case. Figures A.119 (c) and (d) show the Reynolds shear stress and the correlation coefficient of Reynolds shear stress, respectively. The case identifiers for this comparison were 616cnc-LINE10809 for plasma off and 616pnc-LINE10809 for plasma on.

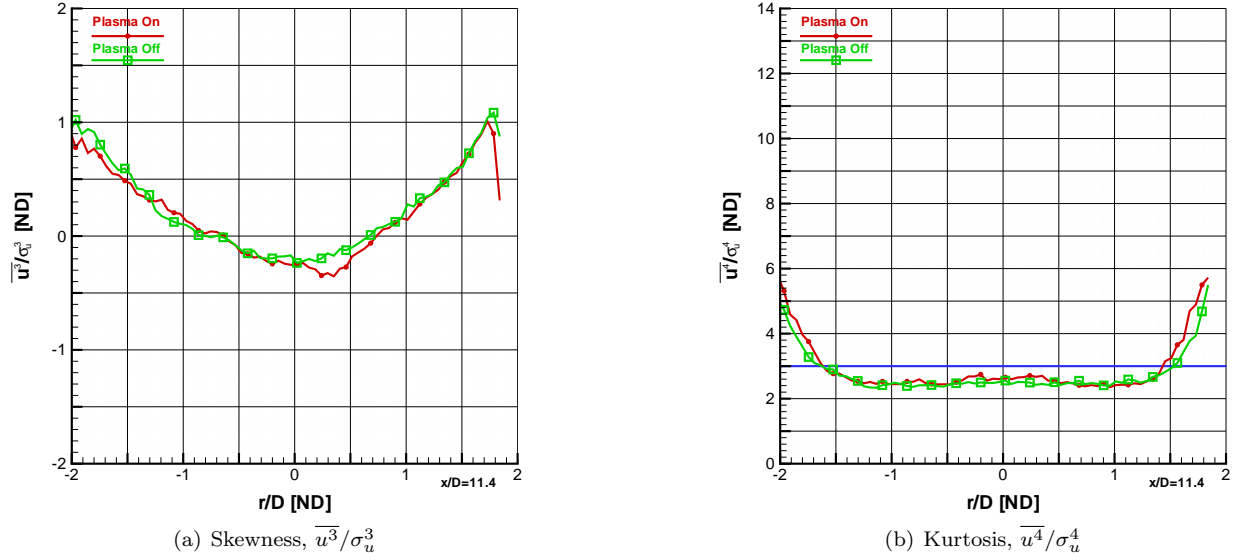


Figure A.120: Comparison of Plasma Effects on Skewness and Kurtosis: Case 616LINE10809

This is the final series of figures on the investigation into the effect of plasma on jet created by developing flow in a constant-diameter tube driven at a Mach 1.9 isentropic pressure ratio, 11.4 diameters from the anode face. The jet diameter is 9.5 mm. The two plots represented above are a comparison between plasma on in red versus plasma off in green. The plasma off case is placed on top of the plasma on case, therefore making it easier to notice small changes between the two cases. Figure A.120 (a) (b) are the measurements of skewness and kurtosis (or flatness), respectively. A Gaussian distribution has skewness of zero, which indicates a distribution of fluctuations is symmetric about the mean. Positive skewness represents a shift toward the right tail (positive fluctuations), while negative skewness is shifted toward negative fluctuations. A Gaussian distribution has kurtosis of three, represented by the blue line. Values lower than three represent a distribution of velocity with higher peakedness than a Gaussian distribution. Conversely, values above three represent flatter distributions. The case identifiers for this comparison were 616cnc-LINE10809 for plasma off and 616pnc-LINE10809 for plasma on.

A.9 Mach 1.1 Converging-Diverging Nozzle at 9 Torr Using Anode with Serrated Conical Feature

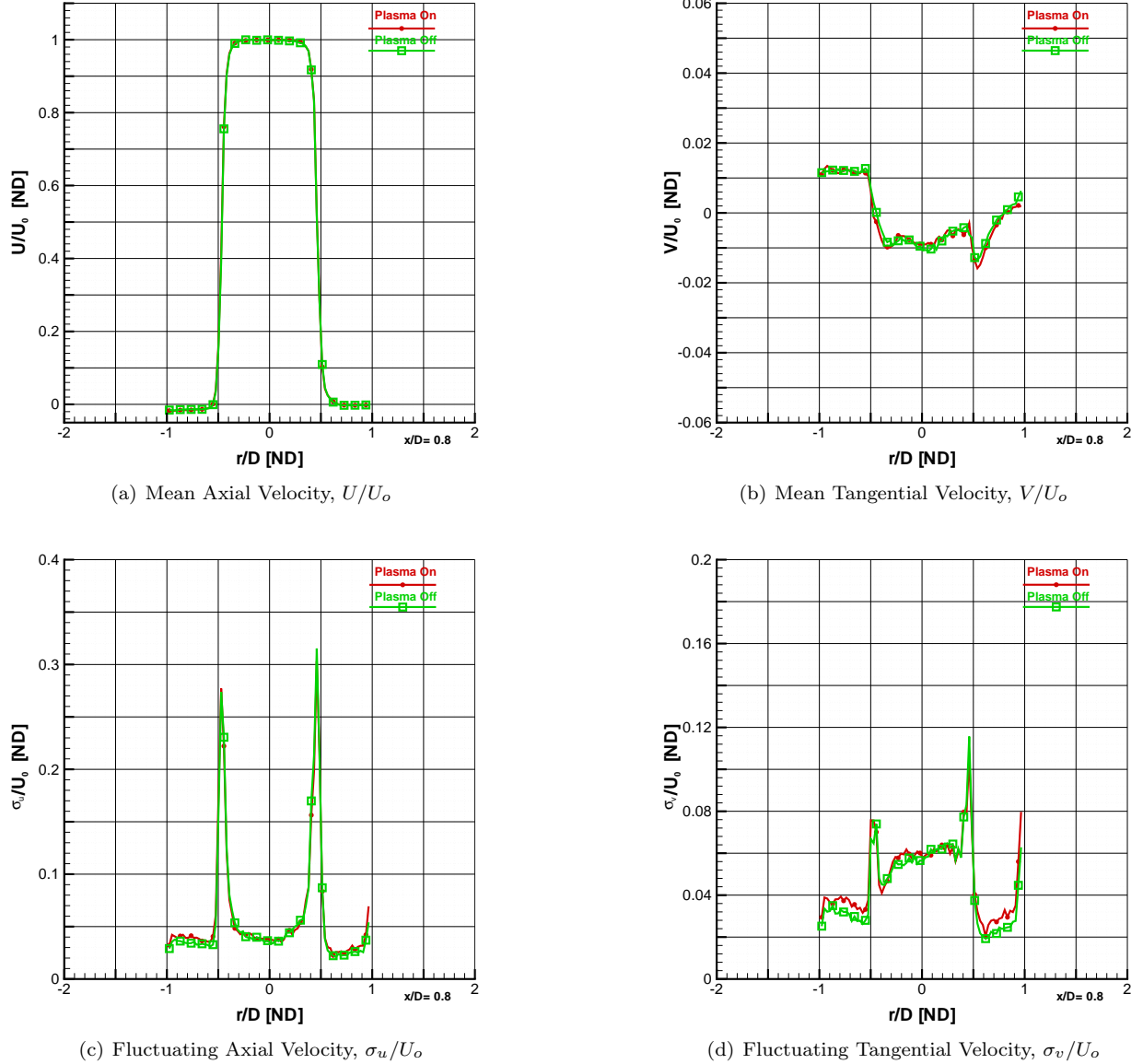
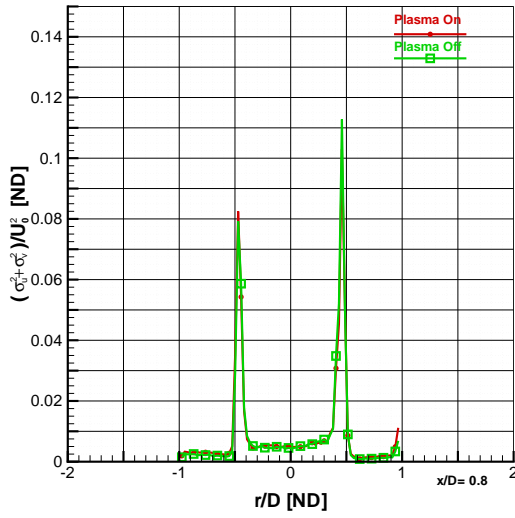
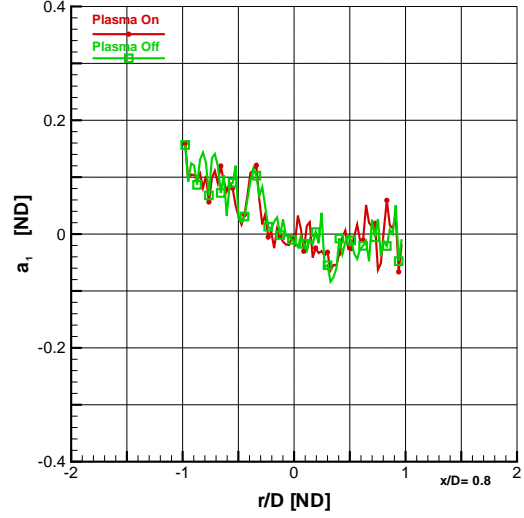


Figure A.121: Comparison of Plasma Effects on Mean Velocity and Fluctuations: Case 614LINE1331

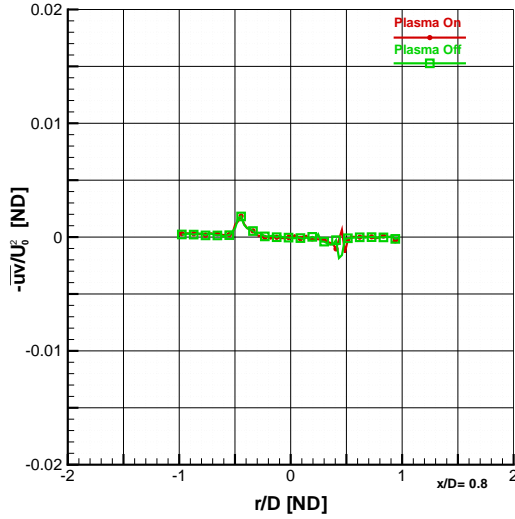
This is an investigation into the effect of plasma on a Mach 1.1 jet, 0.8 diameters from the anode face. The jet diameter is 15.7 mm. The four plots represented above are a comparison between plasma on in red versus plasma off in green. Figure A.121 (a) is non-dimensionalized axial velocity. For these figures, U_o is 347.1 m/s for the plasma off case and 347.0 m/s for the plasma on case. Figure A.121 (b) is the mean tangential component of the velocity. Figures A.121 (c) and (d) show the Reynolds normal stresses.



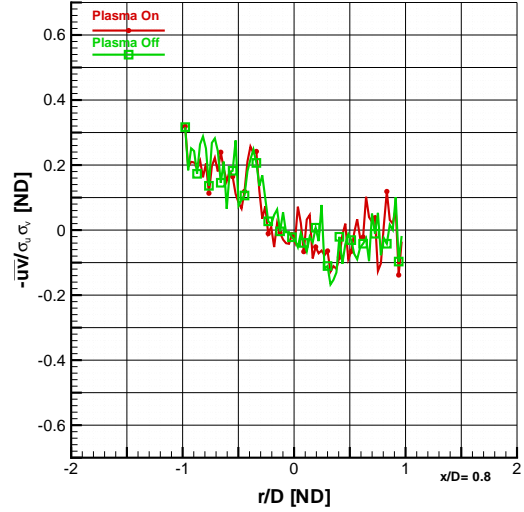
(a) Turbulent Kinetic Energy, $(\sigma_u^2 + \sigma_v^2)/U_o^2$



(b) Structural Parameter, $a_1 = -\overline{uv}/(\sigma_u^2 + \sigma_v^2)$



(c) Reynolds Shear Stress, \overline{uv}/U_o^2



(d) Correlation Coefficient of Reynolds Shear Stress, $-\overline{uv}/(\sigma_u \sigma_v)$

Figure A.122: Comparison of Plasma Effects on Second Moment Fluctuations: Case 614LINE1331

This is a continuing investigation into the effect of plasma on a Mach 1.1 jet, 0.8 diameters from the anode face. The jet diameter is 15.7 mm. The four plots represented above are a comparison between plasma on in red versus plasma off in green. Figure A.122 (a) is non-dimensionalized turbulent kinetic energy and panel (b) is the structural parameter a_1 . At this station, U_o is 347.1 m/s for the plasma off case and 347.0 m/s for the plasma on case. Figures A.122 (c) and (d) show the Reynolds shear stress and the correlation coefficient of Reynolds shear stress, respectively. The case identifiers for this comparison were 614cn-LINE1331 for plasma off and 614pn-LINE1331 for plasma on.

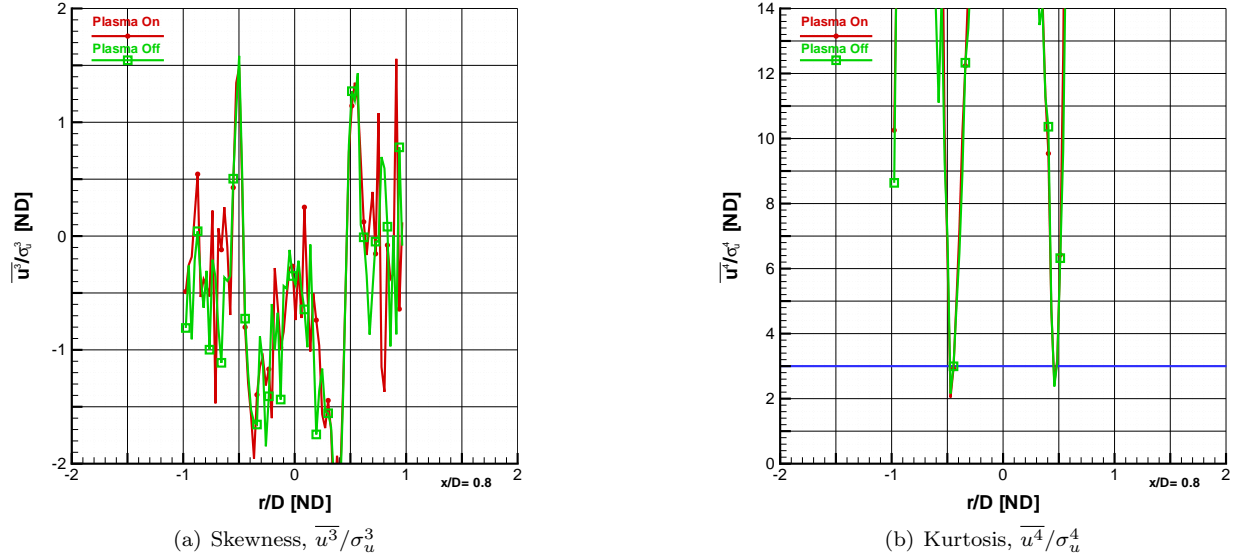
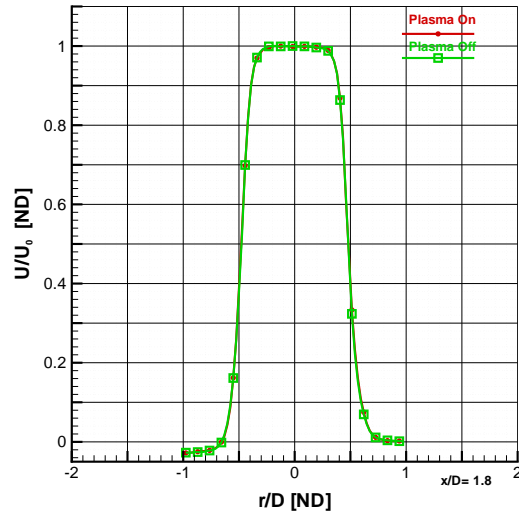
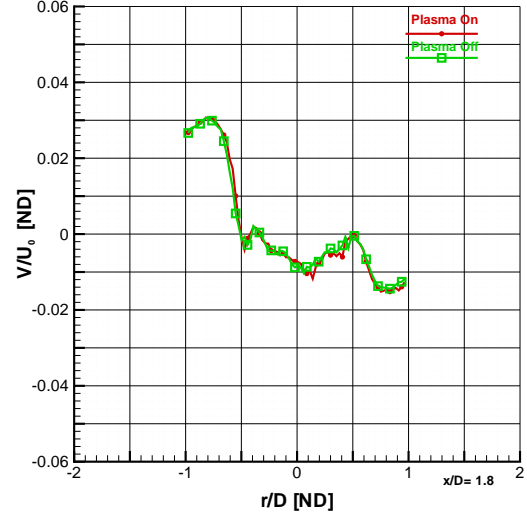


Figure A.123: Comparison of Plasma Effects on Skewness and Kurtosis: Case 614LINE1331

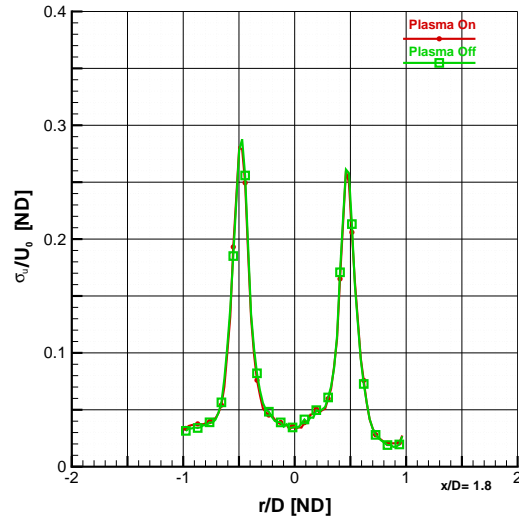
This is the final series of figures on the investigation into the effect of plasma on a Mach 1.1 jet, 0.8 diameters from the anode face. The jet diameter is 15.7 mm. The two plots represented above are a comparison between plasma on in red versus plasma off in green. The plasma off case is placed on top of the plasma on case, therefore making it easier to notice small changes between the two cases. Figure A.123 (a) (b) are the measurements of skewness and kurtosis (or flatness), respectively. A Gaussian distribution has skewness of zero, which indicates a distribution of fluctuations is symmetric about the mean. Positive skewness represents a shift toward the right tail (positive fluctuations), while negative skewness is shifted toward negative fluctuations. A Gaussian distribution has kurtosis of three, represented by the blue line. Values lower than three represent a distribution of velocity with higher peakedness than a Gaussian distribution. Conversely, values above three represent flatter distributions. The case identifiers for this comparison were 614cn-LINE1331 for plasma off and 614pn-LINE1331 for plasma on.



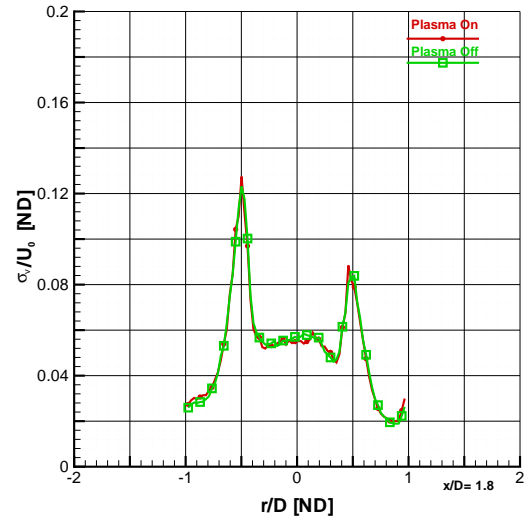
(a) Mean Axial Velocity, U/U_o



(b) Mean Tangential Velocity, V/U_o



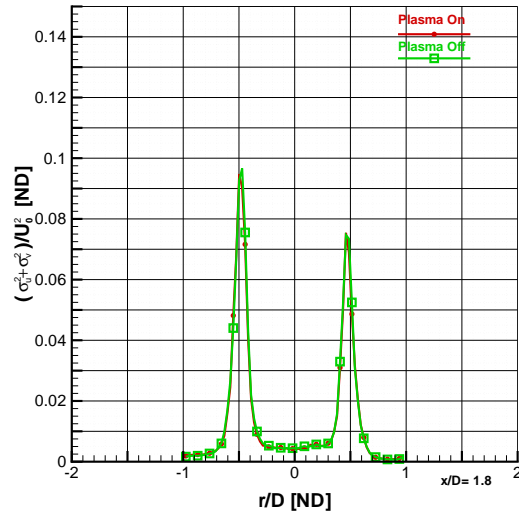
(c) Fluctuating Axial Velocity, σ_u/U_o



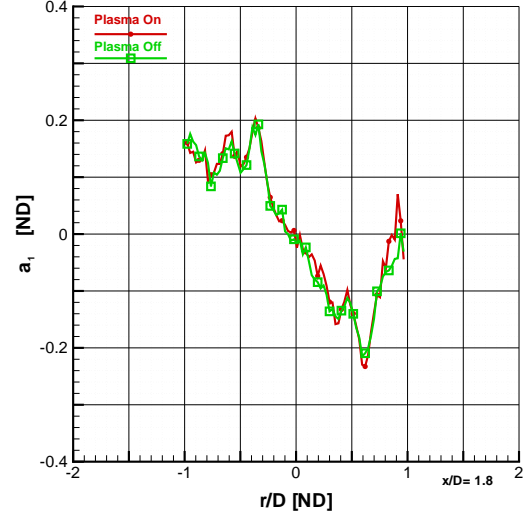
(d) Fluctuating Tangential Velocity, σ_v/U_o

Figure A.124: Comparison of Plasma Effects on Mean Velocity and Fluctuations: Case 614LINE2831

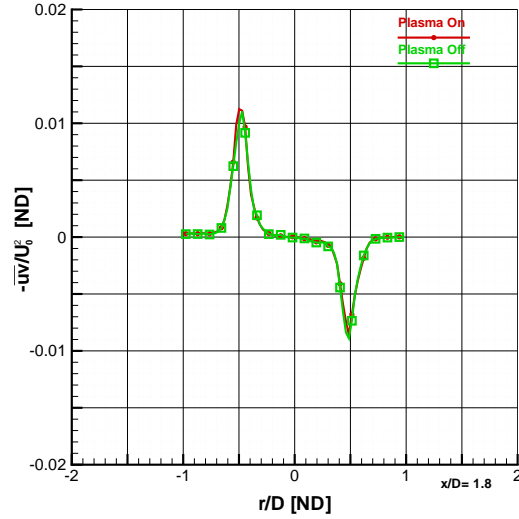
This is an investigation into the effect of plasma on a Mach 1.1 jet, 1.8 diameters from the anode face. The jet diameter is 15.7 mm. The four plots represented above are a comparison between plasma on in red versus plasma off in green. Figure A.124 (a) is non-dimensionalized axial velocity. For these figures, U_o is 346.1 m/s for the plasma off case and 345.8 m/s for the plasma on case. Figure A.124 (b) is the mean tangential component of the velocity. Figures A.124 (c) and (d) show the Reynolds normal stresses in the axial and tangential directions, respectively. The case identifiers for this comparison were 614cn-LINE2831 for plasma off and 614pn-LINE2831 for plasma on.



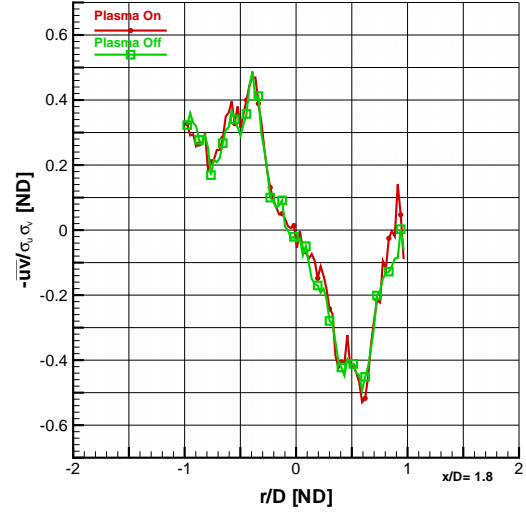
(a) Turbulent Kinetic Energy, $(\sigma_u^2 + \sigma_v^2)/U_o^2$



(b) Structural Parameter, $a_1 = -\overline{uv}/(\sigma_u^2 + \sigma_v^2)$



(c) Reynolds Shear Stress, \overline{uv}/U_o^2



(d) Correlation Coefficient of Reynolds Shear Stress, $-\overline{uv}/(\sigma_u \sigma_v)$

Figure A.125: Comparison of Plasma Effects on Second Moment Fluctuations: Case 614LINE2831

This is a continuing investigation into the effect of plasma on a Mach 1.1 jet, 1.8 diameters from the anode face. The jet diameter is 15.7 mm. The four plots represented above are a comparison between plasma on in red versus plasma off in green. Figure A.125 (a) is non-dimensionalized turbulent kinetic energy and panel (b) is the structural parameter a_1 . At this station, U_o is 346.1 m/s for the plasma off case and 345.8 m/s for the plasma on case. Figures A.125 (c) and (d) show the Reynolds shear stress and the correlation coefficient of Reynolds shear stress, respectively. The case identifiers for this comparison were 614cn-LINE2831 for plasma off and 614pn-LINE2831 for plasma on.

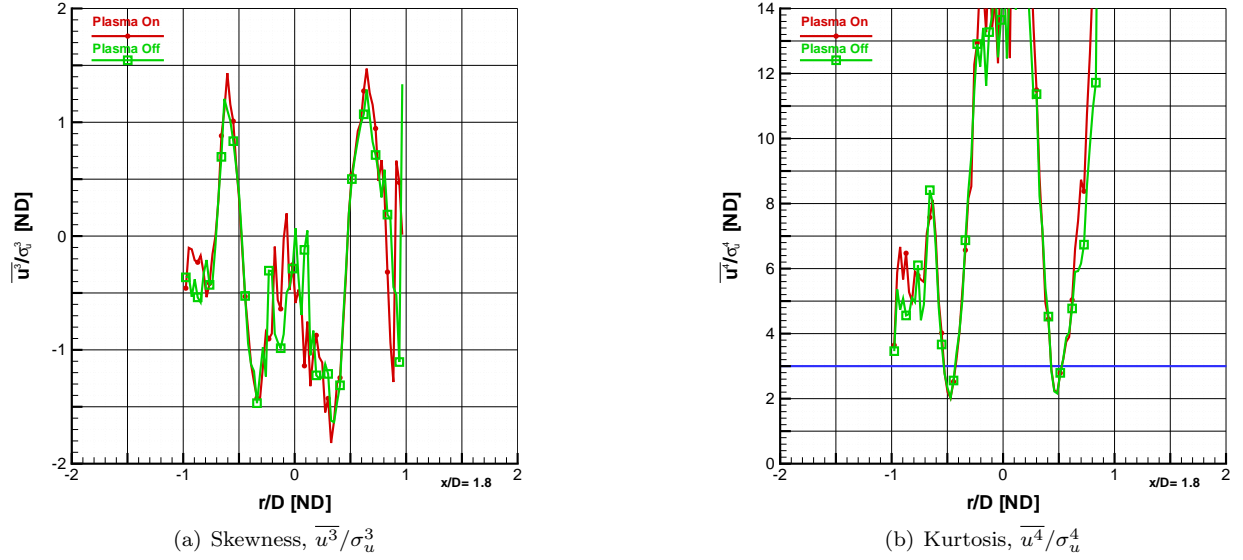
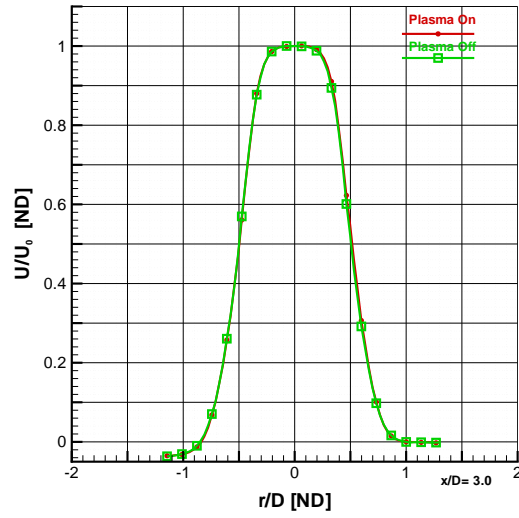
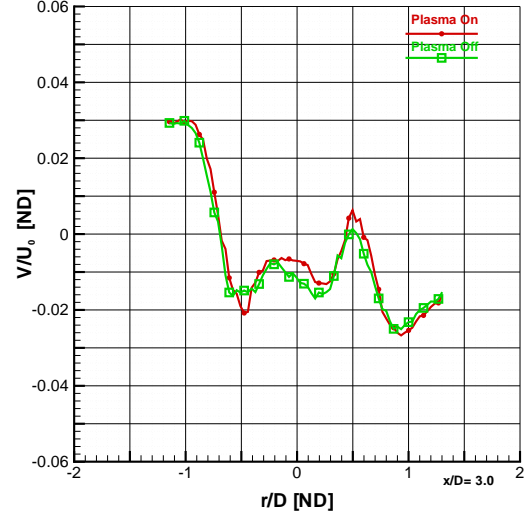


Figure A.126: Comparison of Plasma Effects on Skewness and Kurtosis: Case 614LINE2831

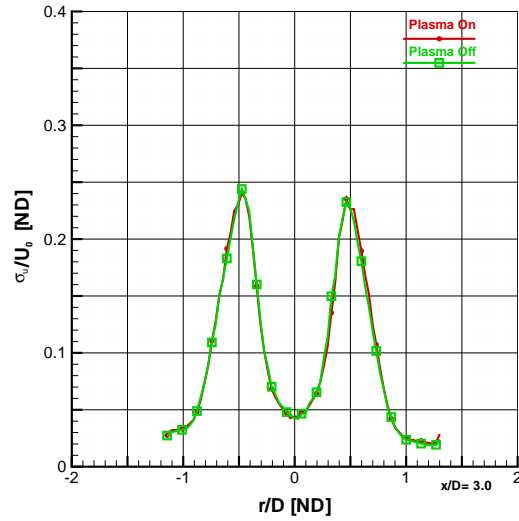
This is the final series of figures on the investigation into the effect of plasma on a Mach 1.1 jet, 1.8 diameters from the anode face. The jet diameter is 15.7 mm. The two plots represented above are a comparison between plasma on in red versus plasma off in green. The plasma off case is placed on top of the plasma on case, therefore making it easier to notice small changes between the two cases. Figure A.126 (a) (b) are the measurements of skewness and kurtosis (or flatness), respectively. A Gaussian distribution has skewness of zero, which indicates a distribution of fluctuations is symmetric about the mean. Positive skewness represents a shift toward the right tail (positive fluctuations), while negative skewness is shifted toward negative fluctuations. A Gaussian distribution has kurtosis of three, represented by the blue line. Values lower than three represent a distribution of velocity with higher peakedness than a Gaussian distribution. Conversely, values above three represent flatter distributions. The case identifiers for this comparison were 614cn-LINE2831 for plasma off and 614pn-LINE2831 for plasma on.



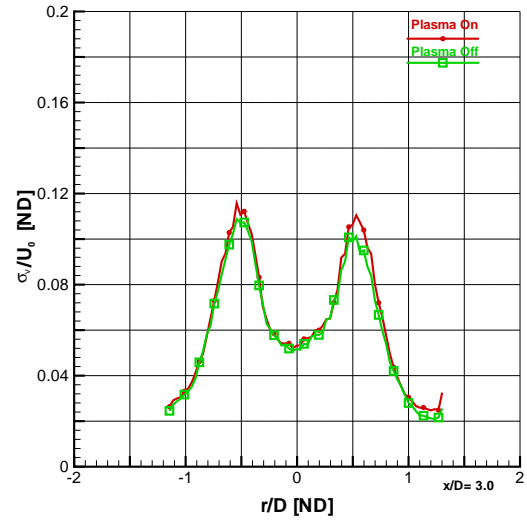
(a) Mean Axial Velocity, U/U_o



(b) Mean Tangential Velocity, V/U_o



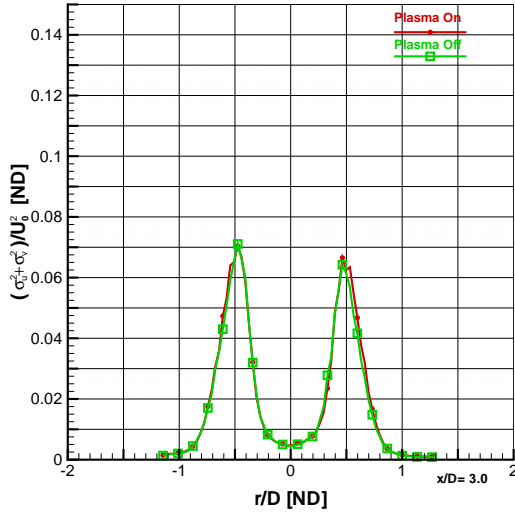
(c) Fluctuating Axial Velocity, σ_u/U_o



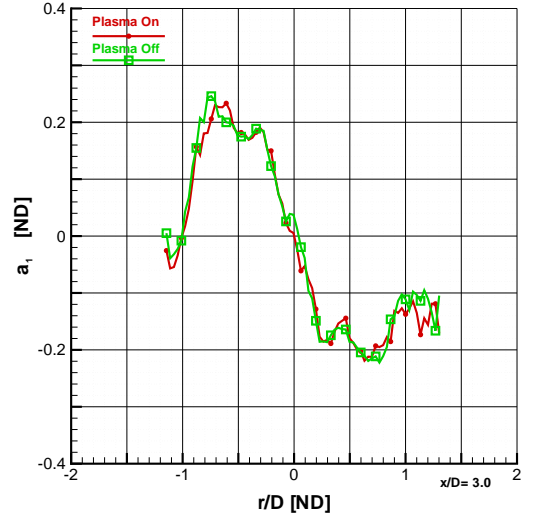
(d) Fluctuating Tangential Velocity, σ_v/U_o

Figure A.127: Comparison of Plasma Effects on Mean Velocity and Fluctuations: Case 606LINE4706

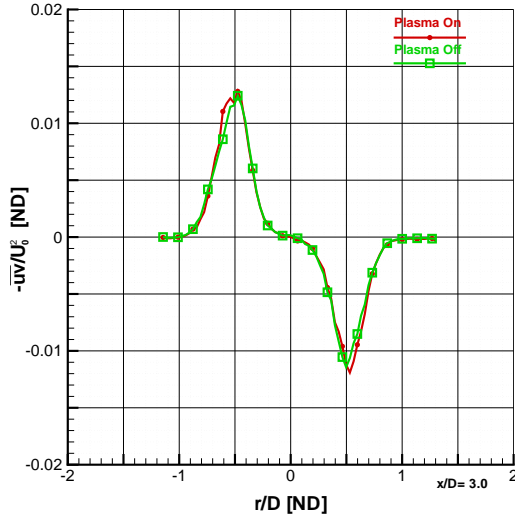
This is an investigation into the effect of plasma on a Mach 1.1 jet, 3.0 diameters from the anode face. The jet diameter is 15.7 mm. The four plots represented above are a comparison between plasma on in red versus plasma off in green. Figure A.127 (a) is non-dimensionalized axial velocity. For these figures, U_o is 343.7 m/s for the plasma off case and 343.0 m/s for the plasma on case. Figure A.127 (b) is the mean tangential component of the velocity. Figures A.127 (c) and (d) show the Reynolds normal stresses in the axial and tangential directions, respectively. The case identifiers for this comparison were 606cnc-LINE4706 for plasma off and 606pnc-LINE4706 for plasma on.



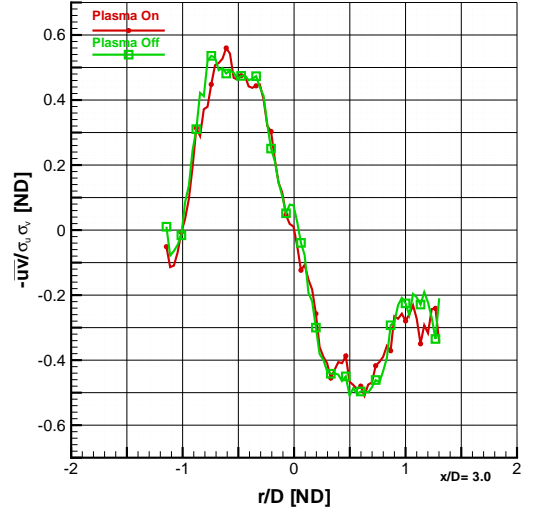
(a) Turbulent Kinetic Energy, $(\sigma_u^2 + \sigma_v^2)/U_o^2$



(b) Structural Parameter, $a_1 = -\overline{uv}/(\sigma_u^2 + \sigma_v^2)$



(c) Reynolds Shear Stress, \overline{uv}/U_o^2



(d) Correlation Coefficient of Reynolds Shear Stress, $-\overline{uv}/(\sigma_u \sigma_v)$

Figure A.128: Comparison of Plasma Effects on Second Moment Fluctuations: Case 606LINE4706

This is a continuing investigation into the effect of plasma on a Mach 1.1 jet, 3.0 diameters from the anode face. The jet diameter is 15.7 mm. The four plots represented above are a comparison between plasma on in red versus plasma off in green. Figure A.128 (a) is non-dimensionalized turbulent kinetic energy and panel (b) is the structural parameter a_1 . At this station, U_o is 343.7 m/s for the plasma off case and 343.0 m/s for the plasma on case. Figures A.128 (c) and (d) show the Reynolds shear stress and the correlation coefficient of Reynolds shear stress, respectively. The case identifiers for this comparison were 606cnc-LINE4706 for plasma off and 606pnc-LINE4706 for plasma on.

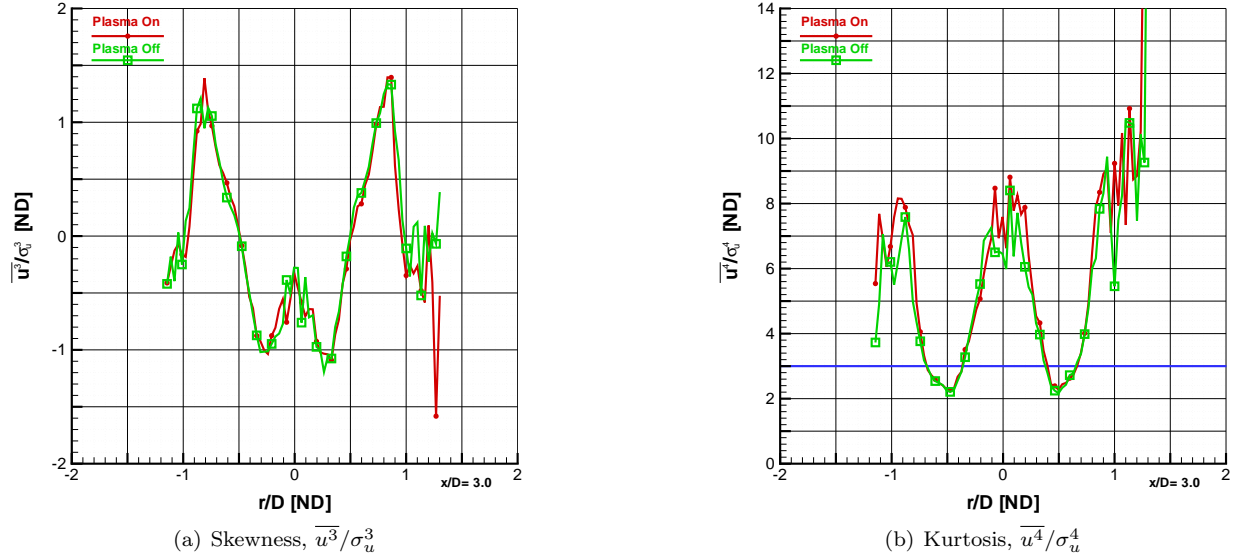
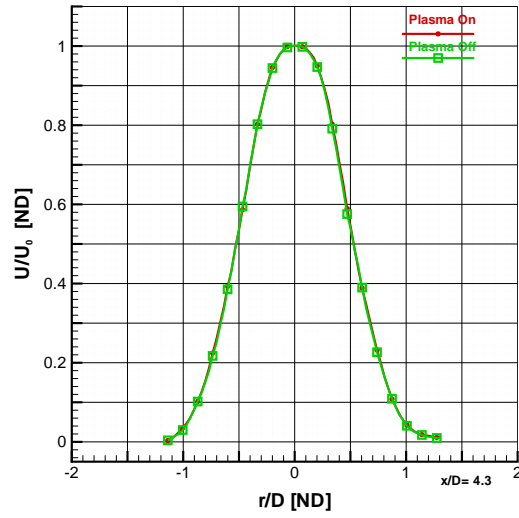
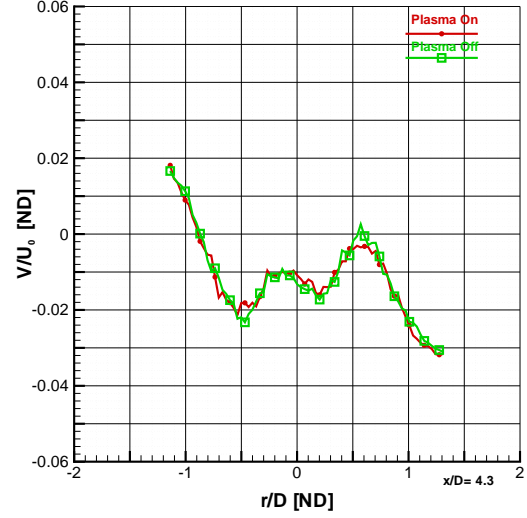


Figure A.129: Comparison of Plasma Effects on Skewness and Kurtosis: Case 606LINE4706

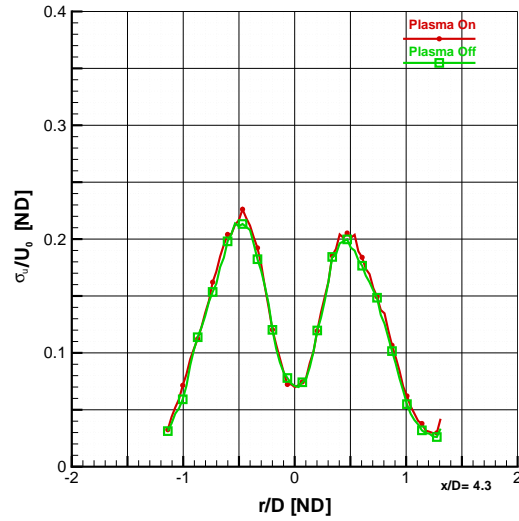
This is the final series of figures on the investigation into the effect of plasma on a Mach 1.1 jet, 3.0 diameters from the anode face. The jet diameter is 15.7 mm. The two plots represented above are a comparison between plasma on in red versus plasma off in green. The plasma off case is placed on top of the plasma on case, therefore making it easier to notice small changes between the two cases. Figure A.129 (a) (b) are the measurements of skewness and kurtosis (or flatness), respectively. A Gaussian distribution has skewness of zero, which indicates a distribution of fluctuations is symmetric about the mean. Positive skewness represents a shift toward the right tail (positive fluctuations), while negative skewness is shifted toward negative fluctuations. A Gaussian distribution has kurtosis of three, represented by the blue line. Values lower than three represent a distribution of velocity with higher peakedness than a Gaussian distribution. Conversely, values above three represent flatter distributions. The case identifiers for this comparison were 606cnc-LINE4706 for plasma off and 606pnc-LINE4706 for plasma on.



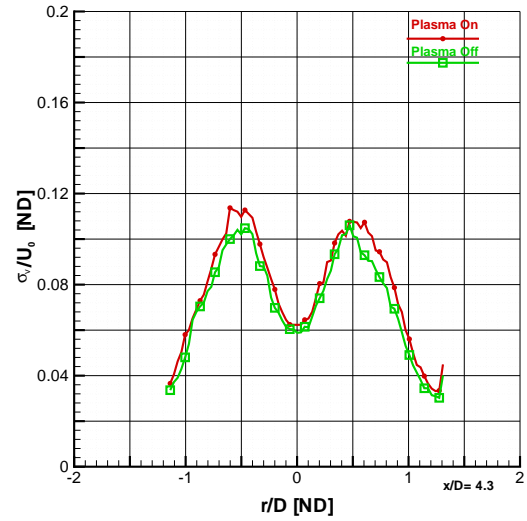
(a) Mean Axial Velocity, U/U_o



(b) Mean Tangential Velocity, V/U_o



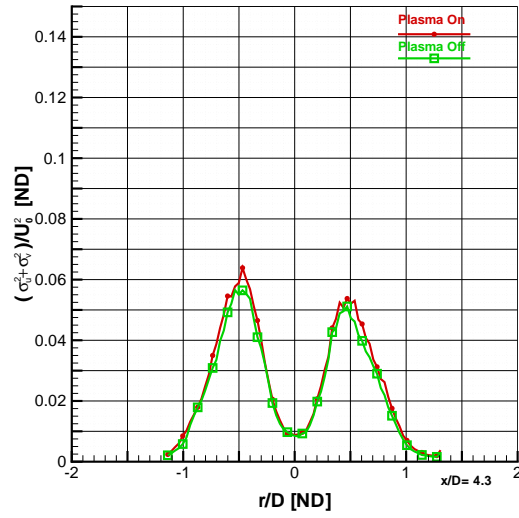
(c) Fluctuating Axial Velocity, σ_u/U_o



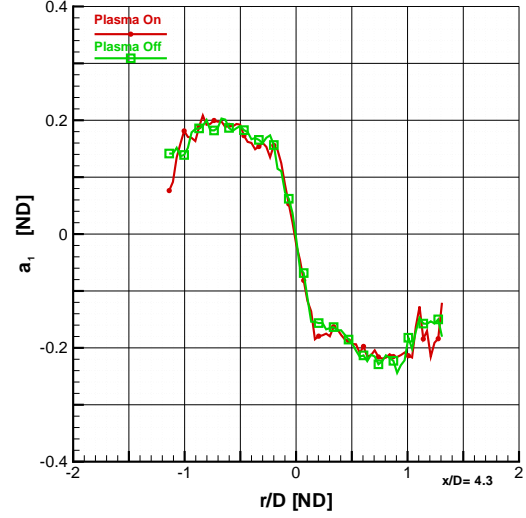
(d) Fluctuating Tangential Velocity, σ_v/U_o

Figure A.130: Comparison of Plasma Effects on Mean Velocity and Fluctuations: Case 606LINE6701

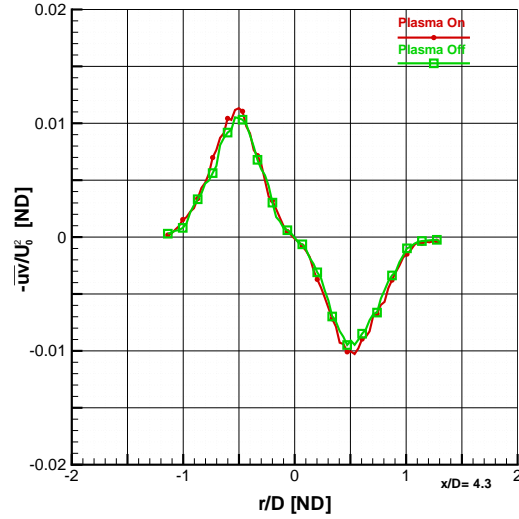
This is an investigation into the effect of plasma on a Mach 1.1 jet, 4.3 diameters from the anode face. The jet diameter is 15.7 mm. The four plots represented above are a comparison between plasma on in red versus plasma off in green. Figure A.130 (a) is non-dimensionalized axial velocity. For these figures, U_o is 338.9 m/s for the plasma off case and 338.5 m/s for the plasma on case. Figure A.130 (b) is the mean tangential component of the velocity. Figures A.130 (c) and (d) show the Reynolds normal stresses in the axial and tangential directions, respectively. The case identifiers for this comparison were 606cnc-LINE6701 for plasma off and 606pnc-LINE6701 for plasma on.



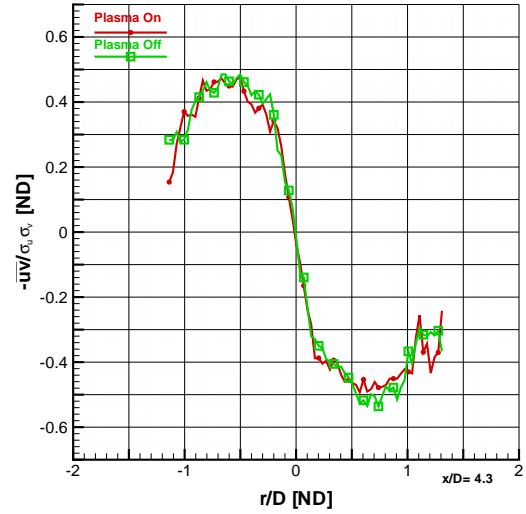
(a) Turbulent Kinetic Energy, $(\sigma_u^2 + \sigma_v^2)/U_o^2$



(b) Structural Parameter, $a_1 = -\overline{uv}/(\sigma_u^2 + \sigma_v^2)$



(c) Reynolds Shear Stress, \overline{uv}/U_o^2



(d) Correlation Coefficient of Reynolds Shear Stress, $-\overline{uv}/(\sigma_u \sigma_v)$

Figure A.131: Comparison of Plasma Effects on Second Moment Fluctuations: Case 606LINE6701

This is a continuing investigation into the effect of plasma on a Mach 1.1 jet, 4.3 diameters from the anode face. The jet diameter is 15.7 mm. The four plots represented above are a comparison between plasma on in red versus plasma off in green. Figure A.131 (a) is non-dimensionalized turbulent kinetic energy and panel (b) is the structural parameter a_1 . At this station, U_o is 338.9 m/s for the plasma off case and 338.5 m/s for the plasma on case. Figures A.131 (c) and (d) show the Reynolds shear stress and the correlation coefficient of Reynolds shear stress, respectively. The case identifiers for this comparison were 606cnc-LINE6701 for plasma off and 606pnc-LINE6701 for plasma on.

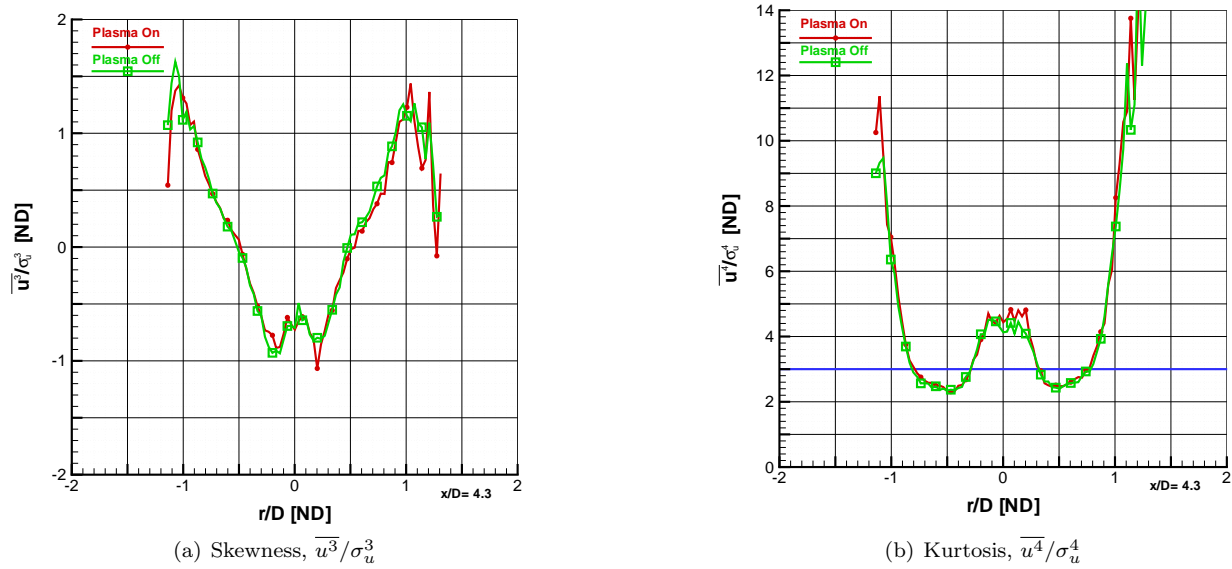


Figure A.132: Comparison of Plasma Effects on Skewness and Kurtosis: Case 606LINE6701

This is the final series of figures on the investigation into the effect of plasma on a Mach 1.1 jet, 4.3 diameters from the anode face. The jet diameter is 15.7 mm. The two plots represented above are a comparison between plasma on in red versus plasma off in green. The plasma off case is placed on top of the plasma on case, therefore making it easier to notice small changes between the two cases. Figure A.132 (a) (b) are the measurements of skewness and kurtosis (or flatness), respectively. A Gaussian distribution has skewness of zero, which indicates a distribution of fluctuations is symmetric about the mean. Positive skewness represents a shift toward the right tail (positive fluctuations), while negative skewness is shifted toward negative fluctuations. A Gaussian distribution has kurtosis of three, represented by the blue line. Values lower than three represent a distribution of velocity with higher peakedness than a Gaussian distribution. Conversely, values above three represent flatter distributions. The case identifiers for this comparison were 606cnc-LINE6701 for plasma off and 606pnc-LINE6701 for plasma on.

Appendix B

Archival of Spectroscopy Based Temperature Measurements

This appendix contains a series of tables of rotational (T_r) and vibrational (T_v) temperatures of images of line spectroscopy of the plasma emissions in the second positive system of diatomic Nitrogen. The temperatures were derived from model matching the recorded spectra.

Each table shows the rotational and vibrational temperatures measured in a grid across the electrode gap, G . The top portion of the table is devoted to rotational temperature, T_r , while the bottom section reports T_v , vibrational temperature. The position from left to right corresponds to jet diameters of vertical displacement from the centerline of the jet. The radial positions are negative for the positions measured vertically below the centerline and positive above the jet center. Each row in the table corresponds to a different location along the gap, beginning near the anode face and progressing downstream towards the cathode. The distance from the electrode (x/D) for each row of temperature measurements is the far left hand column. In some cases, data was taken at only one streamwise location. In those instances, the table was abbreviated with rotational temperatures in the top row, directly over the vibrational temperatures and the location x/D was moved into the upper left corner.

Table B.1: Rotational and Vibrational Temperatures Taken by Line Spectroscopy of the Mach 0.7 Jet at 9 Torr (Case A)

x/D	r/D								
3.2	-1.2	-0.9	-0.6	-0.2	0.1	0.4	0.7	1.0	1.3
T_r [K]	392	338	353	371	478	395	298	358	401
T_v [K]	2917	3072	3169	3323	3380	3435	3365	3079	2839
Note: Jet Exit Diameter D is 20.8 mm and Gap Distance G is 75.8 mm.									

Table B.2: Rotational and Vibrational Temperatures Taken by Line Spectroscopy of the Mach 1.1 Jet at 9 Torr (Case B)

T_r [K]	r/D								
x/D	-1.6	-1.1	-0.7	-0.3	0.1	0.5	0.9	1.4	1.8
0.6	392	325	469	520	0	376	344	401	387
1.9	461	455	330	401	498	406	394	382	408
3.1	399	306	312	386	478	407	394	383	400
4.4	369	320	337	428	443	366	350	448	459
T_v [K]	r/D								
x/D	-1.6	-1.1	-0.7	-0.3	0.1	0.5	0.9	1.4	1.8
0.6	3639	3604	3585	3978	0	3895	3439	3223	3014
1.9	3188	3111	3193	3286	3421	3366	3153	3027	2948
3.1	2994	3065	3173	3278	3349	3354	3170	3072	2977
4.4	3055	3227	3316	3430	3539	3568	3399	3094	3063
Note: Jet Exit Diameter D is 15.6 mm and Gap Distance G is 79.1 mm.									

Table B.3: Rotational and Vibrational Temperatures Taken by Line Spectroscopy of the Mach 1.1 Jet at 9 Torr with Modified Anode (Case B')

T_r [K]	r/D								
x/D	-1.6	-1.1	-0.7	-0.3	0.1	0.5	0.9	1.4	1.8
0.4	0	0	525	434	370	397	499	444	424
1.7	0	0	556	525	578	434	373	449	554
3.0	460	400	348	431	525	441	357	405	431
4.3	374	324	344	433	451	369	351	447	380
T_v [K]	r/D								
x/D	-1.6	-1.1	-0.7	-0.3	0.1	0.5	0.9	1.4	1.8
0.4	0	0	3572	3292	3488	3506	3725	3405	3108
1.7	0	0	3625	3660	3632	3418	3262	3168	3273
3.0	3149	3164	3264	3372	3416	3399	3235	3085	3036
4.3	2991	3152	3246	3344	3465	3494	3321	3032	3036
Note: Jet Exit Diameter D is 15.7 mm and Gap Distance G is 76.7 mm.									

Table B.4: Rotational and Vibrational Temperatures Taken by Line Spectroscopy of the Mach 2.0 Jet at 8 Torr (Case C)

x/D	r/D								
5.8	-2.2	-1.6	-1.0	-0.4	0.1	0.7	1.3	1.9	2.5
T_r [K]	394	416	298	376	475	395	381	391	409
T_v [K]	3005	3151	3325	3446	3502	3519	3336	3118	3049
Note: Jet Exit Diameter D is 11.3 mm and Gap Distance G is 75.8 mm.									

Table B.5: Rotational and Vibrational Temperatures Taken by Line Spectroscopy of the Overexpanded Jet at 8 Torr (Case D)

x/D	r/D								
5.8	-2.2	-1.6	-1.0	-0.4	0.1	0.7	1.3	1.9	2.5
T_r [K]	398	416	301	381	482	398	382	397	413
T_v [K]	3033	3180	3346	3463	3507	3535	3346	3116	3057
Note: Jet Exit Diameter D is 11.3 mm and Gap Distance G is 75.8 mm.									

Table B.6: Rotational and Vibrational Temperatures Taken by Line Spectroscopy of the Mach 1.4 Jet at 5 Torr (Case E)

x/D	r/D								
7.0	-2.6	-1.9	-1.2	-0.5	0.2	0.9	1.5	2.2	2.9
T_r [K]	436	385	340	433	527	373	428	423	450
T_v [K]	3235	3359	3503	3636	3690	3732	3455	3256	3129
Note: Jet Exit Diameter D is 9.5 mm and Gap Distance G is 77.0 mm.									

Table B.7: Rotational and Vibrational Temperatures Taken by Line Spectroscopy of the Effective Mach 0.9 Jet at 5 Torr (Case F)

x/D	r/D								
11.4	-2.6	-1.9	-1.2	-0.5	0.2	0.9	1.5	2.2	2.9
T_r [K]	343	309	395	419	527	453	436	451	481
T_v [K]	3172	3312	3408	3588	3676	3728	3533	3280	3092
Note: Jet Exit Diameter D is 9.5 mm and Gap Distance G is 118.3 mm.									

Table B.8: Rotational and Vibrational Temperatures Taken by Line Spectroscopy of the Effective Mach 1.4 Jet at 5 Torr (Case G)

T_r [K]	r/D								
x/D	-2.6	-1.9	-1.2	-0.5	0.2	0.9	1.5	2.2	2.9
7.2	389	417	361	435	452	388	377	446	461
9.3	411	439	394	489	505	439	422	478	485
11.4	360	374	389	491	501	422	344	434	443
T_v [K]	r/D								
x/D	-2.6	-1.9	-1.2	-0.5	0.2	0.9	1.5	2.2	2.9
7.2	3205	3231	3346	3430	3541	3587	3345	3165	3091
9.3	3279	3307	3463	3622	3720	3704	3475	3297	3219
11.4	3248	3404	3505	3628	3719	3755	3612	3254	3187
Note: Jet Exit Diameter D is 9.5 mm and Gap Distance G is 118.3 mm.									

Table B.9: Rotational and Vibrational Temperatures Taken by Line Spectroscopy of the Effective Mach 1.9 Jet at 5 Torr (Case H)

x/D	r/D								
11.4	-2.6	-1.9	-1.2	-0.5	0.2	0.9	1.5	2.2	2.9
T_r [K]	345	306	322	405	499	415	331	418	435
T_v [K]	3231	3375	3481	3599	3614	3644	3590	3233	3173
Note: Jet Exit Diameter D is 9.5 mm and Gap Distance G is 118.3 mm.									

Table B.10: Rotational and Vibrational Temperatures Taken by Line Spectroscopy of the Highly Underexpanded Jet at 8 Torr (Case U)

T_r [K]	r/D								
x/D	-3.0	-2.2	-1.4	-0.6	0.2	1.0	1.8	2.6	3.4
1.0	299	388	292	168	157	382	454	432	368
1.6	257	384	283	173	148	387	449	349	351
2.2	307	384	279	424	456	372	368	434	368
4.6	304	387	334	417	437	368	364	429	368
7.1	405	426	307	396	405	332	394	410	345
T_v [K]	r/D								
x/D	-3.0	-2.2	-1.4	-0.6	0.2	1.0	1.8	2.6	3.4
1.0	3126	3176	3313	3660	3756	3573	3296	3192	3059
1.6	2986	3056	3189	3595	3626	3447	3193	3100	2935
2.2	2986	2999	3144	3268	3464	3386	3190	3015	2911
4.6	2958	2979	3108	3213	3425	3337	3164	3016	2972
7.1	3065	3227	3405	3532	3669	3644	3368	3133	3145
Note: Jet Exit Diameter D is 8.2 mm and Gap Distance G is 68.0 mm.									

Table B.11: Rotational and Vibrational Temperatures Taken by Line Spectroscopy of the Effective Mach 0.9 Jet at 5 Torr, with Decreased Gap Distance of 76.5 mm

x/D	r/D								
7.1	-2.6	-1.9	-1.2	-0.5	0.2	0.9	1.5	2.2	2.9
T_r [K]	464	415	437	472	501	454	509	539	519
T_v [K]	3084	3210	3317	3486	3674	3762	3516	3275	3158
Note: Jet Exit Diameter D is 9.5 mm and Gap Distance G is 77.4 mm.									

Table B.12: Rotational and Vibrational Temperatures Taken by Line Spectroscopy of the Effective Mach 1.4 Jet at 5 Torr, with Decreased Gap Distance of 76.5 mm

T_r [K]	r/D								
x/D	-2.6	-1.9	-1.2	-0.5	0.2	0.9	1.5	2.2	2.9
2.8	0	330	340	411	357	351	373	445	392
4.9	426	283	343	439	364	375	370	453	387
7.0	412	311	326	418	434	369	362	439	451
T_v [K]	r/D								
x/D	-2.6	-1.9	-1.2	-0.5	0.2	0.9	1.5	2.2	2.9
2.8	0	3227	3308	3379	3511	3447	3271	3160	3154
4.9	3030	3164	3226	3302	3437	3407	3228	3076	3004
7.0	3128	3300	3430	3568	3660	3643	3474	3206	3056
Note: Jet Exit Diameter D is 9.5 mm and Gap Distance G is 76.5 mm.									

Table B.13: Rotational and Vibrational Temperatures Taken by Line Spectroscopy of the Effective Mach 1.9 Jet at 5 Torr, with Decreased Gap Distance of 76.5 mm

x/D	r/D								
7.0	-2.6	-1.9	-1.2	-0.5	0.2	0.9	1.5	2.2	2.9
T_r [K]	444	396	341	439	450	379	449	385	400
T_v [K]	3126	3301	3444	3543	3611	3632	3404	3186	3170
Note: Jet Exit Diameter D is 9.5 mm and Gap Distance G is 76.5 mm.									

Table B.14: Rotational and Vibrational Temperatures Taken by Line Spectroscopy of the Mach 2.0 Jet at 10 Torr

x/D	r/D								
1.4	-2.2	-1.6	-1.0	-0.4	0.1	0.7	1.3	1.9	2.5
T_r [K]	325	285	296	375	317	323	313	390	403
T_v [K]	2887	2983	3048	3147	3300	3268	3137	2888	2705
Note: Jet Exit Diameter D is 11.3 mm and Gap Distance G is 26.2 mm.									

Table B.15: Rotational and Vibrational Temperatures Taken by Line Spectroscopy of the α -Discharge No-Flow Plasma Field

T_r [K]	r/D								
x/D	-2.2	-1.6	-1.0	-0.4	0.1	0.7	1.3	1.9	2.5
0.7	430	393	356	438	518	451	443	506	451
1.3	454	434	462	485	553	498	563	472	483
2.2	480	526	542	552	651	659	592	586	614
3.1	493	535	559	580	675	679	592	579	584
4.0	478	525	545	560	659	665	653	563	571
4.9	483	526	554	573	595	593	590	582	579
5.8	464	472	405	492	595	501	496	514	584
T_v [K]	r/D								
x/D	-2.2	-1.6	-1.0	-0.4	0.1	0.7	1.3	1.9	2.5
0.7	4108	4248	4424	4532	4584	4600	4326	4066	3938
1.3	3706	3804	3926	4088	4166	4121	3827	3756	3653
2.2	3612	3663	3829	3963	3891	3805	3759	3711	3702
3.1	3638	3685	3841	3989	3959	3875	3760	3646	3557
4.0	3652	3715	3863	4018	4012	3916	3727	3667	3543
4.9	3643	3697	3853	3997	4041	3966	3776	3635	3530
5.8	4166	4273	4503	4597	4561	4601	4393	4143	3935
Note: Jet Exit Diameter D is 11.3 mm and Gap Distance G is 75.1 mm.									

Bibliography

- [1] Abbett, M., “Mach Disk in Underexpanded Exhaust Plumes,” *AIAA Journal*, Vol. 9, No. 3, 1971, pp. 512–514.
- [2] Abramovich, G., *Turbulent Jets of Air, Plasma, and Real Gas*, Consultants Bureau, New York, 1969.
- [3] Acton, E., “A Modelling of Large Eddies in an Axisymmetric Jet,” *Journal of Fluid Mechanics*, Vol. 98, 1980, pp. 1–31.
- [4] Adamovich, I., Subramaniam, V., Rich, J., and Macheret, S., “Shock Wave Propagation in Weakly Ionized Plasmas,” AIAA Paper 97–2499, 1997.
- [5] Adamovich, I., Aithal, S., Palm, P., Ploenjes, E., Subramaniam, V., Yano, R., and Rich, J., “Modeling of Vibration-to-Vibration and Vibration-to-Electronic Energy Transfer Processes in Nonequilibrium Flows,” AIAA Paper 98–2750, 1998.
- [6] Adamovich, I., Lempert, W., Utkin, Y., and Rich, W., “Thermal Mode Nonequilibrium in High Speed Gas Dynamics,” AIAA Paper 06–0584, 2006.
- [7] Adamson Jr., T. and Nicholls, J., “On the Structure of Jets from Highly Underexpanded Nozzles into Still Air,” *Journal of the Aero/Space Sciences*, Vol. 26, 1959, pp. 16–24.
- [8] Addy, A., “Effects of Axisymmetric Sonic Nozzle Geometry on Mach Disk Characteristics,” *AIAA Journal*, Vol. 19, No. 1, 1981, pp. 121–122.
- [9] Adelgren, R., Elliott, G., Knight, D., Zheltovodov, A., and Beutner, T., “Energy Deposition in Supersonic Flows,” AIAA Paper 01–0885, 2001.
- [10] Adelgren, R., Elliott, G., Crawford, J., Carter, C., Grosjean, D., and Donbar, J., “Axisymmetric Jet Shear Layer Excitation Induced by Electric Arc Discharge and Focused Laser Energy Deposition,” AIAA Paper 02–0729, 2002.
- [11] Adelgren, R., Elliott, G., Crawford, J., Carter, C., Donbar, J., and Grosjean, D., “Axisymmetric Jet Shear-Layer Excitation by Laser Energy and Electric Arc Discharges,” *AIAA Journal*, Vol. 43, No. 4, 2005, pp. 776–791.
- [12] Adrian, R., “Twenty Years of Particle Image Velocimetry,” *Experiments in Fluids*, Vol. 39, 2005, pp. 159–169.
- [13] Aleksandrov, A., Bychkov, V., Chernikov, V., Ershov, A., Shibkov, V., and Timofeev, I., “Plasma Aerodynamics Investigations in MSU Physical Department (Review of Investigations),” AIAA Paper 05–1433, 2005.
- [14] Anderson, J., *Modern Compressible Flow; with Historical Perspective*, McGraw-Hill, New York, 1982.
- [15] Anderson, J., *Fundamentals of Aerodynamics*, McGraw-Hill, New York, 1991.
- [16] Anderson, R. and Roy, S., “Preliminary Experiments of Barrier Discharge Plasma Actuators using Dry and Humid Air,” AIAA Paper 06–0369, 2006.

- [17] Anon., *DPIV 2.1 32bit PIV Analysis Code: Product Help*, Innovative Scientific Solutions Inc., 2776 Indian Ripple Rd., Dayton OH 45440, 2004.
- [18] Anon., "Equations, Tables, and Charts for Compressible Flow," NACA Report 1135, 1953.
- [19] Anon., *Gemini PIV: Product Data Sheet*, New Wave Research, Inc., 47613 Warm Springs Blvd., Fremont CA 94539, 2003.
- [20] Anon., *Gated Integrators and Boxcar Averagers*, Stanford Research Systems, 1290-D Reamwood Ave., Sunnyvale CA 94089, 2005.
- [21] Anon., *General Purpose 5 or 10 VDC Output Pressure Sensors: Product Specifications Sheet*, Omega Corp., 1 Omega Dr., Stamford CT 06907, 2007.
- [22] Anon., *ICCD Detector Operation Manual*, RS Princeton Instruments, 3660 Quakerbridge Rd., Trenton NJ 08619, 1999.
- [23] Anon., *Instruction Manual: Terranova Model 907 Dual-Hybrid Vacuum Gauge Controller*, Duniway Stockroom Corp., 1305 Space Park Wy, Mountain View CA 94043, 2001.
- [24] Anon., *Kinney KT Series Signe Stage, Triplex Rotary Piston Pumps*, Tuthill Vacuum and Blower Systems, 4840 West Kearney St., Springfield MO 65803, 2003.
- [25] Anon., *MODEL 3475 Condensation Monodisperse Aerosol Generator: Instruction Manual*, TSI Incorporated, 500 Cardigan Road, Shoreview, MN 55126, 1933475th ed., 2004.
- [26] Anon., *Operator Manual for a H5437.1.1A High Pressure Air Compressor*, CompAir UK Ltd., Ranelagh Rd, Ipswich England IP2 0AQ, 2000.
- [27] Anon., *PCO.1600 Cooled Digital 14 Bit CCD Camera System: Product Data Sheet*, The Cooke Corp., 6930 Metroplex Dr., Romulus MI 48174, 2005.
- [28] Anon., *PG-200 Programmable Gate Pulse Generator*, RS Princeton Instruments, 3660 Quakerbridge Rd., Trenton NJ 08619, 1998.
- [29] Anon., *Quanta-Ray PRO-Series Pulsed Nd:YAG Lasers*, Spectra Physics, 1335 Terra Bella Ave., Mountain View CA 94043, 2002.
- [30] Anon., *Quantum Composers Model 565: Product Manual*, Berkeley Nucleonics Corp., 2955 Kerner Blvd., San Rafael, CA 94901, 2006.
- [31] Anon., *ST-138 Controller*, RS Princeton Instruments, 3660 Quakerbridge Rd., Trenton NJ 08619, 2003.
- [32] Anon., *TRIAX 180/190: Specification Sheet*, HORIBA Jobin Yvon, 3880 Park Ave., Edison NJ 08820, 2007.
- [33] Anon., *User Manual, CESAR Generator Model 1350 200V*, Dressler HF-Technik GmbH, 6389 San Ignacio Ave, San Jose CA 95119, 2003.
- [34] Anon., *User Manual, VARIOMATCH Auto-Matching 2-27MHz 5000W*, Dressler HF-Technik GmbH, 6389 San Ignacio Ave, San Jose CA 95119, 2003.
- [35] Aoki, S., Lee, J., Masuya, G., Kanda, T., and Kudo, K., "Aerodynamic Experiment on an Ejector-Jet," *Journal of Propulsion and Power*, Vol. 21, No. 3, 2005, pp. 496–503.
- [36] Appartaim, R. and Johnson III, J., "Turbulence in Plasma-Induced Hypersonic Drag Reduction," *AIAA Journal*, Vol. 40, No. 10, 2002, pp. 1979–1983.
- [37] Arnette, S., Samimy, M., and Elliott, G., "On Streamwise Vortices in High Reynolds Number Supersonic Axisymmetric Jets," *Physics of Fluids A*, Vol. 5, No. 1, 1992, pp. 187–202.

- [38] Artana, G., D'Adamo, J., Leger, L., Moreau, E., and Touchard, G., "Flow Control with Electrohydrodynamic Actuators," AIAA Paper 01-0351, 2001.
- [39] Aupoix, B., "Modeling of Compressibility Effects in Mixing Layer," 3rd international symposium on turbulence and shear flow phenomena, 2003.
- [40] Austin, J., "Rocket Propulsion," AE-434 Class Notes, University of Illinois at Urbana-Champaign.
- [41] Baird, C., Enloe, C., McLaughlin, T., and Baughn, J., "Acoustic Testing of the Dielectric Barrier Discharge (DBD) Plasma Actuator," AIAA Paper 05-0565, 2005.
- [42] Baker, W., *Explosions in Air*, University of Texas Press, Austin, TX, 1973.
- [43] Balcer, B., Franke, M., and Rivir, R., "Effects Of Plasma Induced Velocity On Boundary Layer Flow," AIAA Paper 06-0875, 2006.
- [44] Bar-Meir, G., *Fundamentals of Compressible Fluid Mechanics*, Genick Bar-Meir, Minneapolis, MN, 2007.
- [45] Batchelor, G., "Turbulent Motion," *Reports on Progress in Physics*, Vol. 15, 1953, pp. 101-141.
- [46] Bauer, A., "Normal Shock Location of Underexpanded Gas-Particle Jets," *AIAA Journal*, Vol. 3, No. 6, 1965, pp. 1187-1189.
- [47] Bayly, B., Orszag, S., and Herbert, T., "Instability Mechanisms in Shear-Flow Transition," *Annual Review of Fluid Mechanics*, Vol. 20, 1988, pp. 359-391.
- [48] Beaulieu, W., Bytyurin, V., Klimov, A., Leonov, S., Pashina, A., and Timofeev, B., "Plasma Aerodynamic WT Tests with 1/6 Scale Model of Nose Part of F-15," AIAA Paper 99-4825, 2006.
- [49] Behringer, K. and Fantz, U., "Spectroscopic Diagnostics of Glow Discharge Plasmas with Non-Maxwellian Electron Energy Distributions," *Journal of Physics D: Applied Physics*, Vol. 27, 1994, pp. 2128-2135.
- [50] Benedict, L. and Gould, R., "Towards Better Uncertainty Estimates for Turbulence Statistics," *Experiments in Fluids*, Vol. 22, 1996, pp. 129-136.
- [51] Berkooz, G., Holmes, P., and Lumley, J., "The Proper Orthogonal Decomposition in the Analysis of Turbulent Flows," *Annual Review of Fluid Mechanics*, Vol. 25, 1993, pp. 539-575.
- [52] Birks, J., *Photophysics of Aromatic Molecules*, John Wiley and Sons, New York, 1970.
- [53] Bitjwrin, V., Klimov, A., Leonov, S., VanWie, D., Brovkin, V., Kolesnichenko, Y., and Lutsky, A., "Effect of Heterogeneous Discharge Plasma on Shock Wave Structure and Propagation," AIAA Paper 99-4940, 1999.
- [54] Blackwell, C., Anderson, C., Deneen, J., Carter, C., Kortshagen, U., and Kakalios, J., "The Influence of Thermophoresis Effects During Deposition of Hydrogenated Amorphous Silicon Thin Films with Nanocrystalline Silicon Inclusions," *Materials Research Society*, Vol. 910, No. 7, 2006, pp. 1-6.
- [55] P. Bletzinger, B. G. and Garscadden, A., "Strong Double-Layer Formation by Shock Waves in Non-equilibrium Plasmas," *Physical Review E*, Vol. 67, 2003.
- [56] Bletzinger, P., Ganguly, B., and Garscadden, A., "Influence of Dielectric Barrier Discharges on Low Mach Number Shock Waves at Low to Medium Pressures," *Journal of Applied Physics*, Vol. 97, 2005, pp. 113303-1-6.
- [57] Bletzinger, P., Ganguly, B., Van Wie, D., and Garscadden, A., "Plasmas in High Speed Aerodynamics," *Journal of Physics D: Applied Physics*, Vol. 38, 2005, pp. R33-R57.

- [58] Bogdanoff, D., "Compressibility Effects in Turbulent Shear Layers," *AIAA Journal*, Vol. 21, No. 6, 1983, pp. 926–927.
- [59] Bogey, C. and Bailly, C., "An Analysis of the Correlations Between the Turbulent Flow and the Sound Pressure Fields of Subsonic Jets," *Journal of Fluid Mechanics*, Vol. 583, 2007, pp. 71–97.
- [60] Boguszko, M. and Elliott, G., "Property Measurement Utilizing Atomic/Molecular Filter-Based Diagnostics," *Progress in Aerospace Sciences*, Vol. 41, 2005, pp. 93–142.
- [61] Boguszko, M., Huffman, R., and Elliott, G., "Property and Velocity Measurements in a Supersonic Flow," AIAA Paper 06–1390, 2006.
- [62] Bonnet, J., Gresillon, D., and Taran, J., "Nonintrusive Measurements for High-Speed, Supersonic, and Hypersonic Flows," *Annual Review of Fluid Mechanics*, Vol. 30, 1998, pp. 231–273.
- [63] Bottin, B., "Thermodynamic Properties of Arbitrary Perfect Gas Mixtures at Low Pressures and High Temperatures," *Progress in Aerospace Sciences*, Vol. 36, 2000, pp. 231–273.
- [64] Bowersox, R., "Combined Laser Doppler Velocimetry and Cross-Wire Anemometry Analysis for Supersonic Turbulent Flow," *AIAA Journal*, Vol. 34, No. 11, 1996, pp. 2269–2275.
- [65] Bradshaw, P., Ferriss, D., and Johnson, R., "Turbulence in the Noise-Producing Region of a Circular Jet," *Journal of Fluid Mechanics*, Vol. 19, 1966, pp. 591–623.
- [66] Bradshaw, P., "The Effect of Initial Conditions on the Development of a Free Shear Layer," *Journal of Fluid Mechanics*, Vol. 26, 1966, pp. 225–236.
- [67] Bradshaw, P., "Compressible Turbulent Shear Layers," *Annual Review of Fluid Mechanics*, Vol. 9, 1977, pp. 33–54.
- [68] Broc, A., De Benedictis, S., Dilecce, G., Vigliotti, M., Sharafutdinov, R., and Skovorodko, P., "Experimental and Numerical Investigation of an O₂/NO Supersonic Free Jet Expansion," *Journal of Fluid Mechanics*, Vol. 500, 2004, pp. 211–237.
- [69] Broc, A., De Benedictis, S., and Dilecce, G., "LIF Investigations on NO, O and N in a supersonic N₂/O₂/NO RF Plasma Jet," *Plasma Sources Science and Technology*, Vol. 13, 2004, pp. 504–514.
- [70] Brode, H., "Numerical Solutions of Spherical Blast Waves," *Journal of Applied Physics*, Vol. 26, No. 6, 1955, pp. 766–775.
- [71] Brown, G. and Roshko, A., "On Density Effects and Large Structures in Turbulent Mixing Layers," *Journal of Fluid Mechanics*, Vol. 64, No. 4, 1974, pp. 775–816.
- [72] Brovkin, V., Kolesnichenko, Y., Klimov, A., Leonov, S., Krylov, A., and Ryvkin, M., "Study of Microwave Plasma-Body Interaction in Supersonic Airflow," AIAA Paper 99–3740, 1999.
- [73] Bruun, H., "A Time-Domain Analysis of the Large-Scale Flow Structure in a Circular Jet. Part 1. Moderate Reynolds Number," *Journal of Fluid Mechanics*, Vol. 83, 1977, pp. 641–671.
- [74] Bryant, R., Donham, J., and Driscoll, J., "Acetone Laser Induced Fluorescence for Low Pressure/Low Temperature Flow Visualization," *Experiments in Fluids*, Vol. 28, 2000, pp. 471–476.
- [75] Byun, G. and Simpson, R., "Structure of Three-Dimensional Separated Flow on an Axisymmetric Bump," *AIAA Journal*, Vol. 44, No. 5, 2006, pp. 999–1008.
- [76] Candler, G., Macheret, S., Adamovich, I., and Kelley, J., "Modeling of RF Plasma Kinetics and Aerodynamics of the AEDC Ballistic Range Experiments," AIAA Paper 01–0494, 2001.
- [77] Cercignani, C., *Rarefied Gas Dynamics: From basic Concepts to Actual Calculations*, Cambridge University Press, Cambridge, 2000.

- [78] Chang, L. and Chow, W., "Mach Disk from Underexpanded Axisymmetric Nozzle Flow," *AIAA Journal*, Vol. 12, No. 8, 1974, pp. 1079–1082.
- [79] Charwat, A., "Boundary of Underexpanded Axisymmetric Jets Issuing into Still Air," *AIAA Journal*, Vol. 2, No. 1, 1964, pp. 161–163.
- [80] Laurendeau, N., *Combustion Measurements*, Hemisphere Publishing Corporation, New York, 1991.
- [81] Chintala, N., Meyer, R., Hicks, A., Bao, A., Rich, J., Lempert, W., and Adamovich, I., "Nonthermal Ignition of Premixed Hydrocarbon-Air Flows by Nonequilibrium Radio Frequency Plasma," *Journal of Propulsion and Power*, Vol. 21, No. 2, 2005, pp. 1–9.
- [82] Chow, W. and Addy, A., "Interaction Between Primary and Secondary Streams of the Supersonic Ejector Systems and Their Performance Characteristics," *AIAA Journal*, Vol. 2, No. 4, 1964, pp. 687–695.
- [83] Christensen, K., Soloff, S., and Adrian, R., *PIV Sleuth: Integrated Particle Image Velocimetry (PIV) Interrogation/Validation Software*, Laboratory for Turbulence and Complex Flow, Department of Theoretical and Applied Mechanics, University of Illinois at Urbana-Champaign, Urbana, IL 61801, 2001.
- [84] Chu, B. and Kovasznay, L., "Non-Linear Interactions in a Viscous Heat-Conducting Compressible Gas," *Journal of Fluid Mechanics*, Vol. 3, 1958, pp. 494–514.
- [85] Citriniti, J. and George, W., "Reconstruction of the Global Velocity Field in the Axisymmetric Mixing Layer Utilizing the Proper Orthogonal Decomposition," *Journal of Fluid Mechanics*, Vol. 418, 2000, pp. 137–166.
- [86] Clemens, N. and Mungal, M., "Two- and Three-Dimensional Effects in the Supersonic Mixing Layer," *AIAA Journal*, Vol. 30, No. 4, 1992, pp. 973–981.
- [87] Lowry, H., Stepanek, C., Crosswy, L., Sherrhouse, P., Smith, M., Price, L., Ruyten, W., and Felderman, J., "Scaling Measurements in Compressible Axisymmetric Mixing Layers," AIAA Paper 93–0220, 1993.
- [88] Clemens, N. and Paul, P., "Effects of Heat Release on the Near Field FLOW Structure of Hydrogen Jet Diffusion Flames," *Combustion and Flame*, Vol. 102, 1995, pp. 271–284.
- [89] Clemens, N. and Paul, P., "Scalar Measurements in Compressible Axisymmetric Mixing Layers," *Physics of Fluids*, Vol. 7, No. 5, 1995, pp. 1071–1087.
- [90] Clemens, N., Petullo, S., and Dolling, D., "Large-Scale Structure Evolution in Supersonic Interacting Shear Layers," *AIAA Journal*, Vol. 34, No. 10, 1996, pp. 2062–2070.
- [91] Cohen, L. and Hanson, R., "Emission and Laser-Induced Fluorescence Measurements in a Supersonic Jet of Plasma-Heated Nitrogen," *Journal of Physics D: Applied Physics*, Vol. 25, 1992, pp. 339–351.
- [92] Coleman, H. and Steele, W., *Experimentation and Uncertainty Analysis for Engineers*, John Wiley and Sons, New York, 1989.
- [93] Coles, D., "Prospects for Useful Research on Coherent Structure in the Turbulent Shear Flow," *Proceedings of the Indian Academy of Science*, Vol. 4, 1981, pp. 111–127.
- [94] Copeland, R. and Crosley, D., "Radiative Collisional and Dissociative Processes in Triplet Acetone," *Chemical Physics Letters*, Vol. 115, No. 4, 1985, pp. 362–368.
- [95] Corcos, G. and Sherman, F., "The Mixing Layer: Deterministic Models of a Turbulent Flow. Part 1. Introduction and the Two-Dimensional Flow," *Journal of Fluid Mechanics*, Vol. 139, 1984, pp. 29–65.
- [96] Corcos, G. and Lin, S., "The Mixing Layer : Deterministic Models of a Turbulent Flow. Part 2. The Origin of the Three-Dimensional Motion," *Journal of Fluid Mechanics*, Vol. 139, 1984, pp. 67–95.

- [97] Corke, T. and Matlis, E., "Phased Plasma Arrays for Unsteady Flow Control," AIAA Paper 00-2323, 2000.
- [98] Corke, T., Jumper, E., Post, M., Orlov, D., and McLaughlin, T., "Application of Weakly-Ionized Plasmas as Wing Flow-Control Devices," AIAA Paper 02-0350, 2002.
- [99] Corke, T. and Post, M., "Overview of Plasma Flow Control: Concepts, Optimization, and Applications," AIAA Paper 05-0563, 2005.
- [100] Crist, S., Sherman, P., and Glass, D., "Study of Highly Underexpanded Sonic Jet," *AIAA Journal*, Vol. 4, No. 1, 1966, pp. 68-71.
- [101] Crow, S. and Champagne, F., "Orderly Structure in Jet Turbulence," *Journal of Fluid Mechanics*, Vol. 48, 1971, pp. 547-591.
- [102] Crowe, C., Chung, J., and Troutt, T., "Particle Mixing in Free Shear Flows," *Progress in Energy and Combustion Science*, Vol. 14, 1988, pp. 171-194.
- [103] Cutler, A., Diskin, G., Drummond, J., and White, J., "Supersonic Coaxial Jet Experiment for Computational Fluid Dynamics Code Validation," *AIAA Journal*, Vol. 44, No. 3, 2006, pp. 585-592.
- [104] Dahm, W. and Dimotakis, P., "Measurements of Entrainment and Mixing in Turbulent Jets," *AIAA Journal*, Vol. 25, No. 9, 1987, pp. 1216-1223.
- [105] Dabiri, D. and Gharib, M., "Digital Particle Image Thermometry: The Method and Implementation," *Experiments in Fluids*, Vol. 11, 1991, pp. 77-86.
- [106] Davidor, W. and Penner, S., "Shock Standoff Distances and Mach-Disk Diameters in Underexpanded Sonic Jets," *AIAA Journal*, Vol. 9, No. 8, 1971, pp. 1651-1653.
- [107] Davidor, W. and Penner, S., "Turbulence Structure in Free Shear Layers," *AIAA Journal*, Vol. 4, No. 11, 1966, pp. 1971-1978.
- [108] Davis, M., "Coherence Between Large-Scale Jet-Mixing Structure and its Pressure Field," *Journal of Fluid Mechanics*, Vol. 116, 1982, pp. 31-57.
- [109] Dimotakis, P., "Some Issues on Turbulent Mixing and Turbulence," GALCIT Report fm93-1, 1993.
- [110] Domingo, P. and Benazzouz, T., "Direct Numerical Simulation and Modeling of a Nonequilibrium Turbulent Plasma," *AIAA Journal*, Vol. 38, No. 1, 2000, pp. 73-78.
- [111] Dors, I., Parigger, C., and Lewis, J., "Fluid Dynamics Effects Following Laser Induced Optical Breakdown," AIAA Paper 00-0717, 2000.
- [112] Drain, L., *The Laser Doppler Technique*, JohnWiley and Sons, New York, 1980.
- [113] Duckett, S. and Gilbert, B., *Foundations of Spectroscopy*, Oxford Science Publications, Oxford, 2005.
- [114] Dutton, J., Mikkelsen, C., and Addy, A., "A Theoretical and Experimental Investigation of the Constant Area Supersonic-Supersonic Ejector," *AIAA Journal*, Vol. 20, No. 10, 1982, pp. 1393-1400.
- [115] Eastman, D. and Radtke, L., "Location of the Normal Shock Wave in the Exhaust Plume of a Jet," *AIAA Journal*, Vol. 1, 1963, pp. 918-919.
- [116] Elliott, G., Crawford, J., and Mosedale, A., "Response of a Supersonic Turbulent Boundary Layer to Periodic Surface Roughness," AIAA Paper 07-1142, 2007.
- [117] Elliott, G. and Samimy, M., "Compressibility Effects in Free Shear Layers," *Physics of Fluids A*, Vol. 2, No. 7, 1990, pp. 1231-1240.

- [118] Elliott, G. S., Samimy, M., and Arnette, S. A., "Study of Compressible Mixing Layers Using Filtered Rayleigh Scattering Based Visualizations," *AIAA Journal*, Vol. 30, 1992, pp. 2567–2569.
- [119] Elliott, G., Samimy, M., and Arnette, S., "The Evolution of Large Scale Structure in Compressible Mixing Layers," 9th symposium on turbulent shear flows, 1993.
- [120] Elliott, G., Samimy, M., and Arnette, S., "The Characteristics and Evolution of Large Scale Structures in Compressible Mixing Layers," *Physics of Fluids A*, Vol. 7, No. 4, 1993, pp. 864–876.
- [121] Elliott, G. and Samimy, M., "Rayleigh Scattering Technique for Simultaneous Measurements of Velocity and Thermodynamic Properties," *AIAA Journal*, Vol. 34, No. 11, 1996, pp. 2346–2352.
- [122] Elliott, G., Crawford, J., and Mosedale, A., "Enhancement of Large Scale Structures in Supersonic Axisymmetric Jets Using Laser Excitation," AIAA Paper 98–0331, 1998.
- [123] Elliott, G., Crawford, J., and Mosedale, A., "Forcing Compressible Mixing Layers Using Laser Excitation," *AIAA Journal*, Vol. 36, No. 9, 1998, pp. 1730–1732.
- [124] Elliott, G. and Beutner, T., "Molecular Filter Based Planar Doppler Velocimetry," *Progress in Aerospace Sciences*, Vol. 35, 1999, pp. 799–845.
- [125] Elliott, G. and Glumac, N., "Diagnostics for Aerodynamics and Propulsion," AE-598GSE Class Notes, University of Illinois at Urbana-Champaign.
- [126] Enloe, C., McLaughlin, T., VanDyken, R., and Fischer, J., "Effect of Pressure Gradients on Axisymmetric Hypersonic Boundary Layer Stability," AIAA Paper 04–0844, 2004.
- [127] Enloe, C., McLaughlin, T., and Font, G., "Frequency Effects on the Efficiency of the Aerodynamic Plasma Actuator," AIAA Paper 06–0166, 2006.
- [128] Ershov, A., Ardelyan, N., Chuvashov, S., Shibkov, V., and Timofeev, I., "Probe Diagnostics of Gas Discharges in Supersonic Air Flows," *AIAA Journal*, Vol. 39, No. 11, 2001, pp. 2180–2187.
- [129] Estevadeordal, J., Gogineni, S., Kimmel, R., and Hayes, J., "Schlieren Imaging in Hypersonic Plasmas," AIAA Paper 04–1139, 2004.
- [130] Fabri, J. and Siestrunk, R., "Supersonic Air Ejectors," *Advances in Applied Mechanics*, Vol. 5, 1958, pp. 1–34.
- [131] Fantz, U., "Basics of Plasma Spectroscopy," *Plasma Sources Science and Technology*, Vol. 15, 2006, pp. S137–S147.
- [132] Faure, G. and Shkolnik, S., "Determination of Rotational and Vibrational Temperatures in a Discharge with Liquid Non-Metallic Electrodes in Air at Atmospheric Pressure," *Journal of Physics D: Applied Physics*, Vol. 31, 1998, pp. 1212–1218.
- [133] Ferdman, E., Otugen, M., and Kim, S., "Effect of Initial Velocity Profile on the Development of Round Jets," *Journal of Propulsion and Power*, Vol. 16, No. 4, 2000, pp. 676–686.
- [134] Fiedler, H., "Coherent Structures in Turbulent Flows," *Progress in the Aerospace Sciences*, Vol. 25, 1988, pp. 231–269.
- [135] Fiedler, H. and H.Fernholz, "On Management and Control of Turbulent Shear Flows," *Progress in the Aerospace Sciences*, Vol. 27, 1990, pp. 305–387.
- [136] Finkelstein, N., Gambogi, J., Lempert, W., and Miles, R., "The Development of a Tunable, Single-Frequency Ultraviolet Laser Source for UV Filtered Rayleigh Scattering," AIAA Paper 94–0492, 1994.
- [137] Forkey, J., Cogne, S., Smits, A., Bogdonoff, S., Lempert, W., and Miles, R., "Time-Sequenced and Spectrally Filtered Rayleigh Imaging of Shock Wave and Boundary Layer Structure for Inlet Characterization," AIAA Paper 93–2300, 1993.

- [138] Forkey, J., Lempert, W., Bogdonoff, S., Miles, R., and Russell, G., "Volumetric Imaging of Supersonic Boundary Layers Using Filtered Rayleigh Scattering Background Suppression," *AIAA Paper* 94-0491, 1994.
- [139] Forkey, J., Finkelstein, N., Lempert, W., and Miles, R., "Control of Experimental Uncertainties in Filtered Rayleigh Scattering Measurements," *AIAA Paper* 95-0298, 1995.
- [140] Forkey, J., Finkelstein, N., Lempert, W., and Miles, R., "Demonstration and Characterization of Filtered Rayleigh Scattering for Planar Velocity Measurements," *AIAA Journal*, Vol. 34, No. 3, 1996, pp. 442-448.
- [141] Forkey, J., Lempert, W., and Miles, R., "Corrected and Calibrated I2 Absorption Model at Frequency-Doubled Nd:YAG Laser Wavelengths," *Applied Optics*, Vol. 36, No. 27, 1997, pp. 6729-6738.
- [142] Fourguette, D., Mungal, M., and Dibble, R., "Time Evolution of the Shear Layer of a Supersonic Axisymmetric Jet," *AIAA Journal*, Vol. 29, No. 7, 1991, pp. 1123-1130.
- [143] Fox, J., "On the Structure of Jet Plumes," *AIAA Journal*, Vol. 12, No. 1, 1974, pp. 105-107.
- [144] Freund, J., Lele, S., and Moin, J., "Numerical Simulation of a Mach 1.92 Turbulent Jet and Its Sound Field," *AIAA Journal*, Vol. 38, No. 11, 2000, pp. 2023-2031.
- [145] Fridman, A. and Kennedy, L., *Plasma Physics and Engineering*, Taylor & Francis, New York, 2004.
- [146] el Hak, M. G., *Flow Control, Passive, Active and Reactive Flow Management*, 2000.
- [147] George, C., Candler, G., Young, R., Pfender, E., and Heberlein, J., "Nozzle Optimization for Dissociated Species Transport in Low Pressure Plasma Chemical Vapor Deposition," *Plasma Chemistry and Plasma Processing*, Vol. 16, No. 1, 1996, pp. 43S-56S.
- [148] Gendrich, C. and Koochesfahani, M., "A Spatial Correlation Technique for Estimating Velocity Fields Using Molecular Tagging Velocimetry," *Experiments in Fluids*, Vol. 22, 1996, pp. 67-77.
- [149] Ghosh, S. and Mahesh, K., "Direct Numerical Simulation of the Thermal Effects of Plasmas on Turbulent Flows," *AIAA Paper* 05-0407, 2005.
- [150] Girard, L., Teulet, P., Razafinimanana, M., Gleizes, A., Camy-Peyret, F., Baillet, E., and Richard, F., "Experimental Study of an Oxygen Plasma Cutting Torch: I. Spectroscopic Analysis of the Plasma Jet," *Journal of Physics D: Applied Physics*, Vol. 39, 2006, pp. 1543-1556.
- [151] Glumac, N., Elliott, G., and Boguszko, M., "Temporal and Spatial Evolution of a Laser Spark in Air," *AIAA Journal*, Vol. 43, No. 9, 2005, pp. 1984-1994.
- [152] Glumac, N., "Re: Plots of Fit and Uncertainty Estimation Question," Email Conversation Between R. Huffman and N. Glumac.
- [153] Gilbert, A. and Baggett, J., *Essentials of Molecular Photochemistry*, CRC Press, Boca Raton, FL, 1991.
- [154] Goebel, S. and Dutton, J., "Experimental Study of Compressible Turbulent Mixing Layers," *AIAA Journal*, Vol. 29, No. 4, 1991, pp. 538-545.
- [155] Graftieaux, L., Michard, M., and Grosjean, N., "Combining PIV, POD and Vortex Identification Algorithms for the Study of Unsteady Turbulent Swirling Flows," *Measurement Science and Technology*, Vol. 12, No. 9, 2000, pp. 1422-1429.
- [156] Grant, I. and Owens, E., "Confidence Interval Estimates in PIV Measurements of Turbulence Flows," *Applied Optics*, Vol. 29, No. 10, 1990, pp. 1400-1402.
- [157] Grant, H., "The Large Eddies of Turbulent Motion," *Journal of Fluid Mechanics*, Vol. 4, 1958, pp. 149-190.

- [158] Grau, T. and Messerschmid, E., "Numerical Investigation of a Partially Ionized Air Flow in a Plasma Wind Tunnel," *AIAA Paper* 98-2955, 1998.
- [159] Greenblatt, G., Ruhman, S., and Haas, Y., "Fluorescence Decay Kinetics of Acetone Vapour at Low Pressures," *Chemical Physics Letters*, Vol. 112, No. 3, 1984, pp. 200-206.
- [160] Grossman, F., Monkhouse, P., Ridder, M., Sick, V., and Wolfrum, J., "Temperature and Pressure Dependencies of the Laser-Induced Fluorescence of Gas-Phase Acetone and 3-Pentanone," *Applied Physics B: Lasers and Optics*, Vol. 62, 1996, pp. 249-253.
- [161] Gutmark, E., Schadow, K., and Bicker, C., "Mode Switching in Supersonic Circular Jets," *Physics of Fluids A*, Vol. 1, No. 5, 1989, pp. 868-873.
- [162] Gutmark, E., Schadow, K., and Yu, K., "Mixing Enhancement in Supersonic Free Shear Flows," *Annual Review of Fluid Mechanics*, Vol. 27, 1995, pp. 375-417.
- [163] Hall, J., Dimotakis, P., and Rosemann, H., "Experiments in Nonreacting Compressible Shear Layers," *AIAA Journal*, Vol. 31, No. 12, 1993, pp. 2247-2254.
- [164] Hallberg, M. and Strykowski, P., "On the Universality of Global Modes in Low-Density Axisymmetric Jets," *Journal of Fluid Mechanics*, Vol. 569, 2006, pp. 493-507.
- [165] Han, S. and Peddieson Jr., J., "One-Dimensional Numerical Study of Compressible Flow Ejector," *AIAA Journal*, Vol. 40, No. 7, 2002, pp. 1469-1472.
- [166] Hanson, R., Chang, A., Seitzman, J., and Lee, M., "Laser-Induced Fluorescence Diagnostics for Supersonic Flows," *AIAA Paper* 90-0625, 1990.
- [167] Hanson, R., Mungal, M., Grisch, F., Thurber, M., Smith, S., and Hasselbrink, E., "Temperature and Mixture-Fraction Imaging of Gaseous Flows Using Acetone PLIF," *AIAA Paper* 96-1964, 1996.
- [168] Hart, D., "PIV Error Correction," *Experiments in Fluids*, Vol. 29, 2000, pp. 13-22.
- [169] Heald, M. and Wharton, C., *Plasma Diagnostic with Microwaves*, John Wiley and Son, New York, 1965.
- [170] Hecht, E., *Optics*, Addison Wesley, San Fransico, 2002.
- [171] Heicklen, J., "The Fluorescence and Phosphorescence of Biacetyl Vapor and Acetone Vapor," *Journal of the American Chemical Society*, Vol. 81, 1959, pp. 3864-3866.
- [172] Hertzberg, G., *Molecular Spectra and Molecular Structure. 1. Spectra of Diatomic Molecules*, Van Nostrand, New York, 1950.
- [173] Hileman, J. and Samimy, M., "Turbulent Structures and Acoustic Far Field of a Mach 1.3 Jet," *AIAA Journal*, Vol. 39, No. 9, 2001, pp. 1716-1727.
- [174] Hill, R. and Kiewicki, J., "Data Reduction Methods for Flow-Tagging Velocity Measurements," *Experiments in Fluids*, Vol. 20, 1996, pp. 142-152.
- [175] Hiller, B. and Hanson, R., "Simultaneous Planar Measurements of Velocity and Pressure Fields in Gas Flows Using Laser-Induced Fluorescence," *Applied Optics*, Vol. 27, No. 1, 1988, pp. 33-48.
- [176] Hiller, B., Booman, A., Hassa, C., and Hanson, R., "Velocity Visualization in Gas Flows Using Laser Induced Phosphorescence of Biacetyl," *Review of Scientific Instruments*, Vol. 55, No. 12, 1984, pp. 1964-1967.
- [177] Hoerner, S. and Borst, H., *Fluid-Dyanamic Lift*, Hoerner Fluid Dynamics, Bakersfield, CA, 1985.
- [178] Hoerner, S., *Fluid-Dyanamic Drag*, Hoerner Fluid Dynamics, Bakersfield, CA, 1992.

- [179] Holmes, P., Lumley, J., and Berkooz, G., *Turbulence, Coherent Structures, Dynamical Systems and Symmetry*, Cambridge University Press, Cambridge, 1996.
- [180] Hoyaux, M., *Arc Physics, 2d. Ed.*, Springer-Verlag, New York, 1968.
- [181] Howatson, A., *An Introduction to Gas Discharge, 2d. Ed.*, Pergamon Press, Oxford UK, 1976.
- [182] Hu, H. and Koochesfahani, M., “A Novel Method for Instantaneous, Quantitative Measurement of Molecular Mixing in Gaseous Flows,” *Experiments in Fluids*, Vol. 33, 2002, pp. 202–209.
- [183] Huffman Jr., R., *Mach 2.9 Investigation Into the Flow Structure in the Vicinity of the Wrap-Around Fin*, Master’s thesis, Air Force Institute of Technology, December 1995.
- [184] Huffman Jr., R., Elliott, G., and Boguszko, M., “Turbulence Measurements Using FARRS in a Supersonic Axisymmetric Jet,” AIAA Paper 07–0471, 2007.
- [185] Hultgren, L. and Ashpis, D., “Glow Discharge Plasma Active Control of Separation Control at Low Pressure Turbine Conditions,” *Bulletin of the American Physics Society*, Vol. 47, No. 10, 2002, pp. 167.
- [186] Hultgren, L. and Ashpis, D., “Demonstration of Separation Delay with Glow Discharge Plasma Actuators,” AIAA Paper 03–1025, 2003.
- [187] Hussain, H. and Clark, A., “On the Coherent Structure of the Axisymmetric Mixing Layer: a Flow-Visualization Study,” *Journal of Fluid Mechanics*, Vol. 104, 1981, pp. 263–294.
- [188] Hussain, H. and Zaman, K., “The ‘Preferred Mode’ of the Axisymmetric Jet,” *Journal of Fluid Mechanics*, Vol. 110, 1981, pp. 39–71.
- [189] Hussain, H. and Clark, A., “An Experimental Study of Organized Motions in the Turbulent Plane Mixing Layer,” *Journal of Fluid Mechanics*, Vol. 159, 1985, pp. 85–104.
- [190] Hussain, A., “Coherent Structures and Turbulence,” *Journal of Fluid Mechanics*, Vol. 173, 1986, pp. 303–356.
- [191] Hussain, A. and Zedan, M., “Effects of the Initial Condition on the Axisymmetric Free Shear Layer: Effects of Initial Momentum Thickness,” *Physics of Fluids A*, Vol. 21, No. 7, 1989, pp. 1100–1112.
- [192] Hussein, H., Capp, S., and George, W., “Velocity Measurements in a High-Reynolds-Number, Momentum-Conserving, Axisymmetric, Turbulent Jet,” *Journal of Fluid Mechanics*, Vol. 258, 1994, pp. 31–75.
- [193] Ionikh, Y., Chernysheva, N., Yalin, A., Macheret, S., Martinelli, L., and Miles, R., “Shock Wave Propagation Through Glow Discharge Plasmas: Evidence of Thermal Mechanism of Shock Dispersion,” AIAA Paper 00–0714, 2000.
- [194] Igra, O., “Supersonic Expansion on Non-Equilibrium Plasmas,” *Progress in the Aerospace Sciences*, Vol. 16, No. 3, 1975, pp. 299–366.
- [195] Jacob, J., Rivir, R., Carter, C., and Estevadeoral, J., “Boundary Layer Flow Control Using AC Discharge Plasma Actuators,” AIAA Paper 04–2128, 2004.
- [196] Johnson, G. and Scott, S., “Plasma Aerodynamic Boundary Layer Interaction Studies,” AIAA Paper 01–3052, 2001.
- [197] Kearney, S., Beresh, S., Grasser, T., Schefer, R., Schrader, P., and Farrow, R., “A Filtered Rayleigh Scattering Apparatus for Gasphase and Combustion Temperature Imaging,” AIAA Paper 03–0584, 2003.
- [198] Kim, J., Choi, Y., and Hwang, Y., “Electron Density and Temperature Measurement Method By Using Emission Spectroscopy in Atmospheric Pressure Nonequilibrium Nitrogen Plasmas,” *Physics of Plasmas*, Vol. 13, 2006, pp. 093501–1–7.

- [199] Kimmel, R., Poggie, J., and Schmisser, J., "Effect of Pressure Gradients on Axisymmetric Hypersonic Boundary Layer Stability," AIAA Paper 00-0538, 2000.
- [200] Kimmel, R., "Aspects of Hypersonic Boundary-Layer Transition Control," AIAA Paper 03-0772, 2003.
- [201] Kimmel, R., Hayes, J., Menart, J., and Shang, J., "Effect of Surface Plasma Discharges on Boundary Layers at Mach 5," AIAA Paper 04-0509, 2004.
- [202] Kimmel, R., Hayes, J., Menart, J., and Shang, J., "Application of Plasma Discharge Arrays to High-Speed Flow Control," AIAA Paper 05-0946, 2005.
- [203] Kimmel, R., Hayes, J., Crafton, J., Fonov, S., Menart, J., and Shang, J., "Surface Discharges for High-Speed Boundary Layer Control," AIAA Paper 06-0710, 2006.
- [204] King, G., Lucht, R., and Dutton, J., "Quantitative Dual-Tracer Planar Laser-Induced Fluorescence Measurements of Molecular Mixing," *Optics Letters*, Vol. 22, No. 9, 1997, pp. 633-635.
- [205] Klavuhn, K. and McDaniel, C., "Underexpanded Jet for Testing Laser-Based Combustion Diagnostics," *Journal of Propulsion and Power*, Vol. 17, No. 5, 2001, pp. 1067-1075.
- [206] Koch, J. and Hanson, R., "Temperature and Excitation Wavelength Dependencies of 3-Pentanone Absorption and Fluorescence for PLIF Applications," *Applied Physics B: Laser and Optics*, Vol. 76, 2003, pp. 319-324.
- [207] Koch, J., Hanson, R., Koban, W., and Schulz, C., "Rayleigh-Calibrated Fluorescence Quantum Yield Measurements of Acetone and 3-Pentanone," *Applied Optics*, Vol. 43, No. 31, 2004, pp. 5901-5910.
- [208] Kopal, Z., "Tables of Supersonic Flow Around Cones," MIT Technical Report 1, 1947.
- [209] Korkan, K. and Knowles, L., "Boundary of Underexpanded Axisymmetric Jets in Still Air," *AIAA Journal*, Vol. 7, No. 2, 1969, pp. 362-363.
- [210] Koumoutsakos, P., "Multiscale Flow Simulations Using Particles," *Annual Review of Fluid Mechanics*, Vol. 37, 2005, pp. 457-487.
- [211] Kovasznay, L., "Turbulence in Supersonic Flow," *Journal of the Aeronautical Sciences*, Vol. 20, 1953, pp. 657-647, 682.
- [212] Lamb, H., *Hydrodynamics*, Dover, New York, 6th ed., 1945.
- [213] Lange, N., *Langes Handbook of Chemistry*, Vol. 11, McGraw-Hill, New York, 1973.
- [214] Lau, J., "Effects of Exit Mach Number and Temperature on Mean-Flow and Turbulence Characteristics in Round Jets," *Journal of Fluid Mechanics*, Vol. 105, 1981, pp. 193-218.
- [215] Leger, L., Moreau, E., and Touchard, G., "Electrohydrodynamic Airflow Control Along a Flat Plate by a DC Surface Corona Discharge - Velocity Profile and Wall Pressure Measurements," AIAA Paper 02-2833, 2002.
- [216] Lele, S., "Compressibility Effects on Turbulence," *Annual Review of Fluid Mechanics*, Vol. 26, 1994, pp. 211-254.
- [217] Lempert, W., Jiang, N., Sethuram, S., and Samimy, M., "Molecular Tagging Velocimetry Measurements in Supersonic Microjets," *AIAA Journal*, Vol. 40, No. 6, 2002, pp. 1065-1070.
- [218] Lempert, W., Boehm, M., Jiang, N., Gimelshein, S., and Levin, D., "Comparison of Molecular Tagging Velocimetry Data and Direct Simulation Monte Carlo Simulations in Supersonic Micro Jet Flows," *Experiments in Fluids*, Vol. 34, 2005, pp. 403-411.
- [219] Lepicovsky, J. and Bruckner, R., "Seeding for Laser Velocimetry in Confined Supersonic Flows with Shocks," NASA TM 107265, 1996.

- [220] Lewis Jr., C. and Carlson, D., "Normal Shock Location in Underexpanded Gas and Gas-Particle Jets," *AIAA Journal*, Vol. 2, No. 4, 1964, pp. 776–777.
- [221] Li, Y., Kirkpatrick, A., Mitchell, C., and Willson, B., "Characteristic and Computational Fluid Dynamics Modeling of High-Pressure Gas Jet Injection," *Transactions of the ASME*, Vol. 126, 2004, pp. 192–197.
- [222] Lieberman, M. and Lichtenberg, A., *Principles of Plasma Discharges and Materials Processing*, John Wiley and Sons, New York, 1994.
- [223] Limbaugh, C., Felderman, E., Carver, D., and Spinetti, R., "Plasma Aerodynamics Test Techniques," AIAA Paper 00–2449, 2000.
- [224] List, E., "Turbulent Jets and Plumes," *Annual Review of Fluid Mechanics*, Vol. 14, 1982, pp. 189–212.
- [225] Liu, J., "Coherent Structures in Transitional and Turbulent Free Shear Flows," *Annual Review of Fluid Mechanics*, Vol. 21, 1989, pp. 285–315.
- [226] Loth, E., "Advanced Gas Dynamics," ME-510 Class Notes, University of Illinois at Urbana-Champaign.
- [227] Loth, E., "Compressibility and Rarefaction Effects on Drag of a Spherical Particle," *AIAA Journal*, 2007, Submitted for Publication November, 2006.
- [228] Love, E., Grigsby, C., Lee, L., and Woodling, M., "Experimental and Theoretical Studies of Axisymmetric Free Jets," NASA TR r-6, 1959.
- [229] Lowry, H., Stepanek, C., Crosswy, L., Sherrhouse, P., Smith, M., Price, L., Ruyten, W., and Felderman, J., "Shock Structure of a Spherical Projectile in Weakly Ionized Air," AIAA Paper 99–0600, 1999.
- [230] Lowry, H., Smith, M., Sherrhouse, P., Felderman, J., Drakes, J., Bauer, M., Pruitt, D., and Keefer, D., "Ballistic Range Tests in Weakly Ionized Argon," AIAA Paper 99–4822, 1999.
- [231] Lowry, H., Crosswy, L., J.Mansfield, Keefer, D., Smith, M., and Wavio, N., "Development of an RF Induction Plasma Generator for Ballistic Range Testing," AIAA Paper 00–2625, 2000.
- [232] Lozano, A., Smith, S., Mungal, M., and Hanson, R., "Concentration Measurements in a Transverse Jet by Planar Laser-Induced Fluorescence of Acetone," *AIAA Journal*, Vol. 32, No. 1, 1993, pp. 218–221.
- [233] Lozano, A., Barreras, F., Valino, L., and Marin, C., "Imaging of Gas through a Porous Medium From a Fuel Cell Bipolar Plate by Laser-Induced Fluorescence," *Experiments in Fluids*, Vol. 42, 2007, pp. 301–310.
- [234] Lu, X., Leipold, F., and Laroussi, M., "Optical and Electrical Daignostics of a Non-Equilibrium Air Plasma," *Journal of Physics D: Applied Physics*, Vol. 36, 2003, pp. 2662–2666.
- [235] Macheret, S., Shneider, M., and Miles, R., "Magnetohydrodynamic and Electrohydrodynamic Control of Hypersonic Flows of Weakly Ionized Plasmas," AIAA Paper 02–2249, 2002.
- [236] Mack, L., *Boundary-Layer Stability Theory*, Jet Propulsion Laboratory, California Institute of Technology, Pasedena, CA, 1969.
- [237] Mack, L., "Boundary-Layer Stability Theory," *AGARD Report*, , No. 709, 1984, pp. 3–1–3–81.
- [238] Marcum, S., Parish, J., and Ganguly, B., "Plasma Emission Measurements from Pulsed DC Methane Discharges," AIAA Paper 03–0701, 2003.
- [239] Markides, C. and Mastorakos, E., "Measurements of Scalar Dissipation in a Turbulent Plume with Planar Laser-Induced Fluorescence of Acetone," *Chemical Engineering and Science*, Vol. 61, 2006, pp. 2835–2842.

- [240] Marple, V., "History of Impactors - The First 110 Years," *Aerosol Science and Technology*, Vol. 38, No. 3, 2004, pp. 247–292.
- [241] Martens, S., Kinzie, K., and McLaughlin, D., "Wave Structure of Coherent Instabilities in a Planar Shear Layer," AIAA Paper 94–0822, 1994.
- [242] Martin, J. and Meiburg, E., "Numerical Investigation of Three-Dimensionally Evolving Jets Subject to Axisymmetric and Azimuthal Perturbations," *Journal of Fluid Mechanics*, Vol. 230, 1991, pp. 271–318.
- [243] Mate, B., Graur, A., Elizarova, T., Chirokov, I., Tejeda, G., Fernandez, M., and Montero, S., "Experimental and Numerical Investigation of an Axisymmetric Supersonic Jet," *Journal of Fluid Mechanics*, Vol. 426, 2001, pp. 177–197.
- [244] Matlis, E., Corke, T., and Gogineni, S., "A.C. Plasma Anemometer for Hypersonic Mach Number Experiments," AIAA Paper 06–1245, 2006.
- [245] Matveyev, A. and Silakov, V., "Theoretical Study of the Role of Ultraviolet Radiation of the Non-Equilibrium Plasma in the Dynamics of the Microwave Discharge in Molecular Nitrogen," *Plasma Sources Science and Technology*, Vol. 8, 1999, pp. 162–178.
- [246] McAndrew, B. and MORE, "Supersonic Vehicle Control by Microwave Driven Plasma Discharges," AIAA Paper 02–0354, 2002.
- [247] McComb, W., "Theory of Turbulence," *Reports on the Progress in Physics*, Vol. 58, 1995, pp. 1065–1070.
- [248] McGregor, I., "The Vapour-Screen Method of Flow Visualization," *Journal of Fluid Mechanics*, Vol. 11, 1961, pp. 481–511.
- [249] Melling, A., "Tracer Particles and Seeding for Particle Image Velocimetry," *Measurement Science and Technology*, Vol. 8, 1997, pp. 1406–1416.
- [250] Menart, J., Shang, J., and Hayes, J., "Development of a Langmuir Probe for Plasma Diagnostic Work in High Speed Flow," AIAA Paper 01–2804, 2001.
- [251] Menart, J., Shang, J., Kurpik, A., Kimmel, R., and Hayes, J., "Survey of Plasmas Generated in a Mach 5 Wind Tunnel," AIAA Paper 03–1194, 2003.
- [252] Menart, J., Henderson, S., Shang, J., Kimmel, R., and Hayes, J., "DC Plasma Discharge Effects on a Mach 5 Flow Between Small Plate Electrodes," AIAA Paper 04–2264, 2004.
- [253] Menart, J., Stanfield, S., Shang, J., Kimmel, R., and Hayes, J., "Study of Plasma Electrode Arrangements for Optimum Lift in a Mach 5 Flow," AIAA Paper 06–1172, 2006.
- [254] Merriman, S., Ploenjes, E., Palm, P., and Adamovich, I., "Shockwave Control by Nonequilibrium Plasma in Cold Supersonic Gas Flows," AIAA Paper 00–xxxx, 2000.
- [255] Meyer, R., Palm, P., Plonjes, E., Rich, J., and Adamovich, I., "The Effect of a Nonequilibrium RF Discharge Plasma on a Conical Shock Wave in a $M = 2.5$ Flow," AIAA Paper 01–3059, 2001.
- [256] Meyer, T., Lucht, R., and Dutton, J., "Dual-Tracer PLIF Measurements of Entrainment and Mixing in a Driven Axisymmetric Jet," AIAA Paper 98–3081, 1998.
- [257] Meyer, R., Nishihara, M., Hicks, A., Chintala, N., Cundy, M., Lempert, W., Adamovich, I., and Gogineni, S., "Measurements of Flow Conductivity and Density Fluctuations in Supersonic Nonequilibrium Magnetohydrodynamic Flows," *AIAA Journal*, Vol. 43, No. 9, 2005, pp. 1923–1930.
- [258] Meyers, J. and Komine, H., "Doppler Global Velocimetry: a New Way to Look at Velocity," *Laser Anemometry*, Vol. 1, 1991, pp. 289–296.

- [259] Meyers, J., "Development of Doppler Global Velocimetry as a Flow Diagnostics Tool," *Measurement Science and Technology*, Vol. 6, 1995, pp. 769–783.
- [260] Michalke, A. and Hermann, G., "On the Inviscid Instability of a Circular Jet with External Flow," *Journal of Fluid Mechanics*, Vol. 114, 1982, pp. 343–359.
- [261] Miles, R., Cohen, C., Connors, J., Howard, P., Huang, Markovitz, E., and Russell, G., "Velocity Measurements by Vibrational Tagging and Fluorescent Probing of Oxygen," *Optics Letters*, Vol. 12, No. 11, 1987, pp. 861–863.
- [262] Miles, R. and Lempert, W., "Flow diagnostics in unseeded air," AIAA Paper 90–0624, 1990.
- [263] Miles, R. and Lempert, W., "Two-Dimensional Measurement of Density, Velocity, and Temperature in Turbulent High-Speed Air Flows by UV Rayleigh Scattering," *Applied Physics B*, Vol. 51, 1990, pp. 1–7.
- [264] Miles, R., Lempert, W., and Forkey, J., "Instantaneous Velocity Fields and Background Suppression by Filtered Rayleigh Scattering," AIAA Paper 91–0357, 1991.
- [265] Miles, R., Forkey, J., and Lempert, W., "Filtered Rayleigh Scattering Measurements in Supersonic/Hypersonic Facilities," AIAA Paper 92–3894, 1992.
- [266] Miles, R., Lempert, W., Forkey, J., Finkelstein, N., and Erbland, P., "Quantifying High Speed Air Flows by Light Scattering From Air Molecules," AIAA Paper 94–2230, 1994.
- [267] Miles, R., "Flow Control by Energy Addition into High-Speed Air," AIAA Paper 00–2324, 2000.
- [268] Miles, R., Lempert, W., and Forkey, J., "Laser Rayleigh Scattering," *Measurement Science and Technology*, Vol. 12, 2001, pp. R33–R51.
- [269] Miles, R., Macheret, S., Martinelli, L., Murray, R., Shneider, M., and Ionikh, Y., "Plasma Control of Shock Waves in Aerodynamics and Sonic Boom Mitigation," AIAA Paper 01–3062, 2001.
- [270] Mitchell, B., Lele, S., and Moin, P., "Direct Computation of the Sound Generated by Vortex Pairing in an Axisymmetric Jet," *Journal of Fluid Mechanics*, Vol. 383, 1999, pp. 113–142.
- [271] Moffatt, H. and Tsinober, A., "Helicity in Laminar and Turbulent Flow," *Annual Review of Fluid Mechanics*, Vol. 24, 1992, pp. 281–312.
- [272] Morgan, C., "Laser-Induced Breakdown of Gases," *Reports on Progress in Physics*, Vol. 38, No. 5, 1975, pp. 621–665.
- [273] Morris, P., "Turbulence Measurements in Subsonic and Supersonic Axisymmetric Jets in a Parallel Stream," *AIAA Journal*, Vol. 14, No. 10, 1976, pp. 1468–1475.
- [274] Mosedale, A., Elliott, G., Carter, C., Weaver, W., and Beutner, T., "On the Use of Planar Doppler Velocimetry," AIAA Paper 98–2809, 1998.
- [275] Mosedale, A., Elliott, G., Carter, C., and Beutner, T., "Planar Doppler Velocimetry in a Large-Scale Facility," *AIAA Journal*, Vol. 38, No. 6, 2000, pp. 1010–1024.
- [276] Mungal, M. and Hollingsworth, D., "Organized Motion in a Very High Reynolds Number Jet," *Physics of Fluids A*, Vol. 1, No. 10, 1989, pp. 1615–1623.
- [277] Muntz, E., "Rarefied Gas Dynamics," *Annual Review of Fluid Mechanics*, Vol. 21, 1989, pp. 387–417.
- [278] Murakami, E. and Papamoschou, D., "Eddy Convection in Coaxial Supersonic Jets," *AIAA Journal*, Vol. 38, No. 4, 2000, pp. 628–635.
- [279] Nakai, Y., Fujimatsu, N., and Fujii, K., "Experimental Study of Underexpanded Supersonic Jet Impingement on an Inclined Flat Plate," *AIAA Journal*, Vol. 44, No. 11, 2006, pp. 2691–2699.

- [280] Nathan, G., Hill, S., and Luxton, R., "An Axisymmetric 'Fluidic' Nozzle to Generate Jet Precession," *Journal of Fluid Mechanics*, Vol. 370, 1998, pp. 347–380.
- [281] Nau, W. and Scaiano, J., "Oxygen Quenching of Excited Aliphatic Ketones and Diketones," *Journal of Physical Chemistry*, Vol. 100, 1996, pp. 11360–11367.
- [282] O'Neal, H. and Larson, C., "Primary Processes in the Acetone Photochemical System," *Journal of Physical Chemistry*, Vol. 73, No. 4, 1966, pp. 1011–1022.
- [283] Owen, P. and Thornhill, C., "The Flow in an Axially-Symmetric Supersonic Jet from a Nearly-Sonic Orifice into a Vacuum," Aeronautical Research Council, Reports and Memoranda 2616, 1948.
- [284] Pai, S., *Fluid Dynamics of Jets*, D. Van Nostrand Co. Inc., New York, 1954.
- [285] Palko, C. and Dutton, J., "Velocity Measurements in a Shock-Separated Free Shear Layer," *AIAA Journal*, Vol. 38, No. 7, 2000, pp. 1237–1245.
- [286] Palm, P., Plonjes, E., Lee, W., Frederickson, K., Lempert, W., and Adamovich, I., "RF Energy Coupling to High-Pressure Optically Pumped Nonequilibrium Plasmas," AIAA Paper 01–0637, 2001.
- [287] Papamoschou, D. and Roshko, A., "The Compressible Turbulent Shear Layer," *Journal of Fluid Mechanics*, Vol. 197, 1988, pp. 453–477.
- [288] Papamoschou, D., "Structure of the Compressible Turbulent Shear Layer," *AIAA Journal*, Vol. 29, No. 5, 1991, pp. 680–681.
- [289] Papoulis, A., *Probability, Random Variables and Stochastic Processes*, McGraw-Hill Inc., New York, 1991.
- [290] Paschereit, C., Wygnanski, I., and Fiedler, H., "Experimental Investigation of Subharmonic Resonance in an Axisymmetric Jet," *Journal of Fluid Mechanics*, Vol. 283, 1995, pp. 365–407.
- [291] Patte-Rouland, B., Lalizel, G., and Rouland, E., "Flow Analysis of an Annular Jet by Particle Image Velocimetry and Proper Orthogonal Decomposition," *Measurement Science and Technology*, Vol. 12, No. 9, 2001, pp. 1404–1412.
- [292] Paul, P. and Clemens, N., "Planar Laser-Induced Fluorescence Imaging of Lifted H₂-Air Nonpremixed Flames," AIAA Paper 93–0800, 1999.
- [293] Peters, C. and Altmann, J., "Monodisperse Aerosol Generation with Rapid Adjustable Particle Size for Inhalation Studies," *Journal of Aerosol Medicine*, Vol. 6, No. 4, 1993, pp. 307–315.
- [294] Pierrehumbert, R. and Swanson, K., "Baroclinic Instability," *Annual Review of Fluid Mechanics*, Vol. 27, 1995, pp. 419–467.
- [295] Piper, L., "Further Observations of the Nitrogen Orange Afterglow," *Journal of Chemical Physics*, Vol. 101, No. 12, 1994, pp. 10229–10236.
- [296] Plaschko, P., "Helical Instabilities of Slowly Divergent Jets," *Journal of Fluid Mechanics*, Vol. 92, 1979, pp. 209–215.
- [297] Pope, A. and Goin, K., *High-Speed Wind Tunnel Testing*, John Wiley and Sons, Inc., New York, 1965.
- [298] Pope, S., *Turbulent Flows*, Cambridge University Press, Cambridge, 2000.
- [299] Post, M., *Phased Plasma Actuators for Unsteady Flow Control*, University of Notre Dame, 2001.
- [300] Post, M. and Corke, T., "Separation Control on High Angle of Attack Airfoil Using Plasma Actuators," AIAA Paper 03–1024, 2003.

- [301] Post, M. and Corke, T., "Separation Control Using Weakly-Ionized Plasma Actuators," AIAA Paper 04-0841, 2004.
- [302] Post, M. and Corke, T., "Flow Control with Single Dielectric Barrier Plasmas," AIAA Paper 05-4630, 2005.
- [303] Press, W., Teukolsky, S., Vetterling, W., and Flannery, B., *Numerical Recipes in FORTRAN*, Cambridge University Press, Cambridge, England, 2nd ed., 1986.
- [304] Provenzale, A., "Transport by Coherent Barotropic Vortices," *Annual Review of Fluid Mechanics*, Vol. 31, 1999, pp. 55-93.
- [305] Rabek, J., *Experimental Methods in Photochemistry and Photophysics*, John Wiley and Sons, New York, 1982.
- [306] Radulescu, M. and Law, C., "The Transient Start of Supersonic Jets," *Journal of Fluid Mechanics*, Vol. 578, 2007, pp. 331-369.
- [307] Raffel, M., Willert, C., and Kompenhans, J., *Particle Image Velocimetry: A Practical Guide*, Springer-Verlag, Berlin, 1998.
- [308] Raizer, Y., Shneider, M., and Yatsenko, N., *Radio-Frequency Capacitive Discharges*, CRC Press, Boca Raton, FL, 1995.
- [309] Rahman, A., Yalin, A., Surla, V., Stan, O., Hoshimiya, K., Yu, Z., Littlefield, E., and Collins, G., "Absolute UV and VUV Emission in the 110400nm Region From 13.56MHz Driven Hollow Slot Microplasmas Operating in Open Air," *Plasma Sources Science and Technology*, Vol. 13, 2004, pp. 537-547.
- [310] Raizer, Y., "Breakdown and Heating of Gases under the Influence of a Laser Beam," *Soviet Physics USPEKHI*, Vol. 8, No. 5, 1966, pp. 650-673.
- [311] Raizer, Y., *Laser Induced Discharge Phenomena*, Consultants Bureau, New York, 1977.
- [312] Raizer, Y., *Gas Discharge Physics*, 2d. Ed., Springer-Verlag, New York, 1997.
- [313] Ralchenko, Y., Kramida, A., and Reader, J., "NIST: Atomic Spectra Database," NIST Physics Laboratory Web Site, <http://physics.nist.gov/PhysRefData/ASD/>, 2006.
- [314] Reda, D., "Review and Synthesis of Roughness-Dominated Transition Correlations for Reentry Applications," *Journal of Spacecraft and Rockets*, Vol. 39, No. 2, 2002, pp. 161-167.
- [315] Ritchie, B. and Seitzman, J., "Simultaneous Imaging of Vapour and Liquid Spray Concentration Using Combined Acetone Fluorescence and Phosphorescence," AIAA Paper 04-0384, 2004.
- [316] Robinson, S., "Coherent Motions in the Turbulent Boundary Layer," *Annual Review of Fluid Mechanics*, Vol. 23, 1991, pp. 601-639.
- [317] Root, R., *Laser-induced Plasmas and Applications*, Marcel Dekker Inc., New York, 1989.
- [318] Roth, J., *Industrial Plasma Engineering*, Institute of Physics, Bristol, 1995.
- [319] Roth, J., Sherman, D., and Wilkinson, S., "Boundary Layer Flow Control with a Glow Discharge Surface Plasma," AIAA Paper 98-0328, 1998.
- [320] Roth, J., Sherman, D., and Wilkinson, S., "Electrohydrodynamic Flow Control with a Glow-Discharge Surface Plasma," *AIAA Journal*, Vol. 38, No. 7, 2000, pp. 1166-1172.
- [321] Roth, R., Sin, H., Madhan, R., and Wilkinson, S., "Flow Re-attachment and Acceleration by Paraelectric and Peristaltic Electrohydrodynamic (EHD) Effects," AIAA Paper 03-0531, 2003.

- [322] Samimy, M. and Elliott, G., "Effects of Compressibility on the Characteristics of Free Shear Layers," *AIAA Journal*, Vol. 28, No. 3, 1990, pp. 439–445.
- [323] Samimy, M. and Lele, S., "Motion of Particles with Inertia in a Compressible Free Shear Layer," *Physics of Fluids A*, Vol. 3, No. 8, 1991, pp. 1915–1923.
- [324] Samimy, M., Reeder, M., and Elliott, G., "Compressibility Effects on Large Structures in Free Shear Flows," *Physics of Fluids A*, Vol. 4, No. 6, 1992, pp. 1251–1258.
- [325] Samimy, M. and Wernet, M., "Review of Planar Multiple-Component Velocimetry in High-Speed Flows," *AIAA Journal*, Vol. 38, No. 4, 2000, pp. 553–574.
- [326] Samimy, M., Breuer, K., Leal, L., and Steen, P., *A Gallery of Fluid Motion*, Cambridge University Press, Cambridge, 2003.
- [327] Saric, W., Reshotko, E., and Arnal, D., "Hypersonic Laminar-Turbulent Transition," *Hypersonic Experimental and Computational Capability, Improvement and Validation*, Vol. III, 1998, pp. 2–1–2–27.
- [328] Schlichting, H. and Gersten, K., *Boundary-Layer Theory*, Springer-Verlag, Berlin, 8th ed., 2000.
- [329] Seasholtz, R., Buggele, A., and Reeder, M., "Flow Measurements Based on Rayleigh Scattering and Fabry-Perot interferometer," *Optics and Lasers in Engineering*, Vol. 27, 1997, pp. 543–570.
- [330] Settles, G., *Schlieren and Shadowgraph Techniques: Visualizing Phenomena in Transparent Media*, Springer-Verlag, Berlin, 2001.
- [331] Shakhmatov, V. and Gordeev, O., "CARS Spectroscopy and Optical Interferometry of Glow Discharge Plasma in Nitrogen," *High Temperature*, Vol. 44, No. 2, 2006, pp. 212–220.
- [332] Shang, J., "Developing a Facility for Magnetoaerodynamic Experiments," *Journal of Aircraft*, Vol. 37, 2000, pp. 1065.
- [333] Shang, J., Hayes, J., Harris, S., Umstatted, R., and Ganguly, B., "Experimental Simulation of Magneto-Aerodynamic Hypersonics," AIAA Paper 00–2258, 2000.
- [334] Shang, J., Hayes, J., and Menart, J., "Hypersonic Flow over a Blunt Body with Plasma Injection," *Journal of Spacecraft and Rockets*, Vol. 35, 2002, pp. 367.
- [335] Shang, J., Kimmel, R., Hayes, J., and Tyler, C., "Performance of a Low-Density Hypersonic Magnetoaerodynamic Facility," AIAA Paper 03–0134, 2003.
- [336] Shang, J., Kimmel, R., Hayes, J., and Tyler, C., "Performance of a Low-Density Hypersonic Magneto-Aerodynamic Facility," AIAA Paper 03–0329, 2003.
- [337] Shang, J., "Electromagnetic Field of Dielectric Barrier Discharge," AIAA Paper 05–4633, 2005.
- [338] Shang, J., Menart, J., Kimmel, R., and Hayes, J., "Hypersonic Inlet with Plasma Induced Compression," AIAA Paper 06–0764, 2006.
- [339] Shen, C., *Rarefied Gas Dynamics: Fundamentals, Simulations and Micro Flows*, Springer-Verlag, Berlin, 2005.
- [340] Shibkov, V., Abramova, A., Chernikov, A., Ershov, A., Gromov, V., Karachev, A., Konstantinovskij, R., Shibkova, L., Timofeev, I., and Voskanyan, A., "Microwave Discharges in Supersonic Plasma Aerodynamics," AIAA Paper 04–0513, 2004.
- [341] Shin, J., Narayanaswamy, V., Raja, L., and Clemens, N., "Characteristics of a Plasma Actuator in Mach 3 Flow," AIAA Paper 07–0788, 2007.

- [342] Shirley, J. A. and Winter, M., "Air-Mass Flux Measurement System Using Doppler-Shifted Filtered Rayleigh Scattering," AIAA Paper 93-0513, 1993.
- [343] Shuvalov, V., Levkovich, O., and Kochubei, G., "Approximate Models of Exhaustion of a Supersonic Gas Jet into Vacuum," *Journal of Applied Mechanics and Technical Physics*, Vol. 42, No. 2, 2001, pp. 237-242.
- [344] Shyy, W. and Krishnamurty, V., "Compressibility Effects in Modeling Complex Turbulent Flows," *Progress in Aerospace Sciences*, Vol. 33, 1997, pp. 587-645.
- [345] Similon, P. and Sudan, R., "Plasma Turbulence," *Annual Review of Fluid Mechanics*, Vol. 22, 1990, pp. 317-347.
- [346] Slessor, M., Bond, C., and Dimotakis, P., "Turbulent Shear-Layer Mixing at High Reynolds Numbers: Effects of Inflow Conditions," *Journal of Fluid Mechanics*, Vol. 376, 1998, pp. 115-138.
- [347] Slessor, M., ZHUANG, M., and Dimotakis, P., "Turbulent Shear-Layer Mixing: Growth-Rate Compressibility Scaling," *Journal of Fluid Mechanics*, Vol. 414, 2000, pp. 35-45.
- [348] Sims, J., "Tables of Supersonic Flow Around Right Circular Cones at Zero Angle of Attack," NASA SP-3004, 1964.
- [349] Smith, M., Northam, G., and Drummond, J., "Application of Absorption Filter Planar Doppler Velocimetry to Sonic and Supersonic Jets," *AIAA Journal*, Vol. 34, No. 3, 1996, pp. 434-441.
- [350] Smith, D., "Laser Induced Gas Breakdown and Plasma Interaction," AIAA Paper 00-0716, 2000.
- [351] Smits, A. and Lim, T., *Flow Visualization: Techniques and Examples*, Imperial College Press, London, 2000.
- [352] Smits, A. and Dussauge, J., *Turbulent Shear Layers in Supersonic Flow*, Springer Science+Business Media, New York, 2006.
- [353] Smits, A. and Dussauge, J., *Turbulent Shear Layers*, American Institute of Physics, Woodbury, NY, 2006.
- [354] So, R., Gatski, T., and Sommer, T., "Morkovin Hypothesis and the Modeling of Wall-Bounded Compressible Turbulent Flows," *AIAA Journal*, Vol. 36, No. 9, 1998, pp. 1583-1592.
- [355] Spina, A., Smits, E., and Robinson, S., "The Physics of Supersonic Turbulent Boundary Layers," *Annual Review of Fluid Mechanics*, Vol. 26, 1994, pp. 287-319.
- [356] Staats, G., McGregor, W., and Sprouse, J., "Magnetogasdynamic Experiments Conducted in a Supersonic Plasma Arc Tunnel," AIAA Paper 00-2566, 2000.
- [357] Stalker, R., "Hypervelocity Aerodynamics with Chemical Nonequilibrium," *Annual Review of Fluid Mechanics*, Vol. 21, 1989, pp. 37-60.
- [358] Stanfield, S., Menart, J., Shang, J., Kimmel, R., and Hayes, J., "Application of a Spectroscopic Measuring Technique to Plasma Discharge in Hypersonic Flow," AIAA Paper 06-0559, 2006.
- [359] Stier, B. and Koochesfahani, M., "Molecular Tagging Velocimetry (MTV) Measurements in Gas Phase Flows," *Experiments in Fluids*, Vol. 26, 1999, pp. 297-304.
- [360] Suzen, Y., Huang, P., Jacob, J., and Ashpis, D., "Numerical Simulations of Plasma Based Flow Control Applications," AIAA Paper 05-4633, 2005.
- [361] Tam, C. and Burton, D., "Sound Generated by Instability Waves of Supersonic Flows. Part 1. Two-Dimensional Mixing Layers," *Journal of Fluid Mechanics*, Vol. 138, 1984, pp. 249-271.

- [362] Tam, C. and Burton, D., "Sound Generated by Instability Waves of Supersonic Flows. Part 2. Axisymmetric Jets," *Journal of Fluid Mechanics*, Vol. 138, 1984, pp. 273–295.
- [363] Tam, C. and Hu, F., "On the Three Families of Instability Waves of High-Speed Jets," *Journal of Fluid Mechanics*, Vol. 201, 1989, pp. 447–483.
- [364] Taylor, G., "The Formation of a Blast Wave Very Intense Explosion. I. Theoretical Discussion," *Proceedings of the Royal Society of London. Series A, Mathematical and Physical Sciences*, Vol. 201, No. 1065, 1950, pp. 159–174.
- [365] Taylor, G., "The Formation of a Blast Wave Very Intense Explosion. II. The Atomic Explosion of 1945," *Proceedings of the Royal Society of London. Series A, Mathematical and Physical Sciences*, Vol. 201, No. 1065, 1950, pp. 175–186.
- [366] Tedeschi, G., Gouin, H., and Elena, M., "Motion of Tracer Particles in Supersonic Flows," *Experiments in Fluids*, Vol. 26, 1999, pp. 288–296.
- [367] Tennekes, H. and Lumley, J., *A First Course in Turbulence*, MIT Press, Cambridge, MA, 1972.
- [368] Tenti, G., Boley, C., and Desai, R., "On the Kinetic Model Description of Raleigh-Brillouin Scattering from Molecular Gases," *Canadian Journal of Physics*, Vol. 52, No. 4, 1974, pp. 285–290.
- [369] Teshima, K. and Sommerfeld, M., "Visualization and Numerical Simulation of Supersonic Microjets," *Experiments in Fluids*, Vol. 5, 1987, pp. 197–200.
- [370] Thurber, M., Grisch, F., Kirby, B., Votsmeier, M., and Hanson, R., "Measurements and Modeling of Acetone Laser-Induced Fluorescence with Implications for Temperature-Imaging Diagnostics," *Applied Optics*, Vol. 37, No. 21, 1998, pp. 4963–4978.
- [371] Tilmann, C., Huffman Jr., R., Buter, T., and Bowersox, R., "Experimental Investigation of the Flow Structure Near a Single Wraparound Fin," *Journal of Spacecraft and Rockets*, Vol. 34, No. 6, 1997, pp. 729–736.
- [372] Tilmann, C., Kimmel, R., Addington, ., and Myatt, J., "Flow Control Research and Applications at the AFRL's Air Vehicles Directorate," AIAA Paper 04–2622, 2004.
- [373] Tornblom, O., "Introduction Course in Particle Image Velocimetry," Course Introductory Material: STEM Project, KTH, Department of Mechanics, Stockholm Sweden, March 2004, <http://www2.mech.kth.se/olle/pivkurs/Intro.to.PIV.pdf>.
- [374] Tran, T., Kochat, Y., and Seitzman, J., "Measurements of Liquid Acetone Fluorescence and Phosphorescence for Two-Phase Fuel Imaging," AIAA Paper 05–0827, 2005.
- [375] Tran, T., Kochar, Y., and Seitzman, J., "Measurements of Acetone Fluorescence and Phosphorescence at High Pressures and Temperatures," AIAA Paper 06–0831, 2006.
- [376] Troutt, T. and McLaughlin, D., "Experiments on the Flow and Acoustic Properties of a Moderate-Reynolds Number Supersonic Jet," *Journal of Fluid Mechanics*, Vol. 116, 1982, pp. 123–156.
- [377] Tsai, W. and Yue, D., "Computation of Nonlinear Free-Surface Flows," *Annual Review of Fluid Mechanics*, Vol. 28, 1996, pp. 249–278.
- [378] Turro, N., *Molecular Photochemistry*, W. A. Benjamin Inc, New York, 1967.
- [379] Urban, W. and Mungal, M., "Planar Velocity Measurements in Compressible Mixing Layers," AIAA Paper 97–0757, 1997.
- [380] Urban, W. and Mungal, M., "Control of Transitional and Turbulent Flows Using Plasma-Based Actuators," AIAA Paper 06–3230, 2006.

- [381] Walsh, M., "Influence of Particle Drag Coefficient On Particle Motion in High-Speed Flow With Typical Laser Velocimeter Applications," NASA TN D-8120, 1976.
- [382] Wayne, R., *Principles and Applications of Photochemistry*, Oxford University Press, Oxford, 1988.
- [383] White, F., *Viscous Fluid Flow*, McGraw-Hill, New York, 2nd ed., 1991.
- [384] White, A., Palm, P., Plonjes, E., Subramaniam, V., and Adamovich, I., "Influence of Structural Electric Discharges on Parameters of Streamlined Bodies in Airflow," AIAA Paper 01-3058, 2001.
- [385] Wilkinson, S., "Investigation of an Oscillating Surface Plasma for Turbulent Drag Reduction," AIAA Paper 03-1023, 2003.
- [386] Woodmansee, M. and Iyer, V., "Nonintrusive Pressure and Temperature Measurements in an Underexpanded Sonic Jet Flowfield," *AIAA Journal*, Vol. 42, No. 4, 2004, pp. 1170-1180.
- [387] Woodmansee, M. and Lucht, R., "Experimental Measurements of Pressure, Temperature, and Density in an Underexpanded Sonic Jet Flowfield," AIAA Paper 99-3600, 1999.
- [388] Anon, "FLOWMASTER: Advanced PIV Systems for Quantitative Flow Field Analysis," LaVision Sales Brochure, LaVision GmbH, Goettingen Germany, 2006.
- [389] Wygnanski, I. and Fiedler, H., "Some Measurements in the Self-Preserving Jet," *Journal of Fluid Mechanics*, Vol. 38, 1969, pp. 577-612.
- [390] Wygnanski, I., Sokolov, M., and Friedman, D., "On a Turbulent 'Spot' in a Laminar Boundary Layer," *Journal of Fluid Mechanics*, Vol. 78, 1976, pp. 786-819.
- [391] Yan, H., Aldegren, R., Boguszko, M., Elliott, G., and Knight, D., "Laser Energy Deposition in Quiescent Air," *AIAA Journal*, Vol. 41, No. 10, 2003, pp. 1988-1995.
- [392] Yan, H., Adelgren, R., Elliott, G., Knight, D., Beutner, T., Ivanov, M., Kudryavtsev, A., and Khotyanovsky, D., "Laser Energy Deposition in Quiescent Air and Intersecting Shocks," Fourth workshop on magneto-plasma aerodynamics for aerospace applications, 2002.
- [393] Yano, R., Aithal, S., Subramaniam, V., Contini, V., Palm, P., Merriman, S., Adamovich, I., Lempert, W., and Rich, J., "Experimental Characterization of Shock Dispersions in Weakly Ionized Nonequilibrium Plasmas," AIAA Paper 99-3671, 1999.
- [394] Yano, R., Contini, V., Merriman, S., Aithal, S., Adamovich, I., Lempert, W., Subramaniam, V., Rich, J. W., Plonjes, E., and Palm, P., "Flow Visualization in a Supersonic Nonequilibrium Plasma Wind Tunnel," AIAA Paper 99-3725, 1999.
- [395] Yano, R., Contini, V., Plonjes, E., Palm, P., Merriman, S., Aithal, S., and Adamovich, I., "Supersonic Nonequilibrium Plasma Wind-Tunnel Measurements of Shock Modification and Flow Visualization," *AIAA Journal*, Vol. 38, No. 10, 2000, pp. 1879-1888.
- [396] Yuceil, K. and Otugen, M., "Scaling Parameters for Underexpanded Sonic Jets," AIAA Paper 01-1052, 2001.
- [397] Yuen, L., Peters, J., and R.Lucht, "Pressure Dependence of Laser-Induced Fluorescence from Acetone," *Proceedings of the Indian Academy of Science*, Vol. 36, No. 15, 1997, pp. 3271-3277.
- [398] Yule, A., "Large-Scale Structure in the Mixing Layer of a Round Jet," *Journal of Fluid Mechanics*, Vol. 89, 1978, pp. 413-432.
- [399] Zagarola, M. and Smits, A., "Mean-Flow Scaling of Turbulent Pipe Flow," *Journal of Fluid Mechanics*, Vol. 373, 1998, pp. 33-79.

- [400] Zaman, K. and Hussain, A., "The Mechanics of Vortex Pairing in an Axisymmetric Mixing Layer," *Turbulent Shear Flows 2*, edited by L. Bradbury, F. Durst, B. Launder, F. Schmidt, and J. Whitelaw, Springer-Verlag, Berlin, 1980, pp. 327–343.
- [401] Zaman, K. and Hussain, A., "Vortex Pairing in a Circular Jet Under Controlled Excitation. Part 1. General Jet Response," *Journal of Fluid Mechanics*, Vol. 101, 1980, pp. 449–491.
- [402] Zaman, K. and Hussain, A., "Taylor Hypothesis and Large-Scale Coherent Structures," *Journal of Fluid Mechanics*, Vol. 112, 1981, pp. 379–396.
- [403] Zaman, K. and Hussain, A., "Natural Large-Scale Structures in the Axisymmetric Mixing Layer," *Journal of Fluid Mechanics*, Vol. 138, 1984, pp. 325–351.
- [404] Zaman, K. and Hussain, A., "Axis Switching and Spreading of an Asymmetric Jet: the Role of Coherent Structure Dynamics," *Journal of Fluid Mechanics*, Vol. 316, 1996, pp. 1–37.
- [405] Zaman, K., "Spreading Characteristics of Compressible Jets From Nozzles of Various Geometries," *Journal of Fluid Mechanics*, Vol. 383, 1999, pp. 197–228.
- [406] Zaman, K., "Spreading Characteristics and Thrust of Jets from Asymmetric Nozzles," AIAA Paper 96–0200, 1996.
- [407] Zhao, W., Frankel, S., and Mongeau, L., "Large Eddy Simulations of Sound Radiation from Subsonic Turbulent Jets," *AIAA Journal*, Vol. 39, No. 8, 2001, pp. 1469–1477.
- [408] Zubair, F., Freeman, A., Piatrovich, S., Shockro, J., Ibrahim, Y., and Catrakis, H., "Large Scale Turbulence Suppression Control for Direct Reduction of Aero-Optical Aberrations," AIAA Paper 07–4008, 2007.

Curriculum Vitae

Education

- Ph.D. Candidate, Aerospace Engineering, University of Illinois at Urbana-Champaign, 2007
- Graduate, Air Command and Staff College, Air University, 2006
- Flight Test Engineer, USAF Test Pilot School, 2000
- M.S., Aeronautical Engineering, Air Force Institute of Technology, 1995
Best Thesis Award, School of Aeronautical Engineering
- B.S., Aeronautical and Astronautical Engineering, Purdue University, 1994

Professional Experience

- Ph.D. Candidate, University of Illinois at Urbana-Champaign, 08/2004 - Present
- Flight Test Director, F-22 Combined Test Force, 12/2000 - 07/2004
- Student, USAF Test Pilot School, Class 00A, 01/2000 - 12/2000
- Airborne Instrumentation Branch Chief, USAF Test Pilot School, 07/1998 - 01/2000
- AFTI/F-16 Test Engineer, Air Force Research Laboratory, 12/1995 - 07/1998
- Masters Student, Air Force Institute of Technology, 05/1994 - 12/1995
- Aerospace Engineer Trainee, National Aerospace Intelligence Center, 01/1992 - 05/1994

Papers

- Huffman, R., Elliott, G., Boguszko, M., "Turbulence Measurements Using FARRS in a Supersonic Axisymmetric Jet," AIAA Paper, No. 07-0471, 2007, to be Submitted to Measurement Science and Technology.

- Boguszko, M., Huffman, R., Elliott, G., “Property and velocity measurements in a supersonic flow,” AIAA Paper, No. 06-1390, 2006.
- Rebello, V., Huffman, R., Brown, J., “The Raptor is Now a Fighter: F/A-22 Gun Integration Testing,” Proceedings of the 47th Annual Conference - Society of Experimental Test Pilots, Los Angeles, California, September 2003.
- Sturim, J., Rush, D., Schaefer, C., Germann, K., Huffman, R., Shearer, M.; “Auto Ground Collision Avoidance System Asymmetric Store Evaluation,” Technical Information Memorandum AFFTC-TIM-00-05, Air Force Flight Test Center, Edwards AFB, 2000.
- Huffman, R., Skoog, M., Pineiro, L., Ferm, M., “Application of Ground Collision Avoidance System Nuisance Criteria,” Proceedings of the 21st Congress - International Council of the Aeronautical Sciences, Melbourne, Australia, September 1998.
- Huffman, R., Cawood, M.D., Ferm, M., Skoog, M.A., “The Development of Nuisance Warnings Criteria for Ground Collision Avoidance Systems,” 4th International Conference on Integrated Navigation Systems, St Petersburg, Russia, May 1997.
- Huffman, R., Tilmann, C., Buter, T., Bowersox, R., “Experimental Investigation of the Flow Structure in the Vicinity of a Single Wrap-Around Fin at Mach 2.9,” AIAA Paper, No. 96-2450, 1996.
- Tilmann, C., Huffman, R., Buter, T., Bowersox, R., “Characterization of the Flow Structure in the Vicinity of a Wrap-Around Fin at Supersonic Speeds,” AIAA Paper, No. 96-0190, 1996.